ODESSA ASTRONOMICAL PUBLICATIONS

Volume 36
(2023)

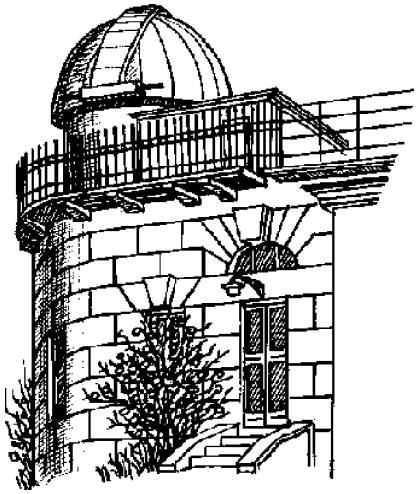

Astronomical Observatory
of Odesa I. I. Mechnikov National University

ODESSA ASTRONOMICAL PUBLICATIONS

Volume 36
(2023)

Address:
Astronomical Observatory, Odesa National University,
T. G. Shevchenko Park, Odesa, 65014, UKRAINE
Tel.: + 38 048 722-03-96
E-mail: astronomical_observatory@onu.edu.ua
http://www.astro-observ-odessa0.1gb.ua

The electronic version of the journal is on the web page: http://oap.onu.edu.ua

Одеські Астрономічні Публікації
Видається з 1946 року (видання відновлено в 1993 р., №6)

Свідоцтво про державну реєстрацію друкованого засобу масової інформації:
серія КВ № 14722-3693Р від 30.10.2008 р.
Журнал включено до списку МОН України наказом МОНУ № 1643 від 28.12.2019 р.

Друкується за рішенням Вченої ради НДІ "Астрономічна обсерваторія" Одеського національного університету імені І.І.Мечникова від 9 листопада 2023 р., протокол №5

Printed in UKRAINE
"ONU" PUBLISHING COMPANY

ISSN 1810-4215

CONTENTS

Cosmology, gravitation, astroparticle physics, high energy physics

Astrophysics (stellar atmospheres, interacting binary systems, variable stars)

Solar system and space environment

Radioastronomy

Sun, solar activity, solar-terrestrial relations and astrobiology

COSMOLOGY, GRAVITATION, ASTROPARTICLE PHYSICS, HIGH ENERGY PHYSICS

https://doi.org/10.18524/1810-4215.2023.36.289962

GALAXY CLUSTER MERGERS: THE USE OF THE COMPUTER MODELING

M. Berkovskyi[1], E. Panko[2], N. Miroshnik[3]

[1] National Centre "Junior Academy of Sciences", under the auspices of UNESCO, Kamianske, Dnipropetrovsk region, Ukraine
[2] Department of Theoretical Physics and Astronomy, I.I. Mechnikov Odessa National University, Odesa, Ukraine
panko.elena@gmail.com
[3] Communal institution "Anatoliy Lyhun Scientific Lyceum" of the Kamianske City Council, Dnipropetrovsk region, Ukraine

ABSTRACT. We show the possibilities of the methods of computer modeling of the galaxy cluster merger process with different initial parameters for the investigation of the features of the clusters after colliding.

We considered the galaxy clusters as evolving objects including through collisions. Computer modeling of galaxy cluster mergers and comparing its results with observational data makes it possible to determine the evolutionary status of real clusters with complex internal structures. Within the study, we analyzed in detail a series of models of the galaxy clusters' merger consequences by ZuHone under different initial conditions like mass ratio, initial collision parameter, or plasma coefficient β. The considered time intervals were from 0 to 4.8 billion years, from 0 to 6 billion years, and from 0 to 10 billion years, depending on the initial conditions.

Based on the images of the simulated galaxy clusters, maps of the distribution of the total mass density and X-ray radiation were created and compared with observations. We showed a good perspective to use this catalog for studying galaxy clusters having compound inner structure.

Keywords: Galaxy clusters: morphology, inner structure; data analysis: modeling.

АНОТАЦІЯ. У дослідженні на основі каталогу змодельованих зіткнень скупчень галактик ("The Galaxy Cluster Merger Catalog: An Online Repository of Mock Observations from Simulated Galaxy Cluster Merg ers", on-line data: http://gcmc.hub.yt/) вивчено можливості методів комп'ютерного моделювання процесу зіткнення скупчень галактик із різними початковими параметрами для дослідження особливостей скупчень після процесу злиття. Ми розглядаємо скупчення галактик як об'єкти, що еволюціонують, зокрема через зіткнення. Комп'ютерне моделювання злиття скупчень галактик і порівняння його результатів зі спостережними даними дає змогу визначити еволюційний статус реальних скупчень зі складною внутрішньою будовою. У рамках дослідження ми детально проаналізували серію моделей наслідків злиття скупчень галактик за різних початкових умов, таких як відношення мас, початковий параметр зіткнення або коефіцієнт плазми β. Було розглянуто часові інтервали від 0 до 4.8 млрд років, від 0 до 6 млрд років і від 0 до 10 млрд років, залежно від початкових умов. Також проаналізовано та порівняно між собою змодельовані результати зіткнень скупчень галактик. На основі зображень змодельованих скупчень галактик побудовано карти розподілу загальної густини маси та рентгенівського випромінювання, які порівняно зі спостереженнями. Наведено приклади аналізу двох реальних збурених скупчень галактик за допомогою мап розподілу загальної густини маси та рентгенівського випромінювання. Зроблено висновок, що порівняння оброблених зображень із реальними дає змогу оцінити параметри скупчень, що злилися, та визначити час цього зіткнення. Показано перспективність використання цього каталогу для вивчення скупчень галактик зі складною внутрішньою структурою. Каталог також буде корисним при викладанні курсу "Позагалактична астрономія".

Ключові слова: скупчення галактик: морфологія, внутрішня структура; аналіз даних: моделювання

1. Introduction

A common modern paradigm about galaxy clusters forming is arising the large-scale structures according to the primordial distribution of the adiabatic fluctua-

tion in the early Universe, as it was studied in a lot of works, beginning from theoretical papers (Zeldovich, 1970 and Peebles, 1969) and observed data analysis (Wen et al., 2009, Dietrich et al., 2012, Parekh et al., 2020). The special place in this study occupies the numerical simulations which are based on the DM distribution (Springel et al., 2005, Vogelsberger et al., 2014, Artale et al., 2017, Cui et al., 2018, Tomoaki et al., 2021). Overdence regions evolved to the galaxies, galaxy groups or clusters in dependence on their own scale. The simulations improve the accuracy of simulations of the dynamics of gas, dark matter, and stars in the expanding cosmological background, starting from an initial state of high-redshift matter fluctuations. Clusters of galaxies form in these simulations at the junction between filaments of gas and dark matter. Depending on the physics used, stars form from cold, dense gas and explode as supernovae, providing a source of energy for the environment and enriching it with metals. Some simulations include the formation of black holes and the resulting feedback from active galactic nuclei. The next growing of these structures occurs, among other things, due to peculiar mowing inside the Hubble flow, and the interaction and collisions of the galaxy groups and clusters appear in their inner structure/substructures.

In the optic, we can see the complex inner structure of galaxy clusters as the peculiarities or regular substructures in the distribution of galaxies. Their main features are reflected in the morphological classification schemes of galaxy clusters. The idea by Strubble & Rood (1987) about the connection between the morphological type and evolutional status of galaxy clusters was improved in the Panko (2013) classification where the influence of the close neighbors is reflected as regular cluster substructures. However, the galaxies are the smallest mass part of galaxy clusters, and hot intracluster gas has also different features in the distribution. In the X-ray range, the distribution of the density and temperature is described in corresponding classification schemes. Buote & Tsai (1995, 1996) developed a method to quantify cluster morphology and substructure by "power ratios" that measure the square of the ratio of high-order multipole moments of the two-dimensional potential to the monopole moment. Weißmann et al. (2013), using the Buote & Tsai (1996) approach discussed regular, intermediate, complex, double as well as relaxed, mildly disturbed, and disturbed X-ray clusters. More, the multeity in X-ray images of galaxy clusters (tails, cold fronts, sloshing, etc.) requires to use of the modern method of comparing the observed data with the models, calculated on powerful computers or supercomputers. The DM distribution inside the galaxy cluster is the most difficult task, but the comparison of the distributions of all three components of the cluster is the key to galaxy cluster evolution.

The aim of the present paper is to use the grids of models to reproduce the effects of collisions of galaxy clusters, to study the distribution of dark matter and hot gas at different initial parameters of the collision on a time scale of up to 4.8 and 10 billion years as well as to compare the grids of models with the observed data.

2. Simulation of Galaxy Cluster Collisions

For the study of the results of galaxy cluster collisions, we used "The Galaxy Cluster Merger Catalog: An Online Repository of Mock Observations from Simulated Galaxy Cluster Mergers" (ZuHone et al., 2018, on-line data: http://gcmc.hub.yt/). The original set of simulations was performed using the computational resources of Argonne National Laboratory and Lawrence Livermore National Laboratory, with this updated and improved set performed using the Pleiades supercomputer at NASA's Ames Research Center. The simulation of collisions of galaxy clusters is represented by three types of simulations, which are divided into one or more subtypes. They are: N-body collisions/hydrodynamic binary collisions, hydrodynamic binary collisions with hard gravitational potentials, and clusters in cosmological simulations, which improve the accuracy of simulations of the dynamics of gas, dark matter, and stars in the expanding cosmological background, starting from an initial state of high-redshift matter fluctuations. All of them differ in initial conditions and approximations. In each type of simulation, certain theories are adopted and there are parameters that make it possible to understand the content of the simulation, namely, DM, DE in the ΛCDM paradigm, H_0, metallicity Z (at usual, $Z \sim 4\,\%$ near the center of galaxy clusters, and $Z \sim 0.5\,\%$ on the object's outskirts, in these models it was assumed $Z = 0.3Z_{\odot}$), velocity dispersion (it allows calculation the mass of such a group by applying the virial theorem), the critical density of the Universe ρ_c, the radius enclosing a volume with a mass density 200 times the critical density ρ_c, at cluster redshift r_{200}, cosmological parameter corresponding to the mass density, which includes baryonic mass and dark matter Ω_m, cosmological constant that corresponds to the fraction of the effective mass of the Universe that is accounted for by dark energy Ω_Λ, the mass ratio between two clusters R, the distance between the centers of clusters d - the initial collision parameter in kpc or Mpc b, and the cosmological epoch of the simulation in Gigayears t, and also magnetic induction and Spitzer viscosity. The typical box size for N-body/Hydrodynamic Binary Mergers was $L = 14.26\,\mathrm{Mpc}$, the finest cell size was $\Delta x_{min} = 6.96\,\mathrm{kpc}$, and primary cluster mass was $M_{200} = 6 \cdot 10^{14} M_{\odot}$. For sloshing of Cold Gas in Galaxy Cluster Cores the corresponded values were:

$L = 10$Mpc, $\Delta x_{min} = 4.88$ kpc and $M_{200} = 10^{15} M_{\odot}/$. The output figure is FITS image.

3. The Grids of Models and the Comparison with the Real Data

The catalog, which we used in the present study, contains interactive static images that show the state of the cluster at a particular moment of its evolution. Depending on the needs of the study, one can use images of various physical quantities (temperature, X-ray radiation, total density or dark matter density, etc.) in 3-axis projections. Since modern researchers mostly use maps of the distribution of physical quantities to compare images of distant space objects, it is worth doing the same with the catalog materials to use them in research. For a basic comparison of several simulations with each other, the creation of distribution maps is not necessary. Thus, after processing the graphical elements and their distribution, we get model grids, which are a good way to conveniently compare the effects of collisions with each other. We can compare the distributions of X-ray emission, temperature, magnetic induction, and dark matter density of the clusters at the beginning and end of the simulation in the same axis projection.

3.1. Comparison with Typical Perturbed Galaxy Clusters

To create clear isolines on the distribution maps, we used the free online graphic editor *Photopea* and the built-in Hue/Saturation, Trace Contour, and Black and White filters with the same parameters. These filters made the image more saturated, highlighted the transition lines between the most contrasting colors of the images, which made it possible to highlight the gradual transition between the values of the physical quantities under consideration with isolines, and converted the images to black and white for easy comparison, respectively. The example of isolines is shown in Fig. 1. The processed image (right panel), one can see isolines separating the transitions between colors within specific values of the considered parameter for the image which is shown in the left panel. Isolines form clear intervals of value, which makes it easy to compare images with critical values that differ by several orders of magnitude.

By comparing the distribution maps of simulated and real clusters (Fig. 2), it is possible to determine, for example, the approximate time of a past or future collision between two objects in a short time. When comparing and extracting the data, attention is first paid to determining the mass ratios of the interacted clusters, which is done using the density distribution

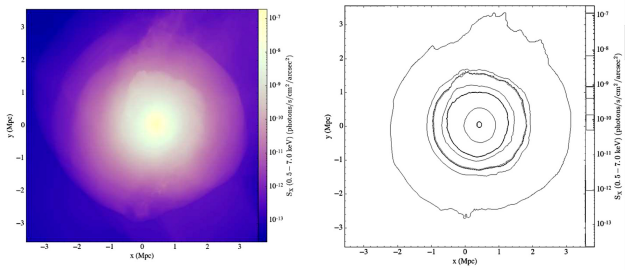

Figure 1: An unprocessed image of the distribution of the X-ray photon flux density of the hot gas of the clusters with the values of the parameters $R = 1:3$ and $b = 1000$ kpc at the end of the simulation $t = 10.00$ Gyr in the z-axis projection, left panel; a map of the distribution of the X-ray photon flux density after applying filters and converting the image to black and white, right panel

maps of the total mass or the dark matter mass. Then, the distance between the centers of the two colliding objects is extracted and the moment in the simulation where this distance is equal to the distance between the real subclumps is found. To update the results, we take into account the distribution of X-rays, so we can determine the degree of perturbation of the object.

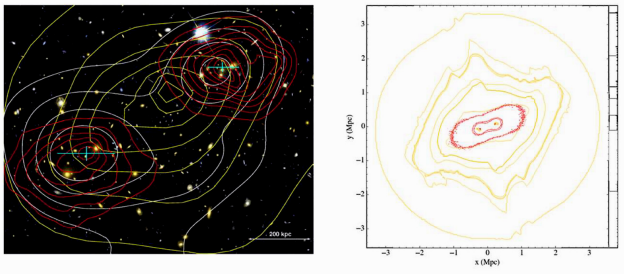

Figure 2: An image of the contours of the surface mass concentration of the MACS J0025.4-1222 cluster (red) and the contours of the X-ray brightness (yellow), left panel; a colored map of the distribution of the total mass density (red) and the X-ray photon flux density (yellow) of the simulated clusters with the values of the parameters $R = 1:1$ and $b = 500$ kpc at the moment of simulation $t = 2.60$ Gyr in the z-axis projection, right panel

3.2. Comparison of the Subtype "A Parameter Space Exploration of Galaxy Cluster Mergers"

We compare the changes in the position of the total mass density concentration and gas distribution with the time of the simulated and real collisions. The dis-

tribution of the hot gas of the galaxy cluster in the simulation with mass ratio $R = 1 : 3$ and $b = 500$ kpc is similar to that of the real colliding clusters 1E2215 and 1E2216. Comparing the changes in the gas distribution with time, we can conclude that the time after which the collision of clusters 1E2215 and 1E2216 will begin approximately is 1.30 billion years. The same comparison for the collision of the MACS J0025.4-1222 cluster found the collision of the MACS J0025.4-1222 cluster (Fig. 2) took place 1.2-1.28 billion years ago.

We can conclude about the simulations of the cluster collisions the next:

- Comparing the results of simulations at fixed values of the parameter R and values of $b = 0$, 500, 1000 kpc within the subtype "A Parameter Space Exploration of Galaxy Cluster Mergers" it follows that at $R = 1 : 1$ the effects of collisions are the simplest – clusters of almost regular shape are formed. At $R = 1 : 3$, the newly formed clusters are disturbed and quite heterogeneous, and at $R = 1 : 10$, the clusters are generally of the correct shape, except for small regions of inhomogeneity in the distribution of baryonic matter.
- Due to the fixed values of the parameters R and b in the subtype "Sloshing of Cold Gas in Galaxy Cluster Cores", the distribution of the photon flux density and temperature values look almost identical. However, in the simulation without taking into account the viscosity, the distribution of hot gas is more heterogeneous compared to the simulation with the Spitzer viscosity.
- In the subtype "Sloshing of the Magnetized Cool Gas in the Cores of Galaxy Clusters", the simulation results look almost identical at values of the plasma coefficient $\beta = 100$, $\beta = 200$, $\beta = 500$, $\beta = 1000$, differing only in that at higher values of plasma – β the central region of the cluster has increasingly higher values of the photon flux density, temperature and magnetic induction.

.

4. Conclusion

The "The Galaxy Cluster Merger Catalog: An Online Repository of Mock Observations from Simulated Galaxy Cluster Mergers" (ZuHone et al., 2018) defines a wide range of calculated parameters of the collided galaxy clusters. Comparing the simulation results and the created distribution maps with typical disturbed galaxy clusters, it follows that 1.2-1.28 billion years have passed since the collision of the MACS J0025.4-1222 cluster, and the time after which the collision of the 1E2215 and 1E2216 clusters will begin is approximately 1.3 billion years. So, the comparison of the calculated images with the real ones makes it possible to assess the parameters of the collided clusters and determine when events occurred. It is possible to use the model grid and catalog in the academic teaching for the "Extra-Galactic Astronomy" course.

Acknowledgements. This research has made use of NASA's Astrophysics Data System.

References

Artale M. C., Pedrosa S. E., Trayford J., et al.: 2017, *MNRAS*, **470**, 1771.
Buote, D., & Tsai, J.: 1995, *ApJ*, **452**, 522.
Buote, D., & Tsai, J.: 1996, *ApJ*, **458**, 27.
Cui W., Knebe A., Yepes G., et al.: 2018, *MNRAS*, **473**, 68.
Dietrich J. P., Werner N., Clowe D., et al.: 2012, *Nature*, **487**, 202.
Parekh V., Lagana T. F., Tho K., et al.: 2020, *MNRAS*, **491**, 2605.
Peebles P.: 1969, *AJ*, **155**, 393.
Springel V., White S.D., Jenkins A., et al.: 2005, *Nature*, **435**, 629.
Struble M.F. & Rood H.J.: 1982, *AJ*, **87**, 7.
Tomoaki A.A., Francisco P., Klypin A.A., et al.: 2021, *MNRAS*, **506**, 4210.
Vogelsberger M., Genel S., Springel V., et al.: 2014, *MNRAS*, **444**, 1518.
Wen Z.L., Han J.L. & Liu A.C.: 2009, *ApJSS*, **183**, 197.
Weißmann A., Böhringer H., Suhada R. & Ameglio S.: 2013, *A&A*, **549**, A19.
Zeldovich Y.B.: 1970, *A&A*, **5**, 84.
ZuHone, J.A., Kowalik, K., et al.: 2018, *ApJSS*, **234**, 4.

https://doi.org/10.18524/1810-4215.2023.36.290808

TOWARDS THEORETICAL MODELLING OF DISTRIBUTION OF MATTER IN UNIVERSE

O.I.Gerasymov [1], L.S.Kudashkina [1,2]

[1] Department of Physics and Environmental Protection Technologies, Odesa State Environmental University, Odesa, Ukraine, *gerasymovoleg@gmail.com*

[2] Department of Mathematics, Physics and Astronomy, Odesa National Maritime University, Odesa, Ukraine, *kuda2003@ukr.net*

ABSTRACT. The description of the distribution of matter in the universe requires not only accurate observations but also adequate approaches to their theoretical interpretation. This paper proposes a method of parameterization of distributions with a morphologically complex topology using structural invariants (for example, Euler), based on which it is possible to distinguish clusters with different topologies (in the observation plane). Based on the introduced classification and appropriate scaling, it becomes possible to estimate the distribution of matter, for example, within the framework of the mean-field model. To study the kinetics of the evolution of matter distribution, it is proposed to introduce the appropriate ordering parameter, which is built based on the calibrating and current values of the Euler-Poincaré invariants. This approach, by constructing phase diagrams for the ordering parameter, allows you to track the details of the kinetics of the evolution of matter distributions, studying, in particular, the temporal hierarchy of relaxation times of intermediate states. The temporal kinetics of this approach are described using simple kinetic equations that describe the relaxation of the ordering parameter field, and the values of invariants determined with the help of appropriate measurements (observations) appear as initial conditions. This approach can be seen as an alternative to other approaches to parameterization of structurally complex systems, such as Voronoi methods, graphs, etc. A comparative analysis of the results of various alternative approaches to the parameterization of topologically complex distributions of matter, which will be conducted in the future, should contribute to the deepening of existing ideas about the nature of the distribution of matter in the Universe.

Keywords: matter distribution, Euler-Poincaré structure invariants, order parameter relaxation.

АБСТРАКТ. Опис розподілу матерії у Всесвіті вимагає не тільки прецизійних спостережень, але й адекватних підходів до їх теоретичної інтерпретації. У нашій роботі пропонується метод параметризації розподілів із морфологічно складною топологією за допомогою структурних інваріантів (наприклад, інваріантів Ейлера-Пуанкаре), на основі якого можна розрізняти кластери з різною топологією (у площині спостереження). На основі такої класифікації та відповідного масштабування з'являється можливість вивчення розподілу речовини, (наприклад, за допомогою моделі середнього поля). Для вивчення кінетики еволюції розподілу речовини пропонується ввести відповідний параметр впорядкування, який будується на основі калібрувальних (асимптотичних) та поточних значень інваріантів Ейлера-Пуанкаре. Такий підхід, шляхом побудови фазових діаграм для параметру впорядкування дозволяє відслідковувати деталі (і, зокрема, немонотонний характер) кінетики еволюції розподілів матерії вивчаючи, наприклад, часову ієрархію часів релаксації проміжних станів глобально неоднорідної системи. Часова кінетика про цьому підході описується за допомогою простих кінетичних рівнянь, які описують релаксацію поля параметру впорядкування, а в якості початкових умов фігурують визначені за допомогою відповідних вимірів (спостережень) значення інваріантів. Запропонований підхід може розглядатися як альтернативний до інших підходів до параметризації структурно складних систем, таких, як методи побудов Вороного, графів та ін. Порівняльний аналіз результатів різних альтернативних підходів до параметризації топологічно складних розподілів речовини, який буде проведено у майбутньому має сприяти поглибленню існуючих уявлень про характер розподілу речовини у Всесвіті.

Ключові слова: розподіл матерії, структурні інваріанти Ейлера-Пуанкаре, релаксація поля параметра впорядкування.

1. Introduction

We explore unexpected connections between cosmological objects and micromechanical systems (granular materials), drawing attention to some common features. To model and understand these phenomena, we focus on using the Euler-Poincaré invariants to describe scaling relationships.

Earlier (Gerasymov, 2015; 2022) has been considered a simple but effective model that characterizes the kinetics of the compaction field in granular materials. This model related packing density to parameters such as the number of impacts or other perturbations. We assumed that these methods, originally developed for granular systems, can be applied to the study of the distribution of matter in the Universe (Gerasymov & Kudashkina, 2022).

The ultimate goal of our study is to quantitatively describe the geometric properties of materials with complex internal structures at different scales. We draw an analogy between the distribution of masses on a cosmic scale, such

as in supergalactic clusters, and the basic structure of granular materials. To do this, we use stereological methods that allow us to qualitatively describe the morphology of objects by analyzing sectional planes and extracting three-dimensional information (Gerasimov & Spivak, 2020).

1) The research addresses the task of quantitatively describing the geometric characteristics of materials with complex internal morphology at micro- and macro-scales.

2) An analogy between the distribution of masses in large-scale systems, such as supergalactic clusters, and the structure of granular materials is examined.

3) The application of stereology methods for qualitative description of the morphology of objects analyzed on sectional planes to extract three-dimensional information is discussed.

2. Method of parameterization of distributions with a morphologically complex topology

Since measurement of absolute density is often impossible both in the Universe and in bulk materials, we turn to various functions and invariants to describe changes in relative density, compare scales, and study dependencies between different systems. Some of the key factors we consider include mean density, density relative to the mean, structural patterns, Euler-Poincaré invariants, modeling, and statistical distributions.

We introduce the concept of the Euler-Poincaré connection as an essential stereological characteristic that helps to describe the morphology of an object. We present basic connectivity parameters for various spatial dimensions such as 3D, 2D, and 1D. This Euler-Poincare connection is the foundation for analyzing the geometric and topological features of structures at different scales.

For example, the scaling dependence for the Universe and granular material can be expressed in terms of the Euler-Poincaré invariants.

$$\frac{\chi_U}{\chi_S} = h(\rho_U, \rho_S).$$

Here f and g are functions that describe the dependence of the characteristic curvature on density and volume for the Universe (U) and for a granular system (S), respectively:

$$\chi_U = f(\rho_U, V_U),$$
$$\chi_S = g(\rho_S, V_S).$$

The scaling dependence ceases to be a power law, that is, limited to one specific form. The use of Euler-Poincaré invariants makes it possible to take into account more complex structural and geometric aspects depending on the dependence between the densities of the objects under consideration.

2.1. Euler-Poincaré invariants

Based on the observed external similarity of clustering, which is characterized by the formation of specific thread-like clusters, both in granular matter and in the distribution of matter in the Universe, it can be assumed that Euler-Poincaré invariants can be used to analyze the topology of particle clusters both in granular materials and groups of galaxies in the Universe.

Euler-Poincaré invariants are numerical characteristics associated with the topological properties of spatial structures. They can be calculated for different spatial regions. Let's consider how these characteristics can be used to analyze the topological properties of both space structures and structures of bulk materials.

Let's say we have a data set that represents the distribution of galaxies in a certain region of space. We can partition this space into segments and then use Euler-Poincaré invariants to analyze the topological properties of these segments. The relationship between the parameters in Euler's formula is expressed:

$$\chi = N_1 - N_2 + N_3,$$

N_1 - the number of facets (cells, grid cells) that fall within the perimeter of the object;

N_2 - the number of grid lines that are cut off by the perimeter of the object and that are located inside the perimeter of the object;

N_3 – number of points of intersection of the object's perimeter with the grid lines.

For example, in Figure 1 the Euler characteristic is $\chi = 7$.

In the context of cosmology, the following correspondence can be established:

N_1 – number of large galaxy clusters or superclusters;

N_2 – void-type structures;

N_3 – boundaries of large structures.

Let us have two segments: one with a high density of galaxies and the other with a low density. For each segment, we can calculate the Euler characteristic χ. If we have a segment with a high density of galaxies, for example, 1 component and 0 voids (if the segment is compact), thus, C=1, H=0, then:

$$C - H = \chi = 1\,.$$

Now, if we have two segments: one with a high density of galaxies, and the other with a low density, then we can compare the resulting values of the Eulerian characteristic.

Let a segment with a high density of galaxies have a characteristic χ_1 and a segment with a low-density χ_2, then:

- If $\chi_1 > \chi_2$, then this may indicate a more complex topology of the segment with a high density of galaxies, possibly the presence of additional components or voids.
- If $\chi_1 < \chi_2$, then the segment with a high density of galaxies may have a simpler topology.

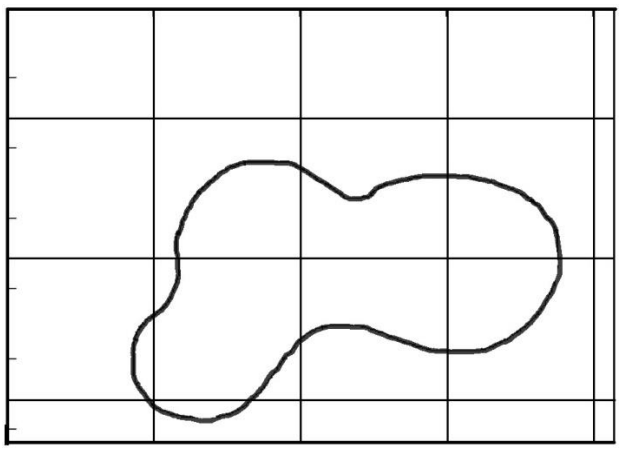

Figure 1: $N_1 = 8$, $N_2 = 11$, $N_3 = 10$, the Euler characteristic is $\chi = 7$.

Quantitative differences in topological properties can give us information about the structure and distribution of galaxies. For example, if a segment with a high density of galaxies has many components, this may indicate the presence of various clusters (clusters or superclusters of galaxies) in that region of space. If a segment with a low density of galaxies has one component, this may indicate a more uniform distribution of galaxies without a clear structure. The number of voids may indicate the presence of regions with a low density of galaxies (Luminet, 2008).

By analyzing topological properties, the presence of filaments and different patterns in the distribution of galaxies can be revealed. You can also analyze the shape of clusters, their boundaries, and relative positions.

Topological properties may change over time, which may indicate dynamic processes of fusion or the formation of new structures.

To assess the connectivity of components, for example, in a flat slice, you can use the connectivity measure:

$$\gamma = \frac{2C}{n(n-1)},$$

where n is the number of galaxies in the slice.

To analyze the shape of structures, you can approximate the shape using the relationship

$$A = \frac{l_1}{l_2},$$

where is l_1 and l_2 – the length of the axes of the ellipse fitted to the structure.

Filaments and patterns can be identified by analyzing the density gradient and looking for local maxima.

Euler-Poincaré characteristics are also suitable for analyzing more complex topological structures, such as waves, which also occur in both granular materials and the Universe (Gerasimov, 2022).

2.2. Order parameter

Euler-Poincaré invariants provide information about the topological characteristics of a structure but do not themselves contain a density or order parameter.

We can try to include the concept of "order" through local characteristics of the structure, such as the ratio of the number of neighbors to the total number of particles in a certain region. This can serve as a measure of organization or structural order in a given area. In the context of granular materials, the concept of "order" may be associated with parameters describing the degree of packing of particles or the characteristics of their interactions (Gerasimov et al., 2021).

In its most general form, the order parameter is defined as follows. Let us have some structure, represented by a set of points in space P_i (i=1, …, N). You can enter a parameter that will evaluate the degree of ordering of this structure. For example, it could be the ratio of the average number of nearest neighbors to the total number of points:

$$\eta_0 = \frac{1}{N}\sum_{i=1}^{N} n_i ,$$

where is n_i – number of nearest neighbors of a point P_i.

For a granular material, the nearest neighbors can be considered the particles with which the particle has contact. In the structure of the Universe, the order parameter can be related similarly to the local organization of galaxies.

Using the Euler-Poincaré characteristics, we give a phenomenological definition of the order parameter.

$$\eta = \frac{\chi - \chi_1}{\chi_{AS} - \chi_1},$$

where are χ – experimentally observed invariant value; χ_1 – some value specified in the experimental conditions; χ_{AS} – the value to which the value of the invariant asymptotically tends.

The introduced definition of the order parameter allows us to track the kinetic stages of the evolution of a distribution parameterized in terms of Euler invariants. This method allows us to interpret the non-monotonicity of the corresponding phase diagram for the order parameter in terms of the hierarchy of characteristic relaxation times of inhomogeneous anisotropic states.

3. Conclusion

A stereological analysis methodology is presented, enabling the assessment of properties of materials and structures with complex morphology based on Euler-Poincaré connectivity.

An analogy between the geometry of mass distribution in the large-scale Universe structure and the morphology of granular materials is identified.

The results provide opportunities for a deeper understanding of the Universe's structure and materials on various scales.

The results presented allow a rough classification of the observed mass distributions on the scale and in the observation plane. Advantages include the possibility of parameterizing arbitrarily complex distributions and the possibility of large-scale extrapolation of topological invariants with allowance for scaling. The disadvantages are the dependence of the obtained results on the choice of the observation plane and the need for aperture scanning to refine the values of the invariants describing the observed distributions.

References

Gerasymov O.I.: 2015, Physics of Granular Materials Odessa: TES, 264.

Gerasimov O.I., Spivak A.Ya.: 2020, Separate problems of the physics of soft matter. Odesa: "Helvetica" publishing house, 200. ISBN 978-966-992-202-1 http://eprints.library.odeku.edu.ua/id/eprint/9015

Gerasimov O.I., Khudyntsev M.M., Klymenkov O.A.: 2021, The latest materials and technologies in the tasks of protection of environmental systems. (Odesa, ODEKU), 78. ISBN 978-966-186-192-2 http://eprints.library.odeku.edu.ua/id/eprint/10207

Gerasimov O.I.: 2022, Physics of complex non-equilibrium systems and processes. (Odesa: ODEKU), 187. ISBN 978-966-186-237-0 http://eprints.library.odeku.edu.ua/id/eprint/11406

Gerasymov O.I., Kudashkina L. S.: 2022, *AApTr*, **33**, 1, 11. doi:10.17184/eac.6466

Luminet J.-P.: 2008, preprint (arXiv: 0802.2236).

https://doi.org/10.18524/1810-4215.2023.36.289964

TRAPPED HOT DARK MATTER IN THE SHELL AROUND THE COMPACT OBJECT

D.L. Khokhlov

Sumy State University (Retired),
Ukraine, *dlkhokhl@rambler.ru*

ABSTRACT. The model of the compact object is considered, being alternate to the black hole. In the model, the accreting protons decay at the Planck scale into positrons and hypothetical Planck neutrinos. The energy of the particles is split in two modes, low and high. The electrons, positrons and Planck neutrinos with the high energy move away. The electrons and positrons with the low energy form the compact object. The Planck neutrinos with the low energy form the shell around the compact object. The Planck neutrinos moving away may be interpreted as the hot dark matter (HDM). The Planck neutrinos in the shell around the compact object may be interpreted as the trapped hot dark matter (THDM). In a recent paper, the concept of the free fall pressure was introduced. In the effective gravity, including the Newton gravity and the free fall pressure, the THDM is hidden for the massive particles but makes deflection of the massless particles. The THDM can be seen in the gravitational interaction of two shells. The gravitational interaction of the galaxies in the Virgo cluster (M60, M87, M84, M86, M49) is studied. The motion of the galaxies is defined by the THDM masses in the shells around the compact objects in the centres of the galaxies, the stellar masses of the galaxies and the HDM mass in the galaxies. The velocities of M60 and M49 toward M87 are estimated to be 678 km s^{-1} and 445 km s^{-1} which are 66% and 59% of the observational values respectively.

Keywords: gravitation; dark matter; galaxies: kinematics and dynamics.

АНОТАЦІЯ. Розглядається модель компактного об'єкта, що є альтернативою чорній дірці. У цій моделі акреціруючі протони розпадаються на Планковській шкалі на позитрони та гіпотетичні Планковські нейтрино. Енергія частинок розщеплюється на дві моди, низьку та високу. Електрони, позитрони та Планківські нейтрино з високою енергією віддаляються. Електрони та позитрони з низькою енергією утворюють компактний об'єкт. Планківські нейтрино з низькою енергією утворюють оболонку навколо компактного об'єкта. Планківські нейтрино, що віддаляються, можуть бути інтерпретовані як гаряча темна матерія (ГТМ). Планківські нейтрино в оболонці навколо компактного об'єкта можуть бути інтерпретовані як захоплена в пастку гаряча темна матерія (ЗГТМ). У недавній статті було запроваджено поняття тиску вільного падіння. У моделі ефективної гравітації, що включає гравітацію Ньютона і тиск вільного падіння, ЗГТМ прихована для масивних частинок, але викликає відхилення безмасових частинок. ЗГТМ можна побачити у гравітаційній взаємодії двох оболонок. Розглядається гравітаційна взаємодія галактик у скупченні Діви (M60, M87, M84, M86, M49). Рух галактик визначається масами ЗГТМ в оболонках навколо компактних об'єктів у центрах галактик, зірковими масами галактик та масами ГТМ у галактиках. Швидкості M60 і M49 у напрямку M87 оцінюються в 678 км $с^{-1}$ і 445 км $с^{-1}$, що становить 66% і 59% значень, що спостерігаються, відповідно.

Ключові слова: гравітація; темна матерія; галактики: кінематика та динаміка.

1. Introduction

General relativity (Misner et al., 1973) predicts the formation of a black hole in the gravitational collapse of a body with a mass above $\sim 3\ m_\odot$. The black hole is bounded by the event horizon of the Schwarzschild radius, $r_g = 2Gm/c^2$. The existence of the event horizon breaking the connection of the gravitating mass of the black hole with an outer observer questions the usual physics.

Khokhlov (2017, 2021) developed the model of the compact object as a thin shell near the Schwarzschild radius, being alternate to the black hole. Khokhlov (2017, 2021) assumed that the liberated gravitational binding (kinetic) energy of the matter (protons and electrons) accreting onto the compact object is split in two modes, with the low energy $E_k^- \approx Gm/2r_g$ and with the high energy $E_k^+ \approx 3Gm/2r_g$ as seen in the local frame of the compact object (hereafter we

use the unity mass of the particle). Half the accreting matter with the low energy retains at the compact object. The inertial force, $F_{in} \approx 2E_k^-/r_g \approx Gm/r_g^2$, balances the gravity of the compact object thus making it stable. Half the accreting matter with the high energy leaves the compact object overcoming the gravity of the compact object. The protons with the high energy are assumed to decay at the Planck scale into positron and hypothetical Planck neutrinos, the mode of the decay of the proton was proposed in Khokhlov (2011).

The footprints of the decay of the protons at the compact objects may be seen in the astrophysical observations. Annihilation of the positrons arising in the decay of the protons at the compact object Sgr A*, now interpreted as a black hole, may explain (Barbieri & Chapline, 2012) an excess of 511 keV radiation from the centre of the Galaxy (Prantzos et al., 2011). The flux of Planck neutrinos may account for the discrepancy between the accretion rate and the luminosity of Sgr A* (Khokhlov, 2014). The spectrum of ultra high energy cosmic rays may be explained by the Planck neutrinos with the energy corresponding to the decay of the proton at the compact object (Khokhlov, 2020a).

Planck neutrino is a candidate for dark matter particle. The concept of dark matter came into being to explain the discrepancy between the dynamical mass and the baryonic mass in the galaxies and in the clusters of galaxies (Trimble, 1987) and references therein. The modern theory suggests the existence of the cold dark matter (CDM) in the universe (Trimble, 1987) and references therein. Now, the dark matter is described within the framework of the ΛCDM cosmological model (Ostriker & Steinhardt, 1995). Several open problems of the ΛCDM model on galaxy scales were under discussion, e.g. (Weinberg et al., 2015; Kroupa, 2012, 2015) and references therein. Planck neutrinos are assumed to be massless particles (Khokhlov, 2011). Therefore, Planck neutrino may be thought of in terms of hot dark matter (HDM). The model of the galaxy with HDM was developed in Khokhlov (2018, 2020b).

In the present paper, we shall consider the model of the compact object based on the assumption that all the accreting protons decay at the Planck scale into positrons and Planck neutrinos. In this case, the compact object consists of the electrons and positrons with the low energy, and the Planck neutrinos with the low energy are placed in the shell around the compact object. We shall treat the Planck neutrinos in the shell around the compact object as the trapped hot dark matter (THDM).

In a recent paper (Khokhlov, 2021), the effective gravity was considered, including the Newton gravity and the free fall pressure. We shall consider the Planck neutrinos (THDM) in the shell around the compact object within the framework of the effective gravity. In this approach, the THDM is hidden for the massive particles but makes deflection of the massless particles. The THDM can be seen in the gravitational interaction of two shells. The approach may be tested in the gravitational interaction of the galaxies containing the supermassive black holes in their centres while interpreting them as the compact objects.

In the present paper, we shall study the gravitational interaction of the galaxies in the Virgo cluster. Specifically, we shall study the motion of the galaxies M60 and M49 toward the central galaxy M87 caused by the THDM mass in the shells around the compact objects of the galaxies, the stellar masses of the galaxies and the HDM masses of the galaxies.

2. Model of the compact object

Following (Khokhlov, 2017, 2021), consider the model of the compact object, being alternate to the black hole. Khokhlov (2017, 2021) think of the compact object as a thin shell of the radius (near the Schwarzschild radius) at which the falling protons reach the Planck energy. The model is based on the assumption of the decay of the proton at the Planck scale into positron and Planck neutrinos (Khokhlov, 2011). Khokhlov (2017, 2021) assumed that the kinetic energy of the accreting matter (protons and electrons) is split in the high and low energy modes. The accreting matter with the low energy retains at the compact object, with the inertial force balancing the gravity of the compact object. The accreting matter with the high energy leaves the compact object, overcoming the gravity of the compact object. The protons with the high energy decay into the positrons and Planck neutrinos. In what follows, we shall consider the model of the compact object in which all the accreting protons decay into positrons and Planck neutrinos, with the kinetic energy of the electrons, positrons and Planck neutrinos is split in the high and low energy modes.

The concept of the free fall pressure opposing the gravity was introduced in Khokhlov (2021). This leads to the effective gravity, including the Newton gravity and the free fall pressure. The gravitational force is established with the velocity of light c while the inertial force due to free fall pressure is established with a free fall velocity v. In the case of the weak gravity, the inertial force due to free fall pressure is suppressed. At the Schwarzschild radius, the free fall velocity is equal to the velocity of light, and the inertial force due to free fall pressure balances the gravity.

Planck neutrino is assumed to be massless particle (Khokhlov, 2011). Consider an approach to description of the gravitational interaction of the massless particle (photon, Planck neutrino) within the framework of the effective gravity. Consider the

massless particle in the gravitational field. In view of the equivalence principle, the massless particle should possess the gravitating mass. Since the massless particle propagates with the velocity of light, the free fall pressure of the massless particle balances its gravity. The effective potential experienced by the massless particle, including the gravitational potential and the inertial potential due to free fall pressure, is zero

$$\Phi_{eff} = \Phi_g + \Phi_{in} = \frac{Gm}{r} - \frac{Gm}{r} = 0 \qquad (1)$$

where G is the Newton constant, m is the mass of the source of gravity. Assume that the perturbation due to free fall pressure comes with a time delay of the size of the massless particle. In this case, a couple of forces due to gravity and free fall pressure act on the massless particle in the gravitational field. The resultant force is zero, but the deflection of the massless particle is twice that of the massive particle. The massless particle is deflected in the gravitational field at an angle

$$\alpha = \frac{4Gm}{c^2 b} \qquad (2)$$

where b is the impact parameter. The deflection of the massless particle eq. (2) is the same as the deflection of light in general relativity (Pauli, 1958).

Consider the behaviour of the electrons, positrons and Planck neutrinos with the low energy. In view of the foregoing reasoning, the massive particles (protons, electrons, positrons) do not experience the gravity of the massless Planck neutrinos. We come to the model of the compact object, consisting of the electrons and positrons with the low energy. The compact object is a shell with the radius close to the Schwarzschild radius, $r_{co} \approx 2Gm_{co}/c^2$. Assume that the positrons and electrons of the compact object are in the chaotic motion in the transverse direction. In the own frame of the compact object, the kinetic energy of the positrons and electrons of the compact object, $E_k^- \approx Gm_{co}/2r_{co}$, produces the centrifugal acceleration of the particles, balancing their gravity. The kinetic energy of the positron (electron) minus its gravitational energy is $E_k^- - E_g \approx -Gm_{co}/2r_{co}$. Therefore, the emission of the electromagnetic radiation by the positrons and electrons of the compact object is suppressed. The remote observer will see the compact object as a black region.

The Planck neutrinos with the low energy are deflected in the gravitational field generated by the mass of the compact object plus the mass of the Planck neutrinos. They are placed in the shell around the compact object. In the frame of the shell, the kinetic energy of the Planck neutrino minus its gravitational energy is $E_k^- - E_g \approx -G(m_{co} + m_{sh})/2r_{sh}$. Assume that the energy (mass) of four Planck neutrinos is $m_\nu = m_p - m_e$ where m_p is the mass of proton, m_e is the mass of electron. The mass of the Planck neutrinos in the shell around the compact object is given by

$$m_{sh} = \frac{(m_p - m_e)}{2m_e} m_{co}. \qquad (3)$$

In view of eq. (2), the radius of the shell is given by

$$r_{sh} = \frac{(m_p - m_e)}{4m_e} r_{co}. \qquad (4)$$

The massive probe particle does not detect the mass of the Planck neutrinos in the shell around the compact object. The mass of the shell eq. (3) is hidden for the massive probe particle. The massless probe particle (photon, Planck neutrino) is deflected by the mass of the shell at an angle eq. (2). The photon lensed by the shell can reveal the hidden mass of the Planck neutrinos. When moving from infinity, the massless probe particle cannot approach the shell closer than twice the radius of the shell. Thus, the massive and massless probe particles experience the Planck neutrinos in the shell around the compact object in different way.

The Planck neutrinos in the shell around the compact object can scatter on the accreting protons. The process of the scattering of four Planck neutrinos on the proton goes at the Planck scale, with the birth of the electron-positron pair (Khokhlov, 2020a). The probability of the scattering of the Planck neutrinos in the shell around the compact object on the accreting protons is given by

$$\frac{1}{\tau} \propto \frac{1}{t_{Pl}} \left(\frac{(E_\nu E_p)^{1/2}}{m_{Pl}} \right)^7 \qquad (5)$$

where t_{Pl} is the Planck time, m_{Pl} is the Planck mass, $E_\nu = (m_p m_{Pl})^{1/2}$ is the energy of four Planck neutrinos of the compact object, $E_p \approx m_p$ is the energy of the accreting proton, taking into account that the relativistic factor of the accreting proton is $v^2/c^2 = r_{co}/r_{sh} \sim 5.5 \times 10^{-3}$. The probability eq. (5) is small thus the interaction of the Planck neutrinos in the shell around the compact object with the accreting protons can be neglected.

Consider the behaviour of the electrons, positrons and Planck neutrinos with the high energy. The positrons and electrons with the high energy can overcome the gravity of the compact object. In the own frame of the compact object, the kinetic energy of the positron (electron) minus its gravitational energy is $E_k^+ - E_g \approx Gm_{co}/2r_{co}$. This energy may be converted into the electromagnetic radiation seen by the remote observer. The luminosity of Sgr A* was explained by the energy $E_k^+ - E_g$ of the electrons leaving Sgr A* (Khokhlov, 2017). The positron from the decayed proton was assumed to have the negligible kinetic energy (Khokhlov, 2017). Later Khokhlov (2020a) showed that the positron and Planck neutrinos share

the energy of the decayed proton. In its own frame, the kinetic energy of the positron is the same as that of the electron. Then, half the energy $E_k^+ - E_g$ of the positrons and electrons leaving Sgr A* may explain the luminosity of Sgr A*. The cosmic rays from Sgr A* may carry away the other half of the energy.

The Planck neutrinos with the high energy can overcome the gravity of the compact object plus the shell of the Planck neutrinos. In the own frame of the compact object, the kinetic energy of the Planck neutrino minus its gravitational energy is $E_k^+ - E_g \approx Gm_{co+sh}/2r_{sh}$. They may be thought of as the HDM distributed in the universe. The Planck neutrinos with the low energy are trapped by the compact object plus the shell of the Planck neutrinos thus may be thought of as the THDM. Since the mass of the Planck neutrinos in the shell is much more than the mass of the compact object, the Planck neutrinos with the low energy are mostly trapped by themselves.

Consider the gravitational interaction of two shells of the Planck neutrinos within the framework of the effective gravity (Khokhlov, 2021). Suppose that the mass of the first shell is less than the mass of the second shell. The effective gravitational potential of the shell is a sum of the gravitational potential and the inertial potential due to free fall pressure equal zero

$$\Phi_{eff,sh} = \Phi_{g,sh} + \Phi_{in,sh} = 0. \tag{6}$$

In the gravitational interaction of two shells, the relative inertial potential of the shells is given by

$$\Phi_{in,sh12} = \Phi_{in,sh2} - \Phi_{in,sh1}. \tag{7}$$

In the frame of the first shell, the effective gravitational potential of the second shell is given by

$$\Phi_{eff,sh2} = \Phi_{g,sh2} + \Phi_{in,sh12} = \Phi_{g,sh1}. \tag{8}$$

This gives the velocity of the first shell toward the second shell

$$v_1 = (2\Phi_{eff,sh2})^{1/2} = \left(\frac{2Gm_{sh1}}{R_{12}}\right)^{1/2} \tag{9}$$

where R_{12} is the distance between the shells. In the frame of the second shell, the effective gravitational potential of the first shell is given by

$$\Phi_{eff,sh1} = \Phi_{g,sh1}. \tag{10}$$

This gives the velocity of the second shell toward the first shell

$$v_2 = (2\Phi_{eff,sh1})^{1/2} = \left(\frac{2Gm_{sh1}}{R_{12}}\right)^{1/2}. \tag{11}$$

The relative velocity of the shells is given by

$$v_{12} = v_1 + v_2. \tag{12}$$

So, in the gravitational interaction of two shells of the Planck neutrinos around the compact objects, the inertial potentials of the shells compensate each other by the value of the smaller inertial potential. As a result, the mass of the Planck neutrinos in the shells around the compact objects can be revealed. For both the shells, the value revealed is equal to the mass of the Planck neutrinos of the smaller shell.

3. Gravitational interaction of the galaxies in the Virgo cluster

Consider the motion of the galaxies due to gravitational interaction of the galaxies in the Virgo cluster. We shall interpret the black holes in the centres of the galaxies as the compact objects, consisting of the electrons and positrons. The compact object is surrounded by the shell of the Planck neutrinos. In view of eq. (3), the mass of the shell of the Planck neutrinos around the compact object is more than the mass of the compact object by a factor of $m_p/(2m_e) = 0.9\times10^3$. The mass of the shell is hidden for the massive probe particle and can be revealed in the gravitational interaction of two shells, with the value revealed equal to the mass of the smaller shell eqs. (9),(11). Remind that we treat the Planck neutrinos of the compact object in terms of the THDM.

We shall consider the gravitational interaction of the galaxies defined by the THDM mass around the compact objects in the centres of the galaxies, the stellar masses of the galaxies and the HDM mass in the galaxies. We shall take the stellar masses of the galaxies as the baryonic masses of the galaxies. The stellar masses of the galaxies can be obtained from their luminosities in the V-band taken from NED, adopting the stellar mass-to-light ratio, $m_{*,\odot}/L_{V,\odot} = 6$. In the HDM model of the galaxy (Khokhlov, 2018, 2020b), the dynamical mass of the galaxy, including the baryonic and the HDM mass of the galaxy, is twice the baryonic mass of the galaxy at most. We shall take the dynamical mass of the galaxy twice the sum of the stellar mass of the galaxy and the mass of the smaller shell around the compact object.

We shall model the gravitational interaction of the galaxies with the use of the foregoing formalism of the gravitational interaction of the shells of the Planck neutrinos around the compact objects. Consider two galaxies with the compact objects in their centres. The velocity of the first galaxy toward the second galaxy is defined by the mass centred on the second galaxy as

$$v_1 \approx \left(\frac{2G(m_{thdm} + m_{*2} + m_{hdm2})}{R_{12}}\right)^{1/2} = \left(\frac{4G(m_{thdm} + m_{*2})}{R_{12}}\right)^{1/2} \tag{13}$$

where m_{thdm} is the THDM mass of the smaller

compact object, m_* is the stellar mass of the galaxy, m_{hdm} is the HDM mass of the galaxy, R_{12} is the distance between the galaxies.

We shall study the motion of the galaxies M60 and M49 toward the galaxy M87 in the centre of the Virgo cluster, assuming that M87 is at rest. We shall estimate the velocity of M60 toward M87 due to gravitational interaction of M60 with M87, M84, M86, M49 and the velocity of M49 toward M87 due to gravitational interaction of M49 with M87, M84, M86, M60. We shall consider the motion of the galaxies in projection, taking the distances between the galaxies in projection and neglecting the radial distances between the galaxies.

Consider the gravitational interaction of M60 and M87. The distance between the galaxies is 0.97 Mpc. The observational mass of the black hole in the centre of M87 is $m_{bh,M87} = 6.5 \times 10^9$ m$_\odot$ (Event Horizon Telescope Collaboration, 2019) that gives the THDM mass of the shell around the compact object, $m_{thdm,M87} = 5.85 \times 10^{12}$ m$_\odot$. The observational mass of the black hole in the centre of M60 is $m_{bh,M60} = 4.5 \times 10^9$ m$_\odot$ (Shen & Gebhardt, 2010) that gives the THDM mass of the shell around the compact object, $m_{thdm,M60} = 4.05 \times 10^{12}$ m$_\odot$. The luminosity of M87 is $L_{V,M87} = 1.34 \times 10^{11}$ L$_\odot$ that gives the stellar mass of M87, $m_{*,M87} = 8 \times 10^{11}$ m$_\odot$. The mass centred on M87 is a sum of the THDM mass of the shell around the compact object in the centre of M60, the stellar mass of M87 and the HDM mass, $m_{M87} = 2(4.05 \times 10^{12} + 8 \times 10^{11}) = 9.7 \times 10^{12}$ m$_\odot$. This mass gives the velocity of M60 toward M87, 294 km s^{-1}.

Consider the gravitational interaction of M60 and M84. The distance between the galaxies is 1.45 Mpc. The direction of M60 toward M84 is close to the direction of M49 toward M87. The observational mass of the black hole in the centre of M84 is $m_{bh,M84} = 1.5 \times 10^9$ m$_\odot$ (Bower et al., 1998) that gives the THDM mass of the shell around the compact object, $m_{thdm,M84} = 1.35 \times 10^{12}$ m$_\odot$. The luminosity of M84 is $L_{V,M84} = 9.33 \times 10^{10}$ L$_\odot$ that gives the stellar mass of M84, $m_{*,M84} = 5.6 \times 10^{11}$ m$_\odot$. The mass centred on M84 is a sum of the THDM mass of the shell around the compact object in the centre of M84, the stellar mass of M84 and the HDM mass, $m_{M84} = 2(1.35 \times 10^{12} + 5.6 \times 10^{11}) = 3.8 \times 10^{12}$ m$_\odot$. This mass gives the velocity of M60 toward M84, 151 km s^{-1}. Projecting it on the direction of M60 toward M87, one gets the same value, 151 km s^{-1}.

Consider the gravitational interaction of M60 and M86. The distance between the galaxies is 1.4 Mpc. The direction of M60 toward M86 is close to the direction of M49 toward M87. The mass of the black hole in the centre of M86 is unknown. Adopt the value, $m_{bh,M86} = 1.5 \times 10^9$ m$_\odot$, which gives the THDM mass of the shell around the compact object, $m_{thdm,M86} = 1.35 \times 10^{12}$ m$_\odot$. The luminosity of M86 is $L_{V,M86} = 1.57 \times 10^{11}$ L$_\odot$ that gives the stellar mass of M86, $m_{*,M86} = 9.4 \times 10^{11}$ m$_\odot$. The mass centred on M86 is a sum of the THDM mass of the shell around the compact object in the centre of M86, the stellar mass of M86 and the HDM mass, $m_{M86} = 2(1.35 \times 10^{12} + 9.4 \times 10^{11}) = 4.6 \times 10^{12}$ m$_\odot$. This mass gives the velocity of M60 toward M86, 169 km s^{-1}. Projecting it on the direction of M60 toward M87, one gets the same value, 169 km s^{-1}.

Consider the gravitational interaction of M60 and M49. The distance between the galaxies is 1.5 Mpc. The direction of M60 toward M49 is at an angle of 62° to the direction of M60 toward M87. The observational mass of the black hole in the centre of M49 is $m_{bh,M49} = 5.65 \times 10^8$ m$_\odot$ (Loewenstein et al., 2001) that gives the THDM mass of the shell around the compact object, $m_{thdm,M49} = 5.1 \times 10^{11}$ m$_\odot$. The luminosity of M49 is $L_{V,M49} = 1.78 \times 10^{11}$ L$_\odot$ that gives the stellar mass of M49, $m_{*,M49} = 10.7 \times 10^{11}$ m$_\odot$. The mass centred on M49 is a sum of the THDM mass of the shell around the compact object in the centre of M49, the stellar mass of M49 and the HDM mass, $m_{M49} = 2(5.1 \times 10^{11} + 10.7 \times 10^{11}) = 3.2 \times 10^{12}$ m$_\odot$. This mass gives the velocity of M60 toward M49, 136 km s^{-1}. Projecting it on the direction of M60 toward M87, one gets 64 km s^{-1}.

Calculate the total velocity of M60 toward M87 due to gravitational interaction of M60 with M87, M84, M86, M49. The total velocity of M60 toward M87 is estimated to be 294 + 151 + 169 + 64 = 678 km s^{-1}. The velocity of M60 toward M87, 1030 km s^{-1} (Wood et al., 2017), was obtained from the X-ray data analysis. Thus, the value obtained from the gravitational interaction of the galaxies may explain 66% of the value obtained from the X-ray data. To obtain the more accurate value one needs to include more galaxies in the study.

Consider the gravitational interaction of M49 and M87. The distance between the galaxies is 1.35 Mpc. The mass centred on M87 is a sum of the THDM mass of the shell around the compact object in the centre of M49, the stellar mass of M87 and the HDM mass, $m_{M87} = 2(5.1 \times 10^{11} + 8 \times 10^{11}) = 2.6 \times 10^{12}$ m$_\odot$. This mass gives the velocity of M49 toward M87, 129 km s^{-1}.

Consider the gravitational interaction of M49 and M84. The distance between the galaxies is 1.55 Mpc. The direction of M49 toward M84 is at an angle of 16° to the direction of M49 toward M87. The mass centred on M84 is a sum of the THDM mass of the shell around the compact object in the centre of M49, the stellar mass of M84 and the HDM mass, $m_{M84} = 2(5.1 \times 10^{11} + 5.6 \times 10^{11}) = 2.1 \times 10^{12}$ m$_\odot$. This mass gives the velocity of M49 toward M84, 109 km s^{-1}. Projecting it on the direction of M49 toward M87, one gets 105 km s^{-1}.

Consider the gravitational interaction of M49 and

M86. The distance between the galaxies is 1.55 Mpc. The direction of M49 toward M86 is at an angle of 14° to the direction of M49 toward M87. The mass centred on M86 is a sum of the THDM mass of the shell around the compact object in the centre of M49, the stellar mass of M86 and the HDM mass, $m_{M86} = 2(5.1 \times 10^{11} + 9.4 \times 10^{11}) = 2.9 \times 10^{12}$ m$_\odot$. This mass gives the velocity of M49 toward M86, 128 km s^{-1}. Projecting it on the direction of M49 toward M87, one gets 124 km s^{-1}.

Consider the gravitational interaction of M49 and M60. The distance between the galaxies is 1.5 Mpc. The direction of M49 toward M60 is at an angle of 41° to the direction of M49 toward M87. The luminosity of M60 is $L_{V,M60} = 1.05 \times 10^{11}$ L$_\odot$ that gives the stellar mass of M60, $m_{*,M60} = 6.3 \times 10^{11}$ m$_\odot$. The mass centred on M60 is a sum of the THDM mass of the shell around the compact object in the centre of M49, the stellar mass of M60 and the HDM mass, $m_{M49} = 2(5.1 \times 10^{11} + 6.3 \times 10^{11}) = 2.3 \times 10^{12}$ m$_\odot$. This mass gives the velocity of M49 toward M60, 115 km s^{-1}. Projecting it on the direction of M49 toward M87, one gets 87 km s^{-1}.

Calculate the total velocity of M49 toward M87 due to gravitational interaction of M49 with M87, M84, M86, M60. The total velocity of M49 toward M87 is estimated to be $129 + 105 + 124 + 87 = 445$ km s^{-1}. The velocity of M49 toward M87, 750 km s^{-1} (Gavazzi et al., 1999), was obtained from the kinematics analysis. Thus, the value obtained from the gravitational interaction of the galaxies may explain 59% of the value obtained from the kinematics analysis. To obtain the more accurate value one needs to include more galaxies in the study.

4. Discussion

In the model considered, the mass of the shell of the Planck neutrinos around the compact object, the THDM mass, is hidden for the massive probe particle but may be seen in the gravitational interaction of the shells of the Planck neutrinos around the compact objects in the centres of the galaxies. We have calculated the velocity of M60 toward M87 due to gravitational interaction of M60 with M87, M84, M86, M49 and the velocity of M49 toward M87 due to gravitational interaction of M49 with M87, M84, M86, M60. The gravitational interaction of the galaxies is defined by the masses of the shells of the Planck neutrinos around the compact objects in the centres of the galaxies (THDM mass), the stellar masses of the galaxies and the HDM mass in the galaxies.

Estimate the contribution of the DM mass, including the THDM and HDM mass, and the stellar mass in the gravitational interaction of the galaxies. The velocity of M60 toward M87 is defined by the THDM mass 36%, the stellar mass 14%, the HDM mass 50%. The velocity of M49 toward M87 is defined by the THDM mass 20%, the stellar mass 30%, the HDM mass 50%. In total, the DM is responsible for 86% of the velocity of M60 toward M87 and for 70% of the velocity of M49 toward M87.

The relative velocity of the Milky Way and M31 was explained by the baryonic mass and the HDM mass in the galaxies (Khokhlov, 2020b). The observational masses of the black holes in the centres of the galaxies are $m_{bh,MW} = 4 \times 10^6$ m$_\odot$ (Ghez et al., 2008; Gillessen et al., 2009) in the Milky Way and $m_{bh,M31} = 2 \times 10^8$ m$_\odot$ (Bender et al., 2005) in M31. Accordingly, the THDM masses of the shells around the compact objects are $m_{thdm,MW} = 3.6 \times 10^9$ m$_\odot$ in the Milky Way and $m_{thdm,M31} = 1.8 \times 10^{11}$ m$_\odot$ in M31. The THDM mass revealed in the gravitational interaction of the shells is equal to that in the smaller shell in the Milky Way which can be neglected in comparison with the baryonic masses in the Milky Way, $m_{b,MW} = 10^{11}$ m$_\odot$ (Khokhlov, 2018), and in M31, $m_{b,M31} = 1.3 \times 10^{11}$ m$_\odot$ (Khokhlov, 2020b). Thus, the THDM mass is not seen in the gravitational interaction of the Milky Way and M31. The DM is responsible for 50% of the relative velocity of the Milky Way and M31.

The light rays are deflected by the THDM. Therefore, the THDM mass may be seen in the lensing of the galaxies. One can measure the total masses of the galaxies in the galaxy-galaxy weak lensing. van Uitert et al. (2011) measured halo masses of the galaxies in the weak lensing analysis, using data for the galaxies from RCS2 and SDSS ($0.08 < z < 0.48$) of stellar masses in the range $m_* \sim 10^{10} - 10^{12}$ m$_\odot$. The halo masses of the galaxies determined in the weak lensing analysis increase with the stellar masses of the galaxies. For the early type galaxies, the halo mass grows from $m_h^e = 1.35 \times 10^{11} h^{-1}$ m$_\odot$ at $m_* = 2.0 \times 10^{10}$ m$_\odot$ to $m_h^e = 7.2 \times 10^{13} h^{-1}$ m$_\odot$ at $m_* = 1.2 \times 10^{12}$ m$_\odot$. For the late type galaxies, the halo mass grows from $m_h^l = 5.6 \times 10^{10} h^{-1}$ m$_\odot$ at $m_* = 2.0 \times 10^{10}$ m$_\odot$ to $m_h^l = 2.2 \times 10^{13} h^{-1}$ m$_\odot$ at $m_* = 6.9 \times 10^{11}$ m$_\odot$. The lensing halo masses of the early type galaxies are greater than those of the late type galaxies. This may be explained by the smaller masses of the shells of the Planck neutrinos around the compact objects (THDM masses) in the centres of the late type galaxies.

Compare the total masses, including the stellar, THDM and HDM masses, of the Milky Way, M31, M87 with the lensing halo masses, corresponding to the stellar masses of the galaxies. Estimate the total mass of the Milky Way, taking the stellar mass of the Milky Way, $m_{*,MW} = 10^{11}$ m$_\odot$, and neglecting the THDM mass. Calculation gives $m_{MW} = 1 + 1 = 2 \times 10^{11}$ m$_\odot$. The corresponding lensing halo mass of the late type galaxy is $m_h^l = 1.4 \times 10^{11}$ m$_\odot$ which is consistent with the total mass of the Milky Way. Esti-

mate the total mass of M31, taking the stellar mass of M31, $m_{*,M31} = 1.3 \times 10^{11}$ m$_\odot$. Calculation gives $m_{M31} = 2(1.3+1.8) = 6.2\times10^{11}$ m$_\odot$. The corresponding lensing halo mass of the late type galaxy is $m_h^l = 2.1 \times 10^{11}$ m$_\odot$ which is lower than the total mass of M31. Estimate the total mass of M87, taking the stellar mass of M87, $m_{*,M87} = 8 \times 10^{11}$ m$_\odot$. Calculation gives $m_{M87} = 2(0.8 + 5.85) = 13.3 \times 10^{12}$ m$_\odot$. The corresponding lensing halo mass of the early type galaxy is $m_h^e = 9.4 \times 10^{13}$ m$_\odot$ which is higher than the total mass of M87.

Consider the gravity of M87 experienced by the massive probe particle within the framework of the HDM model (Khokhlov, 2018, 2020b). The THDM mass is hidden for the massive probe particle. It can experience the baryonic and HDM mass. In the HDM model, the baryonic matter of the galaxy is embedded into the HDM, with the HDM density constant with radius. At some radius r_0, the HDM mass is equal to the baryonic mass. Estimate the radius r_0 for the stellar mass of M87. For the HDM density $\rho_{hdm} = 5 \times 10^{-3}$ m$_\odot$ pc^{-3} (Khokhlov, 2018, 2020b), the HDM mass is equal to the stellar mass of M87, $m_{*,M87} = 8 \times 10^{11}$ m$_\odot$, at the radius $r_0 = 34$ kpc. At $r < r_0$, the probe particle moves along the elliptic orbit. At $r \geq r_0$, the probe particle moves along the parabolic orbit. At $r \geq r_0$, the enclosed dynamical mass is twice the enclosed baryonic mass.

Estimate the enclosed dynamical mass of M87 at 100 kpc from the velocity dispersion profile. Longobardi et al. (2018) used a sample of planetary nebulas to map the velocity dispersion profile of the M87 outer halo, subtracting the contribution of the intra-cluster planetary nebulas. The radial velocity dispersion of the M87 halo at 100 kpc is $\sigma_r \sim 200$ km s^{-1} (Longobardi et al., 2018). In the HDM model (Khokhlov, 2018, 2020b), the enclosed dynamical mass at $r \gg r_0$ is defined by the radial velocity which is twice the radial velocity dispersion, $v_r = 2\sigma_r$. Then, the enclosed dynamical mass of M87 at 100 kpc is $m_{dyn,M87}(< 100$ kpc$) = v_r^2 r/2G = 1.9 \times 10^{12}$ m$_\odot$. The enclosed baryonic mass of M87 at 100 kpc is $m_{b,M87}(< 100$ kpc$) = 9.5 \times 10^{11}$ m$_\odot$. This is comparable with the stellar mass of M87, $m_{*,M87} = 8\times10^{11}$ m$_\odot$. The radial velocity dispersion of the intra-cluster planetary nebulas at 100 kpc is $\sigma_r \sim 800$ km s^{-1} (Longobardi et al., 2018). It is reasonable to think that the intra-cluster baryonic matter is dragged by the motion of the galaxies.

So, the THDM mass of the shell around the compact object in the centre of the galaxy manifests itself in different way depending on the observation method. It is hidden for the objects tracing the gravity of the galaxy. It may be seen in the gravitational interaction of the shells of the Planck neutrinos around the compact objects in the centres of the galaxies thus influencing the motion of the galaxies. In lensing, the THDM mass of the shell around the compact object in the centre of the galaxy gives contribution to the lensing mass of the galaxies.

5. Conclusion

We have considered the model of the compact object, being alternate to the black hole. The model is based on the assumption that the accreting protons decay at the Planck scale into positrons and Planck neutrinos. The energy of the particles is split in two modes, low and high. The compact object consists of the electrons and positrons with the low energy. The Planck neutrinos with the low energy are placed in the shell around the compact object. The mass of the shell is more than the mass of the compact object by a factor of $m_p/(2m_e) = 0.9 \times 10^3$. The electrons, positrons and Planck neutrinos with the high energy move away, overcoming the gravity of the compact object and the shell of the Planck neutrinos. The Planck neutrinos with the high energy may be interpreted as the HDM.

We have considered Planck neutrinos within the framework of the effective gravity, including the Newton gravity and the free fall pressure. The gravitational potential of the Planck neutrinos in the shell around the compact object is balanced by the inertial potential due to free fall pressure. The mass of the Planck neutrinos is hidden for the massive particles. The massless particles (photons, Planck neutrinos) are deflected by the mass of the Planck neutrinos. In effect, the Planck neutrinos in the shell around the compact object are trapped and may be interpreted as the THDM. The THDM mass may be seen in the lensing of the galaxies containing the central compact object (black hole).

In the gravitational interaction of two shells of the Planck neutrinos around the compact objects, the inertial potentials of the shells compensate each other by the value of the smaller inertial potential, revealing the masses of the Planck neutrinos (THDM masses) in the shells, equal to the mass of the Planck neutrinos of the smaller shell. We have studied the gravitational interaction of the galaxies in the Virgo cluster, M60 with M87, M84, M86, M49 and M49 with M87, M84, M86, M60. The gravitational interaction of the galaxies is defined by the revealed THDM masses in the shells around the compact objects in the centres of the galaxies, the stellar masses of the galaxies and the HDM mass in the galaxies. The total velocity of M60 toward M87 due to gravitational interaction of M60 with M87, M84, M86, M49 is 678 km s^{-1} being 66% of that obtained from the X-ray data, 1030 km s^{-1} (Wood et al., 2017). The total velocity of M49 toward M87 due to gravitational interaction of M49 with M87, M84, M86, M60 is 445 km s^{-1} being 59% of that obtained from the kinematics analysis, 750 km s^{-1} (Gavazzi et al., 1999).

References

Barbieri J., Chapline G.: 2012, *Phys. Lett. B*, **709**, 114.

Bender R., Kormendy J., Bower G. et al.: 2005, *ApJ*, **631**, 280.

Bower G.A., Green R.F., Danks A. et al.: 1998, *ApJ*, **492**, 111.

Event Horizon Telescope Collaboration, Akiyama K., Alberdi A., Alef W. et al.: 2019, *ApJ*, **875**, L6.

Gavazzi G., Boselli A., Scodeggio M., Pierini D., Belsole E.: 1999, *MNRAS*, **304**, 595.

Ghez A.M., Salim S., Weinberg N.N. et al.: 2008, *ApJ*, **689**, 1044.

Gillessen S., Eisenhauer F., Trippe S. et al.: 2009, *ApJ*, **692**, 1075.

Khokhlov D.L.: 2011, *Open Astron. J.*, **4 (SI 1)**, 151.

Khokhlov D.L.: 2014, *Phys. Lett. B*, **729**, 1.

Khokhlov D.L.: 2017, *Int. J. Mod. Phys. Appl.*, **4**, 8.

Khokhlov D.L.: 2018, *Open Astron.*, **27**, 294.

Khokhlov D.L.: 2020a, *Open Astron.*, **29**, 40.

Khokhlov D.L.: 2020b, *Odessa Astron. Publ.*, **33**, 11.

Khokhlov D.L.: 2021, *Int. J. Adv. Astron.*, **9**, 28.

Kroupa P.: 2012, *PASA*, **29**, 395.

Kroupa P.: 2015, *Can. J. Phys.*, **93**, 169.

Loewenstein M., Mushotzky R.F., Angelini L., Arnaud K.A., Quataert E.: 2001, *ApJ*, **555** L21.

Longobardi A., Arnaboldi M., Gerhard O., Pulsoni C., Söldner-Rembold I.: 2018, *A&A*, **620**, A111.

Misner C.W., Thorne K.S., Wheeler J.A.: 1973, *Gravitation*, Freeman, San Francisco.

Ostriker J.P., Steinhardt P.J.: 1995, *Nature*, **377**, 600.

Pauli W.: 1958, *Theory of Relativity*, Pergamon Press, London.

Prantzos N., Boehm C., Bykov A.M. et al.: 2011, *Rev. Mod. Phys.*, **83**, 1001.

Shen J., Gebhardt K.: 2010, *ApJ*, **711**, 484.

Trimble V.: 1987, *ARA&A*, **25**, 425.

van Uitert E., Hoekstra H., Velander M., Gilbank D.G., Gladders M.D., Yee H.K.C.: 2011, *A&A*, **534**, A14.

Weinberg D.H., Bullock J.S., Governato F., de Naray R.K., Peter A.H.G.: 2015, *Proc. Nat. Acad. Sci.*, **112**, 12249.

Wood R.A., Jones C., Machacek M.E. et al.: 2017, *ApJ*, **847**, 79.

https://doi.org/10.18524/1810-4215.2023.36.289772

A NEW METHOD OF INVESTIGATION OF THE ORIENTATION OF GALAXIES IN CLUSTERS IN LACK OF INFORMATION ABOUT THEIR MORPHOLOGICAL TYPES

B. Mrzygłód[1], W. Godłowski[2]

[1] Institute of Physics, Uniwersytet Opolski,
ul. Oleska 48, 45-052 Opole, Poland, *blazej.mrzyglod@student.uni.opole.pl*
[2] Institute of Physics, Uniwersytet Opolski,
ul. Oleska 48, 45-052 Opole, Poland, *godlowski@uni.opole.pl*

ABSTRACT. The problem of the formation of structures in the universe is one of the most important issues of modern extragalactic astronomy and cosmology. The tool enabling the verification of a particular formation scenario is analysis the spatial orientation of the galaxies from deprojection of their images. Obtaining correct analysis results obliges to take into account the fact that galaxies are oblate spheroids with the real axis ratio depending on the morphological type, which, however, is not given in most of the currently available astronomical data. According to the approach used in the new method of investigation, on the basis of estimated frequencies of occurrence of given morphological types, obtained using sufficiently numerous observational data, simulations are performed, which enable to recognize new angle distributions used in orientation studies. These distributions already contain information on the frequency of the appearance of galaxies of particular morphological types in clusters, allowing for more accurate results of the statistical tests carried out during the analysis. The method is an extension of results developed in Godłowski 2012 and Pajowska et al. 2019.

Keywords: Galaxies: clusters, orientation, morphological types.

АНОТАЦІЯ. Проблема формування структур у Всесвіті є однією з найважливіших проблем сучасної позагалактичної астрономії та космології. Інструментом, що дозволяє перевірити заданий сценарій, є аналіз просторової орієнтації галактик на основі депроекції їх зображень. Отримання правильних результатів аналізу вимагає врахування того факту, що галактики є сплюснутими сфероїдами, фактичне співвідношення осей яких залежить від морфологічного типу, що не передбачено в більшості наявних на даний момент астрономічних даних. Відповідно до нового підходу, використаного в новому методі, на основі оцінених частот зустрічальності заданих морфологічних типів, отриманих з використанням достатньо великої кількості даних спостережень, проводяться моделювання, які дозволяють отримати нові кутові розподіли, які використовуються в орієнтаційних дослідженнях. Ці розподіли вже містять інформацію про частоту появи певних морфологічних типів у скупченнях галактик, що дозволяє отримувати точніші результати статистичних перевірок, проведених під час аналізу. Цей метод є розширенням результатів, отриманих Godłowski 2012 та Pajowska та ін 2019 рік.

Ключові слова: Галактики: скупчення, орієнтація, морфологічні типи.

1. Introduction

The state of knowledge regarding the formation of structures in the Universe has developed significantly, but this problem still remains one of the most important issues of modern extragalactic astronomy and cosmology. Over the years, the original theories of the formation of galaxies and their structures have been verified many times and have also undergone modifications, resulting in the creation of new versions of the models. The model of hierarchical clustering has remained valid and has been significantly improved.

According to the commonly accepted ΛCDM cosmological model, the Universe is considered to be spatially flat, isotropic and homogeneous on an appropriately large scale, and structures are formed from primordial, adiabatic, self-scaling Gaussian fluctuations (Silk 1968, Peebles & Yu 1970, Sunyaev & Zeldovich 1970, Stephanovich & Godłowski 2015). A standard test of scenarios for the formation of galaxies and their structures, enabling comparison of predicted theoretical results with observations, is the investigation of galaxy

orientation. This results from different predictions regarding the distributions of galaxy angular momentum postulated by individual scenarios of the formation and evolution of cosmic structures (Romanowsky & Fall 2012; Joachimi et al. 2015; Kiessling et al. 2015). These analyses assume that normals to the galaxies planes are their rotation axes, which is especially true for spiral galaxies.

The first application of the research method that became a standard tool for searching galaxy alignments was realized in the paper of Hawley and Peebles (1975). It consisted a statistical analysis of the galaxies angular momenta based on the observed angles of the main axes of the galaxy image, in order to detect possible deviations from the isotropic distribution. However, because the direction of the angular momentum is perpendicular to the direction of the major galaxy axis, the original version of the method only allowed for the analysis of side-viewed galaxies.

The use of galaxies with all possible orientations and locations on the celestial sphere in the study is possible applying a method based on the deprojection of galaxy images, proposed by Öpik (1970), applied by Jaaniste and Saar (Jaaniste 1977, Jaaniste & Sarr 1978) and significantly modified by Flin and Godłowski (Flin & Godłowski 1986, Godłowski 2012, Pajowska, Godłowski et. al 2019). For this purpose, this method, in addition to the positional angles of galaxies, also uses their ellipticities. Obtaining correct results, however, obliges one to take into account the Holmberg effect in the analysis, which consists of the fact that the measured, especially optical, ellipticity of the image of galaxies differs from the true ellipticity of the image (Holmberg 1946, 1958, 1975, Fouque & Paturel 1985), and the fact that galaxies are flattened spheroids with the actual axis ratio depending on their morphological type.

Nowadays, it is becoming increasingly common practice to make high-quality, readily usable astronomical data widely available. Sky surveys such as SDSS, DESI, Euclid, and Kilo-Degree Survey provide the opportunity to create catalogs of galaxy clusters and then conduct studies of the orientation of their members. Like most astronomical data currently published, these surveys do not contain information about the morphological types of galaxies. For this reason, in the case of studies carried out using data that did not contain information about the values of the actual axis ratio of galaxies, the average value of this parameter was used. However, in some cases this solution is insufficient (see Godłowski 2011 and Pajowska 2012). This paper presents a new, improved method of investigation the orientation of galaxies in clusters, allowing for more accurate analysis results using the estimated frequencies of occurrence of given morphological types.

2. New method of investigation of the orientation of galaxies in clusters

The new method of investigation the orientation of galaxies in clusters is an extension of the approach presented in the papers of Flin and Godłowski (1986), Godłowski (2012) and Pajowska et al. (2019). The method calculates two angles determining the spatial orientation of galaxies. The first is the "polar" angle δ_D - the angle between the normal to the galaxy plane and the main plane of the coordinate system. The second one, the "azimuth" angle η, describes the direction between the projection of this normal onto the main plane and the direction towards the zero initial meridian. In the case of a supergalactic coordinate system, the main plane is the supergalactic equator, and these angles can be expressed as the relationship between the latitude and longitude angles, B and L, the position angle P, and the inclination angle i (Figure 1). Deprojection of galaxy images on the celestial sphere gives four solutions for the angular momentum vector. In the absence of information about the direction of galaxy rotation, it is sufficient to examine only the directions perpendicular to the galaxy plane. This fact transfer into the need to take into account two possible settings of galaxies. The formulas for calculating the δ_D and η angles are expressed by the following relationships:

$$\sin\delta_D = -\cos i \sin B \pm \sin i \cos r \cos B, \tag{1}$$

$$\begin{aligned}\sin\eta = (\cos\delta_D)^{-1} [&-\cos i \cos B \sin L + \\ &\sin i\,(\mp\cos r \sin B \sin L \pm \sin r \cos L)],\end{aligned} \tag{2}$$

$$\begin{aligned}\cos\eta = (\cos\delta_D)^{-1} [&-\cos i \cos B \cos L + \\ &\sin i\,(\mp\cos r \sin B \cos L \mp \sin r \sin L)],\end{aligned} \tag{3}$$

where $r = P - \frac{\pi}{2}$. As a result of the reduction of the analysis into two solutions only, it is necessary to consider the sign of the expression: $S = -\cos i \cos B \mp \sin i \cos r \sin B$ and for $S > 0$ should be reversed the sign of δ_D respectively. In the investigation is an uniform distribution of angles on the sphere. For this reason, numerous ranges of δ_D and η angles should be characterized by cosine and uniform distributions, respectively. As part of the study, using statistical methods, the obtained real distributions of these angles are confronted with the theoretical distributions.

The inclination angle can be computed from the image of the galaxy using Holmberg's formula for oblate spheroids (Holmberg 1946)

$$i = \cos^{-1}\left(\sqrt{\frac{q^2 - q_0^2}{1 - q_0^2}}\right), \tag{4}$$

where $q = \frac{d}{D}$ is the ratio of the minor to the major axis diameters, and q_0 is the "true" axial ratio.

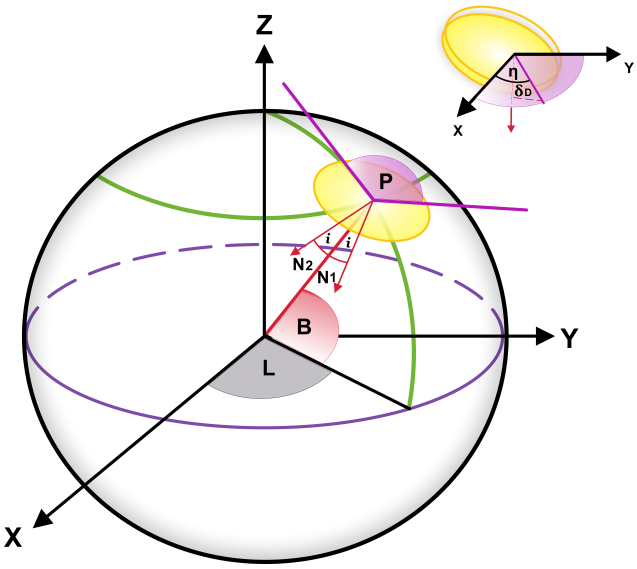

Figure 1: A schematic illustration of angles δ_D (the polar angle between the normal to the galaxy plane and the main plane of the coordinate system) and η (the azimuth angle between the projection of this normal onto the main plane and the direction towards the zero initial meridian). The angle of inclination i is the angle between the normal to the plane of the galaxy a observer's line of sight, while P is the angle of the position in the frame of reference. N_1 and N_2 are possible positions of the normal to galaxy plane directed line segment inside the sphere. L and B are the longitude and latitude of the reference coordinate system.

Each morphological type, using the Heidmann, Heidmann and de Vaucouleurs (HHD) approach, can be assigned a corresponding value of the q_0 parameter. In the absence of information about the morphological types of galaxies, $q_0 = 0.2$ is used (described in Pajowska et al. 2019). An alternative approach was used by Tully in his catalogue (Tully 1988), taking this constant value of q0 and adding 3° to the calculated inclination angle to compensate for the failure to take into account different morphological types of galaxies $i = \cos^{-1}\left(\sqrt{(q^2 - 0.2^2)/(1 - 0.2^2)}\right) + 3°$.

According to the approach presented in the new method, the lack of information about the morphology of galaxies can be compensated by using the estimated frequencies of occurrence of given morphological types. Assuming an isotropic distribution of normals to the plane of the galaxy in space, an isotropic random distribution of inclination angles is generated. By using the known frequencies of occurrence of given morphological types and the HHD approach for parameter q_0, the Holmberg formula can be reversed and a new "isotropic" distribution of the "observed" axial ratio q can be obtained. This allows to perform numerical simulations for the examined clusters of galaxies, which enable to learn new values of the inclination angle i through one of the formulas. Using these new values of i, new values of angles δ_D and η can then be calculate. "Theoretical isotropic distributions" of angles δ_D and η contain information about the frequency of appearance of galaxies of particular morphological types in clusters.

3. Application of a new method of investigation

Determining the effectiveness of a new method requires testing it under controlled test conditions. For this purpose, the Tully Nearby Gaslaxies (NBG) Catalog (Tully 1988) was used to implement the method, which contains all the necessary information about galaxies, in particular about their morphological types and affiliation to structures. It has been carefully screened for the completeness of the sample and the removal of non-galactic objects from it. The galaxies included in the catalog are devoid of background objects and provide relatively even coverage of the entire unobstructed sky (Tully 1987). The use of the Tully's catalog in other research works (Godłowski & Flin 2010, Godłowski 2011, Pajowska 2012) also makes it possible to indicate the correlation of the obtained results.

To implement the method from the NBG Catalog, 18 groups with at least 40 members were used. The actual coordinates of the galaxies were used to calculate the δ_D and η angles. The information on the morphology of galaxies contained in the catalog was used to calculate the estimated frequencies of occurrence of given morphological types.

To analyze the distribution of δ_D and η angles, statistical methods described in the paper Pajowska et al. 2019 were used: the χ^2 test, the First Autocorrelation test, the Fourier test, the Kolmogorov-Smirnov test, the Cramer-von Mises test and the Watson test. The first three of these tests were originally proposed in the paper of Hawley & Peebles 1975. The analyzed range of the test angle theta (equal to $\delta_D + \frac{\pi}{2}$ or η) is divided into a particular number of equal to the width of bins, in this case $n = 18$.

The χ^2 test uses the statistic:

$$\chi^2 = \sum_{k=1}^{n} \frac{(N_k - Np_k)^2}{Np_k} = \sum_{k=1}^{n} \frac{(N_k - N_{0,k})^2}{N_{0,k}} \qquad (5)$$

where N is the total number of galaxies in the cluster, p_k is the probability that the selected galaxy will fall into the k-th bin, and N_k and $N_{0,k}$ are the obtained and expected numbers of galaxies in the k-th bin.

The First Autocorrelation test determines the correlations between galaxy numbers in neighboring angle

bins. The statistic C is given by:

$$C = \sum_{k=1}^{n} \frac{(N_k - N_{0,k})\,(N_{k+1} - N_{0,k+1})}{[N_{0,k} N_{0,k+1}]^{\frac{1}{2}}} \tag{6}$$

where $N_{n+1} = N_1$.

The Fourier test was significantly improved by Godłowski (2012). In the test, deviation from isotropy is a slowly varying function of the angle θ, according to the relationship:

$$\begin{aligned} N_k = N_{0,k}(1 + \Delta_{11}\cos 2\theta_k + \Delta_{21}\sin 2\theta_k + \\ + \Delta_{12}\cos 4\theta_k + \Delta_{22}\sin 4\theta_k + \ldots) \end{aligned} \tag{7}$$

In that case all $N_{0,k}$ are equal. The Fourier coefficients are given by formulas:

$$\Delta_{1J} = \frac{\sum_{k=1}^{n}(N_k - N_{0,k})\cos 2J\theta_k}{\sum_{k=1}^{n} N_{0,k}\cos^2 2J\theta_k} \tag{8}$$

$$\Delta_{2J} = \frac{\sum_{k=1}^{n}(N_k - N_{0,k})\sin 2J\theta_k}{\sum_{k=1}^{n} N_{0,k}\sin^2 2J\theta_k} \tag{9}$$

with standard deviations given by:

$$\sigma(\Delta_{1J}) = \left(\sum_{k=1}^{n} N_{0,k}\cos^2 2J\theta_k\right)^{-\frac{1}{2}} \tag{10}$$

$$\sigma(\Delta_{2J}) = \left(\sum_{k=1}^{n} N_{0,k}\sin^2 2J\theta_k\right)^{-\frac{1}{2}} \tag{11}$$

The probability that the amplitude

$$\Delta_J = \left(\Delta_{1J}^2 + \Delta_{2J}^2\right)^{-\frac{1}{2}} \tag{12}$$

described by the two-dimensional Gaussian distribution, is greater than a certain chosen value is given by the formula:

$$P\,(>\Delta_J) = \exp\left(-\frac{1}{2}\left(\frac{\Delta_{1J}^2}{\sigma(\Delta_{1J}^2)} + \frac{\Delta_{2J}^2}{\sigma(\Delta_{2J}^2)}\right)\right). \tag{13}$$

By using the auxiliary variable $J = \Sigma_i \Sigma_j G_{ij} I_i I_j$, where G is the inverse matrix to the covariance matrix of Δ_{ij}, it is possible to write:

$$P\,(>\Delta_1) = \exp\left(-\frac{1}{2}J\right), \tag{14}$$

where the vector $\mathbf{I}$ is:

$$\mathbf{I} = \begin{pmatrix} \Delta_{11} \\ \Delta_{21} \end{pmatrix}. \tag{15}$$

The probability that the amplitude

$$\Delta = \left(\Delta_{11}^2 + \Delta_{21}^2 + \Delta_{12}^2 + \Delta_{22}^2\right)^{-\frac{1}{2}} \tag{16}$$

described by the four-dimensional Gaussian distribution, is greater than a certain chosen value is given by the formula:

$$P\,(>\Delta) = \left(1 + \frac{1}{2}J\right)\exp\left(-\frac{1}{2}J\right), \tag{17}$$

where vector $\mathbf{I}$ has the form:

$$\mathbf{I} = \begin{pmatrix} \Delta_{11} \\ \Delta_{21} \\ \Delta_{12} \\ \Delta_{22} \end{pmatrix} \tag{18}$$

In Kolmogorov-Smirnov test, the D_n statistic is calculated,

$$D_n = \sup|F(x) - S(x)| \tag{19}$$

which is the largest absolute difference between the theoretical distribution function $F(x)$ and the empirical distribution function $S(x)$, calculated on the basis of an ordered sample, and then the λ statistics is calculated:

$$\lambda = \sqrt{n} D_n. \tag{20}$$

In the Cramer-von Mises test, the W^2 statistic is computed:

$$W^2 = \sum_{i=1}^{n}\left(F(x_i) - \frac{2i-1}{2n}\right)^2 + \frac{1}{12n} \tag{21}$$

where $F(x_i)$ again is theoretical distribution. In the advanced modification, called Watson test, one uses statistic:

$$U^2 = W^2 - n\left(\bar{F} - \frac{1}{2}\right)^2 \tag{22}$$

where the average value $\bar{F} = \frac{1}{n}\sum_{i=1}^{n} F(x_i)$.

The "theoretical isotropic distributions" simulated as part of the new method for three examples of groups differing in size are presented in Figure 2. During the calculations, various variants of calculating the inclination angle were considered. The consequence of comparing the obtained distributions was the statement of a noticeable deviation caused by the addition of 3° to the inclination angle. The method used in some research works (see Tully 1988) to compensate for the failure to take into account morphological types by adding a 3° may therefore not meet its original assumption.

The results of the analysis of the distributions of δ_D and η angles for the Tully groups, performed using the new research method, are presented in Tables 1 and 2. Since the data from the Tully catalog have been subjected to statistical tests many times, e.g. in Godłowski 2011, Pajowska et. al. 2012, Godłowski and Mrzygłód 2023, it is possible to state that the results obtained using the new method are comparable to those obtained for known morphological types. In the case of both

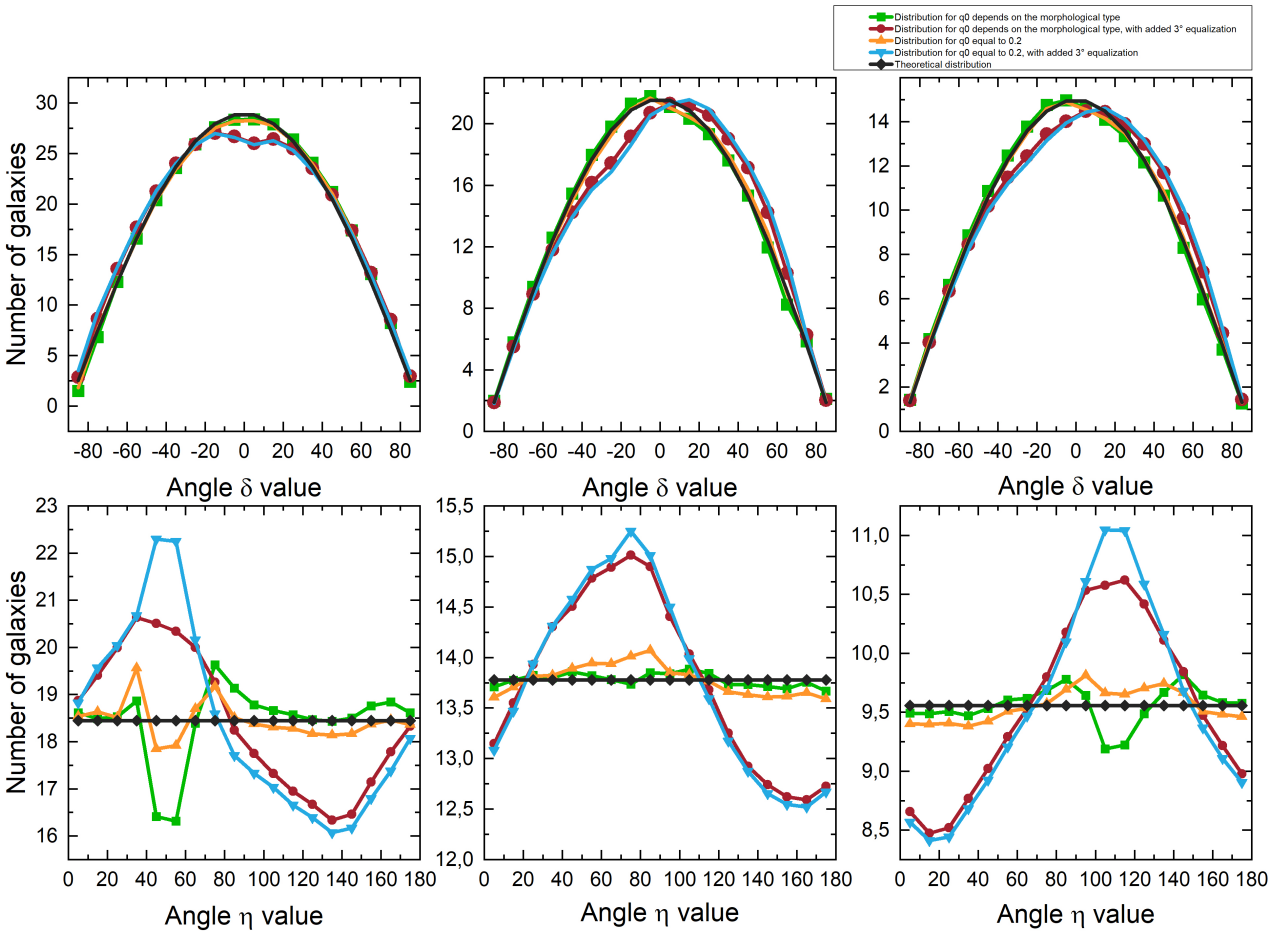

Figure 2: Simulated distributions of the angle δ_D and η for groups 12 (left panels), 21 (center panels) and 52 (right panels)

Table 1: Test for isotropy of the distribution of the angle δ_D of galaxies, obtained using the new method of investigation.

Group	N	χ^2	C	$\frac{\Delta_{11}}{\sigma(\Delta_{11})}$	Δ_1	Δ	$P(\Delta_1)$	$P(\Delta)$	λ	W^2	U^2
11	626	59.24	23.837	-5.127	0.302	0.288	0.0000	0.0000	1.340	0.9076	0.0284
12	332	23.51	0.701	-2.590	0.209	0.195	0.0346	0.1072	0.879	0.2563	-0.2613
13	128	22.40	-2.716	-0.299	0.048	0.174	0.9304	0.8442	0.405	0.0473	-0.1276
14	426	26.87	6.327	-2.483	0.183	0.215	0.0358	0.1166	0.900	0.2252	-0.6374
15	130	9.52	-1.566	-0.042	0.082	0.142	0.7928	0.8999	0.603	0.0975	0.0884
17	80	8.26	-2.106	-0.971	0.183	0.240	0.5284	0.6738	0.722	0.1157	0.1095
21	248	20.46	1.613	-0.759	0.218	0.298	0.0446	0.0695	1.267	0.7711	0.7104
22	126	6.81	-2.527	0.205	0.044	0.053	0.9384	0.9975	0.224	0.0095	-0.1159
23	100	10.41	1.246	0.471	0.073	0.160	0.8812	0.8719	0.438	0.0418	-0.0487
31	210	36.41	19.094	1.667	0.456	0.466	0.0000	0.0001	2.163	2.0593	1.5171
41	192	27.75	11.562	-0.274	0.312	0.392	0.0069	0.0017	1.804	0.9063	-0.6480
42	230	30.49	3.900	-0.431	0.188	0.333	0.1172	0.0522	1.269	0.6391	-0.9776
44	80	23.95	5.304	-0.990	0.316	0.390	0.1277	0.1055	1.213	0.3297	-0.1475
51	228	30.51	7.548	0.933	0.323	0.400	0.0021	0.0013	1.901	1.3166	1.0980
52	172	32.83	9.707	-2.363	0.412	0.399	0.0006	0.0019	1.841	1.0431	1.0122
53	260	21.10	-8.961	-0.429	0.146	0.152	0.2312	0.5331	0.715	0.2149	0.1665
61	258	14.47	1.584	-0.702	0.088	0.198	0.6123	0.3232	0.638	0.1630	-0.5230
64	102	15.93	0.741	0.666	0.227	0.229	0.2564	0.6032	0.904	0.2979	-0.3018

Table 2: Test for isotropy of the distribution of the angle η of galaxies, obtained using the new method of investigation.

Group	N	χ^2	C	$\frac{\Delta_{11}}{\sigma(\Delta_{11})}$	Δ_1	Δ	$P(\Delta_1)$	$P(\Delta)$	λ	W^2	U^2
11	626	51.09	34.516	5.977	0.362	0.364	0.0000	0.0000	2.083	1.4864	1.4824
12	332	38.26	14.673	-0.920	0.361	0.362	0.0000	0.0002	2.096	1.5317	-0.7605
13	128	14.28	-3.196	0.739	0.141	0.279	0.5306	0.2900	0.482	0.0908	-0.0924
14	426	30.46	2.379	1.485	0.206	0.210	0.0113	0.0521	1.801	0.8471	-0.9937
15	130	14.22	-0.256	0.451	0.064	0.198	0.8737	0.6347	0.723	0.1404	0.1404
17	80	34.01	-15.640	-0.414	0.315	0.317	0.1415	0.4103	0.990	0.2576	0.2576
21	248	33.80	3.921	1.321	0.239	0.248	0.0289	0.1073	1.630	0.5451	-0.5519
22	126	18.46	7.166	2.031	0.318	0.405	0.0417	0.0353	1.357	0.4754	0.4349
23	100	27.23	5.659	-1.408	0.473	0.513	0.0041	0.0111	1.571	0.7560	0.6315
31	210	18.66	4.842	1.580	0.202	0.291	0.1164	0.0629	1.289	0.4804	0.4539
41	192	30.01	18.142	3.521	0.451	0.476	0.0001	0.0002	2.036	1.0864	0.9845
42	230	32.96	6.630	-0.174	0.337	0.390	0.0015	0.0015	1.603	1.0393	-0.5294
44	80	19.60	-1.483	0.030	0.273	0.421	0.2254	0.1314	1.120	0.1952	-0.1201
51	228	26.59	-2.132	3.079	0.295	0.298	0.0070	0.0381	1.184	0.3519	0.3292
52	172	42.00	16.865	2.490	0.457	0.514	0.0001	0.0002	2.021	1.4674	1.1505
53	260	11.53	-5.162	0.520	0.047	0.050	0.8673	0.9880	0.266	0.0230	-0.1978
61	258	10.94	2.142	0.849	0.186	0.188	0.1072	0.3355	1.012	0.2731	-0.4037
64	102	52.33	2.005	3.120	0.526	0.683	0.0009	0.0001	2.149	1.5422	1.1508

Table 3: Test for isotropy of the distribution of the angle δ_D obtained using the values of q_0 depending on the morphological type and Fouque and Paturel correction.

Group	N	χ^2	C	$\frac{\Delta_{11}}{\sigma(\Delta_{11})}$	Δ_1	Δ	$P(\Delta_1)$	$P(\Delta)$	λ	W^2	U^2
11	626	29.10	-5.254	-1.302	0.087	0.111	0.3443	0.4907	0.677	0.0710	-0.5891
12	332	12.72	-4.261	-0.935	0.076	0.079	0.6408	0.9215	0.384	0.0455	-0.3625
13	128	27.84	2.881	1.754	0.251	0.438	0.1580	0.0280	0.786	0.2241	0.0307
14	426	19.25	6.103	0.000	0.033	0.219	0.9108	0.0589	0.623	0.1024	-0.7387
15	130	23.10	-7.212	0.799	0.134	0.200	0.5977	0.6819	0.789	0.0932	-0.2091
17	80	5.58	0.524	0.148	0.106	0.244	0.8311	0.7163	0.559	0.0890	0.0890
21	248	19.39	-6.411	0.285	0.084	0.190	0.6978	0.4134	0.889	0.1671	0.1328
22	126	14.82	3.054	0.675	0.120	0.176	0.6707	0.7872	0.707	0.1110	-0.1888
23	100	17.97	-1.012	1.602	0.264	0.318	0.2056	0.3434	0.614	0.1435	-0.0934
31	210	31.90	-0.093	1.240	0.233	0.279	0.0887	0.1243	0.966	0.2677	0.2560
41	192	11.74	5.787	1.044	0.179	0.269	0.2636	0.1864	0.722	0.2679	-0.4889
42	230	17.49	4.119	1.245	0.128	0.279	0.4208	0.0946	0.786	0.1954	-0.4389
44	80	12.06	0.588	-1.046	0.328	0.330	0.1610	0.4258	0.900	0.2598	-0.2228
51	228	17.44	-4.402	0.683	0.092	0.118	0.6561	0.8442	0.552	0.0833	0.0054
52	172	17.94	5.950	-1.504	0.364	0.358	0.0082	0.0450	1.454	0.7803	0.7109
53	260	9.79	-0.320	-0.698	0.077	0.109	0.7056	0.8484	0.523	0.0901	-0.5060
61	258	15.76	0.848	0.780	0.141	0.213	0.3385	0.2690	0.802	0.1902	0.1498
64	102	19.78	-0.098	0.481	0.172	0.226	0.5297	0.6798	0.594	0.0868	-0.1816

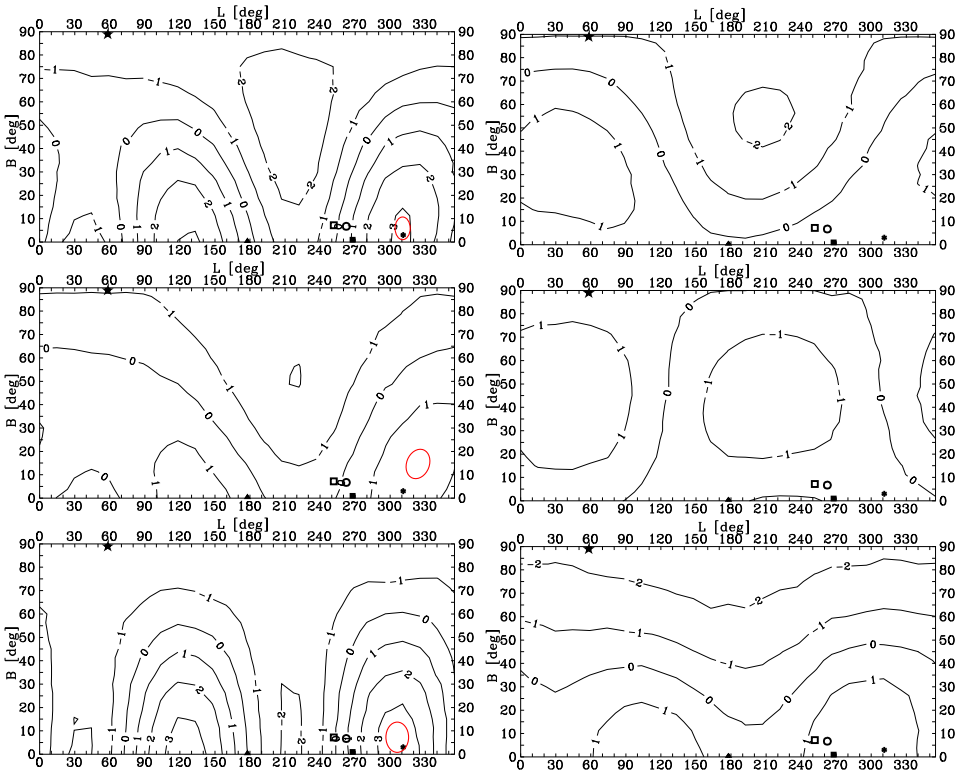

Figure 3: Maps of $s \equiv \Delta_{11}/\sigma(\Delta_{11})$ versus the chosen cluster pole supergalactic co-ordinates (L, B) for the cluster 12. In the maps, the results of the Tully data are shown on the left, while results obtained using the values of q_0 depending on the morphological type and Fouque and Paturel correction are given on the right. The maps are presented for ALL cluster galaxies (upper panel), for Spiral (middle panel) and Nonspiral (bottom panel) sub-samples. In the map important directions have been indicated, as seen from the centre of the considered cluster: 1.) three cluster poles (full star, square and triangle), 2.) the direction to the Local Supercluster centre (open circle), 3.) the direction of the Virgo A cluster centre (open square) and 4.) the line of sight from the Earth (asterisk). Red ellipses mark the maxima that correlate with the line of sight.

delta and eta angles, some groups showed that the distribution was non-random. However, the final result of the papers that analyzed the studied groups was that no significant alignment was observed.

The mere consideration of the morphological type does not lead to "fully satisfactory" analysis results, because there is a strong systematic effect in the NBG catalogue data, generated by the process of galactic axis de-projection from its optical image. This effect makes it significantly difficult to find the real alignment during analysis of the spatial orientation of galaxies in clusters, but it can be analyzed in more detail using the methodology described in Godłowski and Ostrowski 1999. For this purpose, for each angle δ_D for each cluster, is computed the Δ_{11} parameter describing the alignment of the axes galactic relative to the selected pole of the cluster, divided by its formal error $\sigma(\Delta_{11})$, denoted as $s \equiv \Delta_{11}/\sigma(\Delta_{11})$. Changing the position of the pole of the coordinate system along the celestial sphere causes the main plane of the system to also change its position. For each such instantaneous coordinate system, we the parameter s is computed. The maps resulted in this way can be analyzed in terms of the correlation of their maxima with important points on the maps. This procedure makes it possible to easily find both preferred and undesirable alignment directions normal to the galaxy planes, if any existed in these clusters. This is because if the rotation axes of galaxies preferred to be aligned in a certain plane, there would be a deficit in the rotation axis in the direction perpendicular to that plane. However, if the orientation of the rotation axes of galaxies favored a particular direction, then there should be a surplus of galaxies with spins pointing in that direction.

Example maps for cluster 12 are presented in Figure 3. In the left panels, obtained for the original NBG Catalog data, strong maxima are observed that correlate with the line of sight. Taking into account the morphological types of galaxies combined with converting q to standard photometric axial ratios according to the formulas of Fouque and Paturel (1985) makes these maxima disappear, as shown in the right panels. The results of the statistical analysis for the data after taking both of these corrections into

Table 4: Test for isotropy of the distribution of the angle η obtained using the values of q_0 depending on the morphological type and Fouque and Paturel correction.

Group	N	χ^2	C	$\frac{\Delta_{11}}{\sigma(\Delta_{11})}$	Δ_1	Δ	$P(\Delta_1)$	$P(\Delta)$	λ	W^2	U^2
11	626	36.84	14.121	3.574	0.213	0.278	0.0009	0.0001	1.101	0.4450	0.0557
12	332	17.37	2.464	-0.595	0.097	0.154	0.4599	0.4165	0.860	0.2365	-0.5615
13	128	17.12	6.297	1.208	0.165	0.382	0.4194	0.0529	1.110	0.2416	0.2405
14	426	14.96	0.338	0.469	0.112	0.144	0.2655	0.3551	0.775	0.1649	-0.5359
15	130	13.72	2.092	0.132	0.115	0.278	0.6530	0.2863	0.643	0.1576	0.1575
17	80	9.10	0.550	-0.135	0.118	0.229	0.7567	0.7188	0.683	0.1061	0.1052
21	248	17.35	-4.710	-0.031	0.064	0.122	0.7749	0.7616	0.564	0.0917	0.0438
22	126	16.57	-2.571	0.172	0.031	0.242	0.9707	0.4506	0.535	0.0286	-0.0656
23	100	10.16	-0.820	-0.856	0.149	0.174	0.5729	0.8232	0.444	0.0477	-0.0294
31	210	17.31	-0.514	1.270	0.147	0.228	0.3238	0.2418	1.104	0.3029	0.3005
41	192	24.38	0.375	2.631	0.289	0.344	0.0181	0.0228	0.962	0.2555	0.1976
42	230	16.05	0.478	-0.083	0.117	0.221	0.4551	0.2283	0.879	0.2468	-0.4326
44	80	14.05	1.000	0.407	0.096	0.393	0.8306	0.1871	0.472	0.0678	0.0524
51	228	28.58	0.158	1.468	0.150	0.249	0.2769	0.1317	1.214	0.4058	0.3993
52	172	17.63	4.651	1.095	0.310	0.314	0.0161	0.0758	1.339	0.6194	0.5459
53	260	14.85	-4.192	0.113	0.121	0.136	0.3857	0.6592	0.675	0.0943	0.0221
61	258	11.86	0.977	1.316	0.133	0.195	0.3174	0.2960	0.955	0.2249	0.2211
64	102	12.71	2.118	1.805	0.274	0.281	0.1482	0.4019	0.627	0.1198	0.0714

account are presented in Tables 3 and 4. The failure to observe any significant alignment for either group indicates that the orientation of the galaxies in the studied Tully groups is random. These results are therefore analogous to those in other research papers regarding this catalog.

4. Conclusions

Data from the Tully Nearby Galaxies Catalog, combined with the results of research analyzing the groups of galaxies used, made it possible to confirm the effectiveness of the new research method. The obtained results indicate that the method may be important in future studies of galaxy clusters. In the case of any astronomical data, the use of the method will involve carrying out an analysis using the designated "theoretical isotropic distributions", which will be previously compared with the "observational" distributions obtained assuming the value of the parameter q_0 equal to 0.2. Since, according to the current view, in the case of catalogs based on automatic galaxy measurements, the Holmberg effect should not be significant, consequently the new method, unlike in the case of the NBG Catalog, can be used without taking into account the photometric correction. Otherwise, however, it will be necessary to first independently estimate this type of correction.

The results of galaxy investigations of orientation are particularly important because they provide information for testing scenarios of the formation of galaxies and their structures. The result obtained in this paper is consistent with the new version of the hierarchical clustering model, which takes into account tidal effects (Catelan & Theuns 1996), as well as with the Li model (Li 1998). According to the current state of knowledge, the ordering of galaxies in clusters increases with their number. For this reason, in small clusters such as Tully's groups, alignment should not be observed - which has been confirmed.

References

Catelan P., Theuns T.: 1996, *Mon. Not. R. Astr. Soc.*, **282**, 436.

Doroshkevich A.G.: 1973, *ApL*, **14**, 11.

Flin P., Godłowski W.: 1986, *Mon. Not. R. Astr. Soc.*, **222**, 525.

Fouque, P.; Paturel, G.: 1985 *Astron. Astroph.*, **150**, 192.

Godłowski W.: 2011, *Acta Phys. Pol. B*, **42**, 2323.

Godłowski W.: 2012, *Astrophys. J.*, **747**, 7.

Godłowski W., Flin P.: 2010, *Astrophys. J.*, **708**, 920.

Godłowski W., Mrzygłód B.: 2023, *Appl. Sci.*, **13**, 4845.

Godłowski W., Ostrowski M.: 1999, *Mon. Not. R. Astr. Soc.*, **303**, 50.

Hawley D. I., Peebles P.J.E.: 1975, *Astron. J.*, **80**, 477.

Heidmann, J.; Heidmann, N.; de Vaucouleurs, G.: 1972, *Mem. R. Astron. Soc.*, **75**, 85.

Holmberg, E.: 1946, *Medd. Lund. Astron. Obs. Ser. II*, **117**, 3.

Holmberg, E.: 1958, *Medd. Lund. Astron. Obs. Ser. II*, **136**, 1.

Holmberg, E.: *Galaxies and the Universe*; Sandage,

A., Sandage, M., Kristian, J. Eds.; University of Chicago Press: Chicago, USA, 1975; pp. 123.
Jaaniste, J.: 1977 *Tartu Obs.*, 50.
Jaaniste, J.; Saar, E.: *The large scale structures of the Universe.*; Longair, M.S., Einasto, J., Eds.; D. Reidel Publishing Co. (IAU Symposium, No. 79), 1978; pp. 488.
Joachimi, B., et al.: 2015 *Space Sci. Rev.*, **193**, 1.
Kiessling, A., Cacciato, M., Joachimi, B., et al.: 2015, *Space Sci. Rev.*, **193**, 67.
Li, Li-Xin.: 1998, *Gen. Rel. Grav.*, **30**, 497.
Öpik, E. J.: 1970, *Ir. Astron. J.*, **9**, 211.
Pajowska, P.; Godlowski, W.; Panko, E.; Flin, P.: 2012, *J. Phys. Stud.*, **16**, 4901.
Pajowska, P.; Godłowski, W.; Zhu, Z.-H.; Popiela, J.; Panko, E.; Flin, P.: 2019, *J. Cosmol. Astropart. Phys.*, **2**, 5.
Peebles P. J. E.: 1969, *Astrophys. J.*, **155**, 393.
Peebles, P. J. E.; Yu, J. T.: 1970, *Astrophys. J.*, **162**, 815.
Romanowsky, A. J., Fall, S. M.: 2015, *Astrophys. J., Suppl. Ser.* , **203**, 17.
Shandarin S. F.: 1974, *Sov. Astr.*, **18**, 392.
Silk J.: 1968, *Astrophys. J.*, **151**, 459.
Stephanovich, V. A.; Godłowski, W.: 2015, *Astrophys. J.*, **810**, 14.
Sunyaev A. R., Zeldovich Ya.B.: 1970, *Astrophys. Space Sci.*, **7**, 3.
Tully, R. B.: 1987, *Astrophys. J.*, **321**, 280.
Tully, R. B. *Nearby Galaxies Catalogue (NBG)*, 2nd ed.; Cambridge University Press: Cambridge, United Kingdom, 1988.
Zeldovich B. Ya.: 1970, *Astron. Astrophys.*, **5**, 84.

https://doi.org/10.18524/1810-4215.2023.36.289969

MELTING HADRONS, BOILING QUAKRS AND GLUONS

István Szanyi[1], Tamás Biró[1], László Jenkovszky[2], Vladyslav Libov[2]

[1] Wigner Research Centre for Physics,
Budapest, Hungary, *sz.istvan03@gmail.com*
[2] Bogolyubov ITP,
Kyiv, Ukraine, *jenk@bitp.kiev.ua*

ABSTRACT. Resonance spectra (Hagedorn distribution) are critically revised with emphasis on the saturation of hadron states and possible transition to a soup of quarks and gluons. Previous studies in this direction are extended by use of non-linear, complex Regge trajectories whose limited real part supports the idea of saturation of high-mass/spin resonance production.

Keywords: hadrons, resonances, Hagedorn spectrum, Regge trajectories, quarks, gluons.

АННОТАЦІЯ. В роботі проведено аналіз адронних спектрів (розподіл Хагедорна) з акцентом на можливість насичення адронних станів та переходом їх до "варева" (супу) з кварків та глюонів. Основні результати даної роботи такі:

1) досліджено спектр мезонів та баріонів в області великих мас;

2) з'ясована роль критичної температури в статистичній моделі Хагедорна;

3) проаналізовані наслідки конечності спектра Хагедорна;

4) дана статистична інтерпретація фазового переходу від адронів до кварків та глюонів в термінах рівняння стану. Унікальною рисою отриманого рівняння стану є наявність в ньому від'ємної температури та переохолодження речовини.

В більшості відомих теорій та моделей траєкторії Редже є лінійні та реальні функції, що не допускає застосування їх для реальних резонансів. Результати попередніх аналізів в цьому напрямку нами розширено завдяки застосуванню нелінійних комплексних траєкторій Редже, в яких зростання реальної частини є обмежений, що підтверджує насичення процесу народження резонансів з великими масами. Приведені конкретні моделі таких траєкторій, а саме: траєкторії з кореневими порогами та такі, що слідують з дисперсійних співвідношень. Параметри приведених моделей траєкторій Редже верифіковано за допомогою порівняння з експериментальними даними про мезонні та баріонні резонанси. В цілому, робота є внеском в дослідження одної з важливих та загадкових проблем фізики високих енергій – конфайнменту кварків та глюонів на прикладі переходу важких адронних резонансів в новий агрегатний стан речовини, можливо – кварк-глюонну плазму, властивості якої ще до кінця не з'ясовано.

Ключові слова: Адрони, резонанси, спектр Хагедорна, траєкторії Редже, кварки, глюони.

1. Introduction

The spectrum of hadron resonances is among the central problems of high-energy physics since the properties of highly excited resonances are intimately connected with the problem of confinement.The idea of the resonance gas was suggested by Belenky and Landau, who used the Bethe-Uhlenbeck method for non-ideal gases. The field was revitalized in a series of papers by Rolf Hagedorn (Hagedorn), and followers who introduced the notion of limited temperature, that later received various modifications and interpretations . In a recent paper (Szanyi, 2023) we extended Hagedorn's approach by combining statistical physics with the analytic $S-$matrix theory, realized by the Regge-pole model.

Here we the spectrum of hadronic resonances by relating seemingly two different approaches: statistical - that of Hagedorn and Regge.

The density of hadron states follows the law

$$\rho(m) = f(m) \exp(m/T_H), \tag{1}$$

where $f(m)$ is a slowly varying function of mass and T_H is the Hagedorn temperature, originally considered as the limiting temperature but later re-interpreted as the temperature of the color deconfinement phase transition where hadrons "boil"transforming matter into a boiling quark-gluon soup.

Over 50 years after the publication of R. Hagedorn's paper (Hagedorn) on the spectrum of resonances

many important details still remain open. In spite of many efforts, the calculated value of the Hagedorn temperature shows a surprisingly widespread from $T_H = 141$ MeV to $T_H = 340$ MeV, depending on the parametrization and the set of data (baryons, mesons) used. The discrepancies may have different origin, in particular: a) the large uncertainties in the specification and identification of heavy resonances, b) the analytical form of the Hagedorn spectrum, in particular, the form of the function $f(m)$ multiplying Hagedorn's exponential. In the present paper, we address both issues.

Our approach here is limited to the world of observed resonances, summarized by the Particle Data Group and theoretical methods based on analyticity, unitarity, and duality.

Crucial in our paper is the identification of the function $f(m)$ with the derivative of the relevant Regge trajectory. In the spirit of the analytic S-matrix approach, Regge trajectories encode an essential part of the strong interaction dynamics, they are building blocks of the theory. There were many attempts to find analytic forms of the non-linear complex Regge trajectories, based on mechanical analogues (strings), quantum chromodynamics etc. Below we rely on duality and constraints based on analyticity and unitarity, constraining the threshold and asymptotic behaviour of the trajectories. An important constraint, affecting the spectrum near its critical point is the upper bound on the real part of Regge trajectories', coming from dual models with Mandelstam analyticity. Construction of explicit models of the trajectories satisfying the above constraints is a non-trivial problem. In the present paper, we propose explicit models of such trajectories allowing explicit calculations and compatible with the data on resonances.

Below we argue that while Hagedorn's exponential rise comes mainly from the proliferation of spin and isospin degeneracy of states with increasing mass, that can be counted directly, the prefactor $f(m)$ reflects dynamics, encoded in Regge trajectories given that $f(m) = \alpha'(m)$, where $\alpha'(m)$ is the slope of the trajectory.

The low-mass, $m < 1.8$ GeV spectra do not exhibit any surprise by following Hagedorn's exponential. The only open questions are the value of the Hagedorn temperature T_H and possible differences between the spectra for various particles. The spectra beyond $m = 1.8$ GeV are different: on the experimental side, the high-mass resonances tend to gradually disappear, their status becoming uncertain.

The most important issue is the existence of a "melting point"where the resonances are transformed to a continuum of a boiling soup of quarks and gluons. This critical region/point is studied by various methods: statistics and thermodynamics, quantum.

2. Melting hadrons

In this Section we study the relation between the mass density of hadronic states given by the Hagedorn spectrum and the dynamics emerging from Regge pole models, inspecting non-linear Regge trajectories.

In spite of the huge number of papers, the subject remains a topical problem of hadron dynamics with numerous open questions. We address the following issues:

- the behavior of the meson mass spectrum in the high-mass region;
- the role of the critical temperature and the prefactor in $\rho(m)$ in the Hagedorn model of hadronic spectra;
- the finiteness of the Hagedorn spectrum and its consequences.

The expression for pressure in this thermodynamic approach in the Boltzmann approximation is given by:

$$p = \sum_i g_i p(m_i) = \int_{M_1}^{M_2} dm\, \rho(m)\, p(m), \tag{2}$$

with

$$p(m) = \frac{T^2 m^2}{2\pi^2} K_2\left(\frac{m}{T}\right), \tag{3}$$

where M_1 and M_2 are the masses of the lightest and heaviest hadrons, respectively, and g_i-s are particle degenerations.

For fixed isospin and hypercharge a cubic density of states, $\rho(m) \sim m^3$, fits the data. Moreover, the cubic spectrum can be related to collinear Regge trajectories. Indeed, following the arguments of Burakovsky and Horowitz (Burakovsky & Horowitz) , on a linear trajectory with negative intercept, $\alpha(t) = \alpha' t - 1$, some integer values of $\alpha(t) = J$ correspond to states with negative spin, $J = \alpha(t_J)$, with squared masses $m^2(J) = t_J$. Since a spin-J state has multiplicity $2J+1$, the total number of states with spin $0 \le J \le j$ at $t = m(j)^2$ is given by

$$N(j) = \sum_{J=0}^{j} (2J+1) = (j+1)^2 = \alpha'^2 m^4(j). \tag{4}$$

Hence the density of states per unit mass interval is obtained as the derivative of this cumulative quantity,

$$\rho(m) = \frac{dN(m)}{dm} = 4\alpha'^2 m^3, \tag{5}$$

and it grows as the cubic power of the mass. Consequently for a finite number of collinear trajectories, N, the corresponding mass spectrum is given as

$$\rho(m) = 4N\alpha'^2 m^3. \tag{6}$$

A different view on the spectra was advocated by E. Shuryak (Shuryak), who suggested to use a quadratic parametrization, completely different from the conventional form:

$$\rho(m) \sim m^2.$$

In both the statistical bootstrap model and in the dual resonance model, the resonance spectrum takes the form of Eq. (1). In the dual resonance model $f(m) \sim \frac{d}{dm}\Re\alpha(m^2)$. We use non-linear complex Regge trajectories to determine this pre-factor as discussed in the next subsections.

The meson and baryon spectra differ, in particular by their slopes. More important is the question of the asymptotic behaviour of $\rho(m)$ for large masses. In theory, Hagedorn's exponential may rise indefinitely, however, starting from $m \approx 2.5$ GeV resonances are not observed. The question arises whether it is a "technical"issue (the resonances gradually fade becoming too wide to be detected) or there is a critical point where they melt to a continuum transforming the hadron matter to a "boiling soup". This point can be illuminated by means of Regge trajectories, as we demonstrate it in what follows.

We concentrate on the meson spectrum, more specifically that of ρ and its excitations. This familiar trajectory is chosen just as a representative example. Other trajectories, including baryonic ones as well as those with heavy (c and b) flavors will be studied later. We are interested in the high-mass behavior, starting from $m \approx 1.8$ GeV. Beyond this value the exponential behavior of the Hagedorn spectrum is expected to change drastically. We concentrate on its behaviour above 1.8 GeV.

Note that rather than comparing the density of states $\rho(m)$ to the data it is customary to accumulate states of masses lower than m,

$$N_{exp} = \sum_i g_i \Theta(m - m_i), \tag{7}$$

where g_i is the degeneracy of the i-th state with mass m_i in spin J and isotopical spin I, i.e.,

$$g_i = \begin{cases} (2J_i+1)(2I_i+1), & \text{for non-strange mesons} \\ 4(2J_i+1), & \text{for strange mesons} \\ 2(2J_i+1)(2I_i+1), & \text{for baryons} \end{cases}$$

The theoretical equivalent of Eq. (7) is

$$N_{theor}(m) = \int_{m_\pi}^{m} \rho(m')dm', \tag{8}$$

where the lower integration limit is given by the mass of the pion. We identify $f(m)$ in $\rho(m)$ with the slope of the relevant non-linear complex Regge trajectory $\alpha'(m)$. In the next subsection we discuss the properties of these trajectories following from the analytic $S-$matrix theory and duality, and present an explicit example of such a trajectory.

3. Regge trajectories

At low and intermediate masses, light hadrons fit linear Regge trajectories with a universal slope, $\alpha' \approx 0.85$ GeV^2. As masses increase, the spectrum changes: resonances tend to disappear. The origin and details of this change are disputable.

Termination of resonances, associated with a "ionization point"was also studied in a different class of dual models, based on logarithmic trajectories [**?**].

Possible links between the Hagedorn spectra and Regge trajectories appear in the statistical bootstrap and dual models, according to which the pre-factor $f(m)$ in Eq. (1) depends on the slope of the relevant Regge trajectory, $\alpha'(m^2)$, which is constant for linear Regge trajectories.

We extend the Hagedorn model by introducing the slope of relevant non-linear Regge trajectories. Anticipating a detailed quantitative analysis, one may observe immediately that a flattening of $\Re\alpha(s = m^2)$ [1], results in a decrease of the relevant slope $\alpha'(m)$ and a corresponding change in the Hagedorn spectrum. Following Eq. (1) we parametrize

$$\rho(m) = \left(\frac{d}{dm}\Re\alpha(m^2)\right) \times \exp(m/T_H). \tag{9}$$

Based on the decreasing factor $\Re\alpha'$ in Eq. (9) the exponential rise of the density of states slows down near to the melting point around $m \approx 2 - 2.5$ GeV. The cumulative spectrum Eqs. (7) and (8), accordingly tends to a constant value.

Any Regge trajectory should satisfy the followings:

- threshold behavior imposed by unitarity;
- asymptotic constraints: the rise of real part of Regge trajectories is limited, $\Re\alpha(s) \leq \gamma\sqrt{t}\ln t, \quad s \to \infty$;
- compatibility with the nearly linear behavior in the resonance region (Chew-Frautschi plot).

The threshold behavior of Regge trajectories is constrained by unitarity. t-channel unitarity constrains the Regge trajectories near the threshold, $t \to t_0$ to the form

$$\Im\alpha(t) \sim (t - t_0)^{\Re\alpha(t_0)+1/2}. \tag{10}$$

Here t_0 is the lightest threshold, *e.g.* $4m_\pi^2$ for the meson trajectories. Since $\Re\alpha(4m_\pi^2)$ is small, a square-root threshold is a reasonable approximation to the above constraint.

[1] We use the (here positive) variables s or t interchangeably with crossing-symmetry in mind.

In the resonance region below flattening near $m = \sqrt{s} < 2.5$ MeV the meson and baryon trajectories are nearly linear (Chew-Frautschi plot). Fixed-angle scaling behavior of the amplitude constrains the trajectories even more, down to a logarithmic behavior.

There are several reasons why the non-linear and complex nature of the Regge trajectories is often ignored, namely: 1) the observed spectrum of meson and baryon resonances (Chew-Frautschi plot) seem to confirm their linearity; 2) in the scattering region, $t < 0$, the differential cross-section, $d\sigma/dt \sim \exp((2\alpha(t) - 2)\ln s)$ is nearly exponential in t; 3) Dual models, *e.g.* the Veneziano amplitude are valid only in the narrow-width approximation, corresponding to linear Regge trajectories (hadronic strings). Deviation from linearity is unavoidable, but its practical realization is not easy.

4. Models of Regge trajectories

Unitarity imposes a severe constraint on the threshold behaviour of the trajectories:

$$\Im m\alpha(t)_{t\to t_0} \sim (t - t_0)^{\Re e\alpha(t_0)+1/2}, \qquad (11)$$

while asymptotically the trajectories are constrained by dual amplitude with Mandelstam analyticity

$$\left|\frac{\alpha(t)}{\sqrt{t}\ln t}\right|_{t\to\infty} \leq \text{const.} \qquad (12)$$

The above asymptotic constraint can be still lowered to a logarithm by imposing wide-angle power behaviour for the amplitude.

The above constraints are restrictive but still leave much room for model building.

While the parameters of meson and baryon trajectories can be determined both from the scattering data and from the particles spectra, this is not true for the pomeron (and odderon) trajectory, known only from fits to scattering data (negative values of its argument). An obvious task is to extrapolate the pomeron trajectory from negative to positive t-values to predict glueball states at $J = 2, 4, ...$, for which, however, no experimental evidence exists so far. Given the nearly linear form of the pomeron trajectory, known from the fits to the (exponential) diffraction cone, little room is left for variations in the region of particles ($t > 0$).

4.1. Additive thresholds

Apart from the Pomeron trajectory, the direct-channel f trajectory is essential in the proton-proton system. Guided by conservation of quantum numbers, we include two f trajectories, labelled f_1 and f_2, with mesons lying on these trajectories.

The real and imaginary part of the f_1 and f_2 trajectories can be derived from the parameters of the f-resonances.

To be consistent with the meson trajectories, the linear term is replaced by a heavy threshold mimicking linear behaviour in the mass region of interest (M < 5 GeV),

$$\alpha_P(M^2) = \alpha_0 + \alpha_1(2m_\pi - \sqrt{4m_\pi^2 - M^2}) + \\ +\alpha_2(\sqrt{M_H^2} - \sqrt{M_H^2 - M^2}), \qquad (13)$$

with M_H an effective heavy threshold $M = 3.5$ GeV.

The $f_0(500)$ resonance. The experimental data on central exclusive pion-pair production measured at the energies of the ISR, RHIC, TEVATRON and the LHC collider all show a broad continuum for pair masses $m_{\pi^+\pi^-} < 1$ GeV/c^2. The population of this mass region is attributed to the $f_0(500)$. This resonance $f_0(500)$ is of prime importance for the understanding of the attractive part of the nucleon-nucleon interaction, as well as for the mechanism of spontaneous breaking of chiral symmetry. In spite of the complexity of the $f_0(500)$ resonance, and the controversy on its interpretation and description, we take here the practical but simple-minded approach of a Breit-Wigner resonance

$$A(M^2) = a\,\frac{-M_0\Gamma}{M^2 - M_0^2 + iM_0\Gamma}. \qquad (14)$$

The Breit-Wigner amplitude of Eq. (14) is used below for calculating the contribution of the $f_0(500)$ resonance to the Pomeron-Pomeron cross section.

4.2. Dispersion relations

Meson trajectories. The nearly linear real part of the meson trajectory can be elated to its imaginary part by

$$\Re e\,\alpha(s) = \alpha(0) + \frac{s}{\pi}PV\int_0^\infty ds'\,\frac{\Im m\,\alpha(s')}{s'(s'-s)}. \qquad (15)$$

In Eq. (15), PV denotes the Cauchy Principal Value of the integral. The imaginary part is related to the decay width by

$$\Gamma(M_R) = \frac{\Im m\,\alpha(M_R^2)}{\alpha'\,M_R}. \qquad (16)$$

The quantity α' in Eq. (16) denotes the derivative of the real part, $\alpha' = \frac{d\Re e\,\alpha(s)}{ds}$. The relation between $\Gamma(M)$ and $\Im m\,\alpha$(s) requires $\Im m\,\alpha(s) > 0$. In a simple analytical model, the imaginary part is chosen as a sum of single threshold terms

Table 1: Parameters of resonances belonging to the f_1 and f_2 trajectories.

	I^G	J^{PC}	traj.	M (GeV)	M^2 (GeV^2)	Γ (GeV)
$f_0(980)$	0^+	0^{++}	f_1	0.990±0.020	0.980±0.040	0.070± 0.030
$f_1(1420)$	0^+	1^{++}	f_1	1.426±0.001	2.035±0.003	0.055± 0.003
$f_2(1810)$	0^+	2^{++}	f_1	1.815±0.012	3.294±0.044	0.197± 0.022
$f_4(2300)$	0^+	4^{++}	f_1	2.320±0.060	5.382±0.278	0.250± 0.080
$f_2(1270)$	0^+	2^{++}	f_2	1.275±0.001	1.6256±0.003	0.185± 0.003
$f_4(2050)$	0^+	4^{++}	f_2	2.018±0.011	4.0723±0.044	0.237± 0.018
$f_6(2510)$	0^+	6^{++}	f_2	2.469±0.029	6.096±0.143	0.283± 0.040

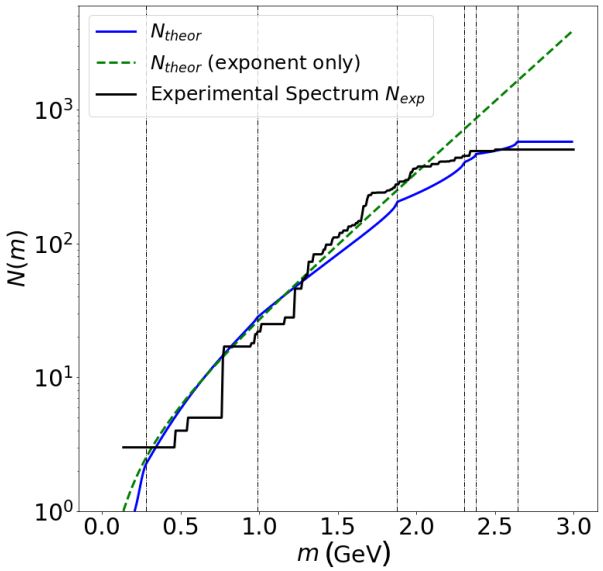

Figure 1: Hadron mass spectrum N_{theor} from Eq. (8) compared with the data. Additionally, N_{theor} obtained from a simple exponential mass density is also shown (dashed line).

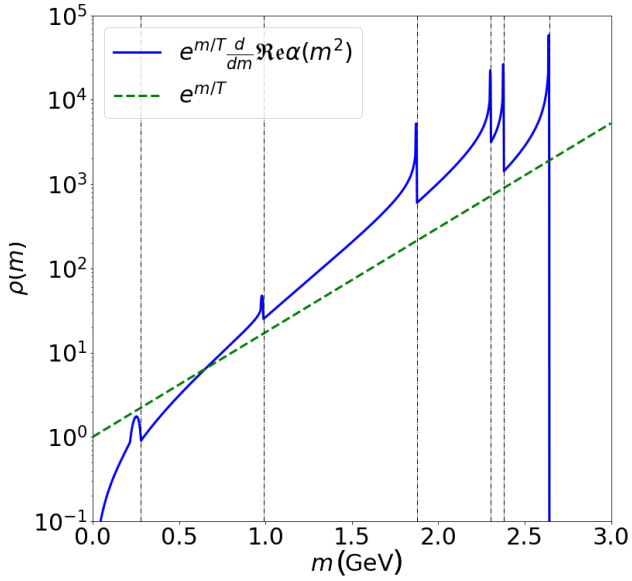

Figure 2: Mass density $\rho(m)$ calculated by using the derivative of the smoothed ρ-meson trajectory as a prefactor. The exponential density without any prefactor is also shown (dashed line), using the same temperature and normalization. Above the highest threshold the derivative, and hence the density vanishes (not seen due to the logarithmic scale).

$$\Im m\,\alpha(s) = \sum_n c_n (s-s_n)^{1/2} \Big(\frac{s-s_n}{s}\Big)^{|\Re e\,\alpha(s_n)|} \theta(s-s_n). \tag{17}$$

The imaginary part of the trajectory shown in Eq. (17) has the correct threshold and asymptotic behaviour. The highest threshold, higher than all the resonance masses lying on the trajectory, is chosen as an effective threshold. This highest threshold ensures that $\Re e\,\alpha(s)$ tends to a constant value for $s \to \infty$.

Calculated mass spectra and mass densities are shown in Fig. 1 and Fig. 2.

Baryon trajectories. The Pomeron-proton channel, $Pp \to M_X^2$ couples to the proton trajectory, with the $I(J^P)$ resonances: $1/2(5/2^+)$, F_{15}, m = 1680 MeV, Γ = 130 MeV; $1/2(9/2^+)$, H_{19}, m = 2200 MeV, Γ = 400 MeV; and $1/2(13/2^+)$, $K_{1,13}$, m = 2700 MeV, Γ = 350 MeV. The status of the first two is firmly established, while the third one, $N^*(2700)$, is less certain, with its width varying between 350 ± 50 and 900 ± 150 MeV . Still, with the stable proton included, we have a fairly rich trajectory, $\alpha(M^2)$.

We use the explicit form of the trajectory, ensuring correct behaviour of both its real and imaginary parts. The imaginary part of the trajectory can be written in

the following way:

$$\mathcal{I}m\,\alpha(s) = s^{\delta}\sum_n c_n\left(\frac{s-s_n}{s}\right)^{\lambda_n}\cdot\theta(s-s_n)\,, \quad (18)$$

where $\lambda_n = \mathcal{R}e\ \alpha(s_n)$. Eq. (18) has the correct threshold behaviour, while analyticity requires that $\delta < 1$. The boundedness of $\alpha(s)$ for $s \to \infty$ follows from the condition that the amplitude, in the Regge form, should have no essential singularity at infinity in the cut plane.

The real part of the proton trajectory is given by

$$\mathcal{R}e\,\alpha(s) = \alpha(0) + \frac{s}{\pi}\sum_n c_n\mathcal{A}_n(s)\ , \quad (19)$$

where

$$\mathcal{A}_n(s) = \frac{\Gamma(1-\delta)\Gamma(\lambda_n+1)}{\Gamma(\lambda_n-\delta+2)s_n^{1-\delta}}{}_2F_1\left(1,1-\delta;\lambda_n-\delta+2;\frac{s}{s_n}\right)\times\theta(s_n-s) + \left\{\pi s^{\delta-1}\left(\frac{s-s_n}{s}\right)^{\lambda_n}\cot[\pi(1-\delta)] - \frac{\Gamma(-\delta)\Gamma(\lambda_n+1)s_n^{\delta}}{s\Gamma(\lambda_n-\delta+1)}{}_2F_1\left(\delta-\lambda_n,1;\delta+1;\frac{s_n}{s}\right)\right\}\theta(s-s_n)\ .$$

The proton trajectory, also called N^+ trajectory, contains the baryons N(939) $\frac{1}{2}^+$, N(1680) $\frac{5}{2}^+$, N(2220) $\frac{9}{2}^+$ and N(2700) $\frac{13}{2}^+$. In the fit, the input data are the masses and widths of the resonances. The quantities to be determined are the parameters c_n, δ and the thresholds s_n. We set $n = 1, 2, x$ and $s_1 = (m_\pi + m_N)^2 = 1.16$ GeV^2, $s_2 = 2.44$ GeV^2 and $s_x = 11.7$ GeV^2.

Other parameters of the trajectory, obtained in the fit, are summarized below: $\alpha(0) = -0.41$, $\delta = -0.46 \pm 0.07$, $c_1 = 0.51 \pm 0.08$, $c_2 = 4.0 \pm 0.8$ and $c_x = (4.6 \pm 1.7)\cdot 10^3$. Taking the central values of these parameters we obtain the following values for the λ's: $\lambda_1 = 0.846$, $\lambda_2 = 2.082$, $\lambda_x = 11.177$.

A typical curve of meson mass spectrum calculated by means of trajectory with additive threshold is shonw in Fig. 1. The resulting mass density is shown in Fig. 1.

5. Boiling quarks and gluons

In the previous section, we inspected the spectrum of resonances by combining two different approaches - statistical (Hagedorn) and dynamical (Regge). We have focused on the region of heaviest resonances, the region where hadrons may melt transforming in a boiling "soup"of quarks and gluons. Melting may happen in different ways, characterized by the details for a phase transition of colorless hadronic states into a quark-gluon soup. In terms of hadron strings this process corresponds to breakdown (fragmentation) of a string. Lacking any theory of confinement providing a quantitative description of interacting string, we will not pursue this model. Instead we use thermodynamics adequate in this situation. To complement the previous section, we present our arguments below related to the possible change of phase from a different, thermodynamic perspective.

The Hagedorn exponential spectrum of resonances Eq. (1) results in a singularity in the thermodynamic functions at critical temperature $T = T_c$ and in an infinite number of effective degrees of freedom in the hadronic phase. Furthermore, the Hagedorn-like mass spectrum is incompatible with the existence of the quark-gluon phase. To form a quark phase from the hadronic phase, the hadron spectrum cannot grow more quickly than a power. This is possible in case of a simple power parametrization $\rho \sim m^k$, compatible with $k \approx 3$, for the observable mass spectrum in the interval 0.2–1.5 GeV. Assuming ideal contributions to thermodynamical quantities we hence take energy density in the form

$$\epsilon = \int_0^\infty \rho(m)T^4\sigma(m/T)dm = \lambda_k T^{k+5}, \quad (20)$$

and obtain the corresponding pressure and sound velocity square as follows[2]:

$$p = \frac{\lambda_k}{k+4}T^{k+5}, \quad c_s^2 = 1/(k+4). \quad (21)$$

It can be shown that the existence of the forward cone in hadronic interactions with non-decreasing total cross sections, *i.e*, pomeron dominance, confirmed by numerous experiments at high energies, results in an asymptotic, $T \gg m$ EOS $p(T) \sim T^6$ where m is a characteristic hadron (e.g. pion) mass. The inclusion of non-asymptotic (secondary) Regge terms produces a minimum in the $p(T)$ dependence at negative pressure, with far-reaching observable consequences.

The unorthodox $p \sim T^6$ asymptotic behavior is orthogonal to the "canonical"(perturbative QCD) form $\sim T^4$. Still, it cannot be rejected e.g. when assuming a screening of the action of large-distance van der Waals forces at high temperatures and densities.

The asymptotic form $\sim T^6$ can be extended to lower temperatures by adding non-asymptotic Regge-pole exchanges. The resulting EOS is

$$p(T) = aT^4 - bT^5 + cT^6, \quad (22)$$

where a, b, c are parameters connected with Regge-pole fits to high-energy hadron scattering. The

[2]Note that the definition of entropy density s, energy density ϵ and velocity of sound c_s in case of $\mu = 0$:

$$s(T) = p'(T),\ \epsilon(T) = Ts - p,\ \ c_s^2 = \frac{dp}{d\epsilon} = \frac{p'}{Tp''} = \frac{s}{Ts'}.$$

remarkable property of this EOS, apart from the non-standard asymptotic behavior, $\sim T^6$, is the appearance of the non-asymptotic term T^5 with negative sign, creating a local minimum with negative pressure. This metastable state with negative pressure can produce inflation of the universe.

The standard bag equation of state assuming, for simplicity, vanishing chemical potential, $\mu = 0$:

$$p_q(T) = \frac{\pi^2}{90}\nu_q T^4 - B, \tag{23}$$

$$p_h(T) = \frac{\pi^2}{90}\nu_h T^4, \tag{24}$$

where $p_q(T)$ and $p_h(T)$ are pressure in the quark-gluon plasma (QGP) and in the hadronic gas phase, respectively, B is the bag constant, and $\nu_{q(h)}$ is the number of degrees of freedom in the QGP (hadronic gas),

$$p_c = B\nu_h/(\nu_q - \nu_h), \;\; T_c = [90B/\pi^2(\nu_q - \nu_h)]^{1/4}. \tag{25}$$

Since $s(T) = dp(T)/dT$, the relevant formula for the entropy density can be rewritten as

$$s(T) = (2\pi^2 T^3/45)\nu_h[1 - \Theta(T - T_c) + \nu_q\Theta(T - T_c). \tag{26}$$

$$s^{(T)} = s(T)/T^3, \;\; s_c^* = s_c/T_c^3, \;\; s_c = \frac{\pi^2 T_c^3}{45}(\nu_h + \nu_q). \tag{27}$$

The above simple bag model EOS can also be modified (Boyko, 1990) by making the bag "constant"T-dependent, $B(T) = AT$, to produce a metastable QGP state with negative temperature:

$$p_q(T) = (\pi^2/90)\nu_q T^4 - AT, \quad p_h(T) = (\pi^2/90)\nu_h T^4. \tag{28}$$

Another important feature of this EOS is that for $\Gamma - \gamma = 0$ it describes second order phase transitions, with singular behavior of the thermal capacity at $T = T_c$. Really, in this case, we have $T - T_c \sim (\Delta s^*)^3$ near $T = T_c$.

Acknowledgements. The work of L.J. was supported by the Simon Foundation and by the DOMUS Program of the Hungarian Academy of Sciences. I.Sz. was supported by the NKFIH Grant no. K133046 and by the ÚNKP-22-3 New National Excellence Program of the Ministry for Innovation and Technology from the source of the National Research, Development and Innovation Fund.

References

Boyko V.G., Jenkovszky L.L., Sysoev V.M.: 1990, *Z. Phys. C*, **45**, 607.

Burakowsky L. and Horowitz L.P.: 1997, *Nucl. Phys. A*, **614**, 373.

Hagedorn, R.: 1965, *Nuovo Cim. Suppl.*, **3**, 147.

Shuryak E.V.: 1980, *Phys. Rep.*, **61**, 71.

Szanyi István et al.: 2023, *Phys. Rev. C*, **107**, 024904.

https://doi.org/10.18524/1810-4215.2023.36.289971

THE STUDY OF X-RAY SPECTRUM OF COMA GALAXY CLUSTER

L. Zadorozhna[1,2], A. Tugay[1], O. Prikhodko[1], D. Malyshev[3], Y. Sahai[1], D. Savchenko[4], N. Pulatova[5,6]

[1] Faculty of Physics, Taras Shevchenko National University of Kyiv, Ukraine
[2] Niels Bohr Institute, University of Copenhagen, Denmark
[3] Institut für Astronomie und Astrophysik Tübingen, Universität Tübingen, Germany
[4] Bogolubov Institute for Theoretical Physics, Kyiv, Ukraine
[5] Main Astronomical Observatory, Kyiv, Ukraine
[6] Max-Planck-Institute for Astronomy, Heidelberg, Germany
e-mail: tugay.anatoliy@gmail.com

ABSTRACT. The X-ray spectrum of the Coma galaxy cluster was studied using the data from the XMM-Newton observatory. We combined 7 observations performed with the MOS camera of XMM-Newton in the $40' \times 40'$ region centered at the Coma cluster. The analyzed observations were performed in 2000-2005 and have a total duration of 196 ksec. We focus on the analysis of the MOS camera spectra due to their lower affection by strong instrumental line-like background. The obtained spectrum was fitted with a model including contributions from the Solar system/Milky Way hot plasma and a power law X-ray background. The contribution of the instrumental background was modeled as a power law (not convolved with the effective area) and a number of Gaussian lines. The contribution from the Coma cluster was modeled with a single-temperature hot plasma emission. In addition, we searched for possible non-thermal radiation present in the vicinity of the center of the Coma cluster, originating e.g. from synchrotron emission of relativistic electrons on a turbulent magnetic field. We compared the results with previous works by other authors and spectra obtained from other instruments that operate in the similar energy range of $1-10$ keV. Careful and detailed spectrum analysis shall be a necessary contribution to our future work – searching for axion-like dark matter particles' manifestations in the Coma cluster.

Keywords: Clusters of galaxies, intergalactic plasma, non-thermal radiation, XMM-Newton, X-ray radiation.

АНОТАЦІЯ. В роботі було досліджено рентгенівський спектр кластера галактик Кома за даними спостережень обсерваторії XMM-Newton. Ми поєднали 7 спостережень, отриманих камерою MOS в регіоні розміром $40' \times 40'$, центрованому на кластері Кома. Ці спостереження були здійснені протягом 2000-2005 років і мають загальну тривалість 196 ксек. Основна увага була приділена аналізу спектрів камери MOS, оскільки вони менше схильні до впливу сильного інструментального фону у вигляді ліній. Отриманий спектр було апроксимовано моделлю, яка враховувала внески від гарячої плазми Сонячної системи/Молочного шляху та фонового рентгенового випромінювання у формі степеневого закону. Внесок інструментального фону було описано степеневим законом (не згладженим з ефективною площею) та декількома гаусовими лініями. Внесок від кластера Кома було описано випромінюванням гарячої плазми з однією температурою. Крім того, ми проводили пошук можливого нелінійного випромінювання в околі центру кластера Кома, наприклад, від синхротронного випромінювання релятивістських електронів в турбулентному магнітному полі. Ми порівняли наші результати з попередніми роботами інших вчених та спектрами, отриманими з інших приладів, які опрацьовують подібний енергетичний діапазон від 1 до 10 кеВ. Ретельний та докладний аналіз спектрів буде важливим для нашої майбутньої роботи - пошуку проявів аксіоноподібних частинок, що можуть бути кандидатами на роль темної матерії, зі спостережень кластеру Кома.

Ключові слова: Скупчення галактик, міжгалактична плазма, нетеплове випромінювання, XMM-Newton, рентгенівське випромінювання.

1. Introduction

Coma cluster (Abell 1656) is a hot gas galaxy cluster well-researched at all wavelengths. The Coma cluster's

distance from the observer is $\sim 99\,\mathrm{Mpc}$, redshift $z = 0.0231$, it contains above 1000 galaxies. It is virialized structure, with a mass about $10^{14} - 10^{15} M_\odot$ and spatial extents of $\mathcal{O}(1\,\mathrm{Mpc})$ (Bower, 2013). Apart from the dark matter component, which constitutes approximately 90% of the cluster's mass, there is an additional approximately 10% of the mass in a hot ionized intracluster medium (ICM). The intracluster medium accounts for the vast majority of a cluster's baryonic mass and produces diffuse X-ray emission due to thermal bremsstrahlung with a typical temperature of $T \sim 10^8\mathrm{K}$ and number density $n \sim 10^{-1} - 10^{-3}\,\mathrm{cm}^{-3}$ (Chen et al., 2007).

Coma cluster's celestial size extends over more than 2° on the sky. Its ICM is an extended X-ray source which size is above 45′. As was evident from radio observations, the Coma cluster itself was formed through the merging of several smaller clusters. The central gas density $n_0 = 3.49 \cdot 10^{-3}\,\mathrm{cm}^{-3}$ and virial parameters – cluster's mass $M_{vir} = 1.2 \cdot 10^{15} M\odot$ and radius $R_{vir} = 2.7\,\mathrm{Mpc}$ were obtained in (Łokas& Mamon, 2003).

Despite a plethora of observations, the characteristics and structure of the intergalactic plasma within clusters remain undefined. Both radio and X-ray observations indicate that the gas within these clusters is turbulent and disturbed (Churazov et al., 2012; Schuecker et al., 2004). The plasma within the clusters is weakly collisional (Zhuravleva et al., 2019), yet its collision rate is augmented by plasma instabilities. Furthermore, the transport processes are intricately tied to the local magnetic field's configuration. Multiple instances of X-ray and radio observations provide evidence for the existence of wave fronts, filaments, and bridges (Churazov et al., 2021). The substructures within the intercluster medium of Coma, notably the gas fluctuations caused by the collision of galaxy clusters, underscore the complex nature of the ICM.

Magnetic fields in ICM play a crucial role in cosmic ray emission and transport processes. The main ways to investigate a cluster's magnetic fields are the Faraday rotation measures (RM) and synchrotron radiation detection. Also, magnetic fields are interconnected with plasma and can persist in its internal structure. But at the same time, the properties of magnetic fields indicate their stochastic turbulent nature. Bonafede et al. (2010) estimated the magnetic field strength $B_0 = 4.7\,\mu\mathrm{G}$ from RM for the center of the Coma cluster. More recent radio observations from LOFAR and the Planck Observatory report correlations between radio synchrotron and soft X-rays, as well as radio – Sunyaev-Zel'dovich (SZ) correlations, which may assist for better identification of the areas with a regular magnetic field (Bonafede et al., 2022).

The lowest limit of magnetic field strength was obtained by Wik et al. (2009) which is equal to $B = 0.2\,\mu\mathrm{G}$. Generally accepted to use the beta-profile for gas density and for a profile of the magnetic field. The anisotropy parameter for Coma cluster $\beta = -0.654$ (Łokas & Mamon, 2003) and $\eta = 0.5$ (Bonafede et al., 2010). The electron radial distribution $n_e(r) = n_0[1 + (r/r_e)^2]^{3\beta/2}$ and the magnetic field profile $B(r) = B_0[n_e(r)/n_0]^\eta$.

For the last twenty years temperature map and a brightnessprofile of cluster core which is relatively homogenous $(8 - 10\,\mathrm{keV})$ with a gradient from the northwest to the cooler southeast $(\sim 7\,\mathrm{keV})$ have been obtained in (Arnaud et al., 2001; Gastadello et al., 2015).

Arnaud et al. (2001) obtained the X-ray spectrum of the central part $(\sim 0.78\,\mathrm{Mpc})$ of the Coma cluster from XMM-Newton EPIC/MOS (the European Photon Imaging Camera/Metal Oxide Semi-conductor) camera observations with total time 173 ksec (5 overlapping observations). The best fit temperature is $kT = 8.25 \pm 0.1\,\mathrm{keV}$ and an abundance 0.25 ± 0.02, the absorption hydrogen column density $n_H = 9.4 \pm 0.9 \cdot 10^{19}\,\mathrm{cm}^{-2}$.

In the study conducted by Nevalainen and Lieu (2003), the best-fit temperature was determined to be $kT = 9.2 \pm 0.7\,\mathrm{keV}$, considering a systematic error of 5% .

The existence of nonthermal emission in the X-ray spectrum of the Coma cluster was first supposed in the work of Fusco-Femiano et al. (1999) and this idea was developed in the articles of Nevalainen & Eckert (2004) and Rephaeli & Gruber (2002). Nevalainen & Eckert (2004) give the upper limit of nonthermal flux as 20 % of the total flux and report the hard X-ray nonthermal electrons population in the energy range of 15-60 keV. However, Wik et al.'s (2011) later research did not corroborate the previous findings in the hard X-ray range, failing to identify the expected Inverse Compton (IC) emissions. Gastadello et al. (2015) determined the upper limit of the IC component within the Coma cluster's core $(12' \times 12')$ at the energy range of $7-10\,\mathrm{keV}$, resulting in a nonthermal flux value $5.1 \cdot 10^{-12}\,\mathrm{erg\,cm^{-2}\,s^{-1}}$. It's important to acknowledge that this value lacks precision due to the intense brightness of the thermal component at the cluster's center and the limited field of view (FoV).

Examination of the Rossi X-Ray Timing Explorer dataset from 1996 and 2000 validates that the utilization of thermal emission from isothermal gas does not yield a satisfactory fit for the spectral distribution of emissions within the inner 1° radial zone Coma cluster. Although it's feasible to achieve spectrum alignment through emissions from gas exhibiting a notable temperature gradient, a more probable scenario encompasses the existence of an additional secondary nonthermal component. In such a scenario, it is estimated that nonthermal emission constitutes approximately 8% of the entire $4-20\,\mathrm{keV}$ flux (Rephaeli & Gruber, 2002).

Angus et al. (2014) provided a detailed review of the

cluster soft X-ray excess in $0.2 - 0.4$ keV and gave an alternative explanation of the phenomenon.

Consequently, the existence of nonthermal X-ray emissions at the cluster center remains subject to debate. However, the possibility of non-thermal emissions cannot be ruled out and necessitates further observations.

2. Extraction and modelling of the spectrum

XMM-Newton stands as a contemporary and advanced X-ray mission, currently in operation. It functions within an energy range of 0.2 keV to 12 keV and is equipped with two MOS and one PN cameras. These cameras exhibit a substantial total effective area that reaches its peak at around 2000 cm^2 at 1.5 keV, boasting a commendable energy resolution of roughly 10% and a relatively extensive field of view spanning a radius of approximately $15'$ radius.

We analysed publicly available observation data files for the Coma cluster from the XMM-Newton X-ray observatory. We used observations ObsIDs: 0124711401, 0153750101, 0300530101, 0300530301, 0300530401, 0300530501, 0300530601, 0300530701 with total exposure 343.8 ksec (see Fig. 1). These data were processed utilizing the *Extended Sources Analysis Software* (ESAS) package, which is accessible as part of the Science Analysis System (SAS). Periods of time impacted by a notably variable background component, such as soft proton flares, were sieved using ESAS scripts named `mos-filter`.

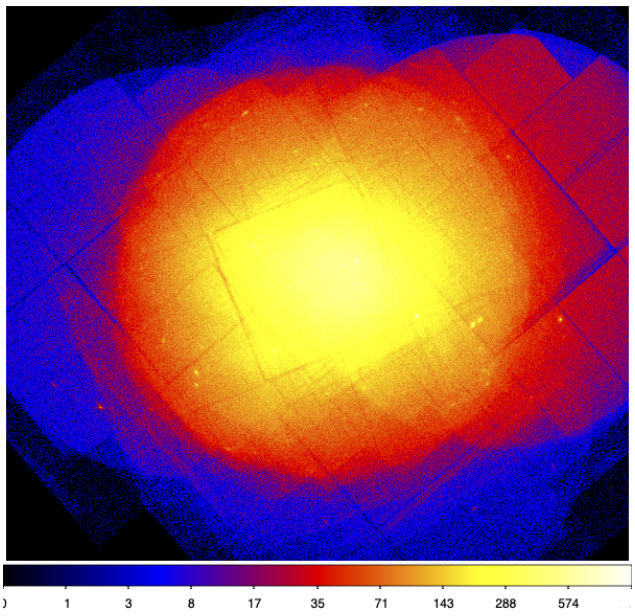

Figure 1: The picture of the Coma cluster is a mosaic of 8 partially overlapping pointings obtained with combined MOS1 and MOS2 cameras. Colors reflect the number of X-ray photons in a pixel.

Table 1: The XMM-Newton background modeling incorporates the most salient instrumental and astrophysical lines. These lines have been adopted from the reference (Malyshev et al., 2022) (TABLE I).

Energy	Line	Origin
0.56	O VII	astrophysical line
0.65	O VIII	astrophysical line
0.81	O VIII	astrophysical line
0.91	Ne IX	astrophysical line
1.34	Mg XI	astrophysical line
1.49	Al-Kα	instrumental line
1.56	Al-Kβ	instrumental line
1.74	Si-Kα	instrumental line
1.84	Si-Kβ	instrumental line
2.11	Au-Mα	instrumental line
2.20	Au-Mβ	instrumental line
4.51	Ti-Kα	instrumental line
5.41	Cr-Kα	instrumental line
5.89	Mn-Kα	instrumental line
5.95	Cr-Kβ	instrumental line
6.40	Fe-Kα	instrumental line
6.49	Mn-Kβ	instrumental line
7.06	Fe-Kβ	instrumental line
7.48	Ni-Kα	instrumental line
8.04	Cu-Kα	instrumental line
8.26	Ni-Kβ	instrumental line
8.63	Zn-Kα	instrumental line
8.90	Cu-Kβ	instrumental line
9.57	Zn-Kβ	instrumental line
9.68	Au-Lα	instrumental line

We implemented the conventional filters and cuts criteria provided by the ESAS software suite. Notably, we eliminated prominent point sources identified through the standard SAS process `edetect_chain`. To derive source spectra and create corresponding response matrices, we focused within the confines of a $14'$ radius circle centered around the source's position. These tasks were accomplished using the ESAS procedure `mos-spectra`. For the purpose of analysis, the obtained spectra were binned with an interval of 60 eV per energy bin, aiming to ensure that the bins remained statistically uncorrelated. We followed the procedure described in the article by Iakubovskyi et al. (2015).

We modeled combined MOS spectra in `Xspec` spectral package. In our spectral analysis, we avoided the background subtraction procedure, since we are dealing with an extended object with a size exceeding the field of view and the proper selection of the region for the estimations of the background spectrum is not possible. We chose the modeled energy range $0.3 - 10.0$ keV. To account for residual calibration uncertainties we added 1% systematic error using `Xspec` parameter `systematic`.

The resulting spectra consist of the Coma

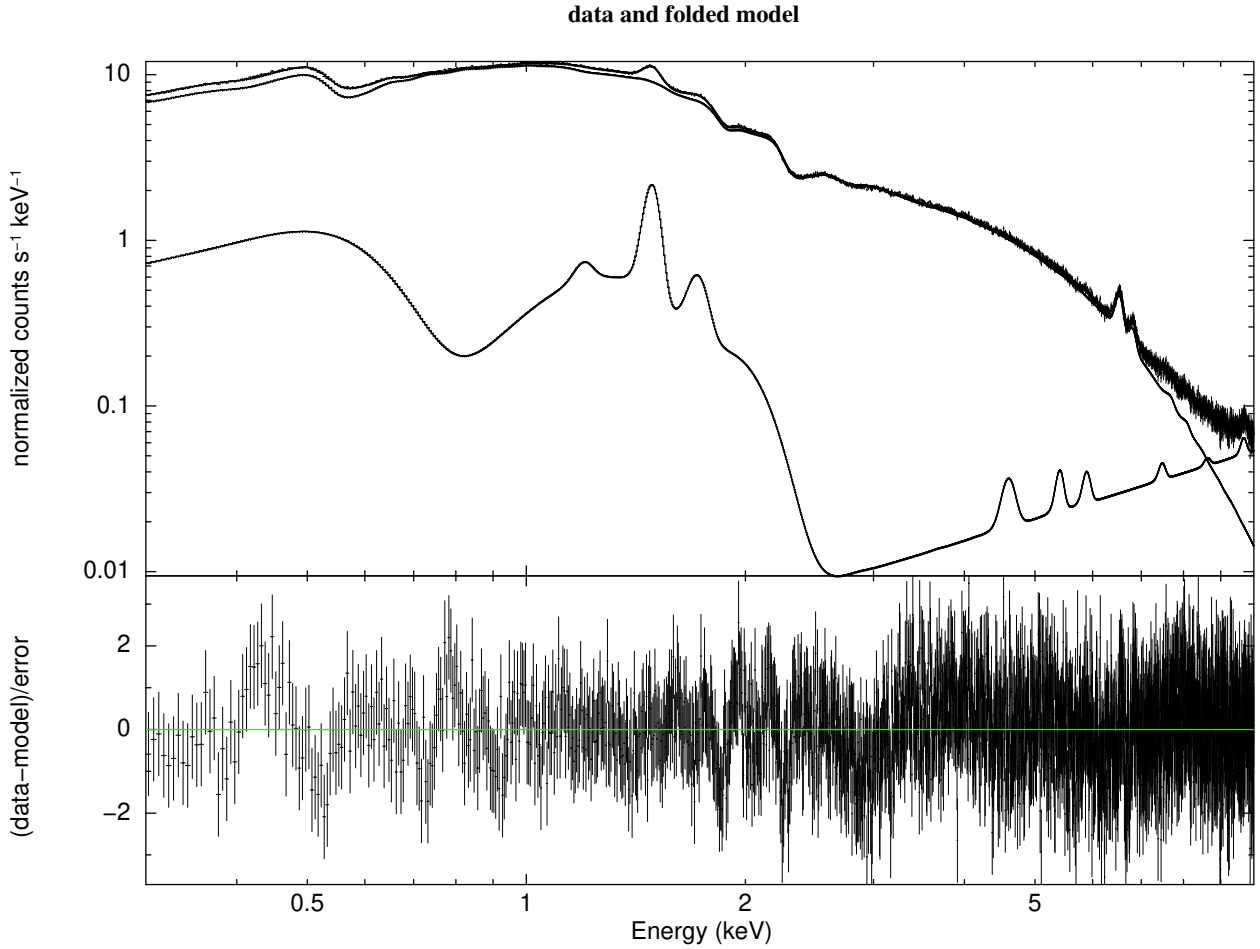

Figure 2: XMM-Newtom/MOS spectrum extracted from Coma cluster central region (top) and residuals with the best-fit model (bottom).

Table 2: Model parameters of MOS1/MOS2 combined spectrum extracted from Coma cluster central region. Column **Value fit 1** displays a set of parameters of the complex model `apec_1 + phabs*(powerlaw_1+apec_2+apec_3)` with adding the instrumental background. The column labeled **Value fit 2** presents a collection of parameters from the intricate model with additional secondary nonthermal component `apec_1 + phabs*(cflux_1*powerlaw_1 + apec_2 + apec_3+cflux_2*powerlaw_2)`, including the contribution of instrumental background. Please note, that in absence of the detection of non-thermal (powerlaw) emission from the Coma cluster we present the limits on the flux of this component for the fixed to 2 powerlaw index.

No	Model Component	Parameter Unit	**Value fit 1**	**Value fit 2**
1	apec_1	kT, keV	0.307 ± 0.018	0.303 ± 0.020
2	apec_1	Abundance	1.000 frozen	1.000 frozen
4	apec_1	Redshift	0.0 frozen	0.0 frozen
5	apec_1	norm, cm^{-3}	$(8.278 \pm 1.941) \cdot 10^{-4}$	$(7.156 \pm 2.010) \cdot 10^{-4}$
6	phabs	n_H, 10^{22} atoms cm^{-2}	$(1.502 \pm 0.491) \cdot 10^{-2}$	$(1.678 \pm 0.632) \cdot 10^{-2}$
7	cflux_1	Emin, keV	–	0.200 frozen
8	cflux_1	Emax, keV	–	10.000 frozen
9	cflux_1	lg10Flux, flux in $\mathrm{erg\,cm^{-2}\,s^{-1}}$	–	-9.624 ± 0.197
7	powerlaw_1	PhoIndex	1.478 ± 0.021	1.491 ± 0.165
8	powerlaw_1	norm, photons $\mathrm{cm^{-2}\,s^{-1}\,sr^{-1}\,keV^{-1}}$	$(2.450 \pm 0.249) \cdot 10^{-2}$	1.000 frozen
9	apec_2	kT, keV	1.002 ± 0.040	0.998 ± 0.041
10	apec_2	Abundance	1.000 frozen	1.000 frozen
11	apec_2	Redshift	0.0 frozen	0.0 frozen
12	apec_2	norm, cm^{-3}	$(6.333 \pm 1.282) \cdot 10^{-4}$	$(6.213 \pm 1.374) \cdot 10^{-4}$
13	apec_3	kT, keV	7.664 ± 0.139	7.656 ± 0.140
14	apec_3	Abundanc	0.542 ± 0.063	0.628 ± 0.252
15	apec_3	Redshift	0.0231 frozen	0.0231 frozen
16	apec_3	norm, cm^{-3}	$(7.658 \pm 0.908) \cdot 10^{-2}$	$(6.628 \pm 2.686) \cdot 10^{-2}$
7	cflux_2	Emin, keV	–	0.200 frozen
8	cflux_2	Emax, keV	–	10.000 frozen
9	cflux_2	lg10Flux, $\mathrm{erg\,cm^{-2}\,s^{-1}}$	–	< -10.4
17	powerlaw_2	PhoIndex	–	2.000 frozen
18	powerlaw_2	norm, photons $\mathrm{cm^{-2}\,s^{-1}\,sr^{-1}\,keV^{-1}}$	–	$1 \cdot 10^{-2}$ frozen
		χ^2/d.o.f.	1926.78/1895	1904.96/1908
		null hypothesis probability	30.0%	51.5%

cluster's thermal radiation of plasma `apec_3` and the astrophysical (Solar System plasma `apec_1`, hot interstellar plasma `apec_2`, cosmic X-ray background `powerlaw_1`), the hydrogen column density for absorption `phabs` and the instrumental (smooth continuum `powerlaw` and line-like `gaussian` features) backgrounds.

We modeled the spectrum with the following `Xspec` syntax `apec_1 + phabs*(powerlaw_1+apec_2+apec_3)` presenting contributions from the described components. For instrumental background, we used `powerlaw+gauss+...+gauss`, not convolved with the effective area. We included in the instrumental background model Gaussian lines, all were reported in (Malyshev et al., 2022) (see Table 1). The fit parameters are summarized in Table 2 (Column **Value fit 1**). The spectrum is shown in Figure 2.

A nonthermal correction was introduced to the aforementioned fitting models through the inclusion of a power law characterized by a freely adjustable spectral index parameter. The normalization of this power law was set in a manner ensuring that the nonthermal contribution to the overall flux remained below 10%. We modeled the spectrum using the following syntax `apec_1 + phabs*(cflux_1*powerlaw_1 + apec_2 + apec_3+cflux_2*powerlaw_2)`. `cflux` is a convolution model to calculate the flux of other model components. The instrumental background was modeled similarly to the previous case. The summary of fit parameters can be found in Table 2 (Column **Value fit 2**). An image of the spectrum was not presented due to the negligible alterations in comparison to the spectrum depicted in Figure 2.

3. Conclusion

We merged a total of 8 overlapping observations captured by XMM/MOS within a $40' \times 40'$ region around Coma cluster center. For our analysis, we harnessed a cumulative observation time of 196 kiloseconds, extending across the years 2000 to 2005. The spectrum was fitted using two distinct models: a single-temperature thermal spectrum and a one-temperature thermal plasma model adjusted by means of a nonthermal correction. The inclusion of a nonthermal spectrum correction within $\sim 10\%$ from total flux did not yield deterioration in the fitting's quality.

Acknowledgements. We are grateful for the discussions with Prof. Oleg Ruchayskiy and Prof. Bohdan Hnatyk. Lidiia Zadorozhna's work is funded by the Scholars At Risk Ukraine (SARU) fellowship at the University of Copenhagen.

This research was made with the support of the Center for the Collective Use of Scientific Equipment "Laboratory of High Energy Physics and Astrophysics"of Taras Shevchenko National University of Kyiv.

References

Angus S., Conlon J.P., Marsh D. et al., 2014, *JCAP*, **09**, 026.

Arnaud M., Aghanim N., Gastaud R. et al. 2001, *A&A*, **365**, L67.

Bonafede A., Feretti L., Murgia M., Govoni F. et al., 2010, *A&A*, **513**, A30 , 1002.0594.

Bonafede A., Brunetti G., Rudnick L. et al., 2022, *ApJ*, **933**, 218.

Bower R., 2013, Clusters of Galaxies. In: Oswalt, T.D., Keel, W.C. (eds) Planets, Stars and Stellar Systems. Springer, Dordrecht.

Chen Y., Reiprich T.H., Böhringer H. et al., 2007, *A&A*, **466**, 805.

Churazov E., Vikhlinin A., Zhuravleva I. et al., 2012, *Mon. Not. R. Astron. Soc.*, **421**, 1123.

Churazov E., Khabibullin I., Lyskova N. et al., 2021, *A&A*, **651**, A41.

Fusco-Femiano R., Fiume D., Feretti L. et al., 1999, *ApJ*, **513**, L21.

Gastaldello F., Wik D., Molendi S. et al., 2015, *ApJ*, **800**, 139.

Iakubovskyi D., Bulbul E., Foster A.R. et al., "Testing the origin of $\sim$ 3.55 *keV* line in individual galaxy clusters observed with XMM-Newton,"[arXiv:1508.05186 [astro-ph.HE]].

Łokas E.L. & Mamon G.A., 2003, *MNRAS*, **343**, 401.

Malyshev D., Moulin E., and Santangelo A., 2022, *Phys. Rev. D*, **106**, 123020.

Nevalainen J., Lieu R., Bonamente M. et al., 2003, *ApJ*, **584**, 716.

Nevalainen J. & Eckert D., "Mapping the nonthermal emission in Coma cluster of galaxies using the FeXXV/FeXXVI line ratio". 2004, https://www.cosmos.esa.int/documents/332006/1107598/nevalainen_j.pdf.

Rephaeli Y. & Gruber D., 2002, *ApJ*, **579**, 587.

Schuecker P., Finoguenov A., Miniati F. et al., 2004, *Astron. Astrophys.*, **426**, 387.

Wik D., Craig L., Filoguenov A. et al., 2009, *ApJ*, **696**, 1700.

Wik D., Craig L., Filoguenov A. et al., 2011, *ApJ*, **727**, 119.

Zhuravleva I., Churazov E., Schekochihin A. et al., 2019, *Nature Astronomy*, **3**, 832.

ASTROPHYSICS

(stellar atmospheres, interacting binary systems, variable stars)

https://doi.org/10.18524/1810-4215.2023.36.290774

THE PROBLEM OF OBTAINING COMBINED GAMMA AND OPTICAL DETECTORS FOR THE REGISTRATION OF FAST NUCLEAR PROCESSES

Marko D. Doikov

Faculty of Physics and Technologies, Plovdiv University "Paisii Hilendarski",

Plovdiv, Bulgaria, *marik.doikov@gmail.com*

ABSTRACT. The physical and technical aspects of the registration of fast physical processes involving nuclear transformations with the help of binary detectors in the γ- and optical ranges are considered We chose a semiconducting perovskite crystal $CsPbBr_3$ as the main element of the detector. Have been presented with geometrical and technologically usable parameters of the $CsPbBr_3$ crystal for its implementations in nuclear medicine, geophysics and astrophysics. One of the objects that allow testing of the developed high-speed spectrographic equipment are lightning discharges in the atmospheres of planets, including the Earth. The thermonuclear nature of γ-bursts detected during thunderstorms was revealed by their spectra. The paper shows the role of the corresponding channels involving high-energy protons and α-particles, leading to the formation of ${}^{11}_{6}C$, ${}^{13}_{7}N$, and ${}^{15}_{8}O$ isotopes. The registration of the γ-spectrum of the flash and its evolution allowed to estimate the character, energy and time scales of the processes necessary for the design and manufacture of multipurpose measuring complexes by us. The inclusion of γ-spectra in the consideration allowed to estimate the correlation between the maximum currents of particles and the productivity of γ-rays. In the experiments planned by us, the magnetic field fluctuations caused by currents are simultaneously recorded by highly sensitive magnetic field detectors. The height of the building of the Faculty of Physics in Smolyan, Bulgaria, is 900 meters above sea level. This makes it possible to place the measuring complex as close as possible to the sources of hard radiation and to carry out measurements in the immediate vicinity. Unlike distant space objects, the perovskite detector registers the positions themselves. This makes it possible to use the methods of positron γ-spectroscopy and accurately determine the parameters of local currents. The technological parameters of the device were determined.

A simulation model was created in Simulink MATLAB, LabVIEW with synchronization of the operation of the listed spectrographs. The characteristic shape of the signal formed by individual γ-quanta with the parameters of the Gaussian function and the total number of these quanta are calculated. The degree of mathematical blinding of neighboring Gaussian functions and its influence on the structure of the final spectrogram in the form of an autocorrelation function is estimated.

The similarity of the time scales of thermonuclear explosion processes on white dwarfs (WD) and the processes of synthesis of ${}^{11}_{6}C$, ${}^{13}_{7}N$, and ${}^{15}_{8}O$ isotopes in the flash head is determined. It is concluded that it is expedient to create a robotic network of lightning observation stations similar to the meteor patrol at the I. I. Mechnikov National University of Ukraine.

Keywords: γ-ray spectroscopy; CsPbBr3 detectors, ionization rays, higher speed interface, rapid nuclear transformation diagnostics, signal-noise relation.

АНОТАЦІЯ. Підвищення чутливості та розширення спектрального діапазону детекторів γ-випромінювання за останні десять років призвело до значних успіхів у галузі природничих і технічних наук. Однією з визначних подій у цій галузі є поява перших повідомлень про створення комерційних кристалів $CsPbBr_3$ у 2016 році, а також заявлена можливість їх застосування в ядерній медицині, геофізиці та астрофізиці. На сьогодні відомо, що кристали $CsPbBr_3$ є напівпровідниками з великим середнім атомним номером 57,35 а. м. u. Ширина забороненої зони 4,5 еВ легко регулюється під час виготовлення кристала та під дією зовнішнього електричного поля. Енергія утворення електронно-діркової пари становить 5,3 еВ. Це дозволяє використовувати спектроскопічне обладнання в експедиційних умовах без використання охолодження. Високі значення добутку швидкості рухливості зарядів μ на час їх життя τ складають $\mu\tau = 8 \cdot 10^{-4}$ см2/В. В даний час середній розмір кристала становить 3x3x0,9 мм. У роботи отримано, що у разі поперечних перерізів детекторів S=9mm^2 отримуються високоточні деталізовані рентгенівські та γ-спектри в діапазоні енергій 0,01 – 1 МеВ. У цьому випадку корпус детектора ефективно поглинає падаючі кванти і має високу продуктивність електронно-діркових пар. У разі енергій, перевищуючих 1,022 МеВ, спектр падаючого випромінювання спотворюється спільною дією, пов'язаною з появою електрон-позитронних пар в інтенсивному навколо ядерному полі кристалічних атомів, розсіюванням Комптона γ-квантів, атомним фотоефектом і когерентним розсіянням квантів на електронах, власною люмінесценцією, оже-електронами. Автором використано колекція емпіричних вимірювань лінійного коефіцієнта поглинання γ-випромінювання, які дозволяють

уникнути непотрібних складних розрахунків і експериментів. Виражена нелінійність k_E дозволяє вибрати оптимальну геометрію детекторів. Зроблено розрахунок із відношення поглинених даного типу γ-квантів до енергії утворення однієї електронно-діркової пари 5,3 еВ. Незважаючи на уявні проблеми теоретичного підходу та вироблення кристалів, точність реєстрації розглянутими детекторами вже досягла кількох процентів. В основній частині статті розглянуто роботу електроніки у режимі підрахунку імпульсів, аналіз форми імпульсів і їх вплив на результуючий спектр . У наших попередніх роботах ми розраховували потоки γ-квантів у вибухових термоядерних процесах. На 1 см^2 детектора від астрофізичного об'єкта за 20 мкс. потрапило 180 фотонів з енергією не більше 10 МеВ. Тому необхідно, щоб детектований γ-спектр міг містить безперервні фонові кванти та лінії випромінювання. Запропоновано алгоритм виділення ліній і неперервного спектра. Зроблено схемні рішення для емуляції генератора сигналів необхідної форми, що утворюються після проходження квантів жорсткого рентгенівського та м'якого γ-випромінювання скрізь кристал $CsPbBr_3$ Надано увагу перспективам розвитку теорії та практики бінарних детекторів нового покоління.

Ключові слова: γ-спектроскопія; Детектори CsPbBr3, іонізаційні промені, високошвидкісний інтерфейс, швидка діагностика ядерних перетворень, зв'язок сигнал-шум.

1. Introduction

The increase in sensitivity and the extension of the spectral range of γ-band detectors in the last decade has led to significant advances in the field of natural and engineering sciences. One of the remarkable events in this field is the appearance of the first reports on the creation of commercial crystals of CsPbBr3 perovskite in 2016. It also explained the possibility of their application in nuclear medicine, geophysics, and astrophysics.

At present, it is known (Liu et al., 2022) that$CsPbBr_3$ crystals are semiconductors with a large average atomic number of 57.35 a. m. u. The band gap of 4.5 eV can be easily tuned during the crystal growth and under the action of an external electric field. The energy of electron-hole pair formation is 5.3 eV. This allows the use of spectroscopic instruments in the field without the need for cooling. High values of the product of the mobility rate μ of the charges and their lifetime τ are $\mu\tau = 8\cdot10^{-4}$ cm^2/V. Currently, the average crystal size is 3x3x0.9 mm. Note that the detector cross section is $S = 9\ mm^2$. Detectors with reduced dimensions make it possible to obtain high-precision, detailed X-rays and γ-spectra in the energy range 0.01 – 1.0 MeV. In this case, the detector body effectively absorbs the incident quanta and has high electron-hole pair productivity.

At energies above 1.022 MeV, the incident emission spectrum is distorted by the combined action associated with the appearance of electron-positron pairs in an intense near-nuclear field of crystal atoms, Compton scattering of γ quanta, atomic photoelectric effect and coherent scattering of quanta by electrons, intrinsic luminescence, Auger electrons, etc. Therefore, measurements of the linear absorption coefficient of γ radiation k_E allow to avoid unnecessary complex calculations and experiments.

The expressed nonlinear character k_E (Liu et al., 2022, Fig. 2 C) allows to choose the optimal geometry of the detectors. In the future, we will be guided by the absorbed energy according to the empirical values of k_E. And only for the energy intervals in which one of the above mechanisms predominates, we will use the values of the exact theoretical cross sections calculated in our previous works. Calculation from the ratio of the absorbed γ-quanta of a given type to the formation energy of an electron-hole pair of 5.3 eV. Despite the apparent roughness of the approach, the accuracy of registration by the marked detectors has already reached several percent (Liu et al., 2022; Lopes et al., 2020). The operation of the considered detectors in pulse-counting mode, saturation modes, and their calibration in section 2. In our previous work, we calculated the fluxes of γ quarks in fast, explosive thermonuclear processes. 180 photons with energies not exceeding 10 MeV were fired from an astrophysical object onto $1cm^2$ of the detector in 20 μs (Doikov D., 2022). The γ spectrum recorded by the detector contains continuous background quanta and emission lines. An algorithm to select the lines and the continuous spectrum is proposed. In section 3, circuit solutions are given for emulating the signal generator of the required shape, formed after the passage of hard x-ray and soft γ-radiation quanta through the CsPbBr3 crystal. The discussion is devoted to the prospects for the development of the theory and practice of the new generation of binary detectors.

2. The selection of the signal type from test objects

The close binary systems with white dwarfs (WD) and companion stars with a Sun-like chemical composition. So-called Cataclysmic Variable Stars (CVs). The accretion from the companion star to the surface of the WD through its hard magnetic field (1000 T) creates the conditions for the production of the induced γ-ray (Doikov D., 2022). The theoretical background γ-ray production forms 10-20 quants at the localization point of the Earth and the space closest to it. The possible thermonuclear explosion produced in formal Earth detector γ-ray fluxes is 100 quants/cm^2/s at time intervals $\Delta\tau \approx 10^{-4}s$. In AM Her type CVs these events repeat several times a year. The use of the considered detector spectrographs in monitoring mode allows the registration of random events of explosive origin in space. In such conditions, the development of binary detector-spectrographs in the γ and optical spectral ranges allows for an increase in the probability of detection of explosion precursors. Other astrophysical objects are not considered in this section because the physical processes in them are more complex, both in time and in the structure of the spectra.

Relaxation times $\Delta\tau_{rel}$ of pulse formation limited by Δτ. Strictly speaking, $\Delta\tau_{rel} \leq \Delta\tau/100$. During this time, a γ quantum must pass through a 0.9 mm thick crystal, transfer energy to the valence electrons, and they must pass through the band gap. As noted in the introduction, the average number$N_{\gamma e}$ of electron-hole pairs from a single γ-quantum will be

$$N_{\gamma e} = \frac{E_\gamma\left(1-e^{-\kappa_\gamma d}\right)}{5{,}3\ eV}\ . \qquad (1)$$

Where $E_\gamma$is the energy of the γ quantum, κ_γ is the coefficient of linear monochromatic extinction. The dependence of $\kappa_\gamma$on γ-quantum energies is presented in (Liu et al., 2022, Fig. 2, B), using data from NIST USA (19 references in this paper). In Fig. 1 we have shown the dependence of $N_{\gamma e}$ on the γ-ray energy E_γ. The saturation of $N_{\gamma e}$only denotes the fact that the radiation length of γ-quats is more from crestal depth.

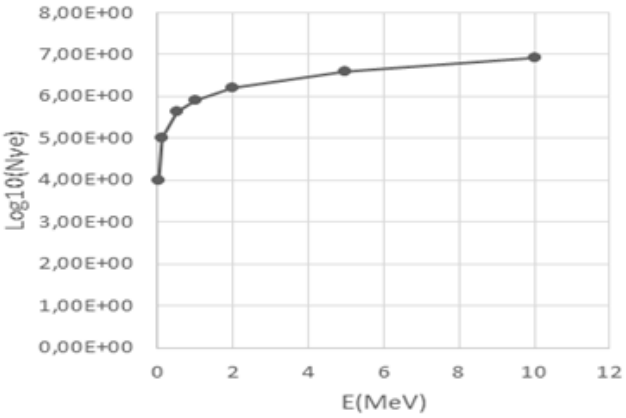

Figure 1: Dependence of the number of injected electrons in the conductivity zone log10($N_{\gamma e}$)) from the γ-ray energy E(MeV).

3. Earth atmosphere

In recent years, the demand for increasing the sensitivity of γ-spectrographs for practical needs in many branches of practical activity has increased sharply. In this work, the main attention is paid to the selection of available equipment and the development of software for monitoring fast processes in plasma with the presence of reactive electrons, protons, and α-particles. In last year's studies, it was shown that under certain conditions, the presence of flows of charged particles accelerated to relativistic speeds in plasma leads to radiative losses of kinetic energy for radiation. The article (Doikov D., 2022) describes in detail the sequence of radiation losses as a function of time and energy regimes. In order to develop the necessary equipment, in our work we calculated the time frame for the processes of induction of hard radiation and the values of the fluxes. Testing such equipment for astrophysical purposes is difficult due to the fact that the Earth's atmosphere absorbs the hard radiation of interest to us. Therefore, alternative sources were sought to calibrate the multichannel spectrograph. A suitable source of broad-spectrum radiation is lightning. It was found that the time intervals for the formation of hard and optical radiation can be divided into 3 stages.

In the first stage, γ-rays appear before the onset of an optical flare. Its duration is 1-10 μs. In the second stage, during an optical flare, a broad spectrum of radiation is observed within 10-100 milliseconds. In the third stage, after the disappearance of the optical radiation, γ-rays are observed for a few more seconds. In contrast to astrophysical problems, the measuring equipment during such a calibration must include a magnetometer and a radio rangefinder. The latter two devices available on the market have a high sensitivity and a low affordable price. The main task is to switch and synchronize the operation of the optical and γ-spectrographs. The accuracy of synchronization of individual elements of a multichannel spectrograph in monitoring mode should be 1-10 ns. Before manufacturing a spectrograph, it is necessary to simulate the registration processes with standard devices placed in the LabVIEW environment. Each individual signal is converted into an equivalent rectangular shape. In reality, the actual shape of the current pulse of the generated signal after the interaction of a hard radiation quantum with the perovskite material is well approximated by the Gaussian function.

The conversion to a square pulse is done in the INTEGRATOR. As with optical and γ-spectrographs, it is necessary to know the resolution and the signal-to-noise ratio. This year's articles have already explained that the signal-to-noise ratio is (80pA / 20pA). And the resolution is already approaching 1 KeV. It is also important to note that the fight against noise when amplifying the signal by applying a potential difference of 0.5-1 kV is carried out exclusively by building an appropriate electronic circuit. In this case, it is not necessary to cool this type of detectors. This leads to the possibility of their use in normal climatic conditions. The proposed design is also convenient for the organization and operation of field monitoring lightning detectors. The first experiment is planned to be carried out near the building of the branch of the Faculty of Physics and Technology in Smolyan. The faculty building is located at an altitude of 900 meters above sea level. In this case, the lightning discharge is much closer to the detectors than at sea level. The portability of the equipment makes it easy to carry and maintain in the field. In particular, in analogy to tornado hunters, they should be placed on the base of a car or a trailer for it.

The present paper consists of 1. Introduction, 3. Chapter, 5. Discussion and 6. Conclusion. Chapter 2 is devoted to the structure and evolution of the flow of γ-quants formed in lightning. Of particular interest is the γ-flare, a precursor of the lightning itself and its structure. Chapter 3 is about signal structure and its movement according to the electronic circuit and the method of its processing. Chapter 4 is devoted to spectral analysis of signals, building temporal correlations between currents at different wavelengths. In discussion, a comparative analysis of multichannel spectrographic of a hard and optical radiations has been carried out. Their importance and indispensability in monitoring of unique explosive processes in astrophysics and geophysics is emphasized. In the conclusion the main new results of the article are carried out. The design and methodological advantages of the simulation method for the design and manufacture of the necessary electronic components of a multichannel spectrograph are given.

The motion of a stream of protons, α-particles of positive ions, and the most common ions in a strong electric field with E is of particular interest. In lightning, the initial velocities of both the accelerated particles and the target molecules are close to thermal.

When an external field E is applied, the entire medium undergoes strong polarization, the effective binding energy of molecular electrons with shielded nuclei becomes smaller, and the medium begins to fill with free electrons. This process leads to the appearance of positive molecular ions and electrons in the flash heads.

The onset of ion motion is accompanied by elastic collisions with neutral molecules and atoms of the atmosphere. In elastic collisions with neutral atoms, atomic and molecular ions have a much higher energy transfer coefficient $\chi_{\alpha.\beta}$ than electrons. The same ratios affect the growth of ion velocities at the distances of their free paths.

As soon as the kinetic energy becomes comparable to the binding energy of molecular and atomic electrons, charge exchange reactions and detachment of electrons from parent atoms and molecules begin.

A further increase in velocity leads to a decrease in the cross section for the interaction of the ion current with the resting atoms of the atmosphere. Atomic and molecular current ions begin to maintain themselves in an ionized state.

The criteria of charge retention depending on the current velocity are described and systematized in detail in (Sigmund, 2014). Let the atomic number of the nucleus of the atom participating in the current Z_1 and the charge of its ion q_1,, the standard Bohr velocity $v_0 = c/137$ and its velocity v. Then, according to Bohr, in the hydrogen-like approximation, by replacing the nuclear charge by the effective charge Z_{1eff}, the following relation is satisfied

$$q_1 = Z_{1eff}\left(1 - exp\left(-\frac{v}{Z_{1eff}^{\frac{2}{3}} v_0}\right)\right) =$$

$$= Z_{1eff}\left(1 - exp\left(-137v/Z_{1eff}^{2/3}\mathrm{c}\right)\right). \qquad (2)$$

Figure 2 shows the ionization characteristics for hydrogen, helium, carbon, nitrogen and oxygen ions under lightning head conditions. When a sufficient velocity v is reached, a state of complete ionization is reached. The q_1 functions shown in the figure indicate zones of spectrum formation over a wide range for waves. In contrast to classical plasma, here a directed ion stream collides with atmospheric atoms that are practically at rest. And the cross sections of all the successive collision processes make it possible to estimate their intensities, which is important for planning an experiment.

In contrast to the differences in particle deceleration processes in the strong electric field of lightning, the acceleration of positive ions and electrons is observed. Figure 1 shows the results of calculations of the degree of ionization of atoms during such a movement. At high speeds, fully charged ions are formed. The velocities marked on the graphs correspond to the kinetic energies of the ions in the range 2.8 – 32 MeV. Collisions of ions with resting atoms of the atmosphere produce both induced

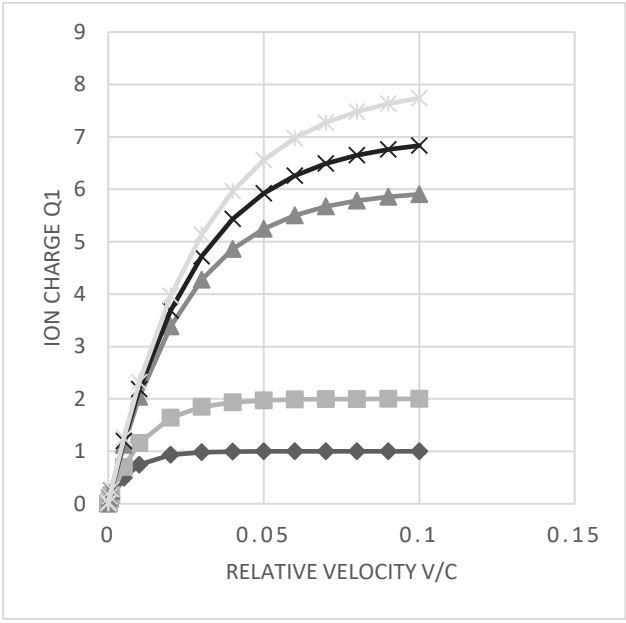

Figure 2: Ionization degree for elements Q1 for elements: ◊ – H, ▪ – He, Δ – C, X – N, * – O in lighting.

gamma rays and proton-excess nuclei. In any case, the appearance of a gamma-ray burst in the flash head is expected. Several μs before the onset of the optical phase of the discharge suggest that classical shock transitions do not manifest themselves in the optics. The developed detector covers the lightning spectra from optical to soft gamma radiation. Preliminary calculations of the total radiation losses show the highest information content in the marked region.

In 2017, slab γ-ray bursts were registered with the help of upgraded detectors installed at nuclear power plants after the well-known Fukushima accident. The registration of bursts coincided with the presence of a lightning storm in the vicinity of the nuclear power plant. The physical aspects of γ-burst formation have been considered in our work (Doikov D. & Doikov M., 2023, in press). Here we also discuss the structure and energy of a storm's γ-flares for modeling the detector's mode of operation. The fact that the building of the Branch of the Faculty of Physics and Technology is located at the altitude of 900 m is also very convenient for the sensor calibration experiment.

This leads to the fact that the detector is as close as possible to the source of γ-radiation. The source of γ-radiation of interest to us is located in the upper part of the lightning. In the so-called upper stage with lengths reaching 1 km. In this lighting current tube, the potential differences reach 10^8 V and the intensity of the electrical field is $(10^6 - 10^7)V/m$. The γ-spectra consists slab background continuous components and (0,511, 1,112) MeV emission line after collisions between accelerated electrons, protons and He ions (Doikov D. & Doikov M 2023, in press). The average statistical values of the characteristic time of formation of γ-flares are well known, which usually occur between 200 – 300 μs. The predicted flux of γ-quanta per 1 cm^2 of the detector surface varies from 100 to 1000 quanta

depending on the mutual distance between the detector CsPbBr3 and the lightning head.

This results in the detector being as close as possible to the source of the γ radiation. The source of γ-rays we are interested in is located in the upper part of the flash. In the so-called upper stage with lengths up to 1 km. In this lightning tube the potential differences reach 10^8 V and the intensity of the electric field is $(10^6 - 10^7)V/m$. The γ-spectra consist of continuous slab background components and the (0.511, 1.112) MeV emission line after collisions between accelerated electrons, protons and He ions (Doikov D.& Doikov M., 2023). The statistical averages of the characteristic γ-flaring times are well known, typically occurring between 200 and 300 μs. The predicted flux of γ quanta per 1 cm^2 of detector surface varies from 100 to 1000 quanta depending on the mutual distance between the detector $CsPbBr_3$ and the flash head.

Pulse reading and counting. Unlike optical radiation, the refractive index of γ and X-ray radiation in crystals is usually very close to 1. Then we can estimate the characteristic time of its motion in the crystal body as the ratio of quantum velocity to the thickness of the absorbing layer d, $\Delta\tau_{ch} \approx d/c \approx 3 \cdot 10^{-11} s$ This time is much smaller than all the other times considered before. The minimum of the ionization relaxation time $\Delta\tau_{ion}$_ion is in the power of $\Delta\tau_{ion} \approx 10^{-8} s$ and corresponds to the times of electron-hole pair formation. In this case, the impulse is a rare event and available for its single account. In other words, each quantum forms its own pulse. From Fig.1 for $E_\gamma = 0.511 MeV$ we have $N_{\gamma e} \approx 4{,}3 \cdot 10^5$. The $CsPbBr_3$ electron-hole lifetime τ is close to $10^{-5} s$. The driving velocity $v_d = \mu E \approx 50 \frac{cm^2}{s} \cdot 5{,}6 \cdot \frac{10^3 V}{cm} \approx 2{,}8 \cdot 10^5 cm/s$. Typical external potential differences are 500 V (Liu et al., 2022), (Doikov M., 2022).

The free path length of the electron-hole pairs in the perovskite semiconductor is $v_d \tau \approx 5{,}6\, cm$ Considering the accuracy of the determination of the carrier mobility in the considered semiconductor for the used energy range, we can conclude that the electron-hole recombination in our perovskite crystal CsPbBr3 is insignificant. It is important to conclude that the current pulls do not decrease, which is important to count the individual events. The pulling amplitude in these conditions we estimate from formula: $I = env_d S \approx 0{,}25 \cdot 10^{-6}$ A. In the case of heavy element semiconductors, we have avalanche breakdown. This type of breakdown is based on the effect of avalanche multiplication of carriers in the thickness of the p-n junction. At a certain value of the reverse bias voltage, the field strength in the p-n junction becomes so large that the minority carriers accelerated in it acquire sufficient energy to ionize the neutral atoms of the semiconductor in the junction. As a result of ionization, an avalanche increase in the number of carriers occurs, creating a reverse current. Avalanche breakdown is typically observed at reverse bias voltages on the order of hundreds of volts. It is typical of relatively thick p-n junctions where each of the minority carriers is present.

Note that an avalanche-like increase in the concentration of charge carriers in the form of electrons and the holes they leave behind leads to an increase in current strength. The drift velocity of the electron-hole pairs does not change significantly. This effect is limited because only the electrons in the outer valence shells of heavy elements have low binding energies. The neighboring valence shells already limit the flow of electrons into the conduction band. Most often we are dealing with outer d- or f-shell electrons.

Part of the energy contributed by the gamma quanta is converted to heat. The resulting shot thermal noise is responsible for a current of amplitude i:

$$i_n = \sqrt{\frac{4k_B T}{R}} \approx \frac{1.23}{\sqrt{R}} 10^{-10} A\,. \qquad (3)$$

Were R to be ohmic resistance of $CsPbBr_3$ crystal in normal room condition. From (Liu et al., 2022) $R \approx 10^{10} \Omega$. Relative currents of individual γ-quants depend on geometry and material properties of this crystal, which we get from Herst's equation in form:

$$\frac{I}{I_0} = \frac{\mu\tau V}{d}\left(1 - e^{-\frac{d^2}{\mu\tau V}}\right) \approx \frac{0.8}{d}\left(1 - e^{-\frac{d^2}{0.8}}\right). \qquad (4)$$

The saturation current I_0 depends on the thickness d and corresponds to the maximum γ-ray flux that does not change with the full current pulse. In the majority of practical cases μτ = 8·10^{-4} cm^2/V. V=500 –1000V. The maximum thickness d at present is close to 1 cm. Figure 3 shows the useful currents for different d.

The maximum current pulls from γ quantum with energy before 1 MeV are produced for crystal thickness d=1 cm. This means that the increase in crystal size must be controlled simultaneously by adjusting the product μτ and the free path of the electron-dot pairs. It was confirmed early on that $\lambda \approx 4.5\, cm$. If $d \leq \lambda$, carriers do not recombine on crystal defects and reach the anodic contact. Fulfillment of these conditions allows for high accuracy of recorded signals. That is, the dispersion of individual pulses reaches minimal values. The spectral resolution is maximal.

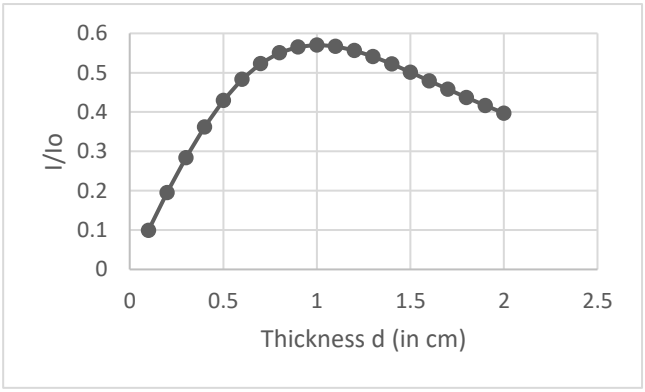

Figure 3: Dependence of the relative to saturation $\frac{I}{I_0}$ useful current from $CsPbBr_3$ crystal with thickness d (in cm).

Background and line γ-ray selections. During the study of the objects listed in this section, a low-amplitude continuous component of the γ spectrum appears. Emission lines appear against this background. Thus, guided by the physical characteristics of the process under consideration, it becomes possible to create a soft pulse processing program. We build the developed software into the pulse analyzer. According to Fig. 1, the pulse amplitude is related to the energy of the γ quantum. At the hardware level, we create a multichannel accumulator of pulses of the same amplitude. The time scale of these processes is limited only by the physical properties of the objects under study. Our research should be carried out in a monitoring mode. In this case, the software for processing the incoming information contains an algorithm for removing spurious signals and taking into account the dark current. To the above, we add that it is important to take into account and correct the natural radioactive background. Based on its average values, we can calibrate the detector used.

4. Emulation and selection of the type of signal from the pulse generator

The presence of heavy elements in the design of the detector leads to a sharp reduction of relaxation times during the formation of a current pulse of the useful signal. In this case, it is convenient to represent the signals as a Lorenz, Gaussian function. For sufficiently small widths and large amplitudes, the Dirac δ functions are used. On the other hand, amplitude, profile, and equivalent width are the most important spectroscopic characteristics for specialists. The physical mechanisms of γ line broadening before the advent of $CsPbBr_3$ γ detectors usually gave values within the error limits (Doikov D., 2022). The processing of the spectra is further complicated by the fact that the line broadening is much smaller than in the optical range. According to bench studies of the instrumental profile of semiconductors containing heavy metals, relaxation processes take much less time than those caused by real physical processes. The width of the instrumental profile in most cases is close to the natural profile of the γ-line. For the convenience of modeling the shape of the current pulse, we will use two profile formulas that are convenient for considering dissipative processes in semiconductors. In spectroscopy, such profiles are called Lorentz or Gaussian emission profiles. The Lorentz contour represents the evolution of some periodic processes in a dissipative physical system. In our case perovskite semiconductor.

$$P(\omega) = \frac{A_0^2}{(\omega-\omega_0)^2+(\gamma/2)^2} \quad . \qquad (5)$$

For ions is shown in the form:

$$P(\omega) = \frac{1}{\sigma\sqrt{2\pi}} e^{-\frac{(\omega-\overline{\omega_0})^2}{2\sigma^2}} \quad . \qquad (6)$$

The dispersion σ, frequencies ω, and $\overline{\omega_0}$ contain physical information about the equivalent width of the signal contour. We will interpret these values later in the next section.

Interference from useful signals. In classical signal theory, there are three main types of interference. These are:

1. Interference with a narrow frequency spectrum of signals caused by the operation of radio stations or sources of natural origin at close frequencies. Directed by the power supply.

2. Impulse interference, which is a chaotic sequence of impulses whose frequency is such that when the next impulse arrives, the processes caused by the previous impulses in the system are completed.

3. Fluctuation interference in the form of internal noise of transmission lines. Caused by the thermal motion of electrons in the conduction band of semiconductor devices. In our case, CsPbBr3 detectors.

These perturbations are such that the system's response to the next perturbation does not have time to fade before the next one arrives. Reactions from such a chaotic sequence are superimposed to form a continuous process. This phenomenon is often observed as a dark current.

We note that all these points are important to us. Point 1 is important for research in the presence of a densely packed, large number of spectral lines of atomic and molecular origin. Or when spectral studies are carried out near wavelengths occupied by strong resonance lines of atoms of the alkaline group of elements of the periodic table of elements of Mendeleev. The most interesting for us is point 2. Here, above the noise, we can expect to observe pulses of hard radiation quanta incident on the detector, quanta of the continuous γ-spectrum and noisy dark current. Of the considered signals represented by formulas (5) and (6), it is more convenient to use the Gaussian function to describe the time evolution of two successive pulses. Let us consider these pulses in the form of two Gaussian functions. With different mathematical expectations a_1, a_2 and variances σ_1, σ_2

$$f_1(t) = \frac{1}{\sqrt{2\pi}\,a_1} exp\left(-\frac{t^2}{2a_1^2}\right);\ f_2(t) = \frac{1}{\sqrt{2\pi}a_2} exp\left(-\frac{t^2}{2a_2^2}\right). \qquad (7)$$

The cross-correlation coefficient $k_{12}(\tau)$ describes the degree of magnitude in the resulting distribution, similar in meaning to the dispersion. $k_{12}(\tau)$ also represents the Gaussian distribution. If $a_{12}^2 = a_1^2 + a_2^2$ then the integral for calculating $k_{12}(\tau)$ has an exact solution and is useful for interpreting hard radiation spectral flux measurement data.

$$k_{12}(\tau) = \frac{1}{\sqrt{2\pi}\,a_{12}} exp\left(-\frac{\tau^2}{2a_{12}^2}\right). \qquad (8)$$

Thus, with a rapid increase in the flux of γ quanta, the indicator of the onset of detector saturation is the cross-correlation function $k_{12}(\tau)$ for each of the signal pairs. Considering that the detectors we design operate in the γ flare monitoring mode, the appearance of a non-zero cross-correlation function is a precursor of the flare itself. The single signal structure in the microscopic interpretation is the result of electron cloud motion in the conductive semiconductor zone. These electrons are injected after interactions between energetic hard radiation quants with heavy elements in the semiconductor (Fig. 1 and formula (1)). In the framework of relaxation time $\Delta\tau_{rel} \approx 10^{-9}s$ in the considered semiconductor, we must know that simultaneous backdown of more than 10^3 quants lead to

saturation of the detector system. The electronic architecture in Fig. 4 means that the hard radiation spectrograph works with overlapping signals. The degree of overlap is calculated from (8). If the inequality $k_{12}(\tau) \ll 1$ is satisfied, the splitting of the signal contours $f_1(t)$and $f_2(t)$ results from the formulas (7) for the free contour zone. In the opposite case, the increase of the dispersion leads to a decrease in the accuracy of the final spectra of the examined physical objects.

5. Registration of the magnetic field and distances from lighting

The directed motion of charged particles observed in lightning should generate local magnetic fields. If magnetic field detectors are placed near lightning, it is possible to measure magnetic field perturbations with sufficient accuracy. It should be noted that modern low-cost detectors available on the market make it possible to measure the local magnetic field with accuracy in the nanotesla range. On the other hand, for currents recorded by lightning, the calculated perturbations of the local magnetic field become comparable with the average magnetic field of the Earth. $\Delta B \approx \mu_0 I/r$. Where $\mu_0 = 4\pi \cdot 10^{-7} Hn/m$, I is the current of the charged particle (electron, proton or α particle). $I \approx 4 \cdot 10^4 - 10^5 A$, r is the distance between detector and illumination $r \approx 10^3 - 10^4$ m.

To determine the distance r from the lightning. A lightning-distance radiometer is suitable and available for sale on Internet platforms such as Amazon or others. In the frequency of radio waves, this device allows you to register lightning storms over long distances.

Thus, in field experiments, the optical and hard lightning spectra obtained as a result of work in monitoring mode can be compared with reliably fixed distances and local magnetic fields. In this case, we have an unambiguous picture of local physical processes in different parts of the lightning discharge.

6. Simulation in LabVIEW environment

First of all, we note that the present research is the pairing of two detectors within a single instrument. It can be called a prototype of a combined γ-optical telescope. We have divided the engineering and physical tasks of building a layout into two parts. The first part is devoted to the physical structure of a current pulse formed in a crystal under the action of an incident γ-quanta. A γ-quantum interacts with a crystal, and an optical quantum interacts with a CCD matrix. Both detectors are placed in the same mount and appear to distant objects as measuring instruments at the same point. In this case, signal synchronization requires taking into account the delay time caused by the operation of the devices involved in the simulation.

To simulate the operation of the detector, we will replace it with a standard pulse generator, and the operation of high-speed analog-to-digital converters with an integrator of individual signals. The resulting time spectrum is then displayed on the third device – an oscilloscope. The most suitable mode of operation of the pulse generator for us is the random signal generation mode. The point is that the processes we are considering take place in a highly turbulent medium. Within an acceptable energy interval, the generation of γ-quants is a random background process. The formation of a spectral emission line does not fit into the framework of such a concept. This means using a separate pulse generator where the waveform is given by a Gaussian function and simply means that it is more likely to be repeated. All of this is shown in Figure 2.

Noise suppression. The dark current of the crystal detector under normal conditions does not exceed 20 pA with a useful signal level of 80-100 pA. The first stage of signal amplification and signal registration is the creation of a significant potential difference in its working area. However, for crystals of the $CsPbBr_3$ type, a weak dependence of the dark current level on the temperature is observed. This simplifies the instrumental methods of noise treatment and brings them to the level of classical methods. Our discussion ends when we approach the saturation state of the detector. In this mode, these crystal degradation processes are already actively manifested. The level of uncontrolled noise increases here due to a decrease in the bandgap of the semiconductor under study.

The system consists of a charge-sensitive preamplifier, a shaping amplifier, and a multi-channel analyzer. Charges in the detectors are directed to the charge-sensitive preamplifier, accumulated on a capacitor, and then converted to voltage, which is then boosted to form a stepped voltage signal. The signal also passes through the preamplifier. One reason an amplifier is needed is to amplify the peak voltage resulting from the long attenuation of the signal's serial output from the preamplifier. An amplifier is therefore essential to accurately determine the height of each pulse. The technique involves modifying the attenuation curve into a narrower pulse shape while maintaining the height ratio of each pulse.

The circuit of a simple RC shaping amplifier is shown on the following page. It is a combination of a differentiator and an integrator. The differentiator acts as an upper pass filter, allowing only the high-frequency component to pass while blocking the constant component. Similarly, the integrator acts as a low-pass filter, allowing only the low-frequency component to pass, resulting in a gradually increasing slope. The output of the shaper amplifier is proportional to the signal level from the preamplifier, which is also proportional to the energy assimilated by the detector. It counts the number of pulses at different intervals and heights by applying a series of pulses with a specific shape to its input.

The multichannel analyzer (MCA) is an important device used in the production of gamma-ray spectra. It counts the number of pulses at different intervals and heights by applying a series of pulses with a specific shape to its input. The MCA consists of several channels, each with a window. If the height of an input pulse is within the window, the MCA records it as a single count in that channel. After a certain amount of time, the MCA produces a statistical output showing the number of samples and the corresponding channel number, which ultimately forms the final spectrum. The channel number is associated with both the pulse height and the gamma energy. By analyzing the spectrum against a known source, a correlation between energy and channel number can be made.

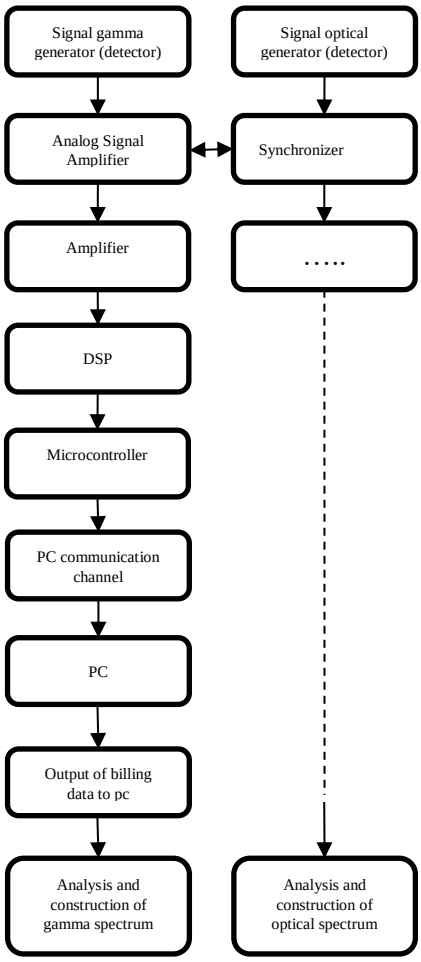

Figure 4: General block diagram of the current pulse motion and its analysis and simulation of the converted pulse

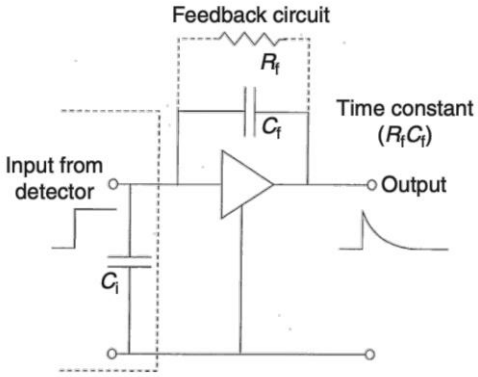

Figure 6: Preamplifier and signal structure (from Feng, 2020)

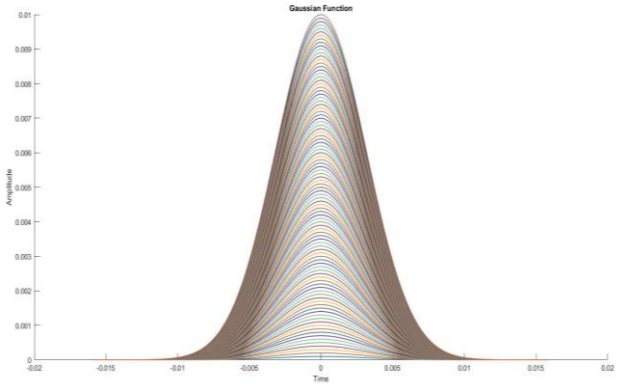

Figure 7: The original current pulls emulated from Palls generator before he enters into the preamplifier (the amplitude and dispersion parameters were configured with a dispersion of 10 μs and an amplitude ranging from 0.1 μA to 10 mA).

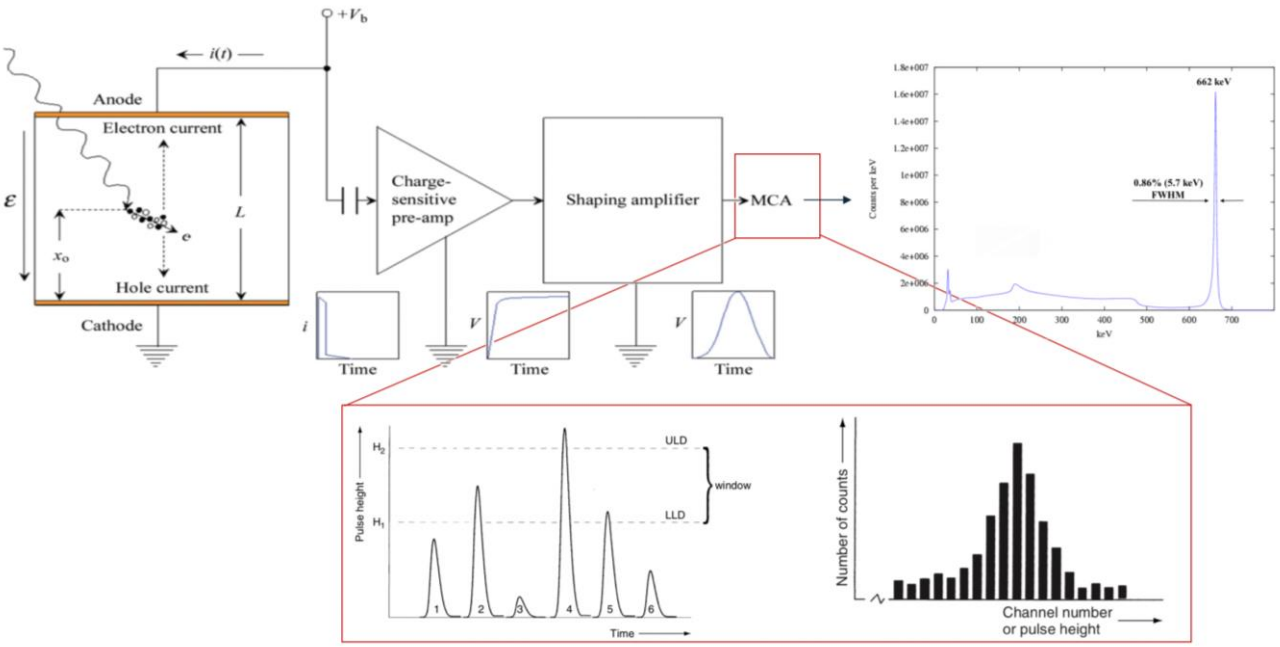

Figure 5: General block diagram of the analog current-potential pulse movement and analyses and simulation of the converted shapes (from Feng, 2020)

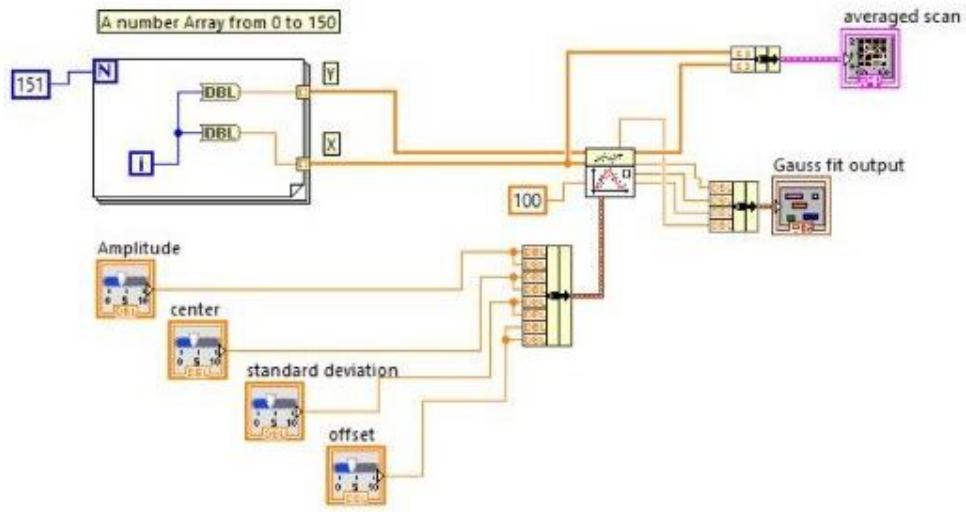

Figure 8: Used general block diagram of the current pulse movement and its analysis and simulation of the converted pulse.

In this paper, the optical part of the detector is referred to separately and considered in many works. For our case we used principles presented in (Rogalski & Bielecki, 2004). However, it is synchronized with the γ detector using a synchronizer. The studied physical processes are often accompanied by the formation of γ and optical spectra. Therefore, a stabilized time scale of the processes is crucial to avoid the loss of registration of the physical events. Our interest in considering the detection of two spectra simultaneously is also because peroxides can also be used to study optical spectra. However, well-available and highly sensitive optical spectrographs are now readily available and inexpensive for high-quality observations.

7. Discussion

The presence of heavy elements in the structure of a semiconductor allowed to solve several problems simultaneously, important solutions to practical problems of spectral diagnostics of fast processes of nuclear origin. First of all, it turned out that perovskite-based CsPbBr3 detector spectrographs are equally good for the construction of spectra of hard radiation and optical. In this paper, some of them are called binary detectors. The quantum states of the valence electrons and the characteristic times responsible for the filling of the conduction band by carriers under the influence of optical and γ-quanta are significantly different. However, they do not affect the formation of a current pulse from each γ- or optical quantum. In our opinion, both detectors should be placed in the same crystal body. The constructive part and the schematic diagram of the device were proposed by (Doikov M., 2022). The design features of binary detectors located in the body of a single crystal CsPbBr3 and the theory of current pulse formation will be the subject of our next work. In the meantime, we will consider the formation of the spectra of γ and optical radiation in single-crystal CsPbBr3 detectors.

8. Conclusion

Modern detector crystals made of the heavy elements Cs, Pb, and Br $CsPbBr_3$ make it possible to comprehensively solve the problems of studying fast processes in plasma, in which quanta of γ and optical radiation are formed simultaneously.

The ability to easily reconfigure the bandgap of a semiconductor makes it possible to preserve its multichannel nature.

Several physical objects have been considered that simultaneously generate gamma and optical spectra. correct processing of the signals coming from the final spectra. In the article, the characteristic times of formation of useful current signals in μs, pulse amplitudes in μA, and times between signals of tens of μs.

In the signal modeling phase, the above characteristics were used. Emulation was done using a signal generator in the LabVIEW environment. For high-speed ADCs presented in the same environment, the supply of the described signals from the detectors was tested.

We have found that the ADC processing of the applied current pulses in terms of amplitude and dispersion allows us to obtain the desired γ and optical spectra without loss and distortion of physical information.

Reference

Doikov D.N.: 2022, *Odessa Astron. Publ.*, **35**, 18.
Doikov M.D.: 2022, *Odessa Astron. Publ*, **35**, 24.
Doikov D.N., Doikov M.D.: 2023, *FAS*, **61**, in press.
Feng Y.: 2020, Master Degree Thesis. Univ. of North Carolina at Chapell Hill, 70 p.
Liu F., Wu R., Wei J., Nie W., Mohite A.D., Brovelli S., Manna L., Li H.: 2022, *ACS Energy Lett.*, **7 (3)**, 1066.
López C.A., María Consuelo Alvarez-Galván C.A., Hong B.-K., Martínez-Huerta M.V., Serrano-Sánchez F., Carrasco F., Castellanos-Gómez A., Fernández-Díaz M.T., Alonso J.A.: 2020, *ACS Omega*, **5 (11)**, 5931.
Ma W., Liu L., Qin H., Gao R., He B., Gou S., He Y., Ouyang X.: 2023, *Sensors*, **23**, 1.
Rogalski A., Bielecki Z.: 2004, *Bull. of the Polish Ac. Of Sciences. Technical Sciences*, **52**, No.1, 43.

https://doi.org/10.18524/1810-4215.2023.36.289978

FLAYERS IN THE PLANETS ATMOSPHERE

D. N. Doikov[1], M. D. Doikov[2]

[1] Dpt of Mathematics, Physics and Astronomy, Odessa National Maritime University, 34 Mechniov str, 65029, Odessa, Ukraine, *dmitro.doikov@gmail.com*

[2] Faculty of Physics and Technologies, Plovdiv University "Paisii Hilendarski", Plovdiv, Bulgaria, *marik.doikov@gmail.com*

ABSTRACT. Planets of the Solar System or exoplanets with atmospheres are complicated to investigate because of the absence of sufficiently intense energy fluxes reflected by their atmospheres. At a sufficiently high brightness of the neighboring star, the atmosphere of the exoplanet gives the absorption spectra of some molecules with a high dissociation potential. If the star's surface temperature is low enough and its activity is low, then the presence of thunderstorm activity in the planet's atmosphere can make it possible to identify it. We show the processes that lead to the formation of flare spectra in the γ- and optical ranges and ways to identify them. It is important to note that current discharges initiate intense nuclear transformations with the formation of proton-rich C11, N13, and O15 nuclei. The spectrum of such a medium is specific and different from the spectra formed by the neighboring star. The statistical irregularity of the frequency of thunderstorms and the variety of conditions in the atmospheres of planets makes it possible to study them due to their illumination in the optical part of the spectrum. It is shown that the integrated optical flow and the detailed γ-spectrum make it possible to trace the time evolution of the lightning head current cord and obtain quantitative values of the current strength. Such fluctuations of the current give changes in the magnetic field of the filament, comparable with the value and even greater than the intrinsic magnetic fields of the planets. To carry out the proposed research, M. Doikov developed a multichannel spectrograph consisting of a γ- and optical spectrometer, a highly sensitive magnetometer, and a radio wave recorder. Its design is discussed in his report. We also note here that the calculations make it possible to determine the statistical parameter of time signals, the operating modes of the equipment, and the selection of the necessary nodes for designing the final working layout of the multichannel spectrometer. The value of the choice of observation site is indicated. In mountainous areas, these are heights of the order of a kilometer. In this case, the devices are near lightning.

Keywords: γ- and optic ray spectra, lighting in planet and exoplanet, rapid nuclear processes, induce γ-ray spectroscopy, positron spectroscopy.

АНОТАЦІЯ. Планети Сонячної системи або екзопланети з атмосферами складні для дослідження через відсутність достатньо інтенсивних власних потоків енергії, відбитих і розсіяними атмосферами. При досить високій яскравості сусідньої зорі атмосфера екзопланети дають спектри поглинання деяких молекул з високим потенціалом дисоціації. Якщо температура поверхні зорі низька і активність мала, тоді наявність грозової активності в атмосфері планети може дозволити її ідентифікувати. Показано процеси, що призводять до формування спектрів спалахів в γ- та оптичному діапазонах та способи їх ідентифікації. Зроблено дослідження струмових розрядів, які ініціюють інтенсивні термоядерні перетворення з утворенням багатих протонами ядр C11, N13 і O15. Доведено, що спектри такого середовища специфічні і відрізняються від спектрів, утворених сусідньою зорею. Отримано, що статистична нерівномірність частоти гроз і різноманітність умов в атмосферах планет дозволяє вивчати їх завдяки їх освітленості в оптичній частині спектру. Показано, що інтегральний оптичний потік і детальний γ-спектр дозволяють простежити часову еволюцію струмового шнура блискавки та отримати кількісні значення сили струму. На малих дистанціях флуктуації струму дають зміни в магнітному полі нитки розрядження, порівнянні з величиною і навіть більші, ніж власні магнітні поля планет. Для виконання запропонованих досліджень, М. Дойковим розроблено багатоканальний спектрограф, що складається з γ- та оптичного спектрометрів, високочутливого магнітометра та реєстратора відстань до блискавок за допомогою радіохвиль. Про його дизайн йдеться в іншої доповіді. Тут також зауважимо, що розрахунки дають змогу визначити статистичні параметри сигналів часу, режими роботи обладнання, та вибрати необхідні вузли для проектування кінцевої робочої схеми багатоканального спектрометра. Вказано значення вибору місця спостереження. Запропоновано розміщувати обладнання у гірських районах де висоти встигають кілометра і вище. У цьому випадку пристрої знаходиться поблизу блискавки і вимірюванні фізичні параметри мало спотворюються атмосферою.

Ключові слова: γ- та оптичні спектри блискавки, блискавки на інших планетах сонячної системі або на екзопланетах, швидкі ядерні процеси, спектроскопія індуційних γ-променів, позитронна спектроскопія.

1. Introduction

In the history of the Earth, thunderstorms took place an important role in the chemical reaction of light gaseous. Until recently, it was believed that lightning had nothing to do with the fusion of nuclei of some common isotopes but was the product of their interaction with cosmic rays. On the other hand, lightning is a classic, widespread source of sharp disturbances in a wide range of radiation from local regions of the current plasma spectrum and different parts of the current cord. With the advent of sensitive spectrometers, fluxes of these radiations began to be recorded in soft γ- and hard X-rays. Of particular interest were the data from the γ-spectrograph placed after control measurements of radiation fluxes from destroyed atomic reactors recorded fluxes of hard quanta during lightning flashes. Moreover, the γ-spectrum indicated the reactions of synthesis of proton-rich nuclei of light elements and contained both positron annihilation products with electrons. It turned out that in atmospheric conditions there are physical conditions for the acceleration of electrons, protons, and helium nuclei – α-particles. The history of consideration of these currents shows that questions has been for electron current components. In our work we drew attention positive ions component in lighting.

The cross sections of nuclear reactions involving protons, He nuclei (α-particles), and Earth atmospheres CNO elements are well studied and presented in the works (Tanaka et al., 1994), (Doikov, 2020). The electrophysical structure of lightning is well-studied. Here we can talk about the characteristic parameters of the electric field of thunderclouds and its structure, and characteristic energies. Potential differences between clouds or clouds and Earth surface are in frame of $\Delta V \approx (10^8 - 10^9)$V, $E \approx 10^6$ V/m, $I \approx 10^5 A$. The given physical parameters of lighting show conditions for the proton, α-particle, and other positive ions acceleration. At sufficient collision energies, reactions occur with the formation of proton-rich nuclei ${}^{11}_{6}C, {}^{13}_{7}N, and\ {}^{15}_{8}O$. The half-life of the listed isotopes does not exceed 20 minutes. Here we should observe the afterglow in the form of γ-lines from the annihilation of positrons and electrons injected into the environment with energy 0.511 MeV. Collisions between protons and α-particles lead to the formation of a background (continuous) γ-spectrum (Doikov D.N.& Doikov M.D. 2023 in press). For its registration, small times registration equipment is required. The presented processes are also accompanied by optical flayers, bursts of radio waves, and disturbance of the magnetic field near the lightning. The optical spectra are recorded by the binary detector developed in the previous work (Doikov M.D, 2022). In this article has been discussed the integration of a magnetometer, a lightning range finder, and a radio recorder into the already mentioned multichannel structure.

All of the above leads to the need to develop appropriate equipment and plan for monitoring lightning activity in the Earth's atmosphere. In this paper, we consider the possibility of observing lightning and its flare activity on other planets. Especially on exoplanets. For the identification of lightning on exoplanets, it turns out to be useful to have a statistical collection of characteristic parameters of their flashes and their features.

2. The physical structure of lighting

The light in the Earth's atmosphere is a combination of the electron, proton and α-particle currents in the conditioned cylindrical space of the corresponding atmosphere. Under the considered physical conditions, in the first microseconds of the discharge between clouds or between clouds and the Earth, the electron current forms a cylindrical structure of the plasma layer. Such a plasma is kept in a compressed state by the pinch effect and dissipates in a confined space. Unlike classical discharges, in our case the electrons, protons and positive ions acquire relativistic velocities and can initiate nuclear transformations. It is important to note that the electron flow is directed from the Earth towards or between the clouds, while the positive ion flow is in the opposite direction. In the first approach, we will calculate the kinematic properties of the plasma components mentioned, which are important for the following, taking into account the characteristics of the electric field mentioned above. We will spend the characteristic time between two successive collisions, taking into account the external Coulomb force, which is reduced due to the strong acceleration of the particles. The formulae presented in the textbooks have been used only for the estimation of the state in lighting.

2.1. The proton and α-particle flux

For protons $a_p = qE/m_p$, α particles $a_\alpha = \frac{qE}{m_\alpha} = \frac{a_p}{4}$ then the binary collision time is $t_b = \sqrt{\frac{2l}{a}}$. Under the conditions of the Earth's atmosphere, we have $t_b \approx 0.45 \cdot 10^{-10} s$ for protons and $t_b \approx 10^{-10} s$ for α particles. In the main part of the illumination observation the full lifetime is close to 0.1 s. Then, theoretically, each proton and α particle undergoes 10^{10} collisions. The change in speed between the collisions is $10^4\ m/s$. In other words, even taking into account the energy loss due to the ionization of the heavy particles, the protons and alpha particles reach relativistic velocities. In terms of kinetic energies, energies of 20 MeV correspond to a proton velocity of $V_p \approx 6 \cdot 10^7 m/s$. To account for this, we use the Bethe-Bloch formula:

$$-\left(\frac{dW}{dx}\right)_{ion} = NS\ . \qquad (1)$$

In illumination $NS \approx 60 - 100\ erg/cm$. The ionization rates during energy loss are

$$-\left(\frac{dW}{dt}\right)_{ion} = \frac{3}{4}\sqrt{2}c\sigma_{ph}\left(\frac{Mc^2}{W}\right)^{\frac{1}{2}} mc^2 ln\left(\frac{4W}{I}\right) n_e\ , \qquad (2)$$

where N – projective ions is the number density in the illumination plasma, z is the charge number of the particle (in our case p or α particles), v_i is the particle velocity, β is the relativistic term $\beta = v_i/c$, $-\left(\frac{dW}{dx}\right)_{ion}$ is the specific ionisation loss over the unit length, I is the mean ionization potential (in eV), I= (13.5 eV) Z≈94eV, and the thermalization times t_l of the fast electrons are:

$$t_I = \int_I^W \frac{1}{-\left(\frac{dW}{dt}\right)_{ion}} dW \approx \frac{3{,}2\cdot 10^{13}}{n_e}\left(\frac{W}{Mc^2}\right)^{\frac{1}{2}} \frac{W}{mc^2 ln\left(\frac{4W}{I}\right)}\ s \approx 8.57\cdot\frac{10^{13}}{n_e} s\ . \quad (3)$$

In air, under normal conditions, the free path length is $l \approx 2{,}65\cdot 10^{-3} cm$. The maximum free path length times of the motion $t_m \approx l/v \approx 10^{-3} cm/4.4\cdot 10^6 cm/c \approx 0{,}17\cdot 10^{-9} s$. The time t_m and t_I show that the transition from the non-relativistic to the relativistic regime gives electrons, protons and α-particles time to undergo several thousand collisions to reach relativistic velocities. This allows us to conclude that ionization losses are included with some delay. In this case, we can observe a pure combination of coincidence between inverse Compton, Bremsstrahlung, and synchrotron effects (CBSE).

Elastic collision. Let's start by estimating the energy loss due to elastic collisions that satisfy the Massey criterion. The collision should be described by a formula of elastic processes of particles α and β with masses m_α, m_β The kinetic energies K_α, K_β are suitable to satisfy the third condition. After each collision, energy ΔK_α is transferred from particle α to particle β.

$$\Delta K_\alpha = -\frac{m_a m_b}{(m_a+m_b)^2}(1-cosv)\left(K_\alpha - K_\beta\right)\ , \quad (4)$$

where v is the scattering angle for the projectile particle colliding with the target particle β, $b \gg a$. Let $\chi_{\alpha\beta}$be:

$$\chi_{\alpha\beta} = \frac{2m_\alpha m_\beta}{(m_\alpha+m_\beta)^2}\ . \quad (5)$$

The$\chi_{\alpha\beta}$ coefficient is called the energy transfer coefficient (or energy exchange efficiency). If the kinetic energy of electrons $K_e < 10\ eV$ and ions $K_i < 10^4 \frac{m_i}{m_H} eV$ for protons, then the Massey criterion for proton, α particle-atom collisions is fairly well met. Since Earth's atmosphere consists mainly of CNO element, some single atoms of inert gaseous, we considered targets mainly like ${}^{12}_{6}C, {}^{14}_{7}N, and\ {}^{16}_{8}O$. The source of proton is atmospheric water, of α-particle is single atoms of ${}^{4}_{2}He$ At the beginning the atmospheric gas is ideal gas. Then free path length l in normal condition is $= \frac{1}{\sqrt{2}\sigma n_\alpha} = 7.1\cdot 10^{-3} cm$, $n_\alpha = 2.65\cdot 10^{21} cm^{-3}$ is numerical density of atmospheric gas, $\sigma = 3.77\cdot 10^{-16} cm^2$is average geometrical cross section of typical molecules N_2. At each distance l the homogeneous electric field accelerated ions and added to proton velocities $\Delta V = \sqrt{2qEl/m_p}$ where N is number of intervals after collision with resting atoms or molecules. Then V(N)= NΔV The next step is to calculate the third multiplier in (4):

$$K_p - K_N = \frac{m_p}{2}(N\Delta V)^2 - \frac{m_p}{2}\left((N-1)\Delta V\right)^2 = \\ = \frac{m_p}{2}(\Delta V)^2(2N-1). \quad (6)$$

After replacing in (4) we get:

$$\Delta K_p = -\frac{m_p m_N}{(m_p+m_N)^2}(1-cosv)\frac{m_p}{2}(\Delta V)^2(2N-1) \quad (7)$$

or for α-particle

$$\Delta K_\alpha = -\frac{m_\alpha m_N}{(m_\alpha+m_N)^2}(1-cosv)\frac{m_p}{2}(\Delta V)^2(2N-1)\ . \quad (8)$$

The next step is averaging over the scattering angles. It should be noted that in the case of intense electric fields, the proton reaches $\Delta V \approx 2.45\cdot 10^6 cm/s$ or in atomic energy unit $K_p \approx 6.26\ eV$. already on the first free path. Then the mean value of the multiplier $\overline{1-cosv} \approx 0.25$ The energy transfer coefficient is $\chi_{pN} \approx 0.104$, then $\Delta K_p = 0.109\cdot 0.25\cdot 6.26 = 0.17 eV$ when N=1. In the following intervals after collisions with nitrogen atoms, the proton velocity increases, which shortens the characteristic time between collisions. Very quickly, even taking into account the inertia of the collision processes, in a fraction of a microsecond, the processes of acceleration and energy transfer become like an avalanche. Let's see what it looks like in reality. First, we estimate how many collisions must occur to satisfy the Messi approximation. To do this, we substitute the value of the limiting kinetic energy for ions into the left side of the equation, taking into account that we are moving protons and α-particles.

$$10^4 \frac{m_i}{m_H} eV = 0.015 eV(2N-1)\ . \quad (9)$$

From (9) we can see that in order to reach the limits of energies at which the Messier approximation is still performed, collisions must occur. This is the case for $N = 6.67\cdot 10^5$. This is followed by the ionization loss modes described by the Bethe-Bloch formula (1). However, in this paper we will use a form that is more convenient for solving the problem. At each further step up to proton energies of 10 MeV. The number of collisions in the light guide N=7·10^8 acts without ionization losses. The distance crossed by protons and α-particles along the flash head is 50-60 meters. Crossing time. The definition of the electron crossing time is given in the formula:

$$t = \frac{1}{N}(l/\Delta V) \approx \frac{1.31\cdot 10^{-10}}{N}\ s\ . \quad (10)$$

Without resorting to plotting the characteristic times of the considered relativistic phase of proton and α-particle motion, we can conclude that all phases of their motion occur almost instantly, compared to the time of a lightning discharge. This means that the rest of the time, which is tens and hundreds of milliseconds, the reactions of nuclear transformations are continuously taking place with the formation of characteristic γ-spectra.

Heavy ions lose a lot of energy in the early stages of their motion, interacting mainly with nitrogen atoms. After passing through 10^5-10^6 collisions, they begin to participate in nuclear interactions, leading to the formation of proton-excess nuclei. Even protons and alpha particles can excite the radiative states of the nuclei of carbon, nitrogen and oxygen (Sigmund, 2014). The result is stimulated gamma radiation. The maximum radiation from the cross-section selection in our previous works is given by the nuclear reaction channel: $\alpha + {}^{14}_{7}N \rightarrow \gamma + \cdots$. presented in Table 1.

Table 1. γ-ray and neutron production cross section

E(MeV)	σγ(P+N14→ →γ+..) mbn	σn(α+N14→ →n+) mbn
7	9298	25,07
8	9635	48,18
9	10060	84,97
10	10540	126,1

2.2. The electron current in lighting

The electric current in lightning is formed in a large spatial slice, is responsible for bursts of electromagnetic energy in different regions of the spectrum, and forms a magnetic field perturbation. The perturbation of the magnetic field is $\Delta B \approx \frac{\mu_o I}{r} \approx 10^{-4}T \approx B_E$Typical currents in lighting are $I \approx 10^4 - 10^6 A$. The maximum time of the magnetic field change is 10 − 100 ms, and $\Delta B_l \approx B_E \approx 10^{-5}T$. The advantage of the detector designed by us is the possibility of synchronized measurements of the magnetic field with accuracy up to one pika Tesla. The induction of electric and magnetic vortex fields generates a wide spectrum of radio emissions. Taking into account the observational data on lightning, in addition to the "classical" radio emission, attention should also be paid to the formation of radio waves of a synchrotron and bremsstrahlung nature. In any case, we are dealing with a continuous spectral distribution. From lightning observations, it is possible to make a realistic estimate of the average velocity by dividing its characteristic scale h by the process time t.

Then we have the average velocity of the electrons $V_e = h/t \approx 10^5 m/s$. In further calculations we take into account that the average angle between the lightning and the direction of the Earth's magnetic field is π/4 rad. Taking into account the non-thermal, directed flow of electrons under the action of an external electromagnetic force, the calculations of the energy losses of electrons for radiation should be divided into two stages. Non-relativistic and relativistic. Observations of lightning storms also show the beginning of a burst of hard radiation before the onset of an electric discharge. That is, before the onset of ionization and the subsequent discharge. The same question arises as in the physics of cosmic rays about the prevalence of the corresponding energy loss mechanism for radiation. First, we consider the strict relations for the energy losses of electrons obtained by Bethe and Heitler (Haykava, 1974) for each mechanism separately. Then we will answer the question about the structure of the radiation produced by each of the given mechanisms. In the same section we will comment on the operation of such mechanisms

If electron energies are more than 10 eV the collisions are ruled by quantum mechanics. However, the electron energy will now be determined by the ratio between their energy losses from interaction with air atoms and the increase in kinetic energy as a result of the work of the electric field. In this paper, we single out only those mechanisms that lead to losses due to their radiation during their movement in the Earth's atmosphere. In the "prequantum mechanic regime" have been no more than 10^3 collisions in the air with normal conditions. At this time no observed optical radiation. But after this beginning concurrence between CBSE these effects produced part of the full energetic loss of already fast electrons including pare production, photo effect, and ionization losses. In this and the next sections, we considered only radiation loss and pair production haw the source of the hard radiation from lighting.

"Runaway electrons". The work of the known mechanisms of energy loss of electrons accelerated by an electric field forms the spectrum of secondary electrons. The distribution function of secondary electrons is such that the main part is represented by low-energy electrons. According to (Gurevich, 2001), high-energy secondary electrons form a stream of relativistic electrons called "runaways". The stream of relativistic electrons, unlike the stream of ions, undergoes an avalanche-like increase in its number. Gurevich proposed the dominance of the Bremsstrahlung emission in the γ-quanta background continuum. Another point of view of the statement in the work (Petrov, 2021). It shows that γ-quanta are formed due to the action of the synchrotron mechanism. However, the proof of the operation of such a mechanism can be only a high degree of polarization and a narrow directivity of the radiation pattern.

Bremsstrahlung emission. Bremsstrahlung emission is usually divided into three types of processes. Under the conditions of a lightning discharge, the deceleration (or acceleration) of charges can be caused either by their attraction or repulsion when electrons and ions approach each other, or by their centrifugal acceleration when moving in external magnetic fields (of Earth and sounder storms with lighting). The presence of multiply charged ions in a lightning discharge leads to a certain probability of the formation of quanta with energies comparable to the binding energies of the last filled level. On the other hand, for relativistic electrons, the time of the dipole interaction of an electron with an ion is exactly proportional to the velocity of the electrons. Bremsstrahlung emission of energy from units of plasma volume within a solid angle in a unit frequency interval in units of time (called emissivity) for electrons with Maxwell-distributed velocities.

$$J_v(T) = \frac{16}{3}\left(\frac{\pi}{6}\right)^{\frac{1}{2}} \frac{n_v Z^2 e^6}{m_e^2 c^3} \left(\frac{m_e}{kT}\right)^{\frac{1}{2}} g e^{-hv/kT} n_e n_i = 5.44 \cdot$$
$$\cdot 10^{-39} \frac{n_v Z^2 g}{\sqrt{T}} n_e n_i e^{-hv/kT} erg/(cm^3 s\ sr\ Hz)\,, \quad (11)$$

$J_v(T)$ in units of erg/(cm^3 s sr Hz). Where n_v is the refractive index, Z is the ion charge, n_e and n_ia are the electron and ion concentrations, g is the so-called Gaunt multiplier (in the optical range $g \approx 1$,, and in the radio range g≈5-6). The rate of plasma energy loss due to bremsstrahlung is:

$$W = 1{,}43 \cdot 10^{-27} T^{1/2} n_e n_i Z^2 (erg/(cm^3 s))\,. \quad (12)$$

After substitution of the data plasma $n_e \approx 10^{19} cm^{-3}, n_i \approx 10^{19} cm^{-3}, T \approx 10^5 K, Z \approx 6$ we have $\approx 1{,}69 \cdot 10^{16} erg/(cm^3 s)$. The rate change in specific heat energy $\Delta U/\Delta t \approx 3{,}66 \cdot 10^{14} erg/(cm^3 s)$. Thus, brems-strahlung losses are the main source of radiation energy and are comparable to changes in heat losses. Together with this, the formula (11) is limited $J_v(T)$ by hard radiation part.

$$J_v(T) \approx 0{,}089 \cdot e^{-\frac{h\nu}{kT}} \approx 0{,}089 \cdot e^{-\frac{h\nu}{8.8\,eV}}\ erg/(cm^3 s\ sr\ Hz). \quad (13)$$

The formula (13) consists of a sharp decrease of the bremsstrahlung intensity in the X-ray region. It has been shown that the bremsstrahlung of the electron component of the plasma under lightning discharges does not form γ-spectra. In lightning we have a different situation. First, fast electrons form a directed flow of fast electrons that is self-sustaining in the combined external electric and magnetic fields. In the lightning head, the electric field gradient is so large that the electron flow reaches relativistic velocities in 0.1 ns, but the avalanche-like ionization has not yet begun. The direction of the electron flow is maintained by two independent factors. The constancy of the direction of the electric field strength and the pinch effect. In this case, the angle between the electric field and the mean magnetic field will be 45 degrees. The energy loss of electrons due to bremsstrahlung without magnetic field and with magnetic field (magnetic bremsstrahlung) is considered separately. In this case, the energy loss is represented by the classical textbook relation (Sigmund, 2014):

$$\begin{cases} -\left(\frac{dE}{dx}\right)_{br}^{rad} = \int_0^{E-mc^2} \frac{N}{A}\sigma_r(E,k)kdk \\ = 4\frac{N}{A}z^2\alpha r_e^2 E \cdot \left(ln\frac{2E}{mc^2} - 1/3\right) \\ mc^2 \ll E \ll 137 \cdot \frac{mc^2}{Z^{\frac{1}{3}}} \\ or\ 0{,}511\ MeV \ll E \ll 35\ MeV \end{cases} \quad (14)$$

and for the relativistic limit of electron energies bremsstrahlung energy loss is:

$$\begin{cases} -\left(\frac{dE}{dx}\right)_{br}^{rad} = 4\frac{N}{A}z^2\alpha r_e^2 E\left[ln\left(191\frac{1}{Z^{1/3}}\right) + \frac{1}{18}\right] \\ 137 \cdot \frac{mc^2}{Z^{\frac{1}{3}}} \ll E\ or\ 35\ MeV \ll E \end{cases}. \quad (15)$$

For further calculations, we also need to know the comparative rate of electron energy loss due to bremsstrahlung, synchrotron radiation, and electron energy loss due to the inverse Compton effect.

$$\begin{cases} -\left(\frac{dE}{dt}\right)_{br}^{rad} = 4Z(Z+1)n\alpha v r_e^2\left[ln\left(\frac{2E}{mc^2}\right) - \frac{1}{3}\right]E \\ 0{,}511\ MeV \ll E \ll 35\ MeV \end{cases}, \quad (16)$$

$$\begin{cases} -\left(\frac{dE}{dt}\right)_{br}^{rad} = 4Z(Z+1)n\alpha v r_e^2\left[ln\left(\frac{191}{Z^{1/3}}\right) + \frac{1}{18}\right]. \\ 35MeV \ll E \end{cases} \quad (17)$$

Where Z is the charge number, α = 1/137, $r_e = \frac{e^2}{mc^2} = 2.82 \cdot 10^{-13} cm$, is the classical electron radius, $\alpha = 2\pi e^2/hc = 1/137$ the thin structure constant.

When studying the interaction of fast electrons with the atmosphere, it usually turns out that the energy of the detected bremsstrahlung quantum is limited by the time of interaction with the atomic field and the energy of the Coulomb field of the nucleus at distances comparable to the de Broglie wavelength. The potential energy of the Coulomb field near the nucleus on such scales is 1.99-2 MeV. Under lightning conditions, the electron undergoes collisions to reach similar energies without losses due to 10^8 collisions. Taking into account the latter, we have an order of magnitude greater number of collisions is 10^10. In this case, the passage length is 1 km and we conclude that the bremsstrahlung quantum of the electron current forms in the lower part of the illumination. However, the proton current generates γ-quanta in the flash head, but their origin is different and is described in the first part of this article. The ratio of the rate of energy losses caused by bremsstrahlung to the rate of ionization losses using the expressions given in this article leads to the relation

$$\eta = \frac{-\left(\frac{dE}{dt}\right)_{br}^{rad}}{-\left(\frac{dE}{dt}\right)_{I}^{rad}} = \frac{\left(\frac{e^2}{hc}\right)}{\frac{W}{mc^2}}\ . \quad (18)$$

The absence of optical radiation has been observed in classical plasma in the pre-optical period at the beginning of the γ-flash of illumination. In this case, according to the formula, we should assume the absence of ions in the presence of electrons that have already reached relativistic velocities. In the atmosphere under consideration, the times of the main radiative transitions are comparable to the times between two successive collisions, and the excited electronic state is removed by the impact interaction. As shown in this section, in classical collisions the electron loses only 0.1% of its kinetic energy for each collision. In order to reach relativistic speeds, it has to undergo about 1000 collisions under the conditions of the Earth's atmosphere. After that, we have optical flyers of light.

Synchrotron emission.

$$-\left(\frac{dE}{dt}\right)_{s}^{rad} = 6{,}5 \cdot 10^{-4} H^2 \left(\frac{E}{mc^2}\right)^2 eV/s\ . \quad (19)$$

Maximum power of synchrotron emission of an electron in a single frequency interval and in a unit solid angle:

$$P_\nu = \frac{1{,}6 \cdot e^3 H}{4\pi mc^2} = 1.7 \cdot 10^{-23} H\ \left(\frac{erg}{s \cdot sr \cdot Hz}\right), \quad (20)$$

where H is expressed in Ersted. The monochromatic radiation decreases at lower frequencies and decreases exponentially at higher frequencies (the hard radiation spectra).

$$P_\nu \sim \nu^{\frac{1}{2}} \exp(-0{,}29\nu/\nu_m)\ . \quad (21)$$

The registration of hard radiation under existing conditions in flash synchrotron radiation according to relation (15) is problematic.

The inverse Compton effect. The relation for this type of energy loss rate:

$$-\left(\frac{dE}{dt}\right)_{c}^{rad} = 2{,}67 \cdot 10^{-14} W_{ph}\left(\frac{E}{mc^2}\right)^2 eV \cdot s^{-1}\ . \quad (22)$$

In the high energy range, the main contribution to radiation losses comes from the last two mechanisms. Bremsstrahlung dominates only in the intermediate energy range.

The main result of the performed calculations is the synthetic cumulative spectrum. In the process of energy acquisition, the electron covers a wide range of radiation and radio waves up to X-rays. In this sense, the question of the nature of gamma radiation remains open. Observations of lightning made it possible to register γ quants are formed

in a few milliseconds before the ignition. One of the mechanisms responsible for the formation of γ quanta is the formation of electron-positron pairs. As in the case of bremsstrahlung, it is necessary to introduce the parameter ξ, where is the ratio of the energy of the emitted photon k to the kinetic energy E of the incident electron u = k/E (Haykava, 1974). Then:

$$\xi = 100\frac{mc^2}{E}\frac{u}{1-u}Z^{-1/3} \quad . \tag{23}$$

The ξ approximation predicts the desired ionization calculations in the ongoing energy loss calculations. All calculations of the interaction of fast electrons with atomic structures and the appearance of the corresponding radiation produced by the energy losses of electrons for radiation begin with its preliminary evaluation.

Pair formation. In quantum electrodynamics, pair formation is an inverse process of bremsstrahlung of fast electrons. From Detail Equilibrium Principle

$$\sigma_{pair}(k,E) = \sigma_r(k,E)\left(\frac{E}{k}\right)^2 \quad . \tag{24}$$

Then if v=E/k, where E is the energy of the electron created.

$$\sigma_{pair}(k,E) = 4\alpha Z^2 r_e^2 G(k,v) \quad . \tag{25}$$

$G(k,v)$ presented in readable form in (Haykava, 1974). The full cross section after integration of the $\sigma_{pair}(k,E)$ ire in a formula:

$$\begin{cases} \sigma_{pair}(k) = \int_{mc^2}^{k-mc^2}\sigma_{pair}(k,E)dE = 4\alpha Z^2 r_e^2 \cdot \\ \cdot\frac{7}{9}ln\frac{2k}{mc^2} - \frac{109}{54} \\ 3{,}423\ MeV \ll k \ll 35\ MeV \\ \frac{7}{9}\ln\left(191Z^{-\frac{1}{3}}\right) - \frac{1}{54} \\ 35MeV \ll k \end{cases} . \tag{26}$$

In the first formula, the left edge of the interval is bounded by the energy values 3.423 MeV. From these relations in 1m is produced 1 positron. In all light channel full number of positrons is 10^7. If position of devices is near current tube the γ-flyers have been detected positrons and γ-quants from annihilation between positrons and electrons.

The mean cross section $\sigma_{pair}(k)$ of pair formation varied in air in the illumination is $10^{-25}cm^2 \le \sigma_{pair}(k) \le 10^{-24}cm^2$. The mean distance of pair formation in air l is $l = \frac{1}{\sigma_{pair}(k)} \approx (10^3 - 10^4)\ cm$. We emphasize that positrons do not annihilate immediately, because they need to experience sufficient deceleration up to thermal velocities. In other words, it is not always possible to attribute γ-flares before a lightning discharge.

In this chapter, we presented the radiation loss of fast relativistic electrons and pair production, and the possible source of γ-ray flashes. From the presented relations the following conclusions can be drawn.

The presence of huge gradients of the potential of the electric field in the places of formation of the lightning head leads to an unusual course of the process of formation of the radiation spectrum before the formation of the lightning discharge itself.

The calculations carried out in the article show that the presence of γ-radiation bursts and the simultaneous absence of an optical manifestation before a lightning discharge indicates that the electrons become ultra-relativistic after a thousand collisions. During this time, the ionized fraction of the gas does not have time to enter the recombination process.

This is possible in the absence of dust fractions and other pollutants, which absorb the electrons that are created and at the same time accelerate the coagulation rate. At the same time, the formation of raindrops is accelerated.

The spectroscopic properties of media that penetrate fast electrons are well studied, and the formulas used are simpler for all energy loss modes considered. In contrast to the extensive list of laboratory physical and extra-atmospheric astrophysical media used in lightning, the applicability of the Maxwell-Boltzmann velocity distribution is not applicable. Namely, all electrons move in one direction in the longitudinal direction, in the transverse direction they are distributed according to Maxwell. At relativistic velocities, the energy fraction of the transverse component of the electron velocities decreases sharply, and all velocities are already in a narrow angular opening. The bremsstrahlung and synchrotron in the ultra-relativistic mode of electron motion in flashes have several peculiarities. They consist in the fact that the possibility and spectrum of synchrotron radiation are limited by the values of the magnetic field of the Earth (or the corresponding planets), while the bremsstrahlung is determined by the influence of the Coulomb field of the nucleus. In the intervals given by us, synchrotron radiation can give rise to soft X-ray quanta. That is, under the conditions considered, synchrotron radiation does not produce γ quanta.

3. The detection in the exoplanets

The existence of a new generation of infrared satellites with its sensitivity is suitable for the search for exoplanets at a new level. In exoplanets with illumination in a short time have been IR excess production. In experiments with exoplanet identification, we propose to use IR photometric observation. The character of short-time IR pulses is specific for energy losses in an exoplanet atmosphere. The very fact of identifying the presence of planetary atmospheres is based on the registration of specific lines of polyatomic and diatomic molecules. These lines are of an electronic vibrational nature. The EXOMOLE project (Giovanna et al., 2007) used this approach and provided valuable information about the presence of polyatomic molecules on exoplanets. The very presence of lightning in planetary atmospheres speaks to their multiphase nature. That is, gas, solid particles and turbulent updrafts are present at the same time. The work function of electrons from the surface of solid particles of methane or its various mixtures with other chemical components of exoplanet atmospheres. The lower the work function emitted from the surface of the solid particle, the higher the probability of electron emission from its surface. In combination with active atmospheric activity, the power of lightning discharges has no fundamental limitations. Of great value in lightning is the backlight, which contains a large amount of scattered radiation. When lightning storms show significant activity, the exoplanet begins to "shine" with much greater intensity in the scattered radiation. The maximum intensity of radiation produced by lightning discharges is in the ultraviolet, as observed in the Earth's

atmosphere. The planet Uranium can be used as a standard for the scattering of ultraviolet radiation, the atmosphere is practically composed of CH4 and NH3 molecules. Scattering by other molecules and small particles of different chemical composition is described by the classical Mie theory. Under normal conditions, the intensity of the scattered emission is given by the formula

$$I = \frac{9\pi^2(1-cos^2\theta)}{2r^2\lambda^4}\left(\frac{n_1^2-n_0^2}{n_1^2+2n_o^2}\right)^2 V^2 I_0 \,. \qquad (27)$$

The cross section registers mainly the illumination with $\theta \approx \pi/2n_1$ are the refractive coefficients. n_0 are the gas phases, V is the molecular volume, $I_0$is the source illumination (from the illumination). The Rayleigh scattering cross section has a simple form:

$$C_s = \frac{8\pi^3(n^1-1)^2}{3N^2\lambda^4} \approx 10^{-17} cm^2 \text{ (For } CH_4) \,. \quad (28)$$

Within order of magnitude, molecules CN_4, NH_3, C_2H_2, H_2O these same cross sections lead to effective scattering of the. The detected large exoplanets are probably composed of H_2 molecules and He atoms. For the planets of the solar system we used the next molecular data, which are presented in Table 2. The column header is: μ is molar masses n is refractive index. J, S, N, U are Jupiter, Saturn, Neptune, and Uran in percent of the corresponding chemical composition.

Table 2. The optical parameters, percent contention, and molecular data for big Sun System planets

μ(g/mol)	n	J	S	N	U
$\mu_H = 2.06$	1,00139	86%	96%	80%	72%
$\mu_{He} = 4.0026$	1,000035	13,9%	3,26	19%	26%
$\mu_{CH_4} = 16{,}04$	1,000441	0,1%	0,1%	0,1%	2%
$\mu_{NH_3} = 17{,}03$	1,000375	0,1%	0,1%	0,1%	0,1%
$\mu_{N_2} = 28{,}013$	1,000297	0,1%	0,1%	0,1%	0,1%
$\mu_{H_2O} = 18{,}015$	1,33	0,1%	0,1%	0,1%	0,1%

The glow of all planets without exception is due to incoming streams of light energy from external sources. Most of the discovered exoplanets are close to their parent star. This causes large temperature gradients and contributes to the occurrence of intense storms (Helling et al., 2012), (Berger et al., 2010), (Christensen, 2009). The presence of cloud layers in the atmospheres is associated with the upper layers of their exospheres, where the total gas pressure is close to the pressure at sea level on Earth. This causes large temperature gradients and contributes to the occurrence of intense storms. The presence of cloud layers in the atmospheres is associated with the upper layers of their exospheres, where the total gas pressure is close to the pressure at sea level on Earth. The possible presence of lightning in the presence of thunderstorms leads to additional "illumination" of the atmosphere (Wilkins, 2022), (Neuber et al., 2019). In this case, laboratory experiments are of interest, where spectra of spark discharges were obtained in media with the chemical composition shown in the table. Surprisingly, the obtained spectra have a maximum in the ultraviolet and with the presence and emission lines of the marked atoms and molecules. However, the maximum of the energy distribution is in the UV. In this case the Raleigh scattering of the present molecules is sufficient. In order to detect an exoplanet, it is necessary, as a contrast, to create a brightness variability on its surface in a narrow band of the spectrum, which is not characteristic for the variability of a star. The irregularity of the lightning discharge variability has several peculiarities. First of all, we notice their time interval. The structure of the flashes requires a detailed study. In this case, it is interesting to carry out laboratory experiments to obtain spectra of spark discharges in media with the chemical composition shown in the table. Surprisingly, the obtained spectra have a maximum in the ultraviolet and with the presence and emission lines of the marked atoms and molecules. However, the maximum of the energy distribution is in the UV. In this case the Raleigh scattering of the present molecules is sufficient. In order to detect an exoplanet, it is necessary, as a contrast, to create a brightness variability on its surface in a narrow band of the spectrum, which is not characteristic for the variability of a star. The irregularity of the lightning discharge variability has several peculiarities. First of all, we notice their time interval. The structure of flashes requires a detailed study. The sequence of physical processes during the formation of a lightning discharge can have its peculiarities for different chemical compositions of the exoplanet's atmosphere. Usually these are molecules and atoms from a Table 2. As an example, we can note cases of variability in the appearance of molecular lines and bands on a time scale in optical and IR spectral regions. This method requires the development of a new instrumental approach and is beyond the scope of this article.

4. Discussion

Lightning discharges in the atmospheres of planets provide an opportunity for local diagnostics of their state and help to check and calibrate the instruments we are developing. In particular, for a binary detector in the γ and optical ranges, the simultaneous presence of different fluxes was important. The γ-ray lightning spectra discovered by Japanese physicists using detectors at the Fukushima nuclear power plant required detailed consideration of the positron sources. We were involved in the separation of the whole set of channels of nuclear transformations and interactions of relativistic electrons with atmospheric atoms considered in this work and in (Doikov M., 2022). A big surprise was the appearance of a γ-flare, recorded by flashes several microseconds before the start of the discharge and its glow in the optics. The detection and study of this phenomenon required the development of a new generation of multichannel spectrographs. The work of (Doikov M., 2022) is devoted to this problem. At present it has become possible to integrate a commercial optical spectrograph into the design of the detector manufactured by us with access to the speed of LabView for its further synchronization with the γ-detector. Currently, the main efforts are focused on the development of the electronic unit of the mock-up γ-spectrograph. In order to diagnose lightning on other planets, it is necessary to thoroughly study their spectral and photometric variability. The structure of the variability of the energy fluxes, their temporal evolution, and the variability of the brightness of the spectral lines are important for identifying exoplanets with atmospheres with thunderstorm activity. The presence of traces of nuclear

reactions involving protons and α-particles makes it possible to reconsider the sources of entry into the atmosphere of the Earth and other planets with thunderstorm activity of isotopes of CNO – elements and new sources of induce γ-ray emissions (Doikov D., 2020) with their participation. The role of lightning in the formation of planetary ionospheric activity should also be reconsidered (Doikov M., 2022). Lightning modulates collective oscillations in the ionosphere at infrasonic frequencies, and these oscillations are recorded by special ground stations. The limited timescales of lightning discharge processes and the energy intervals at which lightning hard radiation is formed provide important information about the environment. Despite the non-relativistic average speed of the electrons of a lightning discharge in the lengths of their one run, their speed quickly reaches relativistic values. According to the second part, the increase in velocity in the non-relativistic regime, taking into account collisions with the main component of the atmosphere with nitrogen molecules and atoms. In the range of ionization and radiation losses of kinetic energy accelerated by an external electric field of a given layer of the atmosphere, it becomes possible to form spectral lines and molecular bands located in the zone of maximum sensitivity of modern spectrographic equipment. The selection and planning of the equipment and observation sites are due to the fact that the base stations are located at relatively high altitudes in the mountainous terrain of the Rhodope Mountains. In particular, the building of the branch of the Faculty of Physics and Technology is located at an altitude of 800 m above sea level. The well-equipped Rozhen Observatory (1800 m above sea level) is also located nearby. In this case, the detection equipment is located near the lightning current, which eliminates the influence of additional distorting factors.

5. Conclusion

This paper considers the motion of relativistic particles in a quiescent atmosphere. Contrary to the results of traditional lightning observations, it was considered that the γ-burst starts before the main optical flash caused by collisions of relativistic electrons. In an external electric field, charged particles accelerate between pair collisions, and the loss of kinetic energy during collisions has the following characteristics Typically, charged particles undergo classical collisions, ionization losses, bremsstrahlung losses, and radiation due to the inverse Compton effect. We have also singled out the energy losses for radiation caused by the production of electron-positron pairs. To determine the efficiency of the kinetic energy losses for γ radiation, we considered the cross section for the production of electron-positron pairs. In this case, the source of γ quanta is the annihilation of newly formed thermalized positrons with thermal electrons. In contrast to the formation of positrons as a result of the decay of proton-rich nuclei, positrons in vapors do not have sufficiently low initial velocities. It takes some time for them to slow down. In our work we have obtained the following results:

1. Starting from zero, the particle moves in a non-relativistic regime with increasing velocity up to 10^5 m/s. γ-rays quants appear only in the relativistic regime of motion. In our case, the appearance of primary γ quants before a lightning discharge can be attributed to the formation of electron-positron pairs and further annihilation of positrons. The calculations performed in the article show small values of the cross sections and the productivity of the γ-quanta.

2. Then, with the onset of a lightning discharge, radiation arises due to the excitation of bound and correspondingly unbound transitions. Mainly the energy distribution in lightning spectra is UV part. Under these conditions, a plasma channel is created along which the accelerated motion of low-energy electrons occurs. Simultaneously, protons, and partially helium nuclei (α-particles) are carried out.

3. After the appearance of the plasma channel, the formation of two currents in opposite directions is shown. Electrons usually move from the Earth's surface toward the clouds or between the clouds. The flow of positive protons and alpha particles toward the Earth or between the clouds. The relativistic electron current should be a source only of background γ-ray quanta after 1 thousand collisions with atmospheric atoms.

4. In this state, after 10 thousand collisions, protons and α-particles acquire relativistic speed and energy and begin to participate in the nuclear transformations of lightning.

5. The currents consisting of the mentioned positive particles participate in nuclear transformations similar to the fission reactions leading to the brewing of proton-rich isotopes. Calculations of the induced γ radiation, carried out in our previous works, have shown that the isotope ${}^{13}_{7}N$ is formed most efficiently by the reaction $\alpha + {}^{14}_{7}N \rightarrow {}^{13}_{7}N + n + \alpha + \gamma$. After the formation of ${}^{13}_{7}N$ the decay is observed in the form of the reaction ${}^{13}_{7}N \rightarrow {}^{13}_{6}C + e^{+}$. Assuming these, we conclude that in illumination is possible to isolate γ-radiation produced by two processes, positron annihilation and the formatted by stimulated emission.

6. The photonuclear reaction with γ-quanta we plan to present in the next paper in volcano lighting.

It should be emphasized that lightning is of interest to us as a natural laboratory for the calibration of monitor-type γ-spectrographs.

References

Berger et al.: 2010, *Ap.J*, **709**, 332.

Christensen et al.: 2009, *Nature*, **457**, 167.

Doikov D.N.: 2020, *Odessa Astron. Publ.*, **33**, 28.

Doikov M.D.: 2022, *Odessa Astron. Publ.*, **35**, 24.

Doikov D.N., Doikov M.D.: 2023, *Astron. & Astrophys. Trans.* (in press)

Giovanna T., Alfred Vidal-Madjar, Mao-Chang Liang et al.: 2007, *Nature*, **448**, 169.

Gurevich A.V., Zybin K.P.: 2001, *Usp. Phys. Nauk*, **171**, № 11, 1177.

Haykava S.: Origin of Cosmic Rays, M.: MIR, 1974, v. 2, 343 p.

Helling C. et al.: 2012, *PSS Sp.Iss.: Outer Planets*, VIII July 10, arXiv:1207.1907 VI[astro-ph. EP], 8 Jul. 2012.

Neuber T. et al.: 2019, *Science*, **367**, Issue 6474, 183, https://doi.org/ 10.1126/ science.aax3872.

Petrov N.I.: 2021, *Scientific Rep.*, **11**:19824, https://doi.org/10.1038/s41598-021-99336-3.

Tanaka S., Yamano N., Hata K. et al.: 1994, *Proc. of 8th Int. Conf. on Rad. Shielding*, Arlington, April 24-28, 2, 965; Am. Nucl. Soc. Inc. https://wwwndc.jaea.go.jp/ftpnd/sae/acl.html

Sigmund P.: 2014, Particle Penetration and Radiation Effects, v. **2**, Springer., Switzerland, 603 p.

Wilkins A.: 2022, *New Scientists*, 26 May 2022.

https://doi.org/10.18524/1810-4215.2023.36.289990

A NEW APPROACH TO THE ANALYSIS OF LIGHT CURVES OF PULSATING RR LYRAE STARS WITH THE BLAZHKO EFFECT

L.E. Keir

Department of Physics and Astronomy,
I.I. Mechnkikov Odessa National University, Odessa, Ukraine,
partneroae@gmail.com

ABSTRACT. We discuss the new approach for the analysis of the long-term dense series of observations of RR Lyr-type pulsating stars with the Blazhko effect. The standard way, namely The frequency analysis of the O–C values for the times of maxima does not allow for to detection of the complex nature of the periodic changes in the shape of the light curves, including bi-cyclicity. We have shown the perspectives of a new approach on the example of the analysis of FI Sge variable observations containing a total of 55 observational nights during a period of five years (AZT-3 Telescope, Mayaki Observational Station, SRI "Astronomical Observatory", I.I. Mechnikov ONU). The study is based on the data obtained by S.N. Udovichenko during the 2013 and 2014 observational seasons as well as on data obtained by S.N. Udovichenko and the author during the 2018 observational season.

Our results show that in order to understand the features in the shape of the light curve variations for RR Lyr type pulsating stars with the Blazhko effect, it is necessary to have data for full cycles of variability over a long time, and not just the moments of maxima.

Keywords: pulsating stars: RR Lyr type: Blazhko effect; data analysis.

АНОТАЦІЯ. Обговорюються результати нового підходу до аналізу довготривалих рядів спостережень пульсуючих зір типу RR Ліри з ефектом Блажка. Стандартний спосіб, а саме частотний аналіз значень O–C для моментів максимумів, не дозволяє виявити складний характер періодичних змін форми кривих блиску, в тому числі бі-циклічність, тобто, форми послідовних максимумів, що систематично розрізняються. Для уточнення періодів пульсацій та ефекту Блажка необхідно використовувати довготривалі щільні ряди спостережень, що охоплюють усі фази кривої блиску. Далі при аналізі необхідно враховувати вплив бі-циклічності, а також різний прояв ефекту Блажка для максимумів, що чергуються. Перспективність нового підходу ми показали на прикладі аналізу даних спостережень FI Sge, що охоплюють загалом 55 спостережних ночей за п'ять років (телескоп АЗТ-3, спостережна станція Маяки, НДІ "Астрономічна обсерваторія" ОНУ імені І.І. Мечникова). Спостереження 2013 та 2014 року було отримано С.М. Удовиченко. Спостереження 2018 року отримано спільно автором та С.М. Удовиченко.

Новий підхід дозволив уточнити період пульсацій FI Sge. Крім того, на підставі довгого ряду спостережень було виявлено новий ефект, а саме, зсув моментів максимумів блиску вбік початкової епохи. З новим значенням періоду та врахуванням виявленого ефекту ми побудували нову фазову криву блиску для повного ряду спостережень. Нова фазова крива відповідає теорії пульсацій для зір типу RR Ліри з ефектом Блажка. Наші результати показують, що для розуміння особливостей форми змін кривої блиску пульсуючих зір типу RR Лір з ефектом Блажка необхідно мати дані для повних циклів змінності протягом тривалого часу, а не лише для моментів максимумів.

Ключові слова: пульсуючи зорі: зорі типу RR Lyr: ефект Блажка; аналіз даних.

1. Introduction

At the present time, the technique for processing observation series of pulsating variable stars is currently established. Typically, the analysis of observational data begins with determining the period of variability. To do this, the brightness values and moments of brightness maxima are determined, and then a phase curve is plotted. In this case, a period of variability is selected such that the scatter of the moments of brightness maxima $(O - C)$ is minimal. However, the way minimizing the scatter of brightness maxima does not give both the good values of the peri-

od and a phase curve for the RR Lyrae-type stars with the Blazhko effect. The fact is that in pulsating variable stars of the RR- Lyrae type, in addition to the Blazhko effect, at least two more features of brightness changes are possible, which are lost with this data processing technique. They are the bi-cyclical effect and the effect of shifting the moments of maximums. Ignoring these phenomena leads to an incorrect determination of the period of variability, a distortion of the position of the observed data on the phase curve, and, ultimately, an incorrect analysis of the physical processes occurring in pulsating variable stars. We will look at the manifestations of both these effects and illustrate them using data for the star FI Sge.

The first effect, "bi-cyclicality" was detail described in 2016, in the review paper by Smolec (2016), where he gave an analysis of the data available at that time regarding observations of pulsating variable stars with the Blazhko effect and highlighted the effect of bi-periodicity (period doubling), discovered due to observations of the Kepler space telescope. The term "period doubling" is used to the effect when two successive pulse cycles show systematically stable, alternating variations in the amplitude of the maxima. These variations for RR Lyrae-type stars were first detected in the observational data of the Kepler telescope (Kolenberg et al., 2010), and the typical light curve is shown in Fig. 1.

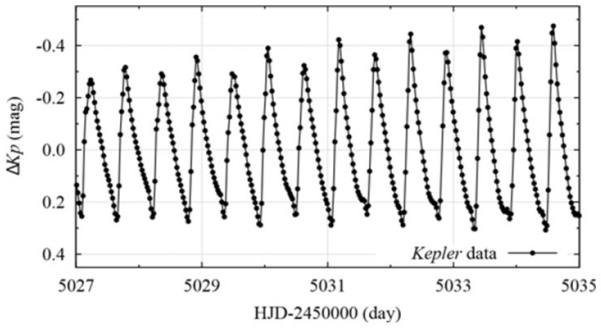

Figure 1: The bi-cyclicity (period-doubling) effect. Average light curve of RR Lyr according to Kepler space telescope data (from Smolec, 2016)

Subsequent studies (Szabo et al., 2010 and Szabo et al., 2014) indicated this effect could not be explained either by two oscillation modes or by oscillations of two different periods. In fact, the bi-periodicity effect is a fairly well-known phenomenon that is observed in type II Cepheids (Soszynski et al., 2011, Smolec et al., 2016). The alternation of amplitude changes is constant, although the pulsations themselves may be irregular for these stars, and modelling shows bi-periodicity may be the beginning of irregular variability (Kovacs & Buchler, 1988). The alternation of amplitude for RR Lyrae-type stars with the Blazhko effect has a different nature. We suppose the use of the term "bi-periodicity" for stars with the Blazhko effect will be false, and we'll use the term "bi-cyclicality" to denote the above effect. Surely, the question is why, for more than 100 years of observations of variable stars with the Blazhko effect from Earth, the bi-cyclicality effect was not discovered? Smolec (2016) explains this by the "unfortunate" average pulsation period for RR Lyrae-type stars, equal to 0.5 days. That is, due to the selection of observations we observe the star with such a period every night practically in the same pulsation cycle. The next pulsation cycle occurs during daylight hours and it is lost.

Fortunately, the pulsation periods of RR Lyrae-type stars do not always exactly coincide with 0.5 days. For example, for the star FI Sge, which was selected for the detailed study, the period of variability noted in the GCVS (Samus et al., 2017) is 0.5047545^d. This means that every night our observations shift along the light curve to the earlier phase, and after 106 cycles (or 53.42 days) we can observe the "previous" cycle. Why did never detect the bi-cyclical effect for FI Sge? The difference in the amplitudes of neighboring cycles reaches 0.1 magnitude, it is not a detection problem even for medium-size telescopes. The problem is determined by the duration of observations and mainly in the methodology for processing observational data of pulsating variable stars with the Blazhko effect. It has always been believed that for pulsating variable stars the most important part of the light curves is the region of the maxima. Determining the moments of the maxima allows to determine the pulsation period and combine all observations into one phase curve and the observation programs were built in accordance with this idea. Thus, the observers themselves increased the duty cycle of the observational data, skipping "unimportan" parts of the light curve. Observations became selective, only the maxima moments, as well as possible changes in their values and phase, were fixed. The base reason for not detecting the bi-cyclicality effect from the Earth is this approach: the short series of fragmentary observations.

The Blazhko effect consists of periodic modulation of the amplitude and period of the star brightness variability. The values of the brightness maxima change by no more than $0.3 \sim 0.4^m$, and the period does not change more than 0.2 of the period. If we place all the observational data on one phase curve, then even if they contain two cycles of different formats, the bi-cyclicality effect is silted up by the Blazhko effect, which has large changes in amplitude. Thus, it was impossible to identify the effect of bi-cyclicality using the short series of observations and a single-period phase curve for all observed data to analyze the variability.

In order not to lose the bi-cyclicality effect during processing, we began to use double the pulsation period when constructing the phase curve. In this way the observational data are automatically divided into two cycles with different formats: the "main" cycle, with a larger maximum amplitude, and the "neighboring" cycle, with a smaller amplitude, and the identification of the bi-cyclical format of bi-cyclical maximum is strongly needed.

2. Observational data and light curve building

We select FI Sge for our detailed study of the RR Lyrae-type stars' light curve possible variations. FI Sge ($RA_{2000.0} = 20^h13^m16.2^s$; $Dec_{2000.0} = +17°30'37''$; type: RRab; $V = 13.2 - 14.3^m$ (p); $E = 2428333.441^d$; $P = 0.5047545^d$; Sp = A2; P(Bl) = 22.4^d according to GCVS (Samus et al., 2017) is the star included in the program of RR Lyrae-type variables of the Scientific Research Institute "Astronomical Observatory" of Odessa I. I. Mechnikov National University. The star was observed for a total of 55 nights during the observation seasons of 2013, 2014, and 2018, at the observation station Mayaki of the SRI "Astronomic Observatory" using AZT-3 telescope equipped CCD Sony ICX429ALL. A total of 5500 frames were obtained in the V photometric band for the entire time of observations, including 26 photometrical maxima. The comparison star was UCAC4-538-127214 $RA_{2000.0} = 20^h13^m14.876^s$, $Dec_{2000.0} = +17°33'39.95''$, $V=13.36^m$). We also used data from Skarka & Cagas (2017), obtained in 2017.

The basis for constructing a phase curve is the period of variability and the initial epoch. Another value of the initial epoch results in a uniform shift of all observed data by a fixed value in time. On the contrary, a change in period leads to a radical change in the location of all observational data on the phase curve. Skarka & Cagas (2017) found another value $P= 0.5047544837^d$ using times of maxima obtained in 2017. We use this value for the building FI Sge light curve for our data set (Fig. 2, left panel). One can clearly see the different positions of the maxima relative to the zero value and the period value is needed if the updating.

We checked the possible influence of the bi-cyclical effect on the light curve and the result is present in Fig. 2, right panel. The maxima positions show a tendency to group together. In addition, we showed the time between neighboring maxima in the bi-cycles exactly corresponds to two pulsation periods, then the time between the maxima of cycles varies from 0.96 to 1.04 phases of the period depending on the location of the cycles (Fig. 3). Moreover, we can suppose the presence of the Blazhko effect for both elements of the bi-cyclisity. So, for FI Sge we must determine the period taking into account both the bi-cyclical and the Blazhko effects.

We concluded an attempt to minimize the scatter of observational data leads to an incorrect choice of period and, as a consequence, to a distortion of the entire picture of the overall phase curve. Therefore, we abandoned the generally accepted method of determining the period and began to look for another method based on a different period search criterion.

3. The Period Search

In our new approach, we assumed that the pulsations of RR Lyrae-type stars are a periodic, continuous process in which the light curves must smoothly transform into each other from night to night. The Blazhko effect should contribute to the dynamics of changes in light curves. The bi-cyclicality effect can be eliminated by considering the light curves of the different parts of bi-cycles (different formats of maxima). We took the longest continuous series of observations in September – October 2018 (15 nights), and analyzed changes in the amplitude, phase and shape of the brightness maximum depending on the selected period. The analysis showed that the best convergence of data and dynamics of changes in light curves for the star FI Sge is provided by a period of 0.50500^d. The difference between this period and that taken from the GCVS for this star is only 0.05%, however, over a large observational interval (5 years), this radically changes the appearance of the phase curve.

Based on the new value of the pulsating period for the star FI Sge, it was possible to determine an additional period of brightness variations equal to 58 pulsation cycles, or 29.29 days. It is impossible to call this value the period of the Blazhko effect, since it is not possible to fit a change in amplitude 0.3^m into this time interval. The dynamic of changes in the amplitude of the maxima for individual series of observations shows that this is impossible. Changes in the brightness amplitude over such a time interval can be no more than 0.1^m. The result is not typical, but it has to be taken into account. The study of the phase curve with a new period revealed identical, discrete, irregular shifts of the moments of the maxima to the initial epoch (Fig. 5). That is, in addition to the Blazhko effect and the bi-cyclicality effect, the star FI Sge has a third effect that complicates the processing of observational data. It should be taken into account that a shift in the moment of maximum in any cycle leads to changes in all subsequent cycles. Based on the above, we assumed the dependence of such shifts on already known effects: the Blazhko effect and the bi-cyclical effect. The bi-cyclicality effect gives us the possibility of the existence of two successive shifts with a difference of 29.29 days,

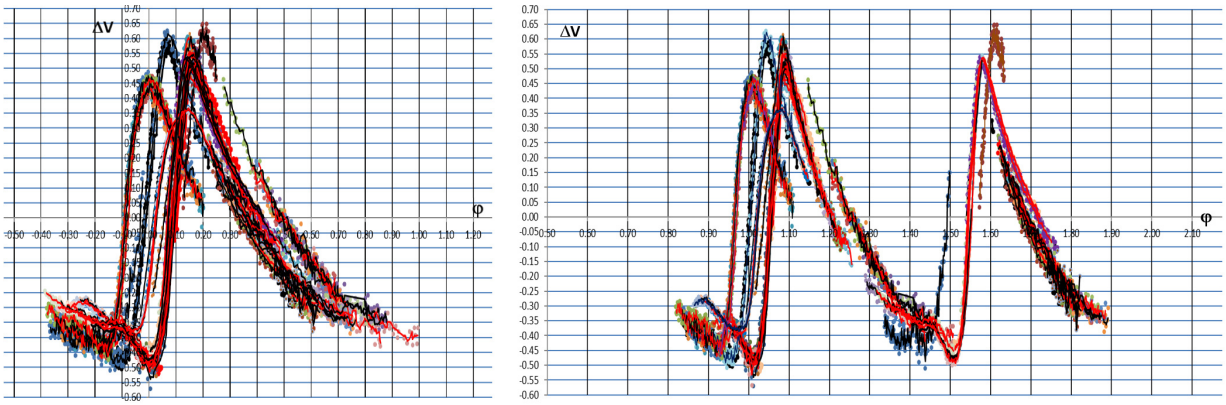

Figure 2: Average light curve of FI Sge for the period P=0.5047544837^d (Skarka & Cagas, 2017) for our data set, left. Bi-cyclical light curve of FI Sge for the same data and period, right

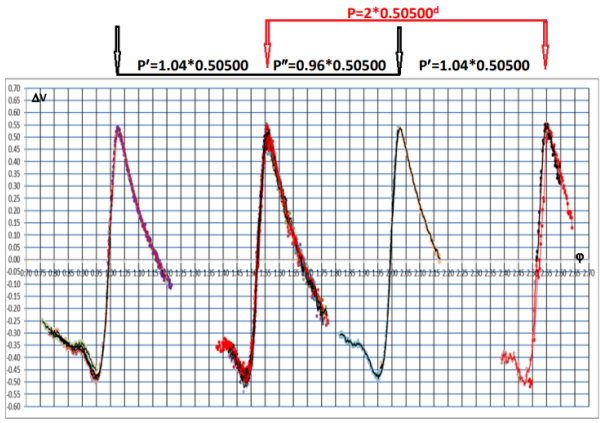

Figure 3: The difference between the tined if maxima for bi-cyclical light curve of FI Sge

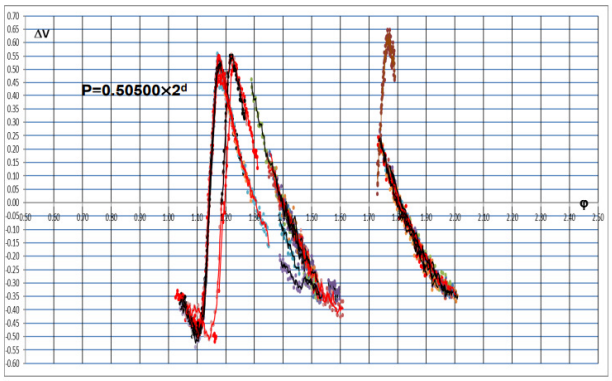

Figure 4: Observations of FI Sge 2018. Manifestation of the effect of displacement if times of maxima to the initial epoch for cycles of different formats

which corresponds to the maximum amplitude of cycles of two different formats, and the Blazhko effect gives a period of 29.29 days. However, between two shifts in the moments of the maxima there are five intervals of 29.29 days, when no shifts occur. It is this periodic order that makes it possible to explain the position of the moments of the maxima over the entire observation interval. It is this order that makes it possible to take into account the shift of the moments of the maxima and to construct for all observational data a common phase curve that corresponds to modern concepts of the theory of pulsations (Fig. 5).

4. Complex Blazhko effect

Above we noted: "The dynamics of changes in the amplitude of the maxima for individual series of observations shows that it is impossible to fit changes in the amplitude of the Blazhko effect ($0.3 \sim 0.4^m$) into the period of change in the moments of the maxima of 29.29 days". We have to assume that during this period there is a modulation of the amplitude up to $\sim 0.1^m$, which has its own local minimum and its own local maximum. Thus, the amplitude of the maximum during three such intervals decreases by 0.3^m and reaches its minimum, then after another three such cycles it increases by $\sim 0.3^m$ and reaches a maximum. After six periods of 29.29 days, that is, after 175.74 days, the amplitude reaches its maximum possible value and a shift maximum occurs in the next cycle. This is a model for a cycle of one of the formats. The same thing happens with a cycle of different formats but with a time shift of 29.29 days. Since cycles of different formats influence each other, displacements occur only when each of the cycles of different formats is at its common maximum. As a result, we observe two consecutive shifts with an interval of 29.29 days

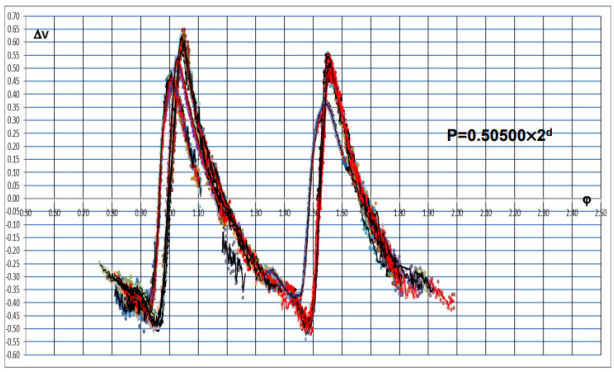

Figure 5: Observations of FI Sge 2018. The final phase light curve, taking into account the effect of bi-cyclicity and the effect of shifts of the brightness maxima

and five gaps between them. Then this entire cycle of changes is repeated periodically. Thus, we believe that the Blazhko effect for this star is a rather complex process, accompanied by shifts in the moments of the maxima to the initial epoch, and its period is 175.74 days. All of the above leads us to the conclusion that the Blazhko effect may be more complex than we imagined, and that the methodology for processing observations for pulsating variable stars with the Blazhko effect needs to be slightly changed.

5. Conclusions

Our analysis of the long-time series of observations of FI Sge allows to make the next conclusion:

Firstly, a much longer series of photometric observations are needed, since the period of the complex Blazhko effect can be more than six months.

Secondly, it is impossible to apply to pulsating stars with the Blazhko effect the method of determining the period by minimization $(O-C)$ values for the moments of maxima, since the existence of a bi-cyclicality effect and the effect of shifting the moments of maxima is leading to errors in determining the period using this method.

Thirdly, to construct the phase curve of such stars, it is necessary to use a double period to divide cycles into formats and be sure to identify observational data according to the bi-cyclical "phase".

Fourthly, if the effect of shifting the moments of maxima is detected, it is necessary to determine its value and the order of periodicity in order to take these shifts into account when constructing the phase curve.

Further studies of pulsating variable stars with the Blazhko effect are very important to clarify the essence of the processes occurring in these stars and to construct a physical theory of the Blazhko effect.

Acknowledgements. This research has made use of NASA's Astrophysics Data System. Author thanks S. N. Udovichenko for providing the data set of FI Sge of the observation 2013 and 2014 seasons and for the assistance in obtaining and data processing. Author thankful to E. Panko for fruitful discussions during the preparation of the paper.

References

Benko J. M., Szabo R.: 2014, Are RRab stars fully radial?, in: *Precision Asteroseismology Proc. IAU Symp. No. 301* /eds. J.A.Guzik, W.J.Chaplin, G.Handler & A.Pigulski, P.383.

Kolenberg K., Szabo R., Kurtz D. W., et al.: 2010, *ApJ*, **713**, L198.

Kovacs G. & Buchler J. R.: 1988, *ApJ*, **334**, 971.

Samus N. N., Kazarovets E. V., Durlevich O. V., et al.: 2017, *Astron. Zh*, **94**, 87.

Skarka M., Cagas P.: 2017, *IBVS*, **6229**, 1.

Smolec R., Soszynski I., Moskalik P., et al.: 2012, *MNRAS*, **419**, 2407.

Smolec R.: 2016, *Proc. of the Polish Astron. Soc.*, **3**, 22.

Soszynski I., Udalski A., Pietrukowicz P., et al: 2011, *Acta Astron*, **61**, 285.

Szabo R., Kollath Z., Molnar L., et al.: 2010, *MNRAS*, **409**, 1244.

Szabo R., Benko J. M., Paparo M., et al.: 2014, *A&A*, **570**, A100.

https://doi.org/10.18524/1810-4215.2023.36.290038

NEW GALACTIC LITHIUM-RICH CLASSICAL CEPHEID: OGLE GD-CEP-0516

V. V. Kovtyukh[1,2]

[1] Astronomical Observatory, Odessa National University, Shevchenko Park, 65014, Odessa, Ukraine

[2] Institut für Astronomie und Astrophysik, Kepler Center for Astro and Particle Physics, Universität Tübingen, Sand 1, 72076 Tübingen, Germany

ABSTRACT. We report the discovery new super-lithium rich beat Cepheid OGLE GD-CEP-0516 which has a lithium abundance of $logA$(Li)≈3.6 dex. It is the sixth known Cepheid of such type in the Galaxy. OGLE GD-CEP-0516 can be considered as the Cepheid which is presently crossing the instability strip for the first time.

Keywords: stars: abundances – stars: variables: Cepheids – stars: individual: OGLE GD-CEP-0516.

АНОТАЦІЯ. У цій статті ми повідомляємо про відкриття нової бімодальної цефеїди, багатої літієм, OGLE GD-CEP-0516. Бімодальні цефеїди — це класичні змінні зорі-цефеїди, які одночасно пульсують у двох (або трьох) радіальних модах.

Детальне фотометричне дослідження OGLE GD-CEP-0516 протягом кількох років показало, що це галактична бімодальна цефеїда з найкоротшим відомим періодом (P1=0.3949599 d, P2=0.3163039 d, P2/P1=0.801). Вона пульсує з амплітудою 0.30 mag в I-діапазоні. Її відстань, яка знайдена за допомогою емпіричного співвідношення період-світність (PL) показує, що вона знаходиться у галактичному тонкому диску, на 0.07 кпк над площиною Галактики. Для цієї цефеїди ми проаналізували спектр UVES з роздільною здатністю R = 42 300, який охоплює інтервал довжин хвиль 4726-6835 Å, відношення сигнал/шум S/N=141. Щоб визначити ефективну температуру, ми використали методику, яка основана на відношеннях глибин лінії. Мікротурбулентна швидкість і прискорення сили тяжіння були знайдені за допомогою стандартного аналізу.

Нова суперлітієва цефеїда OGLE GD-CEP-0516 демонструє наявність сильної резонансної лінії LiI 6707.766 Å і має вміст літію log A(Li) ≈ 3.6 dex. Вміст вуглецю та натрію, визначений для OGLE GD-CEP-0516, близький до сонячних значень, це вказує на те, що ця цефеїда ще не проходила через перший конвективний винос. Це шоста відома класична цефеїда такого типу в Галактиці. OGLE GD-CEP-0516 можна вважати цефеїдою, яка зараз вперше перетинає смугу нестабільності.

Зауважимо, що літій було знайдено в різних цефеїдах: 1) довгоперіодична цефеїда у Великій Магеллановій Хмарі, яка пульсує у фундаментальному періоді; 2) п'ять бімодальних цефеїд Чумацького Шляху, що пульсують або в режими P0/P1 або P1/P2; 3) тільки V1033 Cyg є звичайний пульсатор основної моди з P ≈ 4.9 d. Це може означати, що літій в атмосферах цефеїд міг вироблятися через різні канали, наприклад, через поглинання планети, акрецію субзоряних компаньйонів, забруднення від зорі-супутника, або внутрішнього виробництва Li під час стадії RGB/RC.

Ключові слова: зорі: хімічний склад – зорі: класичні цефеїди.

1. Introduction

Pulsating stars such as classical Cepheids are not only crucial primary distance indicators, but they are also at the crossroad of many fundamental astrophysical problems.

Classical Cepheids are intermediate-mass and massive stars crossing the Instability Strip during the core He-burning stage. Classical Cepheids cover a broad range in stellar mass, namely from ∼2.2 to ∼14 $M_{\odot}$. In an evolved intermediate-mass star one expects the lithium abundance to be severely diluted due to the combined effects of the mass-loss on the Main Sequence and the subsequent first dredge-up. The sensitivity to mass-loss stems from the fact that in B stars (the progenitors of Cepheids) Li remains in only the outer 2% of the star at the end of the Main Sequence. The standard stellar evolution predicts a dilution about a factor of ≈50-60 relative to the initial value. Assuming an initial lithium content of $logA$(Li) = 3.3 dex, this means that Cepheids should have lithium abundances $logA$(Li)<1.5 dex. In contrast, Li-rich Cepheids has

Table 1: Parameters of the lithium-rich Cepheids

Star	Mode	Pobs days	<V> mag	R_G kpc	d pc	l deg	b deg	Remarks
Galaxy :								
OGLE GD-CEP-0516	P2/P1	0.394959	12.666	7.87	2720	285.50	–1.45	This paper
ASAS 075842-2536.1	P2/P1	0.41013	12.260	9.03	2100	243.55	2.35	Kovtyukh et al. (2019)
V363 Cas	P2/P1	0.546597	10.550	8.76	1155	118.46	–2.22	Catanzaro et al. (2020)
ASAS 131714-6605.0	P2/P1	0.913165	11.820	6.85	2200	305.86	–3.64	Kovtyukh et al. (2019)
V371 Per	P1/P0	1.738	10.930	10.61	3200	146.02	–14.65	Kovtyukh et al. (2016)
V1033 Cyg	P0	4.9375119	13.027	7.52	3429	69.94	0.49	Luck & Lambert (2011)
LMC :								
HV 5497	P0	99.156076	11.930	–	–	277.24	–36.17	Luck & Lambert (1992)

Remarks: R_G– Galactocentric distance, d – heliocentric distance.

a strong lithium line with the deduced LTE lithium abundance of $logA(\mathrm{Li}) = 3.3$ dex (see Luck & Lambert, 1992, 2011; Kovtyukh et al., 2019; Catanzaro et al., 2020).

Six super-lithium rich Cepheids have already been reported in the literature. Some useful parameters for the Li-rich Cepheids in the Galaxy and Large Magellanic Cloud (LMC) are gathered in Table 1.

The study of lithium content as a function of effective temperature, rotation, and deepening of the convective zone is a key problem for our understanding of stellar convective mixing and evolution.

In this paper we report the discovery of new Li–rich beat Cepheid OGLE GD-CEP-0516. Beat Cepheids are classical Cepheid variable stars that simultaneously pulsate in two (or three) radial modes. Most beat Cepheid pulsates either in the first overtone and the fundamental modes (P1/P0), or in the second and the first overtone modes (P2/P1). Previous studies clearly established that the period ratio (higher to lower mode) of the P1/P0 pulsators is around 0.72, while that of P2/P0 is closer to 0.80. The period ratios P1/P0 can be measured very accurately and have been found to correlate with the Cepheid masses (or periods), and the abundances of the heavy elements (Kovtyukh et al., 2016; Lemasle et al., 2018).

2. Beat Cepheid OGLE GD-CEP-0516

Extensive photometry of OGLE GD-CEP-0516 over a number of years has clearly shown it to be a Galactic beat Cepheid, with the shortest period known so far (P1=0.3949599 d, P2 = 0.3163039 d, P2/P1 = 0.801, see Udalski et al. 2018). It pulsates with an amplitude of 0.30 mag in the I band. Its distance, which is derived from the empirical period-luminosity (PL) relation, places it in the Galactic thin disk, 0.07 kpc above the Galactic plane (Skowron et al., 2019).

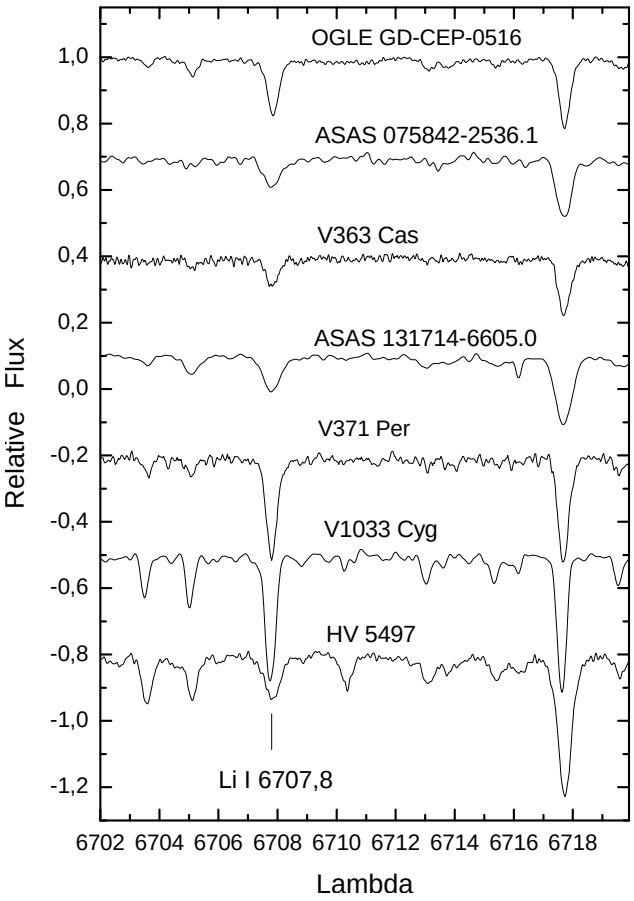

Figure 1: The spectral region around the Li I 6707.8 Å line in the spectra of lithium–rich Cepheids. For the sake of clarity the continuum level was shifted to arbitrary levels.

3. Spectroscopic analysis

For this star we analysed UVES spectrum at R = 42 300 that have been taken using the red arm (#CD3) and cover the wavelength interval 4726–6835 Å, the signal-to-noise ratio S/N=141 (Dekker et al., 2000).

Fig. 1 displays the spectral domain around the Li I 6707.8Å feature for the all Li-rich Cepheids discovered so far in the Milky Way and LMC.

4. Parameters and Abundance

To determine the effective temperature ($T_{\rm eff}$) for OGLE GD-CEP-0516, we employed the method of Kovtyukh (2007), based on $T_{\rm eff}$–line depth relations (we used 59 relations in total, and derived $T_{\rm eff}$= 6526 ± 20, σ = 139 K). The microturbulent velocity $V_{\rm t}$ and gravity log g were found using the standard analysis (see, for example, Kovtyukh et al., 2016). The atmospheric parameters $T_{\rm eff}$, log g and $V_{\rm t}$ are listed in Table 2.

The abundances of different elements were derived in the LTE approximation using atmosphere model interpolated for the atmosphere parameter within the grid of ATLAS9 models by Castelli & Kurucz (2004). We discarded strong lines (with EWs>150 mÅ) due to noticeable damping effects. The oscillator strengths, log gf, were adopted from the Vienna Atomic Line Database (VALD, Ryabchikova et al., 2015, version 2023). The reference solar abundances were taken from Asplund et al. (2009).

The results are given in Table 2.

Table 2: LTE abundance in OGLE GD-CEP-0516. Model 6526/2.4/1.4 ($T_{\rm eff}$, log g, $V_{\rm t}$)

Ion	Code	[El/H]	σ	NL	(El/H)
Li I	3.00	2.44	–	1	3.60
C I	6.00	–0.12	0.07	7	8.44
O I	8.00	–0.00	0.07	3	8.81
Na I	11.00	–0.12	0.09	2	6.20
Mg I	12.00	–0.18	–	1	7.42
Al I	13.00	–0.20	–	1	6.10
Si I	14.00	0.02	0.14	12	7.53
Si II	14.01	0.14	–	1	7.65
S I	16.00	0.28	0.27	3	7.49
Ca I	20.00	0.16	0.15	7	6.54
Sc II	21.01	–0.13	0.25	5	3.12
Ti I	22.00	0.14	0.16	13	5.09
Ti II	22.01	0.03	0.22	5	4.98
V I	23.00	0.01	0.16	3	4.12
V II	23.01	0.05	0.15	2	4.16
Cr I	24.00	0.11	0.16	9	5.87
Cr II	24.01	0.11	0.12	6	5.87
Mn I	25.00	–0.21	0.12	6	5.33
Fe I	26.00	0.01	0.12	149	7.51
Fe II	26.01	0.02	0.10	19	7.52
Co I	27.00	0.08	0.30	2	5.07
Ni I	28.00	–0.03	0.12	28	6.27
Y II	39.01	0.11	0.08	5	2.30
Zr II	40.01	0.02	0.34	2	2.90
La II	57.01	–0.04	0.09	4	1.29
Ce II	58.01	0.05	0.16	5	1.76
Pr II	59.01	0.04	0.19	3	0.85
Nd II	60.01	–0.28	0.10	4	1.24
Eu II	63.01	0.02	0.18	2	0.98

Remark: (El/H) is absolute abundance value on the scale where hydrogen abundance is 12.00.

5. Discussion and Conclusions

We have discovered new lithium Cepheid in the Milky Way, which brings the number of such rare objects to a grand total of seven stars (six in the Galaxy, one in the LMC). This Cepheid (OGLE GD-CEP-0516) shows the presence of strong resonance LiI 6707.766 Å line. The abundances of carbon and sodium determined for OGLE GD-CEP-0516, being close to the solar values, indicate that this Cepheid has never been through the first dredge-up (Adamczak & Lambert, 2014; Takeda et al., 2013, and references therein). Otherwise, we should expect the abundances of these elements to have been significantly altered by the dredge-up.

Note that lithium has been measured in a variety of Cepheids: one very long-period LMC Cepheid pulsating in the fundamental mode, and five double-mode Milky Way Cepheids pulsating either in the P0/P1 or P1/P2 modes; only V1033 Cyg is a common P≈4.9 d fundamental mode pulsator (Table 1). This might indicate that Li observed in the atmosphere of Cepheids could be produced via different channels, for instance via accretion of sub-stellar companions, pollution from a companion star, planet ingestion, or internal production of Li during the RGB/RC stage (for details, see Liu et al. 2014, Kirby et al 2016, Kovtyukh et al. 2019, and references therein).

Acknowledgements. Based on observations collected at the European Southern Observatory under ESO programme ID 105.20MX.

References

Adamczak J. & Lambert D. L.: 2014, *ApJ*, **791**, 58.

Asplund M., Grevesse N., Sauval A.J., Scott P.: 2009,*ARA&A*, **47**, 481.

Castelli F. & Kurucz R.L.: 2004, ArXiv: astro-ph/0405087.

Catanzaro G., Ripepi V., Clementini G. et al.: 2020, *A&A*, **639**, 4.

Dekker H., D'Odorico S., Kaufer A., Delabre B., Kotzlowski H.: 2000, *SPIE*, **4008**, 534.
Kirby E.N., Guhathakurta P., Zhang A.J. et al.: 2016, *ApJ*, **819**, 135.
Kovtyukh V.V.: 2007, *MNRAS*, **378**, 617.
Kovtyukh V., Lemasle B., Chekhonadskikh F. et al.: 2016, *MNRAS*, **460**, 2077.
Kovtyukh V., Lemasle B., Kniazev A. et al.: 2019, *MNRAS*, **488**, 3211K.
Lemasle B., Hajdu G., Kovtyukh V. et al.: 2018, *A&A*, **618**, A160.
Liu Y. J., Tan K. F., Wang L., Zhao G., Sato B., Takeda Y., Li H. N.: 2014, *ApJ* **785**, 94.
Luck R.E. & Lambert D.L.: 1992, *ApJS*, **79**, 303.
Luck R.E. & Lambert D.L.: 2011, *AJ* **142**, 136.
Ryabchikova T., Piskunov N., Kurucz R. L. et al.: 2015, *Physica Scripta*, **90**, 054005.
Skowron D.M., Skowron J., Mróz P. et al.: 2019, *AcA*, **69**, 305.
Takeda Y., Kang D.-I., Han I., Lee B.-C., Kim K.-M.: 2013, *MNRAS* **432**, 769.
Udalski A., Soszyński I., Pietrukowicz P. et al.: 2018, *Acta Astron.*, **68**, 315.

https://doi.org/10.18524/1810-4215.2023.36.290040

THE Hα AND Hβ LINES IN THE SPECTRUM OF CH CYG IN 2016

Kh.M. Mikailov[1], B.N. Rustamov[1,2], A.B. Rustamova[2], A.J. Orujova[2]

[1] Baku State University, Baku, Azerbaijan
[2] Shamakhy Astrophysical Observatory named after N. Tusi, Azerbaijan
mikailovkh@gmail.com

ABSTRACT. We present the results of spectral observations of the symbiotic star CH Cyg, carried out at the Cassegrain focus of the 2-m telescope of the ShAO named after N.Tusi, by using the Shamakhy Fiber Echelle Spectrograph (ShAFES). The spectra of star CH Cyg were obtained with the spectral resolution of R = 28000, between June and November 2016. We also present the results of the comparative analysis of the brightness curve of the star with the main parameters of Hα and Hβ emission lines. During the observation period, both lines exhibited changing profiles characterized by complex structures, predominantly with double peaks. The ratio of the intensities of the blue and red components was typically $I_B/I_R < 1$ for the Hα line and $I_B/I_R \geq 1$ for the Hβ line. A quasi-period of 241 days was found in the variation of the equivalent widths of Hα and Hβ emission lines as well as in the intensities of their components

Keywords: Symbiotic star – CH Cyg; echelle spectra; line profile; radial velocity.

АНОТАЦІЯ. Наводяться результати спектральних спостережень симбіотичної зорі CH Cyg, виконані у фокусі Кассегрена 2-м телескопа ШАО ім. Н. Тусі за допомогою Шамахінського волоконного ешеле-спектрографа (ShAFES). Спектри зорі CH Cyg були отримані зі спектральною роздільною здатністю R = 28000 у період з червня по листопад 2016 р. Також використовуючи фотометричну базу даних змінних зір AAVSO побудовані криві блиску зорі CH Cyg за період наших спектральних спостережень. За профілями емісійних ліній Hα та Hβ були виміряні наступні параметри: променеві швидкості синього та червоного піків випромінювання – RV(I_B та I_R); променеві швидкості центрального поглинання – RV(I_{CA}); еквівалентні ширини емісійних ліній Hα та Hβ – EW; інтенсивності компонентів емісійних ліній Hα і Hβ та їх відношення – I_B/I_R. За період спостережень лінії демонстрували мінливий профіль, що характеризується складною структурою, переважно з подвійним піком. Співвідношення інтенсивностей синьої та червоної компонентів загалом становило $I_B/I_R < 1$ для лінії Hα та $I_B/I_R \geq 1$ для лінії Hβ. Співвідношення інтенсивностей лінії Hβ не так сильно варіюється, як у Hα. Зміна відносин I_B/I_R інтенсивностей синьої (I_B) і червоної (IR) емісійних компонентів лінії Hα корелюється зі змінами променевих швидкостей центрального поглинання (RV(I_{CA})), зі зменшенням відношення I_B/I_R радіальна швидкість центрального поглинання збільшується.

За період спектральних спостережень з червня до листопада 2016 р. яскравість зорі у V-фільтрі зменшилася приблизно на $1^m.5$. Приблизно з 16 по 28 серпня 2016 року яскравість зорі збільшилася приблизно на $0^m.5$ і знову почала зменшуватися. У змінах, еквівалентної ширини та інтенсивності синьої (I_B) та червоної (I_R) емісійних компонент ліній Hα та Hβ, у спектрі симбіотичної зорі CH Cyg, встановлено квазіперіод з характерним часом 241 днів.

Ключові слова: Симбіотичні зорі – CH Cyg; ешеле-спектри; профілі спектральних ліній; променеві швидкості.

1. Introdution

The symbiotic system consists of two completely different types of stars that coexist – interacting, cold red giant – RG (in some cases yellow) and hot compact – WD stars. As a result of strong gravity, the substance flowing from the red giant gathers around this star and forms a disk. This couple is surrounded by nebula as a whole.

By studying symbiotic stars, we simultaneously study 3 different types of space objects: 1. Red giant; 2. White dwarf and accretion disk; 3. Star environment gas and dust nebula. In systems of this type, a powerful flow of matter occurs through the stellar wind from a cold Star, and an accretion disk is formed around a hot compact star. Symbiotic stars can reflect a transitional stage in the evolution of several types of double systems with a powerful flow of matter from a

large-mass star to a small-mass star. (Mikailov, 2010; Mikolajewska et al., 2010).

Among symbiotic stars, CH Cyg is of particular interest and has remained the focus of most researchers until the present time and attracted them due to its inherent characteristics. These features include:

1. CH Cyg is the brightest and closest symbiotic star. The distance to the star, according to measurements by Hippacrosus, is 268±62 pc. Its average visual magnitude of about $m_v = 6^m.5$ at maximum, $m_v = 10^m.5$ at minimum, and it is brighter in infrared region, and its magnitude at a wavelength of 2mkm is $m_k = -1$. (Munari et al., 1997; Belczynski et al., 2000).

2. In the star CH Cyg, both optical and radio domain, directional jet-shaped bipolar eruptions (jets) are observed at a speed of 1200 km/s, the length of which reaches 750 astronomical units. To understand such phenomena and unravel their origin, CH Cygni is the most optimal laboratory (Karovska et al., 2010; Kellogg et al., 2007).

3. CH Cyg pulsates with the exact period (100 and 750 days) characteristic of the cold red giant o Cet (Mira) of the symbiotic system. As a result, the accretion regime changes, and the system shows changes of an even more complex nature. At the same time, such systems with different short and long orbital periods behave differently than other symbiotic stars. The study of the evolution of such a system is of great importance (Hinkle et al., 2009; Hinkle et al., 1993).

4. In the CH Cyg symbiotic system, evidence has been increasing lately indicating the existence of the 3rd Star. Many researchers perceive it as a system of 3 stars. The 756-day short period may be the period of the 3rd star in an invisible inner orbit of a symbiotic pair of M gigants and hot stars with a 15.5-year long period (Mikailov, 2010).

5. CH Cyg is also completely different from other symbiotic stars due to its long activity dynamics. After many years of passivity, activity began in 1963, and after the great flashing in 1977, this activity continues to the present (Mikailov, 2010).

2. Observations and data reduction

Spectral observations symbiotic star CH Cyg, were carried out at the Cassegrain focus of the 2-meter telescope at the Shamakhy Astrophysical Observatory, named after N. Tusi, using the Shamakhy Fiber Echelle Spectrograph (Mikailov et al., 2020) and the CCD matrix with 4096 x 4096 pixels. The spectral resolution was R = 28000, and the wavelength range was 3800-8000 Å in during June – November 2016 were obtained 9 echelle spectrums of star CH Cyg. Processing of echelle spectra was carried out according to the standard method using the new version of the DECH30 program developed by Galazutdinov (http://www.gazinur.com/DECH software.html). A list of all used spectra is given in Table 1.

For the spectral observations period between June – November of 2016, the brightness curve of the star CH Cyg has been constructed using the AAVSO photometric database. As displayed of the figure, the brightness of the star has reduced by approximately $1^m.5$ in the V filter. Around 16 – 28th of august 2016-time interval, the brightness of the star has increased by about $0^m.5$ and started to reduce once again.

3. Results of observations

The following parameters were measured from the available spectra, from the Hα and Hβ emission lines profiles:

a) the radial velocities of the blue and red emission peaks: RV(I_B and I_R);

b) as well as the radial velocities of the central absorption: RV(I_{CA});

c) the equivalent widths in the Hα and Hβ emission lines (EW);

d) the intensities of the Hα and Hβ emission lines components (I_B and I_R) and their ratios I_B/I_R.

Results of measurements of parameters of Hα and Hβ lines is given in Table 1 and 2.

Figure 1 presents the Hα and Hβ emission lines profiles in the spectrum of CH Cyg for the period of our spectroscopic observations (June – November 2016). During the observation period, both lines exhibited changing profiles characterized by complex structures, predominantly with double peaks. The ratio of the intensities of the blue and red components was typically $I_B/I_R < 1$ for the Hα line and $I_B/I_R \geq 1$ for the Hβ line. The Hα and Hβ emission lines (blue and red emission components as well as the central absorption) as a rule, is blue shifted.

As seen in Figure 1 and Table 1, 2: a) The intensity of red (I_R) and blue (I_B) components of H alpha lines show abrupt variations. In two nights, the intensity ratio was $I_B/I_R > 1$, but for the rest of the nights was $I_B/I_R < 1$ displaying strong variability. This variability agrees with the radial velocity of central absorption of Hα lines RV(I_{CA}). As the I_B/I_R ratio reduces, the radial velocity of central absorption increases. b) The intensity ratio of blue and red components of Hβ was $I_B/I_R > 1$ for 6 nights and for the rest 3, it was $I_B/I_R \approx 1$. The intensity ratio doesn't display as much variability as it did in Hα.

A quasi-period of 241 days was found in the variation of the equivalent widths of Hα and Hβ emission lines, as well as in the intensities of their components (Fig. 2).

Table 1: Results of measurements of parameters of profiles of Hα line.

Data	JD	EW (Å)	Rv (km/s)			Int		I_B/I_R
	+2457000		I_R	I_{CA}	I_B	I_R	I_B	
15.05.2016	524.455	15.01	-17.15	-77.00	-113.34	3.88	5.00	1.29
13.06.2016	553.444	5.07	-28.42	-72.53	-113.58	2.20	2.57	1.17
16.07.2016	586.304	8.05	-34.82	-80.01	-109.33	4.54	3.08	0.68
16.08.2016	617.233	18.21	-38.79	-90.67	-115.02	9.67	3.79	0.39
19.08.2016	620.254	13.96	-37.41	-85.58	-117.42	5.82	3.58	0.62
28.08.2016	629.21	13.76	-39.04	-84.20	-120.55	4.77	3.77	0.79
21.09.2016	653.198	10.27	-41.36	-87.6	-119.20	3.47	2.60	0.75
			-15.96		-184.90			
26.11.2016	719.186	34.27	-30.41	-91.23	-118.67	11.16	6.91	0.62
30.11.2016	723.161	41.10	-36.74	-95.65	-120.36	15.75	7.25	0.46

Table 2: Results of measurements of parameters of profiles of Hβ line.

Data	JD	EW (Å)	Rv (km/s)			Int		I_B/I_R
	+2457000		I_R	I_{CA}	I_B	I_R	I_B	
15.05.2016	524.455	10.66	-8.22	-52.60	-102.46	4.81	6.41	1.33
13.06.2016	553.444	5.53	-17.10	-53.41	-107.57	2.49	3.23	1.30
16.07.2016	586.304	6.42	-22.59	-66.40	-97.90	2.98	3.68	1.23
			-44.87		-170.40			
					-216.60			
16.08.2016	617.233	11.82	-14.76	-28.99	-102.56	3.89	5.20	1.34
19.08.2016	620.254	11.33	-13.44	-36.06	-106.75	3.86	5.57	1.44
28.08.2016	629.21	12.08	-10.47	-39.56	-109.46	4.32	5.50	1.27
				-55.36				
21.09.2016	653.198	10.91	-7.85	-35.24	–103.33	4.16	4.08	0.98
				-54.00	-165.41			
26.11.2016	719.186	24.37	-22.94	-54.61	-110.69	9.55	9.28	0.97
				-74.11				
30.11.2016	723.161	25.13	-23.50	-57.75	-110.41	9.74	8.96	0.92
				-79.35				

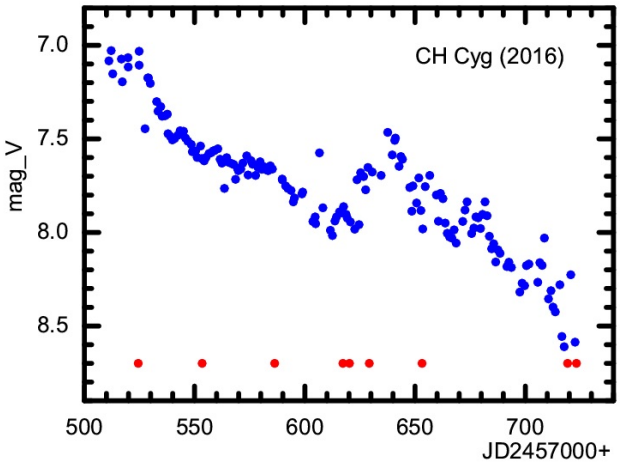

Figure 1: Visual light curve of the CH Cyg star in June – November of 2016. The filled red circles indicate the time of observations.

4. Conclusions

1. Over the period of our spectral observations (June-November 2016) of the symbiotic star CH Cyg, the profiles of the Hα and Hβ lines represent the emission profiles with predominantly double peaks, highly variable intensities of the red (I_R) and blue (I_B) components. The I_B/I_R ratio is < 1 for the Ha line and $I_B/I_R \geq 1$ for the Hβ line.

2. Changes in the I_B/I_R ratios of the intensities of the blue (I_B) and red (I_R) emission component of the Hα line is correlated with changes in the radial velocities of the central absorption (RV(I_{CA}); as the I_B/I_R ratio decreases, the radial velocity of the central absorption increases.

3. During the spectral observation period from June to November 2016, the luminosity of the star in the V-filter decreased by about $1^m.5$. From about August 16 to August 28, 2016, the luminosity of the star increased by about $0^m.5$ and began to decrease again.

4. A quasi-period with a characteristic time of

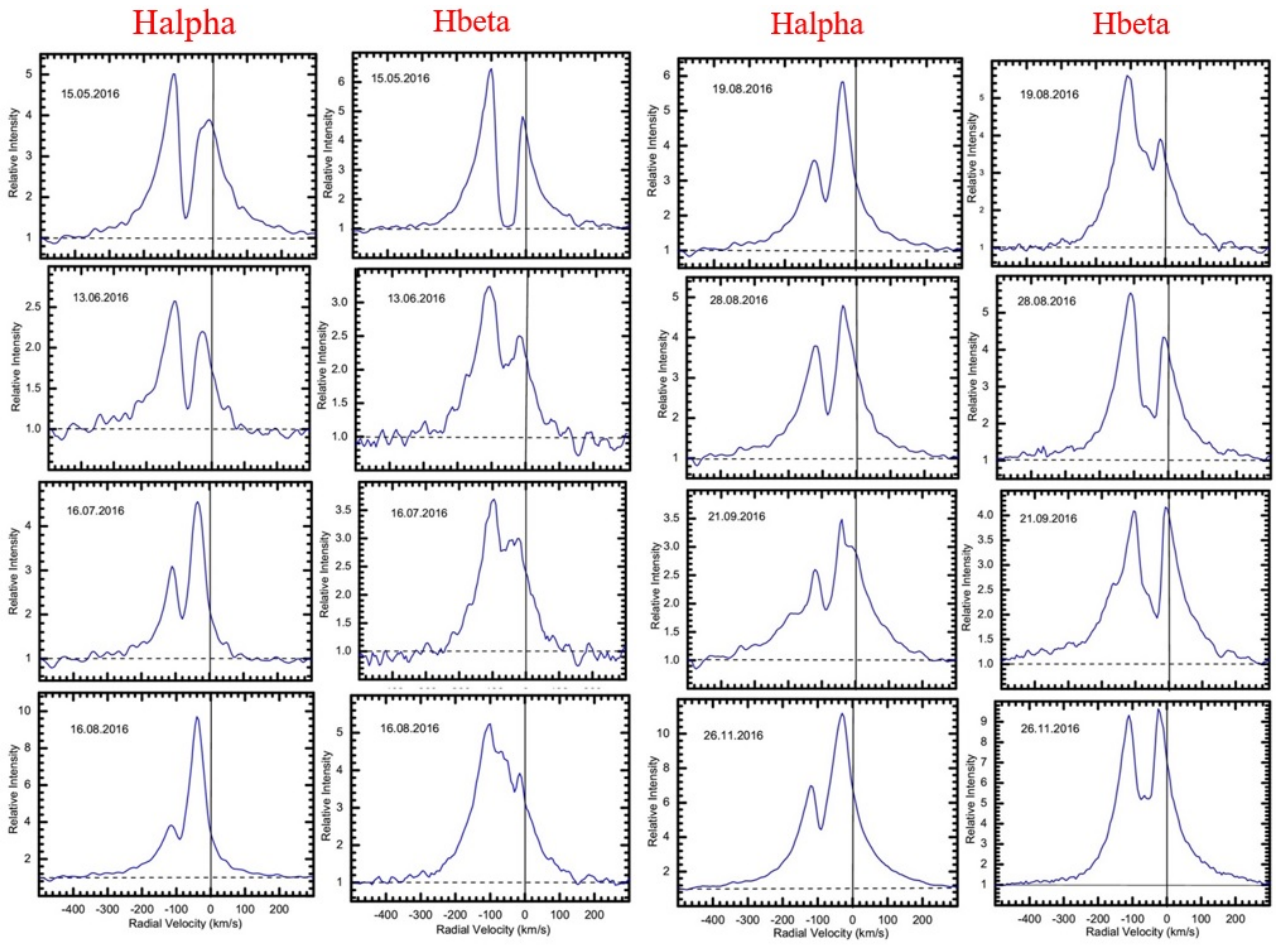

Figure 2: Profiles of Hα and Hβ lines in spectrum CH Cyg.

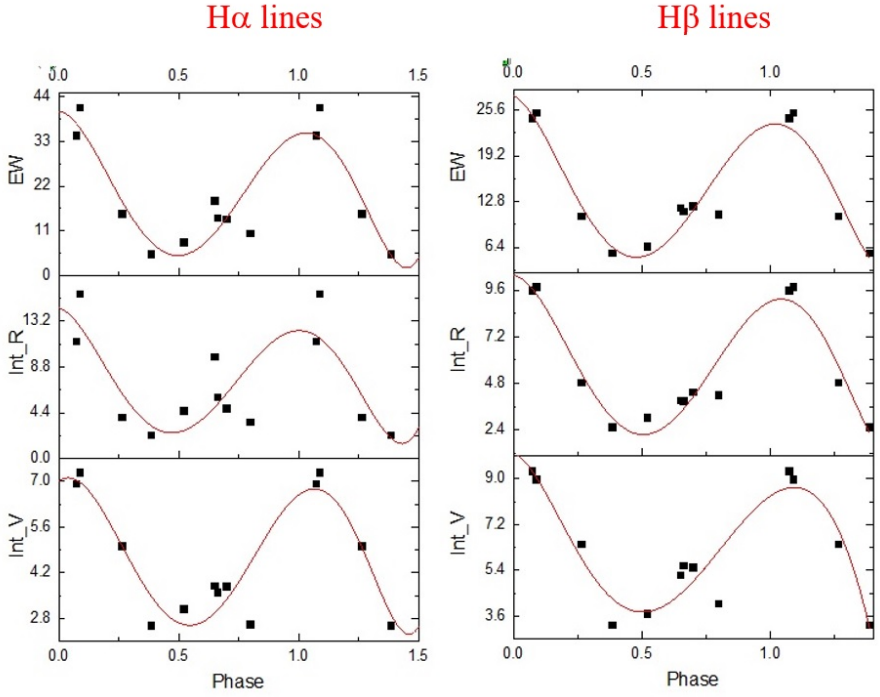

Figure 3: Periodicity in the variabilities of the equivalent widths of Hα and Hβ emission lines, as well as in the intensities of their components.

241 days has been established in the changes in the equivalent width and intensities of the blue (I_B) and red (I_R) emission component of the lines Hα and Hβ in the spectrum of the symbiotic star Cyg.

References

Belczynski K., Mikolajewska J., Munari U. et al.: 2000, *Astron. Astrophys. Suppl.*, **146**, 407.

Galazutdinov G.: http://www.gazinur.com/DECH software.html.

Hinkle K.H., Fekel F.C., Johnson D.S., Scharlach W.W.G.: 1993, *Astron.J, Washington*, **105, Iss. 3**, 1074.

Hinkle K.H., Fekel F.C., Joyce R.: 2009, *Astrophys. J., Washington*, **692**, 1360.

Karovska M., Gaetz T.J., Carilli C. L. et al.: 2010, *Astrophys. J. Lett., Washington*, **710, Iss.2**, 132.

Kellogg E., Anderson C., Korreck K. et al.: 2007, *Astrophys. J., Washington*, **664**, 1079.

Mikailov Kh.M.: 2010, *Ph.D. dissertations on the topic "Creation of echelle spectrometers and spectral study of symbiotic stars" Baku,Azerbaijan*

Mikailov Kh.M, Musaev F.A. , Alekberov I.A. et al.: 2020, *Kinem. and Phys. of Cel. Bod.*, **36**, 22.

Mikolajewska J., Balega Y., Hofmann K., Weigelt G.: 2010, *Mon. Not. R. Astron. Soc.*, **403**, 21.

Munari U., Renzini A., Bernacca B.L.: 1997, *Hipparcos-Venice 97 (ESA SP-402)*, **413**.

https://doi.org/10.18524/1810-4215.2023.36.290042

MANIFESTATION OF STELLAR EVOLUTION IN METAL-DEFICIENT STARS

T.V. Mishenina[1], I.A. Usenko[1], A. Yu. Kniazev[2], T.N. Gorbaneva[1]

[1] Astronomical Observatory, Odessa National University, Odessa 65014-UA, Ukraine, *tmishenina@ukr.net, igus*99*@ukr.net*

[2] Southern African Large Telescope Foundation, South African Astronomical Observatory, P.O. box 9, 7935 Observatory, Cape Town, South Africa, *a_kniazev@saao.nrf.ac.za*

ABSTRACT. Metal-poor stars allow us to establish the early history of the Milky Way, furthermore the stars on advanced evolution stage (e.g. giants, AGB stars etc.) give the opportunity to research the peculiarities of stellar evolution at low metallicity. On the base of the 11m Southern African Large Telescope (SALT) spectra obtained using HRS fibre-fed echelle-spectrograph during 2018 -2020, the atmospheric parameters and elemental abundances of four metal-poor stars HE 1523-0901, HD 6268, HD 121135, and HD 195636 ([Fe/H] ~ -1.5 – -3.0) have been obtained. The iron abundance was determined based on the equivalent widths of absorption lines. The carbon abundance was obtained using the molecular synthesis fitting for the CH (4300-4330 ÅÅ) region, nitrogen from CN at 3883 Å, oxygen from [O] line at 6300 Å and IR triplet at 7770 Å The relationship between the chemical enrichment of stars and their stellar evolution is considered. It may be associated with the processes of mixing inside the stars, and the mechanisms of matter transfer during stellar evolution.

Keywords: stars: abundances – stars: atmospheres – stars: Population II – stars: stellar evolution.

АНОТАЦІЯ. Зорі з бідним вмістом металів дозволяють нам встановити ранню історію Чумацького Шляху, але зорі на просунутій стадії еволюції (наприклад, гіганти, зорі AGB тощо) дозволяють нам вивчати особливості еволюції зір при низькій металевості. На основі спектрів, отриманих за допомогою ешелле-спектрографа з волоконним живленням HRS південноафриканського Великого телескопа (SALT, 11 м) у 2018–2020 рр., досліджено параметри атмосфери та вміст елементів чотирьох бідних на метали зір HE 1523-0901, HD 6268 HD 121135 і HD 195636 ([Fe/H] ~ -1,5 – -3,0) досліджено. Вміст заліза визначали на основі еквівалентної ширини ліній. Вміст вуглецю (і азоту) визначали за допомогою підгонки молекулярного синтезу в області G-смуги CH (4300-4330 ÅÅ), N в області молекулярної смуги CN при 3883 Å, кисню, використовуючи лінії [O] 6300 Å та ІЧ-триплета на 7770 Å. Розглянуто зв'язок між хімічним збагаченням зір і їхньою зоряною еволюцією. Це може бути пов'язано з процесами перемішування всередині зір, тобто з механізмами перенесення речовини в ході їх еволюції. Параметри (log $L/L_{\odot}$ і [C/H]) зір HE1523-0901, HD6269 відповідають області канонічного змішування, зоря HD 121135 можливо не має впливу канонічного екстра-змішування. Введення можливої корекції за відхилення від термодинамічної рівноваги NLTE для значень вмісту вуглецю не змінює висновків про канонічне екстра-змішування в досліджуваних зорях HE1523-0901, HD6269; зоря 195636, швидше за все, є зорею горизонтальної або висхідної гілки гігантів з деякими особливостями хімічного складу та великою швидкістю обертання.

Ключові слова: зорі: вміст – зорі: атмосфера – зорі: Населення II – зорі: еволюція зір.

1. Introduction

Metal-deficient stars ([Fe/H] <- 1.5) researches can provide information about the early nucleosynthesis of the Galaxy and its chemical evolution as a whole, but the stars on advanced evolution stage (e.g. giants, AGB stars etc.) allow us to study the peculiarities of their stellar evolution at low metallicity. The ratios of the CNO elements, the abundances of which changes as a result of nuclear reactions in case of hydrogen burning in advanced cycles may be associated with the processes of mixing inside the stars, and the mechanisms of matter transfer during the course of stellar evolution (e.g., Gratton *et al.*, 2000; Spite *et al.*, 2006). When the star evolves up giant branch (RGB), the outer convective envelope expands inward and the ensuing mixing episode, called the “first dredge-up” (Iben 1964) to alter the star’s surface light element abundance.

First dredge up is expected to be less efficient in metal-poor stars (VandenBerg & Smith 1988; Charbonnel 1994): changes in C and N abundances are very small, and the $^{12}C/^{13}C$ ratio is expected to remain > 30. Gratton et al. (2000) investigated the mixing along the RGB for $-2 \leq$ [Fe/H] ≤ -1 and found that the light elements in lower-RGB stars are in agreement with standard evolutionary models; but in the upper part of the RGB, additional mixing (“second dredge-up”) leads to depletion of carbon and enrichment in nitrogen, but not any O-Na anti-correlation. Later Khan et al. (2018) have indicated that standard stel-

lar models underestimate the depth of efficiently mixed envelopes and an efficiency of significant overshooting increases with a metallicity decreasing.

Spite *et al.* (2006) provided LTE analysis of 32 extreme metal-poor (EMP) giants in order to understand the CNO abundance variations carried out, and found the C–N anti-correlation.

Metal – poor stars with an excess of carbon (CMEP) have aroused special interest, in particular, in the sources of origin of excess of carbon. C underabundance and N overabundance may be associated with canonical extra mixing (e.g., Denissenkov & Pinsonneault, 2008; for the CMEP and CEMP-no stars). Denissenkov & VandenBerg (2003) have proposed to call the thermohaline mixing as an explanation for deep mixing in the envelopes of red giants, because of its universality, as the canonical extra mixing (non-convective) and to use instead of rotational one (e.g. Denissenkov & VandenBerg, 2003) for which viable models to be difficult to construct (e.g. Palacios *et al.*, 2006). To account for extra mixing on the upper giant branch, Stancliffe & Eldridge (2009) used a diffusive prescription for thermohaline mixing based on the work Kippenhahn et al. (1980) and the same parameters choice (introduced by Charbonnel & Zahn, 2007) reproduces the observed abundance trends across a wide range of metallicities, for both CEMP and CEMP-no metal-poor field stars (Stancliffe *et al.*, 2009) and globular cluster stars (Angelou *et al*., 2011). Placco et al. (2014) for the expected depletion of surface carbon abundance have recomputed of the initial carbon abundance of the stars, using the stellar evolution code (Eggleton, 1971; Stancliffe & Eldridge, 2009). Takeda & Takada-Hidai (2013) carried out the non-LTE analysis of C I lines at 1.068-1.069 μm for metal-poor stars and obtained the mean values of NLTE corrections for [C/Fe] about 0.3 - 0.4 dex.

The purpose of this work is to determine the atmospheric parameters and elemental abundances (carbon, nitrogen, and oxygen, i.e. CNO), which are important parts in the analysis of advanced states, for the stars HE 1523-0901, HD 6268, HD 121135, and HD 195636 ([Fe/H] ~ -1.5 – -3.0), in order to research the relationship between the chemical enrichment and their stellar evolution and mixing processes.

2. Observations and spectrum processing

The main parameters of studied stars were taken from the SIMBAD database (Gaia DR2), in particular:

HE 1523-0901: **B** = 12.37; **V** = 11.50 (SIMBAD); π (mas): 0.2772 [0.0434]; **RV** = -163.608 [0.0045] km s^{-1};

HD 6268: **B** = 9.725; **V** = 9.046 (Zacharias *et al.*, 2012; UCAC4); d = 705.9156 pc; π (mas): 1.4166 [0.0440]; **RV** = 39.52 [0.15] km s^{-1};

HD 121135: **B** =10.14; **V** = 9.37 (SIMBAD); d = 755.00 pc; π (mas): 1.3245 [0.0532]; **RV** = 125.60 [0.23] km s^{-1};

HD 195636: **B** = 10.13, **V** = 9.57 (2000, A&A, 355, 27, UCAC4), π (mas): 1.6074 [0.0681]; **RV** = -258.40 [0.3] km s^{-1}.

The spectra of studied stars were obtained using the 11m Southern African Large Telescope SALT (Buckley *et al.*, 2006; O'Donoghue *et al*., 2006) HRS fibre-fed echelle-spectrograph (Barnes *et al*., 2008, Bramall *et al*. 2010, Bramall *et al*., 2012, Crause *et al*., 2014) during 2018–2021 with medium resolution mode (R~ 31000–41000) and high S/N ratio near 50–220 in the ranges of 3900–8700 ÅÅ. All the data were processed using package developed by authors based on the standard system of astronomical data reduction MIDAS. Further spectra processing such as the continuum establishing, line depth and equivalent width (EW) measurements, etc., was conducted using the DECH30 software package by Galazutdinov G.A. http://gazinur.com/DECH-software.html.

The rotational velocity projection was measured by fitting of the observed spectrum with models from Coelho (2014).

3. Atmospheric parameters determination

The effective temperature T_{eff} was determined, due to the independence of the iron abundances obtained for its given absorption lines from the lower-level potential E_{low} of these lines. Gravity log g was obtained from the ionization equilibrium for the Fe I and Fe II abundances. The microturbulent velocity V_t was obtained from the condition of independence for Fe I lines abundances on their equivalent width EW.

The metallicity [Fe/H] was adopted as the iron abundance determined from the Fe I lines. The selection of the parameters was performed using an iterative procedure.

Table 1 represents the stellar parameters of our researching stars.

Table 1: Our determined stellar parameters

Star	T_{eff} (K)	log g	[Fe/H]	V_t (km s^{-1})
HE1523-0901	4450	0.80	-2.82	2.5
HD6268	4700	1.30	-2.56	2.1
HD121135	4950	1.65	-1.37	1.8
HD195636	5450	1.80	-2.75	2.3

In the atmospheres of metal-poor stars the deviations from the Local Thermodynamic Equilibrium (LTE) may influence to the stellar parameters and abundance of iron (see, e.g., Lind *et al*., 2012). But, for such stars Roederer *et al*. (2014) shown that the Fe II abundance determined in the LTE approaches agree with those ones under non-LTE approximations within 0.02 dex. The obtained results enabled Roederer *et al*. (2014) to adopt the iron abundance derived from the Fe II lines as an indicator of the metallicity [Fe/H]. Our values of the iron abundance obtained from the Fe I and Fe II lines are almost similar, and we used the Fe I abundance as the metallicity [Fe/H] value.

4. Abundances determination

The elemental abundances were determined using the LTE approximation and the atmosphere models by Castelli

& Kurucz (2004). The choice of model for each star was made by means of standard interpolation for T_{eff} and log *g*.

The iron abundances were dermined using EWs of lines and WIDTH9 code by R.Kurucz. C, N, O abundances were calculated employing the synthetic spectrum method by a new version of the STARSP software (Tsymbal, 1996) and new version of the VALD3 line list (Kupka *et al.*, 1999). The carbon abundance were determined using the molecular synthesis fitting in the region of the CH G-band (4300-4330 ÅÅ), nitrogen from CN at 3883 Å, oxygen from [O] line 6300 Å and IR triplet at 7770 Å.

The spectrum synthesis fitting of the CH lines to the observed profiles for star HD 6268 are shown in Fig. 1.

To determine the systematic errors in the abundance estimates due to uncertainties in the atmospheric parameter determinations, we have derived the elemental abundances for the target stars from several models with modified parameters (δTeff= ±100 K; δlog g= ±0.2; δVt= ±0.1). The total uncertainty due to the parameter and EW errors for the Fe I and Fe II are 0.11 and 0.12, respectively. The determination accuracy for C, N, O elements varies from 0.15 to 0.21 dex.

The elemental abundances [El/Fe] presented in Table 2.

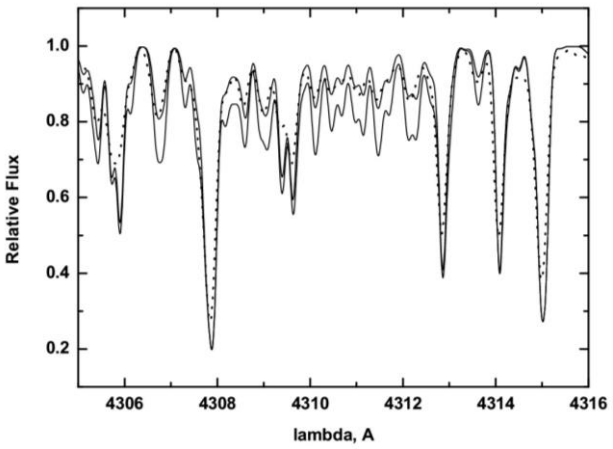

Figure 1: Observed (doted) and calculated (solid lines) spectra in the region of CH lines for star HD 6268.

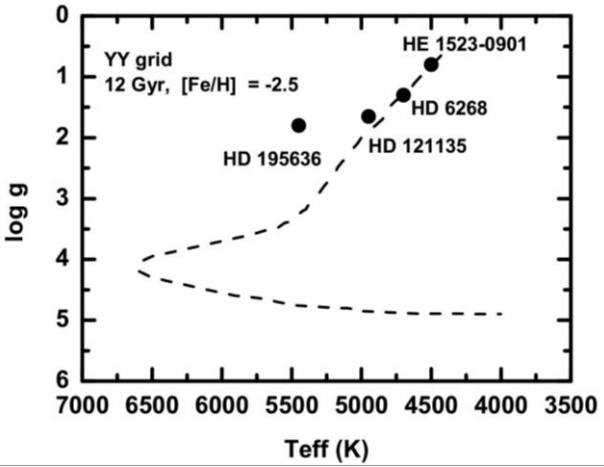

Figure 2: Positions of our stars at evolutionary diagram (Demarque *et al.*, 2004).

5. Results and discussions

We have studied our stars from the point of view of the advanced stages of stellar evolution of metal-poor stars. Positions of our stars at evolutionary diagram (Demarque *et al.*, 2004) illustrated in Fig. 2.

5.1 Stellar evolutionary effects

Some elements abundances, such as Li, CNO, Na, Mg and Al change during evolution and by studying them we can assess the evolutionary effects impact on the atmospheres of clusters and field giants (see, e.g. Charbonnel, 1994; Gratton *et al*., 2000; Spite *et al*., 2006). Table 2 presents the abundances of the C, N, and O, obtained in our research.

Table 2: C, N, O abundances

Elem	HE1523	HD6268	HD121135	HD195636
[C/Fe]	-0.82	-0.79	-0.46	-0.79
[N/Fe]	0.78	0.93		
[O/Fe]	0.78	0.92	1.01	1.20
[Fe/H]	-2.82	-2.54	-1.37	-2.78

Spite et al. (2006) performed the LTE analysis of several extreme metal-poor (EMP) giants in order to investigate the CNO abundance and found out a C–N anti-correlation that agreement the hypothesis that the surface abundances could be modified by the CNO processed material from the inner regions.

In case of our investigated star we found the carbon underabundance (Table 2) that may be agreement with the stellar evolution calculations and associated with canonical extra mixing (Denissenkov & Pinsonneault, 2008). Figure 5 in their paper illustrated variations in the surface C and N abundances (red curve, CEMP stars; black curve, CEMP-no stars black curve) due to canonical extra mixing, at that the extra mixing depth does not seems to depend strongly on the metallicity (Denissenkov & VandenBerg, 2003).

To compare our result with calculation of Denissenkov & Pinsonneault (2008) we computed the value of log $L/L_{\odot}$ based on the classical formula:

$$\text{Log } L/L_{\odot} = \log M^*/M_{\odot} + 4\log T_{eff}^*/T_{eff\odot} - \log g^*/g_{\odot}$$

were $T_{eff\odot}$= 5780 K, log $g_{\odot}$ = 4.44 and assuming that all targets have the same stellar mass $M^* = 0.85M_{\odot}$. The values of log $L/L_{\odot}$ and [C/H] presented in Table 3.

Table 3: log $L/L_{\odot}$ and [C/H] of studied stars

Star	log $L/L_{\odot}$	[C/H]
HE1523-0901	2.42398	-3.44
HD 6268	2.43898	-3.38
HD121135	2.05406	-1.88
HD195636	1.74023	-3.54

With these values of [C/H] and log $L/L_\odot$ the investigated stars, excepted HD 195636, were located in the black curve which corresponds to canonical extra mixing for non-C-enhanced extremely metal-poor stars with the prediction reported in the afore-mentioned study (their Fig. 5).

Placco *et al*. (2014) for the expected depletion of surface carbon abundance have recomputed the initial carbon abundance of the stars, using the stellar evolution code (Eggleton, 1971; Stancliffe & Eldridge, 2009), a grid of 0.8 $M_\odot$ stellar evolution models with a range of initial compositions, [Fe/H] = -1.3, -2.3, -3.3, and -4.3 and for each of these metallicities the values of [C/Fe] = -0.5, 0.0, +0.5, 1.0, respectively. We used their data and taken the correction Δ from Placco *et al*. (2014), recalculated the carbon value [C/Fe] for our targets and eventually obtained the following initial carbon values $[C/Fe]_{ini}$ (Table 4).

Table 4: log $L/L_\odot$ and corrected [C/Fe] of studied stars

Star	**log $L/L_\odot$**	**Δ**	**$[C/Fe]_{ini}$**
HE1523-0901	2.42398	0.90	+0.28
HD 6268	2.43898	0.50	-0.32
HD121135	2.05406	0.35	-0.11
HD195636	1.74023	0.10	-0.69

5.2 The individual target results

Star HE1523-0901 has a small excess of carbon, whereas HD6269 and HD121135 have a small C deficit. Star HD195636 has a large carbon deficit, taking into account this mixing corrections not upper part RGB.

Takeda & Takada-Hidai (2013) using NLTE analysis of C I lines at 1.068–1.069 μm have obtained the mean values of NLTE corrections for [C/Fe] about 0.3–0.4 dex. Used these corrections for our stars, we can see from Fig. 5 (Denissenkov & Pinsonneault, 2008, see their Fig. 5), that new values will move, but remain near the calculated curve, that it does not change our conclusions about the canonical extra-mixing in studied HE1523-0901, HD6269 stars; but the star HD 121135 changes its position and turns out to be far from the calculated curve.

The star HD 195636 have [C/Fe] = -0.79, [O/Fe] = 1.16; Preston (1997) noted that "the low gravity and low metallicity derived from spectrum analysis, and weakness of all CH molecular lines combine to suggest that HD 195636 is in an evolutionary state near the transition between the horizontal branch and asymptotic giant branch (RHB/AGB)". An additive argument by Preston (1997), is a rotational velocity of HD 195636 (Vsini = 25 km/s), the value at 2 times greater than may be if blue horizontal branch axial rotators in globular clusters conserve envelope angular momentum during horizontal branch evolution. We also have a low carbon value, initial [C/Fe] = -0.69, which is lower than our other stars.

The position HD 195636 on the evolutionary diagram (see Fig. 2) confirms Preston's opinion.

6. Conclusion

- The atmospheric parameters and abundances of some key elements, as C, N, O for four target stars were determined to analyze the mixing;
- Such parameters as log $L/L_\odot$ and [C/H] for HE1523-0901 and HD6269 correspond to the region of canonical mixing (Denissenkov & Pinsonneault, 2008), thereas HD 121135 may not be a subject to canonic mixing;
- The initial carbon values [C/Fe] were obtained using mean value of corrections from Placco *et al*. 2014;
- The introduction of a possible NLTE correction (Takeda & Takada-Hidai, 2013) for the value of carbon abundance does not change the conclusions about the canonical extra-mixing in the studied HE1523-0901 and HD6269 stars;
- The star HD195636 is more likely to be a horizontal or ascending giant branch star, with some chemical composition peculiarities.

References

Angelou et al.: 2011, *ApJ*, **728**, 79.
Barnes et al.: 2008, *SPIE 7014*, 70140K.
Bramall et al.: 2010, *SPIE* 7735, 77354F.
Bramall et al.: 2012, *SPIE* 8446, 84460A.
Buckley D.A.H., Swart G.P., Meiring J.G.: 2006, *SPIE*, 6267.
Castelli F., Kurucz R.: 2004, ArXiv *Astrophysics e-prints* astro-ph/0405087.
Charbonnel C.: 1994, *A&A*, **282**, 811.
Charbonnel C., Zahn J.P.: 2007, *A&A*, **476**, L29.
Coelho P.R.T.: 2014, *MNRAS*, **440**, 1027.
Denissenkov P., Pinsonneault: 2008, *ApJ*, **679**, 1541.
Denissenkov P., VandenBerg D. A.: 2003, *ApJ*, **593**, 509.
Demarque et al.: 2004, *ApJS*, **155**, 667. (YY treks)
Galazutdinov G.: 2007, http://gazinur.com/DECH-software.html
Gratton R.: 2000, *A&A*, **354**, 169.
Khan et al.: 2018, *ApJ*, **859**, 156.
Kupka et al.: 1999, *A&ASuppl.*, **138**, 119.
Kippenhahn R., Ruschenplatt G., Thomas H.C.: 1980, *A&A*, **91**, 175.
Lind et al.: 2012, *MNRAS*, **427**, 50.
O'Donoghue D. et al., 2006 *MNRAS*, **372**, 151.
Palacios et al.: 2006, *A&A*, **453**, 261.
Placco et al.: 2014, *ApJ*, **797**, 21.
Preston G. W.: 1997, *AJ*, **113**, 1860.
Roederer et al.: 2014, *AJ*, **147**, 136.
Stancliffe et al.: 2009, *MNRAS*, **396**, 2313.
Stancliffe R. J., Eldridge J. J., 2009, *MNRAS*, **396**, 1699.
Spite et al.: 2006, *A&A*, **455**, 291.
Takeda Y., Takada-Hidai M.: 2013, *PASJ*, **65**, 65.
Tsymbal V.: 1996, *ASP Conf. Ser.*, **108**, 198.

https://doi.org/10.18524/1810-4215.2023.36.291233

TWO TOOLS FOR ESTIMATING STAR CLUSTER PARAMETERS

E. Paunzen[1], M. Piecka[2], J. Supíková[3]

[1] Department of Theoretical Physics and Astrophysics, Masaryk University, CZ-611 37 Brno, Czechia, *epaunzen@physics.muni.cz*
[2] Department of Astrophysics, Vienna University, A-1180 Vienna, Austria, *martin.piecka@univie.ac.at*
[3] Institute of Computer Science, Masaryk University, CZ-602 00 Brno, Czechia, *supikova@ics.muni.cz*

ABSTRACT. A star cluster is a composition of stars held together by the overall gravitational field of the whole cluster. The stars of a given cluster are born in a giant molecular cloud and, as such, can be regarded as objects with almost equal ages. Furthermore, assuming that the initial material in the cloud is perfectly mixed, we may also say that the metallicity of all cluster members is the same. Four parameters (distance, extinction or reddening, age, and metallicity) are standardly used to describe star clusters. Their knowledge is essential for studying galaxies' local and global properties (especially our own Galaxy). However, deriving these parameters may take time and effort. Thanks to the Gaia mission's parallax measurements, we can determine the distances of stars (and clusters) within our Galaxy with unprecedented precision. Therefore, we can remove the distance from the list of free parameters. We developed two different tools for estimating cluster parameters: 1) Metalcode, an automatic tool focused on deriving metallicities of open clusters, and 2) Stellar Isochrone Fitting Tool (StIFT), a tool for fitting a grid of isochrones for any photometric system available. We present both tools in more detail.

Keywords: Galaxy: abundances; Hertzsprung-Russell and C-M diagrams; open clusters and associations: general; stars: abundances.

АНОТАЦІЯ. Завдяки останнім даним GAIA тепер можливо більш детально вивчати найближчі відкриті скупчення. Внутрішня структура та кінематичні характеристики відомі лише для кількох скупчень, таких як Гіади та Плеяди. Однак ці характеристики є важливими як вхідні параметри для моделі, що стосуються формування та еволюції зоряних скупчень. Нещодавні публікації представили однорідний вибір із майже 8 000 галактичних зоряних скупчень (Hunt & Reffert, 2023). Однак оцінка параметрів зоряного скупчення все ще триває. Зоряне скупчення – це композиція зірок, які утримуються разом загальним полем тяжіння всього скупчення. Зорі даного скупчення народжуються у гігантській молекулярній хмарі і можуть розглядатися як об'єкти майже однакового віку. Крім того, припускаючи, що початковий матеріал у хмарі ідеально змішаний, ми також можемо сказати, що металічність усіх членів скупчення однакова. Для опису зоряних скупчень стандартно використовуються чотири параметри (відстань, поглинання або почервоніння, вік і металічність). Їх знання необхідні для вивчення локальних і глобальних властивостей галактик (особливо нашої власної Галактики). Однак визначення цих параметрів може зайняти час і зусилля. Завдяки вимірюванням паралакса, проведеним місією Gaia, ми можемо визначити відстані до зір (і скупчень) у нашій Галактиці з безпрецедентною точністю. Тому ми можемо прибрати відстань зі списку вільних параметрів. Ми розробили два різних інструменти для оцінки параметрів кластерів: 1) Metalcode, автоматичний інструмент, зосереджений на отриманні металічності розсіяних скупчень, і 2) Інструмент підгонки ізохрон зір. (StIFT), інструмент для підгонки сітки ізохрон для будь- якої доступної фотометричної системи.

Ключові слова: Галактика: хімічний склад; діаграми Герцшпрунга-Рассела та C-M; розсіяні скупчення та асоціації; зорі: хімічний склад.

1. Introduction

Star clusters are the most essential astrophysical laboratories for the formation and evolution of individual stars (members) and the Milky Way as a global galaxy. They are physically related groups of stars held together by mutual gravitational attraction. Therefore,

these populate a limited region of space, typically much smaller than their distance from the Sun, so the members are all approximately at the same distance. They are believed to originate from sizeable cosmic gas and dust clouds (diffuse nebulae) in the Milky Way and to continue to orbit the Milky Way through the disk. In many clouds visible as bright diffuse nebulae, star formation still occurs so we can observe the birth of new young star clusters. This process of formation takes only a short time (a few Myrs) compared to the lifetime of the cluster, so, speaking in terms of stellar evolution, all member stars are of similar age. Also, as all the stars in a cluster are formed from the same diffuse nebula, they are all of a similar initial chemical composition. Hence, star clusters are of great interest to scientists:

- The cluster members are all about the same distance from the Sun.
- They have within a few million years approximately the same age.
- The chemical composition of the members is relatively homogeneous within a cluster, but the metallicities of the various open clusters range from about -1.5 to +0.6 dex compared to the Sun.
- The member stars have different masses, ranging from about $120\,M_\odot$ for the most massive stars in very young clusters to less than $0.08\,M_\odot$.

The age and metallicity are, in general, not straightforward to determine for Galactic field stars. Star clusters, on the other hand, represent samples of objects of constant age and homogeneous chemical composition, suited for the study of processes linked to stellar structure and evolution and to fix lines or loci in several of the most important astrophysical diagrams, such as the colour-magnitude diagram (CMD) or Hertzsprung-Russell diagram (HRD). So, any astrophysical phenomenon can be studied for members of star clusters in correlation with age, distance, and metallicity.

A star cluster is a composition of stars held together by the overall gravitational field of the whole cluster. The stars of a given cluster are born in a giant molecular cloud, and as such can be regarded as objects with almost equal ages. Furthermore, assuming that the initial material in the cloud is perfectly mixed, we may also say that the metallicity of all cluster members is the same.

However, deriving the four parameters may not always be simple. One can always use the isochrone fitting technique to determine the distance, the extinction and the age of a cluster. Furthermore, thanks to the parallax measurements from the Gaia mission (Cantat-Gaudin, 2022), we can determine the distances of stars (and clusters) within our Galaxy with unprecedented precision. Therefore, we can remove the distance from the list of the free parameters.

Dealing with the metallicity is not as simple. While isochrone fitting in the CMD can provide fairly precise results (Dias et al., 2021), it is not very sensitive to variations in metallicity and solar metallicity is often assumed. Another approach is to measure the stellar members' spectra and determine their abundances (Heiter et al., 2014). However, this approach can be limited by the distances of the target stars and, therefore, is not suited for the distant clusters.

Here, we present two newly developed tools which significantly improve the situation of fitting cluster parameters and astrophysical parameters of stars. They can be universal used including user-defined isochrone grids, for example

2. The two tools

In the following, we present the two tools in more detail. They have already been successfully applied to star clusters (Paunzen et al., 2021) and individual star groups (Faltová et al., 2021).

2.1. Metalcode

Metalcode[1] is a new, fully automatic procedure capable of computing the four main cluster parameters (distance, reddening, age, and metallicity). The approach is based on the work by Pöhnl & Paunzen (2010) and focuses primarily on determining metallicities of star clusters. The method for determining metallicities, presented in Pöhnl & Paunzen (2010), is based on an iterative approach. It requires a list of stars for which a photometric brightness and a photometric colour are included. In principle, any photometric system can be used while the isochrones are available. Furthermore, an initial estimate of the cluster's distance and the reddening is needed before the method can be used. It is possible to vary the values of these two cluster parameters during the iterations.

Another important part of the method is the isochrone grid which consists of the ($\log L$, $\log T_{\rm eff}$) curves for a given set of age and metallicity values. Before the iterative process is started, the effective temperatures in this grid need to be normalised with respect to the zero-age-main-sequence (ZAMS) – this step is described below.

Overall, the iterative process (Fig. 1) can be summarised in four steps:

1. Assume the initial value of metallicity. In the first iteration, this can be taken to be the solar metallicity value. Any solar metallicity value can be

[1] https://github.com/mpiecka/metalcode

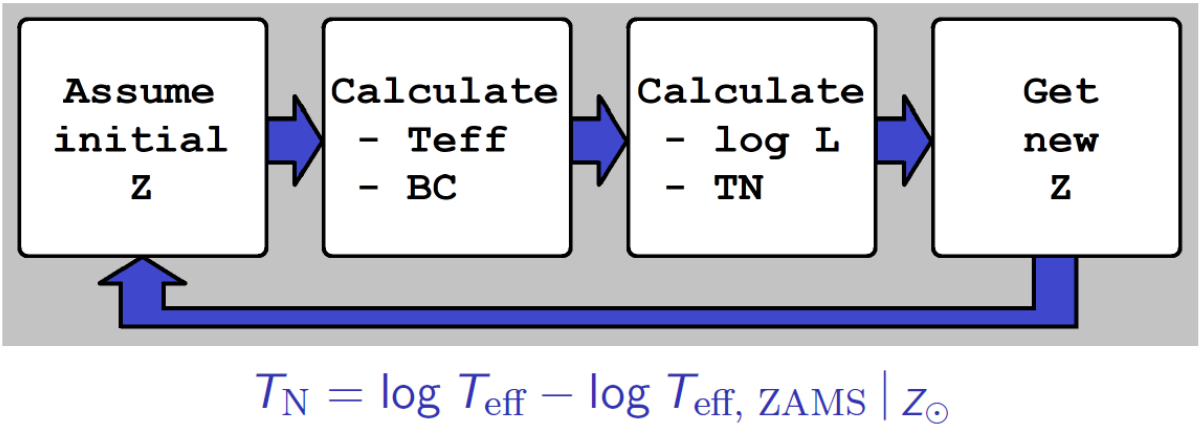

Figure 1: The working flow of metalcode (Sect. 2.1.)

used, but it must be applied consistently during the process.

2. For each of the cluster members, calculate the effective temperature $T_{\rm eff}$ and the bolometric correction BC. Both calibrations are generally based on polynomial relations with the photometric colour and metallicity. Pöhnl & Paunzen (2010) applied the calibrations from Alonso et al. (1996) and Flower (1996). These calibrations require the transformation between Z and [Fe/H].

3. Calculate the luminosity $\log L$ and the normalised logarithmic effective temperature $T_{\rm N}$ for each of the members. The normalisation is performed by subtracting $\log T_{\rm eff}$ from the value on the solar-metallicity ZAMS: $T_{\rm N} = \log T_{\rm eff} - \log T_{\rm eff\,,\,ZAMS}|_\odot$.

4. Compare the distribution of the data points in the ($\log L$, $T_{\rm N}$), or shortly LTN (we will use this abbreviation from now on), diagram with the pre-prepared isochrone grid. Pick the isochrone which best fits the observed data distribution. This gives a new estimate of the metallicity (and of the age).

At the end, the final metallicity value is compared with the initial estimate. The iterations are terminated once the values are the same (or differ by a certain threshold value at most).

This method has been applied several times and proven fairly robust (see Netopil et al., 2016). It was mainly used for stars on the main sequence. The provided results are in good agreement with the spectroscopic observations.

The utilisation of the normalised temperature makes the LTN diagram much more viable for determining metallicities than a CMD or a classical temperature-luminosity diagram. The reason for this is the increased sensitivity to the metallicity change, as already demonstrated in Pöhnl & Paunzen (2010).

Metalcode is a procedure that could apply this method automatically. To do so, it is important first to analyse possible issues. For example, several factors can influence the precision of determining metallicity from the LTN diagram:

- A binary sequence creates an additional distribution of stars, shifting towards negative $T_{\rm N}$ values. This does not affect the results much when the isochrone fitting is performed manually since a skilled researcher can easily distinguish between the two sequences. However, it could influence an automatic procedure.

- Differential extinction can appreciably broaden the width of the MS in the CMD. This broadens the distribution along the horizontal main-sequence "line" in the LTN diagram, which can result in a higher error in the metallicity determination.

- Imperfections in the effective temperature calibrations can cause luminosity-dependent systematic offsets. The effect is further increased when combined with the differential extinction.

For testing purposes, we have written a short code which creates a data set of stars for a synthetic cluster based on the isochrone grid. This code is used to test the above-mentioned sub-procedures, allows us to introduce a binary sequence, and gives us control of the width of the main sequence. Therefore, the influence of various effects can be analysed.

The code is presently equipped with a basic isochrone fitting procedure. Its performance was tested for Johnson BV, 2MASS JKs, and Gaia $GBpRp$ photometric systems.

2.2. Stellar Isochrone Fitting Tool (StIfT)

Stellar Isochrone Fitting Tool (StIfT[2].) is a multiplatform stand-alone tool that estimates the age, radius, mass, and evolutionary phase of a star defined by its $T_{\rm eff}$ and $\log L$. The computation is done by interpolating isochrones from the default grid or custom data set. The tool reacts to the demand for missing features of currently available tools; it offers easier manipulation and provides all necessary options to simplify the work of astrophysicists.

The evolutionary tracks are defined as a parameters grid for different metallicities and ages. StIfT is a tool for interpolating within a user-defined grid of isochrones, for example. Estimating missing characteristics is described in Malkov et al. (2009) and Sichevskij (2017). Firstly, the nearest isochrones are found for a star (x, y) defined by effective temperature and luminosity. Here, four stars are selected as the nearest neighbours of the input star (as shown in Fig. 2).

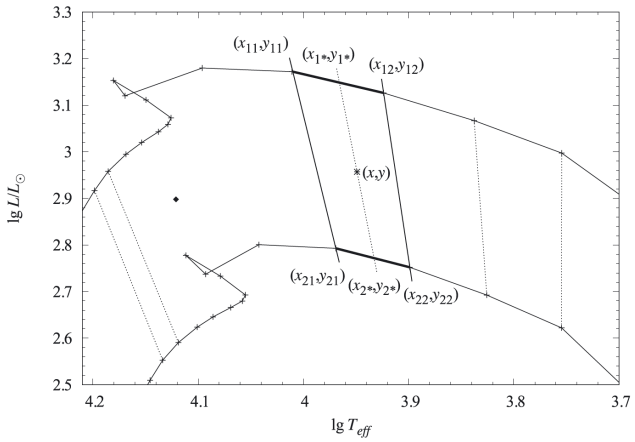

Figure 2: Nearest isochrones (upper and lower tracks) are used for estimating missing parameters, four neighbours create a figure, and a line connects the isochrones with the input star. Credit: Malkov et al. (2009).

Secondly, a line $[(x_{1*}, y_{1*}), (x_{2*}, y_{2*})]$ is found within this area that connects the isochrones and the input star. The x_{2*} coordinate comes as a root of quadratic equation solving the position of line points. Other line points' coordinates are obtained by linear interpolation, for example, the y_{1*} from the following formula:

$$y_{1*} = y_{12} + \frac{y_{12} - y_{11}}{x_{22} - x_{21}}(x_{2*} - x_{22}).$$

The line points are interpolated for the y coordinate and all missing stellar parameters. They are then used in the next step, which requires performing interpolation to get the results for the input point. For example, mass (μ) would be obtained from line points' masses (μ_{1*} and μ_{2*}) by the following formula:

$$\mu = \mu_{1*} + \frac{\mu_{2*} - \mu_{1*}}{x_{2*} - x_{1*}}(x - x_{1*}).$$

This kind of uncertainty creates a standard deviation (σ), which can be calculated as a square root of a sum of squared differences between the mean value (μ) and other values (x) divided by the number of used points (N):

$$\sigma = \sqrt{\frac{\sum(x-\mu)^2}{N}}.$$

Besides estimating the mean value, the StIFT also works with uncertainties. That is, during the process of estimating the result, an error can occur. This comes from using linear interpolation and can be calculated by partial derivation. Another kind of uncertainty comes from using input parameters which are not precise. Other than linear attributes, they must be converted to linear ones to get the correct value. For example, age must be converted from decimal exponent format to years before calculating the deviation and transformed back after. Further, I refer to uncertainty as the combination of interpolation error and standard deviation. The uncertainty for each parameter is obtained from the following formula:

$$uncertainty = \sqrt{error^2 + deviation^2}.$$

In Fig. 3, the GUI version of StIFT is shown. Currently, the tool includes the following features:

- Supported input: filling the form, clicking graph or uploading input file
- Showing results in the result table
- Uploading custom grid data or using default grid data
- Graph representation of grid data
- Exporting result data
- Filtering results based on the evolutionary phase
- Filtering tracks based on the evolutionary phase
- Uncertainty estimation
- Text mode, fast mode

Running the application requires Java 11.

3. Conclusions and Outlook

With the most recent Gaia data releases, studying nearby open clusters in more detail is now possible. The internal structure and kinematic characteristics are only known for a few clusters like the

[2]https://github.com/Johaney-s/StIFT

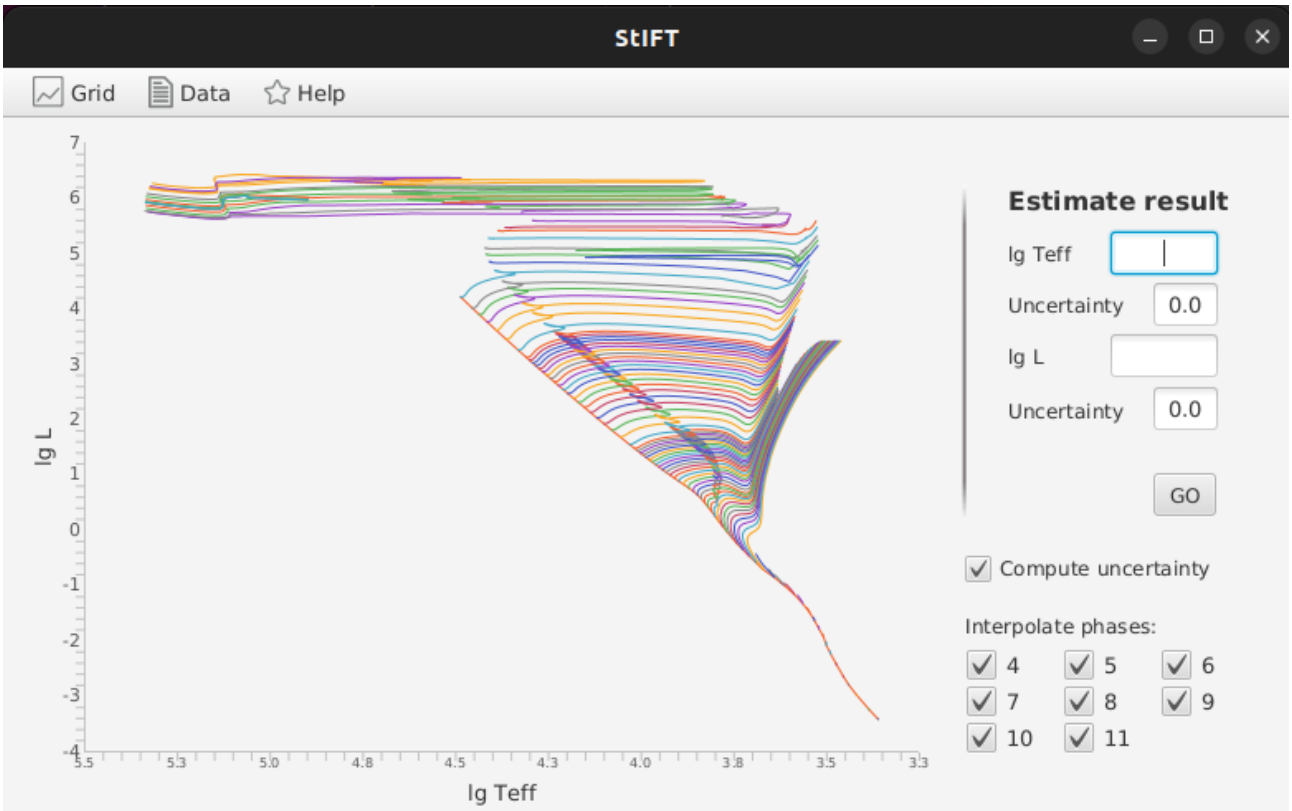

log Teff [K]	log Lum. [L⊙]	log Age [yrs]	Radius [R⊙]	Mass [M⊙]	Phase
3.6826±0.00	4.5340±0.00	$7.1068^{+0.00}_{-0.00}$	$268.2667^{+3.01}_{-2.83}$	$14.6694^{+0.10}_{-0.09}$	$7.0959^{+0.09}_{-0.10}$
4.2120±0.00	2.6776±0.00	$7.3005^{+0.02}_{-0.02}$	$2.7519^{+0.01}_{-0.01}$	$4.6917^{+0.01}_{-0.01}$	$5.1975^{+0.01}_{-0.01}$
4.0990±0.00	2.4005±0.00	$8.2134^{+0.00}_{-0.00}$	$3.3576^{+0.03}_{-0.03}$	$3.5936^{+0.01}_{-0.01}$	$5.6909^{+0.01}_{-0.01}$
3.9214±0.00	1.4584±0.00	$8.8708^{+0.00}_{-0.00}$	$2.5705^{+0.00}_{-0.00}$	$2.0833^{+0.00}_{-0.00}$	$5.7053^{+0.00}_{-0.00}$
3.7407±0.00	0.0730±0.00	$10.1098^{+0.02}_{-0.02}$	$1.2116^{+0.03}_{-0.03}$	$0.9000^{+0.00}_{-0.00}$	$6.7309^{+0.12}_{-0.12}$
3.7116±0.00	0.7935±0.00	$9.4869^{+0.00}_{-0.00}$	$3.1429^{+0.01}_{-0.00}$	$1.4434^{+0.00}_{-0.00}$	$7.9116^{+0.00}_{-0.00}$

Figure 3: A snapshot of the GUI version of StIfT (Sect. 2.2.)

Hyades and Pleiades. However, these characteristics are essential as input parameters for models dealing with the formation and evolution of star clusters (Piecka & Paunzen, 2021).

Recent publications presented a homogeneous selection of almost 8 000 Galactic star clusters (Hunt & Reffert, 2023). However, the estimation of star cluster parameters is still not straightforward and is limited by several observational and theoretical uncertainties. No The homogeneous method allows the age and metallicity estimate for a given distance, and reddening is available.

In this paper, we present two new tools which help to find a solution for this problem. They are user-friendly and can be extended to any new photometric and isochrone set.

Acknowledgements. This work was supported by the grant GAČR 23-07605S.

References

Alonso A. et al: 1996, *A&A*, 313, 873.
Cantat-Gaudin T.: 2022 *Universe*, 8, 11.
Dias W. S. et al: 2021, *MNRAS*, 504, 356.
Faltová N. et al: 2021, *A&A*, 656, A125.
Flower P. J.: 1996, *ApJ*, 469, 355.
Heiter U. et al: 2014, *A&A*, 561, A93.
Hunt E. L. & Reffert S.: 2023 *A&A*, 673, A114.
Malkov O. Yu. et al: 2009, *MNRAS*, 401, 695.
Netopil M. et al: 2016, *A&A*, 585, A150.
Paunzen E. et al: 2021, *MNRAS*, 504, 3758.
Piecka M. & Paunzen E.: 2021, *arXiv:2107.07230*.
Pöhnl H. & Paunzen E.: 2010, *A&A*, 514, A81.
Sichevskij S. G.: 2017, *Astronomy Reports*, 61, 193.

https://doi.org/10.18524/1810-4215.2023.36.290121

SPECTRAL OBSERVATIONS OF THE ALGOL - TYPE BINARY STAR δ LIBRAE

B.N. Rustamov[1,2], Kh.M. Mikailov[1], K.I. Alisheva[1], S.O. Mammadova[2], Sh.A. Agayeva[2], O.V. Maryeva[3]

[1] Baku State University, Baku, Azerbaijan
[2] Shamakhy Astrophysical Observatory named after N. Tusi, Azerbaijan
[3] Astronomical Institute of the Czech Academy of Science, Czech Republic
bayram_rustam@yahoo.com

ABSTRACT. The results of spectral observations of the Algol-type binary star δ Lib are presented. The behavior of Hα and Hβ lines in the star's spectrum during the orbital period phase is described. Based on our measurements of the radial velocities of the Hα and Hβ lines and using published data, the radial velocity curves of both components of the δ Lib system were constructed. In some phases of the orbital period, an absorption component was detected in the blue, or red, part of the Hα and Hβ line profiles. The observed Hα and Hβ absorption lines are attributed to the main component of the binary system δ Lib. It is assumed that the appearance of absorption components at these lines is associated either with suspicion of a third component in the system, or at these phases of the Hα and Hβ lines, the primary and secondary components of the δ Lib system are observed simultaneously.

Keywords: eclipsing – binaries, individual: δ Lib – stars, line spectroscopic – stars, profiles — stars.

АННОТАЦІЯ. Наведено результати спектральних спостережень подвійної зорі типу Алгола δ Lib. Було використано два набори спектрів. Перший був здобутий у фокусі Кассегрена 2-м телескопа Шамахінської Астрофізичної Обсерваторії ім. Н. Тусі на оптоволоконному ешеле-спектрографі ShAFES за допомогою ПЗЗ-матриці у червні 2020 р. Спектри отримані зі спектральною роздільною здатністю R = 56000, у діапазоні довжин хвиль λ = 3900-7500 Å. Другий набір спектрів отримано на 2-м телескопі ім. Л. Перека Астрономічного Інституту Чеської Академії Наук за допомогою ешеле-спектрографа Ондрейова (OES) у фокусі куди у червні та липні 2022 р. Діапазон довжин хвиль λ = 3750-9200 Åта R = 50000. Обробка спектрів проводилася за стандартною методикою, за допомогою нової версії програми DECH 30. Для порівняльного аналізу кривих променевих швидкостей також використані опубліковані дані променевих швидкостей спектральних ліній δ Lib.

Описано поведінку ліній Hα і Hβ в спектрі зорі протягом фази орбітального періоду. За нашими даними променевих швидкостей ліній Hα і Hβ і з залученням опублікованих даних, побудовані криві променевих швидкостей обох компонент системи δ Lib. У деяких фазах орбітального періоду виявлено абсорбційний компонент у синій (фази 0.62 та 0.75) або червоній (фази 0.18 та 0.19) частини профілів ліній Hα та Hβ. Абсорбційні лінії Hα і Hβ, що спостерігаються нами, відносяться до основної компоненти подвійної системи δ Lib.

Передбачається, що поява абсорбційних компонентів у цих ліній пов'язана з тим, що в цих фазах у Hα і Hβ спостерігаються первинний і вторинний компоненти системи δ Lib одночасно, або з підозрою про третій компонент системи, і не виключено, що цей ефект пов'язаний з так званим ефектом Маклафліна – Россітера, який у поодиноких випадках спостерігається у подвійних системах типу Алгола. Попередньо ми надаємо перевагу першій гіпотезі, але надалі всі три гіпотези будуть ретельно досліджені, в міру накопичення спостережного матеріалу.

Ключові слова: затемнювано-подвійні зорі, спектрольно-подвійні зорі, індивідуально: δ Lib.

1. Introdution

δ Librae (= HR 5586 = HD 132742 = HIP 73473) is one of the nearest (∼90 pc) Algol systems. This systems is a close, interacting binary made of A0V + K0IV stars, with V ∼ 4.9 mag and an orbital period close to P = 2.327 days. The hotter and more massive star is A0 and it is on the main sequence; we will refer to it as star A. Its companion, which we call star B, is a cooler and less massive K0 subgiant filling its

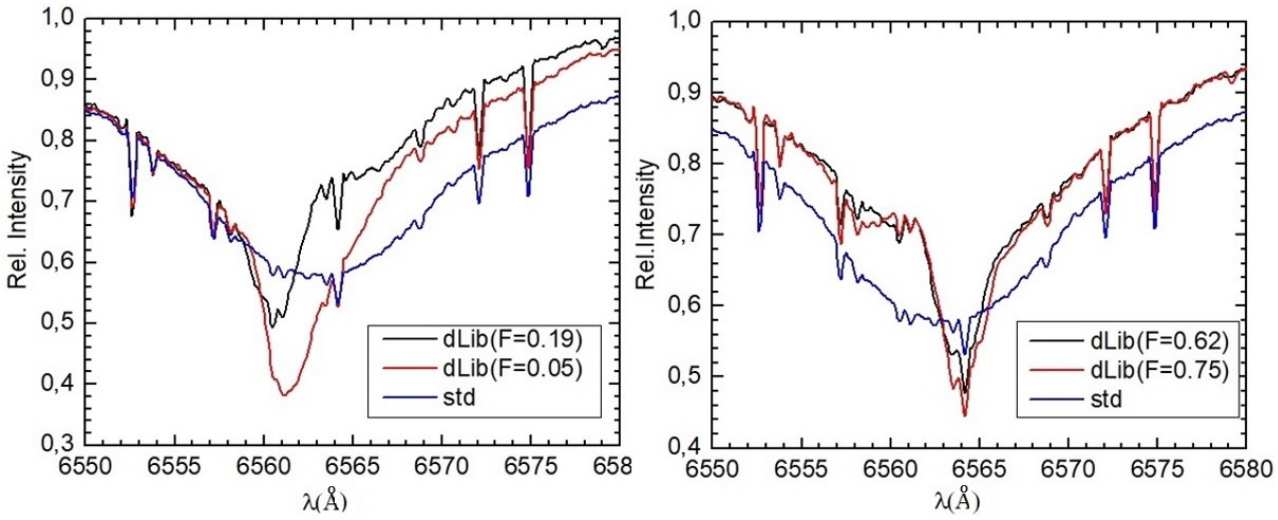

Figure 1: Example the profiles of the standard star and Hα line at close values of orbital phases on δ Lib binary star spectrum

Roche lobe. Matter is being transferred from star B (the donor) to star A (the recipient). (Tomkin, 1978; Budding et al., 2005).

2. Observations and data processing

Two sets of spectroscopic observations were used in the present study. The first one was spectral observations of the Algol-type binary star δ Lib were carried out at the Cassegrain focus of the 2-meter telescope of the Shamakhy Astrophysical Observatory named after N.Tusi, on fiber echelle spectrograph ShAFES (Mikailov et al., 2020), by using CCD matrix STA4150A 4×4 K elements, with an element size of 15 μm. The spectra are obtained at the resolution R = 56000, in the wavelength region $\lambda = 3900 - 7500$ ÅÅ. In June 2020, during four nights, every night two spectra of the studied star, and a complete set of calibration images were obtained, and two spectra of the standard star 109 Vir (sp. AO) were also obtained.

The second set spectrum were carried out at the Perek's 2-m telescope of the Ondrejov observatory from 2022 June and July 2022, with the echelle spectrograph (OES). The OES provides a wavelength range of $\lambda = 3750 - 9200$ ÅÅ and a spectral resolving power of 50000 (Koubský et al., 2004; Kabáth et al., 2020).

Processing of spectra was carried out according to the standard method using the new version of the DECH30 program developed by Galazutdinov (http://www.gazinur.com/DECH software.htm). A list of all used spectra is given in Table 1.

Table 1: Circumstances of spectral observations star δ Lib

No	Date	JD +2450000	Phase	Radial velocity Hα	Hβ
1	07.06.2020	9008.263	0.204	-118.7	-114.7
2	08.06.2020	9009.263	0.634	34.6	25.6
3	09.06.2020	9010.255	0.060	-78.5	-77.3
4	13.06.2020	9014.219	0.763	40.8	24.7
5	10.06.2022	9741.357	0.195	-115.0	-117.0
6	16.06.2022	9747.335	0.763	43.9	33.4
7	02.07.2022	9763.324	0.633	20.6	14.6
8	12.07.2022	9773.317	0.927	-5.0	-8.7
9	16.07.2022	9777.317	0.646	15.1	-15
10	17.07.2022	9778.315	0.074	-70.3	-29.6

3. Results of observations

Orbital phases of δ Lib binary system has been provided according to the date of acquisition of the spectrum shown in Table 1.

Phases computed with Koch's (Koch, 1962) ephemeris:

$$Pr.Min. = 2422852.3598 + 2.32735297E.$$

For a comparative analysis of radial velocity curves, published radial velocity data for spectral lines belonging to both components of the δ Lib binary system were also used (Tomkin, 1978 (date 1977); Bakısh, 2006 (Ondrejov, Rozhen, date: 1996, 1997 and 2003)).

The phases of the components of this star according to radial velocities taken from the published date have been calculated using the same formula.

The profile of Hα and Hβ absorption lines from

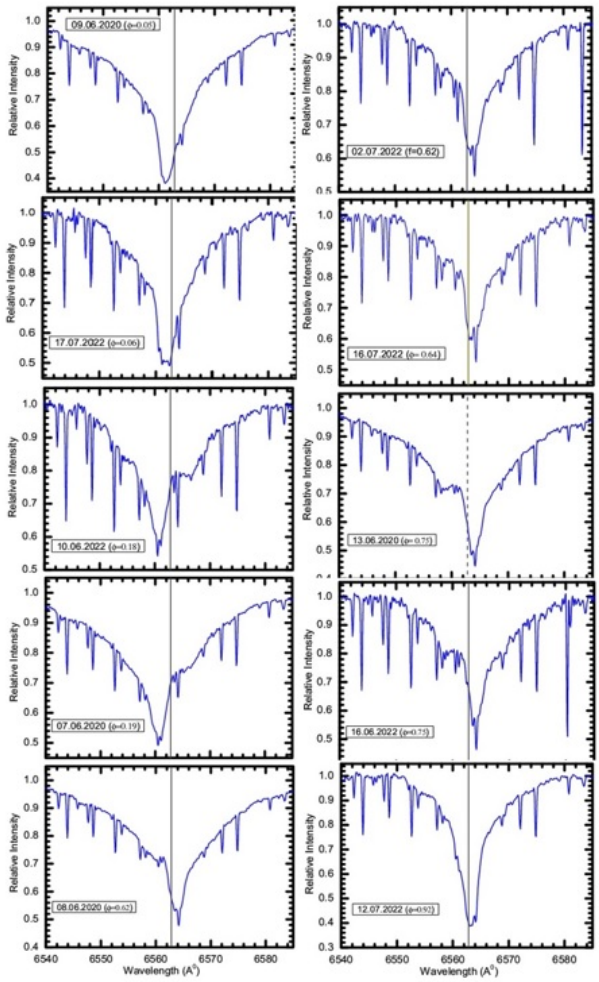

Figure 2: The profiles of Hα lines depending on the phase of the orbital period on δ Lib binary star spectrum

Balmer's series has been constructed and heliocentric radial velocities have been calculated using Galazutdinov's DECH 30 software. The results of measurements of the radial velocities of the Hα and Hβ lines are given in Table 1. Fig.1 presents examples of profiles of the standard star and Hα line at close values of the orbital phases on δ Lib binary star spectrum. Fig. 2 shows with the variations in the profiles of Hα lines depending on the orbital phase of the binary system.

Hα and Hβ lines belong to δ Lib binary system's primary component; the radial velocity curves have been constructed. Figure 3 shows the radial velocity curve of the main component of the delta Lib binary system based on our measurements from the Hα and Hβ lines and from data from the P14 line borrowed from (Tomkin, 1978). As can be seen from Fig.3, our measurements are in satisfactory agreement with the measurements from (Tomkin, 1978).

Figure 4 shows the radial velocity curve of the primary and secondary component of the δ Lib double system based on our measurements and published data from (Tomkin, 1978 (date 1977); Bakısh V., 2006 (Ondrejov, Rozhen, date: 1996, 1997 and 2003)).

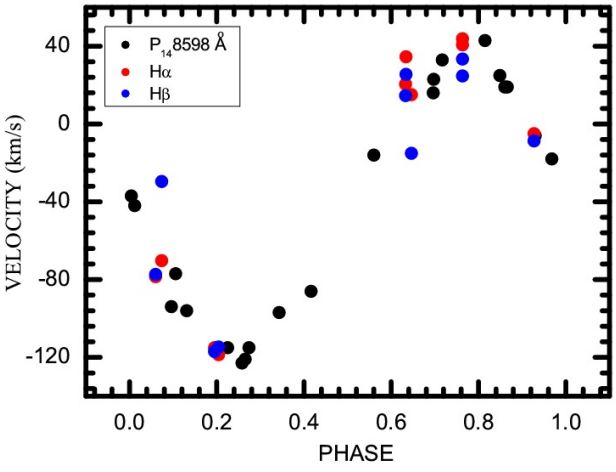

Figure 3: The radial velocity curve of the primary component of the δ Lib Algol type binary system based of our measurements of Hα and Hβ lines (2020-2022) and spectrum P14 8598 Å (Tomkin, 1978 (date 1977)).

A thorough examination has revealed an interesting detail in the spectra of the δ Lib star. In some phases of the orbit of the δ Lib binary system, an absorption detail (depression) is observed on the red and blue wings of the line Hα, namely in the phases 0.18 and 0.19, red, and in the close phases 0.62 and 0.75 in the blue wing of the absorption line Hα an additional absorption detail appears. Fig. 5 for example, shows the fragments of Hα line region with additional absorption detail.

As seen from the radial velocity curves provided at the Fig.4 the lines of the secondary component of the system are not visible at the phase values 0.4 – 0.6 (Bakısh et al., 2006, Ondrejov and Roshen) or 0.35 – 0.7 (Tomkin, 1978). As observed, this phase interval corresponds to the period of the secondary component's eclipse.

In the region of the Ca II 8542 Å and P15 lines in the spectrum δ Lib, in (Tomkin, 1978) a similar picture was found at phase 0.815 on the blue wing and at phase 0.265 on the red wing of the Paschen line, additional absorption is observed. The authors explain this with the appearance of Ca II 8542 Å lines also on the secondary component of the binary system δ Lib.

4. Conclusions

The hypothesis below may be linked to the absorption element observed at the values 0.18 and 0.19 in

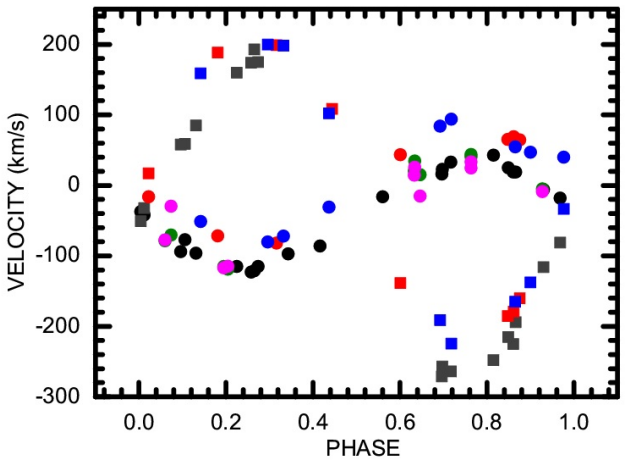

Figure 4: Primary and secondary components radial velocity curves of the δ Lib star Algol type binary system.
Primary component - full circles: **dark** - Tomkin J., 1978 (date 1977); **red** - Bakısh V., 2006 (Ondrejov, date: 1996, 1997 and 2003); **blue** - Bakısh V., 2006 (Rozhen, date:1996, 1997 and 2003); **magenta** - ShAO + Czech (Hα, this work); **olive** - ShAO + Czech (Hβ, this work); **Secondary component – full rectangles**: **dark** - Tomkin J., 1978 (date 1977); **red** - Bakısh V., 2006 (Ondrejov, date:1996, 1997 and 2003); **blue** - Bakısh V., 2006 (Rozhen, date:1996, 1997 and 2003).

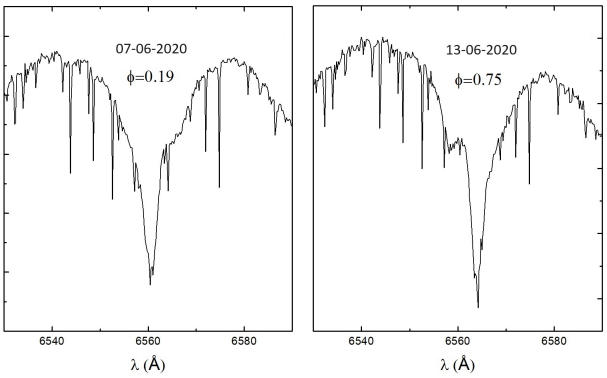

Figure 5: Example the fragments of Hα line region with additional absorption detail.

the direction towards red of Hα lines and at 0.62 and 0.75 towards violet of the orbital phases of δ Lib binary system:

1. The Hα and Hβ lines are visible on the secondary component at the beginning and the end of eclipse.
2. These absorption lines are linked to supposed 3rd component.
3. In close binary star systems, namely Algol type binary systems are related to rarely observed Mclaughlin – Rossiter effect.

All three hypothesis are the discussion topics of the Algol type binary system research. Initially the first hypothesis is preferred, however as the observation material accumulates, all three will be widely researched.

Acknowledgements. Of the coautors: S.O. Mammadova and O.V.Maryeva acknowledges the support of the Innovation Horizon 2020 (2014-2020) under the Marie Sklodowska-Curie Grant Agreement No. 823734.

References

Bakısh V., Budding E., Erdem A. et al.: 2006, *Mon. Not. R. Astron. Soc.*, **370**, 1935.
Budding E., Bakısh V., Erdem A. et al.: 2005, *Astrophys. and Space Sci.*, **296**, 371.
Galazutdinov G.: http://www.gazinur.com/DECH software.html.
Kabáth P., Skarka M., Sabotta S. et al.: 2020, *Publ. Astron. Soc. Pac.*, **132**, 035002.
Koch R.H.: 1962, *A.J.*, **67**, 130.
Koubský P., Mayer P., Čáp J. et al.: 2004, *Publ. Astron. Inst. Czechoslov. Acad. Sci.*, **92**, 37.
Mikailov Kh.M., Musaev F.A., Alekberov I.A. et al.: 2020, *Kinem. and Phys. of Cel. Bod.*, **36**, 22.
Tomkin J.: 1978, *Ap. J.*, **221**, 608.

https://doi.org/10.18524/1810-4215.2023.36.290802

FUNDAMENTAL PARAMETERS OF SUPERGİANT STAR HD40589(A0Iab)

Z.A. Samedov[1,2], U.R. Rustem[2], G.M. Hajiyeva[2], Z.F. Aliyeva[1]

[1] Department of Astrophysics, Faculty of Physics, Baku State University, Baku, Azerbaijan

[2] Division of Physics of stellar atmospheres and magnetism, Shamakhi Astrophysical Observatory of ANAS, Baku, Azerbaijan

zahir.01@mail.ru, ulkergadirova@gmail.com, haciyevagunay@yahoo.com

ABSTRACT. The atmosphere of HD40589(A0Iab) supergiant star of A spectral class was studied using the model atmosphere and parallax methods. The effective temperatures (T_{eff}) and surface of gravity (log g) were determined using a comparison of the observed and calculated values of the photometric quantities [c_1], Q and the equivalent widths of the hydrogen Balmer lines and parallax. Based on the Fe II lines the microturbulent velocity (ξ_t) and metallicity [Fe/H] were determined. Metallicity of the program star is close to the metalicity of the Sun. This shows that our program star and the Sun are formed from the interstellar medium of a similar metallicity.

Keywords: A-type supergiants, fundamental parameters.

АНОТАЦІЯ. У цій роботі були визначені фундаментальні параметри зорі-надгігінта HD 40589 (A0Iab), а саме ефективна температура (T_{eff}), прискорення сили тяжіння (*log* g), мікротурбулентна швидкість (ξt) і металічність [Fe/H]. Відстань до зорі 1734 пк. Висота над площиною Галактики становить 67,5 пк.

Спектри HD40589 були отримані 19 грудня 2019 року за допомогою спектрографа, оснащеного ПЗЗ, що живиться від 2-метрового телескопа Шамахинської астрофізичної обсерваторії (роздільна здатність R=56000, відношення сигнал/шум S/N=150-400). Спектри HD40589 оброблені за програмою DECH 30.

Ефективна температура і прискорення сили тяжіння зорі нашої програми були визначені моделлю атмосфери та методом паралакса. Ефективну температуру та поверхневу силу тяжіння визначали на основі порівняння спостережуваних та розрахункових значень фотометричних величин [c_1], Q та еквівалентних ширин спектральних ліній водневої серії Бальмера, а також за допомогою методу паралакса.

Індекс [c_1] визначається як [c_1]= c_1-0.2(b-y) у фотометричній системі uvby, а індекс Q визначається як Q=(U-B)-0.72(B-V) у системі UBV. Діаграма, що визначає T_{eff} і *log* g дає T_{eff}=10750±150K і *log* g=1.65±0,2. Визначення мікротурбулентної швидкості ґрунтується на дослідженні еквівалентних ширин спектральних ліній заліза. З кожної спектральної лінії можна отримати певний вміст *log* ε. Відхилення від LTE не впливає на лінію FeII. Тому мікротурбулентну швидкість ξ_t і вміст заліза визначали за допомогою ліній FeII. В аналізі використовувалися лише досить слабкі лінії. Ці лінії утворюються в глибоких шарах атмосфери.

У нашому аналізі ми використовували сітку моделей атмосфери Castelli and Kurucz (2003), а атомні дані спектральних ліній були взяті з VALD3.

Металічність зорі [Fe/H]= -0.10. Металічність HD 40589 визначається вперше.

Ключові слова: Надгіганти А-типу, фундаментальні параметри зір.

1. Introduction

In this work the fundamental parameters of our program star HD40589 (A0Iab), namely effective temperature (T_{eff}), surface gravity (log g), microturbulent velocity (ξ_t) and metallicity [Fe/H] were determined. The distance to the star is 1734 pc. The Galactic latitude is 2.23°. The height above the Galactic plane is 67.5 pc. Knowing the effective temperature and surface gravity, the atmosphere models were calculated, and on the basis of these models the chemical composition was determined. The evolutionary parameters of our program star – mass, radius, luminosity, and age were determined. Microturbulence is considered as a broadening mechanism affecting width of the spectral line, therefore, to determine the chemical composition, it is necessary to know accurate value of the microturbulent velocity. The metallicity is one of the main fundamental parameters of stars.

2. Observation material

Spectra of HD40589 were recorded on 19 December 2019 with the help of spectrograph equipped with CCD fed by 2-m telescope of the Shamakhi Astrophysical Observatory of ANAS (resolving power R=56000, signal-to-noise ratio S/N=150−400). The spectra of HD40589 were processed with DECH program (Galazutdinov, 1992).

3. Effective temperature and surface of gravity

As it was mentioned above, the effective temperature and surface gravity of our program star were determined by the atmosphere model and parallax method. This method is described in detail in Lyubimkov, Rachkovskaya and Poklad (2009), Lyubimkov, Lambert and Rostopchin (2010). The effective temperature and surface gravity were determined based on a comparison of the observed and calculated values of the photometric quantities [c_1], Q and

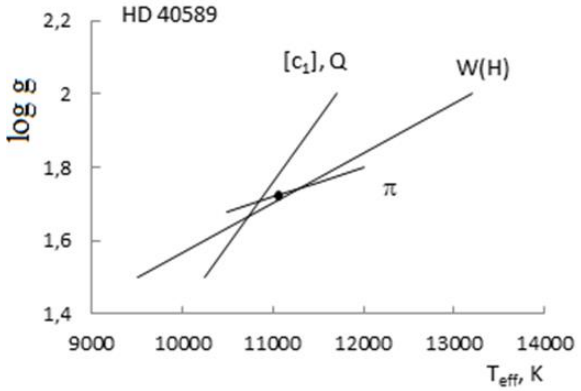

Figure 1: log g–T_{eff} diagrams

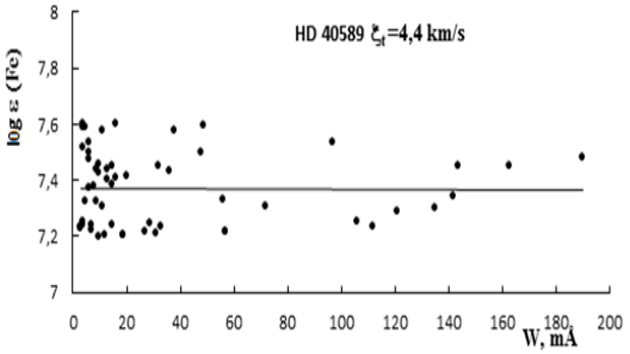

Figure 2: To the determination of the microturbulent velocity

the equivalent widths of the spectral lines of the hydrogen Balmer series, as well as using parallax method.

The index $[c_1]$ is defined as $[c_1]= c_1-0.2(b-y)$ in the uvby photometric system, while the Q index is defined as $Q=(U-B)-0.72(B-V)$ in the UBV system. The observational values $[c_1]$ and Q are determined using the catalogue (Hauck & Mermilliod, 1998). The calculated values of the equivalent widths of the Balmer series lines are given in (Kurucz, 1993). Calculated values $[c_1]$, Q can be found in (Castelli & Kurucz, 2003). Parallax of our program star was measured in (VizieR Online Data Catalog, 2020). The diagram defining T_{eff} and log g is shown in Figure 1: T_{eff}=10750±150K and log g=1.65±0.2.

In (Zorec, Cidale & Arias, 2009) the following value T_{eff}=10970 K for HD40589 is given.

4. The microturbulent velocity

The determination of the microturbulent velocity is based on the study of equivalent widths of spectral lines of iron. From each spectral line one can derive abundance a certain element log ε. Note that the deviation form LTE does not affect the FeII line. Therefore, the microturbulent velocity ξ_t and iron abundance were determined using FeII lines. Only quite weak lines were used in analysis. These lines are formed in deep atmosphere layers.

In our analysis we used Castelli and Kurucz (2003), grid of atmosphere models, and atomic data of spectral lines were taken from the VALD 3 (Ryabchikova et al., 2015).

In Fig.2 the dependence of the abundance log ε(Fe) determined from FeII lines on their equivalent widths W_λ is shown. The slope is about zero, and this is enables us to determine an accurate value of the microturbulent velocity.

From Fig. 2 we can derive the mean iron abundance log ε(Fe) =7.37. The abundance of iron in the Sun is log ε (Fe) =7.47 (Scott, Asplund & Grevesse, 2015). Metallicity of star is [Fe/H]= −0.10. The coincidence between the iron abundance in young nearby stars and that of the 4.5 Gyr old Sun, is interesting from the viewpoint of models of the Galactic chemical evalution (GCE). The question arises: may this result be compatible with models of GCE? One may cite the recent work of Spitoni et al. (Spitoni et al., 2009), where an enrichment of the solar neighbourhood by various metals is studied, in particular, by Fe. One sees from those results that during the Sun's lifetime the Fe abundances in its neighbourhood are predicted to be incresed by about 0.15 dex. The ususal accuracy of the derived abundances in stars seem to be insufficient to detect such a small enrichment. Note that the metallicity of our program star is determined for the first time, thus we cannot compare it to the results of other authors.

5. Main results

1. The effective temperature, surface gravity, and microturbulent velocity of HD40589 (A0Iab) have been determined using the atmosphere model, and parallax methods. The results are following: T_{eff}=10750±150K, log g=1.65±0.2, $\xi_t = 4.4 \pm 0.5$ km/s.

2. Metallicity of this star is log ε(Fe)=7.37±0.12 (in the scale, where the arbitrary hydrogen abundance is 12.00). It has been found that the iron abundance [Fe/H]= −0.10 is close to the solar abundance. This shows that our program star, and the Sun were formed from the interstellar matter of similar metallicity.

References

Castelli F., Kurucz R.L.: 2003, in *Proc. IAU Symp. 210, Modelling of Stellar Atmospheres* /eds. Piskunov N. E., Weiss W.W., Gray D.F., Astron. Soc. Pac., San Francisco, A20.

Galazutdinov G.A.: 1992, *Preprint SAO RAS*, n **92**.

Hauck B., Mermilliod M.: 1998, *A&AS*, **129**, 431.

Kurucz R.: 1993, ATLAS9 Stellar Atmosphere Programs and 2 km/s grid. Kurucz CD-ROM No. 13. Cambridge, Mass.: Smithsonian Astrophysical Observatory, 1993, 13.

Lyubimkov L., Lambert D., Rostopchin S.: 2010, *MNRAS*, **402**, 1369.

Lyubimkov L., Rachkovskaya T., Poklad D.: 2009, *Ap*, **52**, 237.

Ryabchikova T., Piskunov N., Kurucz R.L. et al.: 2015, *PhyS*, **90**, 5.

Scott P., Asplund M., Grevesse N.: 2015, *A&A*, **A26**, 573.

Spitoni E., Matteucci F., Recchi S. et al.: 2009, *A&A*, **504**, 87.

VizieR Online Data Catalog 2020, Available at: (https://ui.adsabs.harvard.edu/abs/2020yCat.1350....0G/abstract) Data Catalog: Gaia EDR3 (Gaia Collaboration)

Zorec J., Cidale L., Arias Y.F.: 2009, *A&A*, **501**, 297.

https://doi.org/10.18524/1810-4215.2023.36.290534

SPECTROSCOPIC INVESTIGATIONS OF POLARIS FIELD STARS

I. A. Usenko,[1,2] A. S. Miroshnichenko,[3,4] S. Danford,[3]
D. G. Turner,[5] D. J. Majaess,[6,7] D. D. Balam[8]

[1] Astronomical Observatory, Odessa National University, Shevchenko Park, Odessa 65014, Ukraine, *igus99@ukr.net*
[2] Mykolaiv Astronomical Observatory, Obsevatorna 1, Mykolaiv 54030, Ukraine
[3] Dept. of Physics and Astronomy, University of North Carolina at Greensboro, P.O. Box 26170, Greensboro, NC 27402, USA, *a_mirosh@uncg.edu; danford@uncg.edu*
[4] Fesenkov Astrophysical Institute, Observatory 23, Almaty, Kazakhstan
[5] Dept. of Physics and Astronomy, Saint Mary's University, 923 Robie Street, Halifax B3H3C3, Nova Scotia, Canada, *David.Turner1@smu.ca*
[6] Washtenaw Community College, 4800 E Huron River Dr., Ann Arbor, MI 48105, USA, *daniel.majaess@gmail.com*
[7] Mount Saint Vincent University, 166 Bedford Hwy, Halifax NS B3M 2J6, Canada
[8] Dominion Astrophysical Observatory, 5071 W Saanich Rd, Victoria, BC V9E 2E7, Canada, *cosmos@uvic.ca*

ABSTRACT. We present the results of an analysis of 28 spectra of 18 Polaris field A–G V stars obtained in 2016–2023. Derived radial velocities and $T_{\rm eff}$ along with distances and reddenings from the Gaia DR3 catalog allowed us to calculate radii of the stars and compare them with calibration relationships "Specral type – Luminosity" for MS stars. As a result, radii and distances for 9 stars were found overestimated compred to those determined photometrically. Therefore, the DR3 distances are unreliable and should be revisited. Accordring to our data for these stars and their photometric distances, 15 objects belong to a possible old open cluster that is currently dissolved in the Polaris field at a distance ∼70–110 pc, while two objects belong to the thick disk, and one belongs to a possible another star group located at a distance of 130 pc.

Key words: Open clusters: Stars: Polaris field stars; radial velocities; main-sequence stars: effective temperatures, radii; GAIA DR3 effective temperatures, distances, reddenings, radii; spectroscopic binaries; pusating variables δ Sct type; thick disc; Individual: HD 5914, HD 10772, HD 11696, HD 14369, HD 14718, HD 16335, HD 66368, HD 90162, HD 163988, HD 203317, HD 209556, HD 224687, HD 224991, Polaris B, BD +86°44, BD +87°16, BD +87°26, BD +88°75. Cepheids: α UMi.

АНОТАЦІЯ. Даються результати аналізу 28 спектрів 18 зір Головної послідовності спектральних класів A-G з поля Полярної, відомої класичної цефеїди, отриманих у 2016-2023 рр. Променяні променеві швидкості та $T_{\rm eff}$ разом із відстанями та почервоніннями, узятими з каталогу Gaia DR3, дозволили нам обчислити радіуси цих зір та порівняти їх з калібрувальними співвідношеннями "Спектральний клас – Світність"для зір ГП. Судячи зі спектрів, HD 90162 дійсно є спектроскопічно-подвійною системою, тоді як HD 14718 і HD 163988 є можливими подвійними. 61% досліджуваних об'єктів – незмінні зорі, а три об'єкти (HD 5914, HD 203317 і HD 224991) можуть бути низькоамплітудними пульсуючими змінними типу δSct. Наші оцінки ефективних температур, отримані за допомогою спектроскопії або фотометрії показали їх приблизну схожість з оцінками з каталогу DR3 для зір спектральних класів F-G, тоді як для більш гарячих зір A-типу різниця становить 300-500 K. Оцінки радіусів зір, розраховані за значеннями $T_{\rm eff}$, почервоніннями та відстанями з DR3 для половини зір виявилися завищеними і невідповідними їх спектральним типам. Перерахунки радіусів і відстаней для зір з використанням наших оцінок $T_{\rm eff}$ із калібрування "Спектральний тип – світність"для зір ГП також підтвердили, що для половини зір оцінки відстані з DR3 ненадійні. Найбільші розбіжності в оцінках відстані між даними DR3 і калібруваннями знаходяться на відстанях більше 130 пк і мають експоненціальний характер. Судячи з отриманих оцінок RV і фото-

метричних відстаней, 15 зір, ймовірно, належать до старого розсіяного скупчення, розчиненого серед зір поля Полярної і розташовані на відстанях ∼70–110 пк, але при цьому два об'єкти належать до товстого диска, а один належить до можливої іншої зоряної групи, розташованої на відстані 130 пс.

Ключові слова: Розсіяні скупчення: Зорі: Полярні зорі поля; радіальні швидкості; зорі головної послідовності: ефективні температури, радіуси; GAIA DR3 ефективні температури, відстані, почервоніння, радіуси; спектроскопічні подвійні; використання змінних δ типу Sct; товстий диск; Індивідуальні: HD 5914, HD 10772, HD 11696, HD 14369, HD 14718, HD 16335, HD 66368, HD 90162, HD 163988, HD 203317, HD 209556, HD 224687, HD 224991, Polaris B, BD +86°44, BD +87°16, BD +87°26, BD +88°75. Цефеїди: α UMi.

1. Introduction

This project is a continuation of our studies of Polaris field stars, which began earlier (Usenko et al. 2018) with the goal to discover whether these stars are members of a sparsely populated open cluster around the nearest Cepheid α UMi (α (2000) = 02 31 49.09; δ (2000) = +89 15 50.79). The main criteria for assessing whether these field stars belonged to the cluster were: 1) proper motions are close to those of Polaris (μ_α = +44.48 mas yr^{-1},μ_δ = −11.85 mas yr^{-1}); 2) radial velocities (RV) are close to that of Polaris (RV = -16.42 km s^{-1}); 3) distances are ∼90–110 pc (Turner 2005). However, estimates of radial velocities and the distances of these stars according to the Gaia DR2 catalog showed a significant scatter, which gave a reason to believe that this cluster may be dissolved among the field stars. Usenko et al. (2018) revealed an obvious discrepancy between the radii of some main sequence stars and their distances from Gaia DR2.

Over the past five years the Gaia database represented in the DR3 catalog has expanded significantly and included a number of important astrophysical parameters, such as $T_{\rm eff}$, log g and A_0, in addition to parallaxes and RVs. This makes it possible to determine accurate distances to the stars in the Polaris field, their spectral types, luminosities and radii as well as the probability of their membership in the cluster mentioned above. Additionally, using new spectra of Polaris field stars it became possible to compare the accuracy of the RVs and effective temperatures. These data will allow us to assess the reliability of the Gaia distance measurements.

As before we performed spectroscopic observations of the Polaris cluster main-sequence stars in order to determine their RV (to establish their membership in the cluster) and effective temperatures (to determine the radii and distances from known spectral types). These objects were taken from Turner et al. (2005).

2. Studied Objects

Table 1 summarizes basic data for the 18 targets that were taken from SIMBAD. According to these data, the stars are located quite close to Polaris, and the vast majority of them have noticeably large proper motions. Nine of these stars (HD 5914, HD 10772, HD 11696, HD 14369, HD 14718, HD 209556, BD +87°16, BD +87°26, BD +88°75) are designated in SIMBAD as stars with a high proper motion (HPMS). The components of their proper motion, as a rule, exceed two dozen milliseconds per year.

However, HD 16335, HD 203317, and Polaris B which meet these criteria are not designated as HPMS. HD 90162 is designated as a spectroscopic binary, and Polaris B is designated as a variable. All these objects are main sequence stars of spectral types from A0 to G0. As it is stated above, the values of μ_α and μ_δ for Polaris are also close to those of these HPMS stars that may serve as a fact of the general spatial dynamics of these stars. The next steps in studying the possible commonality of these stars will be measuring their RVs and determining their effective temperatures.

3. Observations and reduction of spectra

Twenty eight spectra of these eighteen objects were taken in 2016–2023 with the 0.81 m telescope of the Three College Observatory (TCO), located in central North Carolina, USA. They were obtained with an échelle spectrograph manufactured by Shelyak Instruments[1] in a spectral range from 4250 to 7800 Å with a spectral resolving power of $R \sim 12000$ and no gaps between the spectral orders. The data were reduced using the *échelle* package in IRAF.

The DECH30 package (Galazutdinov 2007) was used to measure line depths and RVs. Line depths of some metal lines in the atmospheres of cooler stars (F5–G0 V) were used to determine their effective temperatures. The syntetic spectra method was used for hotter stars. RVs were measured using metal (RV (met)) and hydrogen (H_α, H_β, H_γ,) absorption lines (see Table 2).

4. Radial velocities

Table 2 contains the dates of spectral observations, RV measurements from the TCO spectra, and RV data from other authors as well as from the Gaia DR2 and DR3 catalogs. As can be seen from the table, for more than six years of observations, more than two spectra

[1] http://www.shelyak.com

Table 1: Polaris field objects. Coordinates, proper motions, visual magnitudes and color indices.

Object	α (2000)	δ (2000)	μ_α (mas yr^{-1})	μ_δ (mas yr^{-1})	V (mag)	B-V (mag)	Spec Type
HD 5914⋆	01 33 50.71	+89 00 56.30	+64.873	-33.038	6.46	0.10	A3V
HD 10772⋆	02 03 34.87	+86 55 54.48	+49.208	-13.009	8.11	0.34	F5V
HD 11696⋆	02 34 32.66	+88 28 15.70	+52.918	-47.906	8.13	0.27	A3V
HD 14369⋆	03 40 54.04	+89 06 17.58	-51.778	-30.247	8.11	0.35	F0V
HD 14718⋆	03 17 32.24	+88 40 33.55	-158.016	+42.482	8.61	0.52	G0V
HD 16335	03 04 07.97	+87 01 33.89	-26.672	+18.044	7.84	0.36	F0V
HD 66368	09 21 48.47	+88 34 13.18	-6.429	+12.384	7.13	0.14	A0V
HD 90162 SB	10 49 13.59	+87 51 32.15	-23.671	-5.108	8.78	0.50	F8V
HD 163988	16 48 43.27	+88 09 22.44	-2.222	+12.015	8.11	0.47	F5V
HD 203317	20 47 59.82	+87 32 14.82	+30.650	+24.149	8.52	0.41	F2V
HD 209556⋆	21 36 02.50	+87 47 02.01	+24.927	+33.472	8.37	0.45	F5V
HD 224687	23 59 30.74	+86 42 23.05	+35.745	-1.381	6.74	0.06	A0V
HD 224991	00 02 27.83	+87 01 57.77	+18.454	+8.299	7.84	0.30	F0V
Polaris B VS	02 30 36.09	+89 15 39.20	+41.961	-13.562	8.20	0.57	F3V
BD +86°44	03 28 35.54	+87 23 40.90	-0.124	-3.805	9.14	0.50	F8V
BD +87°16⋆	02 48 59.14	+88 39 39.46	+47.850	-35.107	8.84	0.54	G0V
BD +87°26⋆	03 47 08.90	+87 53 48.25	+41.550	-44.376	8.81	0.48	G0V
BD +88°75⋆	12 37 42.37	+87 58 22.83	-56.249	+17.242	9.08	0.51	F5V

⋆ – High proper motion star (HPMS), SB – spectroscopic binary; VS – variable star (VS).

were obtained for seven stars, which makes it possible to verify the accuracy of the TCO results and compare them with the data from other authors. Noticeable differences between the data shown in Table 2 may indicate variability or binarity of the studied stars. The non-variable (within errors) RVs for HD 10772, HD 11696, HD 14369, HD 16335, HD 66368, HD 209556, HD 224687, BD+87°16, BD+87°26, BD+86°44 and BD+88°75 suggest that 61% of the studied objects are non-variable, single stars.

A significant scatter of the RV data for HD 90162 (over 40 km s^{-1}), which is marked as a spectroscopic binary in SIMBAD, confirms this status. This fact is supported by the apperance of an additional component in the red wing of the H_α line (see Fig. 1). A similar noticeable scatter (∼20 km s^{-1}) in the RV data is characteristic of HD 163988, which may also indicate its binarity. HD 14718 has an RV data scatter within 10 km s^{-1}. These two stars show an asymmetry on the red side of the H_α line core, which may be caused by the presence of a secondary component (Fig. 2).

Polaris B has noticeable differences between recent measurements and those obtained several decades ago. This is unlikely to be related to physical variability of the object, as indicated in SIMBAD, but most likely with its orbital motion. Judging from the minor differences in RVs and spectral types, HD 203317 and HD 224991 may be low-amplitude pulsating δ Sct type variables. Also, the difference between our and earlier RVs from that listed in the DR3 catalog for HD 5914 looks completely unexpected, ∼10 km s^{-1}. If the latter is not erroneous, then HD 5914 can also be suspected of pulsational variability.

Also, average RVs of all the stars, with the exception of HD 14718 and HD 90162, range from +8 to −30 km s^{-1}. This means that all but two of the 16 objects from our list may belong to the same general group. Attention should also be paid to the large RV differences determined from absorption lines of metals and hydrogen for HD 5914, HD 66368, HD 203317, HD 209556, and HD 224687.

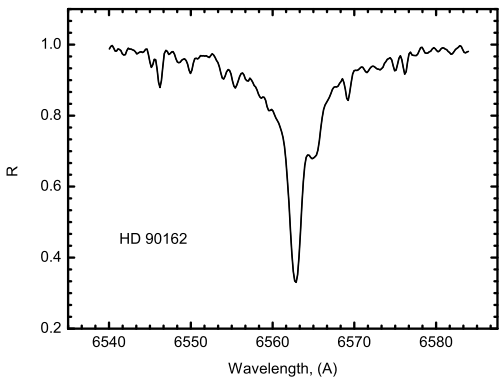

Figure 1: Fragment of the spectrum of HD 90162 in the H_α line region. Presence of the line core of the secondary component is noticeable in the red wing.

Table 2: Radial velocities of Polaris field stars

Object		<RV>						RV(Other authors)	
	HJD 2400000+	Metals	σ	NL	H_α	H_β	H_γ	<RV>	Source
HD 5914	58194.6932	-9.04	3.37	34	-4.17	-3.30	-0.42	-10.0	[b]
	58236.6245	-10.06	2.32	61	-4.09	-2.27	+0.25	-11.0	[c]
								-1.38	[l]
HD 10772	59080.7839	+8.27	2.38	81	+7.00	+6.56	-6.06	+7.83	[l]
	59185.6053	+6.07	2.47	105	+3.28	+3.57	+9.54		
HD 11696	59233.4995	+6.86	1.70	165	+7.69	+7.51	+7.39	+8.26	[j]
								+6.00	[l]
HD 14369	58214.5807	-8.48	2.14	157	-7.82	-6.38	-3.91	-6.56	[k]
	59186.6445	-6.16	1.77	160	-6.75	-6.25	-3.71	-6.76	[l]
	59267.5568	-6.66	2.18	275	-8.36	-5.70	-5.43		
HD 14718	60219.7693	-59.78	2.60	150	-63.40	-61.05	-59.61	-62.7	[f]
								-68.27	[k]
								-61.34	[l]
HD 16335	58182.6840	-27.07	3.02	363	-29.09	-28.79	-27.51	-24.27	[k]
	59225.4923	-27.79	2.78	205	-29.01	-27.14	-26.58	-24.68	[l]
	59267.5108	-27.72	3.02	221	-29.32	-26.31	-25.45		
HD 66368	58158.7237	-7.90	2.79	86	-4.40	-1.99	+8.95	-8.0	[a]
								-8.74	[i]
								-10.64	[l]
HD 90162	59621.7604	-69.18	4.11	150	-68.49	-67.08	-65.70	-23.0	[d]
								-24.97	[i]
								-41.90	[k]
HD 163988	57496.6113	+2.51	2.92	116	+6.21	+3.12	-1.59	-18.9	[b]
								-18.8	[f]
								-2.25	[k]
								-1.34	[l]
HD 203317	58972.7107	-7.64	2.06	30	-0.68	-8.73	-4.48	-7.81	[k]
								-12.35	[l]
HD 209556	58239.6102	-8.66	2.38	51	-13.53	-14.36	-3.40	-5.05	[k]
								-8.62	[l]
HD 224687	58125.5771	-16.34	2.10	30	-13.60	-8.39	-5.55	-17.3	[a]
	59193.5733	-17.42	1.38	47	-14.28	-15.84	-17.21	-18.3	[e]
	59198.5582	-16.98	1.65	54	-11.74	-14.84	-12.86	-17.3	[b]
HD 224991	58240.5511	-3.15	4.30	193	+0.58	+3.76	-1.22	+5.99	[k]
								+4.15	[l]
Polaris B	59248.5809	-19.22	3.39	79	-20.58	-21.96	-20.92	-8.0	[a]
	59255.5298	-19.21	2.60	138	-17.86	-20.96	-24.07	-13.0	[b]
								-18.90	[h]
								-22.25	[k]
BD+86 44	59529.6603	-18.09	2.56	171	-19.77	-19.32	-13.32	-18.60	[k]
	59531.6872	-19.04	2.74	178	-17.70	-20.00	-13.57	-19.11	[l]
BD+87 16	59527.6368	-8.27	1.31	187	-7.54	-8.26	-8.20	-8.38	[l]
BD+87 26	59523.7156	-4.48	2.18	217	-3.58	-6.49	-3.77	-4.10	[k]
								-4.45	[l]
BD+88 75	59622.7052	-9.48	1.74	214	-8.79	-9.88	-9.25	-9.40	[k]
								-10.40	[l]

a – Wilson (1953), b – Gontcharov (2006), c –Young (1939), d – Wilson & Joy (1950), e – Plaskett et al. (1921), f – Nordstroem et al.(2004), g – Pourbaix et al. (2004), h – Usenko & Klochkova (2007), i – 6 m SAO RAS: HJD 2455141.1960, j – 6 m SAO RAS: HJD 2455141.2975, k – Gaia DR2 Catalogue (2018), l – Gaia DR3 Catalogue (2022).

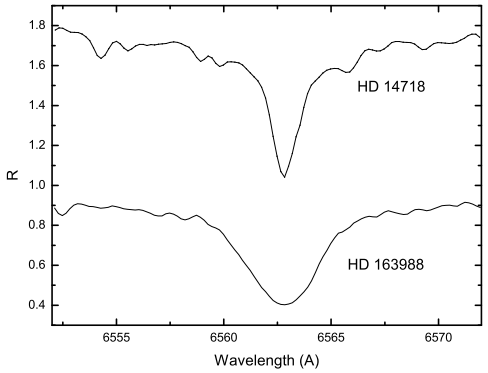

Figure 2: Parts of the spectra of HD 14718 and HD 163988 in the H_α line region.

5. Effective temperatures, reddenings, distances, and radii

All the objects we study are A - G main sequence stars, therefore, one can determine their luminosities from their effective temperatures. Because $T_{\rm eff}$ estimates are independent of the star's reddening, obtaining its spectroscopic estimate through the luminosity and radius allows determining the distance to the object. Conversely, from knowing the star's $T_{\rm eff}$ and distance one can determine its radius and compare it with that calculated from a calibration relationship. Since MS stars having these spectral types, the scatter in estimates of their radii is insignificant. Comparing the obtained estimates of the radius from a calibration, one can estimate the accuracy of the distance measurements. Nowadays we have a database of distances, as well as that of effective temperatures, gravities and reddenings from Gaia DR3, which gives us a convenient opportunity to compare our spectroscopic estimates of $T_{\rm eff}$ with the respective Gaia data and check out the accuracy of distances from this catalog.

Table 3 presents the results of the $T_{\rm eff}$ estimates obtained from our spectroscopy (as described above). Estimates of $\log g$ were determined either by balance of the Fe I and Fe II abundances or by using synthetic spectra. For two stars, $T_{\rm eff}$ were determined from Strömgren photometry. As can be seen from tables, the largest differences between the $T_{\rm eff}$ estimates (from 300 to 600 K) are more noticeable in hotter A–type stars. In latter spectral types, these differences decrease and do not not exceed 170 K. Estimates of $\log g$ are quite close and typical for MS stars. This means that all the objects we study are luminosity type V stars, for which there are calibration relationships that connect $T_{\rm eff}$ with spectral types, colors indices, absolute magnitudes and radii. In our previous study (Usenko et al. 2018) we used calibrations by Pecaut & Mamajek (2013), while in this paper we use improved ones from Mamajek (2022)[2] and Turner (2023)[3].

Table 3: Effective temperatures and gravities of Polaris field stars.

Star	Our results		Gaia DR3	
	$T_{\rm eff}$, K	$\log g$	$T_{\rm eff}$, K	$\log g$
HD 5914	8800 (2)	4.00	8383	-
HD 10772	6900 (2)	4.00	6908	3.7925
HD 11696	7614 (3)	-	7514	3.9808
HD 14369	6721 (3)	-	6621	4.1525
HD 14718	5971 (3)	-	5930	3.8451
HD 16335	7220 (2)	4.00	6772	3.8301
HD 66368	9700 (2)	3.80	10310	3.9897
HD 90162	6175 (1)	3.90	6267	3.8558
HD 163988	6369 (1)	3.50	6509	3.3543
HD 203317	6650 (2)	4.00	6664	3.9941
HD 209556	6301 (1)	4.00	6334	4.1895
HD 224687	9700 (2)	3.80	10055	3.7103
HD 224991	7220 (2)	4.00	7173	3.9197
Polaris B	6900 (2)	4.30	6851	4.1529
BD +86°44	6179 (1)	3.50	6351	3.6227
BD +87°16	6095 (1)	4.20	6076	4.2384
BD +87°26	6169 (1)	3.80	6277	4.1664
BD +88°75	6169 (1)	4.00	6236	4.2091

1 – Lines depths of metal lines, [2] – synthetic spectra, [3] - Strömgren photometry

First, we decided to check how different are the stars' radii calculated from our $T_{\rm eff}$ estimates and those from Gaia DR3, if we assume that the distances and reddenings from DR3 are reliable. The results of our calculations are shown in Table 4. The results shoe that according to DR3 all the objects are located within the distance range from 80 to 290 pc and that their reddenings are insignificant, with the exception of HD 66368, HD 163988, and HD 224687. The differences in the radius estimates do not exceed 0.05 $R_\odot$ for the difference in $T_{\rm eff}$ of 100 K. However, they reach 0.2 - 0.5 $R_\odot$ for the $T_{\rm eff}$ differences from 300 to 500 K.

What is more noticeable is that for the stars located at distances greater than 140 pc, the radii may exceed the estimates typical for MS stars of a given spectral class by a factor of 2–3. From this fact we conclude that the DR3 distances for these stars are erroneous. A similar fact was noted in our previous study (Usenko et al. 2018). To check the accuracy of these distances, we decided to link the estimates of $T_{\rm eff}$ and A_0 from DR3 to their corresponding calibrations from Mamajeck (2023) and Turner (2023). The calculation results are shown in Table 5.

What one should pay attention to in this table:

1. According to the calibrations, for the majority of

[2] http://www.pas.rochester.edu/∼emamajek/EEM_dwarf_UBVIJHK_colors_Teff.txt

[3] http://ap.smu.ca/∼turner/A5500.html

Table 4: Absolute magnitudes and radii of Polaris field stars using our and Gaia DR3 $T_{\rm eff}$, distances, and reddenings.

	V	A_0	d	M_V	Our data		DR3	
Star	(mag)	(mag)	(pc)	(mag)	$T_{\rm eff}$, K	R($R_\odot$)	$T_{\rm eff}$, K	R($R_\odot$)
HD 5914	6.46	0.0	101.7±0.3	1.42±0.01	8800	2.02±0.02	8383	2.22±0.03
HD 10772	8.11	0.0012	107.1±0.6	2.96±0.01	6900	1.63±0.01	6908	1.62±0.01
HD 11696	8.15	0.0003	163.1±1.1	2.09±0.02	7614	1.98±0.02	7514	2.03±0.02
HD 14369	8.10	0.0166	91.7±0.4	3.27±0.01	6721	1.48±0.01	6621	1.52±0.02
HD 14718	8.61	0.0303	102.8±1.6	3.52±0.03	5971	1.67±0.02	5930	1.69±0.02
HD 16335	7.84	0.0075	140.9±1.5	2.09±0.02	7220	1.98±0.02	6772	2.50±0.03
HD 66368	7.10	0.5474	142.3±1.7	0.79±0.03	9700	2.22±0.02	10310	1.96±0.02
HD 90162	8.78	0.0008	194.3±0.5	2.34±0.01	6175	2.68±0.03	6267	2.59±0.04
HD 163988	8.12	0.1522	275.8±2.5	0.77±0.02	6369	5.20±0.06	6509	4.98±0.05
HD 203317	8.52	0.0009	149.3±0.4	2.65±0.01	6650	2.01±0.02	6664	2.00±0.02
HD 209556	8.37	0.0014	87.2±0.2	3.67±0.01	6301	1.40±0.01	6334	1.38±0.02
HD 224687	6.75	0.2893	212.5±2.5	-0.18±0.02	9700	3.47±0.04	10055	3.23±0.04
HD 224991	7.84	0.0184	145.2±0.4	2.01±0.01	7220	2.27±0.03	7173	2.30±0.03
Polaris B	8.60	0.0005	137.2±0.6	2.91±0.01	6900	1.65±0.01	6851	1.67±0.02
BD +86°44	9.14	0.0463	283.5±0.9	1.83±0.01	6179	3.40±0.04	6351	3.22±0.04
BD +87°16	8.84	0.0027	92.4±0.1	4.01±0.01	6095	1.27±0.02	6076	1.28±0.02
BD +87°26	8.81	0.0010	108.4±0.2	3.63±0.01	6169	1.49±0.02	6277	1.49±0.03
BD +88°75	9.08	0.0006	116.2±0.2	3.75±0.01	6169	1.41±0.02	6236	1.38±0.01

the objects, the spectral types determined from the DR3 $T_{\rm eff}$ data are earlier than those given in SIMBAD (see Table 1), or coincide with them. Exceptions are HD 11696, HD 14369, HD 16335, and BD +88°75.

2. Distance estimates to stars derived from the spectral types based on the calibrations, nearly or virtually coincide with the DR3 estimates only for HD 10772, HD 14369, HD 209556, Polaris B, BD +87°16, and BD +87°26. The differences are within 20–30 pc for HD 5914, HD 11696, and HD 66368, while this difference ranges from 40 to 170 pc for the rest of the sample (HD 14718, HD 16335, HD 90162, HD 163988, HD 203317, HD 224687, HD 224991, and BD +86°44) that constitutes half of it.

3. Based on the radii calculated from the $T_{\rm eff}$ and A_0 taken from DR3 and distances from Table 5, one can conclude that the differences between the radii derived from Mamajek and Turner are in the range of 0.05–0.2 $R_\odot$ with the exception of HD 66368 and HD 224687, where this difference exceeds 1 $R_\odot$. If we compare the radii calculated using calibrations with those determined from the DR3 distances, it is clear that only 8 stars coincide within 0.3 $R_\odot$. The rest (HD 5914, HD 14718, HD 16335, HD 66368, HD 90162, HD 163988, HD 203317, HD 224687, HD 224991, and BD +86°44) show the differences from 0.5 to 2.9 $R_\odot$.

Thus, it turns out that for 10 stars out of 18, the radii determined from the distances, $T_{\rm eff}$ and reddenings taken from the DR3 catalog differ significantly from the average values ederived for the corresponding spectral types of the luminosity type V. This means that the DR3 distances for more than half (56%) of the sample are erroneous and need refinement.

Figure 3 shows the relationships of (O-C) in distances - Gaia DR3 distances for two different calibrations from Table 5. There calculated distances (C) were derived using data from Mamajek (2013) and Turner (2023), while the observed (O) values come from the Gaia DR3 catalog. As can be seen from Figure 3, both dependences are close to one another and have an exponential character that indicates that the errors in the distance determination to the target stars increase with increasing DR3 distances, which are larger than 130 pc. This fact means that the Gaia DR3 distances are unreliable.

Therefore, we decided to verify the distances to the stars using photometric data. To do that, we used color-indices (B-V), and thanks to the refined spectral types, intrinsic color indices, color-excesses, and reddenings, the absolute magnitudes for the ZAMS were determined. The latter allowed us to determine the distances. These data are presented in Table 6.

As can be seen from Table 6, the obtained reddening estimates for individual stars differ significantly from those shown in DR3. As for the distance estimates, they are closer to those obtained from the Turner (2023) calibrations. It can be seen that most stars are located in the distance range 70–110 pc and

Table 5: Comparison of absolute magnitudes, distances, spectral types, and radii of the Polaris field stars according to the Gaia DR3 data that is converted from the Mamajek (2022) and Turner (2023) relations.

Star			DR3	Mamajek		Turner			DR3	Mamajek		Turner	
	V	M_V	d	M_V	d	M_V	d	$T_{\rm eff}$	R	SpT	R	Sp	R
	(mag)	(mag)	(pc)	(mag)	(pc)	(mag)	(pc)	K	($R_\odot$)		($R_\odot$)		($R_\odot$)
HD 5914	6.46	1.42	101.7	1.85	83.6	1.99	78.3	8383	2.22	A4V	1.819	A3V	1.71
HD 10772	8.11	2.96	107.1	2.88	111.1	2.98	106.1	6908	1.62	F1V	1.647	F0V	1.60
HD 11696	8.15	2.09	163.3	2.36	143.9	2.47	136.8	7514	2.03	A8V	1.747	A7V	1.71
HD 14369	8.10	3.28	91.2	3.27	91.8	3.40	86.4	6621	1.52	F4V	1.508	F3V	1.37
HD 14718	8.61	3.35	111.0	4.48	66.1	4.76	58.1	5930	1.83	G0V	1.100	F9V	0.95
HD 16335	7.84	2.09	140.9	3.05	90.5	3.15	86.4	6772	2.50	F2V	1.591	F1V	1.54
HD 66368	7.10	0.77	143.4	0.65	151.7	1.37	108.9	10310	1.99	B9V	2.417	B9.5V	1.42
HD 90162	8.78	2.35	193.5	3.83	97.7	4.11	85.9	6267	2.59	F7V	1.312	F7V	1.15
HD 163988	8.12	0.80	271.1	3.44	80.5	3.62	74.1	6509	4.91	F5V	1.449	F5V	1.34
HD 203317	8.52	2.65	149.3	3.21	115.3	3.32	109.6	6664	2.00	F4V	1.529	F2V	1.47
HD 209556	8.37	3.64	88.1	3.71	85.5	3.99	75.1	6334	1.42	F6V	1.353	F7V	1.19
HD 224687	6.75	-0.17	212.0	0.79	136.1	1.46	100.5	10055	3.23	B9V	2.325	B9.5V	1.48
HD 224991	7.84	2.01	145.2	2.61	110.2	2.70	105.8	7173	2.30	F0V	1.717	A8V	1.69
Polaris B	8.60	2.92	136.7	2.94	135.5	3.05	128.8	6851	1.71	F2V	1.630	F0V	1.58
BD +86°44	9.14	1.87	278.3	3.69	120.5	3.88	110.3	6351	3.15	F6V	1.359	F6V	1.25
BD +87°16	8.84	4.01	92.2	4.21	84.3	4.48	74.4	6076	1.28	F9V	1.178	F8V	1.04
BD +87°26	8.81	3.64	108.1	3.77	101.9	4.09	87.9	6277	1.43	F7V	1.333	F7V	1.14
BD +88°75	9.08	3.76	115.9	3.91	108.1	4.18	95.5	6236	1.36	F7V	1.279	F7V	1.13

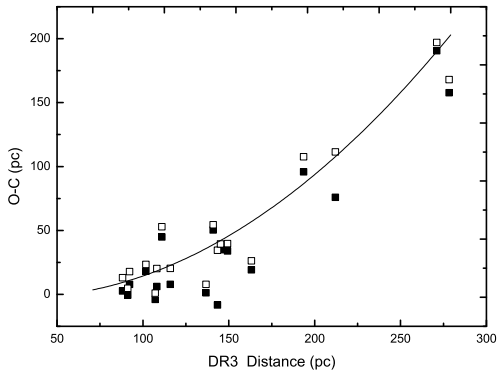

Figure 3: Gaia DR3 distances - (O-C) distances relationship for the Polaris field stars. Filled squares show calculations using Mamajek (2022) calibration, open squares show calculations using that of Turner (2023).

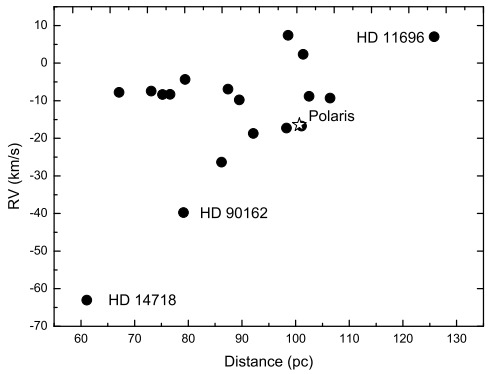

Figure 4: Photometric distance versus RV relationship for the Polaris field stars. Polaris is marked with an open five-point star.

only HD 14718 and HD 11696 fall out of this interval. If we look at the dependence of the average stars' RVs versus these distances, one can see that most stars form the group in a given distance interval with RVs from +7.4 to −26.3 $\mathrm{km\,s^{-1}}$. This can be seen in Figure 4. One obvious (HD 90162) and one probable (HD 14718) drop out of the spectroscopic binaries group, and the star with the greatest reddening, HD 11696, is much further away.

It should be noted that with Polaris' $E_{B-V} = 0.^m02$, $A_V = 0.^m056$, the distance is 100.7 pc. Also, SIMBAD does not contain data on the distances from Gaia DR2 and DR3. This is probably due to difficulties in measuring parallaxes for bright stars.

6. Summary

1. According to the RV values, 15 target stars belong to the same moving group.

2. Two objects, HD 14718 and HD 90162, judging by their RVs, probably belong to the thick disk, while HD 11696 belongs to another group of the Polaris field stars.

3. Judging from the spectra, HD 90162 is indeed a spectroscopic binary, while HD 14718 and HD 163988 are possible binaries.

4. 61% of the studied objects are non-variable stars, and three objects (HD 5914, HD 203317 and HD 224991) can be low-amplitude pulsating variables of the δ Sct type. It is still unclear whether Polaris B is a pulsating variable, as indicated in SIMBAD.

Table 6: Color-excesses, reddenings, absolute magnitudes, and distances for the Polaris field stars.

Star	V (mag)	B-V (mag)	E_{B-V} (mag)	V_0 (mag)	A_V (mag)	M_V (mag)	V_0-M_V (mag)	d (pc)
HD 5914	6.46	0.107	0.017	6.412	0.048	1.99	4.422	76.6
HD 10772	8.11	0.342	0.000	8.110	0.000	3.14	4.970	98.6
HD 11696	8.15	0.270	0.540	6.628	1.522	1.99	5.498	125.8
HD 14369	8.10	0.413	0.058	7.938	0.162	3.23	4.708	87.4
HD 14718	8.61	0.516	0.000	8.610	0.000	4.68	3.930	61.1
HD 16335	7.84	0.379	0.069	7.657	0.183	2.98	4.677	86.2
HD 66368	7.10	0.174	0.174	6.613	0.487	1.56	5.053	102.5
HD 90162	8.78	0.504	0.000	8.780	0.000	4.29	4.490	79.1
HD 163988	8.12	0.475	0.020	8.064	0.056	3.93	4.134	67.1
HD 203317	8.52	0.405	0.045	8.394	0.126	3.26	5.134	106.4
HD 209556	8.37	0.468	0.000	8.370	0.000	4.05	4.320	73.1
HD 224687	6.75	0.081	0.081	6.523	0.227	1.56	4.963	98.3
HD 224991	7.84	0.282	0.000	7.840	0.000	2.82	5.030	101.4
Polaris B	8.60	0.390	0.020	8.544	0.056	3.52	5.024	101.1
BD +86°44	9.14	0.495	0.000	9.140	0.000	4.32	4.820	92.1
BD +87°16	8.84	0.540	0.003	8.832	0.008	4.45	4.382	75.2
BD +87°26	8.81	0.480	0.000	8.810	0.000	4.31	4.500	79.4
BD +88°75	9.08	0.505	0.000	9.080	0.000	4.32	4.760	89.5

5. Our estimates of the effective temperatures obtained using spectroscopy or photometry showed their approximate similarity with the estimates from the DR3 catalog for stars of the spectral classes F–G, while for hotter A–type stars the difference is 300–500 K.

6. Estimates of the stellar radii calculated using $T_{\rm eff}$ values, reddenings and distances from DR3 catalog for half of the stars turned out to be overestimated and inconsistent with their spectral types.

7. Recalculations of the radii and distances for the stars using our $T_{\rm eff}$ estimates and "Spectral type – Luminosity"' calibrations for MS stars also confirmed that for half of the stars the DR3 distance estimates are unreliable.

8. The largest discrepancies in the distance estimates between the DR3 data and the calibrations are found for distances lrger than 130 pc and have an exponential character.

9. Judging from the derived RV estimates and photometric distances, 15 target stars probably still belong to the old open cluster dissolved among the stars of the Polaris field and located at distances of ∼70–110 pc.

10. The distance estimates from the DR3 catalog are extremely unreliable and should be carefully revised.

Acknowledgements. This work has made use of the SIMBAD database, operated at CDS, Strasbourg, France, and data from the European Space Agency (ESA) mission *Gaia* (https://www.cosmos.esa.int/gaia), processed by the *Gaia* Data Processing and Analysis Consortium (DPAC, https://www.cosmos.esa.int/web/gaia/dpac/consortium). Funding for the DPAC has been provided by national institutions, in particular the institutions participating in the *Gaia* Multilateral Agreement.

References

Gaia Collboration et al.: 2018, *A&A*, **616**, A1 (DR2).
Gaia Collaboration et al.: 2023, *A&A*, **674**, A1 (DR3).
Galazutdinov G.A.: 2007, *http://gazinur.com/DECH-software.html*
Gontcharov G.A.: 2006, *Astr.Lett.*, **32**, 759.
Nordström B., Mayor M., Andersen J. et al.: 2004, *A&A*, **418**, 989.
Pecaut M.J., Mamajek E.E.: 2013, *ApJS*, **208**, 9.
Plaskett J.S., Harper W.E., Young R.K., Plaskett H.H.: 1921, *Publ. DAO*, **2**, 1.
Pourbaix D. et al.: 2004, *A&A*, **424**, 727.
Turner D.G., Savoy J., Derrah J., Abdel-Sabour Abdel-Latif M., Berdnikov L.N.: 2005, *PASP*, **117**, 207.
Turner D.G.: 2009, *AIPC*, **1170**, 59.
Usenko I.A., Klochkova V.G.: 2008, *MNRAS*, **387**, L1.
Usenko I.A., Miroshnichenko A.S., Danford S., Kovtyukh V.V., Turner D.G. et al.: 2018, *Odessa Astron. Publ.*, **31**, 113.
Wilson R.E.: 1953, *Gen. Cat. of Stellar Rad. Vel. (GCSRV).*
Wilson R.E., Joy, A.: 1950, *ApJ*, **111**, 221.
Young R.K.: 1939, *Publ. DDO*, **1**, 71.

https://doi.org/10.18524/1810-4215.2023.36.290929

DETERMINATION OF THE TEMPERATURES OF THE CENTRAL STARS OF SELECTED PLANETARY NEBULAE

A.H.Alili, K.I.Alisheva, Kh.M.Mikailov

Baku State University, Baku, Azerbaijan
kamalaalisheva@bsu.edu.az

ABSTRACT. In this work, for planetary nebulae İC 1295, İC 4191, Zanstra temperatures were calculated using the H_β line of the central stars. Respectively, the temperatures 64252 K and 47663 K were determined. The flux in the H_β radiative line used in the calculations, has been determined from the spectra retrieved from the archive of the European Southern Observatory. Our results have been compared with results of the other authors.

Keywords: planetary nebulae, central stars, temperature.

АНОТАЦІЯ. В даній роботі ми дослідили дві планетарні туманості IC 1295 і IC 4191б та визначили температури середовища за допомогою метода Занстра. Лінія Hbeta, яка належить центральним зорям цих туманостей, була використана для цієї цілі. Метод Занстра може бути застосований тільки у разі, коли середовище туманості є оптично товстим в лайманівському континуумі. Всі атоми Гідрогену вважаються такими, що перебувають в незбудженому стані. Температура зорі може бути визначена шляхом порівняння числа квантів до числа квантів, що випромінюютьс у видимій частині спектра. Ми визначили ефективні температури центральних зір туманстей, як 64252 К та 47663 К.

Ключові слова: планетарні туманності, центральні зорі, температура.

1. Introduction

Planetary nebulae (PN) are an advanced stage of the stellar evolution of the low and intermediate mass stars. Central stars of PN (CSPN) are difficult to study because of their faintness in the visible spectral region and contamination of their spectra by the nebular emission. CSPN undergo considerable changes in temperature over their short lifetimes. Therefore, the temperatures of the central stars of planetary nebulae are considered an important quantity that directly characterizes their evolution. The Zanstra method is the most widely used method of the temperature determination methods. The Zanstra method can be applied for determining the temperature of CSPN if two quantities are known: first, the flux in the stellar continuum (or the stellar magnitudes); second, the amount of ionizing photons ($\lambda < 912$Å), as deduced from the total nebular flux at H_β. The ratio of the stellar to nebula fluxes at H_β is equivalent to the temperature of a blackbody between the UV and the visual range, if the nebula is optically thick regarding to the hydrogen ionizing radiations. Considering these two points, in this work for planetary nebulae IC 1295 and IC 4191 the H_β flux was used to determine temperatures of the central stars. For this we used Zanstra method. We discuss our results and compare our values to the temperatures obtained by other authors (Montez et al., 2015; Phillips, 2003) using different methods.

2. Determination of the Zanstra temperature

The Zanstra method can only be applied to nebulae that are optically thick in L_c. At this time, it is assumed that the star radiates as a black body. All neutral hydrogen atoms are assumed to be in unexcited condition (Kostyakova, 1982). Thus, each L_c quantum emitted by the nucleus in the Lyman series limit of hydrogen being swallowed up in the nebula, produces one L_α quantum and one Balmer series quantum. In optically thick nebulae all L_c quanta radiated by the star absorbed by the nebula. In a unit time interval, the number of Balmer quanta emitted by the nebula determines the number of quanta emitted by the star in the ultraviolet region. The temperature of the star can be determined by comparing the number of quanta with number of quanta emitted in the visible region of the spectrum (Pottasch, 1987). If we assume that a star with radius R_s and temperature T radiates as a black body, one can define the luminosity within frequency interval:

$$L_\nu = 4\pi^2 R_S^2 B_\nu(T) \ . \qquad (1)$$

Here, B_ν is the Planck function. Thus,

$$L = \int_0^\infty L_\nu d\nu = \frac{8\pi^6 k^4}{15h^3c^2} R_S^2 T^4. \qquad (2)$$

$\nu \geq \nu_I$, the number of stellar quanta will be:

Table 1:

PN	W (Å)	$F(H_c)$ $\times 10^{-13}$	$F(H_\beta)$ $\times 10^{-11}$	$F(H_\beta)$ $/F_\lambda$	V	E(B-V)	$F(H_\beta)$ $\times 10^{-11}$	Referens
İC 1295	474	0.166	0.39	6586	16.82	0.32		5,8,9
IC 4191	500	3.3	16.5	2471	11.61	0.48	1.02	5,6,8,9

H_β in units $erg \cdot cm^{-2}s^{-1}$.

$$Q_i = \int_{\nu_i}^{\infty} (L_\nu / h\nu)\, d\nu = \frac{8\pi^2 R_s^2}{c^2}\left(\frac{kT}{h}\right)^3 G_i(T) \qquad (3)$$

Here,

$$G_i(T) = \int_{h\nu_i/kT}^{\infty} x^2 (e^x - 1)^{-1}\, dx \quad . \qquad (4)$$

$$\int_{x_0}^{\infty} \frac{x^2 dx}{e^{x_i} - 1} = \sum_{n=0}^{\infty} \int_{x_0}^{\infty} e^{-(n+1)x} x^2 dx$$

By subtracting R_s from formulas (2) and (3) we obtain:

$$Q_i = \frac{15 G_i(T) L}{\pi^4 kT} \qquad (5)$$

When the nebula is optically thick in the Layman's continuum, the star's hydrogen-ionizing quanta will be absorbed by the nebula. The observed $F(H_\beta)$ radiation flux of the nebula will be as follows:

$$4\pi d^2 F(H_\beta) = h\nu(H_\beta) \int n_e\, n(H^+) \alpha(H_\beta) dv \ [erg/s] \qquad (6)$$

Here, the frequency of the $\nu(H_\beta)$- H_β line is the effective recombination coefficient related to the generation of $\alpha(H_\beta)$- H_β quanta. Considering the $(L_\nu = 4\pi d^2 F_\nu)$, (5) and (6) in L/L_0 expression (L_0 is the luminosity of the Sun) of luminosity in terms of the star's radiation flux F_ν, we get the following expression:

$$\frac{F(H_\beta)}{F_\nu} = \frac{15 h\nu(H_\beta)}{4\pi^6 k} \frac{L_0 \alpha(H_\beta) T^3 G_1(T)}{R_0^2 T_0^4 \alpha_B B_\nu} \qquad (7)$$

It is convenient to use the visual region of the spectrum to solve this equation. It can be neglected because the ratio very weakly depends on T_e-, and for calculation one can use $T_e = 10^4 K$. Instead of $F_\nu [erg \cdot cm^{-2}s^{-1}Hz^{-1}]$ it is useful to express $F(H_\beta)$ is $[erg \cdot cm^{-2}s^{-1}]$, $F_{\lambda(vis)} - m_v$, the radiation flux in the visible region of the spectrum is determined by the size of the visible star:

$$F_\lambda = 3.68 \cdot 10^{-9} \cdot 10^{-m_v/2,5} \quad \left[erg/\left(cm^2 \cdot s \cdot Å\right)\right]. \qquad (8)$$

After taking this into account, an expression (7) takes the following form:

$$\frac{F(H_\beta)}{F_\lambda} = 3.95 \cdot 10^{-11} T^3 G_i(T) \ \left[e^{26650/T} - 1\right] [Å]. \qquad (9)$$

Temperatures along the HI line of the central stars of planetary nebulae İC 1295 and İC 4191 were calculated from the last equation. In calculations $F_{\lambda(vis)}$ vs $F(H_\beta)$, an absorption in the interstellar medium was taken into account. İC 1295 and İC 4191 spectra of planetary nebulae gained in 2016, were retrieved from the European Southern Observatory's archive and processed using the DECH30 program (Galazutdinov, 1992). Obtained results are given in the Table 1. In the 3rd column of the Table1, the flux in the continuum is given, and in the 8th column the flux obtained by other authors is shown.

In the 2nd column of the Table 2, Zanstra temperature calculated by us using the line HI is given, while in the 3d column of the Table 2 Zanstra temperature calculated using the line HeII by other authors is given.

Table 2:

PN	T_z(HI)	T_z(HeII)	Reference
İC 1295	64252	98000	1
IC 4191	47663	107200	2

3. Conclusion

Obtained results on $F(H_\beta)/F_\lambda$ ratio as a function of the star's effective temperature exactly coincides with the known graphic dependence from literature. It is also consistent with the results obtained from the atmosphere model provided by Hammer and Mihalas (He/H=0.16) (Phillips, 2003). This shows the accuracy of the spectrum processing results. Since Zanstra method assumes that the nebula is optically thick in the Lyman continuum, and since PN change from optically thick to optically thin in H and He at different times, this can lead to the different estimates of the central star temperature by using either H or He lines. The fact that stellar atmosphere are not well approximated by the blackbody can also contribute to an errors in the Zanstra temperatures (Kwok, 2000).

References

Frew David J., Parker Q.A. and Bojici I.S.: 2016, *MNRAS*, **455**, 1459, doi:10.1093/mnras/stv1516.

http://archive.eso.org/cms.html

Galazutdinov G.: http://www.gazinur.com/DECH software.html

Gleizes F., Acker A. and Stenholm B.: 1989, *A&A*, **222**, 237.

Kostyakova E.B.: 1982, Physics of planetary nebulae, Moscow: "Nauka", 128 p. (in Russian).

Kwok Sun: 2000, The Origin and Evolution of Planetary Nebulae, Cambridge Astrophysics series, p. 243 DOI: https://doi.org/10.1017/CBO9780511529504

Montez R.Jr., Kastner J.H., Balick B. et al.: 2015, *ApJ*, 800:8 (19pp), doi:10.1088/0004-637X/800/1/8.

Phillips J.P.: 2003, *MNRAS*, **344**, 501.

Pottasch S.: 1987, Planetary nebulae, Moscow: "Mir", 351 p. (in Russian).

Pottasch S.R., Beintema D.A. and Feibelman W.A.: 2005, *A&A*, **436**, 953, DOI: 10.1051/0004-6361:20042627.

SIMBAD Astronomical Database – CDS (Strasbourg) (u-strasbg.fr).

SOLAR SYSTEM AND SPACE ENVIRONMENT

https://doi.org/10.18524/1810-4215.2023.36.290220

LIGHT CURVE ANALYSIS OF SIX MAIN BELT ASTEROIDS WITH EARTH MOID LESS THAN 1AU

I.Eglitis [1], K.Nagainis [1], A.Sokolova [1], G.Campbell [2]

[1] Institute of Astronomy, University of Latvia, Raina blvd, 19, Riga, LV 1586, Latvia, *ilgmars.eglitis@lu.lv-mail*

[2] Physica and Astronomy, Brigham Young University, Provo, USA, *ghcampbell25@gmail.com*

ABSTRACT. Six main belt asteroids 1999 HK1 (11411), 1995 AM1 (30968), 1999 XC136 (53454), 1999 JN6 (70055), 1999 UQ9 (86280), 2000 SU2 (93041) with Earth MOID less than 1AU were studied at the Baldone Astrophysical Observatory of the Institute of Astronomy of the University of Latvia in the time span range 2020-2022. The obtained light curve data together with published Minor Planet Center data in the time range 1999-2022 were analyzed with Fourier series, Lomb-Scargle periodogram, and Phase dispersion minimization methods. A plan of analysis step by step is given. The results computed from different observatories' data are compared and mean-weighted periods are obtained. The rotation periods are for asteroids: N11411 P=6.544 h, N30968 P=8.330 h, N53454 P=4.615 h, N70055 P=74.364 h, N86280 P=1.315 or 6.658 h and N93041 P=30.645 h.

Keywords: Main belt asteroids, light curve, rotation period.

АНОТАЦІЯ. Шість астероїдів головного поясу 1999 HK1 (11411), 1995 AM1 (30968), 1999 XC136 (53454), 1999 JN6 (70055), 1999 UQ9 (86280), 2000 SU2 (93041) з MOID Землі менше 1 а.о. досліджувалися в астрофізичній обсерваторії Балдоне Інституту Астрономії Латвійського університету в часовому діапазоні 2020-2022. Отримані дані кривої блиску разом з опублікованими даними Центру малих планет у часовому діапазоні 1999-2022 рр. були проаналізовані за допомогою рядів Фур'є, періодограми Ломба-Скаргла та методів мінімізації фазової дисперсії. Подано покроковий план аналізу. Результати, обчислені за даними різних обсерваторій, порівнюються та отримуються середньозважені періоди. Періоди обертання становлять для астероїдів: N11411 P=6,544 години, N30968 P=8,330 години, N53454 P=4,615 години, N70055 P=74,364 години, N86280 P=1,315 або 6,658 години і N93041 P=30,645 години. Метод рядів Фур'є дає придатні для використання результати аналізу довгих серій спостережень у декілька наступних ночей, коли період обертання не перевищує 7-10 годин. У випадках невеликих серій спостережень, розкиданих протягом великого періоду часу, з різною яскравістю в різних опозиціях, методи L-S і PDM працюють більш надійно. Метод PDM чутливий до невеликої кількості спостережень. Якщо кількість спостережень менше сотні, метод PDM здебільшого не працює. Показана методологія дозволяє аналізувати дані, точність яскравості яких становить один десятковий знак.

Ключові слова: астероїди головного поясу, крива блиску, період обертання.

1. Introduction

The investigation of asteroid properties is important for the development of the evolution theory of the Solar system and the classification of small Solar system objects. Because some of these objects can collide with the Earth, asteroids are also important for having significantly modified the Earth's biosphere. Significantly in the past, but now, every five years Chelyabinsk amount events take part as seen from the observed bolids radar compilation [NASA, 2013]. Asteroids' impact can trigger the creation of life, especially with the delivery of heavy elements to the Earth's surface. It is a crucial moment for the birth and evolution of complex life [Castillo, Vance 2008] and [Houtkooper, 2011] because the carbon-based molecules and some heavy elements serve as the building blocks of life. Asteroid studies will allow us to answer the ambiguous question about the origins of life on Earth. On the other hand, the next step in the human exploration of space will be highly dependent on extracting materials (primarily water and minerals) from the asteroids. It is highly probable that the success and viability of human expansion into space will depend on the ability to exploit space resources. Therefore, a detailed physical and compositional assessment of the population will be required during the next decade before human missions are sent to these objects.

The photometric study of light curves can obtain additional information about size, rotation period, the structure of objects, and the existence of craters and ice fields on the surface, which is very important data for space missions. Asteroids shine due to the Sun's light reflecting on their surface and depend on surface albedo (from surface characteristics: chemical composition; regoliths which cover the object). If an asteroid is not spherical its brightness might vary due to the following factors: the asteroid's

distance to the observer and to the Sun is changing; the asteroid's phase. All of the above plus the shape of the asteroid and its periodic rotation, as well as the precession of the axis of rotation, determines its brightness too. All previous aspects, show the importance and complexity of light curve studies.

2. Data set for analysis

At the Baldone Astrophysical Observatory (IAU Code 069) astronomers operate with a Schmidt-type 1.2-meter telescope installed with two STX-16803 CCDs.The brightness limit in the visual range of the telescope without a filter is 22 magnitude at night with good transparency and calm images. CCD parameters are quantum effectivity of about 80 percent, the size of one pixel is 9*9 microns, and linear size 4096*4096 pixels, which corresponds to 53*53 arcmin of the field of view. In the three last years, the observation has been devoted to the studying dynamics of main belt asteroids in the G(RP) passband, especially those of which the Earth MOID is less than 1 AU. Observations also managed to use nights with a small phase of the Moon. The list of observable asteroids was compiled using the Minor Planet Center NEO checker [MPC, 2023] and MPC light curve database [ALCDEF, 2023]. A sample of studied main belt asteroids with Earth MOID less than 1 AU, with a brightness greater than 18 magnitudes without period data are given in Table 1.

Table 1: list of studied asteroids

Asteroid	Design.	Earth MOID	Sun, P (y)	Absol. mag.
11411	1999 HK1	0.78600	2.50	15.41
30968	1995 AM1	0.76539	3.47	14.39
53454	1999 XC136	0.91428	2.71	15.14
70055	1999 JN6	0.67361	3.59	15.07
86280	1999 UQ9	0.72111	2.58	
93041	2000 SU2	0.83457	3.68	

3. Light curves analysis

The G(RP) magnitudes for reference stars were taken from the GAIA DR2 release [Brown et al. 2018]. For processing one series of observations were used 30-40 reference stars with colors close to the Sun; some brighter and some dimmer, than moving objects. The images were analyzed by calibrated and measured using Lemur software [Savanevych, 2022]. Measurement of magnitudes of objects was made after the application of standard procedures of master flat and master dark images. For further processing selected only that series where the reference star's brightness errors at an average are smaller than 0.05 magnitudes. It helps to discard observations with poor sky instant transparency. Each measurement of an asteroid consists of a time and apparent magnitude couple.

Both values must be corrected for each measurement series because the distance of an asteroid relative to Earth and to the Sun changes. Time changes by reducing to the first moment of observations were made by equation:

$$t_i = t_0 + \frac{D_0 + D_i}{c},$$

where D is the asteroid's distance from the observer.

The magnitudes of all series are corrected depending on the distance from the observer and from the Sun [Zeigler, Hanshaw, 2016]:

$$\Delta m_i = m_i - 5\log(\frac{D_0 R_0}{D_i R_i}),$$

where D is the asteroid distance from the observer and R is the distance to the Sun and R_0, D_0 is the same for the first observation in the first series.

The last is magnitude correction by phase effect:

$$\Delta m_i = (Ph_0 - Ph_i)k,$$

where k is the slope coefficient of the phase diagram for phases in intervals 10 to 30 degrees, Ph_i and Ph_0 are i and the first phase in series, respectively. We thus use linear regression to fit the lightcurve amplitude-corrected data.

After time and brightness corrections, deriving asteroid periods from their lightcurves by the Fourier series analysis method [Pravec, Harris, 2000]. A detailed description of the algorithm is given by [Kwiatkowski et al., 2009].

The Fourier method is very sensitive to gaps in observations, especially when summarizing data from a small series of observations, as well as data from different oppositions, where there are large shifts in the brightness range. In this situation, the Lomb-Scargle (L-S) periodogram [VanderPlas, 2018] and Phase Dispersion Minimization (PDM) [Stellingwerf, 1978] methods.

All brightness data from the whole in Table 2 mentions observatories' measurements of asteroid brightness are analyzed with three methods in the range 0.1 to 100 hours if the number of observations exceeds 70 in the specified passband.

Table 2: observatories from which data are analized

Observatory (IAU Code)/Space mission	Observa-tion period	Passband
Baldone (069)	2022.03-2023.03	G(RP)
Mauna Loa (T08)	2019.01-2022.08	o, c
Haleakala (T05)	2018.05-2022.08	o, c
Catalina Sky Survey (703)	2005.12-2023.05	V, G
Zwicky Transient Facility (I41)	2014.02-2022.08	r, g
Lincoln Laboratory ETS (704)	1999.04-2010.09	c
Catalina Sky Survey (G96)	2019.01-2022.06	G
Ponte Uso (G45)	2014.03-2017.03	r
Transiting Exoplanet Survey Satellite (C57)	2018.09-2018.10	G

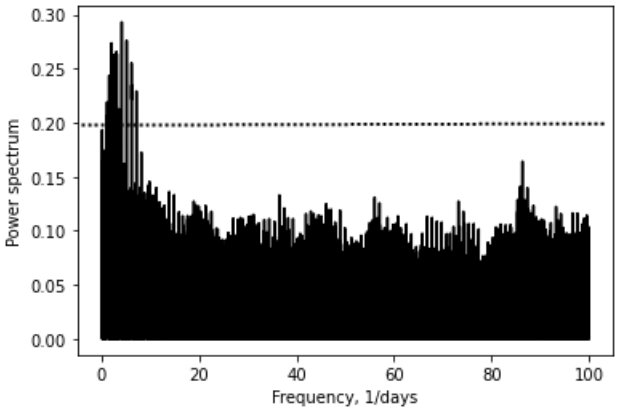

Figure 1: The power spectrum of asteroid N53454, method L-S

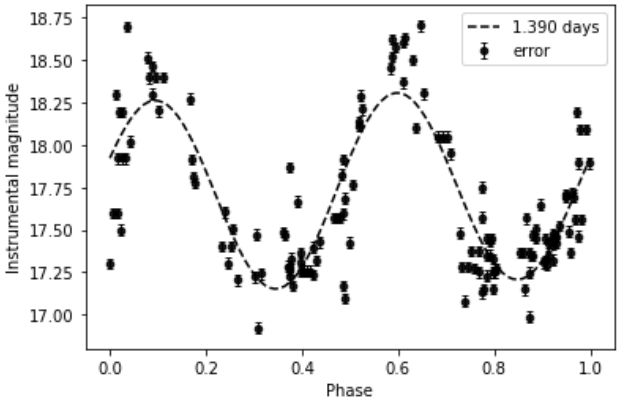

Figure 2: The light curve of asteroid N93041, method L-S

According to the obtained power diagrams, peaks with a probability greater than 20% were selected (see example in Fig. 1).

The surroundings of these separated periods were studied in more detail within a range of plus or minus 2 hours, in order to clarify the possible rotation period. Data from all observatories were similarly analyzed.

Possible periods must satisfy two criteria. A)The light curve should show two maxima and two minimum troughs during one cycle. An example is presented in Fig. 2). B)The shape of the peak in the power spectrum must be similar somewhat resembling a Gaussian distribution (an example is presented in Fig. 3).

All thus allocated periods were cross-correlated. Matching periods from whole observatories with a 3% tolerance were extracted as true rotation period sets. Small discrepancies in values are removed by weighted mean methods. Period values are weighted by the number of observations and by the value of peak probabilities in the power spectrum. The average value is accepted as the true rotation period of the studied asteroids and displaced in Table 3 together with the amplitude of variation in G(RP) passband and their types from [ALCDF, 2023].

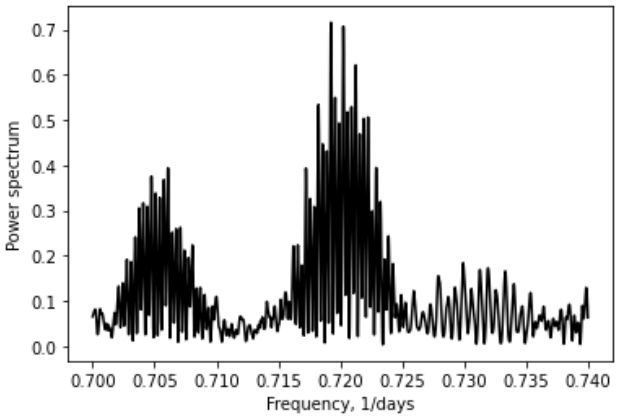

Figure 3: The power spectrum of asteroid N93041, method L-S

Table 3: Results of analyze

Asteroid	Period(h)	error	Ampl.	Type
11411	6.544	0.006	0.8	SE
30968	8.330	0.027	0.4	S
53454	4.615	0.022	0.4	SE
70055	74.364	0.067	0.6	S
86280	1.315 6.658	0.005 0.032	0.4	C
93041	30.645	0.007	1.2	S

4. Conclusion

- Asteroids N70055 and N93041 have great rotation periods: 74.322 h and 30.645 h respectively.
- Asteroid N82680 has two possible rotation periods. The first 1.315 h and 6.658 h. Small amounts of observation don't allow unambiguously choosing the amount of rotation period.
- The Fourier series method gives usable results analyzing long series observation in multiple following nights when the rotation period isn't longer than 7-10 hours.
- In cases of small series of observations scattered over a large period of time, with differences in brightness in different oppositions, the L-S and PDM methods work more reliably.
- The PDM method is sensitive to a small number of observations. If the number of observations is less than a hundred, the PDM method mostly does not work.
- The shown methodology allows analyzing data whose brightness accuracy is one decimal.

Acknowledgements. Text of Acknowledgements. This work has made use of data from the European Space Agency (ESA) mission Gaia (https://www.cosmos.esa.int/gaia), processed by the Gaia Data Processing and Analysis Con-

sortium (DPAC, https://www.cosmos.esa.int/web/gaia/dpac/consortium). Funding for the DPAC was provided by national institutions, in particular, the institutions participating in the Gaia Multilateral Agreement. This research is supported by project 2291 by a «MikroTik» donation administered by the University of Latvia Foundation.

References

ALCDEF: 2022, *Asteroid Lightcurve Data Ex change Format*, https://alcdef. org/php/alcdef-Generate ALCDEFPage.php

Brown A.G.A, Vallenari A., Prusti T. et al.: 2018, *A&A*, **616**, A1, 22.

Castillo J., Vance S.: 2008, *Astrobiology*, **8**, 344.

Houtkooper J.M.: 2011, *Planet Space Sci*. **59**, 1107.

Kwiatkowski T., Kryszczynska A., Polinska M. et al.: 2009, *A&A*, **495**, 967.

MPC: 2023, *Minor Planet Center*, *https://cgi.minorplanetcenter.net/cgi-bin/checkneo.cgi.*

NASA, 2013 *https://www.esa.int/ESA_Multimedia/Images/2016/06/Bolide_airbursts_1994-2013*

Pravec P., Harris A.W.: 2000, *Icarus*, **148**, 12.

Savanevych V.E., Khlamov S.V., Akhmetov, V. S. et al.: 2022, *Astronomy and Computing*, **40**, id. 100605

Stellingwerf R.F.: 1978, *AJ*, **224**, 953.

VanderPlas J.T.: 2018, *AApS*, **236**, id.16, 28.

Zeigler K., Hanshaw B.: 2016, *Minor Planet Bull*., **43**, 199.

https://doi.org/10.18524/1810-4215.2023.36.290222

TEST OPTICAL OBSERVATIONS OF THE COSMOS 1408 FRAGMENTS

O.M.Kozhukhov [1], Y.V.Omelchenko [1], D.M.Kozhukhov [1], O.G.Solomakha [1], M.V.Kulichenko [2], O.V.Shulga [2], Y.S.Kozyrev [2], N.V.Maigurova [2]

[1] National Space Facilities Control and Test Center, State Space Agency of Ukraine, Kyiv, Ukraine, *a.m.kozhukhov@gmail.com*

[2] Research Institute "Mykolaiv Astronomical Observatory", Mykolaiv, Ukraine, *nadya.maigurova@gmail.com*

ABSTRACT. The non-functioning spacecraft COSMOS 1408 (NSSDCA/COSPAR ID: 1982-092A) was destroyed as a result of tests involving Russian anti-satellite weapons on 15 November 2021. This led to the creation of a significant debris cloud that poses a threat to other objects in low Earth orbit (LEO), particularly those in close orbits. More than 1500 of these fragments reached trackable sizes. Such events require rapid and immediate monitoring through all available ground tracking means, including radar and optical observation. The following study presents the results of optical observations of the selected fragments of COSMOS 1408 in Ukraine. These observations were carried out by the telescope OES30 from the National Space Facilities Control and Test Center of the State Space Agency of Ukraine and the Fast Robotic Telescope (FRT) of the Research Institute "Mykolaiv Astronomical Observatory" in February 2022. The observations demonstrated that Ukrainian optical sensors are capable of tracking LEO space debris objects with radar cross-sections (RCS) less than 0.1 square meters when relatively accurate ephemeris data is available. The astrometric reduction has been performed for the acquired frames with fragments of the satellite, which revealed that orbital parameters of a significant part of the targeting objects were close to the orbital parameters of the original satellite before the event. Furthermore, the results of processing the available observations indicated that the range of apogee heights significantly exceeds the range of perigee heights. These findings align with conclusions drawn by previous researchers. In the future, it will be essential to assess the capabilities of sensors for observing the aftermath of object destruction in LEO, especially during the initial hours and days following such events when precise debris orbit data may be lacking.

Keywords: space debris, optical observations.

АНОТАЦІЯ. Недіючий космічний апарат COSMOS 1408 (NSSDCA/COSPAR ID: 1982-092A) був знищений в результаті випробувань російської протисупутникової зброї 15 листопада 2021 року. Це призвело до створення величезної хмари уламків, які становлять загрозу для інших низькоорбітальних об’єктів, що знаходяться на близьких орбітах. Більше 1500 з цих фрагментів мали розміри, які можна відстежувати. Такі події вимагають швидкого та негайного моніторингу за допомогою всіх доступних засобів наземного відстеження, включаючи радіолокаційні та оптичні спостереження. В цьому дослідженні наведено результати оптичних спостережень окремих фрагментів супутника COSMOS 1408, що були отримані в Україні. В спостереженнях приймали участь телескоп OEC30 станції оптико-електронного спостереження Національного центру управління та випробування космічних засобів Державного космічного агентства України та Швидкісний автоматичний комплекс (ШАК) науково-дослідного інституту (НДІ) «Миколаївська астрономічна обсерваторія» у лютому 2022 року. Спостереження показали, що українські оптичні засоби спостереження здатні спостерігати об'єкти космічного сміття на низьких навколоземних орбітах з радіолокаційним перетином менше 0.1 кв. м. при наявності відносно точних ефемеридних даних. Була проведена астрометрична редукція отриманих кадрів з окремими фрагментами супутника, яка показала, що орбітальні параметри значної частини об’єктів, що спостерігалися, були близькими до орбітальних параметрів супутника перед подією. Крім того, результати обробки наявних спостережень вказують на те, що діапазон висот в апогеї значно перевищує діапазон висот в перигеї. Ці висновки узгоджуються з висновками, зробленими іншими дослідниками. У майбутньому буде важливо оцінити можливості спостережень за наслідками руйнування об'єкта на НЗО, особливо в перші години та дні після подібних подій, коли можуть відсутні точні дані про орбіту сміття.

Ключові слова: космічне сміття, оптичні спостереження.

1. Introduction

Spacecraft COSMOS 1408 was destroyed on 15 November 2021 as a result of tests of Russian anti-satellite weapons and the huge cloud of debris that poses a threat to other LEO objects in close orbits was generated. Also known that this event was the reason for the creation of a permanent Internal Task (IT) for the observation of LEO fragmentation events in Working Group 1 of Inter-Agency Space Debris Coordination Committee (IADC WG1).

Table 1: OES30 Specifications (Romanyuk et al, 2021 as OEOS-2)

	OES 30	FRT
Aperture,mm	300	300
Focal length, mm	300	1500
Camera (chip)	QHY-174M GPS (Sony 1/1.2" CMOS IMX174LLJ / IMX174LQJ)	Apogee Alta U9000
Size, pix.	1936x1216	3056 × 3056
Pixel size, μm	5.86	12
Scale without bining ("/pix)	4.01	1.6
FoV (deg^2)	2.89 (130'x80')	1.96 (83'× 83')
Slew rate, deg/s	Up to 10	Up to 20
Tracking	yes	no

In order to monitor the debris cloud special international campaign for observation of fragments of this event was organized in February 2022. The purpose of these observations was to determine whether telescopes with our receivers can observe such debris using standard observation modes and techniques.

2. Equipment and Observation Techniques

Two instruments participated in the observations of COSMOS 1408 debris fragmentations. These were the Type 2 Optoelectronic Observation Station (OEOS-2 or OES30) telescope of the National Space Facilities Control and Test Center of the State Space Agency of Ukraine and the Fast Robotic Telescope (FRT) of the Mykolaiv Astronomical Observatory.

OES30 (or OEOS-2) located near Kyiv. Telescope was installed in 2019 and have modified German with direct drive mount. Standard tracking mode was used for the observations.

Fast Robotic telescope (FRT) was designed and manufactured by NAO in 2004. Maksutov mirror lens and rotating platform with photographic lenses are installed on the parallactic mount telescope. Time delay and integration (TDI) mode with rotation stage are used for the observations.

Some characteristics of the used telescopes are given in the Table 1.

3. Proceeding resuts

3.1 OES30

The observations were made on February 13, 2022. A total of 6 fragments were observed. Observations were carried out with an exposure of 0.3 s with tracking mode. Detailed information about observation frames are given in Table 2, where ID and RCS (S – Small, M – Medium) column given

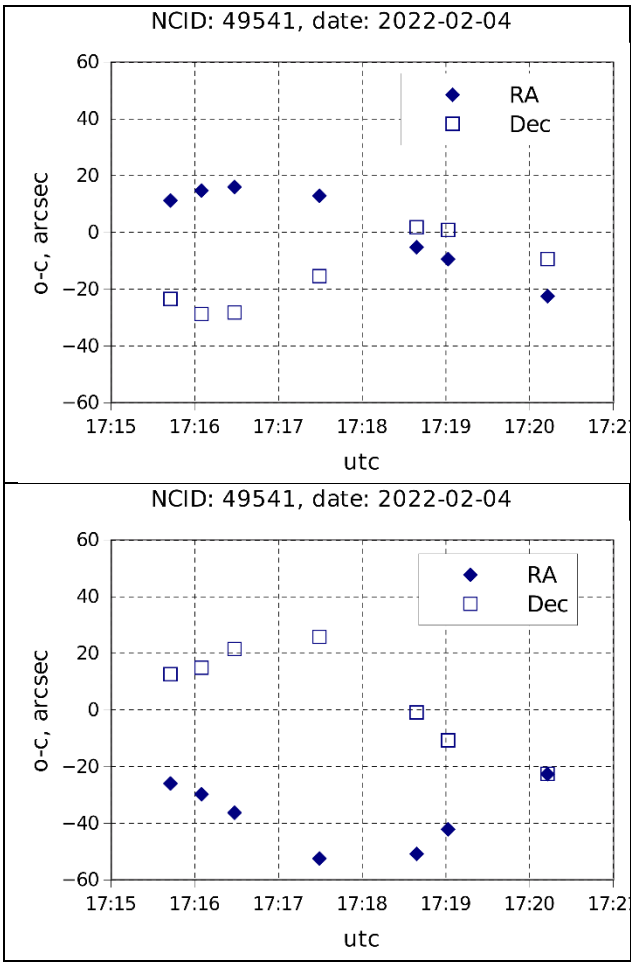

Figure 1: Residual differences (O – C) vs UTC, where O – obtained positions, C – ephemeris data (down – USSPACECOM, up – FindOrb).

according unclassified USSPACECOM (previously NORAD) catalogue (https://www.space-track.org) data. The main orbital parameters close to the observation epoch from USSPACECOM catalogue, are shown in Table 3. As could be shown from tab.3 the objects have similar orbit parameters values.

3.2 FRT

FRT observations were performed on 4 and 11 February 2022. Results of astrometric reductions were shown that positional accuracy of reference stars is about 1 arcsec in both coordinates. The limited magnitude was 13^{mag} with in exposure 1^s. Detailed information about FRT observational data are shown in table 2 and 3.

The Fig. 1 shows the trend of residual differences between the obtained positions (from FRT observations) and the ephemeris data USSPACECOM (https://celestrak.org/NORAD/elements/) and FindOrb software (https://www.projectpluto.com/sat_id2.htm) for the object 49541. It can be noted that the positional differences between the FindOrb ephemeris and obtained observations are smaller

Table 2: Statistics of the observational data

ID	COSPAR ID	N	RCS	Data	Tel
49528	1982-092-R	133	S	Feb.13	OES30
49540	1982-092-AD	88	M	Feb.13	OES30
49582	1982-092-BX	137	S	Feb.13	OES30
49634	1982-092-EB	115	S	Feb.13	OES30
49635	1982-092-EC	120	S	Feb.13	OES30
49662	1982-092-EH	100	M	Feb.13	OES30
49522	1982-092-K	3	M	Feb.04	FRT
49530	1982-092-T	6	M	Feb.04	FRT
49531	1982-092-U	3	M	Feb.04	FRT
49535	1982-092-Y	1	M	Feb.04	FRT
49537	1982-092-AA	1	M	Feb.04	FRT
49538	1982-092-AB	1	M	Feb.04	FRT
49541	1982-092-AE	7	M	Feb.04	FRT
49576	1982-092-BR	1	M	Feb.04	FRT
49590	1982-092-CF	2	M	Feb.04	FRT
49626	1982-092-DT	1	M	Feb.04	FRT
49653	1982-092-EW	1	M	Feb.04	FRT
49694	1982-092-GP	2	M	Feb.04	FRT
49707	1982-092-HC	2	S	Feb.04	FRT
49723	1982-092-HU	2	M	Feb.04	FRT
49784	1982-092-JA	1	S	Feb.04	FRT
49787	1982-092-JD	1	M	Feb.04	FRT
49789	1982-092-JF	1	M	Feb.04	FRT
49822	1982-092-KD	1	M	Feb.04	FRT
50010	1982-092-QW	1	M	Feb.04	FRT
50026	1982-092-RN	1	M	Feb.04	FRT
49530	1982-092-T	1	M	Feb.11	FRT
49694	1982-092-GP	4	M	Feb.11	FRT

than between the ephemeris from USSPACECOM catalogue and observations. However, the small number of points and short arc of observations involved in the initial orbit determination using FindOrb and atmosphere drug influence has not been taken into account.

4. Brief Analysis of Results

The graph (Fig. 2) clearly shows a dense group of objects, whose orbit parameters are close to those of the satellite before fragmentation. Something similar was also observed in the TIRA observations obtained in November 2022. (Cerutti-Maori et al, 2023).

It is also worth noting that the difference in the perigee heights of these objects is much smaller than the difference in the perigee heights (Fig. 3). This is in good agreement with other observations (Fig. 4) (Ramos et al., 2022, Oltrogge D.L. et al. 2022).

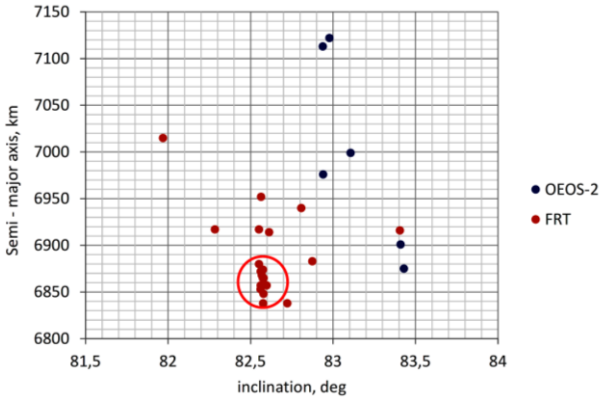

Figure 2: Orbital parameters of the observed fragments: semi-major axis - inclination. The group of objects with orbits close to the COSMOS-1408 orbit before the event is marked with a red circle.

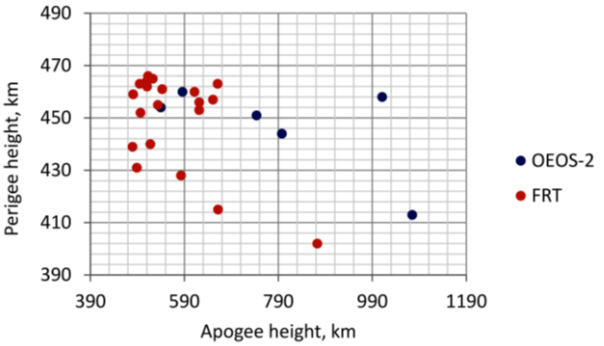

Figure 3: Orbital parameters of the observed fragments: perigee heght – apogee height.

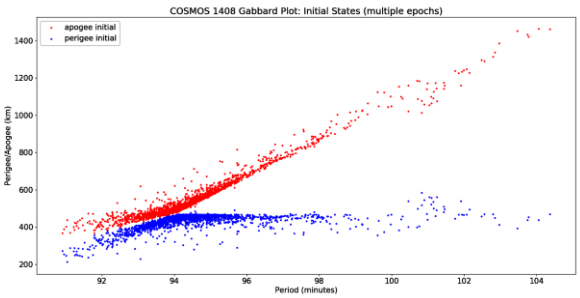

Figure 4: COSMOS 1408 Gabbard Plot-Initial States (Ramos et al, 2022).

5. Conclusion

Ukrainian optical sensors are able to observe LEO space debris objects with RCS less than 0.1 sq. m. in the presence of relatively accurate ephemeris.

The orbital parameters of a significant part of the observed objects were close to the orbital parameters of the original satellite before the event. It can also be observed that the range of apogee heights is much larger than the perigee heights. These facts are also confirmed by reports of observations by other participants that were made earlier.

Table 3: Main orbital parameters of objects for an epoch close to the observation epoch

ID	Epoch (UTC) 2022	Inclination	Semi-major axis, km	Apogee, km	Perigee, km	Tele-scope
49528	02-12 11:34:18	82.978°	7 122	1 075	413	OES30
49540	02-12 17:25:03	83.107°	6 999	798	444	OES30
49582	02-12 11:04:00	82.940°	6 976	744	451	OES30
49634	02-12 17:47:43	83.410°	6 901	586	460	OES30
49635	02-12 10:51:29	82.938°	7113	1011	458	OES30
49662	02-12 17:47:11	83.430°	6875	540	454	OES30
49522	02-03 17:19:52	82.579°	6848	481	459	FRT
49530	02-0312:43:32	83.405°	6 916	622	453	FRT
49531	02-03 17:59:31	82.874°	6 883	583	428	FRT
49535	02-03 12:38:17	82.562°	6 857	495	463	FRT
49537	02-03 18:02:16	82.564°	6952	651	457	FRT
49538	02-03 17:54:24	82.284°	6917	662	415	FRT
49541	02-03 12:16:44	82.808°	6 940	661	463	FRT
49576	02-03 17:26:56	82.598°	6 857	518	440	FRT
49590	02-03 18:27:20	82.551°	6 917	622	456	FRT
49626	02-03 17:57:12	82.561°	6853	497	452	FRT
49653	02-03 19:23:44	82.551°	6880	543	461	FRT
49694	02-03 17:31:11	82.580°	6 865	511	462	FRT
49707	02-03 19:38:58	82.723°	6 838	489	431	FRT
49723	02-03 21:56:30	81.969°	7 015	873	402	FRT
49784	02-03 17:53:08	82.568°	6 868	513	466	FRT
49787	02-03 12:35:04	82.574°	6865	510	464	FRT
49789	02-03 12:54:33	82.613°	6914	612	460	FRT
49822	02-03 12:29:39	82.576°	6874	534	455	FRT
50010	02-03 18:05:18	82.562°	6 872	523	465	FRT
50026	02-03 18:05:21	82.577°	6838	480	439	FRT

In the future, it is necessary to evaluate the capabilities of sensors to observe the consequences of fragmentation of objects on the LEO in the absence of accurate data on the orbits of debris (the first hours and days after the event).

References

Romanyuk Ya.O., Shulga O.V., Shakun L.S. et al.: 2021, *Odessa Astron. Publ.*, **34**, 85.

Cerutti-Maori D., Carloni C., Rosebrock J., Siminski J.: 2023, *Proc. 2nd NEO and Debris Detection Conference, Darmstadt*, Germany, 24-26 January 2023, published by the ESA Space Safety Programme Office, Ed. T.Flohrer, R.Moissl, F.Schmitz, [online] Available at: (https://conference.sdo.esoc.esa.int/proceedings/neosst2/paper/38/NEOSST2-paper38.pdf) [Accessed 7 September 2023].

Ramos C., Hutchinson D., Skrehart B., Gillespie D., McKissock D.: 2022, *Proc. of 23 Advanced Maui Optical and Space Surveillance Technologies Conference (AMOS)*, 283.

Oltrogge D.L., Alfano S., Hall R.: 2022, *Proc. of 23 Advanced Maui Optical and Space Surveillance Technologies Conference (AMOS)*, 1875.

https://doi.org/10.18524/1810-4215.2023.36.290925

COLOR-INDEX DETERMINATION OF LEO SATELLITES USING COLOR IP-CAMERAS

Kulichenko M.O., Kozyryev Y.S., Maigurova N.V., Shulga O.V.

Research Institute "Mykolaiv Astronomical Observatory",
Mykolaiv, Ukraine, niiko4kulichenko@gmail.com

ABSTRACT. The study is devoted to determining the color characteristics of the structural surfaces of artificial satellites. Observations of satellites were carried out in automatic mode using software for detection fast moving object, developed at RI "MAO". The satellite observations equipment consists of Canon EF 85mm f/1.8 USM photographic lens and professional VIVOTEK IP816A-HP network camera. The camera is directed to the zenith and has a field of view (4.9ºx2.8º). The camera has progressive CMOS sensor with Bayer color filter array for producing RGB color image. Coordinate and photometric processing of saved images is carried out using SExtractor and Astrometry.net software along with additional Python scripts. In this paper, we present first results of our LEO satellites observations using network IP-cameras with RGB Bayer filter. To convert the instrumental magnitudes from RGB Bayer system into standard *bp/rp* magnitudes of the Gaia EDR3 photometric system, a system of equations was solved, where the calculated magnitudes in the *bp/rp* photometric system were represented as functions of magnitudes and colors in the instrumental RGB system. The mean differences between the calculated magnitudes and the catalog magnitudes are $(0.03\pm0.15)^{mag}$ and $(0.01\pm0.16)^{mag}$ for *bp* and *rp* band, respectively. The calculated *Brjb_bp* and *Rrjb_rp* magnitudes using obtained transformation coefficients show a good linear correlation with the *bp* and *rp* Gaia EDR3 magnitudes. Only main sequence's stars in the range of $(5\text{-}13)^{mag}$ were used as reference stars for determining the transformation coefficients. The results of determining the color indexes (*Brjb_bp - Rrjb_rp*) for 8 LEO satellites with the obtained transformation coefficients were received. The average accuracy of the obtained values of color indexes is about 0.2^{mag}.

Keywords: RGB-cameras, Photometry Transformations, Gaia *bp/rp* photometric system, color index, LEO satellite.

АНОТАЦІЯ. Дослідження присвячене визначенню кольорових характеристик структурних поверхонь штучних супутників. Спостереження за супутниками проводилися в автоматичному режимі з використанням програмного забезпечення виявлення швидких об'єктів, розробленого в НДІ «МАО». Устаткування для супутникових спостережень складається з фотооб'єктиву Canon EF 85mm f/1.8 USM та професійної мережевої камери VIVOTEK IP816A-HP. Камера направлена в зеніт та має поле зору (4.9°x2.8°). Камера оснащена прогресивною матрицею CMOS із матрицею кольорових фільтрів Байєра для створення кольорового зображення RGB. Координатна та фотометрична обробка збережених зображень здійснюється за допомогою програмного забезпечення SExtractor та Astrometry.net разом із додатковими скриптами Python. У цій статті ми представляємо перші результати наших спостережень супутників LEO з використанням мережевих IP-камер із RGB-фільтром Байєра. Для перетворення інструментальних зоряних величин у системі RGB з фільтрами Байєра в стандартні зоряні величини фотометричної системи Gaia EDR3 *bp/rp* була вирішена система рівнянь, в якій обчислювані зоряні величини в фотометричній системі *bp/rp* були представлені як функції зоряних величин і кольорів в інструментальній системі RGB. Середні залишкові різниці між розрахованими зоряними величинами та величинами з каталогу становлять $(0.03\pm0.15)^{mag}$ та $(0.01\pm0.16)^{mag}$ для смуг *bp* та *rp* відповідно. Розраховані з використанням отриманих коефіцієнтів трансформації величини *Brjb_bp* та *Rrjb_rp* показують хорошу лінійну кореляцію з величинами *bp* та *rp* з каталогу Gaia EDR3. Тільки зорі головної послідовності в діапазоні $(5\text{-}13)^{mag}$ використовувалися як опорні зорі для визначення коефіцієнтів трансформації. Обчислено значення показників кольору *(Brjb_bp – Rrjb_rp)* для 8 супутників LEO з отриманими коефіцієнтами перетворення. Середня точність одержаних значень показників кольору становить близько 0.2^{mag}.

Ключові слова: RGB-камери, фотометричні перетворення, фотометрична система Gaia *bp/rp*, показник кольору, супутник LEO.

1. Introduction

Optical observations of artificial satellites play significant roles in obtaining orbital characteristics, monitoring and catalogization but for object classes identification surface materials, rotation and shape models development, besides the orbits, additional information like physical properties is required. Photometric colors are an important tool in the identification of satellites manufacturers (Vananti et al., 2017) and bus configuration, that includes size and shape of the object, antennae, solar arrays etc. (Zhao et al., 2022) Different photometric systems have also been used for physical characterization of space debris, such as the (BVRI) Johnson-Cousins, the SDSS/Sloan and the infrared bands. In this paper we present first results of the LEO satellites color determination based on data obtained with consumer-level RGB cameras. Such cameras are typically not used in

professional astronomy because of the systematic errors present in the data as a result of the strong intra- and interpixel variations associated with each of the three different colors (RGB) of the Bayer color filter array (Gee et al., 2021). Nevertheless, because the cost of such cameras compared with traditional astronomical CCDs is so much lower, the use of such cameras is, in our opinion, very promising for obtaining mass photometric data. Also, recent works have made strong efforts to produce standard photometry in RGB bands based on high-precision photometry of the EDR3 Gaia catalog. A new set of spectral sensitivity curves, computed as the median of 28 sets of empirical sensitivity curves from the literature, that can be used to establish a standard RGB photometric system was presented in (Cardiel et al., 2021a). This work led to creation of the new catalogs with RGB photometric calibration of Gaia stars (Cardiel et al., 2021b; Carrasco et al., 2023).

2. Observational facilities and technique

The satellite observations equipment consists of Canon EF 85mm f/1.8 USM photographic lens and professional VIVOTEK IP816A-HP network camera, which provides a shooting speed of up to 60 frames per second, a field size of 2 megapixels (1920x1080), a sensitivity of 0.03 lux (color mode), 3D noise suppression in low light conditions, RBF (Radial Basis Function) system for precise focus adjustment, EIS (electronic image stabilization) to control image stability. The camera is directed to the zenith and has a field of view (4.9ºx2.8º), pixel size – 9 arcsec. The RGB Bayer filter system consists of a mosaic of R, G, and B filters on the grid of the photo sensors which cameras are equipped with. Observations of satellites are carried out with frame rate 5 fps in automatic mode using software for detection of the fast moving object, developed at RI "MAO".

The algorithm for detection of moving objects is similar to algorithm for detection of meteors but modified for processing of video stream from different kind of sources and devices (Kulichenko et al., 2019). Another feature of the algorithm is saving color images in standard raster-graphics file formats (such as png) so that the data of each color (R, G, and B) could be processed separately during further photometric reduction.

Average duration of observations for night was 6 hours. During 15 nights 1362 objects were detected. Total number of frames is 41680.

3. Processing

Coordinate and photometric processing of saved images is carried out using SExtractor (Bertin & Arnouts, 1996) and Astrometry.net software (Lang et al., 2010) along with additional Python scripts. Reference stars are obtained using "track-and-stack" technique. Processing of obtained observations included next steps:

1) Frames filtering using software for processing of the CCD images developed in RI "MAO";

2) Extracting stars and cross-match with catalog Tycho-2 for obtaining reduction coefficients using Astrometry.net software. Flux of extracted stars in ADU with subtracted background also saved in result files. Flux values for each color of RGB-image are obtained separately;

3) Obtaining a summary csv-table for all detected stars with measured celestial coordinates and streams from all processed frames using a Python script. The table also includes coordinates and magnitudes from Tycho-2 catalogs for all cross-matching stars.

3.1. Astrometry

Cross-matching procedures with Gaia EDR3 catalog were made by CDS Cross-Match service by TOPCAT software (Taylor M., 2005). The cross-match results are shown in Tab. 1. (O – C) differences and their standard deviations in right ascension and declination are given in column 2, 3, N1- number of common stars with Gaia EDR3 catalog. As you can see from the table, there are no significant systematic differences between obtained coordinates and Gaia EDR3 catalog. The accuracy is almost the same for both coordinates in the B, G, R ranges.

Table 1: Results of cross matching between observational arrays and Gaia EDR3 catalog

Band	(O – C), arcsec		N
	RA	DE	
B	-1.8 ± 7.4	2.1 ± 6.9	175
G	1.2 ± 7.0	-1.1 ± 7.9	272
R	1.2 ±7.3	-0.7 ± 6.7	270

3.2. Photometric transformation and color index determination

The counts from the stars with the subtracted background were converted to the scale of instrumental magnitudes according to the known ratio: $mag = -2.5 * log(FLUX)$.

Differential photometry is achieved by comparing the flux from a target star (within a given radius or aperture) with the flux of the reference stars. The flux measurements of stars were calculated using isophotal mode of SExtractor software. The photometric measure errors for B, G, R files are shown in Fig. 1.

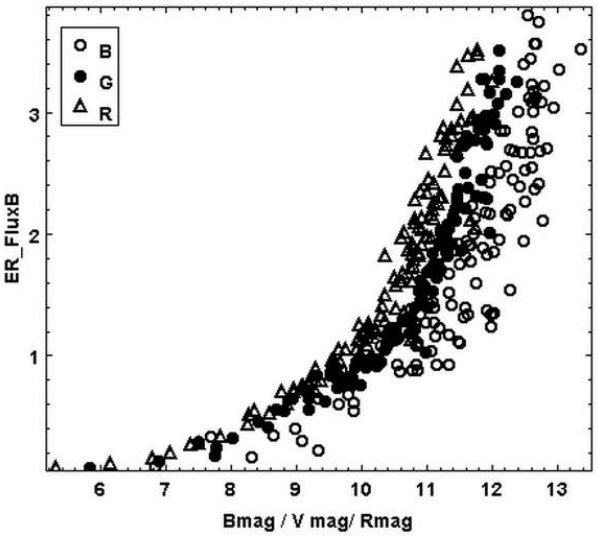

Figure 1: Flux errors for B, G, R bands

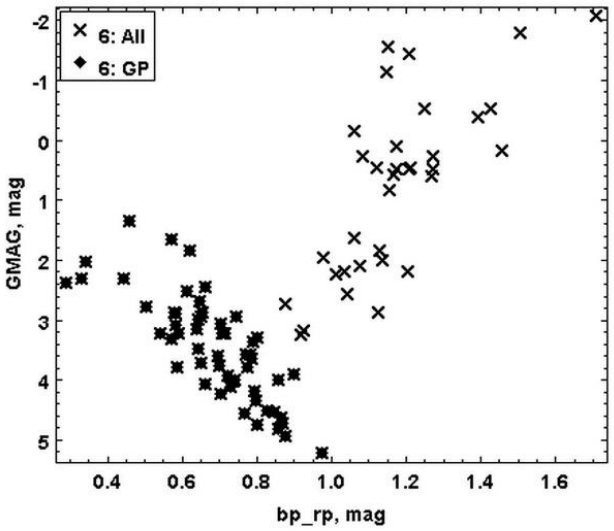

Figure: 2 Hertzsprung-Russell Diagram

To derive the conversion formula that describes the transformation between the instrumental RGB and Gaia *bp_rp* photometric systems only main-sequence stars are selected. The Hertzsprung-Russell diagram plotted using Gaia EDR3 Supplement data provides a way to distinguish stars. As is clear from Fig. 2 main sequence stars are easy visualized as strip from left to right of a HR diagram.

After identify the same stars in B, G, R images, we compared B magnitude with bp Gaia EDR3 magnitude and R magnitude with rp Gaia EDR3 magnitude for individual stars. The relationship between magnitudes can be represented in the form taking into account color differences between Bayer filters:

$$bp\_G = B_0 + C_1 B_{rgb} + C_2(B_{rgb} - G_{rgb}) + C_3(G_{rgb} - R_{rgb})$$
$$rp\_G = R_0 + C_4 R_{rgb} + C_5(B_{rgb} - G_{rgb}) + C_6(G_{rgb} - R_{rgb}),$$

where *bp_G, rp_G* – Gaia EDR3 photometric magnitude, B_{rgb}, G_{rgb}, R_{rgb} – Bayer B, G, and R magnitudes; B_0, R_0 – the zero-points for the Bayer filters. The transformation coefficients were derived by the iterative least square fitting algorithm with 3-sigma clipping method. The calculated values of transformation star coefficients and their errors are presented in Tab. 2 As could be seen from table 2 the accuracy of link between the two systems is 0.15^{mag} for *bp* band and 0.16^{mag} for *rp* band. The *Brjb_bp* and *Rrjb_rp* magnitudes calculated with usage transformation coefficients show a good linear correlation with the *bp* and *rp* Gaia EDR3 magnitudes.

The Fig. 3 presents residual differences between RGB and Gaia *bp* and *rp* photometric magnitudes. As is observable from the Fig. 3 there is no significant systematic differences in magnitudes in the observational range. The random error is determined by the errors of the least squares method solution and mean residual differences between the calculated magnitudes and original catalog magnitudes, are $(0.03\pm0.15)^{mag}$ and $(0.01\pm0.16)^{mag}$ for *bp* and *rp* band respectively.

The Fig. 4 presents residual differences between (*bp_rp)* Gaia color index and calculated color index (*Brgb_bp – Rrgb_rp)* The mean value of the color differences is $(0.02 \pm 0.12)^{mag}$.

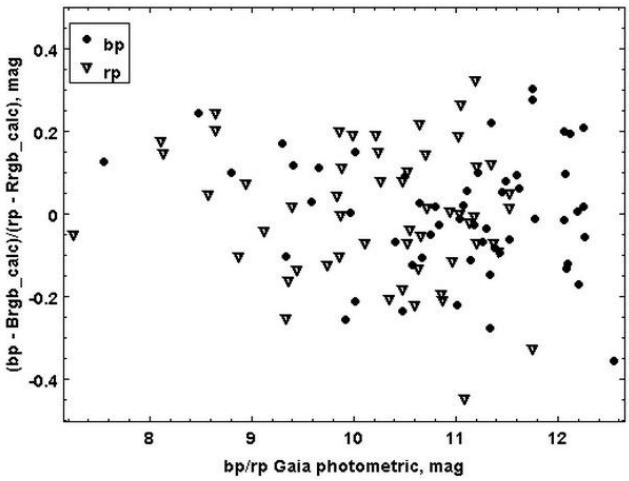

Figure 3: Residuals in magnitude plots for the bp and rp Gaia photometric bands

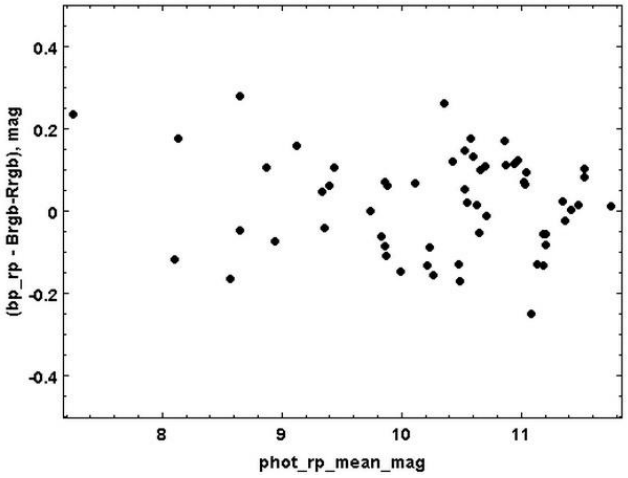

Figure 4: Residuals in color index vs rp band Gaia magnitude

We applied obtained transformation coefficients to the RGB magnitudes of some satellites, whose images were present in the fields with reference stars. Results of the color index determination and identification for selected satellites are shown in Tab. 3. It would be mentioned that 6 satellites were identified by NORAD catalog number. Satellite light-curves for N99005 and N99008 satellites are shown in the Fig. 5.

4. Conclusion

First results of the LEO satellites color index determination from original observations obtained with network RGB color IP-cameras are presented. Derived transformation equations between the RGB instrumental system and the photometric *bp* and *rp* Gaia EDR3 magnitudes are given. The calculated *Brjb_bp* and *Rrjb_rp* magnitudes from the transformation equations has shown a good linear correlation with the *bp* and *rp* magnitudes from

Table2: Transformation coefficients

Band	B_0/R_0	C_1/C_4	C_2/C_5	C_2/C_5	RMS
bp	18.60±0.16	1.12±0.03	-0.77±0.12	-0.03±0.12	0.15
rp	17.39±0.17	1.05±0.03	0.41±0.14	1.01±0.14	0.16

Table3: Results of the color index determination and identification for selected satellites

UTC start 2023-07-	**TMP ID**	**NORAD ID**	**Period, min**	**Incl, deg**	**Apo, km**	**Peri, km**	**RCS***	**N**	***bp*, mag**	**(*bp-rp*), mag**	**Std *(bp-rp)***
12 19:10:54	99001	51654	109.89	87.88	1223	1220	L	88	6.96	−0.3	0.2
12 19:13:32	99003	-	-	-	-	-	U-	194	6.85	−0.17	0.14
12 21:59:55	99004	52790	96.94	50.01	617	608	M	39	5.22	−0.24	0.07
12 23:01:45	99005	45767	95.59	53.05	548	546	L	25	4.93	−0.22	0.07
13 20:24:57	99006	54214	100.78	60.00	816	776	L	133	6.77	−0.31	0.12
13 21:06:51	99007	10730	103.30	114.98	999	830	L	39	7.09	−0.43	0.19
14 19:01:00	99008	-	-	-	-	-	U	36	5.13	−0.48	0.09
14 19:55:34	99009	31571	114.08	51.99	1414	1413	L	50	6.86	−0.26	0.45

* L -large, M – Medium, U – Unknown

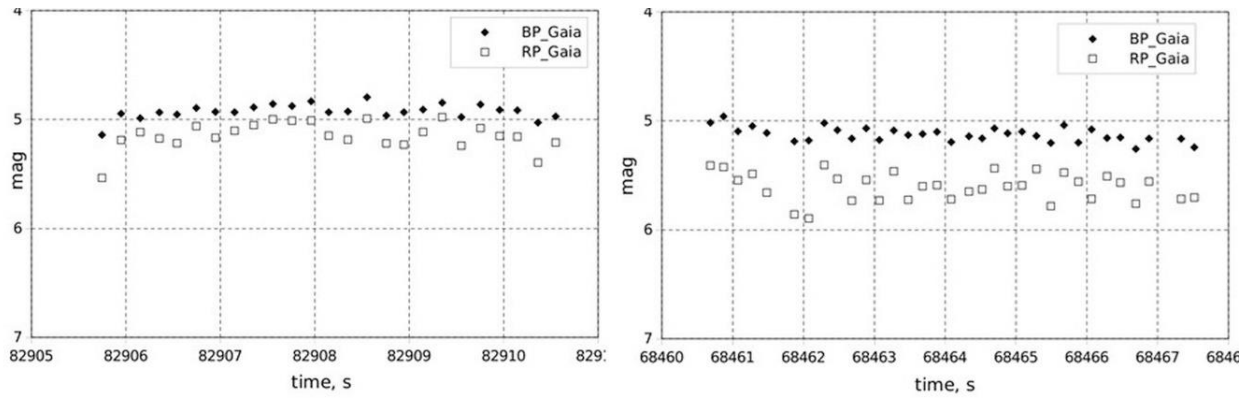

Figure 5: Light-curves for N99005 (right) and N99008 (left) satellites

Gaia EDR3 catalog. The average accuracy of the obtained values of color indexes for LEO satellites is about 0.2 ^{mag}.

Acknowledgements. This work has made use of data from the European Space Agency (ESA) mission Gaia (https://www.cosmos.esa.int/gaia), processed by the Gaia Data Processing and Analysis Consortium.

References

Bertin E. & Arnouts S.: 1996, *A&A Suppl*., **317**, 393. https://doi.org/10.1051/aas:1996164.

Carrasco J.M., Cardiel N., Masana E. et al.: 2023, *Remote Sensing*, **15**, 1767. https://ui.adsabs.harvard.edu/link_gateway/2023RemS...15.1767C/doi:10.3390/rs15071767.

Cardiel N., Zamorano J., Bará S. et al.:2021a, MNRAS, **504**, 3730. https://ui.adsabs.harvard.edu/link_gateway/2021MNRAS.504.3730C/doi:10.1093/mnras/stab997.

Cardiel N., Zamorano J., Carrasco J. M. et al.: 2021b, *MNRAS*, **507**, 318. https://ui.adsabs.harvard.edu/link_gateway/2021MNRAS.507..318C/doi:10.1093/mnras/stab2124.

Gee W., Guyon O., Jovanovic N. et al.: 2021, *J. Astron. Telesc. Instrum. Syst*., **7(4)**, 048001-1. https://ui.adsabs.harvard.edu/link_gateway/2021JATIS...7d8001G/doi:10.1117/1.JATIS.7.4.048001.

Kulichenko M. O., Shulga O. V., Gorbanev Yu. M.: 2019, Odessa Astron. Publ., **32**, 165. https://doi.org/10.18524/1810-4215.2019.32.181908.

Lang D., Hogg D. W., Mierle K. et al.: 2010, *AJ*, **137**, 1782. https://doi.org/10.1088/0004-6256/139/5/1782.

Taylor M.: 2005, *Astron. Data Analysis Software and Systems XIV ASP Conf. Ser.*, **347**, 29.

Vananti A., Schildknecht T., Krag H.: 2017, *Adv. in Space Res.*, **59**, 2488. https://ui.adsabs.harvard.edu/link_gateway/2017AdSpR..59.2488V/doi:10.1016/j.asr.2017.02.033.

Zhao X. F., Zhang H. Y., Yu Y., Mao Y.: 2016, *Adv. in Space Res.*, **58**, 2269. https://doi.org/10.1016/j.asr.2016.09.020.

https://doi.org/10.18524/1810-4215.2023.36.290927

FIRST REPORTED OBSERVATION OF ASTEROIDS 2017 SV39, 2017 ST39, AND 2017 TS7

A. Simon [1,2] and V. Troianskyi [3,4]

[1] Astronomy and Space Physics Department, Taras Shevchenko National University of Kyiv, Glushkova ave., 4, Kyiv, 03022, Ukraine, *andrew_simon@univ.kiev.ua*

[2] National Center «Junior academy of sciences of Ukraine», 38-44, Dehtiarivska St., Kyiv, 04119, Ukraine

[3] Department of Physics and Astronomy FMPIT of Odesa I. I. Mechnykov National University, Pastera Street 42, 65082 Odesa, Ukraine, *v.troianskyi@onu.edu.ua*

[4] Department of Physics and Methods of Teaching, Faculty of Physics and Technology, Vasyl Stefanyk Precarpathian National University, Shevchenko Street 57, 76000 Ivano-Frankivsk, Ukraine

ABSTRACT. In this paper, we show the result of the joint use of the AZT-8 telescope, the Astrometrica software, and the Väisälä method. The paper considers in detail several of the discovered (rediscovered) asteroids: SV39, 2017 ST39, and 2017 TS7 from a long list of small bodies of the Solar System.

Keywords: Minor planets, asteroids, observational.

АНОТАЦІЯ. У цій статті ми показуємо результат спільного використання телескопа AZT-8, програмного забезпечення Astrometrica та методу Вяйсяля. В роботі вказані основні характеристики телескопа AZT-8, що знаходиться в Астрономічній обсерваторії Київського національного університету імені Тараса Шевченка. Докладно розписано метод визначення координат об'єктів на кадрах за допомогою програмного пакету Astrometrica та вказано переваги використання методу Вяйсяля для визначення первинної орбіти небесного тіла. У статті детально розглядаються кілька перевідкритих астероїдів: SV39, 2017 ST39 і 2017 TS7 з довгого списку малих тіл Сонячної системи. Астероїд 2017 SV39 спостерігався 28-го вересня 2017 року, але не був підтверджений іншими обсерваторіями. Астероїд Головного поясу 2017 ST39 спостерігався 28-го вересня та 2-го, 9-го, 10-го жовтня 2017 року; в результаті виявився раніше відкритим астероїдом під номером 536266. Астероїд Головного поясу 2017 TS7 спостерігався 9-го та 10-го жовтня 2017 року; в результаті виявився раніше відкритим астероїдом під номером 540584.

Ключові слова: Малі планети, астероїди, спостереження.

1. Introduction

The Kyiv Comet Station has a long history of patrol observations as well as targeted observation campaigns. Throughout the execution of diverse observational programs, the observatory archive has amassed a substantial volume of scientifically valuable information.

Amidst the ongoing fascination with the exploration and examination of Solar System entities, our endeavor is to extract the utmost additional information from the acquired observations, utilizing contemporary processing tools. In this manuscript, we will delve into the quest for moving objects within a sequence of panoramic images capturing the starry sky. These images were garnered during the observation using the AZT-8 telescope.

2. Observations and data reduction

Observations in Kyiv were made with the AZT-8 telescope (Fig. 1) of the astronomical observatory of the Kyiv Shevchenko National University, which is installed at the Kyiv Comet Station [code: 585]. The AZT-8 reflector, a serial telescope from the Leningrad Optical Mechanical Association. As an imaging detector the FLI PL4710 camera with 63.5 mm Shutter, providing a field of view of 16.2'×16.7' and an image scale of 0.948 arcsec/pixel, was used.

We did standard data reduction (i.e., dark subtracting and flat-fielding); for details, see Oszkiewicz et al., (2019; 2020; 2021; 2023).

2.1. Astrometry

After all standard reductions for single images were done, we started to combine images in order to decrease the value of limiting magnitude on the sum image and so to have a possibility to detect fainter objects. Preliminary information about proper motion of possible asteroids were taken from the Gaia Follow-Up Network for Solar System Objects webpage and was applied during single images stacking. Due to special conditions of observations, all frames had an exposure of 30 seconds and we used from 10 to 100 images depending of brightness of possible asteroid for stacking. Thus time intervals between stacked images and asteroids positions can vary from 5 to 50 minutes.

Images stacking and further astrometrical measurements were done with the use of Astrometrica software.

2.2. Väisälä method

The Väisälä method, as highlighted by Troianskyi et al. (2023b), proves highly valuable in numerous scenarios. Its application becomes particularly prominent when dealing with a brief observing arc that lacks the duration necessary to ascertain the "true" orbit and forecast the object's position over the ensuing week or so. Additionally, this method facilitates the derivation of a reasonably accurate primary orbit, laying the groundwork for subsequent enhancement through one of the iterative methods. Notably, the method finds active utilization in the quest for the primary orbit of small celestial bodies within the Solar System when confronted with limited observational data at the Minor Planet Center (MPC).

3. Results

All objects in this section were observed in the Gaia Follow-Up Network for Solar System Objects. During these observations we had a possibility clearly identify three new asteroids. Two of these asteroids, after recalculating their orbits, were assigned to already discovered objects.

3.1. Asteroid 2017 SV39

Firstly was observed during 28th / 29th of September 2017 night on Kyiv comet station (585). As a result, observations of 8 positions, which cover 35-minute time intervals, were added to the MPC database. In MPS 828365 object received the designation 2017 SV39. Unfortunately, no other observations for this potential asteroid were provided and published on the MPC services.

3.2. Main-belt asteroid 2017 ST39

First observations of this asteroid were done during 28th/29th of September 2017 night on Kyiv comet station (585). Collected data give us a possibility to determine 18 positions of the asteroid for this night and prepared very well for the next observations that were conducted during 02nd/03rd of October 2017 night with 3 more positions, during 09th/10th of October 2017 night with 14 positions and during 10th/11th of October 2017 night with 7 positions. All these observations were published in MPS 891037, MPS 828365 and objects got assignation 2017 ST39. Later it appeared that we rediscovered an object already know under assignations 2007 HU101 and 2015 CX48. This asteroid received its number 536266 and now belongs to the asteroids from the Main Belt.

3.3. Main-belt asteroid 2017 TS7

First observations of this asteroid were done during 09th/10th of October 2017 night with 15 positions and during 10th/11th of October 2017 night with 9 positions (MPS828378). After orbit recalculations by MPC IAU services it appeared that we had rediscovered an object already know under assignations 2000 WN134, 2007 XY37, 2010 RD162 and 2015 DH168. This asteroid received its number 540584 and now belongs to the asteroids from the Main Belt.

Additional observations (MPS 928677) of this object were made on the OMT-800 telescope (Andrievsky et al., 2013; Troianskyi et al., 2014).

Figure 1: AZT-8 telescope

4. Conclusion

The combined use of the AZT-8 telescope, Astrometrica software, and the Väisälä method showed good results in the search for small bodies in the Solar System (2017 SV39, 2017 ST39, 2017 TS7).

Astrometric observations are very important for further research (numerical integration of orbits) of small bodies of the Solar System (Troianskyi & Bazyey, 2018; Troianskyi et al., 2022; Troianskyi et al., 2023a).

Acknowledgements. VT was supported by the National Scholarship Programme of the Slovak Republic - academic year 2023/2024.

References

Andrievsky S.M., Fashchevsky N.N., Podlesnyak S.V. et al.: 2014, *Odessa Astron. Publ.*, **26**, 6.

Oszkiewicz D., Kryszczynska A., Kankiewicz P. et al.: 2019, *A&A*, **632**, A170, doi: 10.1051/0004-6361/201833641.

Oszkiewicz D., Troianskyi V., Fohring D. et al.: 2020, *A&A*, **643**, A117, doi: 10.1051/0004-6361/202038062.

Oszkiewicz D., Wilawer E., Podlewska-Gaca E. et al.: 2021, *Icarus*, **357**, id.114158, doi: 10.1016/j.icarus.2020.114158.

Oszkiewicz D., Troianskyi V., Galad A. et al.: 2023, *Icarus*, **397**, id.115520, doi: 10.1016/j.icarus.2023.115520.

Troianskyi V.V., Bazyey A.A., Kashuba V.I. et al.: 2014, *Odessa Astron. Publ.*, **27**, 154.

Troianskyi V.V., Bazyey O.A.: 2018, *Contributions of the Astronomical Observatory Skalnate Pleso*, **48**, 356.

Troianskyi V., Kankiewicz P., Oszkiewicz D.: 2022, *16th Europlanet Science Congress 2022*, Spain, id.EPSC2022-888, doi: 10.5194/epsc2022-888.

Troianskyi V., Kankiewicz P., Oszkiewicz D.: 2023, *A&A*, **672**, A97, doi: 10.1051/0004-6361/202245678.

Troianskyi V., Kashuba V., Bazyey O. et al.: 2023, *Contributions of the Astronomical Observatory Skalnate Pleso*, **53(2)**, 5-15, doi: 10.31577/caosp.2023.53.2.5.

RADIOASTRONOMY

https://doi.org/10.18524/1810-4215.2023.36.290123

DIRECT IMAGE RECONSTRUCTION IN MULTI-ELEMENT INTERFEROMETRY

A.B.Lozynskyy, O.L.Ivantyshyn, B.P.Rusyn

Karpenko Physico-Mechanical Institute of the National Academy of Sciences of Ukraine, 5, Naukova str., Lviv, 79060, Ukraine, *lozynskyy.a@gmail.com*

ABSTRACT. The Ukrainian VLBI system of decameter radio telescopes URAN successfully solves many scientific problems, but implementing aperture synthesis technology has a number of difficulties. One of them is significant phase distortions in this range caused by an inhomogeneous propagation environment. Therefore, the task arose to develop an alternative technology with the conventional name "Interferovision", which would allow us to restore radio images with a limited number of antennas, operate with broadband signals, not require flatness of the objects scene, and have an extended field of view. A method of direct image reconstruction when observing objects in space, using a multi-element interferometer, is proposed. This method is based on a physically based principle that is similar to holography. The wave front is registered by the antennas of the interferometer, and further processing is equivalent to its playback in reverse and registration of the resulting spatial interference image. There are no special requirements for the radiation of individual points of the source, except for its delta correlation. A finite frequency band is considered, and each point can be characterized by its own spectrum, that is, its own autocorrelation function of radiation. The resolution of the direct reconstruction method depends on its width. With the quasi-monochromatic approximation, the autocorrelation functions of the radiation of all the source points degenerate into sinusoids, and the restoration of the image becomes possible only with the use of the Fourier transformation. A theoretical justification of the method for spaces of different dimensions has been obtained. Interferometric systems of the same rank with many antennas are reduced to a same canonical form with fixed number of virtual antennas placed at the origin of the coordinates and at unit distances on the coordinate axes. The ambiguity of the obtained solution is eliminated by using an additional antenna. A simulation of the proposed method of direct image reconstruction for two-dimensional space was carried out. Despite the low conditionality of the system for estimating the distance, when it increases, the angular characteristics are preserved. Therefore, the method is promising for restoring radio images of space radio sources.

Keywords: multi-element interferometry, image restoration, wide frequency band, wide field of view.

АНОТАЦІЯ. Українська РНДБ система декаметрових радіотелескопів УРАН успішно вирішує багато наукових задач, але імплементація технології апертурного синтезу стикається з рядом труднощів. Однією з них є значні фазові спотворення в цьому діапазоні, викликані неоднорідністю середовища поширення. Тому постало завдання розробити альтернативну технологію під умовною назвою “Інтерферобачення”, яка дозволила б відновлювати радіозображення при обмеженій кількості антен, оперувала широкосмуговими сигналами, не вимагала площинності об'єктної сцени і мала б розширене поле зору. Запропоновано метод прямої реконструкції зображення при спостереженні об’єктів у просторі з допомогою багатоелементного інтерферометра. Цей метод оснований на фізично обґрунтованому принципі, що нагадує голографію. Хвильовий фронт реєструється антенами інтерферометра, а подальший обробіток еквівалентний його відтворенню в зворотному напрямку та реєстрації утвореного просторового інтерференційного зображення. При цьому не висувається спеціальних вимог до випромінювання окремих точок джерела, окрім його дельта-корельованості. Розглядається скінченна смуга частот, причому кожна точка може характеризуватися власним спектром, тобто власною автокореляційною функцією випромінювання. Від її ширини залежить роздільна здатність методу прямої реконструкції. При квазімонохроматичному наближенні автокореляційні функції випромінювання всіх точок джерела вироджуються в синусоїди і відновлення зображення стає можливим тільки з використанням перетворення Фур’є. Отримано теоретичне обґрунтування способу для просторів різних розмірностей. Інтерферометричні системи одного рангу з багатьма антенами приводяться до єдиного канонічного вигляду з (віртуальними) антенами, розміщеними в початку координат та на одиничних віддалях на осях координат. Двозначність отриманого розв’язку усувається введенням додаткової антени. Проведено моделювання запропонованого способу прямої реконструкції зображення для двовимірного простору. Незважаючи на низьку обумовленість системи стосовно оцінки віддалі при її збільшенні, кутові характеристики при цьому зберігаються, тому спосіб є перспективним для відновлення радіозображень космічних радіоджерел.

Ключові слова: багатоелементна інтерферометрія, відновлення зображення, широка смуга частот, широке поле зору.

1. Introduction

Aperture synthesis technology, based on the application of the van Zittert-Zernike theorem, has been widely used in modern radio astronomy (Thompson et al., 2017). It boils down to finding the values of the spatial harmonics of the Fourier transform of the image obtained by many two-element interferometers. For this, the antenna system is divided into pairs and the cross correlation function is determined (Scaife, 2019). An infinite number of spatial harmonics is necessary for the correct solution of the inverse problem – image restoration – which is impossible in principle. Therefore, various methods of interpolation and processing of incomplete data are used, for example, compressed sounding and sparse restoration (Garsden et al., 2015). The resolution and quality of the reconstruction results depend significantly on the set of bases of the antenna system and the applied methods. The implementation of aperture synthesis technology requires the satisfaction of a number of approximation conditions, including: approximation of a plane wave, approximation of the delta-correlation of the source points, approximation of the object field of view to the plane and limitation of its dimensions, approximation of quasi-monochromaticity, approximation of the homogeneity of the waves propagation medium, approximation of the complete filling of the area of interferometric bases. Some of these approximations are quite difficult to ensure, and a number of methods are being developed to reduce the impact of their violation, among them – undersampling and deconvolution, isoplanatism (Schwab, 1984), spectral behavior (Taylor et al., 1999), non-coplanarity (Shopbell et al., 2005), direction-dependent calibration effects (Bhatnagar et al., 2013), etc. The difficulties of taking into account the inhomogeneities of the medium of wave propagation, primarily the non-stationary ionosphere, give rise to the so-called phase problem in low-frequency radio astronomy (Kornienko et al., 2008, 2020). In addition, reconstruction of radio images belongs to the class of inverse problems. Therefore, the search for new stable algorithms for its solution is still relevant today. At the same time, despite all the accompanying problems, the interferometers that are functioning today and new ones that are being built or designed are systems of aperture synthesis.

Another approach is based on the use of the longitudinal correlation function (Koshovy et al., 1998) followed by the Radon transform (Koshovy et al., 2002 & Lozynskyy et al., 2023). Image reconstruction is carried out by inverse Radon transform based on a set of received projections for pairs of antennas. With this technology, the approximation of quasi-monochromaticity becomes unnecessary, the resistance to the influence of the inhomogeneity of the propagation medium increases, and the filling of the area of the interferometric bases is improved. But at the same time, to obtain a strict solution, an infinite number of projections is required, which again requires the use of interpolation procedures.

Lozynskyy et al. (2022) considered a fundamentally different view of the problem of image reconstruction in multi-element interferometry, which correctly poses the inverse problem of image reconstruction. They obtained conclusions about the bijectivity of the transformation of spatial (angular) and difference coordinates. In this work, when considering the problem of positioning with the help of a multi-element interferometer, the method of direct image reconstruction is mentioned. But the essence of the method is not sufficiently revealed there.

2. Direct reconstruction method

The proposed method consists in the fact that each of the antennas of the interferometer registers the sum of wave fronts from different points of the object in some frequency band. At the same time, radiation from different points of the object takes different paths and takes different delays. Further, during processing, the recordings are played back in the opposite direction, which provides an inversion of these delays. At the points in space that correspond to the positions of the object points, the corresponding part of the radiation will interfere constructively, because the differences in the path of the rays for them become zero. The other part will not create interference in this place.

The essential difference between the direct reconstruction method and the aperture synthesis technology is that with its help, a real image is obtained, it physically exists, and is not determined indirectly through the components of the Fourier transform. It can be registered with a test antenna placed in a suitable location, or even visualized in a certain way.

The method of direct reconstruction resembles holography – after recording a section of the wavefront, it can then be playback, resulting in an image. An important feature of holography is that a small particle of the recorded wavefront appears to carry the necessary information about the object, but with reduced contrast. Consider a similar principle in relation to multi-element interferometry.

2.1. Direct problem

Let us have an object consisting of elements (pixels), the radiation of which are random processes $s_i(t)$, collectively stationary in a wide sense. Let us denote by $R_{ij}(\tau)$ the mutual correlation function the radiation of a pair of source elements and write down the condition of their independence, i.e. delta-correlation:

$$R_{ij}(\tau) = \int s_i(t) s_j(t-\tau) dt = \begin{cases} R_i(\tau), & i = j \\ 0, & i \neq j \end{cases}. \quad (1)$$

Let the radiation of the object be received by a multi-element interferometer (Fig. 1). For the k-th element of the interferometer, we write down the sum of the received signals

$$x_k(t) = \sum_i s_i(t - \tau_{ik}) \,. \quad (2)$$

The sum (2) obtained for all k is the starting point for solving the inverse problem.

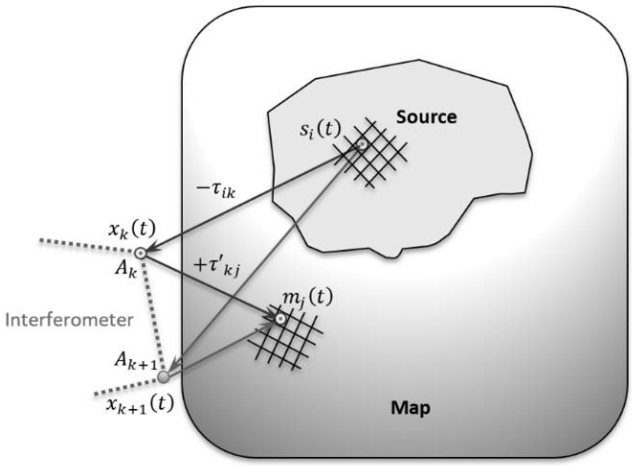

Figure 1: Scheme for determining the intensity of the image element, the resulting beam propagation delay from the i-th element of the source to the j-th pixel of the image through the k-th element of the interferometer is $\tau_{ikj} = -\tau_{ik} + \tau'_{kj}$

2.2. Inverse problem

For each (j-th) pixel of the image, we will form the sum of the signals taken in reverse time, and we will ask whether they interfere (equivalent to playback by the interferometer elements).

$$m_j(t) = \sum_k x_k\left(t - \tau'_{kj}\right). \qquad (3)$$

The intensity of the created signal

$$I\left(m_j\right) = \int\left[\sum_k x_k\left(t - \tau'_{kj}\right)\right]^2 dt\ . \qquad (4)$$

Let's rewrite the square of the sum through the double sum, which will allow us to enter the sign of the integral under the sum

$$I\left(m_j\right) = \sum_l\sum_n \int x_l\left(t - \tau'_{lj}\right)\, x_n\left(t - \tau'_{nj}\right)\, dt\ . \qquad (5)$$

After substituting (2) into (5) and noting the resulting beam propagation delay from the i-th element of the source to the j-th pixel of the image through the k-th element of the interferometer by $\tau_{ikj} = -\tau_{ik} + \tau'_{kj}$, we obtain

$$I\left(m_j\right) = \sum_l\sum_n \int\left[\sum_\alpha s_\alpha\left(t - \tau_{\alpha lj}\right)\right]\times \left[\sum_\beta s_\beta\left(t - \tau_{\beta nj}\right)\right] dt\ . \qquad (6)$$

Let's use the notation of the product of sums by a double sum again

$$I\left(m_j\right) = \sum_l\sum_n\sum_\alpha\sum_\beta \int(\bullet)\,, \qquad (7)$$

where $\int(\bullet) = \int s_\alpha\left(t - \tau_{\alpha lj}\right) s_\beta\left(t - \tau_{\beta nj}\right) dt$. Note that this integral is similar to the integral in (1). After applying (1), we get

$$I\left(m_j\right) = \sum_l\sum_n\sum_\alpha\sum_\beta R_{\alpha\beta}\left(\tau_{\beta nj} - \tau_{\alpha lj}\right). \qquad (8)$$

We consider that on the basis of (1) $R_{\alpha\beta}(\tau)$ is different from zero only if $\alpha = \beta$. This allows you to record the result of transformations in the form

$$I\left(m_j\right) = \sum_l\sum_n\sum_i R_i\left(\tau_{inj} - \tau_{ilj}\right) \qquad (9)$$

or

$$I\left(m_j\right) = \sum_l\sum_n\sum_i R_i\left(\tau_{il} - \tau'_{lj} - \tau_{in} + \tau'_{nj}\right). \qquad (10)$$

The content of the obtained result (10) is as follows. The radiation of the i-th element of the source with a delay τ_{il} reached the l-th element of the interferometer, was recorded and then played back in the reverse direction. At the same time, the delay τ_{il} changed its sign and became equal $-\tau_{il}$. On the way to the j-th pixel of the image, there is an additional delay τ'_{lj}, and the resulting delay will be $\tau_{ilj} = -\tau_{il} + \tau'_{lj}$. Another ray, the n-th, which corresponds to the path through the n-th element of the interferometer, receives a delay $\tau_{inj} = -\tau_{in} + \tau'_{nj}$ in a similar way. It interferes with the previous one, since it is radiated by the same source element, with an amplitude determined by the corresponding correlation function $R_i(\tau)$ based on (1) for $\tau = \tau_{inj} - \tau_{ilj}$. And so in pairs for all elements of the interferometer and for all elements of the source. Note that $R_i(0)$ corresponds to the radiation intensity of the i-th element of the source, that is, the image of the source is formed pixel by pixel in this way.

2.3. Existence and uniqueness of solution

Obtaining an image can be conventionally divided into two stages. At the first stage, signal records are obtained, in which a set of delays corresponds to each element of the source with its spatial coordinates. These delays can be interpreted as difference coordinates. At the second stage, the inverse transformation of coordinates is performed.

Lozynskyy et al., (2022) considered the transformation of spatial and difference coordinates and determined the number of interferometer elements necessary for mutual uniqueness in spaces of different dimensions. The number

of interferometer elements, arbitrary but greater than or equal to the minimum, is described by a canonical equation of the corresponding rank. That is, all interferometric systems of the same rank with many antennas can be reduced to a single canonical form with (virtual) antennas placed at the origin and at unit distances on the coordinate axes. But as it turned out, in some cases the solution of the inverse problem can be ambiguous - the distance from the object to the interferometer can take two values. A detailed analysis of this shortcoming is beyond the scope of this work, it is enough to note that adding one more element to the interferometer completely eliminates the mentioned problem. With a sufficient number of interferometer elements, the transformation of spatial and difference coordinates is bijective. For two-dimensional space, it is 4, and for three-dimensional – 5 elements. If there is no need to determine the distance to the object, but you can limit yourself only to angular coordinates, which is quite acceptable in radio astronomy, then the minimum number of antennas can be reduced by one.

Thus, based on the bijectivity of the transformation of spatial and difference coordinates (displayed as sets of signal delays in records) and the correspondence of the autocorrelation function at zero displacement to the radiation intensity of the source element, the solution of the problem of image reconstruction exists and is unique.

3. Numerical modeling

Numerical modeling of direct and inverse problems was carried out for the case of two-dimensional space. In radio astronomy, such a problem arises when observing radio sources using a 2d interferometer (Lozynskyy et al., 2022). The numerical simulation scheme of the direct reconstruction method is shown in Fig. 2.

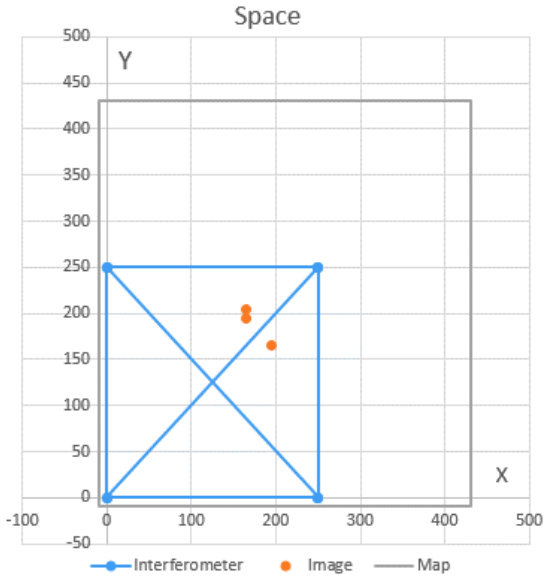

Figure 2: Scheme for numerical modeling of the direct reconstruction method

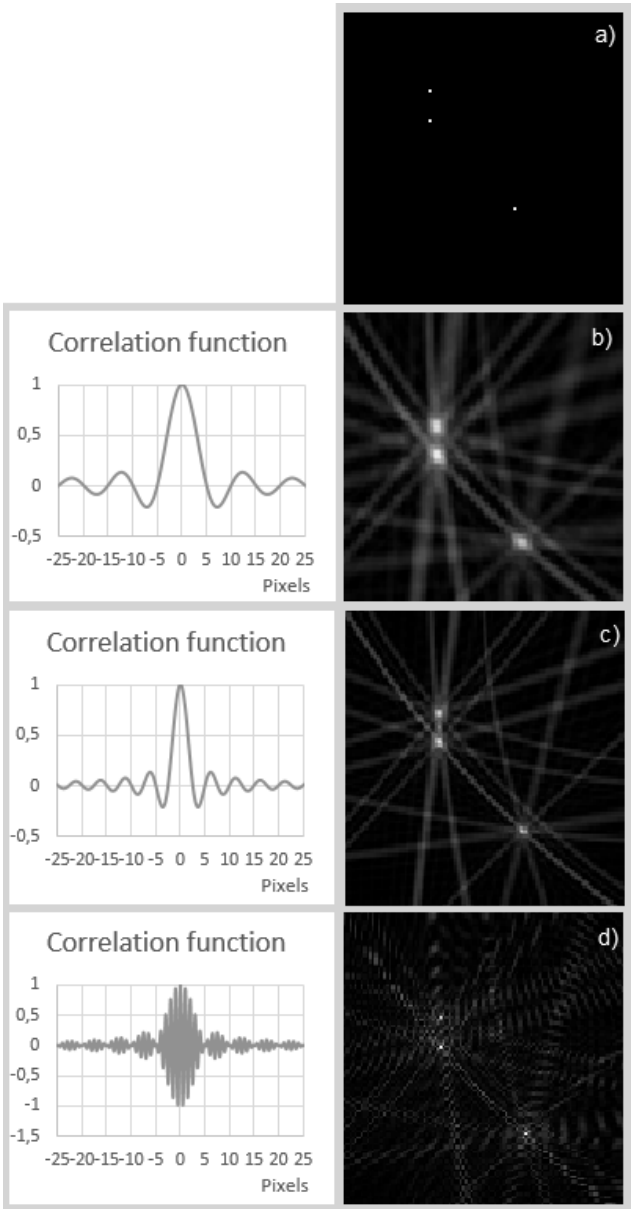

Figure 3: Results of numerical modeling of the direct reconstruction method; a) original image; b-d) reconstructed by setting different autocorrelation functions of the radiation of the object shown on the left

In the space with coordinates *X* and *Y*, 3 pixels of the same intensity are selected, which constitute the model of the original image of the object. 4 interferometer elements are located at the vertices of the square. The part of the space in which the image will be reconstructed is surrounded by a frame.

In Fig. 3 shows the results of numerical modeling of the map section.

4. Conclusion

As follows from the given theoretical reasoning and numerical simulation, the direct reconstruction method allows obtaining results with a limited number of interferometer elements. It is clear that with an increase in the

number of elements, the relative intensity of artifacts will decrease rapidly. The condition that we know the autocorrelation functions of the object's elements is not difficult to ensure in radio astronomy, since the radio radiation with which radio astronomy operates is mostly broadband. A small frequency band is allocated from it by the receiving systems, and the partial autocorrelation functions of all signals become the same and known in advance. However, the method does not impose any requirements on their uniformity. Continuation of research in this direction will make it possible to determine the individual radiation spectra of individual parts of the image, i.e. spectral indices, or, conventionally speaking, "color". Rejection of the quasi-monochromatic approach, besides this, gives a number of positive consequences. For example, increasing the frequency band is equivalent to increasing the sensitivity and immunity to interference.

Separately, it should be noted that with the quasi-monochromatic approximation, the autocorrelation functions of the radiation of all the source points degenerate into sinusoids of the same frequency and the method seems unsuitable in such conditions. However, the amplitude and phase of the mutual correlation function of signals in pairs of interferometer elements appear, and this is already the scope of the well-known aperture synthesis technology.

When implementing the direct reconstruction method, no requirements for objects distance are imposed, on the contrary, it is determined. Moreover, there are no requirements for the flatness of the object of the scene, for the width of the field of view, the interferometer "sees" the entire available space at once.

An important characteristic of the method is the possibility of reconstruction of images of dynamic objects, since only a portion of signals is accumulated, and then only these instantaneous recordings are used. And this creates the basis for observations through the medium of wave propagation with moving inhomogeneities. In this case, the obtained results will resemble speckles.

When observing objects that are distant compared to the size of the interferometer, blurring is observed in the distance estimation, but the angular characteristics are preserved. This effect becomes clear from the analysis of the form of the canonical equation of a multi-element interferometer, in which the direction cosines enter directly, and the distance – inversely, as a unit divided by the distance. The actual angular distribution of radio radiation intensity is important for radio astronomy, so the proposed method is promising for restoring radio images of space radio sources.

References

Bhatnagar S., Rau U. and Golap K.: 2013, *Astrophys. J.*, **770** (2), 91. https://doi.org/10.1088/0004-637X/770/2/91.

Garsden H., Girard J., Starck J. et al. (78 more): 2015, *A&A*, **575**, A90. https://doi.org/10.1051/0004-6361/201424504.

Kornienko Yu.V., Skuratovskiy S.I.: 2008, *Radiofiz. elektron.*, **13** (1), 130.

Kornienko Y., Lyashenko I., Pugach V. and Skuratovskiy S.: 2020, *Kinem. and Phys. of Cel. Bod.*, **36** (1), 37.

Koshovy V.V., Lozynsky A.B.: 1998, *Information extraction and processing*, **12** (88), 37.

Koshovyy V., Lozynskyy A., Lozynskyy B.: 2002, The tomographic technique for reconstruction of the cosmic radio sources images on the basis of radio interferometric data. XXVIIth General Assembly of the International Union of Radio Science. https://doi.org/10.5281/zenodo.7950758.

Lozynskyy A., Ivantyshyn O., Rusyn B.: 2022, *Information and Communication Technologies, Electronic Engineering*, **2** (1), 52. https://doi.org/10.23939/ictee2022.01.052.

Lozynskyy A., Rusyn B., Ivantyshyn O.: 2023, *Electronics and information technologies*, **22**, 3. https://doi.org/10.30970/eli.22.1

Scaife A. M. M.: 2019, *Phil. Trans. R. Soc.*, A378: 20190060. https://doi.org/10.1098/rsta.2019.0060.

Schwab F. R.: 1984, *Astron. J.*, **89** (7), 1076. http://doi.org/10.1086/113605.

Shopbell P., Britton M. and Ebert R.: 2005, Astronomical Data Analysis Software and Systems XIV. Astronomical Society of the Pacific Conference Series, **347**.

Taylor G., Carilli C. and Perley R.: 1999, Synthesis imaging in radio astronomy II. ASP Conference Series, **180**.

Thompson A.R., Moran J.M. and Swenson G.W: 2017, Interferometry and Synthesis in Radio Astronomy, 3rd ed. (Springer, Cham), 872. http://doi.org/10.1007/978-3-319-44431-4.

https://doi.org/10.18524/1810-4215.2023.36.290139

THE LONG-TERM OBSERVATIONS OF THE POWER COSMIC RADIO SOURCES ON THE RADIO TELESCOPE URAN-4 AT THE DECAMETER WAVE RANGE

O.A. Lytvynenko, S.K. Panishko, V.G. Derevyagin

Observatory URAN-4 of the IR NASU, park Shevchenko, 65014, Odessa, Ukraine,
spanishko@ukr.net

ABSTRACT. The radio telescope (RT) URAN-4, located near the city of Odessa, started to work in 1987 as a component of the radio interferometric system URAN, which operates in the decameter range of radio waves and whose elements are placed in several points throughout Ukraine. The first successful VLBI observations of compact cosmic radio sources in the URAN system were carried out on the RT URAN-4–UTR-2 interferometer at the end of 1987. In the same period, a program was launched for regular observations of powerful cosmic radio sources 3C 144, 3C 274, 3C 405, 3C 461 at frequencies of 20 and 25 MHz in the radiometric mode. Later, several stages of modernization of radiometric equipment and systems for automation of observations took place. This made it possible by 2000 to switch to practically continuous radiometric monitoring of a group of these radio sources. Method of measuring and processing of the records of the radio sources passage through RT direction pattern, statistics of the observation records on time periods in dependence on the registration systems of the data obtained during more 35 years observations on the RT URAN-4 are considered in this paper. Some results are given which related to the study of the flux densities of the observing radio sources and ionospheric scintillation effect which is essential at the decameter wavelength range**.**

Keywords: radio astronomical observations; cosmic radio sources; decameter radio wave range.

АНОТАЦІЯ. Радіотелескоп (РТ) УРАН-4, який розміщений поблизу міста Одеса, був введений в стрій в 1987 році як складова частина радіоінтерофероментричної системи УРАН, що працює в декаметровому діапазоні радіохвиль та елементи якої розташовані в декількох пунктах на всій території України. Перші успішні РСДБ спостереження компактних космічних радіоджерел в системі УРАН були проведені на інтерферометрі РТ УРАН-4–УТР-2 в кінці 1987 року. В той же час була запущена програма регулярних спостережень потужних космічних радіоджерел 3С 144, 3С 274, 3С 405, 3С 461 на частотах 20 і 25 МГц в радіометричному режимі. Пізніше пройшло декілька етапів модернізації радіометричної апаратури і систем автоматизації спостережень. Це дозволило до 2000 року перейти до практично безперервного моніторингу групи названих радіоджерел. В роботі розглядаються методика вимірів і обробки записів проходження радіоджерел через діаграму спрямованості РТ, статистика записів спостережень по часовим інтервалам в залежності від системи реєстрації даних, що були отримані за більш ніж 35 років спостережень на РТ УРАН-4. Спостереження в декаметровому радіодіапазоні супроводжується великою кількістю радіоперешкод, які впливають на якість вимірювань. При обробці спостережень кожний запис отримує оцінки якості, що допомагає вибрати записи потрібної якості для конкретної дослідницької задачі. Наведено деякі результати, які стосуються досліджень щільності потоку спостережуваних джерел, зокрема показано, що середньомісячні значення цих величин варіюються протягом циклу сонячної активності. Ефект іоносферних мерехтінь є дуже суттєвим в декаметровому діапазоні радіохвиль. Всі спостережувані радіоджерела мерехтять на неоднорідностях електронної концентрації іоносферної плазми, тому це явище досліджувалось з початку спостережень на РТ. З допомогою розробленої методики обробки до теперішнього часу отримана велика кількість оцінок таких параметрів іоносферних мерехтінь як індекс, період і спектральний індекс. Це дозволило дослідити сезонно-добову залежність параметрів іоносферних мерехтінь, а також їх кутові залежності.

Ключові слова: радіоастрономічні спостереження; космічні радіоджерела; декаметровий діапазон радіохвиль

1. Introduction

The radio telescope (RT) URAN-4 is a component of the radio interferometric system URAN whose elements are placed in several points throughout Ukraine. The URAN system is intended for the investigations of cosmic objects with high resolution at the decameter range of radio waves. Particularities of this wave range are the essential influence of ionosphere, high level of the background cosmic radiation, presence of the large level of interferences which have different origin. Working range defines characteristics of the RT antenna and possibility to observe the different cosmic sources.

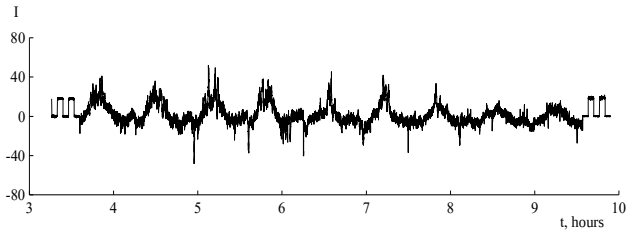

Figure 1: The example of the observation record of the radio source 3C 274 at the frequency 20 MHz during day

RT URAN-4 (Galanin et al., 1989) is located in the village Mayaky near Odessa and it is a multi-element antenna array with size 238×28 m. It includes antenna with phasing system, hardware complex, and precise time system and data registration. Direction pattern (DP) width at half power level, frequency 25 MHz, zenith position of the beam is $(2{,}7 \times 22)°$. The observations on the RT are carried out at four channels: at two frequencies (20 and 25 MHz) and for two polarizations (A and B). To separate the cosmic radio source signal from background noise the modulation measurement mode is used – signals of two half of the antenna array are multiplied.

RT not used most of the time in the interferometric measurements. Therefore for greater efficiency of its work the monitoring program of the studying of relative density flux non-stationarity of the power cosmic source was adopted. Four radio sources were chosen for this two of which are the supernova remnants (3C 144, 3C 461) and others two are the radio galaxies (3C 274, 3C 405).

The purpose of the paper is an overview of the RT URAN-4 work over a period of more than 35 years.

2. Data of the observations and processing

2.1. Observations

The observations at the RT URAN-4 are carried out as records of several passages of each radio source through RT DP during day. For calibration of relative measurements of flux densities the calibration step of the noise generator which is recorded in the beginning and in the end of measurement session is used (Derevyagin et al., 2019). The example of the observation record of the radio source on the RT is showed in the Figure 1.

2.2. Processing

The processing of each source record is carried out by the fitting of calculating function of the RT DP to the observing record of cosmic radio source (Panishko & Lytvynenko, 2019). As a result of processing the different characteristics of record were measured, for example, such as record amplitude and also the ionosphere scintillation parameters – index, period and spectral index. Data is stored in the text files of computer memory. The example of processing of the radio source record which obtained on the RT is showed in the Figure 2. The ionosphere scintillation parameters which estimated from record are given.

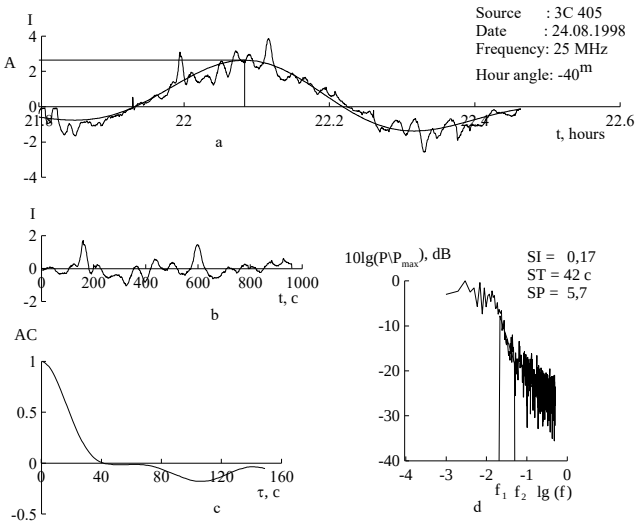

Figure 2: Example of the processing of the radio source record: a – row obtained from observations with fitting DP; b – high frequency part in the center of record (observation row without fitting direction pattern) that associated with ionospheric scintillations; c – autocorrelation function; d – power spectrum of the signal scintillations

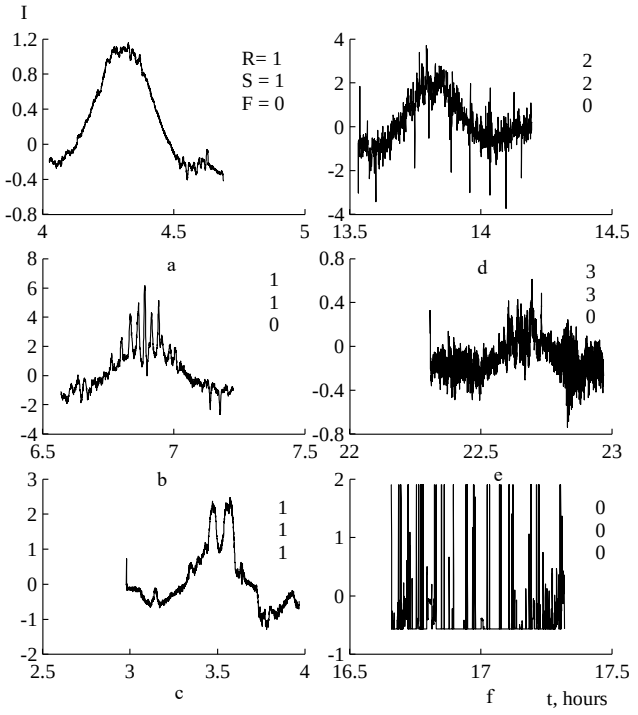

Figure 3: The examples of radio source records with different level of the interferences: a – record of good quality; b – record of good quality with scintillations; c – presence of the intensive fluctuations; d – record of satisfactory quality; e – the interferences strongly distort the record; f – the large interferences, record is not processed

2.3. Accounting of the radio interferences

Observations at the decameter radio wave range are accompanied by the presence of a large amount of interference of various origins. To account for them during processing, each record is evaluated as follows: 1) quality of the fitting of DP calculating function (R: 0..3); 2) presence of the interferences in a central part of record (S: 0..3); 3) presence of the intensive fluctuations which distort the overall form of the record (F: 0..1). The radio source records with different level of the interferences are showed in the Figure 3. When analyzing data, these ratings help select records of acceptable quality for a particular research problem.

3. Analysis of the observation data obtained at the RT URAN-4

3.1. Time intervals

There are some time intervals in the working of RT URAN-4 those characterized of several systems of data registration (Derevyagin et al., 2019):

1. From 1987-1990 regular observations of four radio sources carried out by sessions near 10 days during month. Measurements were written to paper tape of self-recorder. Processing was fulfilled manually with ruler.
2. In the 90s first automatical registration was developed that permitted to process of data using computer program but observations carried out very sporadically.
3. Regular measurements on RT began from 1998 and continued up to 2001. During this time new system of automatical measurements and digital registration with time interval 1 s was developed. From 2002 the registration system of observations was upgraded – automatical record of calibration step was appeared and time interval became 2 s. Measurements in such format continued up to April 2007. This data processed by computer program.
4. From 2007 up to 2010 regular observations on RT URAN-4 did not carried out due to technical occasions and were resumed in 2011. In this time next version of system of automatical measurements and digital registration was developed, time interval 1 s. This format uses in present time and new program of computer processing was created for it.

3.2. Statistics of the observation data

For the entire period of work of the RT URAN-4 the large amount of observation data was obtained. Statistics of the radio source records which observed at the RT is showed in the Table 1 for the above time intervals.

Distribution of the number of records depending on the record quality is showed in the Table 2 in percentages. When analyzing data, records with ratings 1 and 2 are usually used, this is about 40 percent of all recorded data, as follows from the table.

Table 1: Statistics of the radio source records which obtained at the RT URAN-4

Time interval, years	**Number of the obtained records**
1987-1990	8712
1998-2007	198340
2011-2023	446772
Sum	653824

Table 2: Distribution PR of the observation record number N in the dependence from a quality estimation R

R	**N**	**PR, %**
0	256993	40
1	51623	8
2	201774	31
3	134722	21

3.3. Influence of the solar activity cycle on the measurements of the flux densities of cosmic radio sources

Long-term observation data allows studying the behavior of the relative flux densities of cosmic radio sources including due to the impact of the solar activity. During solar cycle the concentration and temperature of the electron plasma particles in the higher atmosphere and, particularly, in the ionosphere are changed, that leads to a change in the nature of the interaction of radiation from the cosmic radio sources and the earth's ionosphere (Yakovlev, 1985). The behavior of the monthly mean values of the relative flux densities of the observing radio source during solar cycle at the frequency 25 MHz is showed in the Figure 4. You can notice a decrease in these values during maximum phase of solar cycle. The trend (sold line) is indicated by a polynomial of the fifth degree.

3.4. Ionospheric scintillations

The effect of the ionospheric scintillations is essential for observations at the decameter radio wave range (Crane, 1977). All observing radio sources are scintillated on the irregularities of the ionospheric plasma. The studying of this effect is carried out at the RT URAN-4 from the beginning of work that made it possible to obtain, in particularly, a seasonal-daily dependence (Lytvynenko & Panishko, 2015), which is well expressed for all ionospheric scintillation parameters (index, period and spectral index). Figure 5 shows the seasonal-daily dependence for a spectral index on the monthly mean values.

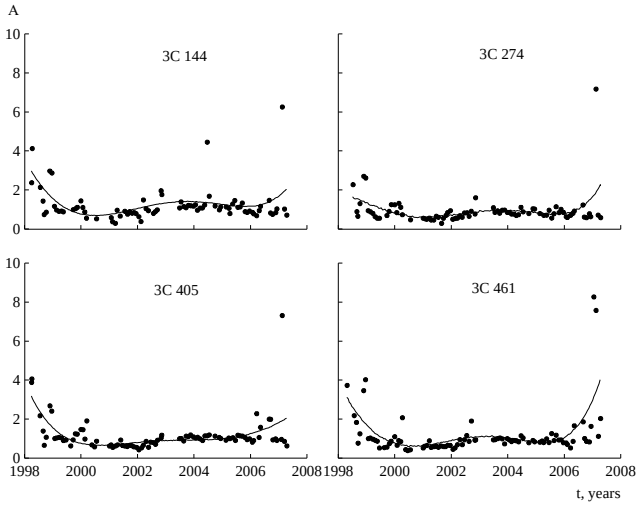

Figure 4: Absorption effect in the maximum of 23-th cycle of the solar activity on the monthly mean values of relative flux densities of the radio sources

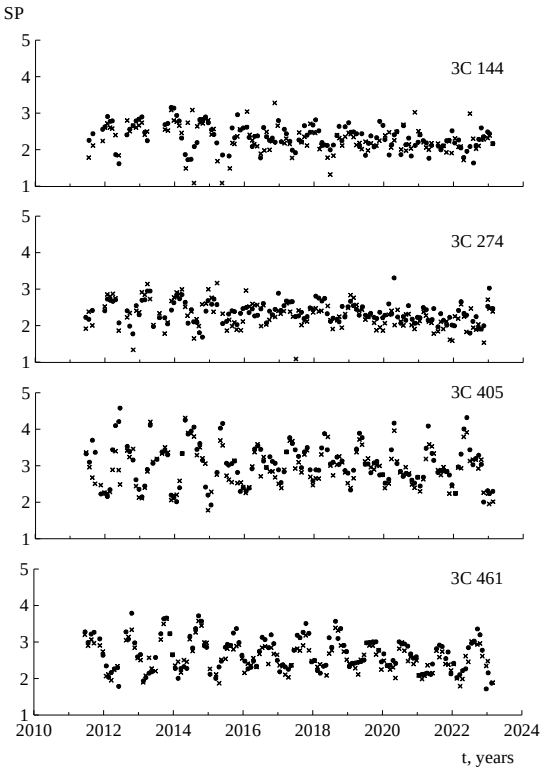

Figure 5: Seasonal-daily dependence of the ionospheric scintillation spectral index

Figure 6 shows the dependencies for the mean values of ionospheric scintillation parameters which calculated for each radio source (Panishko & Lytvynenko, 2019). Figure 6a (the inversely proportional dependence of an index on a period of ionospheric scintillations) and Figure 6b (the dependence of a scintillation period on an angle between direction on the radio source and a power line of the geomagnetic field) confirm that irregularities which caused ionospheric scintillations are stretched along geomagnetic field lines. At the same time, the magnitude of a spectral index depends on the height above horizon on which radio source are observed (Figure 6c). This connects with the reflective layer thickness (Lytvynenko et al., 2022) which changes with height.

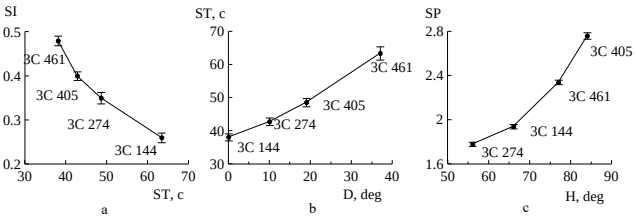

Figure 6: The angular dependencies of the ionospheric scintillation parameters: a – index–period; b – period–angle between the direction on the source and geomagnetic line; c – spectral index–height above the horizon

Conclusions

1. Using monitoring program long-term series of observations of power cosmic sources (3C 144, 3C 274, 3C 405, 3C 461) were obtained at the frequencies 20 and 25 MHz during 1987-2023.

2. Automatical digital registration from 1998 by means of the computer processing was allowed to get the values of relative fluxes and ionosphere scintillation parameters of the sources that observed. Keeping system of data with convenient access to original observations and processing results was designed.

3. Long-term measurements enabled the studying of regularity in the behavior of several values for several time intervals. In particular the effect of the absorption in the Earth's ionosphere of the radiation from cosmic radio sources in the maximum of the solar activity cycle was found. Also the seasonal-daily dependence of ionosphere scintillation index, period and spectral index and angular dependencies of the scintillation parameters were derived from observation data.

References

Galanin V.V., Inyutin G.A., Kvasha I.M. et al.: 1989, Kinematics and physics of celestial bodies, **5**, 87.

Derevyagin V.G., Kravetz R.O., Lytvynenko O.A. et al.: 2019, Proc. of 12th WS «Solar influences on the magnetosphere, ionosphere and atmosphere», Primorsko, Bulgaria, 84.

Panishko S.K., Lytvynenko O.A.: 2019, Radio physics and radio astronomy, **24**, 44.

Yakovlev O.I.: 1985, Propagation of radio waves in space (Nauka, M.), 216.

Crane R. K.: 1977, Proc. IEEE, **65**, 180.

Lytvynenko O.A., Panishko S. K.: 2015, OAP, **28**, 235.

Lytvynenko O., Panishko S., Derevyagin V.: 2022, Proc. of the 14th WS "Solar Influences on the Magnetosphere, Ionosphere and Atmosphere", Primorsko, Bulgaria, 41.

https://doi.org/10.18524/1810-4215.2023.36.290136

DECAMETER TYPE IV BURST WITH UNUSUAL HIGH POLARIZATION

V. N. Melnik [1], A. I. Brazhenko [2], A.V. Frantsuzenko [2], V. V. Dorovskyy [1], M. V. Shevchuk [1]

[1] Institute of Radio Astronomy, Kharkov, Ukraine, melnik@rian.kharkov.ua

[2] Institute of Geophysics, Gravimetrical Observatory, Poltava, Ukraine

ABSTRACT. We present results of observations of Type IV burst with unusual high polarization equalled in maximum phase about 100%. This burst was registered both by URAN-2 and NDA radio telescopes on 13 July 2022. It continued for about 5 hours and consisted of sub-bursts with high frequency drift rates and had short durations. We associate it with the weak CME, which propagated in the East direction in the form of thread-like structure. Theoretical description of sub-burst in the plasma mechanism of radio emission allow explaining their high polarization, high drift rates and short durations.

Keywords: Type IV bursts, CME, Sub-bursts, Frequency drift rates, Durations, Polarization, Plasma model of radio emission.

АНОТАЦІЯ. Ми обговорюємо результати спостережень сплеску IV типу з незвично великою поляризацією, яка досягає в максимальній фазі 100%. Цей сплеск було зареєстровано радіотелескопами УРАН-2 (Україна) та НДА (Франція) 13 липня 2022 року. Цей сплеск тривав біля 5 годин і мав тонку структуру у вигляді суб-сплесків з великою швидкістю дрейфу та малою тривалістю. Ми пов'язуємо цей сплеск з корональним викидом мас (CME), який розповсюджувався практично в східному напрямку у вигляді ниткоподібної структури. Теоретичний розгляд властивостей субсплесків за допомогою плазмового механізму радіовипромінювання дозволяє пояснити їх високу поляризацію, великі швидкості дрейфу та малу тривалість в рамках єдиного підходу.

Ключові слова: Сплески IV типу, сплеск з корональним викидом мас (CME), субсплески, частота швидкості дрейфу, тривалість, поляризація, плазмова модель радіовипромінювання.

1. Introduction

Type IV bursts were identified as a separate group of solar bursts by Boischot in 1957 (Boischot, 1957). At first they were observed at frequencies of meter and decimetre ranges (Stewart, 1985) and later in the decametre range (Gergely & Kundu, 1974). In the decametre range Type IV bursts continued from tens of minutes to some hours. They have fine structure in the form of sub-bursts similar to usual Type III bursts with smaller frequency drift rates (Mel'nik et al., 2008a; Melnik et al., 2010; Antonov et al., 2014; Bouratzis et al., 2015) and sometimes larger drift rates (Dididze et al., 2019). Durations of these sub-bursts can be both smaller (Melnik et al., 2010; Dididze et al., 2019) and larger (Mel'Nik et al., 2008a) than that for usual Type III bursts. In the meter range Type IV bursts also have similar sub-bursts (Bouratzis et al., 2015; Alissandrakis et al., 2019; Bouratzis et al., 2019) so-called fiber-bursts. Radio fluxes of decametre Type IV bursts do not exceed 1000 s.f.u. as a rule and their polarization is about 40% (Mel'nik et al., 2008a). At the same time observations of meter Type IV bursts showed that polarization could be frequently more than 85% (Smerd & Dulk, 1971) and even up to 100% (Liu et al., 2018). Historically at first a synchrotron mechanism of radio emission (Boischot, 1957) was proposed for an explanation of Type IV burst properties. Later preference was given to gyro synchrotron mechanism (Kai, 1969; Dulk, 1970) and finally to plasma mechanism offered in 1981 (Duncan, 1981).

The connection of decametre Type IV bursts with CME was studied in (Mel'nik et al., 2008a). It was found that among 13 Type IV bursts observed by radio telescope UTR-2 in frequency band 10-30 MHz for the period 2003-2006 12 of them were accompanied by CMEs. Later Hillaris et al. (2016) showed that 45 out of 48 decametre Type IV bursts observed with WIND/Waves at frequencies <14 MHz during 1998 – 2012. So we can conclude that decametre Type IV bursts and CMEs are connected with each other very closely. Moreover, it was shown (Melnik et al., 2018a; Melnik et al., 2020) that the sources of meter-decameter Type IV bursts observed on 2013 November 7 and 2017 September 6 were CME's cores.

In this paper properties of Type IV burst in the frequency band of 26 – 70 MHz with high polarization of up to 100% are discussed. We suppose that this burst can be associated not with a bright CME but with very weak CME. Besides this burst consists of sub-bursts with high frequency drift rates and small durations. Model, which agrees with the unusual properties of this Type IV burst, is discussed in the frame of radio emission plasma mechanism.

2. Observations

The radio telescope URAN-2 (Poltava, Ukraine) observed the solar radio emission from 4:50 UT to 16:50 UT on 13 July 2022. This radio telescope (Brazhenko et al., 2005) is a rectangular array with an effective area of

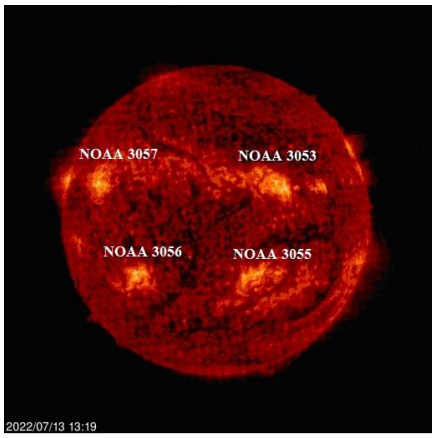

Figure 1: Solar disk on 13 July 2022 according to SOHO with active regions NOAA 3053, 3057, 3055 and 3056.

$28000m^2$ operated in the frequency band of 8 – 33 MHz. This antenna array has a size of $238m$ in East–West direction and $118m$ in North–South direction and a beam size of 3.5◦ × 7◦ at a frequency of 20 MHz. The signals were recorded with a digital spectrum analyzer (DSPz) (Ryabov et al., 2010; Zakharenko et al., 2016), which allows us to carry out observations with frequency-time resolution of 4 kHz – 100 ms, and dynamic range of 90 dB in the working frequency band. This radio telescope can also measure polarization of solar radio emission in the frequency band of 8-33 MHz.

This day active regions NOAA 3053 and 3057 in the northern hemisphere and NOAA 3055 and 3056 in the southern hemisphere were present on the solar disk (Figure 1). Some weak flares were detected this day and three very weak CMEs at 4:24:05, 9:36:07 and 13:25:48 were marked as poor events by catalogue SOHO-LASCO (https://cdaw.gsfc.nasa.gov/CME_list/UNIVERSAL_ver1/2022_07/univ2022_07.html).

At the same time radio emissions in the decametre and meter ranges were strong enough. From the beginning of the observations with URAN-2 there was weak storm of Type III bursts with fluxes not higher than 10 s.f.u. with some single Type III bursts reaching up to 200 s.f.u. (Figure 2a).

The Type IV burst at the frequency range of 26 – 33 MHz began at 7:00 UT and lasted untill 12:00 UT approximately (Figure 2a). The radio telescope NDA (Nancy, France) also registered this burst in the frequency band of 26 – 70 MHz from the beginning of its observation this day (Figure 2b).

As for the standard decametre Type IV bursts (Mel'Nik et al., 2008a) the flux of this burst was increasing from the background level, which in this case was about 1-2 s.f.u., to the maximum value approximately equalled 100 s.f.u. in 1-2 hours (Figure 3a). After that starting from about 10:00 UT the flux was decreasing during 2 hours to the background level. The polarization of Type IV burst also uniformly increased from the beginning to approximately 8:40 UT. During about 1 hour, from 8:40 to 9:40 UT, maximum polarization was 100%. Then it uniformly decreased to the end of the burst. In spite of the observations by NDA were begun practically from the maximum phase of the burst

Figure 2c showed that its polarization was mainly left handed and was practically 100%. Given Type IV burst has fine structure in the form of sub-bursts similar to standard Type III bursts as usual (Melnik et al., 2008a). Generally, such sub-bursts have higher and smaller frequency drift rates and durations compared with decametre Type III bursts for which standard values are –(2-4) MHz/s and 6-12 s correspondingly (Mel'nik, et al., 2005).

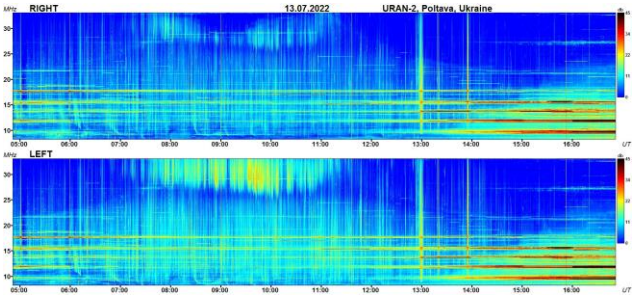

a)

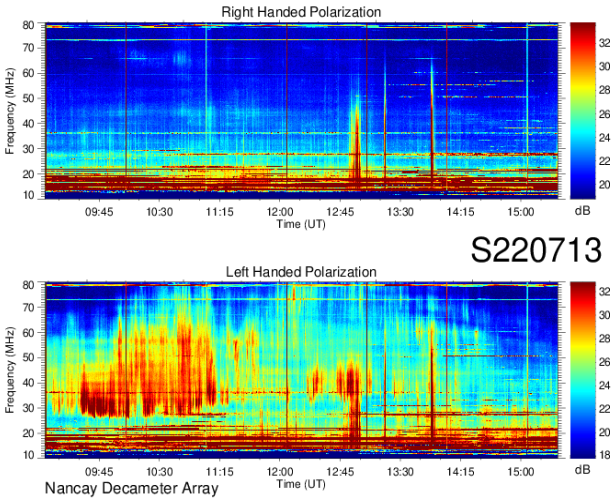

b)

Figure 2: The dynamic spectra of solar radio emission on 13 July 2022 according to URAN-2 (a) and NDA (b). Both spectra show left handed polarization mainly and absence of right one.

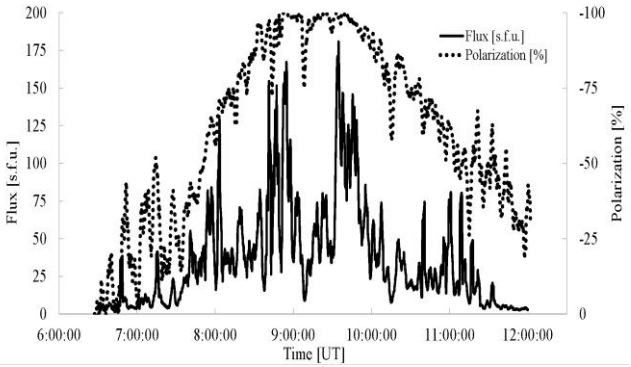

Figure 3: Flux and polarization in the form of a hump of the Type IV burst at frequency 32 MHz (URAN-2).

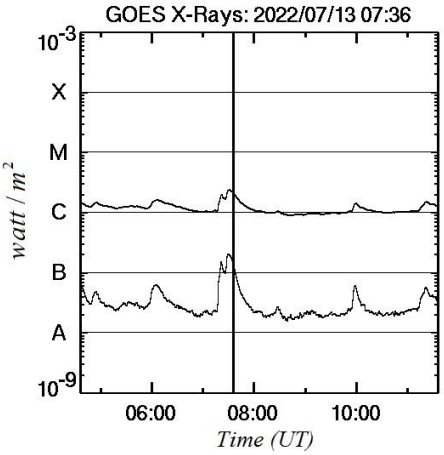

Figure 4: Flare in active region NOAA 3057 (N15 E52) in X-ray emission at 1-8A (upper curve) and at 0.5-4A (low curve) at 7:30 UT.

But usually these differences are not large, up to ten percents. In this case properties of sub-bursts distinguished very importantly. We measured parameters of sub-bursts such as durations, drift rates, fluxes and polarization at the rise, maximum and fall phases of Type IV burst and found that durations, drift rates, fluxes and polarizations were 0.6–2.6 s, -6 – -21 MHz/s (and sometimes positive), 50–700 s.f.u. and 90–100% (at the maximum of Type IV burst) correspondingly. Such parameters especially durations and drift rates remind single fast decametre Type III bursts (Melnik et al., 2008b) whose frequency drift rates were essentially higher and their durations were noticeably shorter than those of standard decametre Type III bursts (2–4 MHz/s and 6–12 s correspondingly). Those decametre Type III bursts were continuation of high frequency fast Type III bursts (so called Type III-like bursts) (Young et al., 1961; Elgaroy, 1980).

As we noticed already earlier practically all decametre Type IV bursts were associated with bright coronal mass ejections (CME). Most of them have standard structures consisting of bright leading edge, a dark void and a bright core (Aschwanden, 2004). Moreover, we put arguments (Melnik et al., 2018a; Melnik et al., 2020) that in those cases the sources of Type IV bursts are CME cores.

This day, as we said above, there were only weak CMEs and only CME at 9:36:07 UT can be associated with the Type IV burst observed by URAN-2 and NDA. This CME could be initiated by the flare at 7:30 (Figure 4). It was not practically seen in the optical band it was not seen practically but the differential optical emission (Figure 5) showed a thread-like structure of this CME, which had the length more than 4Rs at 11:36:00 UT. In this case it is reasonable to suppose that electron beam responsible for fast sub-bursts propagate along this thread-like structure of the CME.

3. Discussion

The main property of the discussed Type IV burst is its high polarization with maximum value of 100%. In our point of view, it is connected with the fact that sub-bursts of this Type IV burst are fast Type III bursts.

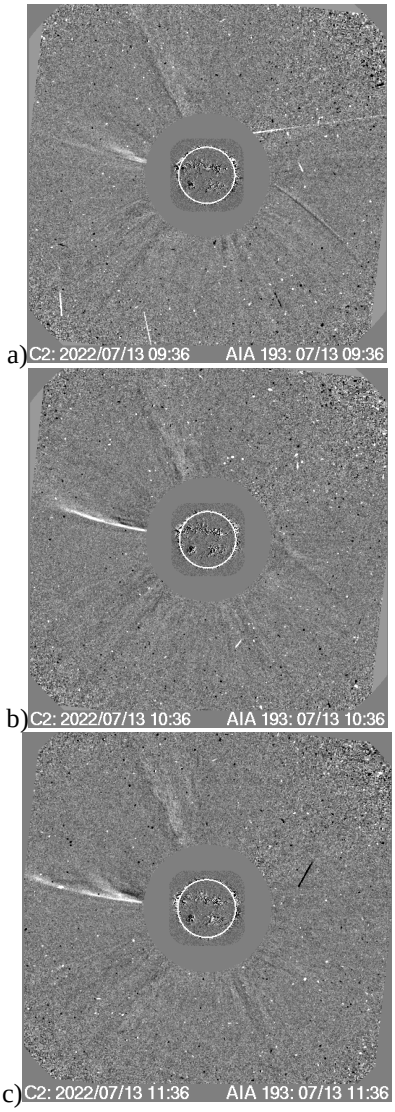

Figure 5: Differential optical radio emission according to SOHO at three different moments 9:36, 10:36 and 11:36 UT, which coincide with weak CME with velocity of 495 km/s and angular width of 12° (https://cdaw.gsfc.nasa.gov/CME_list/UNIVERSAL_ver1/2022_07/univ2022_07.html).

Let us consider the possible connection of high polarization of sub-bursts with their large drift rates in the plasma mechanism of radio emission. In the plasma theory of Type III bursts the Langmuir waves (Z-mode in plasma with magnetic field), l, generated by fast electrons, are transformed into O- or X- modes of electromagnetic waves, t, in the processes of scattering on ions, i, $l + i = t + i$ (Ginzburg & Zhelezniakov, 1958). According to the conservation of energy in these processes the frequency of electromagnetic wave equals to frequency of Langmuir wave $\omega_t = \omega_l$. Then if the frequency of Langmuir wave ω_l is smaller than the frequency $\omega_{pe} + \omega_{Be} / 2$ ($\omega_{pe} = \sqrt{4\pi e^2 n / m}$ is the plasma frequency, $\omega_{Be} = eB / mc$

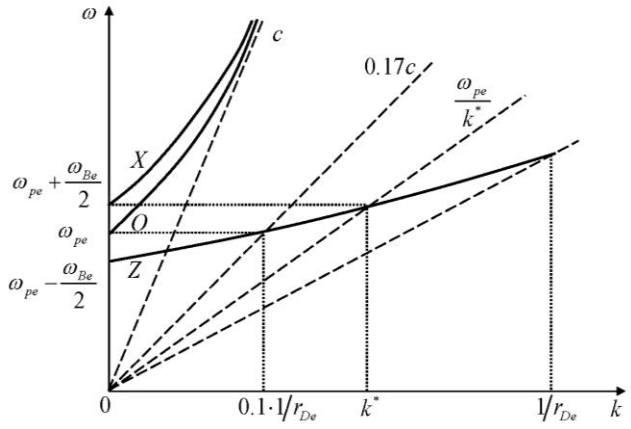

Figure 6: Dispersion curves for X-, O-, and Z-modes for plasma in a magnetic field (Achiezer et al., 1974).

is the electron cyclotron frequency) (Figure 5), Langmuir waves are transformed into O-mode only. At that the wave number of Langmuir wave k_l should be smaller than $k^* = \sqrt{\omega_{pe}\omega_{Be}/3}/v_{Te}$ (corresponding phase velocity is $v^* = \omega_{pe}/k^* = \sqrt{3\omega_{pe}/\omega_{Be}}\cdot v_{Te}$) (Melnik et al., 2018b). If the frequency of Langmuir wave ω_l is larger than $\omega_{pe} + \omega_{Be}/2$ then Langmuir waves can be transformed both into O- and X- modes. It is well known (see, for example, Zlotnik, 1981; Melrose, 1985) that the degree of the polarization is defined by the difference of X- and O-waves. In the first case electromagnetic waves have practically 100% O-polarization and in the second case the polarization is smaller.

As we said earlier sub-bursts of Type IV burst had high negative frequency drifts and even positive ones. As was shown in (Melnik et al., 2008b) large negative drifts and positive drifts (Melnik et al., 2015) of Type III-like bursts are explained by the approximate equality of velocity of electron beams responsible for these bursts and group velocity of electromagnetic waves generated by these beams. In the case of propagation of these electrons to the direction to the viewer this velocity is equal to $v_s = 5\cdot10^9 cm/s = 0.17c$ ($c = 3\cdot10^{10} cm/s$ is the speed of light) (Melnik et al., 2008b). If electrons move under the angle θ to the viewer then this velocity is $v_s = \frac{5\cdot10^9}{\sqrt{\cos\theta}} cm/s$. Under supposition that electron beams propagate along thread-like structure of CME the angle θ was $\theta = 52^\circ$ the velocity v_s was $v_s = 6.4\cdot10^9 cm/s$. If electron velocity is larger than these values then frequency drift rates of corresponding Type III bursts will be positive (Melnik et al., 2015). In the plasma mechanism of radio emission the fast electrons with velocity v_s generate Langmuir waves with wave numbers $k_s \approx \omega_{pe}/v_s$ mainly (Drummond & Pines, 1962; Vedenov et al., 1962). Interaction of these waves with beam electrons leads to the formation of a plateau on the electron distribution function from the maximum velocity v_s to some minimum velocity $v_{\min}$ during the time τ according to the equation (Vedenov & Ryutov, 1975)

$$v_s/v_{\min} + \ln(v_{\min}/v_s) = 1 + \frac{\pi}{\Lambda}\omega_{pe}\frac{n'}{n}\tau \qquad (1)$$

where n' and n are densities of fast electrons and background plasma and Λ is the Coulomb logarithm. In order to the generated Langmuir waves are transformed into O-mode it is necessary that $v_{\min}$ is greater than v^* (or $k_{\min} < k^*$, see Figure 5). For the very case when $v_{\min} = v^*$ ($k_{\min} = k^*$), the time τ of establishing plateau from v_s to $v_{\min}$ is equal approximately to sub-burst duration $\tau = 1s$ at frequency $f_{pe} = 30MHz$, magnetic field equal 2G we find from equation (1) that the density of fast electrons is about $n' = 0.2cm^{-3}$. So the beam of fast electrons with such density and the velocity a little smaller than $v_s = 6.4\cdot10^9 cm/s = 0.21c$ is a source of electromagnetic waves with 100% O-mode and high frequency drift rate. If $k_{\min} > k^*$ some of Langmuir waves will be transformed into X-mode (see Figure 5) and polarization will be smaller. If the velocity of fast electrons will be larger than $v_s = 6.4\cdot10^9 cm/s = 0.21c$ then corresponding sub-bursts will have positive drift rates and polarization will be also high.

In (Melnik et al., 2017) analysing interferometer observations of decametre Type III bursts we showed that sources sizes were approximately equal to $L \approx \tau\cdot v_b$, where τ is the Type III duration and v_b is the velocity of Type III electrons. Supposing that this estimate is true for the sub-bursts we can find brightness temperatures of sub-bursts radio emission

$$T_b = 5.5\cdot10^{29}\frac{\lambda^2 S}{\Theta_p\Theta_t} \qquad (2)$$

where S is the flux $[W/m^2Hz]$, Θ_p and Θ_t are source diameters [minutes] in equatorial and polar directions, and λ is the wavelength [m]. So we found brightness temperatures for the sub-bursts of Type IV burst, which are in the limits from $4\cdot10^{10}K$ to $5\cdot10^{12}K$ supposing that $\Theta_p \approx \Theta_t$. It means that in the plasma theory of radio emission such temperatures can be produced due to induced regime of transformation of Langmuir waves to electromagnetic ones (Melrose, 1985; Suzuki & Dulk, 1985; Mel'Nik & Kontar, 2003).

4. Conclusion

Type IV burst with high polarization up to 100% was observed by radio telescopes URAN-2 and NDA on 13 July 2022. Its duration was about 5 hours and frequency band was from 26 MHz to 50 MHz. Another peculiarity of

this burst was fine structure in the form of sub-bursts with high negative and sometimes even positive drift rates. These sub-bursts were short and their durations were in the range from 1 to 2.6 s mainly. According to these parameters these sub-bursts are similar to decametre Type III-like bursts (Melnik et al., 2008b). Besides these sub-bursts have high polarization up to 100%. We propose the interpretation of these properties in the frame of plasma mechanism of radio emission in the processes of $l + i = t + i$ with the generation of O-mode of electromagnetic waves. It allows estimating the density of fast electrons, which are the sources of sub-bursts.

Interesting peculiarity of the discussed Type IV burst is the absence of bright coronal mass ejection, CME, which usually accompany decametre Type IV bursts. In this case only very weak optical CME in the form of thread-like structure accompanied this Type IV burst.

Acknowledgements. All authors acknowledge funding from the NASU (National Academy of Sciences of Ukraine) project “Complex researches of sporadic radio emission of the Sun during 25 cycle of solar activity” (RADIUS) 0122U000616.

References

Achiezer A.I., Achiezer I.A., Polovin R.V., Sitenko A.G., Stepanov K.N.: 1974, Elektrodinamika plazmy, (Moscou), 720 p.

Alissandrakis C.E., Bouratzis C., Hillaris A.: 2019, *Astron. Astrophys*., **627**, A133.

Antonov A.V., Melnik V.N., Konovalenko A.A. et al.: 2014, *Radio Phys. Radio Astron.*, **19**, 295.

Aschwanden M.J.: 2004, Physics of the Solar Corona. An Introduction, (Springer, Chichester), 818.

Boischot A.: 1957, *Academie des Sciences Paris Comptes Rendus*, **244**, 1326.

Bouratzis C., Hillaris A., Alissandrakis et al.: 2015, *Solar Phys.*, **290**, 219.

Bouratzis C., Hillaris A., Alissandrakis C.E. et al.: 2019, *Astron. Astrophys*., **625**, A58.

Brazhenko A.I., Bulatsen V.G., Vashchishin R.V. et al.: 2005, *Kinem. i Fiz. Neb. Tel, Suppl.* **5**, 43.

Dididze G., Shergelashvili B.M., Melnik V.N. et al.: 2019, *Astron. Astrophys*., **625**, A63.

Drummond W.E., Pines D.: 1962, *Nucl. Fusion Suppl.*, **3**, 1049.

Dulk G.A.: 1970, *Proc. Astronomical Society of Australia*, **1**, 372.

Duncan R.A.: 1981, *Solar Phys.*, **73**, 191.

Ginzburg V.L., Zhelezniakov V.V.: 1958, *Soviet Astron.*, **2**, 653.

Gergely T.E., Kundu M.R.: 1974, *Solar Phys.*, **34**, 433.

Hillaris A., Bouratzis C., Nindos A.: 2016, *Solar Phys.*, **291**, 2049.

Elgaroy O.: 1980, *Astron. Astrophys*., **82**, 308.

Kai K.: 1969, Proc. *Astronomical Society of Australia*, **1**, 186.

Liu H., Chen Y., Cho K., et al.: 2018, *Solar Phys*., **293**, 10.

Mel'nik V.N. , Konovalenko A.A., Abranin E.P. et al.: 2005, *Astron. & Astrophys. Trans.*, **24**, 391.

Melnik V.N., Rucker H.O., Konovalenko A.A. et al.: 2008a, In: Wang, P. (ed.) *Solar Type IV Bursts at Frequencies 10-30 MHz*, 287.

Melnik V.N., Konovalenko A.A., Brazhenko A.I. et al.: 2010, Bursts in emission and absorption as a fine structure of Type IV bursts. In: Chakrabarti, S. K., Zhuk, A. I., and Bisnovatyi-Kogan, G. S. (eds.) *American Institute of Physics Conference Series*, **1206**, 450.

Melnik V.N., Brazhenko A.I., Konovalenko A.A., et al.: 2018a, *Solar Phys.*, **293**, 53.

Melnik V.N., Rucker H.O., Brazhenko A.I. et al.: 2020, *Astrophys. J.*, **905**, 5.

Mel'nik V.N., Konovalenko A.A., Rucker H.O., Rutkevych B.P., Dorovskyy V.V.: 2008b, *Solar Phys.*, **250**, 133.

Melnik V.N., Brazhenko A.I., Konovalenko A.A. et al.: 2015, *Solar Phys.*, **290**, 193.

Melnik V., Shepelev V., Brazhenko A. et al.: 2017, *Sun and Geosphere*, **12**, 105.

Melnik V.N., Brazhenko A.I., Frantsuzenko A.V., et al.: 2018b, *Solar Phys.*, **293**, 26

Mel'nik V.N., Kontar E.P.: 2003, *Solar Phys*. **215**, 335.

Melrose D.B.: 1985, In: McLean D.J., Labrum N.R. (eds.) *Solar Radio Physics*, 177.

Ryabov V.B., Vavriv D.M., Zarka P. et al.: 2010, *Astron. Astrophys*., **510**, A16.

Smerd S.F., Dulk G.A.: 1971, *Solar Magnetic Fields*, *IAUS* **43**, 616.

Stewart R.T.: 1985, In: McLean D.J., Labrum N.R. (eds.) *Solar Radio Physics*, 361.

Suzuki S., Dulk G.A.: 1985, In: McLean D.J., Labrum N.R. (eds.) *Solar Radio Physics*, 289.

Vedenov A.A., Velikhov E.P., Sagdeev R.Z.: 1962, *Nucl. Fusion Suppl.*, **2**, 465.

Vedenov A.A., Ryutov D.D.: 1975, In: Leontovich M.A. (ed.) *Reviews of Plasma Physics*, **6**, 1.

Young C.W., Spencer C.L., Moreton et al.: 1961, *Astrophys. J.*, **133**, 243.

Zakharenko V., Konovalenko A., Zarka P. et al.: 2016, *J. Astron. Instrum*. **5**, 1641010.

Zlotnik E.Ya.: 1981, *Astron. Astrophys*., **101**, 260.

https://doi.org/10.18524/1810-4215.2023.36.290137

THE JET KINETIC LUMINOSITIES FOR THE UTR-2 SOURCES WITH THE STEEP LOW-FREQUENCY SPECTRA

A.P. Miroshnichenko

Institute of Radio Astronomy of NASU, Kharkiv, Ukraine
a.p.miroshnichenko@gmail.com

ABSTRACT. Earlier we have determined that the UTR-2 radio sources with steep linear spectra possess greater jet propagation velocity and lesser characteristic age than the UTR-2 radio sources with steep break spectra. Also examined galaxies and quasars with steep break spectra display greater mean values of the central black hole masses and mass accretion rates, than corresponding these for galaxies and quasars with steep linear spectra. Besides, as we have determined, the radio structure of the UTR-2 steep-spectrum sources is giant, its linear size has Mpc-scale. The source's giant structure is formed by jets with enveloped radio lobes. So, this indicates on the powerful jets of the radio sources with the steep low-frequency spectra. Since the source jets are connected with the accretion disk of the source, it is important to examine relations of their physical characteristics. With this purpose we obtain estimates of the jet kinetic luminosity for the UTR-2 steep-spectrum sources on the assumption of the equality of the corresponding mass accretion rate and the jet matter flux. Using our calculated values of the jet propagation velocity and the mass accretion rate for the UTR-2 steep-spectrum galaxies and quasars, we estimate their jet kinetic luminosities. The obtained values of the jet kinetic luminosities are ~ 10^{45} erg/s, pointing out the great power of jets for the examined steep-spectrum sources. It is essential, that the examined objects display the relation of their kinetic luminosity and corresponding redshift (cosmological evolution).

Keywords: Steep-spectrum radio sources, jets, galaxies, quasars, mass accretion rate, kinetic luminosity.

АНОТАЦІЯ. Раніше ми отримали, що радіоджерела з каталогу УТР-2, які мають круті лінійні спектри, мають більшу швидкість поширення джетів і менший характерний вік, ніж УТР-2 джерела з крутими спектрами зі зламом. Також досліджувані галактики і квазари з крутими спектрами зі зламом проявляють більші середні величини мас центральних чорних дір і темпів акреції маси, ніж відповідні величини для галактик і квазарів з крутими лінійними спектрами. Крім того, ми отримали, що радіоструктура УТР-2 джерел з крутими спектрами є велетенською, її лінійний розмір має мегапарсековий масштаб. Ця велетенська структура джерел формується джетами та їхніми радіопелюстками. Отже, це вказує на потужні джети радіоджерел з крутими низькочастотними спектрами. Оскільки джети джерела пов'язані з акреційним диском джерела, важливо дослідити співвідношення їх фізичних характеристик. З цією метою ми отримуємо оцінки кінетичної світності джетів для УТР-2 джерел з крутими спектрами, припускаючи рівність відповідного темпу акреції маси та потоку речовини джета. Використовуючи обчислені нами величини швидкості поширення джетів і темпу акреції маси для УТР-2 галактик і квазарів з крутим спектром, ми одержали оцінку кінетичної світності їхніх джетів. Отримані значення кінетичної світності джетів становлять ~ 10^{45} ерг/с , вказуючи на велику потужність джетів розглянутих джерел з крутими спектрами. Важливо, що досліджувані об'єкти показують залежність їхньої кінетичної світності відносно відповідного червоного зміщення (космологічну еволюцію).

Ключові слова: Радіоджерела з крутим спектром, джети, галактики, квазари, темп акреції маси, кінетична світність.

1. Introduction

It is known that extragalactic radio sources – galaxies and quasars contain active nuclei. In active nuclei of galaxies and quasars the supermassive black hole accretes the surrounding matter. Modern studies show the structure of the active galactic nuclei at the scales by order of some tenth of light year (Fig. 1). This structure includes the supermassive black hole, accretion disk with its crown, gas-dust torus and extended jets – narrow beams of energetic particles. The emission of accretion disk is connected with optical and high-frequency radio emission. The crown of accretion disk is emitter of X-rays. The gas-dust torus is connected with infrared emission, and jets and their radio lobes are bright regions of low-frequency radio emission. At the decameter wavelengths – at the lowest frequency range for the ground radio telescopes – the jets may be very intensive at the steep spectrum of synchrotron radiation of the source. Indeed, the UTR-2 steep spectrum sources (with value of the spectral indices $\alpha \geq 1$) possess the great luminosity at the decameter wavelengths.

2. Estimate of the jet kinetic luminosities for the UTR-2 sources with the steep low-frequency spectra

As we have derived before (Miroshnichenko, 2010 – 2021), sources with the steep low-frequency spectra from

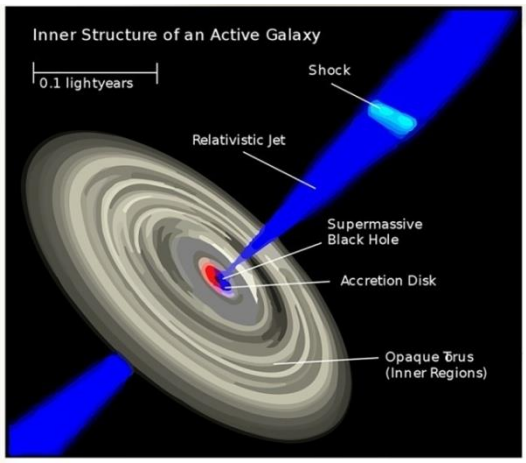

Figure 1: The scheme of active nucleus of radio source

the UTR-2 catalogue (Braude et al., 1978, 1979, 1981, 2003) have great monochromatic luminosity at the decameter band (the monochromatic luminosity at the frequency 25 MHz is ~ 10^{28} W/(Hz·sterad), the giant radio structure (its linear size is ~ Mpc), the great characteristic age (10^8 years), the sublight jet propagation velocity (~ 0.1 s), the great mass of the central black hole (10^8 – 10^9 Mo). These sources have two spectral types: S (steep linear radio spectrum) and C+ (steep break radio spectrum) (Fig. 2). For determining of the characteristics of the steep-spectrum sources, we examine the sample of these sources from the UTR-2 catalogue (78 galaxies and 55 quasars with steep linear radio spectrum, and 54 galaxies and 36 quasars with steep break radio spectrum). Corresponding identifications of the sample sources in the centimeter, infrared, optical, X-ray bands have been made with the NED data base. As the result we have composed 4 subsamples: 53 galaxies with steep linear spectrum (Gs), 37 galaxies with steep break spectrum (Gc+), 45 quasars with steep linear spectrum (Qs), 29 quasars with steep break spectrum (Qc+).

Before (Miroshnichenko, 2019) we have determined that the UTR-2 sources with steep linear spectrum possess greater jet propagation velocity than the UTR-2 radio sources with steep break spectrum:

G_S $< V_j > = 2.97*10^9$ (+- $0.67*10^9$) cm/s ;

Gc+ $< V_j > = 5.78*10^8$ (+- $4.09*10^8$) cm/s ;

Q_S $< V_j > = 3.12*10^9$ (+- $0.31*10^9$) cm/s ;

Qc+ $< V_j > = 1.65*10^9$ (+- $0.45*10^9$) cm/s .

Also, the examined galaxies and quasars with steep break spectrum display greater mean values of the central black hole masses and mass accretion rates, than corresponding ones for galaxies and quasars with steep linear spectrum (Miroshnichenko, 2018).

Since the source jets are connected with the accretion disk of the source, it is important to examine relations of their physical characteristics. The process of accretion on the black hole of source is characterized by the mass accretion rate $\left(\frac{dM}{dt}\right)_{Edd}$ (Shakura & Sunyaev, 1973). In the theory of accretion disks it is usually assumed that the luminosity of the disk is bounded by the Eddington luminosity (Frank et al., 2002; Li, 2012). The Eddington luminosity L_{Edd} is the limit luminosity of source when the light pressure is balanced with the gravity force (Shakura & Sunyaev, 1973).

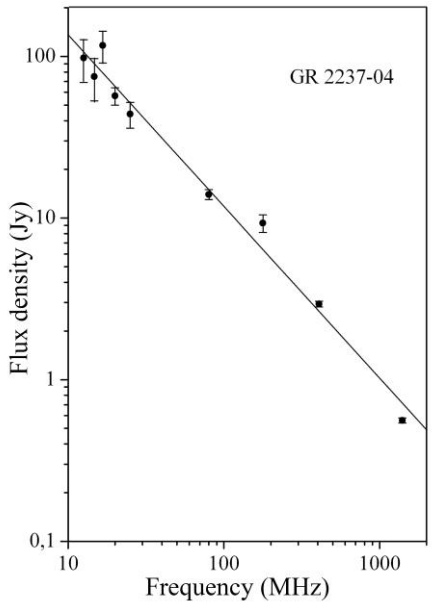

a)

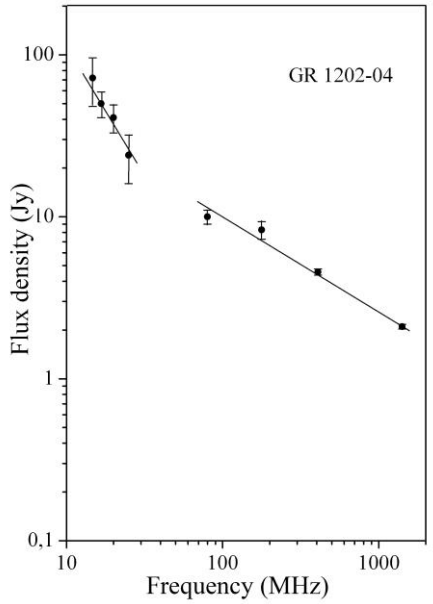

b)

Figure 2: Examples of spectral types S (a) and C+ (b) for steep-spectrum sources from the UTR-2 catalogue

We obtain the estimate of the kinetic luminosity of jets for examined sources from the assumption about the approximate equality of the mass accretion rate and the jet matter flux:

$$L_k = \frac{\dot{M}_j V_j^2}{2} \quad ,$$

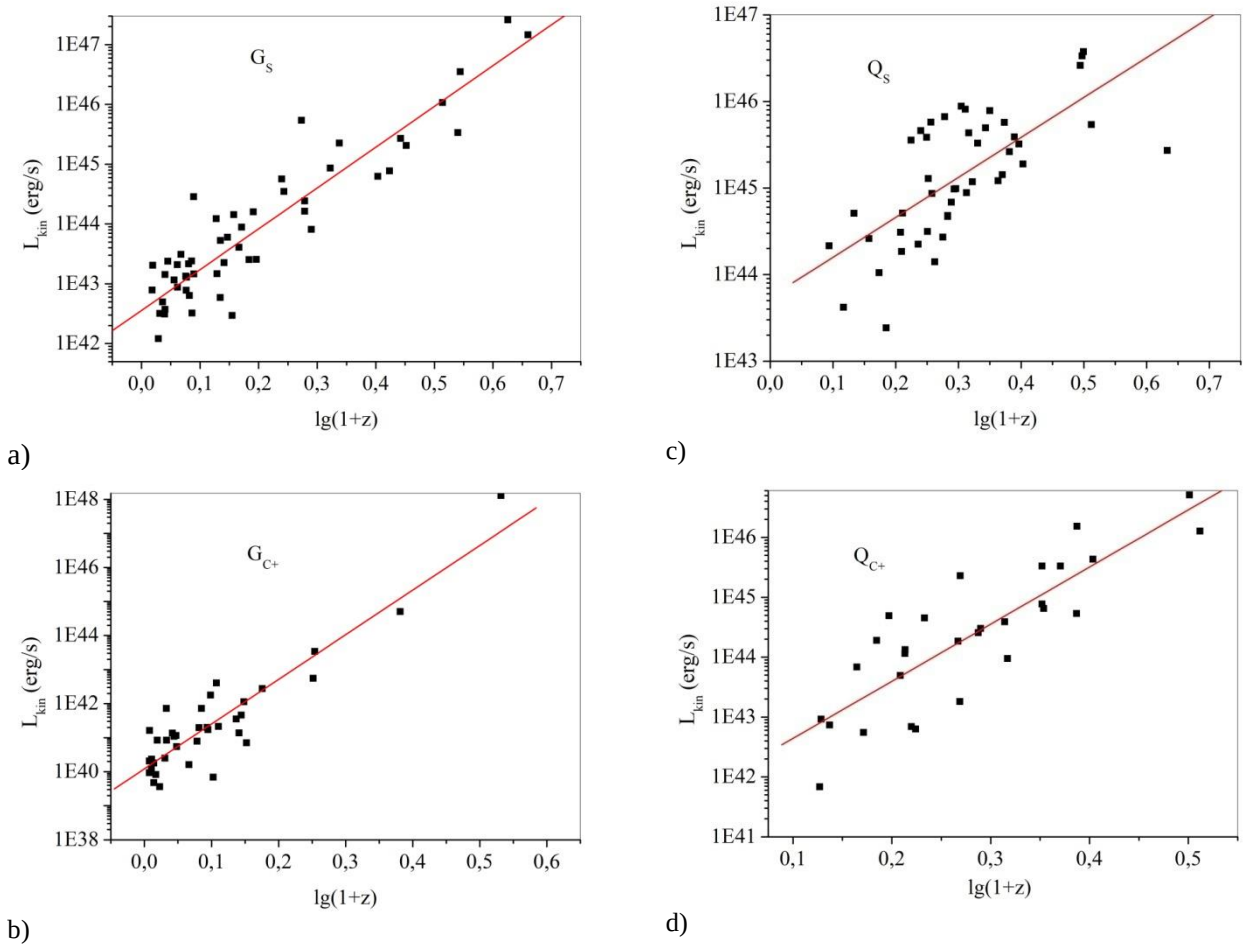

Figure 3: The relation of jet kinetic luminosity and redshift for G_S (a), G_{C+} (b), Q_S (c) and Q_{C+} (d).

where $\dot{M}$ is the jet matter flux, Vj is the jet propagation velocity. Then we obtain:

$$L_{kinet} = \frac{\dot{M}V_j^2}{2} = \frac{\left(\frac{dM}{dt}\right)_{Edd} V_j^2}{2}.$$

The derived values of the kinetic luminosity point out the powerful jets of source with low-frequency steep spectrum:

G_S $\langle L_{kinet} \rangle = = 8.90(\pm 5.58)\cdot 10^{45}\ erg/s$;

G_{C+} $\langle L_{kinet} \rangle = = 3.52(\pm 3.52)\cdot 10^{46}\ erg/s$;

Q_S $\langle L_{kinet} \rangle = = 4.41(\pm 1.20)\cdot 10^{45}\ erg/s$;

Q_{C+} $\langle L_{kinet} \rangle = = 3.35(\pm 1.83)\cdot 10^{45}\ erg/s$.

Since the examined objects cover the redshift range z = 0,017 to z = 3,57, we consider the relation of the obtained kinetic luminosities and the corresponding redshifts. The sample objects with steep break spectrum display considerable relationship from redshift in comparison with the linear spectrum objects (see Fig. 3(a,b,c,d)):

G_S k = 0.91

$L_{kinet} = 6.82(\pm 0.42)\lg(1+z) + 42.55(\pm 0.11)$;

G_{C+} k = 0.91

$L_{kinet} = 13.12(\pm 0.99)\lg(1+z) + 40.09(\pm 0.15)$;

Q_S k = 0.70

$L_{kinet} = 4.62(\pm 0.73)\lg(1+z) + 43.74(\pm 0.23)$;

Q_{C+} k = 0.84

$L_{kinet} = 9.54(\pm 1.17)\lg(1+z) + 41.69(\pm 0.35)$.

3. Conclusion

To continue the study of radio sources with steep low-frequency spectra from the UTR-2 catalogue, the estimates of the jet kinetic luminosity in these sources have been derived.

The obtained estimates of the jet kinetic luminosities point out the great power of jets of the steep-spectrum sources (10^{45} erg/s).

The relationship of the kinetic luminosity of jets and redshift (as cosmological evolution) is revealed, especially, for sources with steep break spectrum.

Acknowledgements. This research has made use of NASA's Astrophysics Data System Bibliographic Services.

References

Braude S. et al.: 1978, *Astrophys. Space Sci.*, **54**, 37.
Braude S. et al.: 1979, *Astrophys. Space Sci.*, **64**, 73.
Braude S. et al.: 1981a, *Astrophys. Space Sci.*, **74**, 409.
Braude S. et al.: 1981b, *Astrophys. Space Sci.*, **76**, 279.
Braude S. et al.: 2003, *Kinet. Phys. Celest. Bod*., **19**, 291.
Frank J., King A., Raine D.: 2002, Accretion Power in Astrophysics. (Cambridge Univ. Press, Cambridge).
Li L.-X.: 2012, *MNRAS*, **424**, 1461.
Miroshnichenko A.: 2012a, *Radio Physics and Radio Astronomy*, **3**, 215.
Miroshnichenko A.: 2012b, *Odessa Astronomical Publications*, **25**, 197.
Miroshnichenko A.: 2013, *Odessa Astronomical Publications*, **26**/**2**, 197.
Miroshnichenko A.: 2014, *in Multiwavelength AGN Surveys and Studies*, Cambridge, 96.
Miroshnichenko A.: 2015, *Odessa Astronomical Publications*, **28**/**2**, 238.
Miroshnichenko A.: 2017, *Odessa Astronomical Publications*, **30**, 236.
Miroshnichenko A.: 2018, *Abstracts of IX Scientific Conference "Selected Issues of Astronomy and Astrophysics"I, Franko National University of Lviv*, 32.
Miroshnichenko A.: 2019, *Astrophys Space Sci.*, **364**, A92.
Miroshnichenko A.: 2021, *Radio Physics and Radio Astronomy*, **26**, 165.
Shakura N., Sunyaev R.: 1973, *Astron. Astrophys.*, **24**, 337.

https://doi.org/10.18524/1810-4215.2023.36.290141

INTERFEROMETRIC OBSERVATIONS OF THE QUIET SUN AT DECAMETER WAVELENGTHS UNDER STRONG RADIO FREQUENCY INTERFERENCE

V. Shepelev[1], R. Vashchishin[2], V. Dorovskyy[1], V. Melnik[1], M. Shevchuk[1]

[1] Institute of Radio Astronomy of the NAS of Ukraine, Kharkiv, Ukraine. shep@rian.kharkov.ua

[2] Gravimetric Observatory of the Institute of Geophysics of the NAS of Ukraine, Poltava, Ukraine. vrv.uran2@gmail.com

ABSTRACT. Studies of the quiet Sun radio emission were carried out in a wide range of wavelengths from extremely short up to decameter ones. At the longest wavelengths, the measurements of angular sizes of the solar corona were previously carried out using the UTR-2 radio telescope in the scanning mode. We have developed a simple interferometric technique for measuring the angular diameter of an extended radio source. It uses a set of interferometers formed from the antenna sections of the north-south and east-west arms of the UTR-2 radio telescope to measure the size of the quiet Sun in the equatorial and polar directions. The first interferometric observations with this approach were carried out using the receivers and software of the URAN interferometers back in 2014. That study allowed us to determine equatorial and polar solar sizes at the fixed frequencies of 20 and 25 MHz. To expand the frequency range of the studies in the following observations, we used broadband digital DSPZ receivers in the correlation mode. However, in the daytime, broadband observations are complicated by radio frequency interference of various types, which often significantly exceed the level of wanted signals. To limit the effect of RFI, software has been developed that automatically detects and mitigates narrowband and impulse interference in a recorded signal. The paper describes the methods of RFI mitigation and criteria for the degree of signal clearing, which are used in this software. We also present the measurement results of the angular parameters of the quiet Sun radio emission, which were obtained by the interferometric method in the frequency range of 10 – 30 MHz. The observations were carried out during the minimum of solar activity in 2018 – 2020.

Keywords: quiet Sun, interferometer, decameter range, interferences.

АНОТАЦІЯ. Дослідження радіовипромінювання спокійного Сонця проводилися в широкому діапазоні довжин хвиль від гранично коротких до декаметрових. На найбільших довжинах хвиль вимірювання кутових розмірів сонячної корони за допомогою радіотелескопа УТР-2 раніше проводилися в режимі сканування. Ми розробили просту інтерферометричну методику для вимірювання кутового діаметра протяжного радіоджерела. В ній використовується низка інтерферометрів, сформованих із секцій північно-південної та східно-західної антени радіотелескопа UTR-2 для вимірювання розміру спокійного Сонця в полярному та екваторіальному напрямках. Перші інтерферометричні спостереження з таким підходом були проведені за допомогою приймачів і програмного забезпечення інтерферометрів УРАН ще в 2014 році. Ці дослідження дозволили визначити екваторіальні та полярні розміри Сонця на фіксованих частотах 20 і 25 МГц. Для розширення частотного діапазону досліджень у наступних спостереженнях використовувалися широкосмугові цифрові приймачі DSPZ у кореляційному режимі. Однак у денний час широкосмугові спостереження ускладнені радіочастотними завадами різного типу, які часто значно перевищують рівень корисних сигналів. Щоб обмежити вплив радіочастотних завад, було розроблено програмне забезпечення, яке автоматично виявляє та видаляє вузькосмугові та імпульсні завади в зареєстрованих сигналах. У статті описано методи боротьби з такими завадами та критерії ступеня очищення сигналу, які використовуються в цьому програмному забезпеченні. Ми також наводимо результати вимірювань кутових параметрів радіовипромінювання спокійного Сонця, отримані інтерферометричним методом в діапазоні частот 10 – 30 МГц. Спостереження проводилися під час мінімуму сонячної активності в 2018 – 2020 роках

Ключові слова: спокійне Сонце, інтерферометр, декаметровий діапазон, інтерференція.

1. Introduction

Radio emission of the quiet Sun has been studied since the 1940s in a wide range of wavelengths from millimeters to meters. Individual observations were also made at frequencies close to the decameter range. Thus, in 1971, observations were made using the Arecibo radio telescope (Aubier et al, 1971) and the flux density, equatorial diameter, and brightness temperature of the quiet Sun at the frequencies of 29.3 and 36.9 MHz were obtained. Later, at close frequencies, studies were performed with the Clark

Lake (Erickson et al, 1977), UTR-2 (Abranin et al, 1986), and Gauribidanur (Sastry, 1994) radio telescopes. It was found that the parameters of the quiet Sun change depending on the period of solar activity. Most of these studies, including those with UTR-2, used scanning radio heliographs (Stanislavsky et al, 2013). As it is known, when an object is scanned by a beam, the output signal is a convolution of the brightness distribution of the observed radio source and the telescope beam pattern. The true size of the object is easily determined by the width of the response if the angular dimensions of the source significantly exceed the width of the beam. With their close dimensions, antenna smoothing leads to an increase in the width of the response compared to the real size and must be taken into account. So, for example, the width of the beam pattern of the UTR-2 radio telescope at the frequency of 25 MHz is 25' and is close to the angular diameter of the quiet Sun at this frequency. In addition, measurements by the scanning method are complicated by the fact that the beam patterns of array antennas used in low-frequency radio astronomy have a significant level of side lobes. furthermore, correlation-type radiometers, which are used on UTR-2 to eliminate the influence of the galactic background, have sign-changing side lobes, the two-dimensional picture of which is quite complex and changes noticeably depending on the orientation of the telescope beam. All this makes it much more difficult to take into account the effect of antenna smoothing when determining the true size of the source.

Alternatively, an interferometric method is used to measure the angular size of radio sources. The north-south and east-west antenna arrays of the UTR-2 radio telescope consist of several identical sections spaced at a distance of 225 m, which can be used to create some interferometers with baselines of up to 1575 m in the north-south direction and up to 675 meters in the east-west. This structure of the radio telescope and the identical parameters of its sections made it possible to develop a simple interferometric technique (Shepelev, 2015) for studying the angular structure of extended sources, such as solar radiation. This technique was used in observations of the quiet Sun conducted in 2014 (Melnik et al, 2018). In this study, we used receivers of the URAN interferometers (Rashkovsky et al, 2012) with a bandwidth of 250 kHz operated at fixed frequencies in the decameter range. Note that these receivers have an effective algorithm for suppressing narrowband interference at the signal recording stage. This algorithm made it possible to carry out observations during the daytime in conditions of a large amount of radio frequency interference. In these observations, the flux density, size, and brightness temperature of the quiet Sun were measured at 20 and 25 MHz. It was also shown that the dependence of the normalized visibility function on the length of the interferometer baseline (Fig. 1) is in good agreement with the calculation for a source with a Gaussian brightness distribution according to the well-known expression:

$$\gamma_n = \exp\left(-\left(\frac{\pi\theta L}{2\sqrt{\ln(2)}\lambda}\right)^2\right), \qquad (1)$$

where L is the length of the interferometer baseline, θ is the angular diameter of the source at half brightness, and λ is the wavelength.

In this case, by measuring the visibility function on two arbitrary baselines, one can determine the angular size using the formula

$$\theta = \frac{2\lambda\sqrt{\ln(2)}}{\pi}\sqrt{\frac{\ln(\gamma_1/\gamma_2)}{\left(L_2^2 - L_1^2\right)}}, \qquad (2)$$

where L_1 and L_2 are the lengths of the interferometer baselines, γ_1, and γ_2 are the visibilities measured on these baselines.

Observations were conducted at two frequencies and showed that it is necessary to expand the frequency range of observation for a more accurate determination of the model of the solar corona and to determine how parameters of the quiet Sun depend on the wavelength.

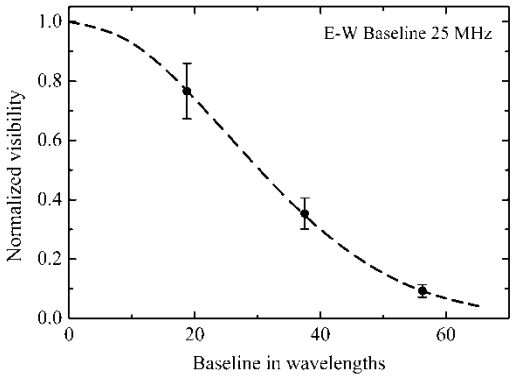

Figure 1: Normalized visibility of the quiet Sun in the east-west direction at 25 MHz and calculated dependency for radio source with Gaussian brightness distribution

2. Broadband observations

The UTR-2 radio telescope is equipped with broadband digital spectral polarimeters DSPZ (Zakharenko et al., 2016) capable of recording signals in the range from 8 to 33 MHz which can be used for interferometric study according technique described. These receivers have two inputs and form at their output a complex dynamic cross-spectrum that is the dependence of covariance of two input signals on frequency and time. Two receivers connected to outputs of the sections of the arrays of the UTR-2 radio telescope form two interferometers with different baselines and allow measuring the angular size of the quiet Sun according to expression (2) in the entire frequency range. To demonstrate the possibility of such a study in a wide frequency range we observed the Sun during the week of April 2015 (Shepelev et al, 2017).

This experiment showed that the main problem with broadband observations during the daytime is the large amount of radio frequency interference, especially in the long-wave part of the range. This problem is aggravated by the use of individual sections of UTR-2 as interferometer antennas, which have a wider beam than that of the entire telescope. In addition, the radiation of the quiet Sun is quite weak at decameter waves and does not have frequ-

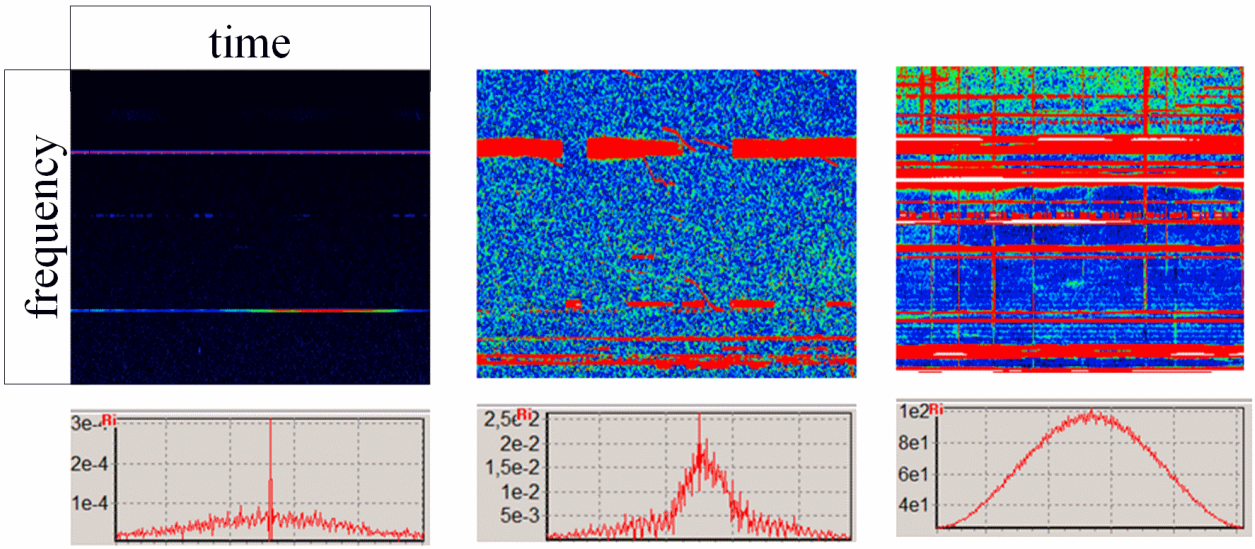

Figure 2: Interference in decameter range

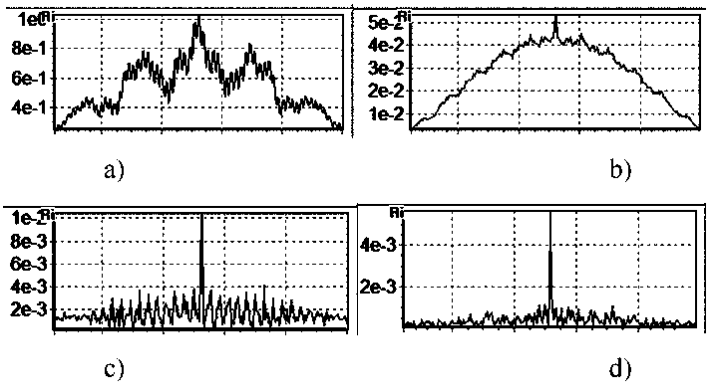

Figure 3: Correlation functions of the "dirty" signal (a) and after two (b), three (c), and four (d) cleaning iterations

ency-time features that make it possible to distinguish it from the interference background.

The broadband DSPZ receivers cannot mitigate interference during observations, which is inherent in URAN receivers, but they have a high dynamic range, which eliminates signal distortion, so interference can be removed at the signal processing stage. To solve these problems, software was developed that allows:

- select a frequency-time frame of the registered with DSPZ correlation dynamic spectrum (cross-spectrum) with a width of up to ΔF = 1 Mhz in frequency and several minutes in time;
- carry out automatic cleaning of this area from narrowband and pulse interference;
- perform coherent integration of the signal in the selected frame;
- calculate the visibility functions and the size of the radiation source;
- visualize processing and results.

The dependence of the module of the visibility function on the differential delay of the input signals of the interferometer (correlation function) serves as an indicator of the presence of interference and a criterion for cleaning the signal since it is significantly different for a wide-band signal of a radio source and narrow-band interference. As is known, the spectrum of the signal at the output of the interferometer and its correlation function are related by a pair of Fourier transforms.

The width of the main lobe $\Delta\tau$ of the correlation function of the useful signal is determined by the width of the spectral window ΔF so that $\Delta\tau \sim 1/\Delta F$. With the selected frame band of 1 MHz, the correlation function has a delta shape with the width $\Delta\tau \sim 1\mu s$. Interference has much narrower spectra, and therefore broader correlation functions. Hence, an obvious way to determine the contribution of radio frequency interference to the signal power of the observed source is the analysis of the entire form of the correlation function. However, with a high level of interference and their large quantity, it is quite difficult to separate the contribution of the signal and interference. In some cases, the interference contribution significantly exceeds the level of the useful signal. Figure 2 shows screenshots of the processing software: dynamic spectra

and corresponding averaged correlation functions for three different cases. The upper row shows frames of dynamic spectra with a width of 1 MHz (vertically) and one minute (horizontally). The bottom row is the correlation function of the signal and interference sum.

Here, the interference level increases from left to right, and the correlation function changes accordingly from a simple situation where the signal contribution can be easily determined to a case where the signal is difficult to detect. It is obvious that preliminary cleaning of the dynamic spectrum is necessary. One of the most effective filtering methods, which was used in the URAN receivers, operates according to the following algorithm:

– signal spectrum modules in frequency channels are integrated in a few seconds to increase sensitivity;
– statistical characteristics of the sequence of signal levels in spectrum channels are calculated;
– channels with signal level that exceeds the value of the average level by more than 4 σ (σ is a standard deviation) are considered to be affected by interference and are removed;
– this procedure is cyclically repeated a given number of times.

It was found that in most cases two to four iterations are enough to significantly improve the shape of the correlation function, which is an indicator of the correctness of processing. The goal is to bring it closer to the delta function characteristic of a "pure" signal. Figure 3 demonstrates screenshots of the software, which show the correlation functions of the signal with interference before and after several iterations of the described processing. Note that the level of the correlation function in Fig. 3a is more than two orders of magnitude higher than the level of the "purified" signal in Fig. 3d.

Short pulse interferences that significantly affect the signal level during time averaging can also be removed using a similar algorithm.

New interferometric observations of the quiet Sun and their processing using this software were carried out in the summer of 2018-2020 during the minimum solar activity. Four DSPZ receivers were used to form pairs of interferometers in each direction from the NS and EW antenna sections. Interferometer baselines were 225 and 450 m or 225 and 675 m at different times. The full receiver frequency recording range of 8–32 MHz was used, but a limited range of 10–30 MHz was used for processing. The most reliable data were obtained at frequencies from 15 to 30 MHz, except frequencies close to 27 MHz, where powerful broadband interference is observed. An example of the dependence of the angular size of the quiet Sun on the operational frequency obtained in observations with strong interference, which demonstrates the capabilities of the software, is shown in Fig. 4.

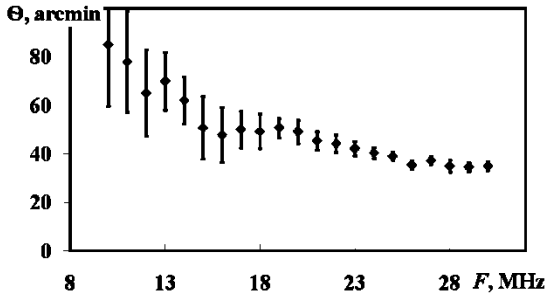

Figure 4: Polar diameter of the quiet Sun as a function of frequency

3. Conclusion

Radio astronomy observations of the quiet Sun at decameter wavelengths with interferometers and broadband DSPZ radio receivers showed a significant influence of radio frequency interference on the data quality.

The software has been developed for the mitigation of narrowband and pulsed interference of various origin.

The use of the cleaning algorithms during data processing made it possible to determine the parameters of the studied radio sources of continuum radio emission under conditions of strong radio frequency interference, which significantly exceeded the level of useful signals

Acknowledgements. V.A. Shepelev acknowledges the Europlanet 2024 RI project funded by the European Union's Horizon 2020 Research and Innovation Programme (Grant agreement No. 871149).

References

Abranin E.P., Bazelian L.L.: 1986, *Kharkov Izdanie IRE AN USSR*, 393.
Aubier M., Leblanc Y., Boischot A.: 1971, *Astron. & Astrophys.*, **12**, 435.
Erickson W.C., Kundu M.R., Mahoney M.J., Gergely T.E.: 1977, *Solar Phys*., **54**, 57.
Melnik V.N., Shepelev V.A., Poedts S. et al.: 2018, *Solar Phys.*, **293**, 97.
Rashkovsky S.L., Belov A.S., Ivanov A.S. et al.: 2012, *Radiophys. and Radioastron*. (in Russian), **17**, 3, 207.
Sastry C.V.: 1994, *Solar Phys*., **150**, 285.
Shepelev V.A.: 2015, *Radiophys. and Radioastron*. (in Russian), **20**, 1, 20.
Shepelev V.A., Melnik V.N., Vashchishin R.V.: 2018, *Odessa Astron. Publ*., **31**, 159.
Stanislavsky A.A., Koval A.A., Konovalenko A.A.: 2013, *Astron. Nach.*, **334**, 1086.
Zakharenko V., Konovalenko A.A., Zarka P. et al.: 2016, *Astron. Instrum*, **5**, 4.

https://doi.org/10.18524/1810-4215.2023.36.290143

ABOUT RESEARCH PROGRAMS AT THE RADIO TELESCOPE "URAN-4" IRA NASU – MONITORING OF FLUXES OF POWERFUL RADIO SOURCES, STUDY OF THE SUN'S SUPERCORONA, OBSERVATIONS OF SOLAR ECLIPSE

A.L. Sukharev, M.I. Ryabov, V.V. Galanin, V.G. Komendant

Odessa observatory "URAN-4" Institute of Radio Astronomy of the National Academy of Sciences of Ukraine (IRA NASU)

ABSTRACT. During 2020–2023, an initiative series of observation programs was carried out on a radiometer designed and manufactured by V.V. Galanin. Among them are observations of ionospheric scintillations of powerful radio sources Cas A, Cyg A, Vir A, Tau A, Per A, on the URAN-4 radio telescope (IRA NASU) at frequencies of 20 and 25 MHz. The observations were carried out at various states of Solar and geomagnetic activity and allow us to analyze the response of the ionosphere in the region of the Odessa Magnetic Anomaly to disturbing events. It was found that the radio source 3C 84 (Per A) is the least noisy at the location of the URAN-4 antenna and is well suited for studying the ionospheric response during magnetic storms. The recorded scintillation periods of the studied radio sources, on "calm" days, are in the range of 1-2 minutes. During magnetic storms, the periods of scintillations are reduced to 10-30 seconds. The paper considers the features of the response of scintillations of different radio sources to a magnetic storm, since they shine through different spatial regions of the ionosphere. Of particular interest are observations of the radio source Tau A (3C 144), which annually, in June, shines through the Solar Supercorona. Processing scans of such observations of the 3C 144 source shows an increase flux variations with an average "period" of about 5-10 seconds. Observations were also made to record the features of radio background variations during partial Solar eclipse. It is shown that during a Solar eclipse, the level of background radio noise increases significantly. At the same time, the background level on the next day after the eclipse was still quite high. A more detailed analysis of this effect is planned and, if possible, repeated observations.

Keywords: ionospheric scintillations, radio sources, antenna array, geomagnetic variations, magnetic anomaly

АНОТАЦІЯ. Протягом 2020 – 2023 років, було виконано ініціативну серію програм спостережень на радіометрі, спроектованому та виготовленому В.В. Галаніним. Серед них спостереження іоносферних мерехтінь потужних радіоджерел Cas A, Cyg A, Virg A, Tau A, Pers A, на радіотелескопі URAN-4 (IRA NASU) на частотах 20 і 25 МГц. Спостереження проводилися за різних станів сонячної та геомагнітної активності та дозволяють аналізувати відгук іоносфери в регіоні Одеської Магнітної Аномалії на обурюючі події. Було встановлено, що радіоджерело 3C 84 (Perseus A) є найменш зашумленим, у місці розташування антени URAN-4 і добре підходить для вивчення іоносферного відгуку під час магнітних бур. Реєстровані періоди мерехтіння досліджуваних радіоджерел, у «спокійні» дні, перебувають у інтервалі 1-2 хвилини. Під час магнітних бур, періоди мерехтіння зменшуються до 10-30 секунд. У роботі розглянуто особливості відгуку мерехтінь різних джерел на магнітну бурю, оскільки вони просвічують різні просторові області іоносфери. Особливий інтерес становлять спостереження радіоджерела Taurus A (3C 144), який щорічно, у червні, просвічує надкорону Сонця. Обробка сканів таких спостережень джерела 3C 144 показує посилення варіацій із середнім «періодом» близько 5-10 секунд. Також було проведено спостереження щодо реєстрації особливостей варіацій радіофону під час часткового Сонячного затемнення. Показано, що під час Сонячного затемнення рівень фонового радіо-шуму значно підвищується. При цьому рівень фону наступного дня після затемнення був досить високим. Планується докладніший аналіз цього ефекту за наявності можливостей проведення повторних спостережень.

Ключові слова: іоносферні мерехтіння, радіоджерела, антенна решітка, геомагнітні варіації, магнітна аномалія.

1. Introduction

During the development of the anomalous 25th solar cycle (beginning in December 2019), the most important task is to study the ionospheric response to extreme manifestations of solar and geomagnetic activity. One of the most scientifically based and widely used methods for studying the Earth's ionosphere and the effects of space weather manifestations is the method of ionospheric scintillations of discrete space radio sources [1, 2]. The main contribution to the scintillations of signals from discrete radio sources is made by inhomogeneities, with transverse dimensions to the line of sight, of order of size the Fresnel zone: $\Lambda_{fr} = \sqrt{\lambda r}$, where λ – wavelength, and r – distance to the scattering layer. These

inhomogeneities focus or defocus signals from cosmic radio sources. At the same time, extended radio sources with angular dimensions θ which exceed the angular size of the Fresnel zone $\theta_{fr} = \Lambda_{fr} / r \sim \sqrt{\lambda / r}$ will not have scintillations, because the addition of oscillations coming to the observation point from different areas of these sources will be incoherent [3, 4]. Ionospheric scintillations strongly depend on the state of the Earth's ionosphere and magnetosphere under the influence of solar activity, and therefore are excellent indicators of space weather. Although this method has been used since the 1950s, many unresolved questions remain. These include the connection between ionospheric scintillation and geomagnetic pulsations, as well as the connection between ionospheric scintillation and variations in cosmic ray fluxes. In addition, the influence of large regional magnetic anomalies on the ionospheric response during extreme space weather events is poorly understood. This work uses data from the URAN-4 (IRA NASU) low frequency radio telescope, operating in the 10-30 MHz range. A unique feature of this radio telescope is its location near the Odessa regional geomagnetic anomaly. The dome of the anomalous field of this anomaly, according to satellite data, extends to ionospheric heights, which makes it possible to study its response to solar activity [5].

2. Brief description of the low-frequency radio telescope URAN-4 and processing observational data

The low-frequency decameter radio telescope, URAN-4 (operated by the Institute of Radio Astronomy of the National Academy of Sciences of Ukraine (IRA NASU)) (began observations in 1987) is a phased array with electronic control of the antenna beam direction. The antenna consists of 128 pairs of vibrators located on an area the size 232.5 x 22.5 meters and oriented in the east-west direction. Thus, the antenna receives a signal in two linear polarizations A and B. The antenna beam pattern has the size 2.7° x 22° at a frequency of 25 MHz. URAN-4 is one of the elements of the national low-frequency radio interferometric system URAN, Ukraine. In very-long-baseline interferometer mode, the angular resolution reaches 2 arcseconds. The sensitivity with a frequency bandwidth of 14 kHz is 100 Jy (and in interferometer mode – 10 Jy) at a frequency of 25 MHz [42]. The hardware complex includes an upgraded antenna control device and a radiometer for recording radio emissions, which was developed and constructed by IRA NASU researcher Valery Galanin. This device controls discrete movement of the antenna's beam pattern when observing radio sources and sets the required observation mode. Currently, observations are carried out at frequencies of 20 and 25 MHz. The radiometer operates in various modes: full power, modulation mode, average power, using the telescope design in the form of two halves of the antenna. The radiometer is made on an ATMEL AT90S8515 microcontroller with a communication circuit with a control computer. The REGICEA software for antenna control and observation planning was written in the Delphi programming language. The resulting observation file contains the time in Julian dates, the total power (*P*) and the differences between the two halves of the antenna (*M*). The main operating mode is modulation ($P - M$). In modulation mode, random uncorrelated noise is suppressed and the noise track of the signal is significantly reduced, which is especially important when observing weak sources (for example, 3C 84). Figure 1 shows an example of recording in modulation mode for the 3C 405 source and in full power mode for the 3C 461 source. The program for monitoring fluxes of powerful radio sources was started on the initiative of the authors (M.I. Ryabov and V.V. Galanin) from the moment of commissioning the URAN-4 radio telescope continues in present time.

Monitoring fluxes of radio sources and their scintillations is carried out in the mode of multiple passage of radio sources through the antenna's beam pattern. Supernova remnant 3C 144 (Taurus A) and radio galaxy 3C 274 (Virgo A) were recorded in the hour angle interval from -120m to +120m with a step of 40 min (7 scans in total). Radio galaxy 3C 405 was recorded in the interval of hour angles from -120m to +80m with a step of 40 min (6 scans in total). The most powerful radio source in the northern sky in the decameter range, supernova remnant 3C 461 (Cassiopeia A) was recorded in the hour angle interval from -60 m +120m with a step of 60 min (4 scans in total). Thus, the total monitoring time was 13 hours 20 minutes. And as a result of this 36-year monitoring, important data were obtained on seasonal-diurnal variations in the fluxes of radio sources and their scintillations over a period of 22–25 solar cycles [6, 7].

The main objects for studying ionospheric scintillations are the powerful radio galaxies 3C 274 (Virgo A), 3C 405 (Cygnus A), 3C 84 (Perseus A), as well as the remnants of supernova explosions 3C 461 (Cassiopeia A) and 3C 144 (Taurus A). Over 36 years of observations on the URAN-4, unique observational material was obtained on changes in the fluxes of radio sources and their scintillations during different cycles of solar and geomagnetic activity in the region of the Odessa magnetic anomaly.

Radio fluxes from space sources are written to the output file as relative values, in decibels (*dB*), relative to a highly stable noise generator (calibrated in antenna temperatures in Kelvin (*K*)). The amplitudes of the calibration steps were selected experimentally for each radio source in the sample.

Figure 2 shows a typical view of recording fragments of radio sources 3C 405 and 3C 144 (sequential passage through the antenna's beam pattern) on URAN-4. This allows us to immediately see the features, similarities and differences in the ionospheric responses to bursts of solar and geomagnetic activity for the entire sample of analyzed sources, on the final flux record.

The sampling rate in the output data file with records the sum and difference of the signals from two halves of the antenna, at frequencies 20 and 25 MHz, is 1 Hz (1 measurement per second). As can be seen from previous figures, ionospheric scintillation is superimposed on the sinusoidal trend from the registration of the antenna's beam pattern scans radio source. To isolate ionospheric scintillations, a semi-automatic method of data preprocessing and subsequent construction of digital dynamic spectra (using Short-Time Fourier Transform

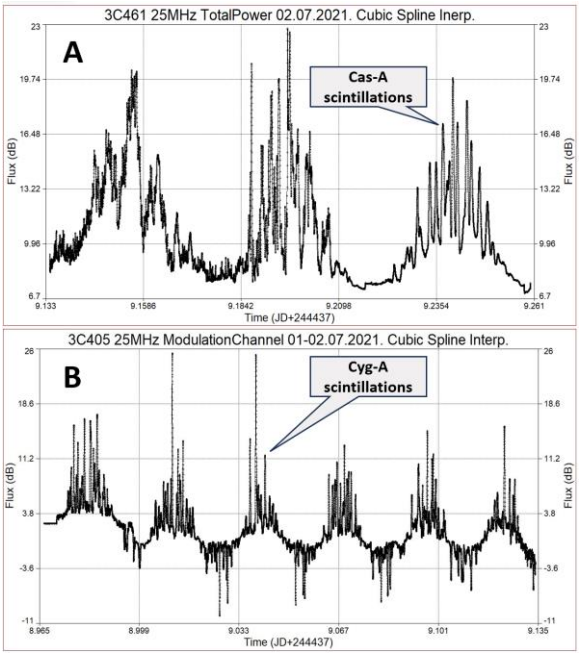

Figure 1: Examples of source scan records: A) 3C 461, frequency 25 MHz, full power with cubic smoothing spline interpolation; B) 3C 405, frequency 25 MHz, modulation mode with cubic smoothing spline interpolation. Records received 1-2 Jul 2021.

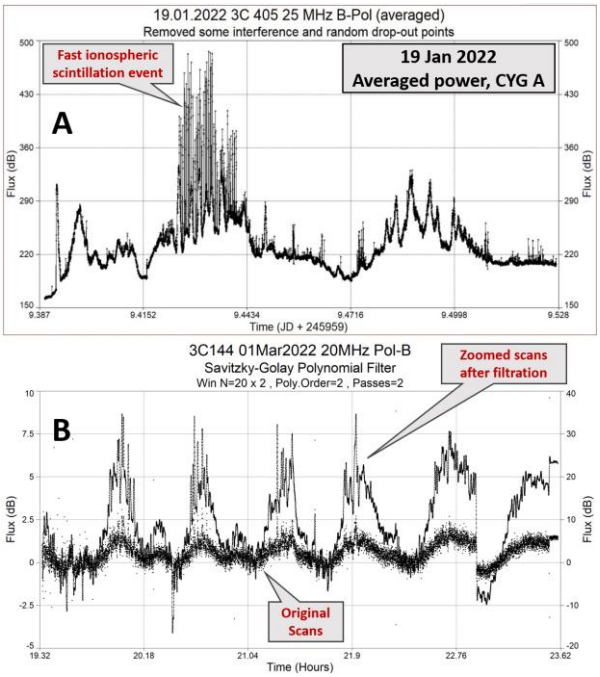

Figure 2: The figure shows: A) An example of a recording (Jan 19, 2022) of average power (the average value of the sum and difference signals of the half-antennas) for the radio source 3C 405 (frequency 25 MHz, linear polarization B). The average power graph has wider scan peaks, which is useful when recording scintillations, but is suitable for high-power sources. This example shows a scintillations burst with a characteristic time of about a minute; B) Example of original and smoothed recordings (Mar 1, 2022) modulation mode, for source 3C 144 (frequency 20 MHz, linear polarization B). Savitzky-Golay filter was used for smoothing [8] (graphs are shifted relative to each other for better visibility).

(STFT) and fast continuous wavelet transform methods) was developed and implemented. Due to the complex interference environment in the decameter range, the antenna's beam pattern (which under normal conditions is well described by the function *sin (x)/x*) is deformed. Under such conditions, data preprocessing consists of the following steps:

1) removal of the strongest radio interference and random outliers (manually).

2) smoothing the recording of radio source scans using three different approaches depending on the level of data noise. For low-noisy data, the Savitzky-Golay filter was used (most often for sources 3C 461 and 3C 84); when the noise was high enough, with weak impulse noise, data interpolation using a smoothing cubic spline with cross-validation was used, where smoothing level is automatically determined using procedure so-called cross-validation [9] (usually for sources 3C 405 and 3C 274). This method allows us to draw scans of radio sources and variations in the radio flux even in the case of noise bursts caused by interference during tens of minutes. In the case of strong continuous noise, which is often recorded in the direction of the 3C 144 source, the Loess method (Locally estimated scatterplot smoothing) implementation of the locally-weighted least-squares procedure with Gaussian weighting function was used [10]. This method can isolate scintillations in the presence of fairly long-term interference, which is not uncommon at the URAN-4 location, and was most often used for observations of 3C 144, since the noise in the direction of this source is often greater than for the rest of the sources in the sample.

3) Since ionospheric scintillations are superimposed on the sinusoidal trend, the trend is removed to isolate them and subsequent analysis. This is complicated by the fact that the main shape of scans of radio sources often differs from the theoretical one due to radio-interference. In this work, the main method for identifying scintillations was FFT filtering with a Hamming spectral window [11]. Spectral windowing is used to reduce spectrum leakage so that components in low spectral power data can be selected and recovered. Thus, even weak scintillations can be clearly distinguished from a noisy background. The Hamming spectral window does not completely attenuate to zero at the edges of the rolloff, and typically the filter can recover the full range of data with 1% edge effects at the beginning and end of the data series. An example of FFT filtering is shown in Figure 3.

Despite the relative simplicity and effectiveness of the FFT band-pass filtering method, in some cases it can leave a small false wave in the data, which can be noticeable on days with no or weak scintillation. Therefore, in 2023, the decomposition of observational data into individual quasiperiodic and noise-like components by the Caterpillar-SSA method began to be used (more details about this method are described in the work [12]), which made it possible to significantly eliminate distortions from filtering in recordings of weak scintillations.

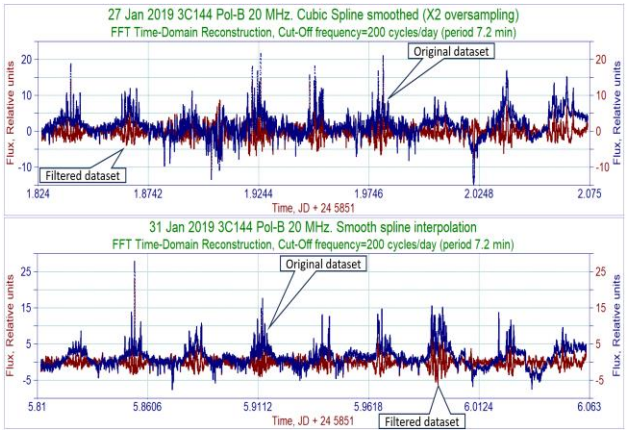

Figure 3: Initial and FFT-filtered data from radio source 3C 144 (frequency 20 MHz, linear polarization B), such that the time scale varies less than 7 minutes (cutoff frequency 200 cycles/day). Top panel – record 27 Jan 2019, bottom panel – record 31 Jan 2019.

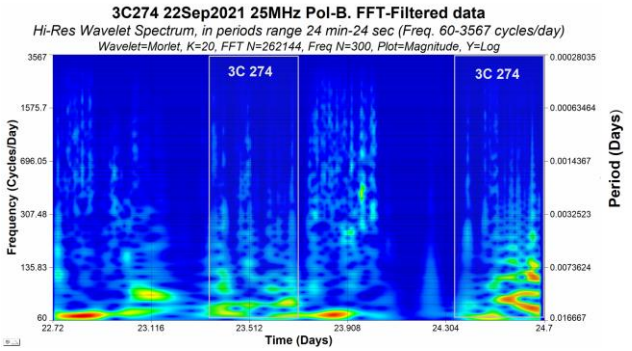

Figure 4: An example of a wavelet spectrogram (frequency 25 MHz, polarization B, period band from 24 seconds to 24 minutes) of the development of ionospheric scintillations during sequential recording of a sample of radio sources in the time interval 22-24 Sep 2021, during weak geomagnetic disturbances. In the graph, source 3C 274 is highlighted by rectangles. The change in noise and quasi-harmonic components of variability is clearly visible; as the time scale decreases, variations in the radio flux become completely noise. Quasi-harmonic variations here are concentrated mainly in a band of periods 10-20 minutes.

4) Finally, after the above-described pre-processing of the data and their normalization, spectrograms were constructed. In low-frequency astronomy, standard practice for this is to use the STFT method (for example [13]). But this method has a number of disadvantages (dependence of the spectrogram from the window width and the amount of window overlap), so the method of "continuous" wavelet transform was additionally used, which was calculated through FFT (for analytically specified wavelets, for example Morlet) (comparative review in [14]). Representations were used in visualization: Magnitude: $\sqrt{R^2+I^2}$, PSD SSA (Surface Integral Sum Squared Amplitude Power): $2(R^2+I^2)$, decibels (dB): $10\log_{10}(R^2+I^2)$, where R – real part, I – imaginary part, of wavelet transform.

3. Results of observations of ionospheric scintillations of cosmic radio sources

The following sections discuss some results of the study features of the manifestation ionospheric scintillations of cosmic radio sources on geomagnetically disturbed and calm days. As shown in Figure 4 (22-24 Sep 2021), during the days of ionospheric storm development, the scintillation spectrum varies significantly from source to source, and even the same source 3C 274 has completely different types of scintillation.

It is worth noting that the band of periods 10-20 minutes corresponds to large-scale wave activity of the ionosphere, for example, the passage of acoustic (2-4 minutes) and gravitational waves (5-20 minutes). These waves arise not only in the *F*-layer of the ionosphere, but also in the *D*-layer (altitude about 100 kilometers), which is also evident from variations in the total electron content determined from properties of the GPS signal [15]. More details about ionospheric waves are described in the work [16]. In the period band 5 minutes – 30 seconds, in mid-latitudes, quasi-periodic scintillations in the range 10-30 MHz appear infrequently, they are mainly recorded in circumpolar regions (for example, according to data from the Kilpisjärvi Atmospheric Imaging Receiver Array (KAIRA) [17]). In mid-latitudes, quasiperiodic ionospheric variations, their registration and study are significant scientific interest, since they are a consequence of the formation of a spatial periodic structure of ionospheric irregularities passing through the beam of the antenna array.

3.1 Cassiopeia A (3C 461)

Supernova remnant Cassiopeia A (3C 461) together with Cygnus A (3C 405) are the most powerful radio sources in the Northern Hemisphere sky in the decameter radio range and, accordingly, the most popular for research. Figure 5 shows examples of STFT spectrograms of source 3C 461 for Sep 27-28, 2021 (quiet geomagnetic field) and Jul 2, 2021 (weakly disturbed geomagnetic field). The example shows that even weak geomagnetic disturbances often lead to a shortening of the "period" of scintillations, from 24 seconds to 16 seconds. In general, this is often true for other sample sources as well. During strong magnetic storms, the "periods" of 3C 461 scintillations are shortened to 10 – 5 seconds. For 3C 461, quasi-periodic flux variations are sometimes recorded, with periods of several minutes. During some strong magnetic storms of 2022, quasi-periodic variations of about 1 minute or 30 seconds, and lasting 10 – 15 minutes, were recorded at a frequency of 20 MHz in both linear polarizations A and B.

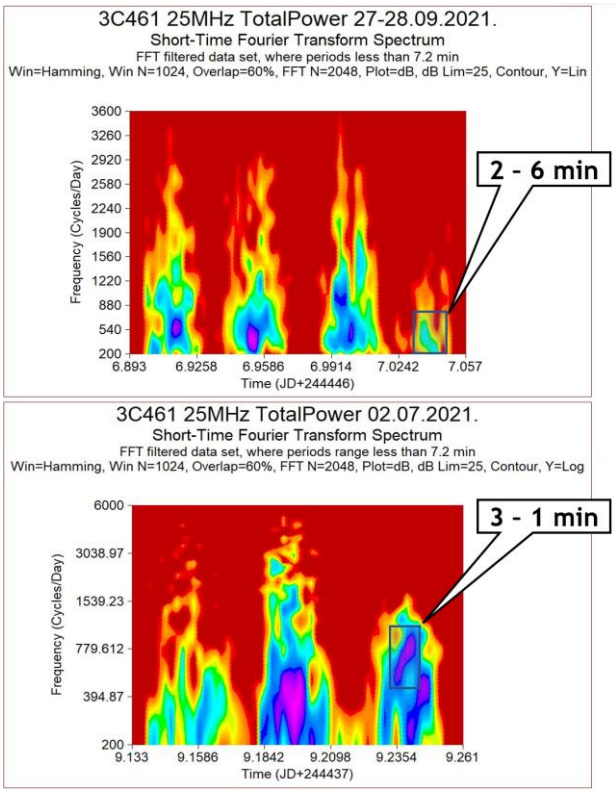

Figure 5: Examples of STFT spectrograms of source 3C 461 at a frequency of 25 MHz, obtained on Sep 27-28, 2021, quiet geomagnetic field (upper graph) and Jul 2, 2021, weakly disturbed geomagnetic field (lower graph), linear polarization A. Rectangles show events of quasiperiodic variations of radio flux of Cassiopeia A (the range of periods is shown by flags on the figure).

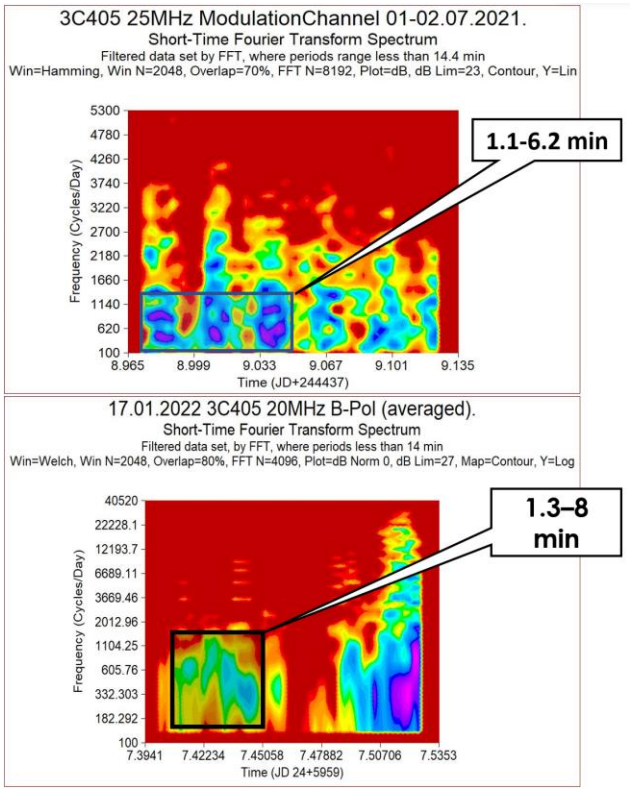

Figure 6: Examples of STFT spectrograms of source 3C 405 at a frequency of 25 MHz, weakly disturbed geomagnetic field, 1-2 Jul 2021 (top graph) and at a frequency of 20 MHz, magnetic storm, 17 Jan 2022 (bottom graph), linear polarization B. Rectangles on the graphs areas are highlighted quasi-periodic variations of the radio flux and flags mark the ranges of changes in the "periods" of oscillations.

3.2 Cyg A (3C 405)

The giant radio galaxy Cygnus A (3C 405) is one of the most popular radio sources for studying the ionosphere in the decameter radio range. The signal from it is powerful and at the same time almost free from noise and radio-interference. Ionospheric scintillations from this source are very intense and change rapidly over time, showing a complex time-frequency structure. Figure 6 shows examples of STFT spectrograms for the 3C 405 source at frequencies of 25 MHz (1-2 Jul 2021) and 20 MHz (17 Jan 2022). On 1-2 Jul 2021 there was a weakly disturbed geomagnetic field, and on 17 Jan 2022 there was a magnetic storm of medium intensity. During a magnetic storm, a significant change in the quasi-period of variations was noted from approximately 1.3 minutes to 8 minutes, increasing with time. During weak geomagnetic disturbances, short-lived "bursts" of quasi-periodic scintillations are sometimes recorded in a period band of approximately 1 – 6 minutes, as shown in this example. Also, at source 3C 405, during some magnetic storms, high-intensity and broadband scintillations of a noise-like appearance are observed, occupying a band of periods in the spectrogram, usually from 10 minutes to 4 seconds. In the sample of sources under study, a similar type of "noise-like" spectrogram was observed at source 3C 274.

3.3 Virgo A (3C 274)

Another giant radio galaxy 3C 274 (Virgo A) in the studied sample of radio sources is similar in properties to ionospheric scintillations to 3C 405, however, fewer quasi-periodic manifestations of scintillations were observed at this source. Scintillations are mostly noise-like and broadband (example in Figure 7). Observation sessions lasting several days, in 2020 and 2022, showed that the maximums of the FFT power spectra of 3C 274, during weak geomagnetic disturbances, lie in the range of 1 – 3 minutes or less. Rare quasiperiodic flux variations with periods from 30 seconds to 1 minute, and duration 5 – 12 minutes, corresponded to geomagnetic storms caused by geoeffective solar coronal mass ejections.

3.4 Taurus A (3C 144)

The radio source 3C 144 is one of the actively studied objects in decameter radio astronomy. The fact is that this powerful radio-bright object (the remnant of a supernova explosion) annually approaching the Sun on the celestial sphere (in June), shining through the quite dense layers of outflowing solar wind, which are called the supercorona. During this period, intense scattering of radio waves from

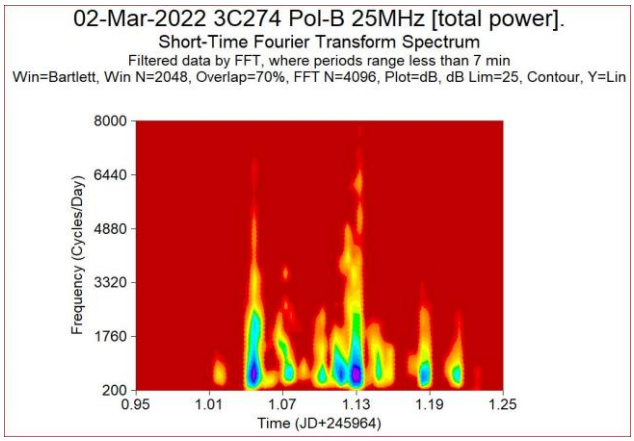

Figure 7: An example of a STFT spectrogram of source 3C 274, for a recording obtained on March 2, 2022 (weak geomagnetic disturbances) at a frequency of 25 MHz, polarization B. Noise-like broadband scintillations are clearly visible here.

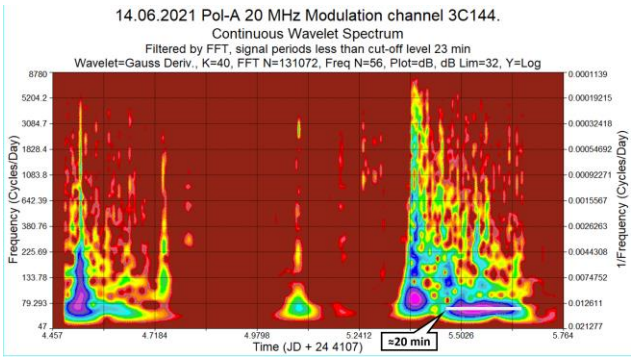

Figure 8: An example of extreme amplification of scintillations of the radio source 3C 144, at an angular approach to the Sun on June 14-15, 2021. Wavelet spectrogram at a frequency of 20 MHz, polarization A. In addition, on June 15, 2021, a quasiperiodic component of variability is visible with a period of about 20 minutes and a duration in several hours (marked with a flag in the figure).

source 3C 144 occurs on plasma clouds of the solar wind (interplanetary scintillation effect). However, this type of scintillations cannot be detected on the URAN-4 antenna array, because their period is on average about 1 second or less. But, besides this, the high turbulence of the supercorona plasma, caused by solar wind from flares, coronal mass ejections [18], provides complex effects on the radio signal of a source. An interesting effect was observed on June 14-15, 2021, when 3C 144 approached the minimum angular distance from the Sun. Figure 8 shows the wavelet spectrum of 3C 144. It can be seen that on June 14 and 15 there was an extreme increase in scintillation at 3C 144, while the rest of the sources from the observation session scintillated much weaker (almost "empty" spectrum between scans of 3C 144). The amplitude of scintillations 3C 144 was 4 times greater than the source 3C 461. This type of effect is discussed in more detail in the article [19].

The exact nature of this effect is not known, but is possibly related to coronal mass ejections or magnetized plasma clouds that may provide lens-like amplification to the observed radio emission. More details about such effects are described in the works [20, 21, 22, 23]. Variations in the radio-flux with a period of about 20 minutes are most likely have ionospheric origin, the passage of moving ionospheric irregularities or ionospheric waves [24]. Therefore, studying records of the annual passage of 3C 144 through the solar supercorona is always with scientific interest, and such observations continue to be carried out on the URAN-4 antenna array.

3.5 Perseus A (3C 84)

The radio source 3C 84 has the smallest flux in the decameter range from the studied sample of radio sources. However, there is minimal interference and distortion in the direction to this source, which makes it important for studying ionospheric disturbances at the URAN-4 location.

At the same time, the properties of 3C 84 ionospheric scintillations are somewhat different from other radio sources in the sample. The maximums of the FFT power spectra show that the main spectral power of the signals falls on the period range of 40 seconds – 1.5 minutes, on days of a quiet geomagnetic field. Figure 9 shows wavelet spectrograms of 3C 84 for Oct 9, 2020 (quiet geomagnetic field) and Apr 8, 2021 (weak geomagnetic disturbances). Noise-like scintillations are predominating. However, in a number of magnetic storms (Jun 12, 2021), fairly stable scintillations appear on the spectrograms with periods of about 50, 25, 16 seconds, which exist for 2 – 3 hours, and sometimes longer. On days of a quiet geomagnetic field, stable quasi-periodic variations are occasionally recorded with a period of about 1.5 minutes – 40 seconds, and a manifestation duration of 2 – 3 hours (23 Sep 2021). In comparison with other radio sources of the studied sample, 3C 84 has much less frequent variations of the radio-flux in the period band of 20 – 5 minutes.

3.6 Effects of a solar eclipse on radio noise levels

Interesting observations were obtained during the annular solar eclipse on June 10, 2021. It was not the Sun observed on the URAN-4 antenna, but the background cosmic noise at frequencies of 20 MHz, 25 MHz (the antenna beam was directed to the zenith). As a result, it turned out that the cosmic background on the day of the eclipse and the next day, June 11, 2021, showed noticeable noisy variations, more intensive than in the records of the cosmic background on June 8-9, 2021. Spectrograms of radio background recordings are shown in the figure 10.

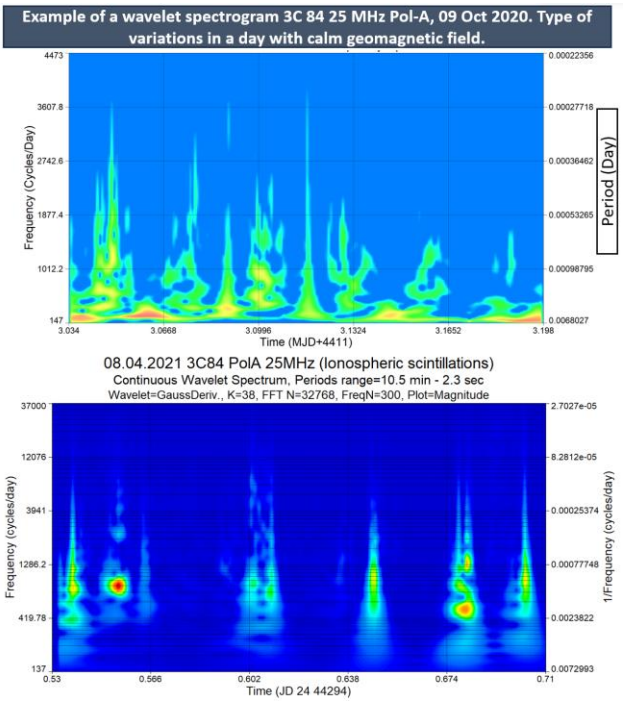

Figure 9: Example of wavelet spectrograms for source 3C 84. The top graph is a quiet geomagnetic field, Oct 9, 2020, frequency 25 MHz, polarization A. Many irregular bursts are visible, which is typical of ionospheric scintillations. Bottom graph – weak geomagnetic disturbances, 8 Apr 2021, frequency 25 MHz, polarization A. This is an interesting example of episodic noise-like scintillations of 3C 84.

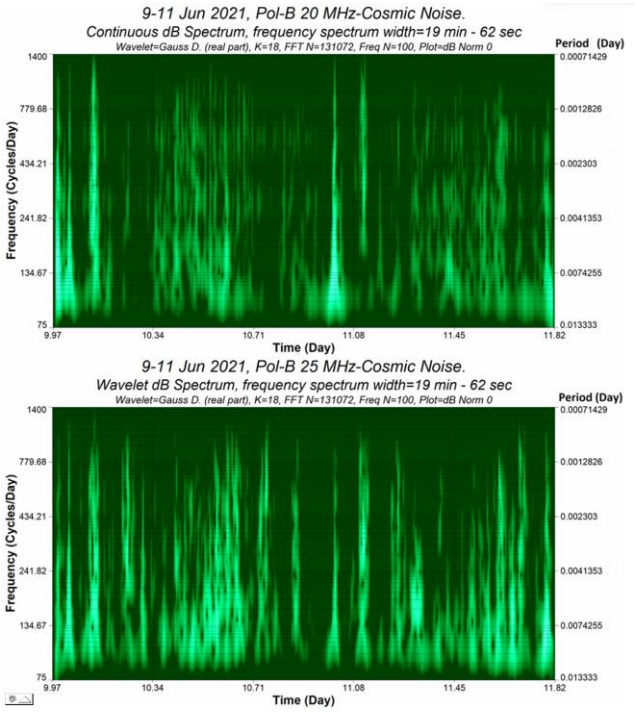

Figure 10: The figures show wavelet spectrograms of 20 MHz (upper plot) and 25 MHz (bottom plot) (B-linear polarization) obtained on June 10-11, 2021. The cosmic background records were cleaned of radio interference and additionally smoothed.

Increase in the intensity of radio noise was also observed by other researchers in different years of solar eclipses [25]. This is usually associated with a decrease in the electron concentration, a decrease in absorption in the ionosphere, which leads to an increase in the intensity of the noise received by the antenna [26]. However, it is interesting that the noise level on the day after the eclipse was still quite high. Also, there could be an increased level of radio-interference here. This is a very strange observational effect, showing that absorption in the ionosphere was still low even the day after the solar eclipse, but the reason for this effect is not clear. Something similar was observed in work [27] when the signal from a radio station increased during a solar eclipse, but a noticeable increase in the signal partially persisted the next day after the solar eclipse.

Analysis of observations showed, on June 8, 2021, two days before the partial solar eclipse visible in Ukraine, the amplitude of the sky background noise, when the antenna beam was set to the zenith, was much less than during the solar eclipse on June 10, 2021 and after it on June 11, 2021. Intensity of radio variations in the noise background, on a time scale of less than 8 minutes, was much weaker than on the day of the Solar Eclipse, and the low-frequency component of the spectrum (20.6 – 8 minutes) also has a lower intensity.

3.7 Interrelation with geomagnetic field variations in the Odessa anomaly zone

An important feature of the decameter radio range is that the observed scintillations of cosmic radio sources are almost completely (with the exception of some contribution of interplanetary scintillations for individual radio sources) determined by the dynamic processes of the ionosphere, under the influence of solar and geomagnetic activity. Seasonal-daily ionospheric effects during the solar activity cycle can be so great that they even exceed long-term intrinsic changes fluxes of the radio sources. For example, seasonal-diurnal effects significantly reduce the observed appearance of the secular decrease Cassiopeia A flux in the decameter range [28, 29, 30, 31]. This makes the decameter range especially interesting for searching and studying the interrelation between ionospheric scintillation and fast variations of geomagnetic induction, during magnetic disturbances and storms caused by different manifestations of solar activity.

Large magnetic anomalies in the Earth's lithosphere may have a quite high height of the anomalous field dome, which is recorded by satellites at altitudes of about 200-300 kilometers and even higher [32]. As is known, the most intense ionospheric scintillations are formed when radio waves pass through the *F*-layer of the ionosphere at altitudes of about 200 – 350 kilometers. Thus, large magnetic anomalies can influence the formation and structure of plasma irregularities, forming a special response of the ionosphere to solar activity events. In addition, local factors also play an important role in the

formation of geomagnetic variations in mid-latitudes [33]. Another important feature is the location of the seismically active Vrancea Zone in Romania, approximately 500 kilometers (290 km in a straight line) from Odessa. As is known, seismically active zones can produce ionospheric waves, including those with periods of tens of minutes (for example, [34]). Currently, this relationship is very poorly studied, especially in Europe, often due to the lack of large low-frequency radio telescopes in areas of magnetic anomalies. Therefore, the location of the URAN-4 antenna array in the area of the Odessa regional magnetic anomaly provides a unique opportunity to study this relationship. Conducted studies of short-period geomagnetic variations in the Odessa magnetic anomaly, which fall within the range of periods of observed ionospheric variations on the URAN-4 antenna array, showed a significant difference in their properties and structure from the variations that were observed at the magnetic station in the Kiev region (Dymer), where the geomagnetic field close to normal [35, 36, 37, 38]. In the summer of 2022, to conduct simultaneous observations of scintillations of radio sources and geomagnetic field disturbances, the LEMI-008 magnetometer of the Institute of Geophysics of the National Academy of Sciences of Ukraine was installed next to the URAN-4 antenna array. This makes it possible to obtain data for cross-spectral FFT analysis and identify similarities and differences in the development of magnetic storms based on geomagnetic and ionospheric variations. Fast geomagnetic variations are also induced in the ionosphere, but are associated with electric currents (field-aligned currents) and the interaction of the ionosphere and magnetosphere Earth. These include resonant geomagnetic variations [39]. Thus, ionospheric activity is studied as if in two dimensions. Preliminary results indeed showed a relationship between the prevailing periods of ionospheric scintillations of 30 seconds – 1 – 2 – 3 minutes and geomagnetic variations, using observations of the radio galaxies 3C 405 and 3C 274. An example of fast geomagnetic variations (*Bx* component of the geomagnetic field) with periods of about 1 minute and 30 seconds, shown in Figure 11. In winter wartime conditions, the magnetometer worked in the center of a magnetic anomaly in the basement on the territory of the Astronomical Observatory of the Odessa I.I. Mechnikov National University. On 22 Feb 2022 there was a weak geomagnetic storm, and on 13 Feb 2022 there was a magnetic storm of medium intensity. The variations shown in the example (falling in the period range Pc3 – Pc4 [40]), during weak and medium magnetic storms, were rarely observed in this form on spectrograms. Observations on URAN-4 of ionospheric scintillations of the radio galaxies 3C 405 and 3C 274, during weak and medium geomagnetic storms, showed that the average periods (in the bands of greatest spectral power) also had values of about 30 seconds and 1 – 2 – 3 minutes. But in general, since it was not possible to obtain complete sessions of simultaneous radio-magnetometric recordings, a clear relationship could not be detected. Solving this problem remained the goal of further work because placement a magnetometer in the summer 2023 in the Mayaki village, where URAN-4 is located.

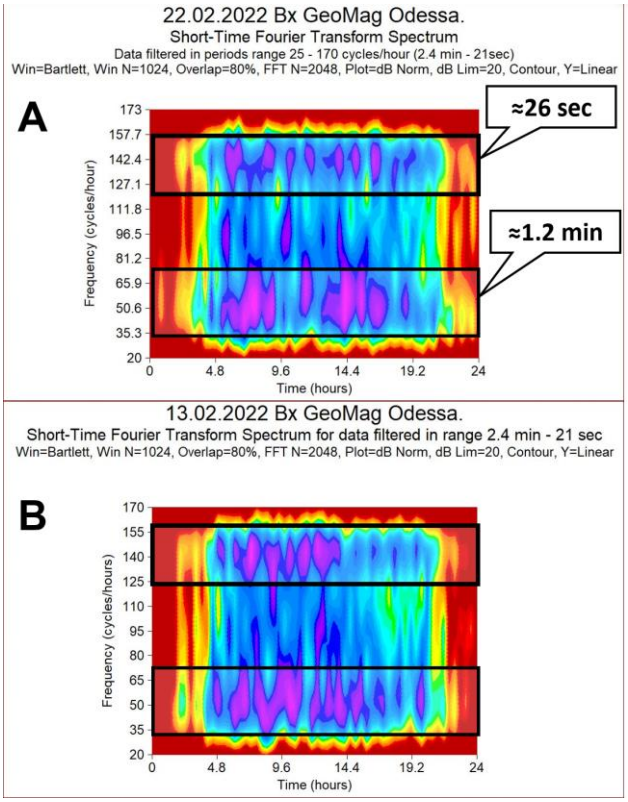

Figure 11: Examples of rapid variations in the geomagnetic field induction, component *Bx*, obtained at the Odessa Astronomical Observatory on 22 (top graph) and 13 (bottom graph) Feb 2022. Here you can see bands of quasi-regular oscillations falling in the pulsation range Pc3 (10 – 45 seconds) – Pc4 (45 – 150 seconds). Radio sources 3C 405 and 3C 274 often show similar average periods of ionospheric scintillations.

The interrelation between fast geomagnetic and ionospheric variations has been observed previously [41]. But these effects, in the case of using radio scintillations from cosmic radio sources, have been observed rarely, especially little information about the influence of geomagnetic anomalies on the correlation between ionospheric and geomagnetic variations. They are quite difficult to register, due to the fact that the decameter radio range is often very noisy. High-intensity geomagnetic variations appear in mid-latitudes most often during fairly strong magnetic storms (although there are exceptions), and moments of coincidence between the times of intense magnetic storms and the absence of radio-interference in the decameter range do not occur often. Nevertheless, long-term complex observations of the radio telescope-magnetometer system have great perspective. They will allow us to evaluate the response and contribution of the Odessa Magnetic Anomaly to the manifestation of space weather effects.

4. Conclusion

The creation of a joint measuring complex radio telescope – magnetometer IRA NASU and the Institute of Geophysics NASU (head of department M.I. Orlyuk)

provides a unique opportunity to identify the reaction and contribution of the Odessa magnetic anomaly to regional manifestations of space weather. Using a radiometer that was designed and manufactured by V.V. Galanin conducted many sessions of observing ionospheric scintillations of cosmic radio sources 3C 461, 3C 405, 3C 274, 3C 144 and 3C 84 near the Odessa Regional Geomagnetic Anomaly. The following main results were obtained:

1. A semi-automatic processing technique (data smoothing, removal of the sinusoidal trend of the antenna's beam pattern, bandpass filtering, to identify frequency bands of interest with intense ionospheric scintillation, calculation of STFT and wavelet spectrograms) was developed and tested on real radio sources observations on the phased array URAN-4 IRA NASU.

2. It is shown that the program for monitoring fluxes of powerful cosmic radio sources at URAN-4 provides an ionospheric response in the form of different amplitude, shape (quasi-periodic or noise), and changes in the frequency and phase of ionospheric scintillations over time. These indicators differ significantly for each of the radio sources in the sample during the development of geomagnetic disturbances.

3. The average periods corresponding to the bands of the highest spectral power for ionospheric scintillations in the URAN-4 location, usually vary in the range of 30 seconds – 1 – 2 – 3 minutes. On days of strong geomagnetic disturbances, scintillations periods can be shortened to tens of seconds or less.

4. Observations of ionospheric scintillations of radio galaxies 3C 405 and 3C 274 and comparison of them with fast geomagnetic variations (during magnetic storms) showed good agreement in the period bands corresponding to the Pc3 and Pc4 pulsations. In addition, coincidences are also observed for periods of about 3 minutes.

5. Mostly, ionospheric scintillations have an irregular, non-periodic structure. Nevertheless however, quasiperiodic variations are occasionally observed (more often during geomagnetic disturbances), with a change in period and amplitude in the range of 1 – 10 minutes.

6. Observations of changes in the intensity of background radio emission during the solar eclipse on June 10, 2021 at frequencies of 20 and 25 MHz showed an increase in background radio noise both during the eclipse and on the following day, June 11, 2021.

7. In the period band of 10–20 minutes, quasiperiodic variations of the radio flux predominate, probably associated with wave activity of the ionosphere (acoustic-gravity waves, moving ionospheric irregularities) caused by external influences. A possible contribution to these processes is the proximity of the Vrancea seismically active zone in Romania.

8. An important result of this work was the successful application of a new technique for processing ionospheric scintillation observations of the entire set of observed sources under the monitoring program. This allows us to significantly expand the list of scientific tasks in which the URAN-4 antenna array can be used. Among these tasks is the organization of comprehensive radio astronomy and magnetometric research together with foreign partners from the Ventspils International Radio Astronomy Center in Latvia) and the University of Oulu in Finland (Sodankyla Geophysical Observatory).

References

1. Vasilyev R., Globa M., Kushnarev D., Medvedev A., Ratovsky K.: 2017, ArXiv, https://doi.org/10.48550/arXiv.1702.01966
2. Cander L.R. Ionospheric Irregularities and Waves. In: Ionospheric Space Weather. Springer Geophysics, 2019. Springer, Cham. https://doi.org/10.1007/978-3-319-99331-7_7
3. Bovkoon V.P., Zhouck I.N.: 1981, *Astrophys. & Space Sci.*, **79**, 165.
4. Warwick James W.: 1964, *Radio Science J.*, **68D**, No. 2, 179.
5. Galanin V.V., Komendant V.H., Yasinski V.V.: 2021, *Odessa Astron. Publ*., **34**, 74.
6. Galanin V.V., Lytvynenko O.A., Derevyagin V.G., Kravetz R.O.: 2018, *Odessa Astron. Publ*., **31**, 128.
7. Gorbynov A., Sukharev A., Ryabov M., Bezrukovs V., Orbidans A.: 2021, *Galaxies*, **9**, No. 2, 30.
8. Hannibal H. Madden: 1978, Anal. Chem., **50**, No. 9, 1383.
9. Breaz Nicoleta: 2004, *Acta Universitatis Apulensis 7*, ResearchGate https://www.researchgate.net/publication/237262065
10. Garimella, Rao Veerabhadra: 2017, A Simple Introduction to Moving Least Squares and Local Regression Estimation. United States, Web ver. doi:10.2172/1367799
11. Tipton Carl: 2022, *Johnson Matthey Technol. Rev.*, 2022, **66**, No. 2, 169.
12. Hassani H., Thomakos D.: 2010, *Statistics and its Interface*, **3**, 377.
13. Allen J.: 1977, *IEEE Transactions on Acoustics, Speech, and Signal Processing*, **25**, Iss. 3, 235.
14. Wang Yun, He Ping: 2023, *RAS Techniques and Instruments*, **2**, Iss. 1, 307.
15. Lay Erin H., Shao Xuan-Min, Kendrick Alexander K., Carrano Charles S.: 2015, *J. of Geophys. Research: Space Physics*, **120**, Iss. 7, 6010.
16. Zawdie Kate, Belehaki Anna, Burleigh Meghan et al.: 2022, *Front. Astron. Space Sci.*, **9**, 1.
17. McKay-Bukowski Derek, Vierinen Juha, Virtanen Ilkka I.: 2015, *IEEE Transactions on Geoscience and Remote Sensing*, **53**, Iss. 3, 1440.
18. Yadav Vipin K.: 2016, *Universal Journal of Physics and Application*, **10**, Iss. 6, 193.
19. Galanin V.V., Derevjagin V.G., Kravetz R.O.: 2012, *Odessa Astron. Publ*., **25**, Iss. 2, 186.
20. Gosling J.T.: 1975, *Rev. of Geophys*., **13**, Iss. 3, 1053.
21. Vlasov V.I.: 2013, *Geomagnetism and Aeronomy*, **53**, Iss. 2, 137.
22. Bothmer V., Schwenn R.: 1998, *Ann. Geophysicae*, **16**, 1.
23. Galanin V.V., Derevjagin V.G., Kravetz R.O.: 2013, *Odessa Astron. Publ*., **26/2**, 243.
24. Munro G.H.: 1950, *Proc. of the Royal Soc*., **202**, Iss. 1069, 208.
25. Bhattacharya R., Nag A., Guha R., Bhoumick A., De S., Bhattacharya A.B.: 2010, *Indian Journal of Physics*, **84**, 1587.

26. Bossolasco M., Elena A.: 1962, *Geofisica pura e applicata*, **51**, 155.
27. Chandra H., Sharma Som, Lele P.D., Rajaram G., Hanchina A.: 2007, *Earth, Planets and Space*, **59**, 59.
28. Guglya L., Ryabov M., Panishko S., Sukharev A.: 2012, *Odessa Astron. Publ*., **25**, Iss. 2, 207.
29. Ryabov M.I., Panishko S.K., Guglya L.I.: 2011, *Odessa Astron. Publ*., **24**, 159.
30. Ryabov M.I., Serokurova N.G.: 1998, *Inform. Bull. of the Ukrainian Astron. Association*, **12**, 93.
31. Ryabov M.I., Serokurova N.G.: 1993, *Astron. & Astrophys. Trans.*, **4**, No.1, 29.
32. Kotsiaros S.: 2020, In: *Encyclopedia of Solid Earth Geophysics* /Gupta H.K. (eds). Encyclopedia of Earth Sciences Series, Springer, Cham. https://doi.org/10.1007/978-3-030-10475-7_276-1
33. Chen Chieh-Hung, Lin Jing-Yi, Gao Yongxin, Lin Cheng-Horng: 2021, *J. of Geophys. Res.: Solid Earth*, **126**, Iss. 3, e2020JB021416
34. Afraimovich E.L., Perevalova N.P., Plotnikov A.V., Uralov A.M.: 2001, *Ann. Geophysicae*, **19**, 395.
35. Ryabov M.I., Sukharev A.L., Orlyuk M.I., Sobitnyak L.I., Romenets A.A.: 2019, *Radiophys. and Radioastron.*, **24**, No. 1, 68.
36. Sobitnyak L.I., Ryabov M.I., Orlyuk M.I., Sukharev A.L., Romenets A.O., Sumaruk Yu.P., Pilipenko A.A.: 2020, *Radiophys. and Radioastron.*, **25**, No. 4, 324.
37. Sukharev A.L., Orlyuk M.I., Ryabov M.I., Romenets A.A.: 2018, *Radiophys. and Radioastron*., **23**, No. 2, P. 116-127
38. Sukharev A., Orlyuk M., Ryabov M., Sobitniak L., Bezrukovs V., Panishko S., Romenets A.: 2022, *Astron. & Astrophys. Trans*., **33**, Iss. 1, 67.
39. Klibanova Y.Y., Mishin V.V., Mikhalev A.V., Tsegmed B.: 2019, *Geodynamics & Tectonophysics*, **10**, Iss. 3, 673.
40. Menk F.W.: 1998, *J. Geomag. Geoelectr.*, **40**, 33.
41. Tedd B.L., Cole K.D., Dyson P.L.: 1989, *Planetary and Space Science*, **37**, Iss. 9, 1079.
42. Galanin V.V., Inyutin G.A., Kvasha I.M., Panishko S.K., Pisarenko Ya.V., Rashkovskij S.L., Ryabov M.I., Serokurova N.G., Tsesevich V.P., Sharykin N.K.: 1989, Kinem. & Phys. of Cel. Bod., **5**, 87.

https://doi.org/10.18524/1810-4215.2023.36.290182

THE DICHOTOMY OF THE MECHANISMS OF DECAMETER RADIO EMISSION FROM JUPITER: THE INFLUENCE OF STREAMER INHOMOGENEITIES AND MHD PERTURBATIONS IN THE SOURCE

N.O.Tsvyk

Institute of Radio Astronomy of the NAS of Ukraine,
Kharkiv, Ukraine, *natalitsv69@gmail.com*

ABSTRACT. There are analyzed a model of the source of DAM radiation bursts which are activated under the MHD waves excitation in the Jupiter lower magnetosphere in a presence of ionized streamer-like inhomogeneities of limited thickness (1-100 km). There was studied the formation of an anisotropic kinetic distribution of electrons, which leads to the generation of Jupiter DAM radiation bursts under the various scenarios. It was investigated the influence of gas-dust flows in the Io-Jupiter tube, the ionization processes and the diffusion effects in the streamer plasma to the creation the cone-type kinetic distribution of electrons. On the other hand, it has been shown that Alfven waves, due to the fluctuations of electric fields, are to form of both cone-like electron distribution (primarily on the streamer periphery) and beam-like distribution with the beams of accelerated electrons (primarily inside the streamer), which further run along the streamers at speeds of about 0.1*c* and have been modulated by a "longitudinal" MHD wave with a length of about 1000 km and a period of about 1 second.

The streamer oscillations in the direction tangential to the magnetic field lines lead to the excitation the fast magneto-sonic waves (at about the ion cyclotron resonance frequencies). The beams of accelerated electrons of along the magnetic field lines generate the plasma waves in the same direction (at about the electron cyclotron resonance frequency). At the same time, plasma perturbations create a stratification of the steamer-tube structure into ultrafine threads of ionized plasma, and they contribute to the ultrafine modulation of bursts of DAM radiation with millisecond periods.

Finally, it is shown in detail how all these processes lead to activate the Jupiter DAM radiation bursts in that source at the frequency of electron cyclotron resonance by different generation mechanisms, such as the Maser Cyclotron or Cherenkov mechanisms of generation, and with different burst's properties.

Keywords: DAM radio emission, bursts, MHD waves, magnetosphere inhomogeneity, Jupiter.

АНОТАЦІЯ. Досліджено модель джерела декаметрового випромінювання Юпітера, яке формується в умовах збудження МГД хвиль в нижній магнітосфері Юпітера в присутності неоднорідності магнітосфери у вигляді іонізованих стимерів товщини 1-100 км. Проаналізовано механізми виникнення анізотропного кінетичного розподілення електронів, за яких виникають умови для активної генерації декаметрового випромінювання такого джерела у вигляді сплесків за різними сценаріями. Показано, що газові течії в потоковій трубці Io – Юпітер та ефекти дифузії плазми в стримерах призводять до створення кінетичного розподілення електронів конусного типу. З іншого боку, показано, що альвенівські хвилі, завдяки коливанням електричних полів, регулюють утворення кінетичного розподілення електронів як конусного типу (переважно, на периферії стимера), так і пучкового типу (всередині стримера). В останньому випадку, виникає прискорення пучків електронів до швидкостей біля 0.1*c* (де '*c*' – швидкість світла), які надалі убігають вздовж стримерів і модулюються продольною Альвенівською хвилею з довжиною біля 1000 км і періодом біля 1 секунди.

Коливання плазми стримерів в дотичному до ліній магнітного поля Юпітера напрямку призводять до збудження швидкого магнітного звука, а прискорені пучки електронів генерують плазмові хвилі в цьому ж напрямку. Розшарована таким чином плазма стримерів формує профіль стримера з неоднорідним і анізотропним розподіленням електронів, який рухається разом з МГД хвилями зі швидкістю біля 0.001*c* і стає надалі джерелом електромагнітного ДКМ випромінювання. Відповідний рух джерела з такою швидкістю призводить до дрейфу частоти сплесків біля 0.2 МГц/сек, як і спостерігається в L-сплесках ДКМ випромінювання Юпітера. При цьому, плазмові хвилі-збурення створюють розшарування стимера на тонкі нитки іонізованої електронної плазми, та сприяють надтонкій модуляції електромагнітних сплесків ДКМ випромінюваня, як в S- сплесках.

Всі ці процеси сприяють генерації ДКМ випромінювання Юпітера у вигляді L- та S- сплесків, та відповідають різним сценаріям і механізмам генерації випромінювання. Зокрема, L- сплески можуть бути пов'язані з Мазерним випромінюванням активної плазми джерела на периферії стимерів, яка активується швидкими МГД хвилями, а S- сплески можуть бути пов'язані з Черенковським випромінюванням швидких пучків електронів, яке збуджується першочергово і переважно

в вигляді плазмових хвиль в джерелах всередині стримерів, та перетворюється надалі в спостережуване електромагнітне радіо випромінювання сплесків.

Ключові слова: декаметрове радіовипромінювання, сплески, МГД хвилі, неоднорідність магнітосфери, Юпітер.

1. Introduction: the observed properties of Jupiter DAM radio emission

Jupiter is the brightest planet of the DAM radio emission, which power gives up to 10^7Jy in bursts (see: Ryabov & Gerasymova, 1990, Ryabov, et al., 2014). The dynamical spectrum of the Jupiter's bursts are observed of various forms and types, and the main of that types are long (L) and short (S) bursts in Jupiter DAM radiation, that have burst-variation by frequency and time. So, the L bursts lasts of 0.3-5 s, and that bursts have the frequency drift of ~200 kHz/s, which may correspondent to move of this source velocity by about 0.001c (where c is the light velocity). The S bursts lasts of 0.002-0.03 s, and they have the fast drift of a burst frequency, ~20 MHz/s, that correspondent to the fast source velocity up to 0.1c (see: Ryabov, Zarka, et al., 2014, Boev, et al., 1993, Tsvyk, 2019). All the bursts are observed as the extra ordinary X-type polarized EM waves, and there are radiated in the direction of near perpendicular to the magnetic fields lines at the sources in the southern or northern Jupiter hemisphere.

The Jupiter's bursts are connected with the generation mechanisms which work with the anisotropic electron distribution in the source (see: Wu, 1985, Melrose, 1986, Ryabov & Gerasymova, 1990, Boev & Luk'yanov, 1991). So, it may be the Maser cyclotron instability with cone-like anisotropic electron distribution, $f(v_{e\_|\_}) \gg f(v_{e||})$, or the Cherenkov instability of plasma wave in the presents of the electron beams with the electron distribution of $f(v_{e\_|\_}) \ll f(v_{e||})$. The last way of a burst radiation must have the wave transformation processes, where the plasma wave is converted to the EM wave by resonance wave-coupling process, or by the linear conversion that came in the density-inhomogeneous plasma (see: Boev & Luk'yanov, 1991, Boev, et al., 1993).

In this report, we are represented and analyzed a model for the source of the DAM radiation that activated the burst under the MHD waves in the presence of ionized streamer-like inhomogeneities in the lower magnetosphere of Jupiter, in different generation mechanisms. The further, by the way, we are to study the dichotomy of Jupiter DAM radio emission that differ to the Maser Cyclotron or Cherenkov mechanisms of generation.

2. The model of an active source and the main processes

We will be investigated the processes in the gas-dust flux tube such as the ionization process by streamer-like structures, the plasma diffusing processes, and the MHD waves of streamer oscillations, and the last one the process of the EM wave emission by Maser Cyclotron or Cherenkov radiation mechanisms. There are analyzed a model of the source that give us the DAM radiation bursts which activated by the MHD waves in the presence of the ionized streamer-like inhomogeneities that was formed in the lower Jupiter magnetosphere.

It is the well-known effects of the Satellite-Jupiter interaction, which excites us the strong Alfven-wing with the current pulses in the Io-Jupiter flux tubes and others as the standing waves (see, for example, Ryabov & Gerasymova, 1990). The current direction change with 300-seconds-period, and it give us the 300-seconds-modulation in Jupiter sporadic DAM radiation by Alfven-wings, that corresponds to the shearing the Jupiter magnetosphere to the large-scale flux-tubes of about 1000 km diameters. The streamer which we will be considered now is not that wing-tube structures, but they are the more fine structures inside of these tubes.

In even and other of that wing-tubes, the gas particles (ions, gas atoms and dust) move nearly along the magnetic lines and fall to the Jupiter. The thermal and electric interaction of volcanic dust with stones, and with the low-ionized plasma and gas, that have been ones injected by Io (or by Sun, or by another Jupiter satellite), will be created the ionized streamer in the form of the plasma streamer-tubes of width of about a_x~ 100 km, that is much shorter then width of the main Io-Jupiter flux tube.

The streamer plasma may creates by Saha-Langmuir electron ionization mechanisms (see: Smirnov, 1995, Boev, et al. 2001), that comes when the gravity-accelerated dust-stone fluids is interacted with gas matter (n_a) and have heat the plasma high then 4000 K:

$$n_e^{\,2}/(n_a - n_e) \propto Const \cdot T_e^{\,3/2} \cdot \exp(-\varepsilon / k_b T_e) .$$

In Jupiter magnetosphere we have T_a<1000K (for gas matter), T_e~3000K (for electron matter) (see: Boev, et al., 2001). The streamer plasma is some more hitting, pinch-compressed and stratified matter, and the streamer structure may be justified by observations when we observe the different frequency drifts of DAM bursts in dynamical spectra.

There may be run the next plasma processes in that streamer-stratified plasma: the ionization; the streamer-pinching processes; the adiabatic effects in the streamer flows; the plasma-rain processes; the coupling of the streamers (by the current flows coupling or in the magnetic field reconnection processes); the streamer MHD-wave excitations (see latter); the streamer stratification effects; the plasma diffusing out the streamer (with ambipolar flow).

So, the pinching effects are supported the streamer formation, because of the plasma compression by the j_z-pinching effects or by the j_θ-pinching effects (see: Kadomtsev, 1963, 1988). The first way, the current of $j_z(r_x)$ are supported the streamer magnetic field to grow as $\mathbf{B} \sim (\mathbf{B}_{0z}+\mathbf{B}_\theta)$, and this leads to the localization of a streamer matter within its flux tube. The next one is the j_θ-pinching effects, when the current of $j_\theta(r_x)$ will take place at the streamer stabilization processes with the added of an longitude streamer magnetic field of the value dB_z. In additionally, the geometry of the streamer is anisotropic, due to the fact that the magnetic field lines B_{0z} converge and the width of the streamer decreases towards the surface of

Jupiter (at low z_j), and therefore the transverse electron velocities in the fluxes and their distribution change adiabatically as: $\frac{{v_{e\_|\_}}^2}{B_{0z}(z_j)} = Const$ (Kadomtsev, 1963). All of these effects support the formation of a 'static' streamer structure, and the other way, the streamer plasma diffusion both and the fluxes geometry effects are leading to the anisotropization of the electron distribution, and the fluctuation of pinching current leads to the dynamical effects by the MHD waves excitation.

The further in the section 3 we will study on the MHD-wave excitations effects in detail, because of it leads to the pumping dynamically of the anisotropic electron distributions, and then, that give us the arising the EM bursts waves radiation in different ways, and it may explain us the formation of the Jupiter DAM bursts (in the section 4).

3. The features of MHD waves inside the streamer

Here we are studied how the MHD waves are excited and transported in the streamers along or in transverse directions to the magnetic field lines, in using the basic theory of MHD hydrodynamic, see: Kadomtsev (1963), Akhiezer (1974). The next study is how these waves can affect to the kinetic distribution of electrons through fluctuations in electric fields, and we will see these effects too.

The MHD waves in the streamer matter need to see in 3D-geometry (like to the Sun streamer study, see: Appert, et al., 1974, Edwin & Roberts, 1983), and in the MHD equations there must be account the low-ionized plasma conditions of multi-components fluids (electron, protons/ions and neutral gas atoms) (see: Braginskyi, 1963). So, that way the equations of moving fluids in the low frequency, for Alfven and fast magneto-sonic waves, will have the main term in that accounted the neutral gas inertia, and the Alfven wave velocity will dependent not from ion density (n_i~n_e), but from the neutral gas density (n_a, when $n_a >> n_e$), that give us the much slowly Aflven velocity then in the classic case:

$$c_{A\_gas} = \sqrt{B_{0z}/(4\pi n_a m_p)} = c_{Ai}\sqrt{n_i/n_a}\,.$$

And then, in high frequency, the fast MHD wave velocity grows up to the c_{Ai} value.

At this reason, in Jupiter magnetosphere it may realize some cases on the MHD wave velocities and its dispersion. At first, the fast MHD wave velocity in low-ionized plasma depends on the degree of ionization and on the wave frequency. So, in the streamer, c_A velocity at a large wavelength (small k_A) not varied in streamer width, because of c_A~c_{A_gas}, and because that the MHD waves not be dumping strongly. The wave field values, B_w, E, both and the current density fluctuation values, j, n_{wi}, v_i, v_{we} , are dependent on the streamer width coordinates, r_x, and they be limited by streamer width r_x~a_x, because of variations of a plasma density, $n_{i0}(r_x)$.

There are considered now the main properties of the 3D-MHD waves in the in streamer-stratified plasma. We take the wave deviation of the plasma parameters as a function of $\propto Fct(r,\theta)\cdot\exp(ik_z z + im_k\theta - i\omega t)$. These streamer waves ware studied (for example) by Edwin& Roberts (1983), Bembitov, et al. (2014) in solar plasma conditions, but now we will look for E-fields and electron wave velocity oscillations which can be found by using Maxwell's and MHD wave equations at Akhiezer (1974).

Let us begin to consider from Alfven waves properties in the {z, r_x, θ}-geometry, which will be mainly propagate along the magnetic lines with $\mathbf{k_A} = (k_{zA}, k_{rA}(m_k)\}$~$\mathbf{k_{zA}}$. That waves may be excited at the resonance frequency in the helical mode (m_k=1) with $\omega_{res} << \omega_{Bi}$, by the Helical instability (see Kadomtsev, 1963), where:

$$\omega_{A(Hel)} \cong c_A \cos\theta\,(1 + \left(k_{zA} - \frac{m_k b_\theta}{a_x}\right)^2 - \frac{m_k b_\theta}{{a_x}^2})^{1/2}$$

Here is: $b_\theta = B_{\theta A}/B_{z0}$. In the Jupiter magnetosphere conditions, this Helical-kink Alfven mode (m_k=1) are running along the magnetic field lines, with the $\lambda_{A,z}$ -lengths that are high then streamer width (a_x), and it will be compared 3000km, that is high-scales of Jupiter magnetosphere at low z_j-altitudes. That wave frequency is about ω_{res} ~1 s^{-1} ($\omega_{res} << \omega_{Bi}$), and resonance Alfven wave length is $\lambda_{A,res}$ ~ $2a_x/b_\theta$ ~ 1000km, when the streamer width is a_x~1-100 km.

It should be note that the parameters of that 3D Alfven waves are limited by the thickness of the streamer, and maximum of Alfven wave frequency ω_{Bi} goes down outside the streamer. There are no wave density fluctuations by time, alternatively, we have the static plasma density dependence in the streamer, $n_{i0}(r_x)$. The magnetic field and electric fluctuations in the Alfven waves are connected with j_z-pinching oscillation, and they have $B_\theta(r_x)$, $E_z(r_x)$, $E_r(r_x)$ components. Because of the streamer cylindrical geometry, the r_x-dependence of the field components comes to zero in the streamer core, $B_\theta(0) = E_r(0) = 0$; but $E_z(0)$ field in the streamer core is a big value. Out in the streamer core, the Alfven waves have the plasma (ion and electron) particle fluctuations in the θ–direction mainly with $v_{e\theta}(r_x)$~$v_{i\theta}(r_x)$, where $\mathbf{v_e} = \mathbf{v_i} - \mathbf{j}/(en_e)$; and they have a non-zero current fluctuations $j_{er}(r_x)$, $j_{ez}(r_x)$, and an electron velocity is differ then ion ones in z_j- and r_x- directions, $v_{ez,r}(r_x) \gg v_{iz,r}(r_x)$. Because of the streamer geometry, the r_x-dependence of current and transverse velocity components comes to zero in the streamer core, $j_{r,\theta}(0)\rightarrow 0$ and $v_{e\_|\_}(0) = (v_{er}^2(0) + v_{e\theta}^2(0))^{1/2}\rightarrow 0$. Alternatively, we have non-zero z-component of electron velocity, $v_{ez}(0)$, in the streamer core, and that sketch of electron velocity distribution within the streamer have been represented in Fig. 1.

The electric field oscillations in the Alfven wave lead to the pumping of the electron kinetic distribution of various types inside and outside the steamer core. Thus, the electrons swing with velocity $\mathbf{v_e}$ along the streamer and is accelerated inside the streamer core to the high-velocity electron beam, up to $v_{e\ beam}$~c_{Ai}~$0.1c$. Alternatively, in the streamer periphery, the transverse velocities $v_{er,\theta}(r_x)$ of much number of electrons are raised dynamically, and we have to pumping the cone-like electron distribution in that place.

The next type of MHD waves that may be interested in the 'streamerring' Jupiter magnetosphere is the fast magneto-sonic (FMS, or Helicon) waves. Those waves may be generated partly at the deep streamer core as the waves which propagate along the magnetic field lines in added to the Alfven waves of low-frequency fluctuations (λ_{ms_x}),

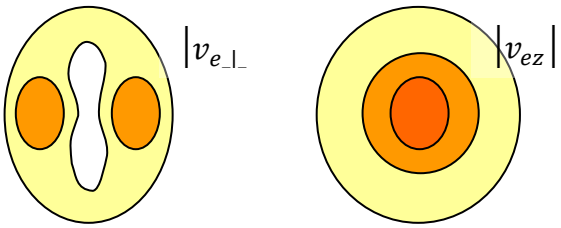

Figure 1: The sketch of the streamer at z_j=const, which show the v_e-electron velocity fluctuations in the case of Alfven wave have been excited. Thus, the electrons are accelerated inside the streamer core to the electron beam because of v_{ez} oscillations, and there are pumping the cone-like distributions in the streamer border because of $v_{e\_|\_}$ oscillations.

when the wave-energy is partly converted from Alfven type to the FMS waves. The other way, the fast magneto-sonic waves will be exited in the perpendicular direction to the magnetic field line mainly due to the plasma diffusion processes in the streamer periphery places, as the small-size magneto-sonic waves at high frequency of about ion-cyclotron and up to "plasma cyclotron hybrid" frequency. The fast magneto-sonic waves have a view a sausage radial fluctuation at **k**={k_z,k_r}, or a kink-surface streamer mode (m_k=1,2..) at **k**={k_z,k_θ} on e-plasma density profile. The fast magneto-sonic turbulence may lead to the fast plasma diffusion and to the streamer stratification. The pinching effects are "joining" the plasma in the streamer frame, to interrupt the plasma diffusion and plasma stratification processes.

The magnetic and electric field fluctuations in the FMS waves are connected with the j_θ -pinching oscillation and they have $B_z(r_x)$, $B_r(r_x)$, $E_\theta(r_x)$ field components. Because of the streamer cylindrical geometry, the field components comes to zero at a streamer core, $B_r(0) = E_\theta(0) = 0$. These fast MS-waves have the main plasma (ions, electrons) particle fluctuation in the r_x- and θ-direction with $v_{ir}(r_x) \sim v_{er}(r_x)$, and they have an electron and current fluctuations in θ- direction: $v_{e\theta}$, $j_\theta(r_x)$. Thus, under the fast MS-waves influence, the transverse velocities $v_{er,\theta}$ of number of electrons are raised dynamically in the streamer periphery, and this way the cone-like type of an electron distribution are pumping at the streamer border.

Finally, we stop briefly at the low MS waves and at the plasma waves inside the streamer. So, the low MS waves may be exited in the streamer at the low-frequency sausage modes which have the plasma density fluctuation v_i in z-direction mainly, and this wave is transported along the streamer. It is very slow mowing wave, because c_s/c_A<0.0001, and it be exist when the electron temperature be higher than ion ones. The magnetic oscillations in these waves are small, so the electric field oscillations are potentially and have the components E_z, E_r which connects with the current oscillations, $j_{z,r}$. So, the electron oscillations in this wave will have $v_{ez} \gg v_{er}$, $v_{ez} \leq v_{iz}$, and they may lightly support the injection process of electron beam together with Alfven waves, but not give us of high velocity of beam which we observed.

The beam, that have arisen inside the streamers core, will generate the plasma waves in Cherenkov instability at nearly the electron Debye wave-lengths, $\lambda_l \sim {k_{De}}^{-1} \sim v_{Te}/\omega_{pe}$, and at the frequency $\omega_l \sim \omega_u = ({\omega_{be}}^2 + {\omega_{pe}}^2)^{1/2}$. This plasma wave has an electron density, velocity and current oscillations, $n_e(r_x)$,$v_{e\theta,r}(r_x)$, $j_{r,\theta}(r_x)$, and the ion wave oscillations are extremely small. Electric and magnetic fields in the plasma wave are the circular polarization modes, and the *E*-field component transforms to the longitude fields E_z at frequency up to the upper hybrid resonance, ω_u. Plasma wave velocities at high frequencies have characteristics of anomalous dispersion waves, and it transports the energy out the streamer when the wave velocity directed inside the streamer. The wave polarization change at the frequency, in which the plasma wave comes to anomaly dispersion region.

4. The influence of MHD waves on the EM bursts radiation

The electron kinetic distribution in the streamer-like magnetosphere may change by adiabatic effects in the magnetic flux $B_z(z_j)$ -tubes of in the gas-dust Io-Jupiter flows, or by plasma diffusion in the streamer structures, or by pumping effects at the electro-magnetic forces of MHD waves influence. So, that is way will be formed mainly the cone-type kinetic distribution of electrons for first of two cases. Alternatively, under MHD waves, the fluctuations of electric field depended on the site place in the streamer, and it changed on the MHD wave length and period.

Thus, due to the MHD wave oscillations, the kind of the kinetic electron distribution is varied by streamer radius as that the cone-like electron distribution form at medium and high speeds, primarily on the streamer periphery, and to the beam-like electron distributions form with an electron beam of that have been accelerated to speeds of about $0.1c$ in the streamer core. This leads to the dichotomy of DAM bursts that connected with activation the EM waves by MHD waves of different types.

Here is we consider how the EM waves radiate in the bursts in the sources (see: Wu, 1985, Melrose, 1986, Ryabov & Gerasymova, 1990, Boev & Luk'yanov, 1991). The EM waves are generated when it defined that resonance condition in electron velocity:

$$\omega + \frac{m_k \omega_{Be}}{\Gamma(v_e)} - k_z v_{ez} = 0 \ ,$$

where it is $\Gamma(v_e) = (1 - {v_e}^2/\mathrm{c}^2)^{-1/2}$, and this give us the EM burst be excited by two ways: for $m_k = -1$ (one way) when it is generated the Maser DAM radiation (X-EM), and for $m_k = 0$ (second way) when radiation comes in the plasma waves that will transform further to the DAM radiation (of X-EM mode). So, when the condition for the burst generation has been realized, the bursts radiate. The type of generation mechanism depends on the e-particles distribution, and the Maser mechanism works in the places where is the cone-like kinetic electron distribution realized in the source, alternatively, Cherenkov radia-

tion corresponds to the places with the beam-like electron distribution.

Here is the Alfven wave deviate the kinetic velocities distribution in scratch profile $f\{v_e; z_j, r_x, \theta; t\}$ that move with c_A velocity along the Jupiter magnetic field lines. This is give us to observe the slow drift of the frequency of the bursts radiation in the frequency-time dynamical spectra df/dt ~200 kHz/s, and this drift can be seen in the L-bursts.

Let us consider how to form the short (S) and narrow (N) bursts of the Jupiter radiation. One way, they may radiate by the short FMS waves (λ_{ms}~0.1-1 km) that modulate the streamer border surface, so, it may be give us to observe the fast-drift of the EM radiation which varied in (*f*-*t*) spectra. And, the second way, in the case of when the electron beams are running in the streamer core strongly along the magnetic field lines with the velocity up to v_{ez}~0.1c, and this may excite the Cherenkov generation of Plasma waves, and it give us the second way of S-burst radiation with the frequency drift of df/dt ~ 20 MHz/s. So, in variation the plasma density in the streamer may give us the finest burst profiles with splitting and other features.

Finally, we have show that all these processes lead to the activation of the bursts of Jupiter's DAM radiation in that source at the frequency close to the electron cyclotron resonance, with different generation mechanisms and with different bursts properties.

5. Conclusion

The streamer-like structure, that arise by ionization process in Jupiter magnetosphere, supports the anisotropization of kinetic electrons of both as cone-type and beam-type distributions, that further leads us to the generation of Jupiter's DAM burst radiation under different scenarios. The cone-type kinetic distribution of electrons arise under adiabatic and diffusion effects, and under the influence of the MHD waves, due to the fluctuations of wave electric field. That way we have the streamer to be an effective source to DAM radiation by Maser generation mechanism, that be changed dynamically.

The Alfven waves move along the streamer and pump the electron distributions of both "cone-like" (primarily on the streamer periphery) and "beam-like" type of accelerated electrons (with the electron beam speeds of about 0.1c, in the streamer core). These Alfven waves have lengths of about ~ 1000 km and periods of ~ 1 second. The streamer's fast magneto sonic waves (of short-lengths and moving in out or tangential to streamer direction) also support the "cone" electron distribution, and may modulate of DAM bursts.

The beams of accelerated electrons, that can arise in the streamer core, will generate the plasma waves in the tangential to streamer direction (at about the electron cyclotron resonance frequency). This wave radiation will be converted to EM mode and may give us to see the fast-moved (S) bursts of DAM radiation.

References

Akhiezer A.I., Akhiezer I.A. et al.: 1974, Plasma electrodynamics (*in Russian*), Moscow: Nauka, Glav. red. phys.-mat. Literatury /eds. Akhiezer A.I., 719 p.

Appert, K. et al.: 1974, *Phys. Fluids*, **17**, 1471.

Bembitov D.B. et al.: 2014, *Ann. Geoph*., **32**, 1189.

Boev A.G., Luk'yanov M.Yu.: 1991, *Sov. Astron.*, **68**, 853.

Boev A.G., Luk'yanov M.Yu., Tsvyk N.: 1993, *Kinemat. Phys. Celest. Bod.*, **9**, 37.

Boev A.G., Udal'tsova N.M., Yantsevich A.A.: 2001, *Radiophys. Radioastron*., **6**, 252.

Bragynskyi S.I.: 1963, The questions of plasma theory (*in Russian*), **1**, 183, Moscow: Gos. izdatel'stvo literatury po nauke i tekhnike /ed. Leontovich M.A.

Edwin P.M., Roberts B.: 1983, *Solar Phys*., **88**, 179.

Kadomtsev B.B.: 1963, The questions of plasma theory (*in Russian*), **2**, 132, Moscow: Gos. izdatel'stvo literatury po nauke i tekhnike /ed. Leontovich M.A.

Kadomtsev B.B.: 1988, Nonlinear phenomena in the plasma (*in Russian)*, Moscow: Nauka, Glav. red. phys.-mat. Literatury /eds. Akhiezer A.I.

Melrose, D.B.: 1986, *J.Geohys.Res*., **91**, A7, 7970.

Ryabov B.P., Gerasymova N.N.: 1990, Decameter sporadic radioemission of Jupiter (*in Russian*), Kyiv: Naukova dumka.

Ryabov V.B., Zarka P. et al.: 2014, *Astron. Astroph.*, **568**, A53.

Smirnov B.M.: 1995, The physics of the low ionized gas (*in Russian)*, Moscow: Nauka, Glav. red. phys.-mat. Literatury, 424 p.

Tsvyk N.O.: 2019, *Odessa Astron. Publ.*, **32**, 105.

Wu C.S.: 1985, *Space Sci. Rev*., **41**, 215.

https://doi.org/10.18524/1810-4215.2023.36.290189

ANGULAR STRUCTURE OF THE RADIO GALAXY 3C280 AT DECAMETER WAVELENGTHS

R.V. Vashchishyn[1], V.A. Shepelev[2], O.A. Litvinenko[3], G.S.Podgorny[2], A.V. Lozinsky[4]

[1] Gravimetric Observatory of IGP NASU, Poltava, Ukraine, *vrv.uran2@gmail.com*

[2] Institute of Radio Astronomy of NASU, Kharkiv, Ukraine, *vshep258@gmail.com*

[3] URAN-4 Laboratory of IRA NASU, Odesa, Ukraine

[4] Physical and Mechanical Institute of NASU, Lviv, Ukraine

ABSTRACT. The image of the 3C280 radio galaxy at decimeter wavelengths consists of two emission regions, the centers of which are separated by about 13 arc seconds. These regions are lobes of the radio galaxy with bright compact components or hot spots embedded in them. We present the results of a study of the source structure in the decameter wavelength range, carried out with the URAN-1 – URAN-4 radio interferometers using a especially technique developed. We show, that at the decameter wavelengths, the source model contains two extended components with the size and position as the lobes have in the decimeter range and a compact detail corresponding to one of the hot spots. The radio emission of other hot spots is not detected at the decameter waves due to their low flux density. The spectra of the radio galaxy components and their variation in the range from decameter to decimeter wavelengths are determined in this study. It is found, that extended lobes provide about 70% of 3C280 flux at low frequencies in contrast to the high-frequency image of the radio galaxy, where compact hot spots predominate in the source radiation.

Keywords: radio source, interferometer, decameter range, brightness distribution, decameter model.

АНОТАЦІЯ. Зображення радіогалактики 3С280 на дециметрових довжинах хвиль складається з двох областей випромінювання, центри яких рознесені приблизно на 13 кутових секунд. Ці області є пелюстками радіогалактики з яскравими компактними компонентами або вбудованими в них гарячими плямами. Наведено результати дослідження структури джерела в декаметровому діапазоні довжин хвиль, що були виконані на радіоінтерферометрах УРАН-1 – УРАН-4 за спеціально розробленою методикою. Ми показуємо, що на декаметрових хвилях модель джерела містить два протяжних компонента з розміром і положенням пелюсток, як у дециметровому діапазоні та компактну деталь, що відповідає одній із гарячих плям. Радіовипромінювання інших гарячих плям на декаметрових хвилях не реєструється через їх малу густину потоку. У цьому дослідженні визначено спектри компонентів радіогалактики та їх зміну в діапазоні від декаметрових до дециметрових довжин хвиль. Виявлено, що протяжні пелюстки забезпечують близько 70% потоку 3С280 на низьких частотах, на відміну від високочастотного зображення радіогалактики, де компактні гарячі плями переважають у випромінюванні джерела.

Ключові слова: радіоджерело, інтерферометр, декаметровий діапазон, розподіл яскравості, декаметрова модель.

1. Introduction

Radiogalaxy 3C280 is a compact FRII radio source with a steep spectrum. It is located in a distant galaxy cluster and has a redshift of z=0.996. A massive elliptical galaxy identified with this radio source is located at its center. (Zirm, 2003). Quite powerful, with an interesting morphology, 3C280 attracted our attention with its complex angular structure at high frequencies (Allen et al., 1972; Clark et al., 1966; Wraith, 1972; Wilkinson, 1972; Mullin et al., 2006; Laing, 1981; Bovkun et al., 1981; Readhead et al., 1976) and the almost complete absence of data about it in the decameter range. In this work, we want to conduct investigations of this source at the lowest frequencies, not limited by the transparency of the ionosphere, and obtain the angular brightness distribution. We also want to find out what possible changes in its structure may occur and determine their probable causes.

From numerous radio images of 3C280 obtained at different times, for analysis and comparison, we chose maps obtained with MERLIN interferometers and the VLA supersynthesis system (Mullin et al., 2006).

On the map obtained at the VLA at a frequency of 1.4 GHz (Xu et al., 1995) with a resolution of 1.5" (see Fig. 2), extended regions of diffuse synchrotron radiation – lobes – are clearly visible. They are located symmetrically to the east and west relative to the center of the source, which contains the galactic nucleus (due to low flux at these frequencies, it is not visible). The eastern lobe is about 3", and the western lobe is about 4". Hot spots on this map, due to its low resolution, are not completely resolved. In the eastern lobe, the hot spot has a radial shape and is located in the

center of the lobe; in the western one, it is slightly elongated in the northwest direction and lies closer to the edge.

On the contrary, no lobes are observed on the maps from (Mullin et al., 2006), which have a resolution of 0.35" and 0.06". However, hot spots are clearly visible. Several compact brightness regions are visible in place of the elongated hot spot on the map at 1.5" resolution.

So, having at our hands a system of decameter radio interferometers URAN and a map obtained at VLA at 1.4 GHz (Xu et al., 1995), which have approximately the same resolution, we decided to compare the brightness distribution of 3C280 at high and low frequencies.

2. Observations and data processing

Observations of 3C280 were carried out using the Ukrainian decameter VLBI network URAN (Megn et al., 1997) simultaneously at frequencies of 20 and 25 MHz. Interference oscillations were formed by multiplying the signals from the north-south antenna of the UTR-2 radio telescope with the signals from the antennas of the URAN system. The measurements were carried out in separate sessions in the autumn-winter period for several days at hourly angles of ±240 minutes relative to the culmination. The data obtained at each hourly angle were averaged for all observation days, and then the weighted average value of the visibility module and its error were calculated. An example of the experimental values obtained and their errors for the URAN-1 and URAN-2 interferometers are shown in Fig. 1 by symbols *1* and *3*.

As is known, the inverse Fourier transform of a similar set of values obtained on different bases represents the source brightness distribution. For this, the necessary conditions are the availability of information about the phase, good filling of the spatial frequency plane, and a sufficient signal-to-noise ratio. However, at decameter waves, wavefront distortions due to the influence of ionospheric irregularities on the propagation of radio waves lead to a phase shift of the measured visibility between antennas more than 2π radians. Also, the signal-to-noise ratio at large bases can be about 1, and the coverage of the *uv*-plane in our observations is not sufficient. All this makes it impossible to use this method of image restoration, therefore to determine the radio brightness distribution of sources in the decameter range, we use a model selection method without information about the phase of the visibility function.

Quite well known, this method has proven its effectiveness in many ours the investigations we have conducted. It is described in (Megn et al., 2001) and consists of representing the real source brightness distribution in the form of a model consisting of a certain number of elliptical components with arbitrary axes orientation and a Gaussian radio brightness distribution.

The process of obtaining a model consists of a sequential step-by-step change of the initial parameters (dimensions, fluxes, coordinates, inclination, etc.) and repeated calculations of the interferometer response. This operation aims to minimize the sum of the least squares of deviations between the calculated response and the experimental one. In this way, the resulting model is consistent with the experimental dependences of the visibility modulus on the hour angle for all bases and frequencies.

To facilitate the calculation of the decameter model, its correctness, and accuracy, we use a priori information from the literature to find the parameters of the initial approximation. We take such information from digital maps of the source, obtained at frequencies as close as possible to ours, and with an angular resolution no worse than that of the URAN-3 radio interferometer, which has the largest base of about 900 km. From the selected map, we calculate the dependence of the visibility modulus on the hour angle for interferometers with our geometry. Next, we select a simple model using the least squares method. The interferometer responses from this model and from the map should be as close as possible.

In our case, to determine the initial parameters for the search of a decameter model, we used the 3C280 digital map, obtained at VLA at a frequency of 1.4 GHz with a resolution of 1.5" (Xu et al., 1995). The model calculated from this map is presented in Fig. 2, and its parameters are summarized in Table 1.

Fitting the model to the digital map made it possible to identify the structural components of the high-frequency image – two lobes and two hot spots: one in the western lobe and one in the eastern. At the same time, in the western lobe the hot spot has a small visible extent (see Fig. 2). On

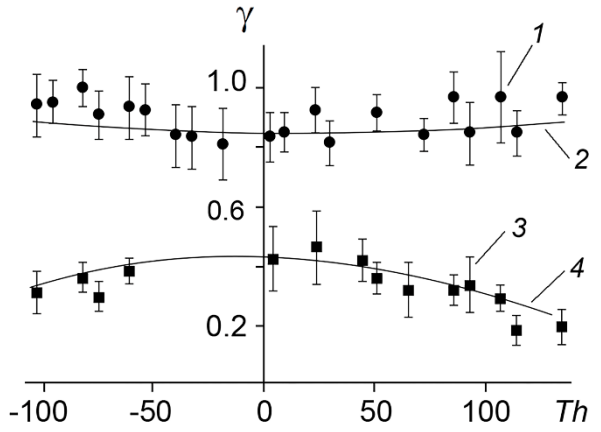

Figure 1: Visibility modulus at a frequency of 25 MHz: *1*, *2* – experimental and calculated for URAN-1; *3*, *4* – experimental and calculated for URAN-2

Table 1: Model from the 1.4 GHz map

Detail	α, "	δ,"	S/S_0	θ, "	*a/b*	ψ, °
HS_E	6,34	0	0,19	1,5	1	0
BCA1	-6,34	0	0,29	1,2	1	0
BCA2	-6,02	0,5	0,32	2.9x2,0 (2,4)	1,41	-50
$Lobe_E$	6,34	0	0,07	2,4	1	0
$Lobe_W$	-3,9	0,8	0,13	5,3x3,3 (4,2)	1,6	72

Notes: α, δ– coordinates of the components relative to the conventional geometric center of the source; *S/S0* – share in the total flux; θ – size; *a/b* – ellipticity; ψ– position angle; BCA1,2 – bright compact regions in the western lobe.

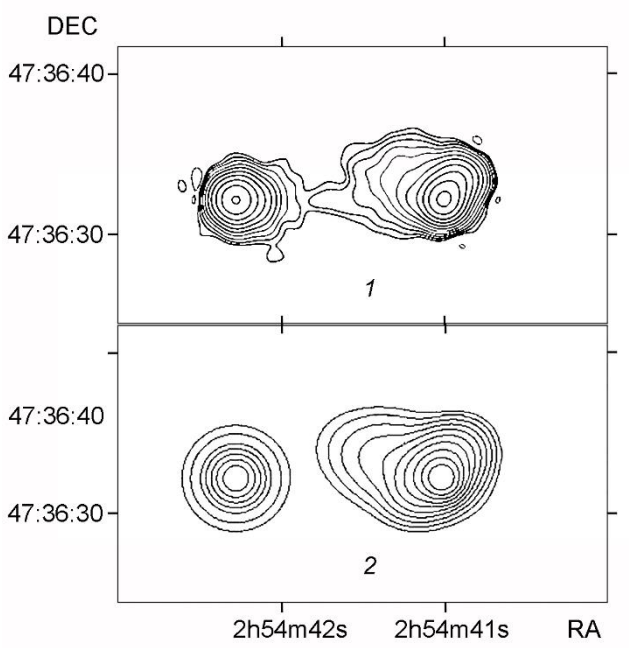

Figure 2: Radio galaxy 3C280 at 1.4 GHz: *1* – map from (Xu et al., 1995); *2* – model

Table 2: Decameter model of 3C280

Detail	α''	δ''	S/S_0	θ''_{25}	θ''_{20}	*a/b*	ψ°
HS_W	-6,34	0	0,3	1,7	2,1	1	0
$Lobe_E$	5,6	0	0,3	2,5	2,9	1	0
$Lobe_W$	-3,9	0,8	0,4	4,3	4,6	1,6	72

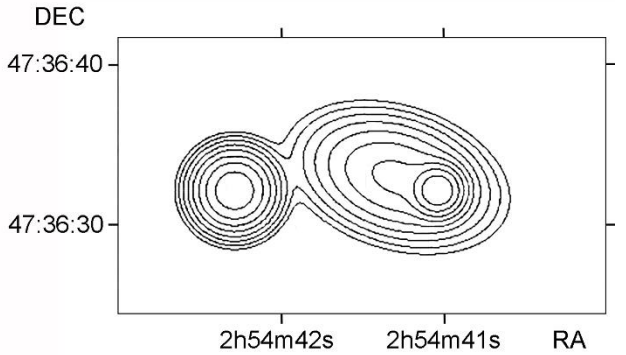

Figure 3: Model 3C280 obtained at 25 MHz

the ultra-high-resolution map from (Mullin et al., 2006), as discussed above, in place of the elongated hot spot, several compact brightness regions are there. To better match the interferometric response, we modeled it as two nearby compact bright regions.

3. Results

Comparison of the visibility modulus experimental dependences on the hour angle with the ones fitted to the high-frequency map for all decameter interferometers made it possible to identify their differences. They occur due to changes in the spectral characteristics of the source components at low frequencies. Thus, for URAN-2 the experimental visibility is about 40% instead of the calculated 75%; on URAN-4 it is 25% instead of the calculated 45%; the response from the URAN-3 interferometer turned out to be below 8% instead of the calculated 17% at the maximum of fluctuations. All these changes are due to an increase in the share of the flux of extended components, and an increase in the size of compact components, including the scattering. The experimental response from the URAN-1 interferometer is quantitatively equal to the calculated one since the image of the radio galaxy does not contain large formations (>20") with low surface brightness. Therefore, URAN-1 sees all detected components in 3C280 as point sources and does not resolve them.

To search the decameter model, we extrapolated the resulting high-frequency model to low frequencies, taking into account all our knowledge about the spectral characteristics of the components and the scattering angle of radio emission in the interstellar medium. Next, we selected the flux ratios of the components, then their ellipticity and inclination. In this model (see Table 2), the sizes of the components, compared with those given in Table 1, changed by the value of the scattering angle. In our case, according to (Shyshov, 2001), at 25 MHz it is 0.9", and at 20 MHz it is 1.47". Two bright compact regions in the western lobe, which simulated an elongated hot spot at high frequencies, are observed as one. On high-resolution maps (Mullin et al., 2006), the position of this region in the group of spots corresponds to a hot spot with the highest brightness and small size. The coordinates of the hot spots have not changed; the eastern lobe has shifted slightly towards the center.

Comparing the fluxes of components of high-frequency and decameter images given in Table 1 and Table 2, it should be noted that in the decameter range, about 70% of the flux density is formed by extended elements – lobes. Their radiation, compared to hot spots, has a steeper spectrum. The western hot spot accounts for 30%. Our data are consistent with the size and flux of the scintillating component at 25 MHz obtained in (Bovkun, 1981). Since radiation from the eastern hot spot is not observed at low frequencies, we can say with confidence that in (Bovkun, 1981) and (Readhead, 1976) the scintillating component is the western hot spot. At high frequencies, about 80% of the radiation is formed by hot spots.

For example, in Fig. 1 solid curves *2* and *4* show the calculated hourly dependencies of the decameter model for the URAN-1 and URAN-2 interferometers, in Fig. 3 – model that we obtained at 25 MHz. Here the radio image is presented in isophotes on a logarithmic scale. Systematic errors do not exceed 15%.

Fig. 4 shows the spectral characteristics of 3C280. The data obtained in this work is shown at frequencies of 20 and 25 MHz.

The full spectrum of the source was fitted by linear approximation of literature data (Vigotti et al., 1999; Roger et al., 1986; Kuehr et al., 1981; Herbig et al., 1992) using the least mean squares method from 10 to 5000 MHz. In the region from 20 to 1000 MHz, it is linear and does not have any curvatures caused by various known mechanisms (Herbig et al., 1992).

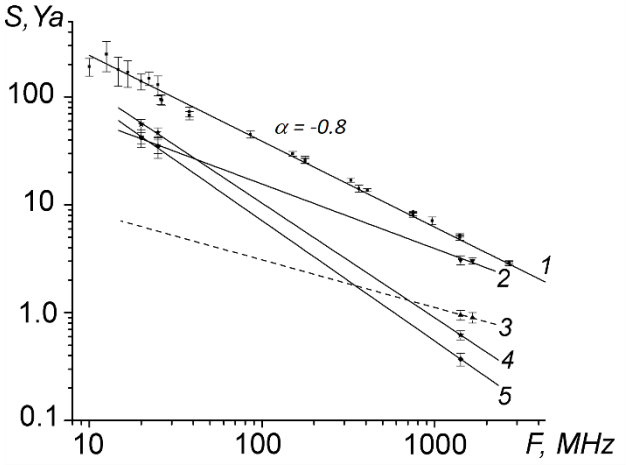

Figure 4: The spectrum of 3C280 and the probable spectra of its components: *1* – total spectrum of the source; *2*, *3* – western and eastern hot spots; *4*, *5* – western and eastern lobes

Since we do not have information about any curvature of the spectra of extended components, we assume them linear in this range. Its were approximated from data taken from digital maps obtained at frequencies of 1.658 GHz on MERLIN ("MERLIN/e-MERLIN is a National Facility operated by the University of Manchester at Jodrell Bank Observatory on behalf of STFC, part of UK Research and Innovation") and 1.4 GHz on VLA (Xu et al., 1995), as well as taking into account our data at 20 and 25 MHz.

As can be seen from the figure, the change in the image from high to low frequencies is determined by the spectra of the components. At decimeter and especially centimeter waves, hot spots have the greatest brightness. Extended details, and lobes, are practically not observed. With increasing the length of the wave the redistribution of fluxes occurs: extended regions emit long waves more intensely, while compact regions become noticeably weaker due to the lower values of their spectral indices. Thus, the emission intensity of the eastern hot spot at decameter waves turned out to be insufficient for stable detection by our instrument.

4. Conclusion

For the first time, the angular structure of the radio galaxy 3C280 was studied using the interferometric method in the decameter wavelength range. Models of the brightness distribution at frequencies of 20 and 25 MHz were obtained, and the probable spectral characteristics of the radio source were determined. It was found that:

1) The sizes of extended components did not change with decreasing frequency. In place of the group of compact bright regions, which at 1.4 GHz formed a slight elongation of the western hot spot, only one remained, the brightest, with a flux fraction of 30%. Its size is determined by scattering on the interstellar medium;

2) About 70% of the total flux at low frequencies is formed by extended components - lobes, while at high frequencies 80% of the radiation is provided by hot spots. The size and contribution of the compact component to the flux of decameter radiation are consistent with the results of studies of 3C280 previously conducted at 25 MHz by the scintillation method on inhomogeneities of the interplanetary plasma;

3) The eastern hot spot flux lies below the sensitivity threshold of our instrument and does not affect the interferometric response.

Acknowledgements. V.A. Shepelev acknowledges the Europlanet 2024 RI project funded by the European Union's Horizon 2020 Research and Innovation Programme (Grant agreement No. 871149).

The authors express their gratitude to David Williams from the Jodrell Bank Observatory for providing the necessary materials for this work.

References

Allen, L.R., Anderson, B., Conway R.G. et al.: 1972, *Mon. Not. R. Astron. Soc.*, **124**, 477.
Bovkun, V. P., Zhuk, I. N., Men, A. V.: 1981, *Soviet Astronomy Letters*, **7**, 192.
Clark B.G., Hogg D.E.: 1966, *Astrophys. J*, **145**, 210.
Herbig T., Readhead A. C. S.: 1992, *Astron. Astrophys. Suppl. Ser.*, **81**, 83.
Kuehr H., Witzel A., Pauliny-Toth I. I. K. et al.: 1981, *Astron. Astrophys. Suppl. Ser.*, **45**, 367.
Laing R. A.: 1981, *Mon. Not. R. Astron. Soc.*, **195**, 261.
Megn A.V., Braude S.Ya., Rashkovsky S.L., et al.:1997, *Radio phys. radio astron.*, **2**, 4, 385.
Megn A.V., Rashkovsky S.L., Shepelev V.A.: 2001, *Radio phys. radio astron.*, **6**, 1, 9.
Mullin L. M., Hardcastle M. J., Riley J. M.: 2006, *Mon. Not. R. Astron. Soc.*, **372**, 113.
Readhead, A. C. S., Hewish, A.: 1976, *Mon. Not. R. Astron. Soc.*, **176**, 571.
Roger, R. S., Costain, C. H., Stewart, D. I.: 1986, *Astron. Astrophys. Suppl. Ser.*, **65**, 485.
Shyshov V.I.: 2001, *Astron. J.*, **78**, 3, 229.
Vigotti M., Gregorini L., Klein U. et al.: 1999, *Astron. Astrophys. Suppl. Ser*. **139**, 359.
Wilkinson P. N.: 1972, *Mon. Not. R. Astron. Soc.*, **160**, 305.
Wraith P. K.: 1972, *Mon. Not. R. Astron. Soc.*, 160, 283.
Xu W., Readhead A. C. S., Pearson, T. J. et al.: 1995, *Astrophys. J. Suppl. Ser.*, **99**, 297.
Zirm W.: 2003, *Astrophys J*, 585, 90.

https://doi.org/10.18524/1810-4215.2023.36.290586

MOTIONS OF THE COMPONENTS OF AGNS ACCORDING TO VLBI MOJAVE DATA AS INDICATORS OF THE ACTIVITY AND SPATIAL STRUCTURE OF THE JET

Zabora D.[1], Ryabov M.[2], Sukharev A.[2], Bezrukovs V.[3], Bazyey A.[1]

[1] Faculty of Mathematics, Physics and Information Technologies ONU, Ukraine

[2] Institute of Radio Astronomy of the National Academy of Sciences of Ukraine (IRA NASU), Ukraine

[3] Ventspils International Radioastronomy Centre of Ventspils University of Applied Sciences, Latvia

ABSTRACT. The system of ten radio telescopes VLBA (Very Large Baseline Array), with a maximum baseline of about 8,600 km, of the National Radio Astronomy Observatory of the USA (NRAO USA) carries out systematic monitoring observations of about 500 active galactic nuclei (AGN), the results are presented in the MOJAVE database. The resulting angular resolution (~0.47 arcseconds at a frequency of 15.4 GHz) is enough to separate the close surroundings of the AGN and its jet. The results of corresponding observations make it possible to compare the features of movement in the jet with the processes of activity of the AGN, as well as to study its spatial structure.

The MOJAVE database contains the spectral densities of the radio fluxes of the AGN, radio images for each epoch of observations at the frequency of 15.4 GHz, and "Separation jet" diagrams (showing the angular separation of the jet components over time). This information makes it possible to study the movement of these components. In this work, a general analysis of movement patterns of the components of the 3C 273 jet was performed. In the published papers of the MOJAVE team, a similar analysis wasn't presented for all jet's features.

Keywords: Active galactic nucleus**,** Separation jet, Relativistic jet, 3C 273, variations.

АННОТАЦІЯ. Система з десяти радіотелескопів VLBA (Very Large Baseline Array), з максимальною довжиною бази близько 8,600 км, Національної Радіоастрономічної Обсерваторії США (NRAO USA) проводить систематичні моніторингові спостереження близько 500-та активних ядер галактик (АЯГ), результати яких представлені у базі даних MOJAVE. Результуючої кутової роздільної здатності (~0.47 тисячних кутової секунди на частоті у 15.4 ГГц) достатньо для розділення близького оточення АЯГ та його джета. Результати відповідних спостережень дозволяють зіставляти особливості руху у джеті з процесами активності АЯГ, а також вивчати його просторову структуру.

У базі даних MOJAVE представлені спектральні щільності радіопотоків АЯГ, радіозображення на кожну епоху спостережень на частоті 15.4 ГГц та діаграми "Separation jet" (що демонструють кутове відхилення компонент джета у часі). Ця інформація й дозволяє вивчати рух цих компонент. У цій роботі, було проведено загальний аналіз патернів руху компонент джета 3C 273. В опублікованих статтях команди MOJAVE, подібний проведеному аналіз не було представлено для усіх особливостей джетів.

Ключові слова: Активні ядра галактик, розділений джет, релятивістський джет, 3C 273, змінність.

1. Introduction

The high level of radiation and kinetic energy of the Active Galactic Nuclei (AGN) jets is provided by active processes in the "accretion disk – core – jet" system. According to the AGN standard model (Fig. 1), the source of its huge energy release is the gravitational energy of an accretion disk matter, which falls on the supermassive black hole in the center. The accretion disk is formed from surrounding matter (gas clouds, stars) that falls on the central supermassive black hole. The core is the region where matter is injected into the jet. Here active processes, that lead to the appearance of jets, are realized.

A common phenomenon for AGNs are relativistic jets — collimated jets of relativistic plasma that are ejected in a direction (mostly) perpendicular to the plane of accretion disk and are observed at distances up to tens or hundreds of kiloparsecs from the core.

Behind the disk plane there is a dust torus, which makes a significant contribution to the IR emission of many AGNs.

The use of aperture synthesis systems and VLBI observations in radio astronomy (including space radio telescopes) has made it possible to study the structure of jets and the processes occurring there. They include the presence of compact plasma releases from the core, shock waves, plasma flows, standing knots, etc. Currently, the

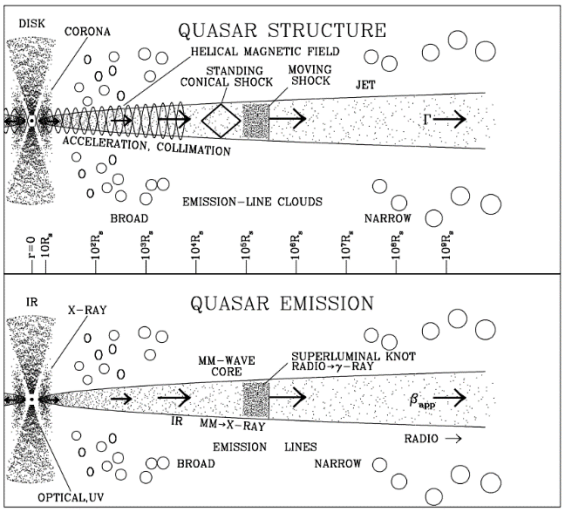

Figure 1: Scheme of an AGN structure (Marcher, 2009)

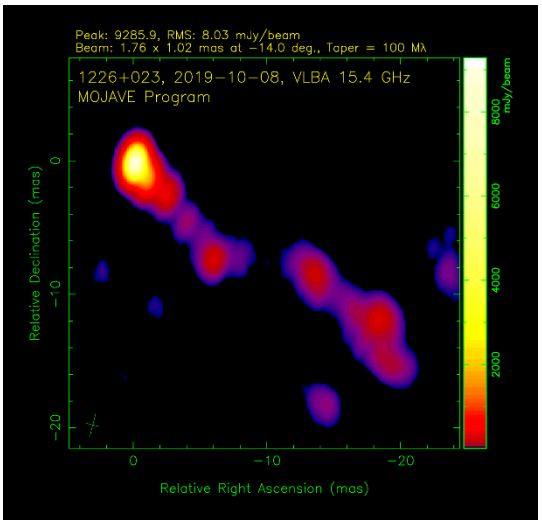

Figure 2: Parsec-scale radio image of 3C 273 obtained from the MOJAVE VLBI observing program database

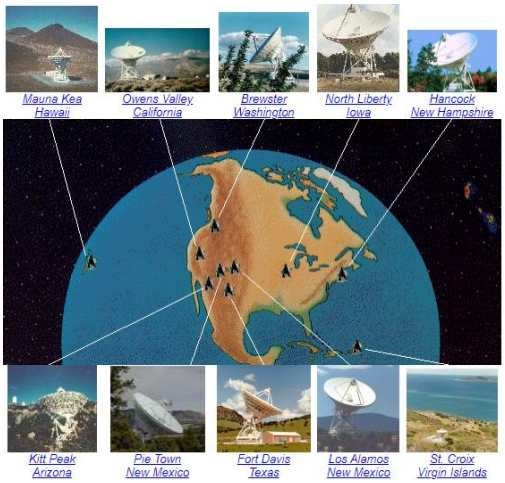

Figure 3: Very Long Baseline Antenna Array (VLBA)

structure of jets is also being studied using orbital space telescopes in the optical, X-ray, infrared and gamma-ray bands (Hubble and Webb Space Telescopes, Chandra X-ray Space Telescope, etc.).

The mechanism by which the matter of the accretion disk is accelerated to relativistic speeds, leading to the formation of jets, remains a subject of debate (especially if we are talking about a specific source), but the most likely mechanisms are those associated with strong magnetic fields in the vicinity of the black hole and its rotation. Particularly notable are the Blandford-Znajek (Blandford & Znajek, 1997) and Blandford-Payne (Blandford & Payne) processes.

The BZ process can serve as a mechanism for the rotational energy of a black hole extraction through its magnetosphere, while the BP process can serve as a mechanism for extracting the rotational energy of an accretion disk through the MHD process. However, the processes of jet formation under various conditions of interaction between the accretion disk and the black hole are studied in more detail using numerical calculations within MHD approach, generalized to the case of general relativity (for additional information, please refer to Yosuke, 2022).

Shock waves that appear as a result of ejections of matter into the jet and manifestation of core activity, as well as magnetic fields in the jet, accelerate relativistic particles that produce synchrotron radiation (mainly in the radio band) (Marcher, 2009). Overall, all these processes form the observed radio image of the core-jet system (Fig. 2).

Active galactic nuclei and their jets aren't isolated systems. The surrounding galactic and extragalactic medium have a direct influence on AGN and jets. As the results of numerical simulations show, galactic matter feeds the central engine, and extragalactic medium (and galactic too) can slow down the particles of the jet's matter, as a result significantly shortening it or even preventing its formation (Tanner & Weaver, 2022).

Active galactic nuclei include objects such as radio galaxies, Seyfert galaxies, quasars and blazars. The difference between them, in general terms, is explained by the orientational unification AGN model due to the different angles of disk-jet system to the observer's line of sight. The blazar is observed when the angle of the radio loud jet is close to the line of sight. Otherwise, if there is the loud radio jet, a quasar (one-sided jet) or a radio galaxy (when relativistic jets are visible from both poles of the disk) is observed. If there is a weak jet, Seyfert (I or II type) is observed (Urry & Padovani, 1995).

2. VLBI program for monitoring active galactic nuclei jets (MOJAVE)

The monitoring of relativistic jets of AGNs (MOJAVE) program has a database of ~500 radio sources (radio galaxies, quasars, blazars, Seyfert galaxies) observed by the VLBA radio interferometer of the National Radio Astronomy Observatory (NRAO USA).

VLBA is a radio interferometric network of ten 25-meter radio telescopes of the same design. Observations are carried out at frequencies from 0.3 GHz – 96 GHz with the largest base of 8.611 km, which allows achieving angular resolutions up to 0.17 – 22 thousandths of an arc second (https://public.nrao.edu/telescopes/vlba/).

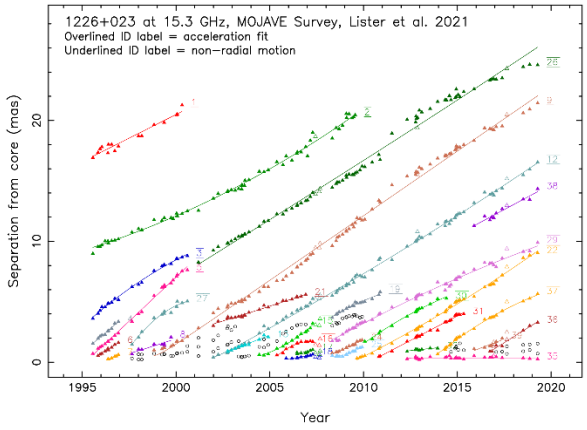

Figure 4: Diagram of Separation jet of the 3C 273

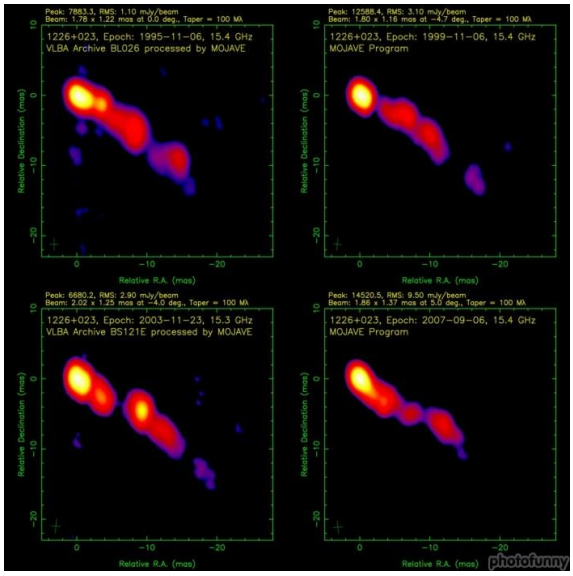

Figure 5: Evolution of 3C 273 radio images over time

Based on the interferometric picture that is taken as a result of observations by the VLBA network, the image is restored by fitting Gaussian surfaces into the brightest ejected components. The accuracy of image reconstruction is confirmed by cross-identification between epochs and authors. The entire process of obtaining radio images is described in detail in the papers (Lister et al., 2009; 2019; 2021).

The MOJAVE database contains both radio images of active nuclei with their jets at a frequency of 15.4 GHz and "Separation jet" diagrams (for most radio sources, Fig. 4). They represent the angular separation of individual components (marked in different colors) from the core over time (https://www.cv.nrao.edu/MOJAVE/allsources.html).

3. Research results of quasar 3C 273

The subject of research in this paper is the kinematics of jet based on the "Separation jet" diagram of the quasar 3C 273 from the MOJAVE VLBI monitoring database. The observational data obtained by the MOJAVE team allow a detailed analysis of the variability of the spatial structure of its jet. In Fig. 5, VLBI radio images of 3C 273 are shown with an interval of ~4 years between "neighbouring" ones. They show the ejection of bright components into the jet, their movement and escape from visibility over time.

The "Separation jet" diagram of quasar 3C 273 in Figure 4 is very representative, since it contains both moving components and slow and stationary ones.

Quasar 3C 273 is located in the constellation Virgo at $z \sim 0.1576$ redshift and is one of the most actively studied AGNs, as well as one of the closest and brightest quasars (Schmidt, 1963).

A team of authors (Ryabov et al., 2016) carried out studies of this object to identify the main periods of radio flux variability based on monitoring observations from the Michigan Radio Astronomy Observatory using wavelet analysis approach. Subsequently, in paper (Zabora et al., 2022), using observational data on variations of the core flux of this source according to MOJAVE data, changes in the core and jet fluxes were separated. The article (Volvach et al., 2023) considers the possibility of the presence of a binary black hole in 3C 273, and also calculated the masses of black holes in the binary system based on quasiperiods of variability of radio fluxes at different frequencies. The results of these calculations are in good agreement with calculations based on spectroscopic observations (Paltani & Turler, 2005).

Many works have been dedicated to the study of the kinematics and structure of the 3C 273 jet. For example, in work (Okino et al., 2022) the kinematics of the jet and the break of its collimation were researched, a similar was studied in work (Akiyama et al., 2018). In paper (Savolainen et al., 2006), was considered the velocity gradient in the direction perpendicular to the jet axis, and the non-ballistic motion of certain components was also determined. The article (Qian et al., 2001) discusses variations of the Lorentz factor of jet 3C 273 and also proposes descriptive models.

Also, the kinematics of the components of AGN jets of a large sample was descripted by participants in the MOJAVE program in a series of articles (Lister et al., 2009; 2019; 2021). In these works, a general statistical analysis was carried out, the methodology for constructing radio images, "Separation jet" diagrams, etc. was described.

4. Results of research of the "core-jet" system kinematics of 3C 273

For the 3C 273 quasar, from the "Separation jet" diagram, an angular distance of components (from the core) of its jet in time were obtained. A total of 31 components were studied over a 25-year observation period from 1995 to 2020 (Fig. 4). For each of them the speed of their radial motion in the jet was determined. The results are presented in Table 1.

The table shows the observation time interval for each of the components, their average speed $\bar{V}$ in thousandths

of arcsec per year; average speed for the jet in the same units $\langle\bar{V}\rangle$; relative deviation of the average for the component from the average for the jet $\frac{\bar{V}-\langle\bar{V}\rangle}{\langle\bar{V}\rangle}$; amplitude velocities for a component $V_{\max}, V_{\min}$ and their corresponding relative deviations from the average for the same component $\frac{V_{\max,\min}-\bar{V}}{\bar{V}}$.

Table 1: Main parameters of the components of jet 3C 273.

№	Observation interval, years	$\bar{V}$, $\frac{mas}{year}$	$\frac{\bar{V}-\langle\bar{V}\rangle}{\langle\bar{V}\rangle}$	$V_{\max}$, $\frac{mas}{year}$	$\frac{V_{\max}-\bar{V}}{\bar{V}}$	$V_{\min}$, $\frac{mas}{year}$	$\frac{V_{\min}-\bar{V}}{\bar{V}}$
1	1995.57 – 2000.32	0.79	-0.02	3.60	3.54	-3.22	-5.05
2	1995.57 – 2009.56	0.78	-0.03	8.57	9.94	-7.96	-11.15
3	1995.57 – 2000.61	1.04	0.28	3.15	2.03	-0.48	-1.47
4	1995.57 – 1996.93	1.31	0.62	2.63	1.01	0.23	-0.83
5	1995.57 – 2000.61	1.44	0.78	2.23	0.55	0.33	-0.77
6	1995.84 – 1996.93	1.00	0.24	1.48	0.48	0.45	-0.55
7	1996.37 – 1996.93	0.66	-0.19	1.02	0.55	0.30	-0.55
8	1997.65 – 1999.73	0.54	-0.34	1.51	1.80	-0.14	-1.27
9	1998.83 – 2019.28	1.06	0.31	5.42	4.09	-2.65	-3.49
12	2001.99 – 2019.28	0.93	0.15	6.46	5.92	-2.91	-4.11
13	2002.74 – 2004.92	0.60	-0.26	1.45	1.41	-0.68	-2.12
15	2004.44 – 2007.29	0.90	0.11	3.02	2.35	-0.20	-1.22
16	2005.37 – 2007.29	0.62	-0.23	2.05	2.30	-0.27	-1.44
17	2006.45 – 2007.29	0.30	-0.63	0.79	1.67	-0.22	-1.76
18	2005.87 – 2007.29	0.23	-0.71	0.88	2.74	-0.03	-1.14
19	2008.33 – 2010.89	0.73	-0.10	4.00	4.50	-0.80	-2.10
21	2001.99 – 2006.92	0.50	-0.38	1.43	1.87	-0.65	-2.31
22	2009.62 – 2019.28	0.92	0.14	2.18	1.37	0.26	-0.71
24	2008.33 – 2009.93	0.71	-0.12	2.60	2.64	0.27	-0.62
25	2008.33 – 2009.92	0.51	-0.37	2.80	4.47	-0.63	-2.23
26	2001.2 – 2019.29	0.99	0.22	12.57	11.73	-6.27	-7.35
27	1997.65 – 2000.61	1.18	0.45	2.64	1.24	0.18	-0.85
29	2008.33 – 2019.29	0.72	-0.11	7.61	9.50	-2.28	-4.14
30	2010.07 – 2014.42	0.88	0.09	2.44	1.77	0.06	-0.93
31	2010.82 – 2015.35	0.81	0.00	1.73	1.13	-0.26	-1.32
32	2012.33 – 2013.95	0.16	-	0.60	-	-0.63	-
35	2012.32 – 2019.28	0.00	-	0.86	-	-2.52	-
36	2016.74 – 2019.28	0.98	0.21	2.20	1.26	-0.20	-1.21
37	2013.96 – 2019.28	0.93	0.15	2.82	2.03	0.27	-0.71
38	2015.9 – 2019.28	0.83	0.03	2.80	2.38	-1.11	-2.34
39	2015.9 – 2017.39	0.58	-0.28	1.38	1.36	0.21	-0.64
$\langle\bar{V}\rangle = 0.81$			$\frac{s_{\bar{V}}}{\langle\bar{V}\rangle} = 0.34$	$\left\langle\left\lvert\frac{V_{\max}-\bar{V}}{\bar{V}}\right\rvert\right\rangle = 3.02$		$\left\langle\left\lvert\frac{V_{\min}-\bar{V}}{\bar{V}}\right\rvert\right\rangle = 2.22$	

At the end of table, the standard deviation $s_{\bar{V}}$ of the average velocity of components from the average for jet, normalized to the average speed over the jet $\langle \bar{V} \rangle$, is placed. It is indicative in the context of dispersion of the velocities of the components in the jet.

The average absolute deviations of amplitude velocities $\left\langle \left| \frac{V_{\max,\min} - \bar{V}}{\bar{V}} \right| \right\rangle$ of the components are also placed. Despite the somewhat complex concept, they are indicative in the context of spread of velocities for one component on average over the jet.

Stationary and slow-moving components ($\bar{V} <\sim 0.2$ *mas / year*) were not taken into account when calculating the values at the end of the table.

The results show a predominance of moving components. Stationary and slow-moving components in the picture plane are presented: No. 32 and 35 according to MOJAVE numbering.

The standard deviation of the average velocities shows significant variation in velocities between components. However, the speed of the component varies, as a rule, by an order of magnitude greater than the average speed of the components in the jet.

Figure 6 shows a histogram of the distribution of average velocities of the moving components (except for the 32nd and 35th) in comparison with the normal distribution with parameters $\langle \bar{V} \rangle = 0.81$ and $s_{\bar{V}} = 0.28$. The observed distribution is close to normal. This may indicate that the process of ejection of components into the jet is quasi-regular.

Fig. 7, 8 show diagrams of distributions of peak (maximum/minimum) velocities of the components of jet 3C 273. They are showing significant asymmetry ($A_S^{V_{\max}} \sim 2.1$, $A_S^{V_{\min}} \sim -2.3$).

The overwhelming majority of events associated with the achievement of maximum speed by the jet components are in the range of up to 4 $mas/year$.

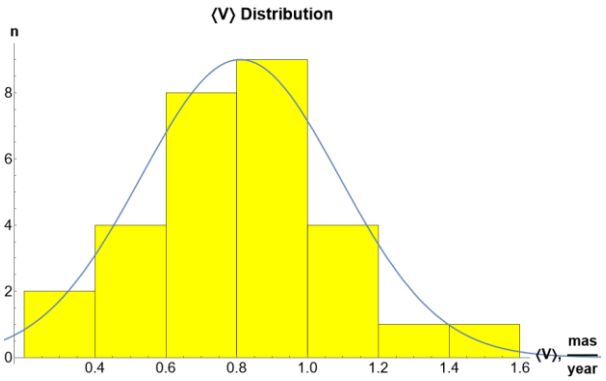

Figure 6: Distribution of average velocities of the moving components of jet 3C 273

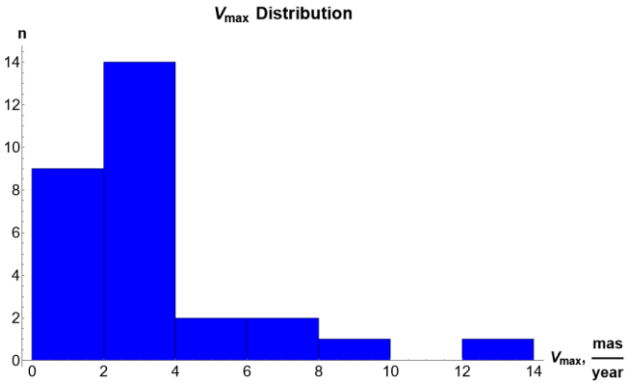

Figure 7: Distribution of maximum velocities of the moving components of jet 3C 273

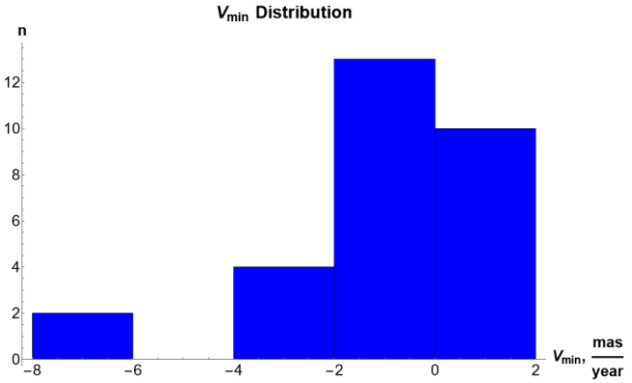

Figure 8: Distribution of minimum velocities of the moving components of jet 3C 273

Higher velocities occur sporadically and will be the subject of further research.

The values of the minimum component velocities may reflect braking processes in jets. The overwhelming number of such events correspond to speed intervals (-2 to +2), which may reflect the presence of a quasi-regular structure of the jet, which determines the deceleration of the movement of the components.

5. Features of the motion kinematics of individual components of jet 3C 273

Farther, to determine the average values of the angular velocity of movement of some components, a single three points linear smoothing was performed. This allows to reduce the influence of random errors on its values.

The 2nd component (Fig. 9) over 15 years shows a monotonic increase in angular velocity on average 0.79 $\frac{mas}{year}$ with an acceleration of 0.02 $\frac{mas}{year^2}$.

A smoothed diagram of the dependence of angular velocity on time shows the variable nature of its changes: we can suspect its three-year cyclicity. From 1996 to 1999, the angular velocity was 0.68 $\frac{mas}{year}$, from 2000 to

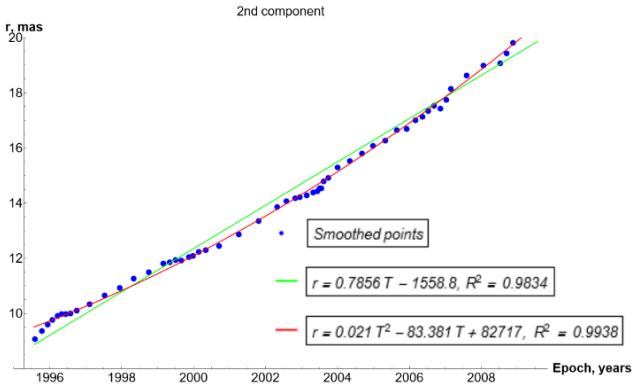

Figure 9: Smoothed "Separation jet" for the 2nd component, comparison with linear and quadratic approximation of the initial points

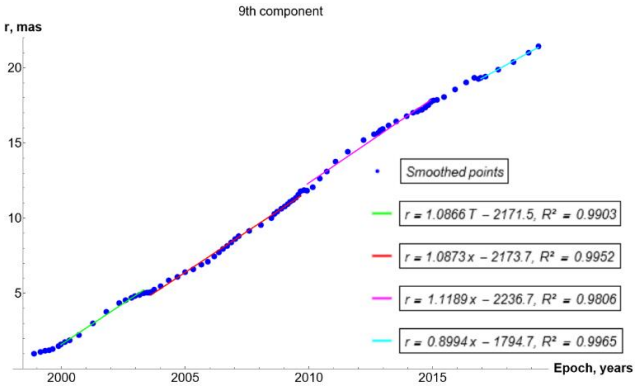

Figure 11: Smoothed "Separation jet" for the 9th component, comparison with piecewise linear approximation

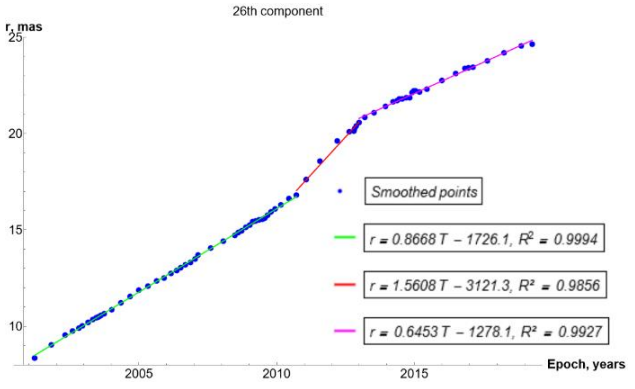

Figure 10: Smoothed "Separation jet" for the 26th component, comparison with piecewise linear approximation

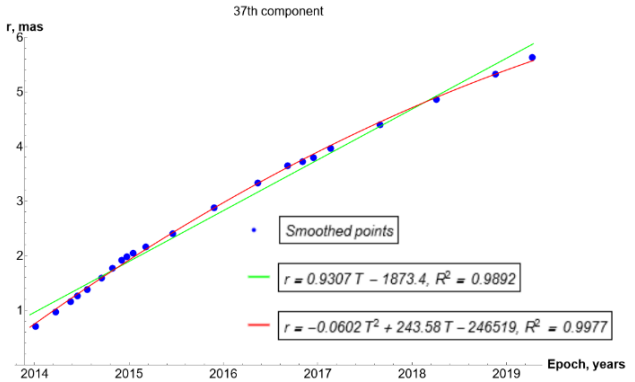

Figure 12: Smoothed "Separation jet" for the 37th component, comparison with linear and quadratic approximation of the original points

2003, the angular velocity was 0.73 $\frac{mas}{year}$, from 2003 to 2006, 0.90 $\frac{mas}{year}$, from 2006 to 2009, 1.09 $\frac{mas}{year}$. In 1996, 1999, 2003, 2006 and 2009 there are time intervals of the order of a month, during which the angular velocity of the component is nearly unchanged.

The 26th (Fig. 10) component in 2001-2010 moves with a constant angular velocity of 0.87 $\frac{mas}{year}$, then the speed increases to 1.56 $\frac{mas}{year}$, but in 2013 it decreases to 0.65 $\frac{mas}{year}$.

The 9th (Fig. 11) component during the observation period shows a changing angular velocity: in 2001-2003 it was 1.09 $\frac{mas}{year}$, then a significant slowdown follows. Speed returns to 1.09 $\frac{mas}{year}$ in 2003-2009, in 2009 the component almost stops. From 2009 to the end of 2012, the angular velocity is about 1.12 $\frac{mas}{year}$. From the end of 2012 to 2019, the angular velocity decreases on average to 0.90 $\frac{mas}{year}$.

The 37th (Fig. 12) component moves with an average speed of 0.93 $\frac{mas}{year}$, but throughout the entire observation interval the angular velocity decreases with an acceleration of 0.06 $\frac{mas}{year^2}$.

6. Conclusion

The MOJAVE project has unique data from long-term monitoring observations of a sample of ~500 active galactic nuclei, which make it possible to study the variability and structures of them and their jets. In this work, the kinematics of the jet components of the quasar 3C 273 was studied. A number of results were obtained:

1. Data were obtained on the angular distances from the core of the 31 components of jet 3C 273 on the observation epochs for the 1995 – 2020-time interval (~25 years) for further calculation of their velocities and the dynamics of their changes.
2. The "Separation jet" diagram demonstrates the presence of both stationary/slow and fast components, the number of which predominates. Calculations show that the average velocities of the jet components differ significantly from each

other. However, not as much as the velocities of the components themselves change.

3. The average component velocities have a distribution that is close to normal, this can reflect quasiregular nature of core activity.
4. The nature of minimum/maximum component velocities changes don't correspond to the normal distribution and correspond to episodic processes of manifestation of AGN activity and variations in the spatial structure of the jet.
5. The individual features of changes in velocities of the selected components of jet 3C 273 were analyzed. They demonstrate episodes of acceleration, braking and stationary states. Thus, the components of the jet are also "test bodies" that reflect the spatial structure of the magnetic fields in the jet.

References

Akiyama K., Asada K., Fish V. et al.: 2018, *Galaxies*, **6**, 15. https://doi.org/10.3390/galaxies6010015

Blandford R. D., Znajek R. L.: 1977, *MNRAS*, **179**, 433. https://doi.org/10.1093/mnras/179.3.433

Blandford, R.D., Payne, D.G.: 1982, *MNRAS*, **199**, 883. https://doi.org/10.1093/mnras/199.4.883

Hiroki O., Kazunori A., Keiichi A. et al.: 2022, *ApJ*, **940**, 17. https://doi.org/10.3847/1538-4357/ac97e5

Lister M.L., Cohen M.H., Homan D.C. et al.: 2009, *AJ*, **138**, 1874. https://doi.org/10.1088/0004-6256/138/6/1874

Lister, M. L., Homan, D. C., Hovatta, T. et al.: 2019, *ApJ*, **874**, 19. https://doi.org/10.3847/1538-4357/ab08ee

Lister M.L., Homan D.C., Kellermann K.I. et al: 2021, *ApJ*, **923**, 19. https://doi.org/10.3847/1538-4357/ac230f

Marcher A.P.: 2009, eprint (arXiv:0909.2576) https://doi.org/10.48550/arXiv.0909.2576

Paltani, S., Türler, M.: 2005, *A&A*, **435**, 811. https://doi.org/10.1051/0004-6361:20041206

Qian, S., Zhang Xi., Krichbaum T.P. et al.: 2001, *Chin. J. Astron. Astrophys.*, **1**, 236. doi:10.1088/1009-9271/1/3/236

Ryabov M.I., Sukharev A.L., Donskikh A.I.: 2016, *Radio physics and radio astronomy*, **21**, 161.

Savolainen, T., Wiik, K., Valtaoja, E. et al: 2006, *A&A*, **446**, 71. https://doi.org/10.1051/0004-6361%3A20053753

Schmidt, M.: 1963, *Nature*, **197**, 1040. https://doi.org/10.1038/1971040a0

Tanner R., Weaver K.A.: *AJ*, **163**, 17. https://doi.org/10.3847/1538-3881/ac4d23

Urry, C. M., Padovani, P.: 1995, *Publ. Astron. Soc. Pac.*, **107**, 803. https://doi.org/10.1086/133630

Volvach A., Volvach L., Larionov M.: 2023, *Galaxies*, **11**, 96. https://doi.org/10.3390/galaxies11050096

Yosuke, M.: 2022, *Universe*, **8**, 85. https://doi.org/10.3390/universe8020085

Zabora et al.: 2022, *AApTr*, **33**, 89. https://doi.org/10.17184/eac.6470

SUN, SOLAR ACTIVITY, SOLAR-TERRESTRIAL RELATIONS AND ASTROBIOLOGY

https://doi.org/10.18524/1810-4215.2023.36.290196

THE RELATIONSHIP OF THE INTENSITY OF THE SCR PROTON FLUX WITH THE PARAMETERS OF TYPE II SOLAR RADIO BURSTS

E.A.Isaeva

Institute of Radio astronomy of NAS of Ukraine, <*isaevaode@gmail.com*>

ABSTRACT. 112 solar proton events (SPEs) were processed for the period from November 24, 2000 to December 20, 2014, which were accompanied by type II radio bursts. For the analysis, used original records of solar radio emission from a solar radio spectrograph in the range of 25-180 MHz, as well as original records of the flux intensity proton of solar cosmic rays (SCR) protons I_p with energy E_p in the range > 0.8-850 MeV according to data from the GOES series of devices. In this case, superimposed proton events were always separated and identified with the corresponding solar proton flares, and the maximum proton flux intensity I_p of superimposed proton events was determined from the level of the previous proton event.

Based on data from the solar radio spectrograph, regression models were obtained for 91 type II bursts that established the relationship between the frequency drift velocity $V_{i,j}$ and the frequency of type II bursts $f_{i,j}$, and for 73 type II bursts it was possible to obtain regression models which established the relationship between the intensity of type II bursts $I_{i,j}$ and type II burst frequency $f_{i,j}$ in the range 25-180 MHz. Detailed studies have shown that the intensity of type II bursts $I_{i,j}$, as well as the frequency drift velocity $V_{i,j}$, strongly depends on the frequency of type II burst $f_{i,j}$ and monotonically changes with time t_i along the harmonics of type II bursts.

As a result, the relationship between the maximum values of the SCR proton flux intensity I_p and the calculated values of the frequency drift velocity $V_{i,j}$ and intensity of type II bursts $I_{i,j}$ was investigated. A comparative analysis showed that the relationship between the intensity of the SCR proton flux I_p and the intensity of type II bursts $I_{i,j}$ is much stronger than with the frequency drift velocity $V_{i,j}$, where the correlation coefficient r is 0.82 and 0.71, respectively, for protons with energies E_p > 30 MeV. The relationship between the proton flux intensity I_p and the frequency drift velocity $V_{i,j}$ and the intensity of type II bursts $I_{i,j}$ was also studied as a function of the proton energy E_p and the frequency $f_{i,j}$ of type II radio bursts. It was shown that the strongest relationship between the intensity of the SCR proton flux I_p with the frequency drift velocity V_i and with the intensity of type II bursts $I_{i,j}$ is observed with subrelativistic SCR protons with energies E_p in the range > 30-100 MeV and for type II radio bursts at a frequency $f_{i,j}$ in the range 40-160 MHz.

Keywords: Proton events, proton flux intensity, frequency drift velocity, type II burst intensity.

АНОТАЦІЯ. Опрацьовано 112 сонячних протонних подій (СПП) за період з 24.11.2000 по 20.12.2014 роки, які супроводжувалися радіосплесками II типу. Для аналізу використовувалися оригінальні записи радіовипромінювання Сонця з сонячного радіоспектрографа в діапазоні 25-180 МГц, а також оригінальні записи інтенсивності потоку протонів сонячних космічних променів (СКП) I_p з енергією E_p в діапазоні > 0.8-850 МеВ за даними з апаратів серії GOES. При цьому накладені протонні події завжди поділялися та ототожнювалися з відповідними сонячними протонними спалахами, а максимальна інтенсивність потоку протонів I_p накладених протонних подій визначалася від рівня попередньої протонної події.

За даними із сонячного радіоспектрографа для 91 сплеску II типу були отримані регресійні моделі, що встановлюють зв'язок між швидкістю частотного дрейфу $V_{i,j}$ і частотою сплеску II типу $f_{i,j}$, а також для 73 сплесків II типу вдалося отримати регресійні моделі, що встановлюють зв'язок між інтенсивністю сплесків II типу $I_{i,j}$ і частотою сплесків II типу $f_{i,j}$ у діапазоні 25-180 МГц. Детальні дослідження показали, що інтенсивність сплесків II типу $I_{i,j}$ як і швидкість частотного дрейфу $V_{i,j}$ сильно залежить від частоти сплеску II типу $f_{i,j}$ і монотонно змінюється з часом t_i вздовж гармонік сплесків II типу.

В результаті було досліджено зв'язок максимальних значень інтенсивності потоку протонів СКП I_p з розрахунковими значеннями швидкості частотного дрейфу $V_{i,j}$ та інтенсивності сплесків II типу $I_{i,j}$. Порівняльний аналіз показав, що зв'язок інтенсивності потоку протонів СКП I_p з інтенсивністю сплесків II типу $I_{i,j}$ значно сильніший, ніж зі швидкістю частотного дрейфу $V_{i,j}$ де коефіцієнт кореляції r дорівнює 0.82 і 0.71, відповідно для протонів з енергією E_p > 30 МеВ. Також було досліджено зв'язок інтенсивності потоку протонів I_p зі швидкістю частотного дрейфу $V_{i,j}$ та інтенсивністю сплесків II типу $I_{i,j}$ залежно від енергії протонів E_p та від частоти $f_{i,j}$ радіосплесків II типу. Було показано, що найбільш сильний зв'язок інтенсивності потоку протонів СКП I_p зі швидкістю частотного дрейфу $V_{i,j}$ і інтенсивністю сплесків II типу $I_{i,j}$ спостерігається з субрелятивістськими протонами СКП з енергією E_p в діапазоні > 30-100 MeV і для радіосплесків II типу на частоті $f_{i,j}$ в діапазоні 40 -160 МГц.

Ключові слова: протонні події, інтенсивність потоку протонів, швидкість частотного дрейфу, інтенсивність сплеску II типу.

1. Introduction

It is currently believed that solar cosmic rays (SCRs) can be accelerated either in the region of flare energy release or at shock wave fronts, which can be generated by both flares and coronal mass ejections (CMEs) (Reames, 1999). The results obtained to date do not allow us to draw an unambiguous conclusion about which acceleration process is dominant.

The presence of a strong connection between the flux of SCR protons and the parameters of microwave radio bursts (Akinyan et al., 1977, 1978; Chertok, 1982; Chertok et al., 1987; Melnikov, Epifanov, 1979; Melnikov et al., 1986, 1991; Isaeva, 2010, 2018, 2020) definitely indicates the acceleration of SCR protons in the flare region. However, there are many indications that shock waves also play an important role in the acceleration of solar cosmic rays (Gopalswamy et al., 2002; Cliver et al., 2004).

Previously, in works (Tsap & Isaeva, 2011, 2012, 2013), some questions regarding the connection between the flux of SCR protons and the parameters of type II radio bursts were considered. In the course of studies of the relationship between the frequency drift velocity of meter-decameter type II bursts and the intensity of the proton flux I_p of SCRs of different energies, two types of events were discovered, which, according to Tsap (Isaeva and Tsap, 2011), suggests the generation of shock waves both in the region of flare energy release and and a moving coronal mass ejection (CME). The works (Isaeva & Tsap, 2011; Tsap and Isaeva, 2012, 2013) present the results of a study of the efficiency of SCR acceleration by coronal and interplanetary shock waves, and also provide arguments in favor of a model of a two-stage proton acceleration process (Wild et al., 1963; Tsap & Isaeva, 2012). A comparative analysis showed that the acceleration of protons by coronal shocks is more effective than by interplanetary shocks, and that the main acceleration of protons occurs in the flare region and additionally at the shock wave fronts (Tsap & Isaeva, 2012).

A study of the fine spectral structure of meter-decameter radio bursts of type II showed that there is a fairly strong connection between the intensity of the proton flux and the relative distance $b_i = (f_{i2}-f_{i1})/f_{i1}$ between the 1-st and 2-nd harmonics of type II bursts at a given time t_i , where the correlation coefficient r between the studied values is $\approx$ 0.70, while the relationship between the frequency drift velocity V_i and the proton flux intensity I_p turned out to be weak, where the correlation coefficient r between I_p and V_i does not exceed ≈ 0.40 (Tsap & Isaeva, 2013) .

However, further studies of the fine spectral structure of meter-decameter radio bursts of type II in the range 25-180 MHz showed that if instead of the frequency drift velocity V_i we use the parameter $V_{II} = (f_2-f_1)/(t_i-t_0)$, which to some extent characterizes the speed of displacement of the shock wave front over time t_i, where f_1 and f_2 are the frequencies at the 1-st and 2-nd harmonics at a given time t_i, and t_0 is the start time of a type II burst at the 1-st harmonic at a frequency of 180 MHz, then there is a fairly strong connection between the proton flux intensity I_p and parameter V_{II}, where the correlation coefficient r between the studied parameters is ≈ 0.79 (Isaeva, 2018), which is quite comparable with what is obtained from the parameters of microwave bursts (Melnikov et al., 1991; Isaeva, 2018). It should also be noted that a strong relationship between the proton flux intensity I_p and parameter V_{II} is observed in a narrow frequency range of 25-60 MHz. Moreover, as a result of detailed studies of the fine structure of type II radio bursts, a number of features were discovered. It has been shown that the relative distance b_i between harmonics of type II radio bursts varies monotonically over time (Isaeva, 2019; Tsap, Isaeva, Kopylova, 2020). All 112 type II radio bursts are characterized by a monotonic decrease in the relative distance b_i between harmonics to a minimum value $b_{min,1}$ with a subsequent increase (Isaeva, 2019, 2020;). A strong relationship was also found between the intensity of the proton flux I_p and the frequency $f_{min,1}$ at the 1-st harmonic at the time of the minimum relative distance between the harmonics of a type II burst (Isaeva, 2018, 2019, 2020). Recent studies have also been related to the study of the fine structure of type II radio bursts in the range 25-180 MHz. As a result of these studies, a strong relationship was discovered between the proton flux intensity I_p and the frequency drift velocity $V_{i,2}$ and the intensity of type II bursts $I_{i,2}$ at the 2-nd harmonic of type II radio bursts.

2. Initial data

For the analysis, we used original recordings of the dynamic spectra of solar radio emission in the range of 25-180 MHz according to data from the Solar Radio Spectrograph (SRS) (http://www.ngdc.noaa.gov/stp/space-weather /solar-data/solar-features/solar-radio/rstn-spectral/), as well as original records of the proton flux intensity I_p of solar cosmic rays (SCR) with energy E_p in the range > 0.8-850 MeV according to data from the GOES series of devices (https://satdat.ngdc.noaa.gov/sem/goes/data/new_avg/).

3. Processing solar proton events

We processed 112 proton events associated with type II radio bursts for the period from November 24, 2000 to December 20, 2014. For the analysis, the maximum values of the proton flux intensity I_p with energy E_p > 0.8-850 MeV were used. Superimposed proton events were separated and identified with corresponding solar flares according to protonity criteria. Then, in each channel, the maximum intensity of the proton flux I_p from the pre-flare level was determined. For superimposed proton events, the proton flux intensity I_p was determined from the level of the previous proton event. Fig. 1 shows an example of the processing of overlaid proton events in April 2001.

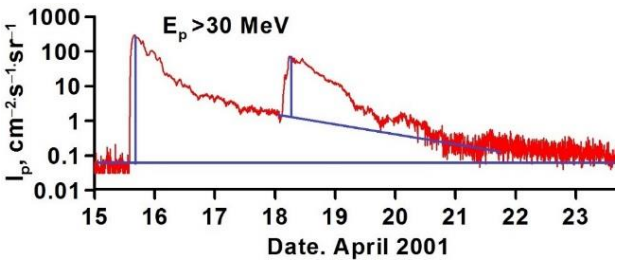

Figure 1: Example of processing superimposed proton events in April 2001

4. Processing of type II solar radio bursts in the range of 25-180 MHz

4.1. Determination of the frequency drift velocity $V_{i,j}$ of type II radio bursts

Harmonics of type II bursts were approximated using linear regression model (1)

$$\lg f_{i,j} = k1_j \cdot \sqrt{t_i} + k2_j \,, \qquad (1)$$

where $f_{i,j}$ is the frequency at time t_i, $k1_j$ and $k2_j$ are linear regression coefficients, i=1…n – sample number, j=1,2 – harmonic number. Start timing for all events corresponded to the beginning of the first harmonic at 180 MHz. This model (1) gives a fairly good approximation for all 112 type II radio bursts (Isaeva, Tsap; 2017), which made it possible to study the dynamics of the parameters of type II radio bursts over time t_i. Therefore, having previously determined the coefficients $k1_j$ and $k2_j$ in the regression model (1), and then differentiated expression (1) by time t_i, it is possible to determine the instantaneous values of the frequency drift velocity $V_{i,j}$ (2) of type II bursts in any time t_i in the range 25-180 MHz (Tsap, Isaeva, Kopylova; 2023).

$$V_{i,j} = \frac{\ln 10}{2}\frac{k1_j f_{i,j}}{\sqrt{t_i}} = \frac{(k1_j \ln 10)^2}{2}\frac{f_{i,j}}{\ln f_{i,j} - k2_j \ln 10} \,. \qquad (2)$$

4.2. Determination of the intensity of type II radio bursts $I_{i,j}$ in the range 25-180 MHz

Based on the original data from SRS, a dynamic spectrum was built on the computer screen, where all processing took place. Using two different linear regressions, which differed only in the values of the linear regression coefficients of type (1), the width of the 2-nd harmonic was limited, as shown in Fig. 2. When the harmonics of type II radio bursts were visible on the background of powerful continuum radiation of type IV, then the procedure was type IV burst filtering.

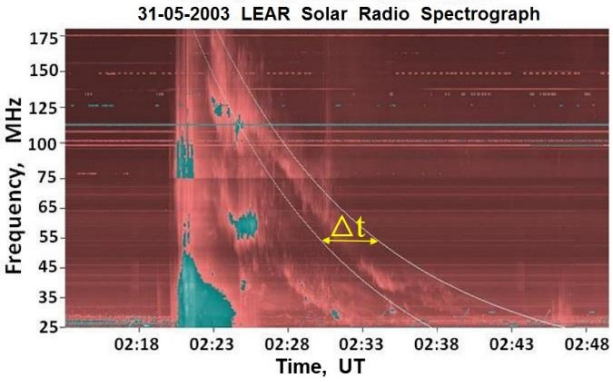

Figure 2: An example of identifying the width of the 2-nd harmonic of type II radio bursts

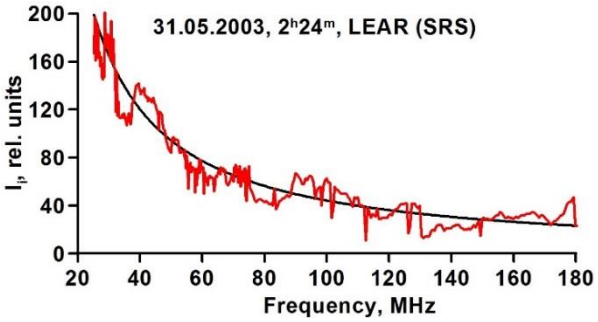

Figure 3: The observed intensity $I_{i,2}$ of a type II burst at the 2-nd harmonic is shown in red, and the calculated intensity in black.

Then, on the time interval Δt_i at a given frequency $f_{i,2}$ at the 2-nd harmonic, the maximum intensity values of the type II burst $I_{i,2}$ were determined. In Fig. 3 shows in red the observed values of the maximum intensity $I_{i,2}$ at a given frequency $f_{i,2}$ with filtering of type IV continuum radiation, and in black the calculated values of the intensity $I_{i,2}$ of a type II radio burst. As a result of this procedure, only 73 dynamic spectra out of 112 were processed, since against the background of a powerful continuum type IV burst it was not always possible to distinguish the width harmonic of a type II burst.

4.3. Relationship between frequency $f_{i,j}$ and intensity of type II radio bursts $I_{i,j}$ in the range 25-180 MHz

In order to understand how the intensity of type II bursts $I_{i,j}$ is related to the frequency $f_{i,j}$, a procedure was performed to average the intensity maxima of type II bursts $I_{i,j}$ at a given frequency $f_{i,j}$ for 73 bursts. The results of this procedure are shown in Fig. 4 a) and b) at the 1-st and 2-nd harmonics, respectively. In Fig. 4 a) and b) it is clear that when the harmonics of type II bursts go beyond the powerful continuum burst of type IV in the frequency range 25-50 MHz, then a clear relationship is visible between $I_{i,j}$ and $f_{i,j}$. In this regard, filtering of the continuum radiation of type IV bursts was performed.

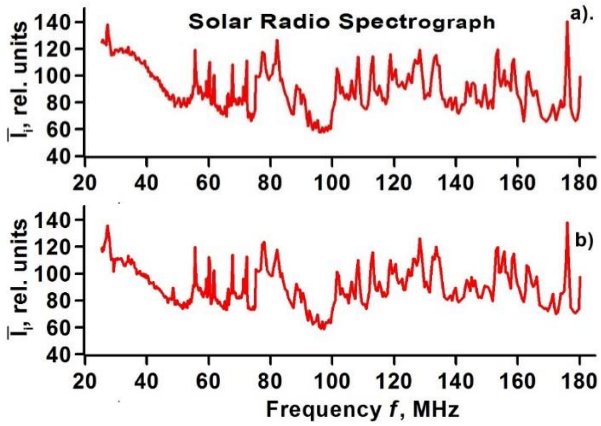

Figure 4: Averaged intensity values of type II bursts $I_{i,j}$ at a given frequency $f_{i,j}$ for 73 type II bursts at the 1-st (a) and 2-nd (b) harmonics, respectively

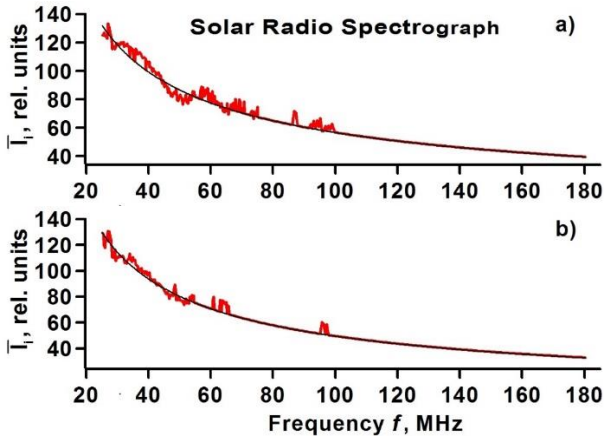

Figure 5: Averaged intensity values of type II bursts $I_{i,j}$ at a given frequency $f_{i,j}$ for 73 type II bursts after filtering type IV continuum radiation at the 1-st (a) and 2-nd (b) harmonics, respectively.

In Fig. 5 a) and b) shows the dependence of the average intensity values of type II bursts $I_{i,j}$ after filtering the continuum radiation of type IV bursts on the frequency of type II bursts $f_{i,j}$.

In Fig. 5 a) and b) it is clear that the intensity of type II bursts $I_{i,j}$ strongly depends on the frequency of type II radio burst $f_{i,j}$, where the dependence of the intensity $I_{i,j}$ on the frequency $f_{i,j}$ can be quite accurately approximated by equation (3), where $k1_j$ and $k2_j$ – linear regression coefficients (3).

$$\lg I_{i,j} = k1_j \cdot \lg f_{i,j} + k2_j \qquad (3)$$

4.4. Elimination of a gain jump when prcessing dynamic spectra, as well as filtering type IV continuum radiation

Fig. 6 a) shows an example of a sharp change in gain at the boundary of two frequency bands 25-75 and 75-180 MHz for the proton event of 04.18.2001, accompanied by a powerful type IV burst, as well as a type II burst according to data from LEAR (SRS), and Fig. 6 b) shows the procedure for bringing the gain in both bands to the same gain value, as well as filtering outliers, type IV continuum emission and zero values in the spectrum for the 2-nd harmonic of a type II burst.

5. Relationship between the intensity of the SCR proton flux I_p and the drift velocity $V_{i,2}$ and the intensity of type II bursts $I_{i,2}$ at the 2-nd harmonic in the range 25-180 MHz

A comparative analysis has shown that there is a fairly strong connection between the intensity of the SCR proton flux I_p and the frequency drift velocity $V_{i,2}$. In Fig. 7 a) shows a scatter diagram between the frequency drift velocity $V_{i,2}$ at a frequency $f_{i,2}$ = 70 MHz and the proton flux intensity I_p with energy E_p > 30 MeV for 91 proton events, where the correlation coefficient r between the studied parameters is ≈ 0.71. The black line in Fig. 7 a) shows the calculated values of the proton flux intensity $I_{p,c}$, calculated

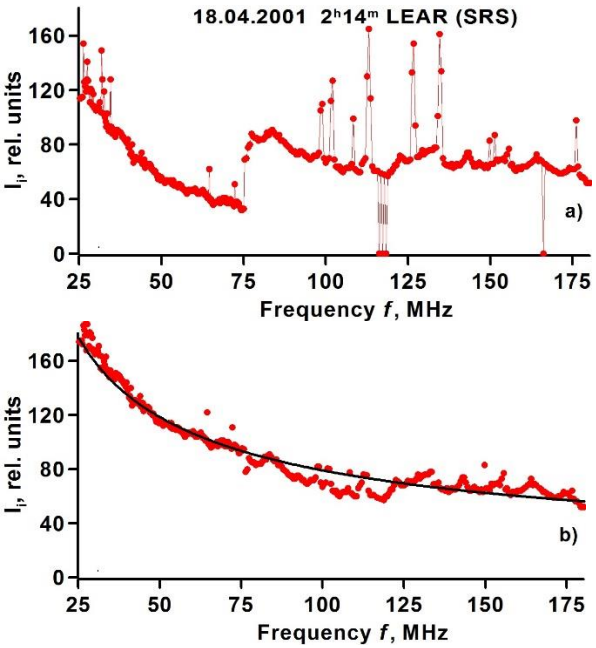

Figure 6: a) An example of a sharp gain reduction in the 25-75 MHz band is shown; b) An example of bringing the gain to one value is shown, as well as the result of filtering outliers and zero intensity values $I_{i,2}$ at the 2-nd harmonic.

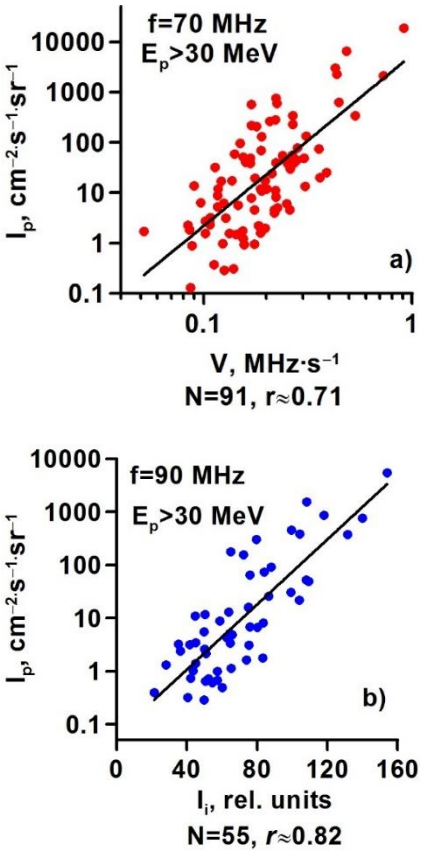

Figure 7: Dependence of the flux intensity of SCR protons I_p with energy E_p > 30 MeV on the frequency drift velocity $V_{i,2}$ (a) and the intensity of type II bursts $I_{i,2}$ (b).

using the regression model (4), which establishes a connection between the frequency drift velocity $V_{i,2}$ and the observed values of the proton flux intensity I_p with energy E_p > 30 MeV.

$$\lg I_p \approx \lg I_{p,c} = 3.4 \cdot \lg V_{i,2} + 3.7 \quad (4)$$

As a result of detailed studies of the relationship between the SCR proton flux and various parameters of type II radio bursts, a strong relationship was discovered between the intensity of the proton flux I_p and the intensity of type II bursts $I_{i,2}$. Moreover, the connection between I_p and $I_{i,2}$ is much stronger than with the frequency drift velocity $V_{i,2}$. In Fig. 7 b) shows a scatter diagram between the intensity of the proton flux with E_p >30 MeV and the intensity of type II bursts $I_{i,2}$ at a frequency $f_{i,2}$ = 90 MHz for 55 proton events, where the correlation coefficient r between I_p and $I_{i,2}$ is approximately 0.82. The black line in Fig. 7 b) shows the calculated values of the proton flux intensity $I_{p,c}$, calculated using the regression model (5), establishing a relationship between the intensity of type II bursts $I_{i,2}$ and the observed values of the proton flux intensity I_p with energy E_p > 30 MeV.

$$\lg I_p \approx \lg I_{p,c} = 0.031 \cdot I_{i,2} - 1.196 \quad (5)$$

It should be noted that when studying the connection between I_p and $I_{i,2}$, the heliolongitudinal attenuation of the proton flux was not taken into account, since taking into account the heliolongitudinal attenuation coefficient leads to a decrease in the correlation between I_p and $I_{i,2}$, while taking into account the heliolongitudinal attenuation between I_p and $V_{i,2}$ leads to an increase in the correlation. It was not possible to establish the reason for the decrease in the correlation between the proton flux I_p and the intensity of type II burst $I_{i,2}$ taking into account the heliolongitudinal attenuation coefficient of the proton flux.

The relationship between the intensity of the SCR proton flux I_p and the frequency drift velocity $V_{i,2}$ and the intensity of type II bursts $I_{i,2}$ was also studied depending on the proton energy E_p in the range >1-850 MeV and on the frequency of type II radio bursts $f_{i,2}$ in the range 25- 180 MHz. A comparative analysis showed that the relationship between the SCR proton flux I_p and the frequency drift velocity $V_{i,2}$ and the intensity of type II bursts $I_{i,2}$ largely depends on the proton energy E_p (Fig. 8 a). In Fig. 8 a) red color indicates the dependence of the correlation coefficients r between I_p and $V_{i,2}$, and blue color between I_p and $I_{i,2}$. In Fig. 8 a) it is clear that the strongest connection between I_p and $V_{i,2}$ and $I_{i,2}$ is observed for subrelativistic protons with E_p >30-100 MeV and sharply decreases for protons with energy E_p >850 MeV.

If we consider the relationship between the intensity of the proton flux I_p with $V_{i,2}$ and $I_{i,2}$ from the frequency of the type II radio burst $f_{i,2}$ in the range 25-180 MHz, then as can be seen in Fig. 8 b) the connection I_p with $V_{i,2}$ and $I_{i,2}$ remains almost constant. The sharp drop at low frequencies $f_{i,2}$ < 30 MHz is due to the fact that at the edges of the spectrum it is not possible to accurately determine the behavior of the regression model (6), which was obtained from data in the range 25-180 MHz. In order to obtain a more accurate model (6), data is needed at frequencies <25 MHz and >180 MHz. Thin lines in Fig. 8 a) and b) show the dependences of the correlation coefficients I_p with $V_{i,2}$ and $I_{i,2}$ on the energy E_p and on the frequency $f_{i,2}$ without taking into account the heliolongitudinal attenuation of the SCR proton flux.

6. Conclusion

The results obtained related to the study of the relationship between the intensity of the flux of SCR protons and the frequency drift velocity and intensity of type II bursts definitely indicate the important role of coronal shock waves in the acceleration of subrelativistic SCR protons. However, a sharp decrease in the relationship between the intensity of the flux of SCR protons I_p with energy E_p > 850 MeV with the frequency drift velocity $V_{i,2}$ and the intensity of type II bursts $I_{i,2}$ indicates that high-energy SCR protons with energy E_p > 850 MeV are probably accelerated in the flare region in current layers.

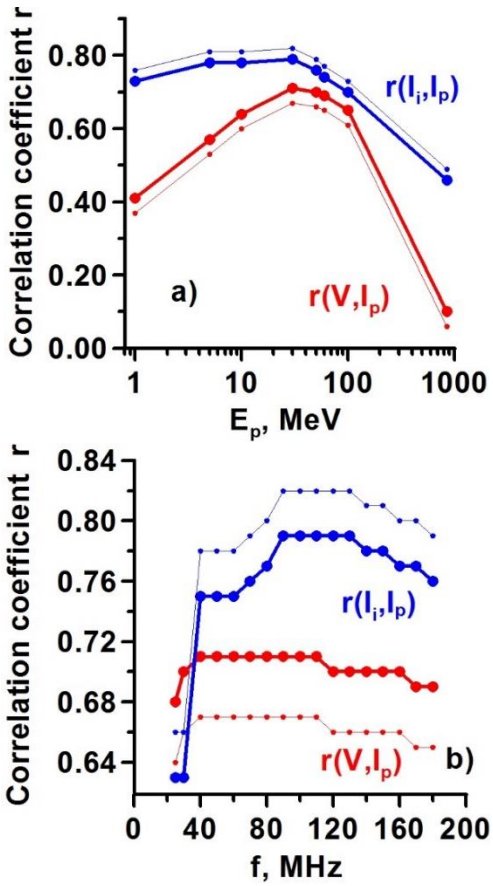

Figure 8: a) Relationship between the intensity of the proton flux I_p and the frequency drift velocity $V_{i,2}$ (red) and the intensity of type II bursts $I_{i,2}$ (blue) from the proton energy E_p; b) Relationship between the proton flux intensity I_p and the frequency drift velocity $V_{i,2}$ (red) and with the intensity of type II bursts $I_{i,2}$ (blue) from the type II radio burst frequency $f_{i,2}$. Thin lines show the values of the correlation coefficients without taking into account the heliolongitudinal weakening of the SCR proton flux.

References

Akin'yan S., Fomichev V., Chertok I.: 1977, *Geomagnetizm i Aeronomiya*, **17**, № 1, 10.

Akin'yan S., Fomichev V., Chertok I.: 1978, *Geomagnetizm i Aeronomiya*, **18**, № 4, 577.

Cliver E., Kahler S., Reams D.: 2004, *Astrophys. J.*, **605**, 902.

Chertok I.: 1982, *Geomagnetizm i Aeronomiia*, **22**, 182.

Chertok I.: 1987, *Geomagnetizm i Aeronomiia*, **27**, 362.

Gopalswamy N., Yashiro S., Michalek G. et al.: 2002, *Astrophys. J.*, **572**, 103.

Isaeva E., Tsap Yu.: 2011, *Bull. of the Crimean Astrophys. Obs.*, **107**, 78.

Isaeva E., Tsap Yu.: 2017, *Odessa Astron. Publ.*, **30**, 222.

Isaeva E.: 2018, *Odessa Astron. Publ.*, **31**, 132.

Isaeva E.: 2019, *Odessa Astron. Publ.*, **32**, 97.

Isaeva E.: 2019, *Odessa Astron. Publ.*, **32**, 122.

Isaeva E.: 2020, *Odessa Astron. Publ.*, **33**, 79.

Melnikov V., Podstrigach T., Kurt V. et al.: 1986, *Kosmicheskie Issledovaniia*, **24**, 610.

Melnikov V., Podstrigach T., Daibog E. et al.: 1991, *Cosmic Res.*, **29**, № 1, 87.

Reames D.: 1999, *Space Sci. Rev.*, 1999, **90**, 413.

Tsap Yu., Isaeva E.: 2012, *Bull. of the Crimean Astrophys. Obs.*, **108**, 52.

Tsap Yu., Isaeva E.: 2012, *Geomagnetism and Aeronomy*, **52**, № 7, 921.

Tsap Yu., Isaeva E.: 2013, *Cosmic Research.*, **51**, № 2, 108.

Tsap Yu., Isaeva E., Kopylova Yu.: 2020, *Astron. Lett.*, **46**, № 2, 144.

Tsap Yu., Isaeva E., Kopylova Yu.: 2023, *Geomagnetism and Aeronomy*.

Wild J., Smerd S., Weiss A.: 1963, *Ann. Rev. Astron. Astrophys.*, **1**, 291.

https://doi.org/10.18524/1810-4215.2023.36.290216

ANOMALOUS MAGNETIC REGIONS ON THE SUN

N.N. Kondrashova[1], V.N. Krivodubskij[2]

[1] Main Astronomical Observatory, National Academy of Sciences of Ukraine, Kyiv, Ukraine
kondr@mao.kiev.ua
[2]Astronomical Observatory, Taras Shevchenko National University of Kyiv, Kyiv, Ukraine
krivod2@ukr.net

ABSTRACT. We studied the anomalous magnetic regions observed near the minima of solar cycles 24 and 25. The peculiarity of these areas was the deviation of their configuration from Hale's law of magnetic polarity and Joy's law about the inclination of the axes of bipolar groups to the latitudinal direction. Therefore, they belong to the class of so-called anti-Hale active regions. We paid special attention to the flare activity of anti-Hale regions, as this is important for forecasting space weather and magnetic storms in the Earth's atmosphere.

The detected anomalies of the surface magnetism of the active regions studied by us may indicate the influence of the mechanisms of the deep small-scale dynamo on their evolution. In this regard we analyzed the possible mechanisms of the formation of anti-Hale magnetic regions. In particular, such mechanisms can be the mechanisms of a small-scale magnetic dynamo. In connection with this an urgent problem today is the search for observed evidence of the existence of the theoretically proposed by Brandenburg A. et al. (2012) of a new physical entity – a small-scale magnetic field hidden in the solar depths, excited by two qualitatively different mechanisms of a small-scale dynamo (SSD). The first mechanism is the SSD of macroscopic MHD (SSD1), while the second is the diffusion SSD of classical MHD (SSD2). However, the small contributions of these sources are very difficult to distinguish observationally. To solve this complication, Sokoloff, Khlystova and Abramenko (2015) proposed a test for separating the contributions of two sources based on a statistical probabilistic model. Such an important feature of the differences between of the two SSD is the behavior of the percentage of anti-Hail groups of sunspots (in relation to the total number of spots) in the minima of solar cycles. According to statistical studies of long series of observations Sokoloff, Khlystova and Abramenko (2015) found that the percentage of anti-Haile groups of spots increases during minima of the solar cycles, suggesting in favor of SSD2.

We believe that the detected magnetic anomalies of the studied regions may be caused by the influence of a SSD2 in the depths of the convective zone of the Sun, since this source gives the most noticeable contribution to the surface magnetism near cycle minima.

Keywords: solar convective zone, magnetic fields, turbulent dynamo, magnetic activity of the Sun, sunspots, solar flares.

АНОТАЦІЯ. Ми дослідили аномальні магнітні області, що спостерігалися поблизу мінімумів сонячних циклів 24 і 25. Особливість цих областей полягала у відхиленні їх конфігурації від закону магнітної полярності Хейла і закону Джоя про нахил осей біполярних груп до широтного напрямку. Тому вони належать до класу т. зв. антихейлівських активних областей. Ми звернули особливу увагу на спалахову активність антихейлівських областей, оскільки це важливо для прогнозування космічної погоди та магнітних бур в атмосфері Землі.

Виявлені аномалії поверхневого магнетизму досліджених нами активних областей можуть свідчити про вплив на їхню еволюцію механізмів глибинного маломасштабного динамо. В зв'язку цим ми проаналізували можливі механізми утворення антихейлівських магнітних областей. Зокрема, такими механізмами можуть бути механізми маломасштабного магнітного динамо. В зв'язку з цим актуальною проблемою сьогодення є пошук спостережених доказів існування теоретично запропонованої в роботі Brandenburg A. et al. (2012) нової фізичної сутності – прихованого в сонячних глибинах маломасштабного магнітного поля, що збуджується двома якісно різними механізми маломасштабного динамо (ММД). Перший механізм – це ММД макроскопічної МГД (ММД1), а другий – дифузійне ММД класичної МГД (ММД2). Однак мізерні внески цих джерел дуже важко розрізнити за допомогою спостережень. Щоб вирішити цю проблему Sokoloff, Khlystova and Abramenko (2015) запропонували тест для розділення внесків двох джерел на основі статистичної імовірнісної моделі. Такою важливою особливістю відмінностей між двома ММД є поведінка відсоток антигхейлівських груп сонячних плям (по відношенню до загальної кількості плям) у мінімумах сонячних циклів. Відповідно до статистичних досліджень тривалої серії спостережень Sokoloff, Khlystova and Abramenko (2015) виявили, що відсоток антихейлівських груп плям зростає під час мінімумів сонячних циклів, що свідчить на користь ММД2.

Ми вважаємо, що виявлені магнітні аномалії досліджених областей можуть бути викликані впливом ММД2 в глибинах конвективної зони Сонця, оскільки це джерело дає найбільш помітний внесок у поверхневий магнетизм поблизу мінімумів циклів.

Ключові слова: сонячна конвективна зона, магнітні поля, турбулентне динамо, магнітна активність Сонця, сонячні плями, сонячні спалахи.

1. Evolution and flare activity of the anti-Hale active regions

We selected to analysis several anomalous magnetic regions observed near minimum of 24 and 25 cycles of the solar activity. Anti-Hale sunspots regions NOAA 10792, 10715, 10875, 10930, 12673, 13088 are the clear examples of violation of Hale's and Joy's laws. We used the magnetograms obtained by the Helioseismic and Magnetic Imager (SDO) (Scherrer et al., 2012) and the Michelson Doppler Imager (SOHO) (Sherrer et al., 1995).

Active region (*AR*) *NOAA 10792*, first seen on 30 July 2005, in latitude N12, was typical anomalous magnetic region. The magnetic field of this region was not regular. The magnetic poles were rotated 180 degrees compared other ARs in northern hemisphere (Fig. 1). Therefore, this region belongs to the class of anti-Hale magnetic configurations. The oppositely oriented regions occur side by side in the same latitude zone. Therefore, they cannot be part of the same magnetic flux system. The region evolved rapidly, and its most complex magnetic configuration was βγδ. 13 flares of C class and five M class flares occurred in it. One X1.3 class flare was the most powerful. This flare produced a coronal mass ejection (CME).

AR NOAA 10715 (29.12.2004 – 10.01.2005). Active region appeared in latitude N04. The orientation of this anomalous magnetic region differs by 90 degrees from the orientation prescribed by Hale's law (Fig. 2). This fact indicates that fluctuations exist over whole range of orientation angles. The region produced four M class flares, 19 C class flares. The most powerful event was X1.7 class flare.

AR NOAA 10875 (23.04.2006 – 6.05.2006). The region was large and had a complex magnetic field (Fig. 3). Two M class and 15 C class flares occurred in this region. One M8 class flare caused a shortwave radio blackout.

AR NOAA 10930 (5.12.2006 – 18.12.2006*)*. This magnetic region (Fig. 4) produced very high flare activity. There were 31 C class, four M class and three X class flares in this region. One X9.0 class flare was the most powerful. This flare caused a geomagnetic storm.

AR NOAA 12673 (29.08.2017 – 10.09.2017). The region appeared on the solar disk on 29 August 2017 in latitude S08 as unipolar spot and developed rapidly. Orientation of the magnetic region was different by 90 degrees from the orientation prescribed by Hale's law (Fig. 5). The number of the sunspot increased. Its magnetic configuration became more complicated from α up to βγδ. There were 39 C class, 17 M class, and four 4 X class flares in this region. The number of more powerful flares increased over time. One X9.3 class flare was the most powerful. X-ray and UV radiation from this flare caused a strong shortwave radio blackout over Europe, Africa and the Atlantic Ocean. This magnetic region also produced several CMEs and strong geomagnetic storms.

AR NOAA 13088 (24.08.2022 ─ 30.*08.2022*). The region appeared on 24 August 2022 in the western part of the solar hemisphere and developed rapidly (Fig. 6). The number and the area of the spots increased. The configuration of its magnetic field has become more complex up to βγ class. This region produced 120 C class and 25 M class flares, several CMEs during two transitions through the solar disk. One M8.6 class flare was the most powerful, and one M 4 class flare caused a shock wave through the atmosphere of the Sun and a CME. The magnetic region produced several CMEs and geomagnetic storms.

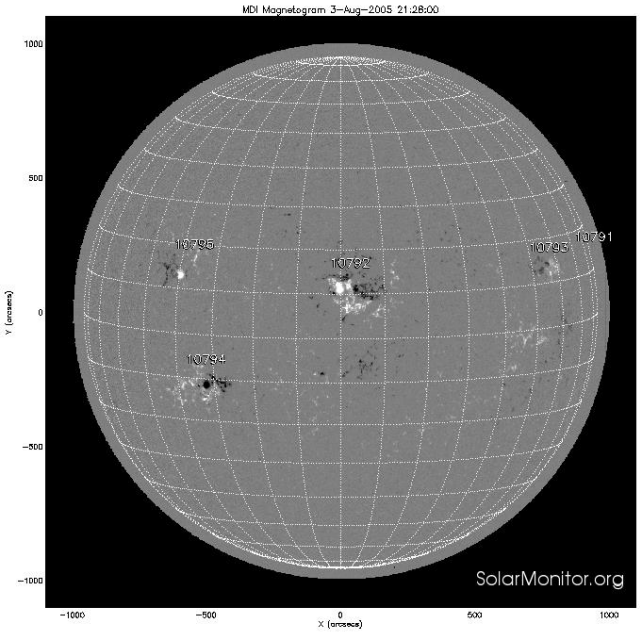

Figure 1: Magnetogram of the Sun on 3 August 2005 (SOHO/MDI). In the center of the figure/disk is the anti-Hale magnetic region NOAA 10792. White and black colors indicate areas of positive and negative polarity of the magnetic field, respectively.

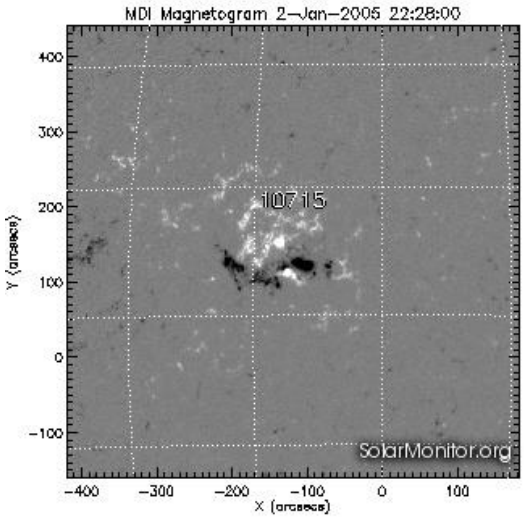

Figure 2: Magnetogram of the active region NOAA 10715 on 2 January 2005 (SOHO/MDI).

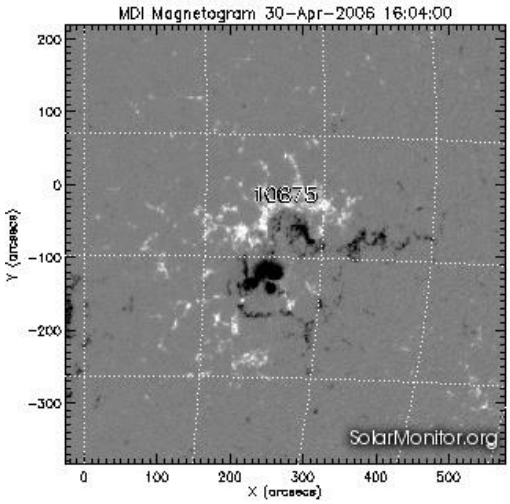

Figure 3: Magnetogram of the active region NOAA 10875 on 30 April 2006 (SOHO/MDI).

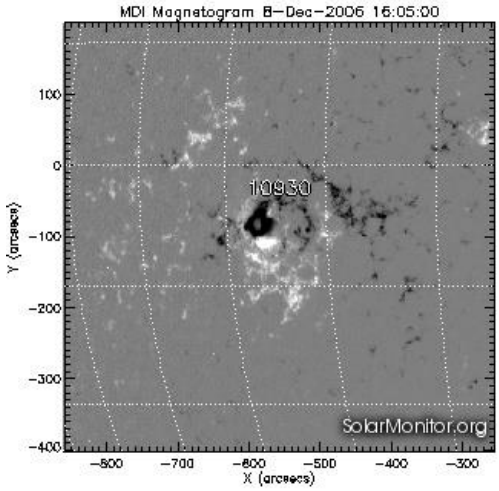

Figure 4: Magnetogram of the active region NOAA 10930 on 8 December 2006 SOHO/MDI).

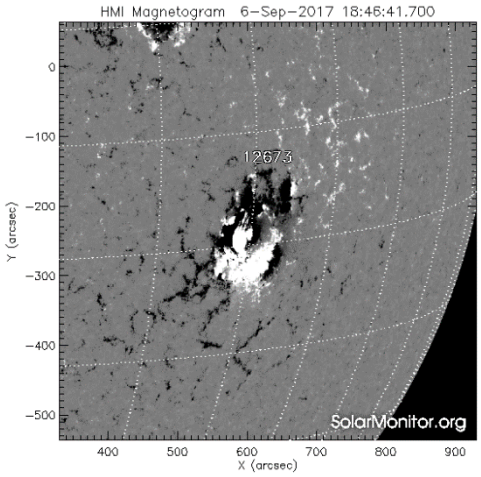

Figure 5: Magnetogram of the active region NOAA 12673 on 6 September 2017 (SDO/HMI).

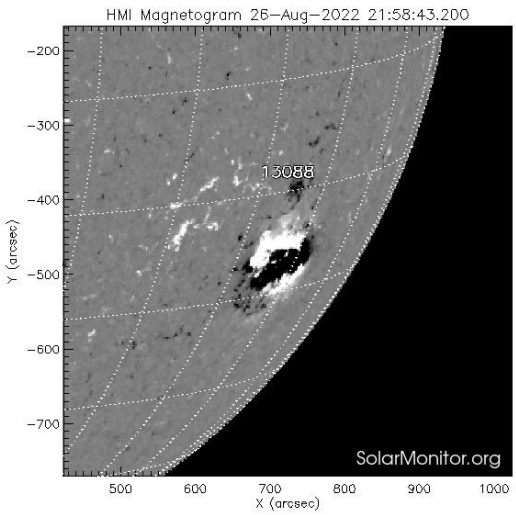

Figure 6: Magnetogram of the active region NOAA 13088 on 26 August 2022 (SDO/HMI).

2. Dynamo mechanisms of small-scale magnetic fields

Next, we will briefly discuss the possible mechanisms contributing to the appearance of anti-Hale active regions [Krivodubskij and Kondrashova, 2023]. In work Sokoloff, Khlystova and Abramenko (2015) based on the processing of observational data for 1920 - 2004 from the Mount Wilson Catalog, it was found that in the "royal zone" a small number of bipolar groups of sunspots were always observed, which had the "wrong magnetic polarity". Sokoloff, Khlystova and Abramenko (2015) called them "violators of Hale's law". They believe that the appearance of anti-Hale bipolar groups is related to operation of the small-scale turbulent dynamo in the solar convective zone (SCZ).

Therefore, an urgent problem today is the search for observed evidence of the existence of the theoretically proposed by Brandenburg, Sokoloff and Subramanian (2012) of a new physical entity – a small-scale (fluctuating) magnetic field, excited by mechanism of a small-scale dynamo (SSD), the action of which is hidden in the depths of the SCZ.

Besides, the situation is complicated by the fact that in the depths of the SCZ can function simultaneously two qualitatively different excitation mechanisms of fluctuating fields (small-scale dynamo of macroscopic MHD and the fluctuation dynamo of classical MHD).

The first mechanism ensures the generation of small-scale magnetic fields due to the interaction of turbulent motions with the global magnetic field (small-scale dynamo 1 of macroscopic MHD: SSD1). Within the framework of macroscopic MHD, in the presence of a weak primary magnetic field, two components of magnetism are excited in the SCZ. They are namely next: the global magnetic field **B** and the fluctuating (small-scale) magnetic field **b** (Krause and Rädler, 1980**)**. The excitation of the fluctuating magnetic field **b** (SSD1) is described by the hydromagnetic equation

$$\frac{\partial \mathbf{b}}{\partial t} = \mathrm{rot}\left[(\langle \mathbf{U} \rangle \times \mathbf{b}) + (\mathbf{u} \times \langle \mathbf{B} \rangle) + \mathbf{G} - \nu_m \,\mathrm{rot}\,\mathbf{b}\right],$$

where **U** is the velocity of regular differential rotation, **u** is the velocity of turbulent convection, $\mathbf{G} = \mathbf{u} \times \mathbf{b} - \langle \mathbf{u} \times \mathbf{b} \rangle$, $\nu_m = c^2/4\pi\sigma$ is the coefficient of magnetic viscosity, σ is the gas-kinetic electrical conductivity.

While the second mechanism (diffusive small-scale dynamo 2 of classical MHD) causes the self-excitation of magnetic fluctuations due to turbulent pulsations of highly conductive plasma (SSD2). Chaotic hydrodynamic movements with velocity **u** excite fluctuating electric currents $\mathbf{j} = -e n \mathbf{u}$ in highly conductive plasma (e is the electron charge; *n* is the concentration of electrons in the plasma). If the magnetic field is frozen in the highly conductive plasma, these fluctuating electric currents **j**, in turn, generate fluctuations of the magnetic induction $\mathrm{rot}\,\mathbf{h} = \mathbf{j}/(c/4\pi)$. The amplitude of the generated magnetic fluctuations *h* can be estimated from the condition of equal distribution of the densities of the kinetic $\rho u^2/2$ and magnetic $h^2/8\pi$ energies of small-scale pulsations (Priest, 1982)

$$\rho u^2/2 \approx h^2/8\pi$$

(here ρ is the plasma density).

The fundamental difference between the two quoted small-scale dynamo mechanisms is as follows.

In the SSD1 mechanism, electric currents, which are necessary for the excitation and subsequent reconstruction of magnetism, are generated as a result of the interaction of fluctuating and regular plasma movements ***with the primary magnetic field.***

In contrast, the SSD2 mechanism provides self-excitation of the magnetic fluctuations ***in the absence of a primary magnetic field***. Generation of electric currents is provided by turbulent movements in highly conductive plasma

The small contributions of two sources of small-scale magnetic fields **b** and **h**, localized in the depths of the Sun, to the surface magnetism are very difficult to distinguish with the help of observations.

Therefore, researchers face the fundamental physical problem of how to find tiny surface manifestations of the small-scale action of two dynamo mechanisms in the interior of the Sun.

3. Search for surface tracers of a deep small-scale magnetic dynamo

Sokoloff, Khlystova and Abramenko (2015) assumed that tracers of small-scale dynamo action in the interior of the Sun may be hidden in the statistics of bipolar groups of sunspots, which violate Hale's law of magnetic polarity and Joy's law of inclination of the axes of bipolar groups to the latitudinal direction. The essence of the proposed criterion is that deep small-scale magnetic fields under certain conditions can lead to violations of Hale's and Joy's laws of observed magnetism on the surface of the Sun.

According to Hale's law of east-west magnetic polarity orientation (Hale et al., 1919; Hale and Nicholson, 1925) during one 11-year cycle in one hemisphere (northern or southern), the head and tail spots of bipolar magnetic groups always have the same opposite magnetic signs. On the other side of the equator, the signs of the head and tail spots are opposite. This situation persists throughout the current cycle, and then, when a new cycle begins, the signs of the spots are reversed. At the same time, the axes of bipolar groups of spots are oriented at a small angle to the "east-west" latitudinal direction (Hale et al., 1919), so that the western head (leading in relation to rotation) spots are on average closer to the equator than the eastern tail spots (Joy's law of magnetic polarity orientation north-south). The average tilt angle of the axes of bipolar groups is about 4°, increasing from a few degrees (for groups near the equator) to 8-10° for high-latitude groups (Howard, 1991).

Hale and Nicholson (1925) as a result of statistical analysis of bipolar groups of spots from 1913 to 1924, found that 2.4% of active regions do not obey the law of magnetic polarities of groups established by them. Similar estimates of the deviation from Hale's law were obtained in subsequent studies by many authors over almost a century. As for the violations of Joy's law, they are to a greater extent characteristic of the anti-Hale bipolar groups of spots. More 70 years ago Richardson (1948) found that in anti-Hale groups, the tilt angles of their axes relative to the equator are, as a rule, greater than the tilt angles of groups of spots that comply with Hale's law.

The study of tilt angles of active magnetic regions allows us to make assumptions about the mechanism of the emergence of anti-Hail groups of spots and its localization in the SCZ. In paper (Munoz-Jaramillo, Navarrete and Campusano, 2021), the inclinations relative to the equator of regular and anti-Hale groups covering four solar cycles were studied. Anti-Hail groups were found to belong to a separate population. This indicates the mechanism of their origin, which differs from the excitation of a regular toroidal field by the Ω effect. In particular, Bekki and Cameron (2023) found that violations of Joy's law are inherent to bipolar magnetic regions shallowly rooted in the subphotospheric convection layers. Therefore, it can be assumed that this mechanism is a subsurface fluctuating small-scale dynamo.

Statistical analysis of deviations from Hale's and Joy's laws over long periods of time allows us to reveal differences in the evolution of the observed manifestations of the two sources of small-scale fields **b** and **h**, since the contribution of the two deep dynamo mechanisms to the surface magnetism changes with the phase of the solar cycle in different ways.

Such an important feature is the behavior of the of anti-Hail groups of sunspots during the cycles. In the case of small-scale dynamo 1 (magnetic field **b**), the percentage of anti-Hale groups is independent of cycle phase. Whereas the percentage of anti-Hale groups associated with small-scale dynamo 2 (magnetic field **h**), should reach its maximum value at solar minima, as the global toroidal magnetic field weakens at this time.

Therefore, the variations of magnetic anomalies make it possible to separate the tiny contributions of deep two small-scale dynamo mechanisms to surface magnetism. In this connection, the task of identifying the harbingers of a small-scale dynamo in the solar depths from observations is gaining relevance.

With this in mind, we conducted an analysis of literature data of statistical studies of long series of observed violations of Hale's and Joy's laws, which can be caused by the presence of deep small-scale magnetic fluctuations of various origins.

In the work Sokoloff, Khlystova and Abramenko (2015) on the basis of processing the data of different catalogs for the period 1917 - 2004, it was demonstrated that the percentage of anti-Hale groups of spots increases during the minima of solar cycles. This testifies to the operation of a random small-scale turbulent dynamo 2 (diffusive dynamo) within the SCZ, the efficiency of which becomes noticeable near the minima of the cycles, when the global toroidal magnetic field weakens.

In this regard, we note the two-layer dynamo models proposed in papers of Benevolenskaya (1998), and Popova, Zharkova and Zharkov (2013). These models are based on the idea of two dynamo sources separated in space. The first dynamo source is located near the bottom of the SCZ, while the second one operates near the solar surface. Currently, it seems that the near-surface source of excitation in the two-layer dynamo models is consistent with the theoretical concept of the excitation of magnetic fluctuations by the mechanism of the *diffusion* small-scale dynamo 2, which is localized in the upper part of the SCZ.

4. Discussion and conclusions

We selected to analysis several anomalous magnetic regions observed ***near minima*** of 24 and 25 cycles of the solar activity. The peculiarity of these ARs consisted in the deviation of their observed surface magnetic configuration from Hale's law of the magnetic polarity of spot groups and Joy's law of tilting the axes of bipolar groups to the latitudinal direction.

In recent decades, thanks to the use of data from observations of space vehicles, evidence has emerged that rare superactive ARs which violated Hale's and Joy's laws had a strong tendency to produce X-ray bursts, strong proton events, and strong magnetic storms (Tian et al., 2002; Tian et al., 2005; Abramenko, 2021; Xu et al., 2022). With this in mind, we paid attention to the flare activity of anti-Hale regions. It was established that all ARs investigated by us generated significantly high flares activity. Considering the relevance of detecting periods of increased levels of flares for the purpose of space weather forecasting, the study of Ars, characterized by violations of Hale's and Joy's laws, becomes important.

We analyzed two qualitatively different possible dynamo-mechanisms of formation of anti-Hale magnetic regions. In the case of small-scale dynamo 1 (macroscopic MHD), the percentage of anti-Hale groups is independent of cycle phase, whereas the percentage of anti-Hale groups associated with diffusive small-scale dynamo 2 (classical MHD) should reach its maximum value at solar minima.

The ARs studied by us were observed near the minima of cycles 24 and 25. Therefore, we assume that the detected observed magnetic anomalies may indicate the influence of the fluctuating small-scale diffusion dynamo 2 of the classical MHD on the evolution of the studied ARs, since this source gives the most noticeable contribution to the surface magnetism ***near the cycle minima***.

Acknowledgements. The work was carried out with the support of the Ministry of Education and Science of Ukraine, state budget grant number 22BF23-03 under the program "Astronomy and space physics" of Taras Shevchenko National University of Kyiv.

References

Abramenko V.I.: 2021, *Mon. Notic. Roy. Astron. Soc*., **507**, 3698.

Bekki Y., Cameron R.H.: 2023, *Astron. and Astrophys.*, **670**, id. A101, 18 p.

Benevolenskaya E.E.: 1998, *ApJ*, **509**, L49.

Brandenburg A., Sokoloff D., Subramanian K.: 2012, *Space Sci. Rev*., **169**, 123.

Hale G.E., Ellerman F., Nicholson S.B., Joy A.H.: 1919, *ApJ*, **49**, 53.

Hale G.E., Nicholson S.B.: 1925, *ApJ*, **62**, 270.

Howard R.F.: 1991, *Solar Phys*., **136**, 251.

Krause F., Rädler K.-H.: 1980, Mean Field Magnetohydrodynamics and Dynamo Theory, Berlin: Akademie-Verlag, 271 p.

Krivodubskij V.N., Kondrashova N.M.: 2023, *Kinem. and Phys. Cel. Bod.*, **39**, No.6, 58.

Munoz-Jaramillo A., Navarrete B., Campusano L.E.: 2021, *Ap. J*., **920**, id. 31, 11 p.

Popova E., Zharkova V., Zharkov S.: 2013, *Ann. Geophys*., **31**, 2023.

Priest E.R.: 1982, Solar Magnetohydrodynamics. Dordrecht: D. Raidel Company, 471 p.

Richardson R.S.: 1948, *ApJ*, **107**, 78.

Scherrer P.H., Bogart R.S., Bush R.I. et al.: 1995, *Solar Phys*., **162**, 129.

Scherrer P.H., Schou J., Bush R.I. et al: 2012, *Solar Phys.*, **275**, 207.

Sokoloff D., Khlystova A., Abramenko V.: 2015, *Mon. Notic. Roy. Astron. Soc*., **451**, 1522.

Tian L., Liu Y., Wang J.: 2002, *Solar Phys*., **209**, Iss.2, 361.

Tian L., Alexander D., Liu Y., Yang J.: 2005, *Solar Phys*., **229**, Iss.2, 63.

Xu Zh., Yan X., Yang L. et al.: 2022, *Ap. J. Lett*., **937**, id. L11, 9 p.

https://doi.org/10.18524/1810-4215.2023.36.290538

THE EARTH'S MAGNETIC FIELD AND THE LARGE-SCALE MAGNETIC FIELD OF THE SUN: THE SOLAR-TERRESTRIAL CONNECTION

M.I. Orlyuk, A.A. Romenets

S.I. Subbotin Institute of Geophysics, National Academy of Sciences of Ukraine, Kyiv, Ukraine
orliuk@ukr.net; romenets@ukr.net

ABSTRACT. The paper presents the results of a joint analysis of the Earth's main magnetic field (core field) B_{IGRF} and the large-scale magnetic field (LSMF) of the Sun. Selected 11- and 22-year periods of LSMF and B_{IGRF} variations are well manifested in both fields and are usually modulated by solar activity. Even 11-year cycles for which the direction of the Sun's magnetic field coincides with the direction of the Earth's magnetic field are characterized by the minimum values of sanspot numbers, and odd cycles with opposite directions of magnetic fields have larger values of sunspot numbers. The rotation rate of two- and four-sector structure of the Sun source of LSMF varied with about 11-year and 22-year cycle. Longer changes in the magnetic fields of the Sun and the Earth with a period of about 75 years have also been revealed.

The rotation periods of the Sun source global field (28,0-28,5 days) were maximum at the middle of the 20th century in the period 1940÷1960 years. This maximum of solar activity corresponds to temporal gradient of geomagnetic field. It is shown that the gradient of the geomagnetic field B_{IGRF} depends on the rate of change in the length of the day. So, according to the results of the study, the rotation modes of the Sun and the Earth cause different periodic changes in their magnetic fields.

Keywords: geomagnetic field, solar activity, magnetic field of the Sun, space weather.

АНОТАЦІЯ. У статті представлені результати спільного аналізу основного магнітного поля Землі (поля ядра) B_{IGRF} і великомасштабного магнітного поля Сонця (ВМПС). При цьому 11- та 22-річні періоди варіацій ВМПС і B_{IGRF} добре проявляються в обох полях і зазвичай модулюються сонячною активністю. Парні 11-річні цикли, для яких напрямок магнітного поля Сонця збігається з напрямком магнітного поля Землі, характеризуються мінімальними значеннями чисел сонячних плям, а непарні цикли з протилежними напрямками магнітних полів мають більші значення чисел сонячних плям. Швидкість обертання дво- та чотирисекторної структури сонячних джерел ВМПС змінювалася з приблизно 11-річним та 22-річним циклом. Виявлено також більш тривалі зміни магнітних полів Сонця і Землі з періодом близько 75 років. Період обертання джерел ВМПС (28,0-28,5 доби) був максимальним в середині 20 століття в 1940÷1960 роках. Цей максимум сонячної активності відповідає часовому градієнту геомагнітного поля. Показано, що градієнт геомагнітного поля B_{IGRF} залежить від швидкості зміни тривалості дня. Отже, згідно з результатами дослідження ротаційні режими Сонця та Землі зумовлюють різноперіодні зміни їх магнітних полів.

Ключові слова: геомагнітне поле, сонячна активність, магнітне поле Сонця, космічна погода

1. Introduction

The study of solar-terrestrial relations is a determining condition for forecasting short-term and long-term changes in space weather. One of the main factors of space weather, which affects a number of terrestrial systems, including the biosphere, is the perturbation of the geomagnetic field. The majority of works in this direction are aimed at studying the relationship between geomagnetic and solar activity in a relatively short-period frequency range (Georgieva et al., 2022; Du, 2011; Sukharev et al., 2022). In this regard, the authors performed an analysis of the long-term changes of the B_{IGRF} magnetic field of the Earth with the large-scale magnetic field of the Sun and solar activity and proposed a mechanism of their potential relationship.

2. Data and methodology

Digital data from sites (DGRF/IGRF…: Solar Cycle…) and graphical data (Obridko et al., 2021; Matsakis, McCarthy, 2023), which were partially generated into digital data, were used for the research. For a joint analysis of temporal changes of the B_{IGRF}, day length, LSMF and Solar activity trend and variation components of long-term and short-term changes were selected using statistical analysis methods.

3. Spatio-temporal structure of the geomagnetic field induction B_{IGRF}

The maximum values of the main magnetic field B_{IGRF} of the Earth for 2020 are characteristic for the negative magnetic pole ($B_{IGRF,1950}$ = 69 000 nT, $B_{IGRF,2020}$ = 66 900 nT) (located near the Earth's geographical North Pole) and positive (located near the Antarctic coast opposite Australia), and the minimum ones for the near-equatorial regions of the South Atlantic (the so-called South Atlantic Anomaly) ($B_{IGRF,\ 1950}$ = 24 500 nT, $B_{IGRF,\ 2020}$ = 22 300 nT) (see Fig. 1 *a*, *b*) (Orlyuk & Romenets, 2020; 2022].

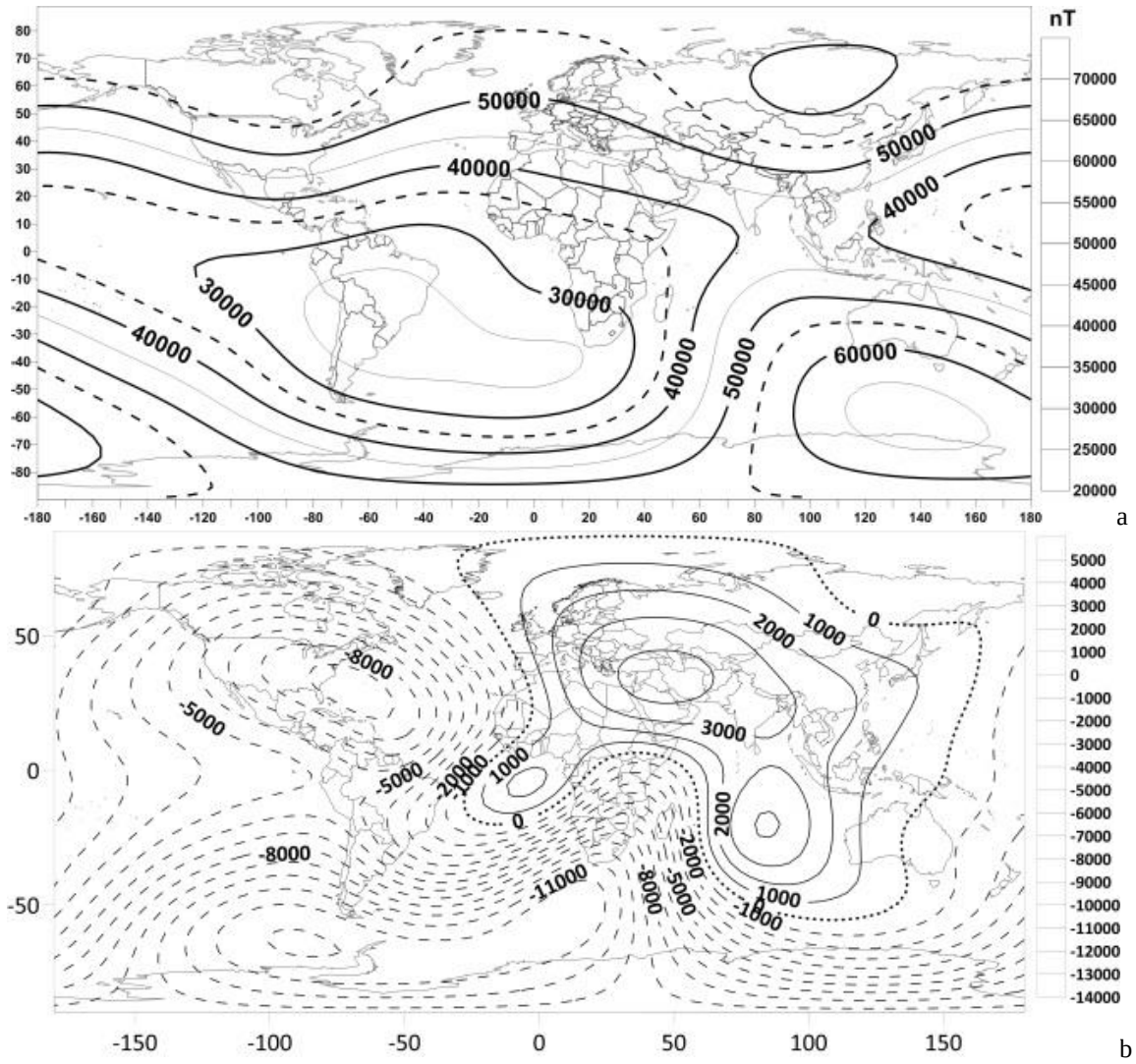

Figure 1: The normal component of the geomagnetic field B_{IGRF} value for 2020 (*a*), and for 1950-2020-time interval temporal changes (*b*)

The maximum field decreases from 1950 to 2020 (from –5500 to –7400 nT, from –80 to –100 nT/year) are located near the Atlantic coast of Central America, as well as in the region the Drake Strait and between Africa and Antarctica. Field increase maxima (2100÷3500 nT, 40÷60 nT/year) are typical for Europe and the Indian Ocean (see Fig. 1*b*)

For the period from 1950 to 2020 the average B_{IGRF} value on the planet's surface decreased by 1797 nT (from 47 603 to 45 806 nT).

The time trend of these changes seems interesting, namely: against the background of a general decrease in the field (at a rate of about –25 nT/year), its sharp jumps are observed (up to –45 nT/year in 1960—1965; –58 nT/year in 1980—1985; –32 nT/year in 2000—2005) after which over the next 15 years there was a less intensive decrease in its changes (to –18 nT/year in 1975; –12 nT/year in 1995; –2 nT/year in 2015). From all this it can be concluded that, starting from 1985 to the present, there is a slowdown in the geomagnetic field decrease (Orlyuk & Romenets, 2022).

More significant changes in the B_{IGRF} geomagnetic field are observed for the time interval 1900-2020. The average value of geomagnetic field induction in the epoch of 1900 is B_{IGRF}=49140 nT, and in the epoch of 2020 – B_{IGRF}=45803 nT. For 120 years, the main magnetic field decreased by 3337 nT (Fig. 2) (Orlyuk & Romenets, 2023).

4. Comparison of temporal changes of the geomagnetic field and length of day

For the time interval 1900-2022, 3 regional extremes can be distinguished regarding changes in the geomagnetic field and the length of the day. The extremes of changes in the B_{IGRF} geomagnetic field fall on the following years: 1917.5±2.5 (-90 nT/year); 1945.5±2.5 (-25 nT/year); 1982.5±2.5 (-70 nT/year) (Fig. 2). The regional extremes of the change in the length of day (relative to the norm) fall on 1905.0±2.5 (4 msec/year; 1936±2.5 (0.3 msec/year); 1972.5 ±2.5 (3 msec/year). An anti-correlation between the extreme values of changes in the geomagnetic field and the length of the day was revealed.

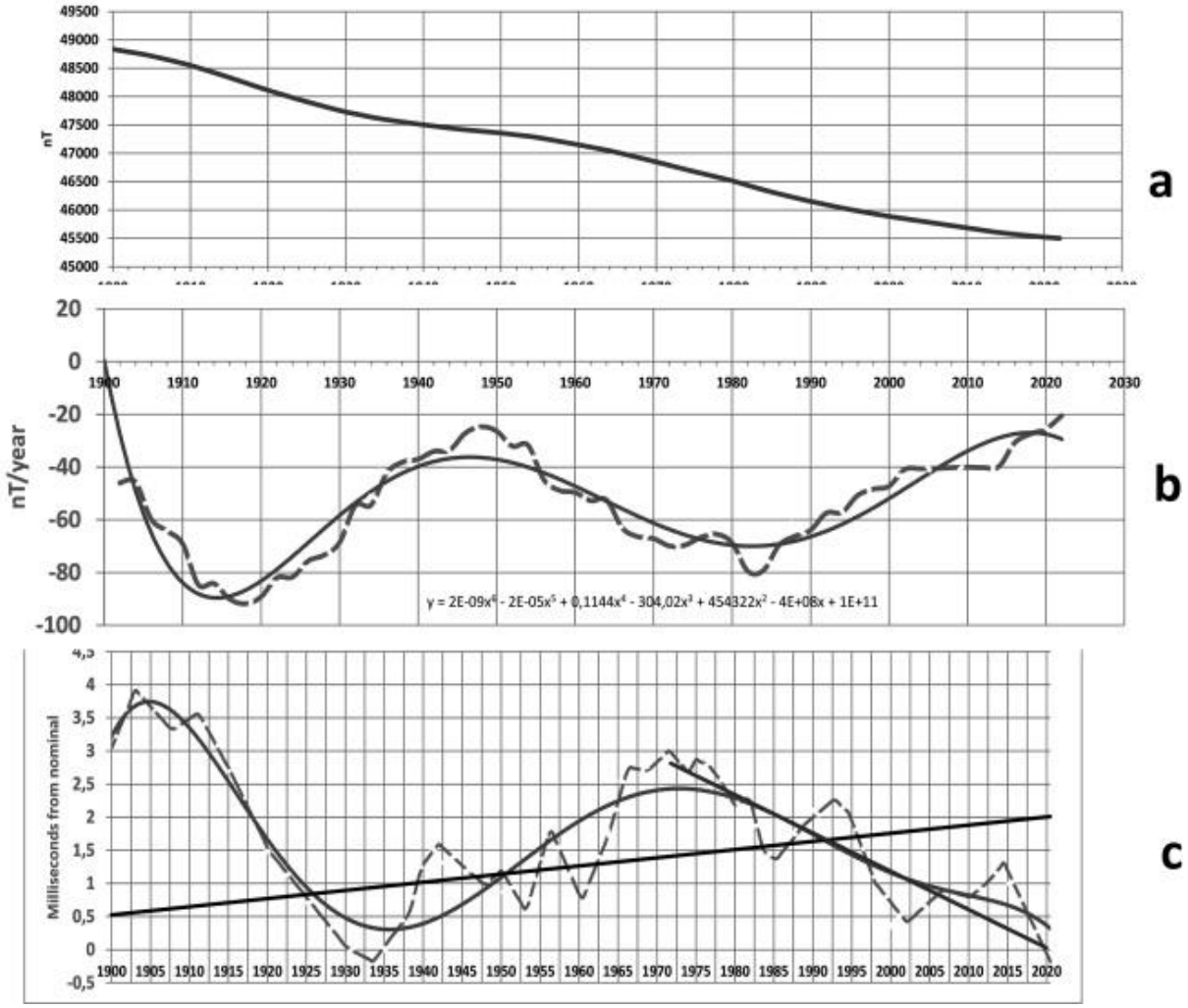

Figure 2: Changes in the average values of the geomagnetic field (a) on the Earth's surface, its temporal gradient (dashed line – raw data; solid line – polynomial approximation)(b) and length of day for the time interval 1900-2022 year (dashed line – raw data, solid line – polynomial approximation and trend (Matsakis & McCarthy, 2023))(c).

The extremes of the change in the length of day precede the extremes of the change in the geomagnetic field by approximately: 12.5 years (1917.5-1905) for the first extreme; 9.5 years (1945.5-1936) – the second; 10.0 years (1982.5-1972.5) – for the third.

Taking into account the accuracy of the determination of the peaks of the corresponding extremes, it is possible to assume an 11-year cycle of their alternation (correlation coefficient r=-0.93 when the curve of length of the day is shifted 11 years ahead).

5. The structure of the large-scale magnetic field of the Sun

Solar and interplanetary large-scale magnetic fields (LSMF) are observed in the form of the sector structure (SS) (Fisk, 2001; Bandic et al., 2023).

5.1 Solar background magnetic field (SBMF)

The rotation rate of two-sector structure of SBMF varied with about 11-year cycle. Four-sector structure had about 22-year cycle of the rotation period. The maximal rotation rate of four-sector structure was observed during maximum of even cycles (14, 16, 18, 20, 22) and minimal rate of the rotation was observed during maximum of odd cycles (15, 17, 19, 21) (Leiko, 2005).

5.2 Interplanetary magnetic field.

The main rotation period (about 27-day period) of the two-sector structure of IMF varied with about 22-year cycle: maximal value of the rotation period of IMF was during about 1952–1956, 1976, 1997 (Leiko, 2005).

The regional component of the rotation speed of the large-scale magnetic field of the Sun changes from 27.5 days for

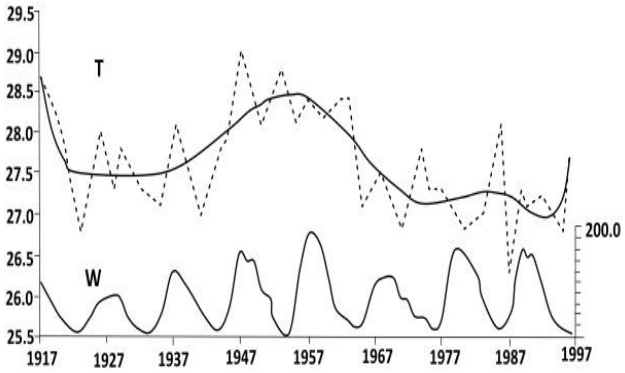

Figure 3: The rotation period (T) as a function of the 11-year cycle (W) (Obridko et al., 2021).

the time interval 1920-1940 to 27.0 days in 1965-1990. During 1945-1965 the speed of rotation was 28.0-28.5 days (Fig. 3).

An analysis of the spectrums of the whole cycles showed that during the 20th–23rd cycles the rotation period of IMF and SMMF was greater in even cycles and smaller in odd cycles. During the 18th–19th cycles the rotation period of IMF was greater during odd cycle and smaller during even cycle. Possibly, this fact is indicative of a change of the rotation regime of IMF in the middle of the 20th century, and this is an indirect confirmation of the Sun's rotation change. The rotation of the source surface global field decelerates as the activity of the local fields grows during both the 11-year and longer cycles. The rotation periods were maximum at the middle of the 20th century, i.e., in the period of the high cycles 18 and 19. At the minimum of the cycle, the frequency increases, i.e., the rotation rate increases (Fig. 3).

22-year Hale cycle of the solar activity starts at the maximum odd 11-year cycles and the change of the LSMF sign in the maxima of even cycles. Hale cycle begins at the maximum activity of an odd 11-year cycle LSMF at the north pole of the directed from the Sun (positive during the decline phase of the odd cycle and during the growth phase of the activity of the 11-year cycle). The direction of the LSMF is defined as positive when the magnetic field in the northern hemisphere is directed away from the Sun, and negative – towards the Sun (Sumaruk T. & Sumaruk P., 2020). At the cycle minimum, the heliospheric current sheet lies in the plane of the solar equator, while at the maximum, it can be tilted up to 90° (Obridko et al., 2021).

Hale cycles are characterized by the following regularity: negative III (1957-1979) and V (2000-2021 (?)) cycles have one low-intensity cycle in its middle (20 and 24), and positive cycle IV is characterized by an intense 11-year cycle (22). Accordingly, the odd Hale cycles are characterized by the minimum values of the time gradient of the B_{IGRF} field (see Fig. 4) (Orlyuk & Romenets, 2022).

6. Discussion of results

According to the above, cyclical changes of the LSMF and the induction module of the main magnetic field of the Earth B_{IGRF} are observed. First of all, we note that the LSMF changes both in direction and in amplitude and the B_{IGRF} field has a constant direction of the induction vector (negative in the northern hemisphere) and an uneven nature of its rate of decrease (see Fig. 5). Selected 11- and 22-year periods of LSMF and B_{IGRF} variations are well manifested in both fields and are usually modulated by solar activity (see Figs. 3, 4). Therefore, the dependence of solar activity on the ratio of the direction of the LSMF and B_{IGRF} is observed. As can be seen from Fig.5, even 11-year cycles for which the direction of the Sun's magnetic field coincides with the direction of the Earth's magnetic field are characterized by the minimum values of sanspot numbers, and odd cycles with opposite directions of magnetic fields have larger values of sunspot numbers. Odd cycles of polarity change LSMF are characterized by a wider spectrum of values of sunspot numbers.

Longer changes in the magnetic fields of the Sun and the Earth with a period of about 75 years have also been revealed.

The analysis of different periodic variations of magnetic fields indicates their potential connection with the rotational regime of the Earth and the Sun (Lesur et al., 2022; Obridko et al., 2021).

The rotation rate of two- and four-sector structure of the Sun source of LSMF varied with about 11-year and 22-year cycle. The maximal rotation rate of four-sector structure was observed during maximum of even cycles and minimal rate of the rotation was observed during maximum of odd cycles. Such a manifestation of the dependence of the speed of rotation of LSMF sources on solar activity can be explained by the effect of "skating rotation".

The rotation periods of the Sun source global field (28,0-28,5 days) were maximum at the middle of the 20th century in the period 1940÷1960 years. This maximum of solar activity corresponds to temporal gradient geomagnetic field dB_{IGRF}/dt =35-40 nT/year. For this reason, it is worth paying attention to the close connection of the temporal gradient of the geomagnetic field with the change in the gradient of LOD (correlation coefficient r=0.72), i.e. with the change in the rotation mode of the Earth (see Fig. 5). According to the (Orlyuk & Romenets, 2022), the twentieth cycle is the axis of a kind of symmetry with respect to changes in solar and geomagnetic activity, and length of day, namely, cycles 21, 22, 23 and 24 are almost a mirror image of cycles 19, 18, 17 and 16 of solar and geomagnetic activity. Therefore, it can be assumed that the 25th cycle should be similar to the 15th cycle.

Figure 5 shows the 15th cycle of solar activity as a dotted line, which in terms of morphology and intensity corresponds to the solar activity of the 25th cycle.

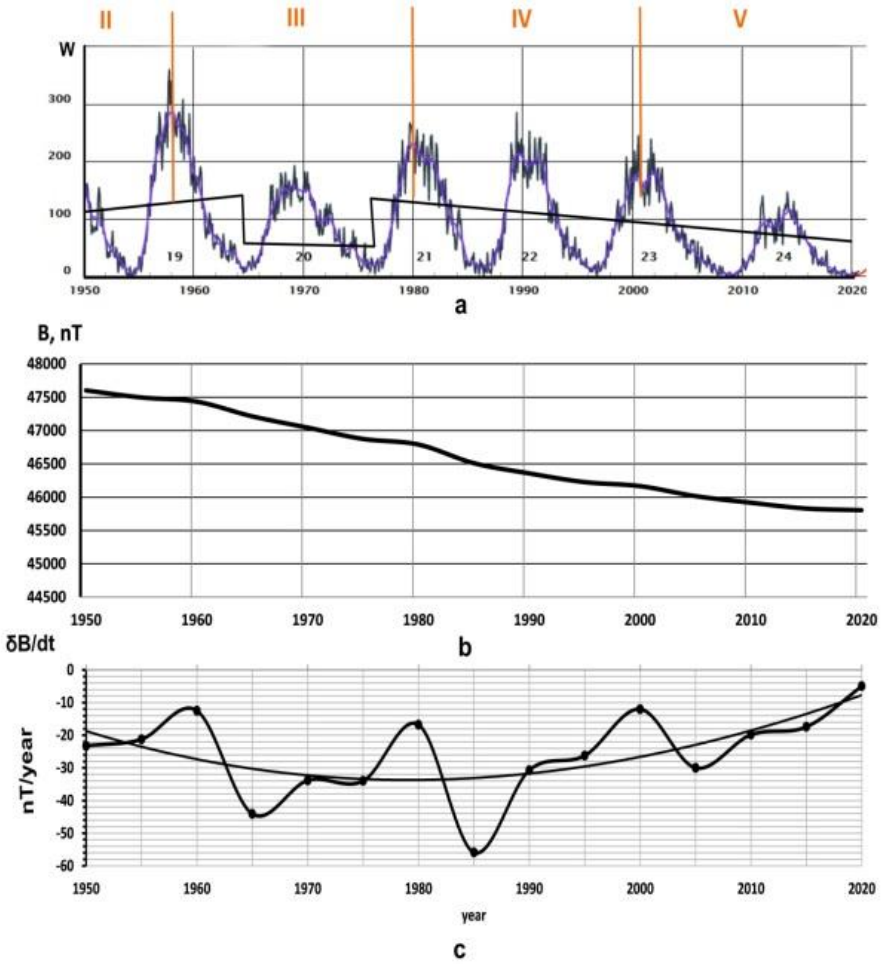

Figure 4: Comparison of 19-24 cycles of solar activity (a) with changes in the average values of the geomagnetic field (b) on the Earth's surface and its time gradient (c) for the time interval 1950÷2020.

References

Bandić M., Verbanac G., Živković S.: 2023, *Sci. Rep.*, Received: 20 January, Accepted: 5 June 2023. www.nature.com/scientificreports.

DGRF/IGRF Geomagnetic Field Model 1945-2025 (IGRF-13) https://ccmc.gsfc.nasa.gov/modelweb/models/igrf_vitmo.php

Fisk L.A.: 2001, *Journal of geophysical research*, **106**, no. a8, pages 15, 849-15, 857, August 1.

Georgieva K., Kirov B., Nagovitsyn Yu.A.: 2022, *Proc. of the Fourteenth Workshop "Solar Influences on the Magnetosphere, Ionosphere and Atmosphere"*. https://doi.org/10.1098/rspa.2016.0404.

Leiko U.M.: 2005, *Kinem i Fiz. Neb. Tel*, **21**, 187.

Lesur V., Gillet N., Hammer M. D., Mandea M.: 2022, *Surveys in Geophysics*, **43**, 41. https://doi.org/10.1007/s10712-021-09662-4

Matsakis D., McCarthy D.: 2023, Will We Have a Negative Leap Second? //Inside GNSS.

Obridko V.N., Pipin V.V., Sokoloff D., Shibalova A.S.: 2021, *MNRAS*, **504**, Iss. 4, https://doi.org/10.1093/mnras/stab1062.

Orlyuk M.I., Romenets A.A.: 2020, *Geofizicheskiy Zhurnal*, **42**, № 4, 18. DOI: https://doi.org/10.24028/gzh.0203-3100.v42i4.2020.210670

Orlyuk M.I., Romenets A.O.: 2022, *Dopov. Nac. akad. nauk Ukr.*, №1. ISSN 1025-6415. https://doi.org/10.15407/dopovidi2022.01.072.

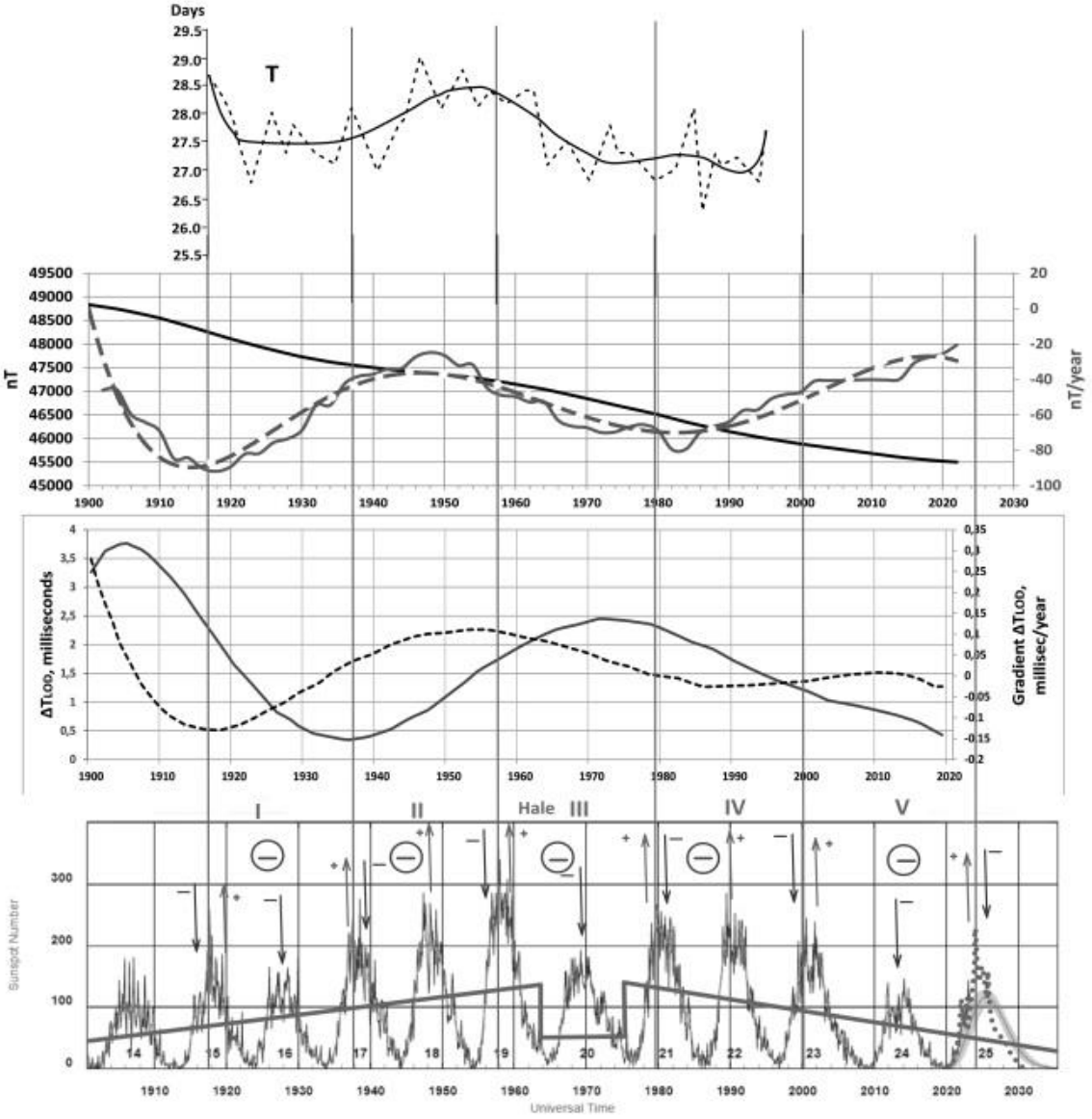

Figure 5: Dynamics of the large-scale field of the Sun and the Earth's magnetic field in connection with their rotation mode and solar activity.

Orlyuk M.I., Romenets A.A.: 2023, in *Book Abstracts 15-th Workshop "Solar Influences on the Magnetosphere, Ionosphere and Atmosphere", Primorsko, Bulgaria*, June 05-09, 30.

Solar Cycle progression https://www.swpc.noaa.gov/products/solar-cycle-progression

Sukharev A, Orlyuk M., Ryabov M., Sobitniak L., Bezrukovs V., Panishko S., Romenets A.: 2022, *Astron. & Astrophys. Trans.*, **33**, No. 1, https://doi.org/10.17184/eac.6481

Du Z. L.: 2011, *Ann. Geophys.*, **29**, 1341.

Sumaruk T.P., Sumaruk P.V.: 2020, *Geofizicheskiy Zhurnal*, **42**, No 5, 183. https://doi.org/10.24028/gzh.0203-3100.v42i5.2020.215081

https://doi.org/10.18524/1810-4215.2023.36.290217

SPECTRAL STUDY LOWER SOLAR ATMOSPHERE OF THE ACTIVE REGION SITE WITH THE ELLERMAN BOMB AND ACCOMPANYING Hα-EJECTIONS

M. N. Pasechnik

Main Astronomical Observatory, NASU, Kyiv, Ukraine, *rita@mao.kiev.ua*

ABSTRACT. The results of studying in details the features formation and development of the Ellerman bomb (EB) and accompanying Hα-ejections arose on the NOAA 11024 active region site, are presented. This site was in the region of emerging new magnetic flux. Spectral data with high spatial and temporal resolution were obtained with the French–Italian solar telescope THEMIS on July 4, 2009. Spectra with the Hα line and with the spectral region λλ ≈ 630 nm were used. Stokes I profiles were obtained with an interval corresponding to 160 km on the Sun surface.

The Hα line profiles obtained for different periods of EB development were asymmetric with an excess of emission in the short-wavelength wing. The temporal variations of intensity in the Hα line wings at distances ±0.1 and ±0.16 nm from its center indicated that two periods can be distinguished in EB evolution: the preheating phase and the flaring phase, during which the gradual and pulse energy release occurred.

Hα-ejections (surges) are small-scale eruptions of cold matter in the solar atmosphere. In all spectra they were visible in the absorption. The surge profiles were projected onto the blue or red Hα line wing. Its Doppler shifts were used to calculate the line-of-sight velocities (Vlos) of chromospheric matter in surges. The velocity distribution in the surges indicated their multi-flow structure. One of the surges showed signs of plasma vortex motions. Most surges occurred with a high velocity – Vlos up reached -110 km/s, and down to 90 km/s.

We obtained temporal Vlos variations in a wide interval (140 ─ 490 km) of photospheric heights for the area of EB development and its immediate surroundings. At all photospheric levels predominantly upward motions were found. In the central part of the EB in the upper layer of the photosphere the Vlos varied between -0.5 ÷ 0.2 km/s, in the lower layer – -1.1 ÷ -0.1 km/s. An increase the core intensity of all photospheric lines was correlated in time with an increase of the emission intensity in the Hα line wings.

The new observational data for the Ellerman bomb and accompanying Hα-ejections, which have been obtained and analyzed, can be used to verify existing and create new theoretical models.

Keywords: Sun, chromosphere, photosphere, Ellerman bomb, surges, line-of-sight velocities.

АНОТАЦІЯ. Представлено результати детального вивчення особливостей формування та розвитку бомби Еллермана та супутніх їй Hα-викидів, що виникли на ділянці активної області NOAA 11024. Ця ділянка знаходилася в області появи нового магнітного потоку. Спектральні дані з високою просторовою і часовою роздільною здатністю було отримано на французько-італійському сонячному телескопі THEMIS 4 липня 2009 року. Ми використали спектри з Hα-лінією (центральна частина) та з спектральною областю λλ ≈ 630 нм. Профілі Стокса I було отримано з інтервалом, що відповідає 160 км на поверхні Сонця.

Профілі лінії Hα, отримані для різних періодів розвитку БЕ, були асиметричними з надлишком емісії в короткохвильовому крилі. Зміни інтенсивності в крилах лінії Hα на відстанях ±0,1 і ±0,16 нм від її центру вказували на те, що в еволюції БЕ можна виділити два періоди: фазу попереднього нагріву і спалахову фазу, під час яких відбувалося поступове та імпульсне виділення енергії.

Hα-викиди (сьоржі) це невеликі виверження холодної речовини в сонячній атмосфері. На всіх спектрах їх видно в поглинанні. Профілі сьоржей проектувалися на синє або червоне крило лінії Hα. Їх доплерівські зсуви було використано для розрахунку променевої швидкості ($V_{пром}$) хромосферної речовини в сьоржах. Розподіл швидкостей у сьоржах свідчить про їх багатопотокову структуру. Один зі сьоржів мав ознаки руху плазмового вихру. Більшість сьоржів з'являлися з великою швидкістю – Vlos вгору досягала -110 км/с, а донизу – до 90 км/с.

Ми отримали часові варіації $V_{пром}$ у широкому інтервалі (140 ─ 490 км) фотосферних висот для області розвитку БЕ та її околиці. На всіх рівнях фотосфери виявлено, переважно, висхідні рухи. У центральній частині БЕ у верхньому шарі фотосфери Vlos коливалася в межах -0,5 ÷ 0,2 км/с, у нижньому шарі – -1,1 ÷ -0,1 км/с. Збільшення інтенсивності в ядрах всіх фотосферних ліній корелювало в часі зі збільшенням інтенсивності емісії в крилах лінії Hα.

Нові дані спостережень для бомби Еллермана та супутніх їй Hα-викидів, які було отримано і проаналізовано, може бути використано для перевірки

існуючих і створення нових теоретичних моделей.

Ключові слова: Сонце, хромосфера, фотосфера, бомба Еллермана, сьоржі, променеві швидкості.

1. Introduction

Among the many manifestations of solar activity, such fine scale, short and impulsive events as Ellerman bombs and chromospheric ejections play an important role. They arise in the lower solar atmosphere as a result of magnetic reconnection processes during the interaction between the new emerging magnetic flux and the already existing magnetic field. Such small-scale magnetic reconnections can affect the energy balance of the solar chromosphere – they effectively help inject dense plasma into the upper atmosphere. EBs are often accompanied by small, short-term chromospheric surges (Fang et al., 2006). Since their dynamics is the movement of plasma along the force lines of the magnetic field, surges are useful for studying the structure of the magnetic field and its changes. Many articles emphasize the importance of detailed studies into the formation and development of individual chromospheric structures such as EBs and Hα-ejections based on observational data with high spatial and temporal resolution. Also, special attention should be paid to how these dynamic phenomena interact with each other (Nelson et al., 2013).

2. Observational material

Spectropolarimetric observations of the active region NOAA 11024 were carried out with the telescope THEMIS on Tenerife (Canary Islands) on 4 July 2009. Spectral data with high spatial (below 1 arcsec) and temporal (about 3 seconds) resolution were obtained. During observations from $9^h52^m35^s$ to $10^h11^m26^s$, 400 spectra were obtained. We used two spectral regions, containing the chromospheric line Hα (central part) and the photospheric lines FeI λ 630.15, 630.25, 630.35 nm, and the TiI λ 630.38 nm. Figure 1 presents Hα spectrum. The field of THEMIS vision is divided into three parts. The spectrum number and the time it was received are given. The position of the EB (two long emission bands in the Hα line wings), pore and surges (dark details) that existed on the site at that time are indicated. The site which we are investigating is marked L1, its length was 10 Mm. It was located in the region of the emerging a new magnetic flux in the form of a serpentine magnetic field (Valori et al., 2012). The AR site without active formations and located outside the region of the emerging magnetic flux is marked L2. The availability of this site spectrum gave us an opportunity to study the changes that took place in the solar atmosphere at the L1 site under the influence of the developing EB and chromospheric surges.

3. Ellerman bomb

3.1. Chromosphere

The spectra were used to obtain Stokes I profiles of Hα line with an interval corresponding to the distance of 160 km on the Sun's surface. Figure 2 shows the Hα line profiles for the EB central part with the maximum emission intensity increase in the blue wing up to 73% (profile 1) and in the red wing up to 35% (profile 2), which occurred at a distance of approximately ±0.16 nm from the line core. For comparison, profile 3 for section L2 is shown. The work (Pasechnik, 2021) detailed the features of the EB development during our observations. Figure 3 shows temporal variations of the emission intensity (EB light curves) in the short-wave (blue curve) and long-wave (red curve) Hα line wings at distances of ±0.16 nm from its center for the EB central part. The numbers indicate the moments of intensity peaks. Two periods can be distinguished from the obtained EB light curves. The first period, during which the intensity changed little, lasted approximately 8 min (9:57:05 – 10:05:21 UT). It consisted of three intensity peaks with a time interval of 1 min 45 sec. The second period of approximately 6 min (10:05:21 – 10:11:26 UT), during which EB brightness was increasing, consisted of five intensity peaks (interval ~1 min). The light curves of the studied EB obtained in this work show that we observed two phases of its evolution: the preheating phase and the flaring phase, during which the gradual and pulse energy releases occurred.

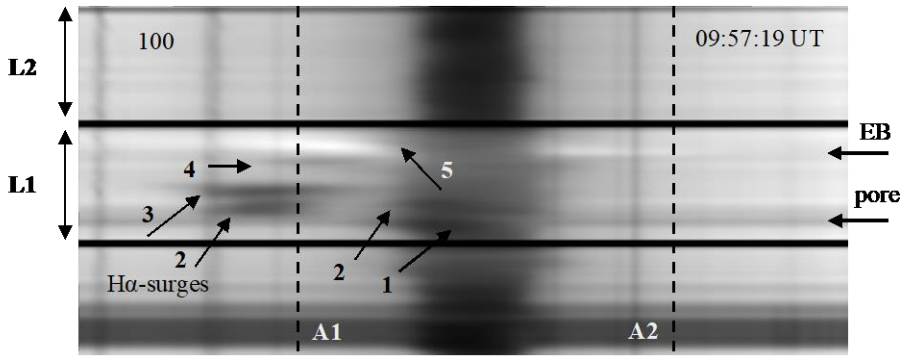

Figure 1: Hα-spectrum of the AR site. EB – Ellerman bomb. L1, L2 – see text. The numbers in the fig. correspond to the surge numbers. Vertical lines **A** are the photometric sections across spectra at the distances of ±0.16 nm from the line center.

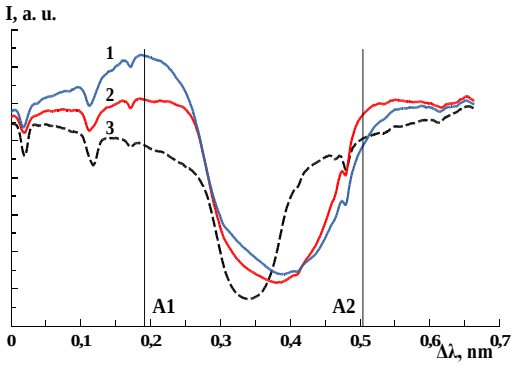

Figure 2: Profiles of the Hα line for EB region (1 and 2) and profile (3) for the AR site L2. **I** is given in arbitrary units.

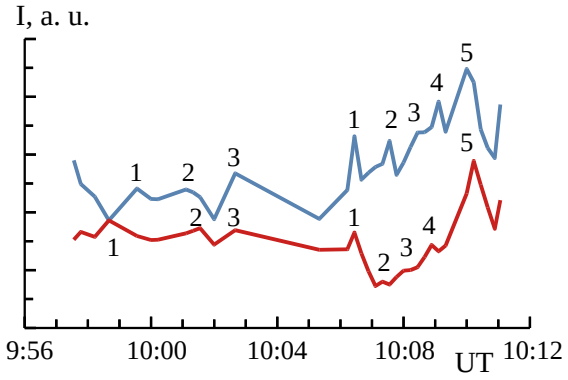

Figure 3: Temporal variations of the emission intensity (EB light curves) in the Hα line wings at the distances of ±0.16 nm from the line core, in the short-wave (blue line) and long-wave (red line) wings.

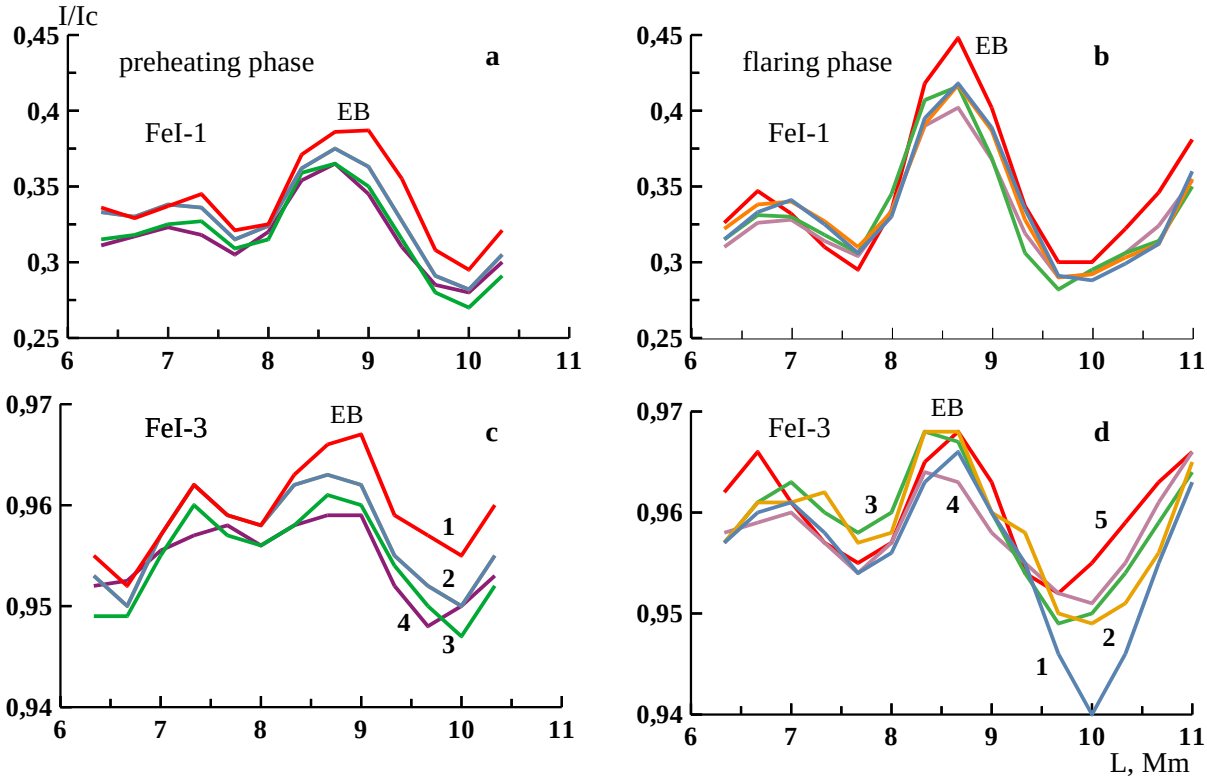

Figure 4: Variations of the photospheric line central intensities along the spectrograph slit at different observation moments: a, c – 9:57:05, 9:59:41, 10:01:06, 10:02:31 UT, curves 1-4, respectively; b, d – 10:06:31, 10:07:42, 10:08:25, 10:09:22, 10:10:32 UT, curves 1-5, respectively.

3.2. Photosphere

The spectral region of λλ≈ 630 nm was used to study the changes of physical conditions at different photospheric levels in the process of EB evolution. This region includes lines that are formed in a wide range of heights: two strong Fraunhofer lines FeI λ 630.15, 630.25 nm and two weak lines: FeI λ 630.35, TiI λ 630.38 nm, they are in the text designated – FeI-1, FeI-2, FeI-3 and TiI, respectively. The central intensities of the two first and two last lines should be formed in the upper and lower photospheric layers.

Figure 4 shows variations of the photospheric lines central intensities I/Ic along the spectrograph slit at different observation moments. The area where the EB was located is very different in the upper and lower photosphere of increased intensity. The greatest increase I/Ic (red curves)

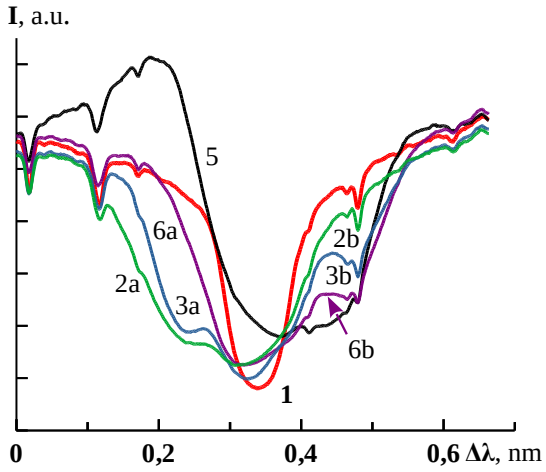

Figure 5: The Hα line profiles (2 -6) for AR site L1 for the observation moment of 10:07:42 UT and profile (1) for the AR site L2. The numbers correspond to the surge numbers.

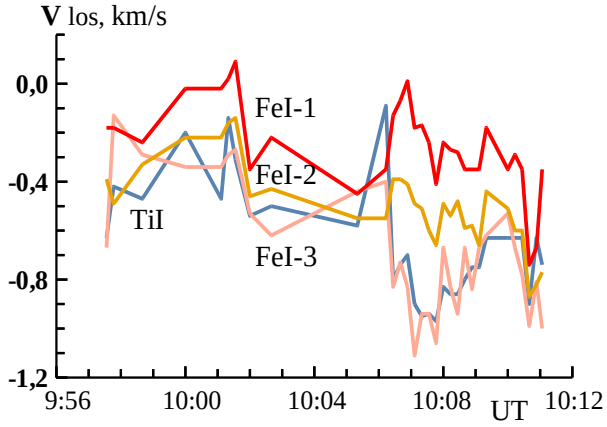

Figure 6: Temporal variations of the line-of-sight velocities matter in the EB central part in the upper (FeI-1 and FeI-2 lines) and in the lower (TiI and FeI-3 lines) photospheric layers. Negative velocity values correspond to motions directed toward the observer.

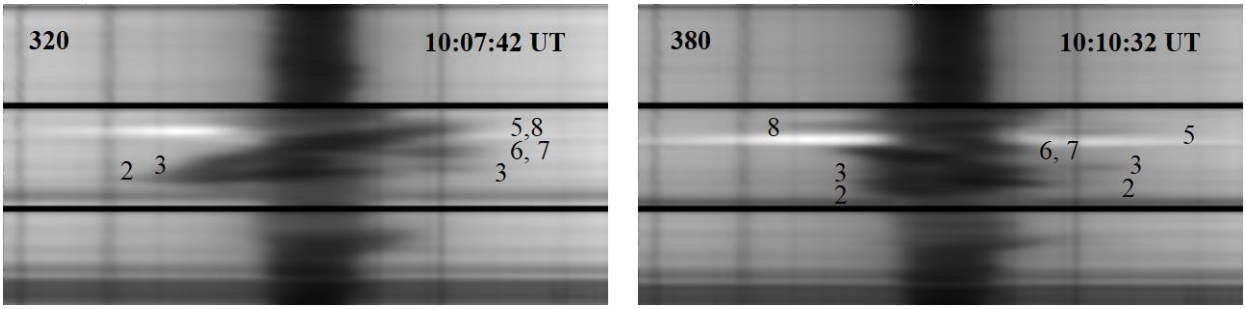

Figure 7: Hα-spectra of the AR site. The numbers correspond to the surge numbers.

occurred simultaneously at all photospheric levels. Horizontal movement of matter took place near the EB area (panel d). Figure 5 shows that an increase the central intensity of all the studied photospheric lines was correlated in time with an increase of the emission intensity in the Hα line wings (Fig. 3).

We obtained temporal Vlos variations in a wide interval (140 ─ 490 km) of photospheric heights for the area of EB development and its vicinity. At all photospheric levels predominantly upward motions were found (Fig. 6). At the same time, a noticeable decrease of the Vlos magnitudes was observed at the EB location. In the central part of the EB in the upper layer of the photosphere the Vlos varied between -0.5 ÷ 0.2 km/s, in the lower layer – -1.1 ÷ -0.1 km/s. A similar Vlos distribution in the photosphere was obtained in (Pasechnik, 2019). Perhaps it is characteristic of EBs formed in the emerging magnetic flux region. The largest changes of Vlos occurred during the Hα-ejection formation near the EB and which had signs of plasma vortex motions. At that time, downward matter flows with Vlos of 0.2 km/s were observed in the upper photosphere.

4. Hα-ejections

The features of the formation and development of all Hα surges that existed in the AR site during our observations were investigated. Figure 1 shows the spectrum was obtained at the beginning of the observations. Surges 1 and 2 occurred on different sides near the pore, surges 4 and 5 – near and above the EB area development and surge 3 – in the middle part of the site. Surges 1, 3 and 5 consisted of one jet. Surges 2 and 4 consisted of two jets – dark details are visible in the blue wing and in the Hα line core. Figure 8 shows the shape of the Hα line profiles obtained for the places of maximum intensity of various surges on the 320 spectrum (Fig. 7). Depending on whether the upflows or downflows was observed in the serge, the serge profile was projected onto the blue (profiles 2a, 3a) or red (profiles 3b, 6b) Hα line wing. If the surge profile was projected onto the line core, there was Hα profile distortion and a shift of its central part to the red or blue side (profile 2b, 6a, 5). Doppler shifts of these components were used to calculate the chromospheric matter Vlos in surges. The Vlos values in the L2 section did not exceed ±2 km/s. Changes in Vlos

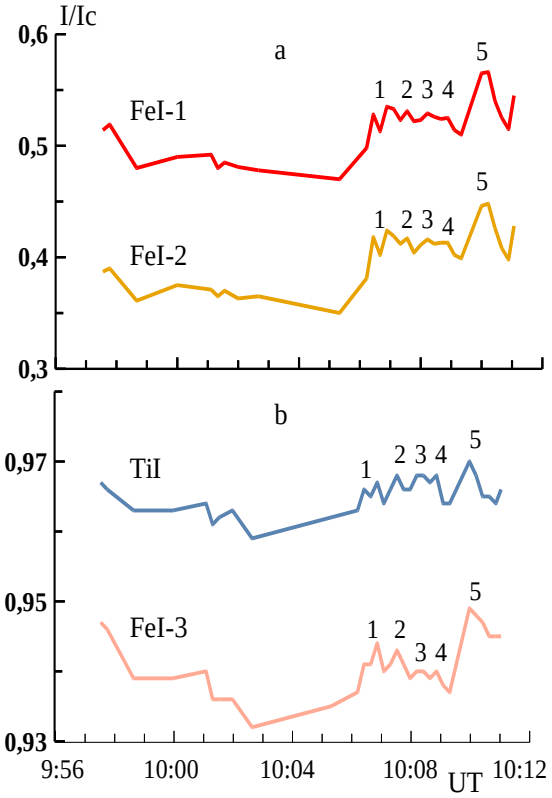

Figure 8: Temporal variations of the Fraunhofer lines central intensity, which are formed in the upper (a) and lowers (b) layers of the photosphere for the EB central part.

of the chromospheric matter along the cross section at the surges maximum intensity site were determined. Figure 9 shows changes in the matter movement along a cross section in one of the surges. It can be seen that this surge was very structured. Most of the velocities change curves consisted of several segments. This means that the serge consisted of several smaller jets, that is, it had a multi-flow structure. The evolution of the serge looks like this: the serge appears with a high upward movement velocity up to -90 – -100 km/s, over time the it decreases, but not uniformly, sometimes accelerating, then slowing down, surge reaches a certain height or the top of the magnetic loop and under the force gravity action returns along the same trajectory or along the second part of the loop. The 380 spectrum was obtained during the 5th highest intensity peak in the EB light curve (Fig. 7). The Hα line is very fibrous. Surges are visible in both line wings. The Hα line central part was completely covered by dark details, a system of arc-shaped Hα-ejections, the so-called Arch Filament System, was formed, under which the EB developed.

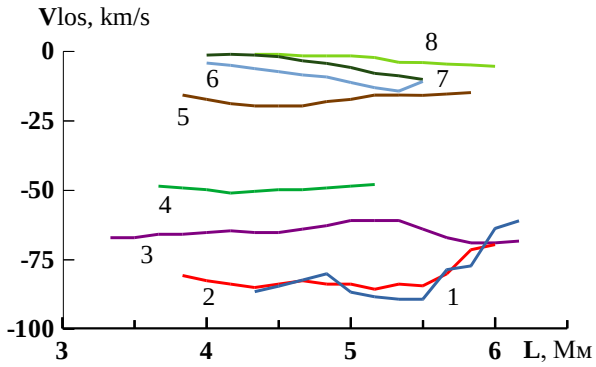

Figure 9: Changes in Vlos along the cross-section of surge 3 at different moments of observation: 9:57:05, 9:57:19, 9:57:46, 9:58:16, 9:59:12, 10:01:06, 10:01:20, 10:02:31 UT - curves 1-8, respectively.

5. Conclusion

We obtained and analyzed new observational data for the Ellerman bomb and accompanying Hα-ejections: for the EB preheating phase; changes in chromospheric matter Vlos along the cross section of the serges; followed the formation so-called Arch Filament System and studied the changes that occurred at the photospheric different levels under the influence EB.

The features of the change in the Hα line wings intensity as well as the chromospheric and photospheric matter Vlos indicate that the EB and accompanying Hα-ejections, which arose and developed in the AR site under investigation, were the result of magnetic reconnections caused by the emergence of a new serpentine magnetic flux and its interaction with a pre-existing magnetic field or between the magnetic loops of the flux itself.

Acknowledgements. Very grateful to E.V. Khomenko and R.I. Kostyk for providing us with the data of the THEMIS observations and the codes for their processing.

References

Fang C., Tang Y. H., Xu Z., et al.: 2006, *Astrophys. J.*, **643**, 1325.
Nelson C. J., Doyle J. G., Erdelyi R., et al.: 2013, *Solar. Phys.*, **283**, 307.
Pasechnik M.N.: 2019, *Kinem. Phys. Cel. Bod.*, **35**, 55.
Pasechnik M.N.: 2021, *Kinem. Phys. Cel. Bod.*, **37**, 3.
Valori G., Green L. M., Demouli P., et al.: 2012, *Solar. Phys.*, **278**, 73.

https://doi.org/10.18524/1810-4215.2023.36.290585

COMPARATIVE ANALYSIS OF MAGNETIC STORMS IN THE ODESSA MAGNETIC ANOMALY REGION WITH PLANETARY AND IONOSPHERIC STORMS DURING THE MONITORING PROGRAM AT RT "URAN-4" (1987 – 2010)

L.I. Sobitnyak[1], M.I. Ryabov[1], M.I. Orlyuk[2], A.L. Sukharev[1], D.M. Ryabov[3], A. Romenets[2], Yu. Sumaruk[2]

[1] Odesa observatory «URAN-4» of the Radio Astronomical Institute of the NAS of Ukraine

[2] Institute of Geophysics by S.I. Subbotin name of the NAS of Ukraine, Kyiv, Ukraine

[3] State University of Intelligent Technologies and Telecommunications, Odesa, Ukraine

ABSTRACT. This work is a continuation of the study of the response of the Odesa geomagnetic anomaly to the manifestations of solar and planetary geomagnetic activity. Not far from the territory of this magnetic anomaly there is the geomagnetic observatory "Odesa" and the decameter radio telescope "URAN-4" of the RI NASU. A catalogue of magnetic storms for the period 1987-1994 and 2000-2009 was compiled for the monitoring program of high-power space radio sources at RT "URAN-4" using the database of the geomagnetic observatory "Odesa". In this paper, a comparative analysis of the features of the manifestations of geomagnetic storms in the zone of the Odesa magnetic anomaly, planetary storms and ionospheric storms in the 22nd and 23rd cycles of solar activity is carried out. The main results are as follows. The magnetic anomaly amplifies the effects of regional manifestations of planetary magnetic storms. The number of different types of magnetic storms and the dynamics of their changes in the Odesa anomaly differ significantly in the 22nd and 23rd cycles of solar activity. Comparisons have shown that the duration of magnetic storms in the Odessa anomaly is longer than the duration of planetary magnetic and ionospheric storms. According to the data of the «URAN-4» radio telescope, geomagnetic storms form various manifestations of the effects of ionospheric flickers and flux changes for space radio sources depending on the time of their observations. For the region of the Odesa geomagnetic anomaly, such comprehensive studies have not been carried out before. The conducted studies will become an important basis for understanding the influence of magnetic anomalies on the dynamics of the ionosphere during periods of solar and geomagnetic activity.

Keywords: geomagnetic anomaly, geomagnetic storms, solar activity, low-frequency radio astronomy, space weather.

АНОТАЦІЯ. Дана робота є продовженням дослідження реакції Одеської геомагнітної аномалії на прояви сонячної та планетарної геомагнітної активності. Недалеко від території цієї магнітної аномалії знаходяться геомагнітна обсерваторія «Одеса» та декаметровий радіотелескоп «УРАН-4» РІ НАНУ. Для програми моніторингу потужних космічних радіоджерел на РТ "УРАН-4" з використанням бази даних геомагнітної обсерваторії "Одеса" складено каталог магнітних бур за період 1987-1994 та 2000-2009 років. У роботі проведено порівняльний аналіз особливостей проявів геомагнітних бур в зоні Одеської магнітної аномалії, планетарних та іоносферних бур у 22-му та 23-му циклах сонячної активності. Основні результати такі. Магнітна аномалія підсилює наслідки регіональних проявів планетарних магнітних бур. Кількість різних типів магнітних бур та динаміка їх зміни в Одеській аномалії суттєво відрізняються у 22-му та 23-му циклах сонячної активності. Порівняння показали, що тривалість магнітних бур в Одеській аномалії перевищує тривалість планетарних магнітних та іоносферних бур. За даними радіотелескопа «УРАН-4», геомагнітні бурі формують різні прояви ефектів іоносфери. мерехтіння та зміни потоку космічних радіоджерел залежно від часу їх спостережень. Для району Одеської геомагнітної аномалії такі комплексні дослідження раніше не проводились. Проведені дослідження стануть важливою основою для розуміння впливу магнітних аномалій на динаміку іоносфери в періоди сонячної та геомагнітної активності.

Ключові слова: геомагнітна аномалія, геомагнітні бурі, сонячна активність, низькочастотна радіоастрономія, космічна погода.

1. Introduction

The data of the geomagnetic field disturbance records in the area of the Odesa magnetic anomaly during the monitoring of the fluxes powerful space radio sources at the RT "Uran-4" from 1987-1994 and 2000-2009 were used.

Changes in the fluxes of space radio sources in the decameter range and their flickering depend on the state of the ionosphere and correlate with geomagnetic disturbances. On geomagnetic observatory "Odesa"

Institute of Geophysics NAS Ukraine since 1948 measurements of a magnetic field of Earth. Until 2009, recordings of geomagnetic field disturbances were carried out in analog mode with subsequent processing and calculation of hourly K indices.

At the same time measurements of K-index and three elements of a magnetic field (horizontal component (H), vertical component (Z) and inducement (D)) are registered. Basis of these data the catalog of magnetic storms in the 22nd and 23rd cycles of solar activity was compiled. The catalog magnetic storms for period monitoring program on RT "URAN-4" IRA NASU (1987-1994 and 2000-2009) indicates the date and time of the beginning and end of the storm, the duration of the storm, the amplitude for three elements of the magnetic field: H, Z, D, the characteristics of magnetic storms with indication of active periods. In this edition of the catalog, sum of hourly daily values measurements of the K-index have been added.

The magnetic station "Odesa" is located near a zone of a magnetic anomaly. On the other hand, Odesa magnetic anomaly located radio telescope "URAN-4" RI NANU. To identify changes in geomagnetic activity due to the presence of a magnetic anomaly, a comparative analysis of the catalogs of magnetic storms was carried out. The catalog of magnetic storms for the magnetic anomaly zone was compared with the catalogs of planetary magnetic and ionospheric storms.

From the beginning of observations in 1987 year at a radio telescope "URAN-4" the fluxes monitoring of high-power galactic and extragalactic radio sources is carried out. A comparative analysis of the catalogs is carried out in order to reveal the contribution of geomagnetic activity to the change in the flux of radio sources.

2. Geomagnetic observatory «Odesa»

The geomagnetic observatory «Odesa» was founded by the Novorossiysk Imperial University, in the territory of a Botanical Garden, at the beginning of the XX century. It was officially commissioned in 1896. In 1936 it was transferred to the village of Stepanivka (near Odesa) by the Odesa State University. World War 2th the station became to belong to the Institute of Geophysics NAS Ukraine. From 1948 to 2010, analog measurements of the Earth's magnetic field were conducted at the «Odesa» magnetic observatory (Guglia et al., 2018). The magnetometers are located in a deep underground room, which makes it one of the best in Ukraine in terms of noise immunity, and the large distance from *Odesa* (36 km) excludes the contribution of technogenics noise to the measurements of the geomagnetic field induction. At the same time measurements of three elements of a magnetic field are registered: horizontal component (H), vertical component (Z) and declination (D). The recorded data on magnetic storms were presented in tabular form (Fig. 1).

3. Magnetic anomaly zone

The magnetic observatory "Odesa" is situated near the intensive magnetic anomaly. Since the dome of the geomagnetic field extends to an altitude of about 90 km, into the ionosphere layer, where the variation (rapidly

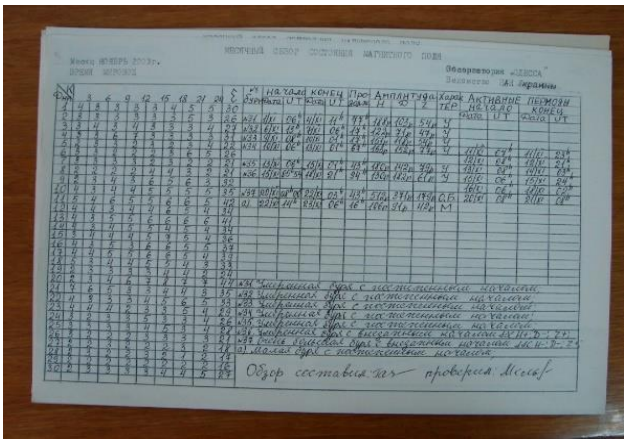

Figure 1: An example of the data table of the geomagnetic observatory "Odesa"

variable) component of the geomagnetic field is formed, regional magnetic anomalies can affect the manifestation of the variability of the geomagnetic field. When processing long-term, long-term observational data, the influence of the magnetic anomaly on the geomagnetic activity of the Earth was revealed (Maksymchuk & Orlyuk, 2018; Ryabov et al., 2019; Sukharev et al., 2018; Orlyuk et al., 2015).

The map of the distribution of the anomalous geomagnetic field over the territory of Ukraine (Orlyuk et al., 2018) is shown in Figure 2. The identification of the magnetic anomaly influence on geomagnetic activity comparison of characteristics of magnetic storms at according to the magnetic observatories "Odesa", planetary magnetic storms and ionospheric storms.

3.1. Electronic catalog of magnetic storms

On the basis of data of magnetic observatory «Odesa» the catalog the magnetic storms is made (Sobitnyak et al., 2018). This issue of the catalog for 1987-1995 and 2000-2009 years include: date and time of the beginning and end of a storm, the storm duration, and amplitude on three elements of a magnetic field are specified: H, Z, D, the characteristic of magnetic storms with the indication of the fissile periods (Orlyuk et al., 2009).

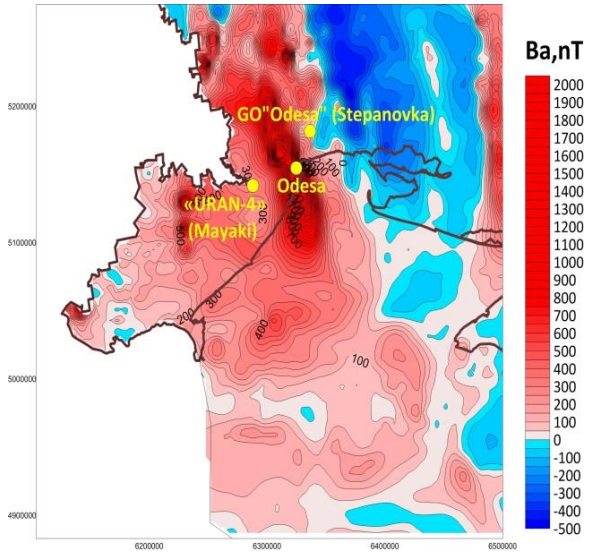

Figure 2: Map of the Odesa Magnetic Anomaly Zone

Figure 3: Radio telescope «URAN-4» IRA NASU

The catalog was compiled to identify the reasons for the change in the level of the flux of space radio sources, according to observations at the «URAN-4» radio telescope at the Odesa Observatory of the Radio Astronomy Institute of the National Academy of Sciences of Ukraine (Figure 3), which have been carried out since 1987.

Data on changes in the fluxes of powerful radio sources during periods of extreme states of solar activity are presented in (Sobitnyak et al., 2017). In paper Sobitnyak et al. (2017) also presents the results of calculating multiple correlation analysis models, which demonstrates the dependence of changes in the radio sources fluxes on the main indicators characterizing the state of space weather.

The total number of minor, moderate, strong and extreme storms shown Figure 4 (Period 22 solar cycle) and Figure 5 (period of 23 solar cycle).

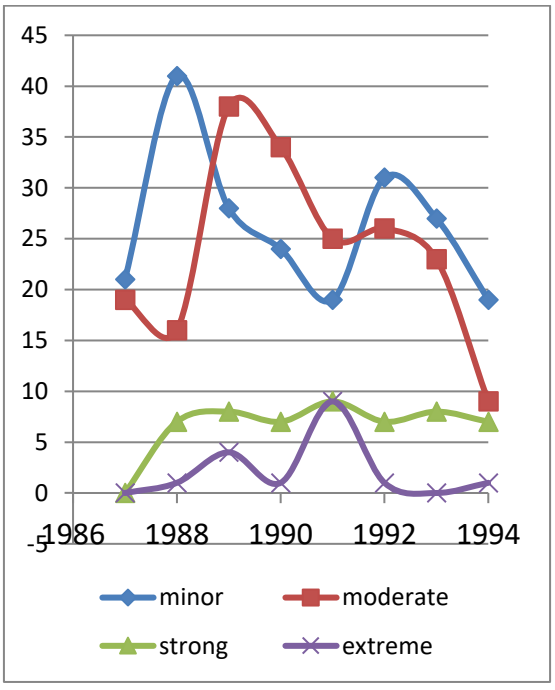

Figure 4: The number of magnetic storms in the Odesa magnetic anomaly in the 22nd cycle of solar activity.

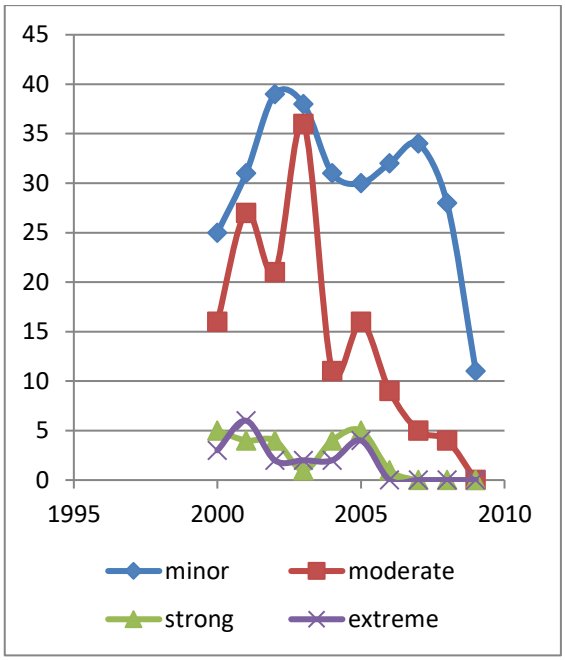

Figure 5: The number of magnetic storms in the Odesa magnetic anomaly in the 23nd cycle of solar activity

It is interesting that the maximum number of different types of magnetic storms in the zone of the Odesa magnetic anomaly falls on different phases of the solar cycle. Moreover, these trends differ in the 22nd and 23rd solar cycles.

Thus, in the 22-nd cycle, the number of minor magnetic storms shows a maximum in the growth phase of the cycle in 1988 (41 storms) and in the decline phase of the cycle in 1992 (31 storms). Moderate magnetic storms show a maximum number of them (38 storms) in the year of the maximum of the cycle in 1989 and a consistently high level of their number (23 – 26 storms) during the decline of the solar cycle in 1991-1993. Strong magnetic storms in cycle 22 are characterized by changes in their number in the range from 7 to 9 during the growth phase to the maximum and the phase of decline. The maximum number of extreme magnetic storms in cycle 22 was recorded during the maximum of the cycle in 1991 (9 storms).

The 23rd solar cycle is characterized by other trends in the distribution of the annual number of different types of magnetic storms. Thus, for minor magnetic storms, the maximum number of magnetic storms was observed during the maximum cycle in 2002 (39 storms) and the recession phase in 2003 (38 storms). The additional period of maximum number of minor magnetic storms was in the phase of the cycle decline in 2007 (34 storms). At the same time, the period with an annual number of storms of more than 30 (from 2001 to 2008) was quite long.

The number of moderate magnetic storms in cycle 23 is characterized by the presence of three maxima: in 2001 (27 storms), 2003 (36 storms), 2005 (16 storms). Strong magnetic storms were most severe during the maximum of the cycle in 2000-2022 (4-5 storms per year). The number of extreme magnetic storms peaked in 2001 (6 storms) and 2005 (4 storms).

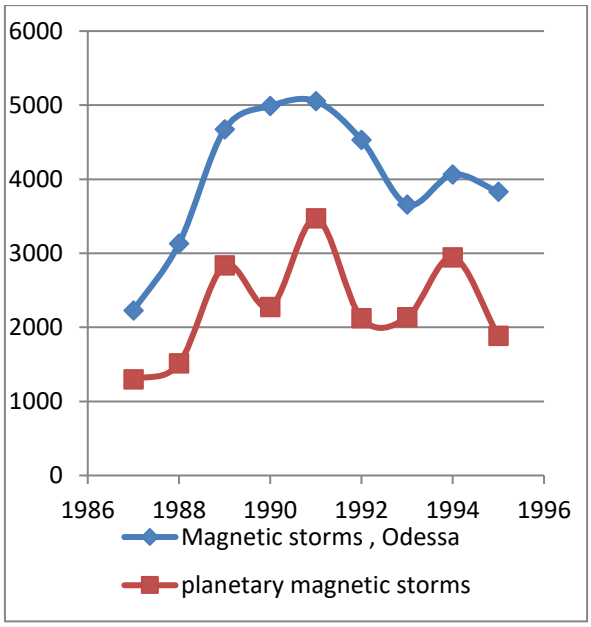

Figure 6: The total annual duration (in hours) of magnetic storms in the zone of the Odesa magnetic anomaly and planetary magnetic storms (22 cycles of solar activity).

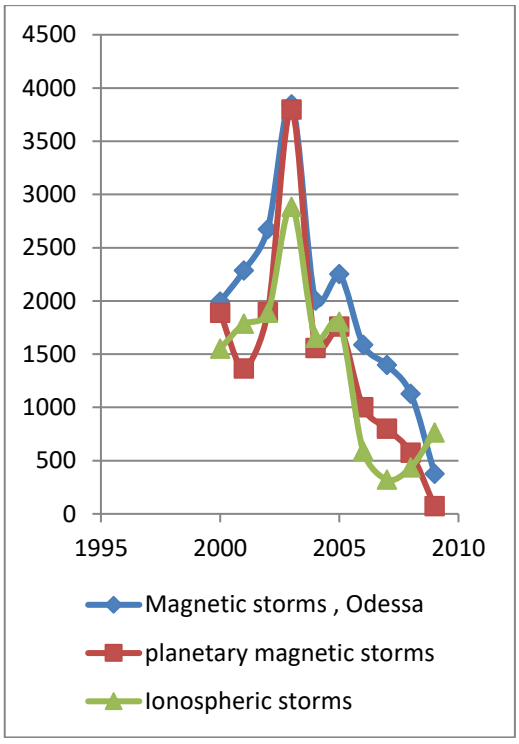

Figure 7: The total annual duration (in hours) of magnetic storms in the zone of the Odesa magnetic anomaly, planetary magnetic and ionosphere storms (22 cycles of solar activity)

3.2. Comparative analysis of the duration of magnetic storms in the zone of the Odesa magnetic anomaly with planetary magnetic storms

The peculiarities of the manifestation of magnetic storms in the Odesa magnetic anomaly are clearly manifested in the comparison of their total annual duration with similar data for planetary magnetic and ionospheric storms.

Figure 6 shows a comparison of these values for period 22-th of the solar cycle. Here, the total annual duration of magnetic storms in the zone of the Odesa magnetic anomaly significantly exceeds the duration of planetary magnetic storms. The maximum annual duration of magnetic storms in the Odesa magnetic anomaly is 5,000 hours (reached during the maximum of the 22nd solar cycle with a separate maximum at the phase of the cycle decline (1994 at the level of 4,000 hours). Planetary magnetic storms are characterized by the presence of three maxima in 1989 (3,000 hours), 1991 (3,500 hours) and the decline phase of the cycle in 1994 (3,000 hours).

Another trend appeared in the 23rd solar cycle (Fig. 7). Here, the maximum duration of magnetic storms in the Odesa magnetic anomaly, planetary storms (4,000 hours) was recorded at the phase of the cycle decline in 2003. The same trend is characteristic of ionospheric storms (lasting about 3,000 hours). The secondary maximum for all storms also occurred during the decline phase of the cycle in 2005.

In the period from 2017 to 2023, the magnetometer of the Institute of Geophysics of NASU measured the dynamics of geomagnetic storms and disturbances in the center of the Odesa magnetic anomaly (territory of the Astronomical Observatory of Odesa I.I. Mechnikov National University) and in the location of the radio telescope "URAN-4" of IRA NASU.

The magnetic anomaly is strong enough for the dome of the anomalous field to be detected at a high altitude, about 100-150 kilometers according to high-precision satellite observations. Thus, it can affect the formation of ionospheric inhomogeneities, acoustic and "gravitational" ionospheric waves. The analysis of long-term data showed that even the classic solar-diurnal fluctuations of the geomagnetic field in the Odesa region differ from those in other regions, GO «Kyiv» (Dymer vill., Kyiv reg.) and GO «Lviv» (Yavoriv vill., Lviv reg.). The Odesa geomagnetic anomaly appears to be the only regional anomaly where the URAN-4 low-frequency telescope and the GO «Odesa» (Stepanivka vill., Odesa reg.) are located. Already the first works on the analysis of long-term data of geomagnetic variations showed that in the Odesa region the structure and manifestation of fast geomagnetic variations with periods of 1-2 minutes and 30-5 seconds are much different from the Lviv and Kyiv regions. For example, in the Odesa region, there are much more manifestations of quasi-periodic geomagnetic variations with periods of 1 minute - 30 seconds during geomagnetic storms. Also, the manifestation of geomagnetic pulsations of the Pc3 and Pc4 type during extreme magnetic storms is much clearer in measurements in Odesa than in other Ukrainian geomagnetic measurement points.

The range of periods of geomagnetic pulsations of the Pc5 type is from 150 to 600 seconds. They are usually caused by magnetospheric currents associated with magnetic storms. Pc5 type pulsations are the strongest and longest of regular geomagnetic pulsations. Pc5 pulsations effectively transfer solar wind energy into the magnetosphere and further into the ionosphere. During the

powerful geomagnetic storms of 2022-2023, according to the data of the LEMI-008 magnetometer, which was installed at the Odesa Astronomical Observatory, the structure of frequency-time changes of Pc5-type pulsations, which have a range of periods from 150 to 600 seconds, and their amplitude of tens nanotesla, were studied. They are commonly observed during magnetic storms, when streams of solar wind and charged particles reach Earth's magnetosphere. Pulsations of the Pc5 type arise as a result of the interaction of these flows with the Earth's magnetosphere, which leads to the formation of electric currents. These currents, in turn, cause disturbances in the geomagnetic field. This is a fairly new work, and previously, there were no such detailed studies of the dynamics of fast geomagnetic variations and the features of their manifestation in geomagnetic storms of different types and strengths for the Odesa geomagnetic anomaly. In addition, dozens of manifestations of unusual wave activity were investigated in the range of periods from 3 hours to 1 hour, which appeared in the form of long-lived quasi-periods with a change in the value of the period and amplitude within 1-2 days (Sukharev et al., 2022; Sobitnyak et al., 2014).

4. Conclusion

1. On the base of data of geomagnetic observatory «Odesa» the catalog the magnetic storms is made. This issue of the catalog for 1987- 1995 and 2000-2009 years include: date and time of the beginning and end of a storm, the storm duration, amplitude on three elements of a magnetic field are specified: H, Z, D, the characteristic of magnetic storms. In the latest edition, the catalog has been supplemented with data on the daily total values of the K- index.

2. The comparison duration of magnetic storms according to the geomagnetic observatory "Odesa" is longer than at planetary magnetic and ionosphere storms in period 22 and 23 solar cycles.

3. The dynamics of the data on the number of types of magnetic storms in the zone of the Odesa magnetic anomaly in cycles 22 and 23 differs significantly.

4. Thus, the Odesa magnetic anomaly significantly intensifies the ionospheric effects of solar and geomagnetic activity.

5. It is planned to create a catalog of magnetic storms according to the Odesa station for the entire monitoring period of space radio sources at the RT «URAN-4» in order to identify manifestations of geomagnetic disturbances during radio astronomical observations and their contribution to changes in radio source fluxes on decameter waves.

6. These studies will be supplemented by a comparative analysis of the characteristics of magnetic storms in the magnetic anomaly zone (Odesa) with data from other magnetic observatories.

References

Guglia L.I., Orlyuk M.I., Ryabov M. I., Suharev A.L., Orliuk I.M.: 2013, *Odessa Astron. Publ*., **26**, No. **2**, 263.

Maksymchuk V., Orlyuk M.: 2018, *COBS Journa*l (Special Issue: IAGA Workshop 2018), No. **5**, 49.

Orliuk M., Sumaruk Yu., Sumaruk T., Romenets A., Melnychuk I.: 2009, in *Proc. of the IAGA11th Scientific Assembly in Sopron*, Hungary.

Orlyuk M. I., Romenets A., Marchenko A., Orliuk I. M., Ivashchenko I.: 2015, *Geofizicheskiy Zhurnal*, **37**, No. **2**, 73. DOI: https://doi.org/10.24028/gzh.0203-3100.v37i2.2015.111307.

Orlyuk M., Marchenko A., Romenets A., Bakarjieva M.: 2018, *COBS Journal* (Special Issue: IAGA Workshop 2018), No. **5**, 40.

Ryabov M.I., Sukharev A.L., Orlyuk M.I., Sobitnyak L.I., Romenets A.A.: 2019, *Radio Phys. Radio Astron.,* **24**, No. **1**, 68. DOI: https://doi.org/10.15407/rpra24.01.068.

Sobitnyak L.I., Ryabov M.I., Sukharev A.L., Orlyuk M.I., Orliuk I.M., Romenets A.A.: 2014, *Odessa Astron. Publ*., **27**, Iss. 1, 101.

Sobitniak L.I., Ryabov M.I., Sukharev A.L., Panishko S.K.: 2017, *Radio Phys. Radio Astron*., **22**. No. 4, 294. DOI: https://doi.org/10.15407/rpra22.04.294

Sobitnyak L.I., Ryabov M.I., Sukharev A.L., Orlyuk M.I., Romenets A.O., Sumaruk Yu.P.: 2018, *Odessa Astron. Publ*., **31**, 163. DOI: https://doi.org/10.18524/1810-4215.2018.31.146662.

Sukharev A.L., Orlyuk M., Ryabov M.I., Romenets A.A.: 2018, Radio phys. radio astron., **23**. No. **2**, 116. DOI: https://doi.org/10.15407/rpra23.02.116.

Sukharev A., Orlyuk M., Ryabov M., Sobitniak L., Bezrukovs V., Panishko S., Romenets A.: 2022, Astron. & Astrophys. Trans., **33**, Iss. **1**, 67.

https://doi.org/10.18524/1810-4215.2023.36.288658

SOLAR AND GEOMAGNETIC ACTIVITY IN 19-25 CYCLES

T.P. Sumaruk [1], P.V. Sumaruk [1], A. Neska [2]

[1] Institute of Geophysics of the National Academy of Sciences of Ukraine, Kyiv, Ukraine, *taras.sumaruk@gmail.com*

[2] Institute of Geophysics, Polish Academy of Sciences, Warsaw, Poland, *anne@igf.edu.pl*

ABSRACT. The paper presents the results of the analysis of changes solar and geomagnetic activity in 19−25 Wolf cycles. A forecast of the maximum geomagnetic activity cycle 25 is made.

Solar activity is presented by sunspot number R_Z, geomagnetic activity is expressed by the energetic index calculated from the data of the "Lviv" and "Belsk" geomagnetic observatories. By annual averages R_Z values, the 11-year window was used to obtain the solar activity minimum (around 1711, 1810, 1901, and 2009). The minimum of 2009 was one of the smallest in the observed data, and we took it as the beginning of the 24th cycle and the 100-year solar activity cycle. The maximum of the 24th cycle occurred in 2014 for R_Z and in 2015 for energetic index.

Cycle 25 began in 2019 according to R_Z, and in 2020 according to energetic index. For cycles 19−25 solar activity is 1−2 years ahead of magnetic activity. The identified quasi-biennial variations over the studied period and the lag of geomagnetic activity from solar activity allow us to predict the magnitude of geomagnetic activity and its maximum in cycle 25.

According to our calculations, the maximum of geomagnetic activity will occur around 2026 and its magnitude will be 1.5−2 times higher than the maximum of the 24th cycle.

Key words: Solar and geomagnetic activity, solar cycle.

АНОТАЦІЯ. У роботі викладено результати аналізу змін сонячної та геомагнітної активності у 19−25 циклах Вольфа. Зроблено прогноз максимуму геомагнітної активності у 25 циклі.

Сонячну активність виражено сонячними числами R_Z, геомагнітну активність виражено енергетичним індексом, вичисленим за даними геомагнітних обсерваторій «Львів» та «Бельськ». Усереднивш всі наявні річні значення R_Z, 11-річним біжучим вікном отримано мінімуми сонячної активності вікових циклів (близько 1711, 1810, 1901, 2009).

Мінімум у 2009р. був один з найменших у спостережуваних даних, прийнято нами за початок 24 циклу а також 100-літнього циклу сонячної актвності. Максимум 24 циклу наступив у 2014 році за R_Z, та у 2015 за енергетичним індексом. 25 цикл розпочався у 2019 році за R_Z, та у 2020 за енергетичним індексом. Протягом 19−25 циклів сонячна активність випереджає магнітну на 1−2 роки. Виділені квазідворічні варіації за досліджуваний період та відставання геомагнітної активності від сонячної дозволяють нам спрогнозувати величину геомагнітної активності та її максимум у 25 циклі.

За нашими розрахунками максимум геомагнітної активності наступить близько 2026 року а його величина буде у 1.5−2 рази більша за максимум 24 циклу.

Ключові слова: Сонячна і геомагнітна активність, сонячний цикл.

1. Introduction

Solar and geomagnetic activity (SA and GA) has been studied by many authors since the beginning of instrumental observations of the Sun and the Earth's magnetic field (Petrovay, 2020) for more than 500 years. However, a strong law of the relationship between the SA and the GA has not been established so far. Despite the use of satellite observations by humans, which has brought us several orders of magnitude closer to solving this problem. The main reason is that the Sun-Earth system is a nonlinear system. This is confirmed by the works of (Czernogor, 2008; Shuman, 2015), so there can be no single law or model of the relationship between the SA and the GA.

To show the relationship between SA and GA in 19−25 cycles of their development patterns and, on this basis, to make a forecast of GA for 25 SA. We used the data of SA expressed by R_Z and the values of the large-scale solar magnetic field (SMF), GA was expressed by the energy index describing the energy supplied from the solar wind to the magnetosphere during the studied period.

2. Solar activity

In this paper, the SA was expressed by two characteristics: the R_Z numbers taken from (https://www.sidc.be/SILSO/datafiles) and the sign of the Sun's large-scale magnetic field. It is known that the SA varies periodically: quasi-biennial variations (QBV), 11-year cycles (Schwabe-Wolf), 22-year cycles (Hale), 60−80-year cycles, 100-year cycles (Heisberg), 200-210-year cycles, and others. A characteristic feature of these cycles: for 11-year cycles, the Gnevyshev-Ohl rule, which means that even cycles are weaker in terms of the amplitude

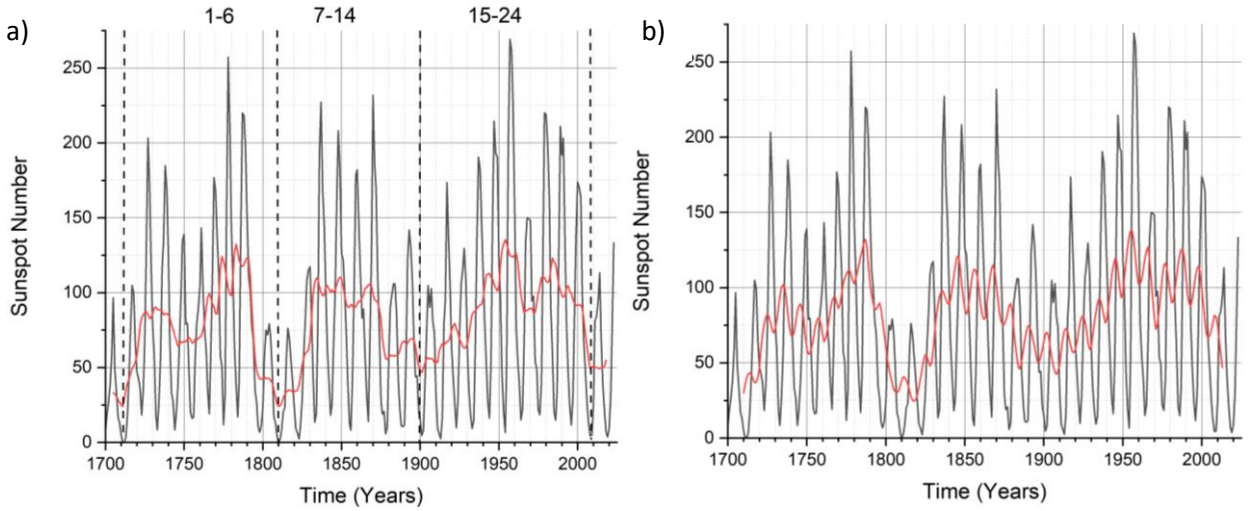

Figure 1: a) Yearly averages of sunspot number Rz (black lines), and a 11-year smoothed curve of Rz (red lines) for the interval 1700-2023; b) Yearly averages of sunspot number Rz (black lines), and a 22-year smoothed curve of Rz (red lines) for the interval 1700-2023.

Table 1: Periods of solar activity and the nature of their changes (years of the beginning, maximum and nature of changes in the SA cycles)

Period	beginning	Maximum	nature of changes in the SA
11	2019	2025	increasing
80–100	2009	2059	increasing
200– 210	1850	1956	decreasing
350 – 360	~1750	~1900	decreasing

of changes in solar numbers R_Z than the odd ones that follow them. Over the past 250 years, this rule has been violated in 4−5, 8−9, 22−23 SA; for 22-year Hale cycles, the sign of the SMF at the north pole of the Sun is characteristic; for the QBV the zug (duration) of oscillations is characteristic. Table 1 shows the periods of solar activity and the nature of their changes (years of the beginning, maximum and nature of changes in the SA cycles).

By averaging all available R_Z with an 11-year running window (red curve), we identified 100-year SA cycles (Fig. 1a). The minima (the beginning of the cycle) were observed in 1711, 1810, 1901, and 2009. In addition, in the 100-year SA cycles, we distinguish two-humped maxima with minima of 1SA, 11SA, and 20SA, which fall out of the general rule of SA growth in terms of amplitude (Krivodubskiy, 2016; Orliyuk & Romenets, 2023), in our opinion, this is a manifestation of a half-century cycle with a period of ~40−50 years. Averaging all the available R_Z with a 22-year running window (red curve), we similarly distinguish 100-year SA cycles (Fig. 1b) with the same SA minima (starts) as when averaging with an 11-year window. This pattern confirms the correctness of the definition of 100-year cycles. The last of the observed 100-year cycles began in 2009 with one of the lowest R_Z=4.2 for the entire observation period.

3. Geomagnetic activity

The geomagnetic activity in this study was expressed by the average annual values of the energy index $\sum(H - S_q)$ (Sumaruk & Sumaruk, 2007), determined from the data of the mid-latitude geomagnetic observatory "Lviv" and "Belsk". This index is quickly calculated from the data of mid-latitude geomagnetic observatories and characterizes the energy supplied from the solar wind to the magnetosphere (its corpuscular part) and correlates well with other GA indices such as K_p, AE, aa etc. (Sumaruk et al., 2012).

The physical meaning of the $\sum(H - S_q)$ index is as follows. The horizontal component (H) of the total magnetic induction vector B best reflects external sources of geomagnetic variations, therefore, it characterizes the magnetosphere-ionosphere current system well and therefore is proposed to be used to determine the GA. The solar diurnal variation (S_q) of the horizontal component (H) characterizes the wave radiation of the Sun. The integral sum $\sum(H - S_q)$ shows the field change caused by the corpuscular radiation of the Sun. By integrating this value over the required time interval, we obtain the characterization of the field disturbance over this interval.

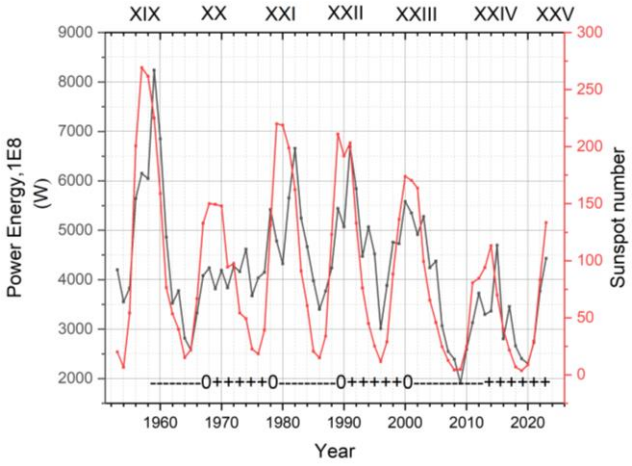

Figure 2: Values of the mean annual values of the energy (GA) entering the magnetosphere in 19-25SA (black curve), sunspot number R_z (red curve), and the sign of the SMF are presented.

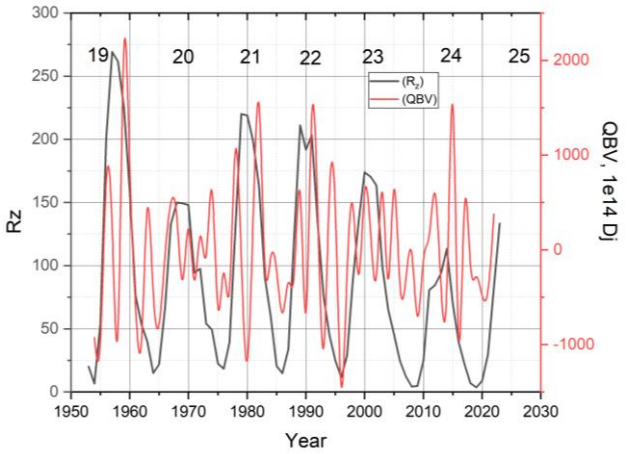

Figure 3: Quasi-biennial variations (red curve) of GA and solar activity (black curve) for 18-25 SA.

Table 2: Average monthly values of energy entering the magnetosphere during the years of minima (the beginning of 19-25 cycles) of SA and GA

Year	1955	1965	1975	1986	1996	2009	2020
E, Je14	3830	2576	3677	3403	3007	1908	2403

Using $\sum(H - S_q)$ as the GA index, we can quickly calculate the energy entering the magnetosphere from the solar wind based on the data of the mid-latitude observatory. The results of our calculations are in good agreement with those of other authors (Akasofu, 1981; Levitin, 2005; Chernogor, 2008; Echer, 2011).

Fig. 2 shows the values of the mean annual values of the energy (GA) entering the magnetosphere in 19−25SA (black curve), sunspot number R_Z (red curve), and the sign of the SMF are presented. The lag in the phase of the GA maxima from the SA by 1−2 years is clearly distinguished.

Table 2 shows the average monthly values of energy entering the magnetosphere during the years of minima (the beginning of 19−25 cycles) of SA and GA. This energy is directly proportional to the number of all geomagnetic disturbances that occurred in these years. The value of the average energy received during the 19−25 SA minima was the lowest in 2009. A similar result was obtained by the authors of (Hajra et al., 2014), which confirms the conclusions of other authors about the "small Maunder minimum" and extremely low GA in 24SA (Vaquero et al., 2011). A similar SA minimum was observed at the end of the nineteenth century, which is associated with the Heisberg cycle (Echer, 2012).

The number of recurrent geomagnetic disturbances was also characteristic for 19−24 SA. Recurrent disturbances were considered to be those that repeated two or more times in a 27-day cycle. The maximum recurrence for the studied period was observed in 2378−2395 revolutions of the Sun (according to Bartels) from November 23, 2007 to January 27, 2009. At this time, the number of solar flares was extremely low, although perturbations of the Earth's magnetic field were observed. Recurrent geomagnetic disturbances were repeated in 17 revolutions of the Sun. The disturbances occurred on days 1−4 and days 16−20 of the Barthelian rotation. Obviously, they were caused by recurrent long-term solar plasma flows (for example coronal holes, etc.) located at the active longitudes of the Sun. As shown in (Sumaruk, 2010), the ratio of the number of recurrent storms to the number of storms with sudden onset was maximum at the beginning of 24SA (1.5−4 times higher than the previous minimums of 19−23SA).

4. Quasi-biennial variations of geomagnetic activity

In the spectrum of SA expressed by a number of R_Z numbers or other indices, along with the other periods described above, the period 2−4 years is often distinguished (Gnevyshev, 1977; Apostolov, 1985). The same quasi-biennial variations (QBV) have been found in the parameters of the interplanetary environment (Okhopkov, 1998) and geophysical processes (Fadel et al., 2002). In the initial phase of the SA, the period of individual oscillations is more than three years, and in the minimum SA it is less than two years.

Since the QBVs are manifested in all parameters of solar activity, in variations of the solar wind and ionosphere, and in meteorological phenomena (Ivanov-Kholodny et al., 2003), we attempted to identify the QBVs in the variations of the geomagnetic field in the middle latitudes (Sumaruk & Sumaruk, 2009b). As the initial data of the magnetic activity measure we chose the monthly

Table 3: A selection of early forecasts for Cycle 25(Petrovay, 2020)

Category	Minimum	Maximum	Peak amplitude	References
Internal precursors	2019.9	2023.8	175 (154–202)	Li et al. (2015)
External precursor				
Polar precursor			117±15	Table 1 here
Polar precursor			136±48	Pesnell and Schatten (2018)
Helicity			117	Hawkes and Berger (2018)
SoDA		2025.2±1.5	120±39	Based on Pesnell and Schatten (2018)
Rush-to-the-poles	2019.4	2024.8	130	Petrovay et al. (2018)
Model-based: SFT				
SFT			124±31	Jiang et al. (2018)
AFT	2020.9		110	Upton and Hathaway (2018)
Model-based: dynamo				
2x2D	2020.5±0.12	2027.2±1.0	89±14	Labonville et al. (2019)
Truncated	2019–2020	2024 ± 1	90±15	Kitiashvili (2016)
Spectral				
Wavelet decomposition tree		2023.4	132	Rigozo et al. (2011)
Attractor analysis				
		2024.0 ± 0.6	103±25	Singh and Bhargawa (2017)
Simplex projection analysis				
Simplex proj./time- delay		2023.2 ± 1.1	154±12	Sarp et al. (2018)
Neural networks				
Neuro-fuzzy		2022	90.7±8	Attia et al. (2013)
Spatiotemporal		2022–2023	57±17	Covas et al. (2019)
Cycle 24 (comparison)	2008.9	2014.3	116	

average sums of deviations of the horizontal component of the magnetic field for a given year at the "Lviv" and "Belsk" geomagnetic observatories from the quiet level of the field $\sum(H - S_q)$. The quiet level is taken as the daily course of the same component averaged over five internationally quiet days for each month. Since the amplitudes of S_q-variations change with the season, seasonal variations of activity caused by changes in the ionospheric conductivity are excluded in the values $\sum(H - S_q)$.

To identify the QBV in GA, we used the methodology proposed in (Ivanov-Kholodny & Chertoprud, 1992) for identifying the QBV in SA, which consists in subtracting the value of the selected parameter for the same month in the previous and next year from the double monthly average value of the selected parameter.

In Fig. 3 shows the QBV (red curve) of GA and SA (black curve) for 18−25 SA. As we can see, in each of the 11-year cycles studied, there are 3 to 4 zigzags of GA fluctuations. The amplitude of changes in the QBV in the cycle depends on the phase of the SA and the observation cycle. For example, in 19SA and 23SA, the amplitudes of the QBV are almost the same and amount to ~1000 e14 J, but in 18SA, 21SA, 22SA, 24SA, 25SA the amplitudes of oscillations increase in the cycle with the QBV amplitudes at the maximum of the cycles and at their decline being several times larger than the QBV at the beginning and end of the cycle, and the maximum of the QBV occurs with a delay from the maximum of the SA, as we observe (see Fig. 2) in the GA as well. This pattern has an explanation, since after the maximum of the SA, the number of recurrent geomagnetic disturbances begins to increase, which leads to an increase in the GA. In addition, as shown in (Eher et al., 2012), we observe the maximum values of the solar wind speed in the phase of the SA decline. This phase of the SA is dominated by high-speed flows coming from coronal holes (Tsurutani et al., 1995). High-speed flows cause the growth of the southern component (B_z) of the interplanetary magnetic field and the stretching of the Parker helix, and hence lead to an increase in GA and an increase in the amplitudes of the QBV at the decline of SA. According to the aa- index, GA minima also lag behind the SA minima by a period of ~1 year (Kane, 2002; Hathway, 2010).

As shown in (Sumaruk & Sumaruk, 2009a), there is a clear dependence of recurrence on the sign of the SMF. The recurrence is minimal in years of changing the sign of the SMF, i.e., in years of large SA, and the maximum recurrence is in years of minimum solar activity. The peaks of recurrence were observed in 1976 and 1995. In these years, the SMF was positive. As we can see, the 22-year Hale cycle is clearly manifested.

Table 3, taken from (Petrovay, 2020), shows the 25SA forecasts - forecast method, years of minimum and maximum, maximum R_z value, and their authors (links in the original). As we can see, most authors predict a maximum SA in 2025±1 year.

5. Conclusions

Using the fact that the second tsug of the QBV variations in 25SA has not yet begun the figure shows a dashed line (see Fig. 3) and according to the above pattern, it should be larger in amplitude than the first tsug in 25SA; the number of recurrent geomagnetic disturbances should be high, since the solar SMF has a positive sign, and the 100-year SA cycle is on the growth branch; the energy entering the magnetosphere has now reached the maximum values of 24SA and continues to grow; analyzing table 3 on the 25SA maxima, it can be concluded that the maximum GA in 25SA will occur around 2026±1 year and will be comparable in magnitude to 23SA.

References

Akasofu S.-I.: 1981, *Space Sci. Rev*., **28**, 121.

Apostolov E.M.: 1985, *Bull. Astron. Inst. Czechsl*., **36**, № **2**, 97.

Chernogor L.F. On the nonlinearity in nature and science: 2008, Kharkiv: Kharkiv V.N.Karazin National University, 528 p.

Fadel G.M., Semenov A.I., Shefov N.N., Suhodoev V.A., Martsvaladze N.M.: 2002, *Geomag. and Aeron*., **42**, № **2**, 203.

Gnevyshev M.N.: 1977, *Solar Phys*., **51**, № **1**, 175.

Gvishiani, A.D., Starostenko, V.I., Sumaruk, Y.P. et al.: 2015, *Geomagn. and Aeron.*, **55**, 299.

Ivanov-Kholodny G.S., Mogilevsky E.I., Chertoprud V. Yu.: 2003, *Geomag. and Aeron*., **43**, № **2**, 161.

Ivanov-Kholodny G.S., Chertoprud U.Yu.: 1992, *Astronom. Trans*., **3**, № **1**, 81.

Levitin A.E.: 2005, *Izvestiya RAS*., **70**, № **10**, 1525.

Krivodubskiy V.N.: 2016, in Proc. *VIII Scientific conference "Selected issues of astronomy and astrophysics"*, Lviv, Ukraine, 25.

Kane R.P.: 2002, *Ann. Geophys*., **20**, 1519.

Hathaway D.H.: 2010, *Liv. Rev. Solar Phys*., **7**, 1.

Orlyuk M.I., Romenets A.A.: 2023, in Proc. *15-th Workshop "Solar Influences on the Magnetosphere, Ionosphere and Atmosphere"*, Primorsko, Bulgaria, June 05-09, P. 30. Solar Cycle progression https://www.swpc.noaa.gov/products/solar-cycle-progression

Okhopkov V.P.: 1998, *Geomag. and Aeron.*, **38**, №**2**, 159.

Petrovay K.: 2020, *Living Rev. Sol. Phys*., **17**, 2.

Sumaruk T., Sumaruk Yu.: 2007, *Publs. Inst. Geophys. Polish Acad. Sci. Monographic*, **C-99 (398)**, 374.

Sumaruk T.P., Sumaruk P.V.: 2009a, *Space science and technology*, **15**, № **1**, 56. https://doi.org/10.15407/knit2012.03.046

Sumaruk T.P., Sumaruk P.V.: 2009b, *Dopov. Nac. akad. nauk Ukr.*, № **1**, 114. http://dspace.nbuv.gov.ua/handle/123456789/7742

Sumaruk T.P., Sumaruk P.V., Sumaruk Yu.P.: 2012, *Space science and technology*, **18**, № **3**, 46. http://doi.org/10.15407/knit2012.03.046

Tsurutani B.T., Gonzalez W.D., Gonzalez A.L.C., Tang F., Arballo J.K., Okada M.: 1995, *J. Geophys. Res*., **100**, 21717.

Echer E., Tsurutani B.T., Gonzalez W.D.: 2011, in: *Comparative Magnetic Minima: Characterizing quiet times in the Sun and Stars Proceedings IAU Symposium No. 286*.

Vaquero J.M., Gallego M.C., Usoskin I.G., Kovaltsov G.A.: 2011, *Astrophys. J. Lett.*, **731**, 24.

Hajra R., Echer E., Tsurutani B.T., Gonzalez W.D.:2014, *J. Geophys. Res. Space Physics*, **119**, 2675.

Наукове видання

Одеські Астрономічні Публікації

том 36 (2023)

Англійською мовою

Технічний редактор *В. В. Ковтюх*
Комп'ютерна верстка *С. Л. Страхова*

Підписано до друку 27.11.23. Формат 60x84/8.
Ум. друк. арк. 22,32. Тираж 50 прим. Зам. №

Видавець і виготовлювач
Одеський національний університет імені І.І. Мечникова
Свідоцтво суб'єкта видавничої справи ДК № 4215 від 22.11.2011 р.
65082, м. Одеса, вул. Єлісаветинська, 12, Україна
Тел.: (048) 723 28 39
e-mail: druk@onu.edu.ua